FACULTY OF ENGINEERING AND ARCHITECTURE

A Computational Understanding of Nuclear Quantum Effects and the Structural Organisation of Confined Water in Nanoporous Materials

Aran Lamaire

Doctoral dissertation submitted to obtain the academic degree of
Doctor of Engineering Physics

Supervisor
Prof. Veronique Van Speybroeck, PhD
Department of Applied Physics
Faculty of Engineering and Architecture, Ghent University

September 2024

GHENT UNIVERSITY

ISBN 978-94-6355-879-2
NUR 928
Wettelijk depot: D/2024/10.500/84

Members of the Examination Board

Chair

Prof. Hennie De Schepper, PhD, Ghent University

Other members entitled to vote

Bernd Ensing, PhD, Universiteit van Amsterdam, the Netherlands
Prof. Lukáš Grajciar, PhD, Charles University, Czech Republic
Prof. Jan Ryckebusch, PhD, Ghent University
Prof. Dimitri Van Neck, PhD, Ghent University
Prof. Toon Verstraelen, PhD, Ghent University

Supervisor

Prof. Veronique Van Speybroeck, PhD, Ghent University

This research has been conducted at the **Center for Molecular Modeling**, in collaboration with:

- The Centre for Membrane Separations, Adsorption, Catalysis and Spectroscopy for Sustainable Solutions (cMACS) at KU Leuven (prof. I. Vankelecom)
- The Multifunctional Materials & Composites (MMC) Laboratory at the Department of Engineering Science, University of Oxford (prof. J.-C. Tan)
- The Laboratory of Computational Science and Modelling (COSMO) at the École Polytechnique Fédérale de Lausanne (EPFL) (prof. M. Ceriotti)
- The Adsorption and Advanced Materials Laboratory (A^2ML) at the Department of Chemical Engineering and Biotechnology, University of Cambridge (prof. D. Fairen-Jimenez)

Preface

We shall not cease from exploration, and the
end of all our exploring will be to arrive where
we started and know the place for the first time.
T.S. Eliot (1888–1965)

Gedurende de voorbije zeven jaar had ik het voorrecht om me tijdens dit doctoraat te kunnen verdiepen in de wondere wereld van de kwantummechanica. Na een eerste kennismaking met academisch onderzoek en de concepten van moleculaire modellering tijdens mijn masterproef, kreeg ik de kans om mij hierin ook verder te bekwamen bij het nastreven van een doctoraat. Zoals bij elk gedegen leerproces werd deze ervaring niet enkel gekenmerkt door intellectuele uitdagingen, maar ook door een persoonlijke groei, waarin verschillende mensen een belangrijke rol speelden. Zonder hen zou dit doctoraat niet uitgegroeid zijn tot wat het nu is.

Eerst en vooral zou ik graag mijn promotor Veronique bedanken. Dankzij jouw vertrouwen in mij als doctoraatsstudent werd dit onderzoek mogelijk. Ook in een grote onderzoeksgroep zoals het CMM sta je erop om voor iedereen tijd vrij te maken om het overzicht te behouden op ieders persoonlijke vooruitgang en daarbij de langere termijn niet uit het oog te verliezen. Bedankt ook voor het vertrouwen in mij als lesgever en om mij meteen vanaf het begin van mijn doctoraat te betrekken bij Kwantummechanica II. Deze verrijkende ervaring in zowel onderzoek als onderwijs zal ik blijven koesteren.

Vervolgens wil ik ook graag mijn bureaugenoten op het CMM bedanken. Bedankt Alexander, Sander en Maarten om van elke werkdag ook een dag onder vrienden te maken. In een vaak eindeloos gedraai van schermen, geschuifel van stoelen of na een lange uiteenzetting (al dan niet aan het bord), kon ik steeds op jullie rekenen om nieuwe ideeën af te toetsen, figuren te verbeteren of scripts te helpen debuggen. Het maakte ook onze band buiten de kantoormuren hechter, waarbij de concerten, gezelschapsspelletjes

en Italiëreizen zeker zullen bijblijven. Bij de vele herinneringen die we samen nog tegoed hebben, kunnen we deze alvast af en toe eens oprakelen.

Ook met andere collega's, die vaste waarden werden in ons bureau, werden vriendschappen gesmeed. Bedankt Sven om ook na mijn masterthesis steeds bereid te blijven om advies te geven of teksten na te lezen. Je niet-aflatende streven naar excellentie en perfectie in zowel onderzoek als onderwijs, met oog voor detail, werd steeds op prijs gesteld en was vaak ook bijzonder leerrijk. De onvermijdelijke flauwe grappen en woordspelingen neem ik er dan maar bij. Bedankt Jelle om mij in mijn masterthesis vertrouwd te maken met nucleaire kwantumeffecten en voor alle begeleiding bij het begin van mijn doctoraat, ook als CMM-peter. Na je vertrek op het CMM bleef je steeds geïnteresseerd in de voortgang van mijn doctoraat en werd je ook een voortreffelijke reiscompagnon. Samen met jou werd ook Kurt een vaste reisgezel de voorbije jaren, die van de CMM-keukentafel over Qwistet en gezelschapsspelletjes ook uitgroeide tot de meest toegewijde concertganger. Bedankt Kurt voor al je enthousiasme en om mijn 'pre-concert talks' schijnbaar nooit beu te raken. De laatste persoon die dit lijstje vervolledigt, is Siebe. Bedankt Siebe om mij je klankbord te maken voor al je fysicavragen. Als lunchwekker durft er al eens een anomalie op te treden, maar je verzuchtingen of verpozingen in ons kantoor, waarin alles en iedereen gefileerd kan worden, zijn intussen niet meer weg te denken. Met je rijbewijs wordt dit gelukkig ook op verplaatsing mogelijk in de toekomst.

Graag wil ik ook al mijn collega's op het CMM bedanken. Bedankt Wim en Daan om gedurende het laatste jaar van mijn doctoraat de rol van bureaugenoten op te nemen. Jullie feedback op vragen, niet in het minst voor figuren, was erg nuttig. Bedankt Ruben en Massimo voor de aangename samenwerking in verschillende projecten, in het bijzonder als *proton hopping musketeers*. Tot slot ook een welgemeende dankjewel voor Leen en Mieke om telkens paraat te staan voor alle praktische bekommernissen tijdens mijn doctoraat, zeker ook ter voorbereiding van mijn verdediging.

Voor de welgekomen afwisseling buiten het CMM wil ik ook al mijn overige vrienden bedanken, in het bijzonder Emmelie en Charlotte waarmee het steeds leuk is om herinneringen op te halen aan middelbaar. Op het conservatorium bedank ik graag mijn leerkrachten, Karin, Jeroen, Erik, Renaat en Guillaume, om mij naast het wetenschappelijke ook muzikaal verder te doen groeien. Bedankt Anouk, Isabel en Hanne voor al het samen musiceren.

Finaal wil ik ook graag mijn broer, zus, ouders en grootouders bedanken die telkens weer onmisbaar zijn. Dankjewel mama en papa voor jullie onvoorwaardelijke steun bij alles wat ik doe. Bedankt voor alle kansen die ik van jullie gekregen heb. Zonder jullie was ik nooit de persoon geworden die ik

nu ben. Dankjewel broer en zus om er steeds voor mij te zijn, met trots uit te kijken naar mijn verdediging en voor alle helpende handen wanneer er nood aan was. Dankjewel oma en opa om jullie onvoorwaardelijke liefde aan ons allemaal door te geven.

Aran Lamaire
Gent, september 2024

Contents

List of Symbols

Throughout this dissertation, italicised variables represent scalars, italicised and bold-faced variables represent vectors, and bold-faced variables represent matrices.

Alphanumeric symbols	
acc	Acceptance probability
C_V	Isochoric heat capacity
$\mathbf{C}$	Collection matrix
D	Diffusion coefficient
e	Elementary charge
E	Energy
$E_k^{(e)}$	Potential energy surface for electronic energy level k
$E_{xc}[n(\boldsymbol{r})]$	Exchange-correlation functional of the electron density
F	Helmholtz free energy
$F[n(\boldsymbol{r})]$	Universal functional of the electron density
$\boldsymbol{F}_\alpha$	Force on nucleus α
h	Planck constant
$\hbar$	Reduced Planck constant ($\hbar = \frac{h}{2\pi}$)
$\hat{H}$	Hamiltonian operator
$\mathbf{H}$	Hessian matrix
$J[n(\boldsymbol{r})]$	Hartree energy functional of the electron density
k	Reaction rate constant
k_B	Boltzmann constant
$\mathcal{L}$	Loss function
m_i	Mass of electron i
M_α	Mass of nucleus α
N	Number of electrons in a molecular system
$n(\boldsymbol{r})$	Electron density
$n_0(\boldsymbol{r})$	Ground-state electron density
N_n	Number of nuclei in a molecular system
p	Probability

P	Pressure
$\boldsymbol{P}_\alpha$	Momentum vector of nucleus α
q	Collective variable
$q^{(c)}$	Centroid collective variable
$q^{(k)}$	Collective variable for bead k
$q^\ddagger$	Collective variable at the transition state
r_{gyr}	Radius of gyration
$\boldsymbol{r}_i$	Position vector of electron i
$\boldsymbol{R}_\alpha$	Position vector of nucleus α
$\boldsymbol{R}_\alpha^{(c)}$	Centroid position vector of nucleus α
S	Entropy
t	Time
T	Temperature
$\hat{T}_e$	Kinetic energy operator of the electrons in a molecular system
$T_e^{(s)}[n(\boldsymbol{r})]$	Kinetic energy functional of the electron density for a non-interacting system represented by a Slater determinant
$\hat{T}_n$	Kinetic energy operator of the electrons in a molecular system
V	Volume
$\hat{V}_{ee}$	Coulomb repulsion operator between the electrons in a molecular system
$\hat{V}_{ne}$	Coulomb attraction operator between the electrons and the nuclei in a molecular system
$\hat{V}_{nn}$	Coulomb repulsion operator between the nuclei in a molecular system
V_i^b	Bias potential of umbrella i
$\boldsymbol{x}_i$	Spatial and spin coordinates of electron i ($\boldsymbol{r}_i$, σ_i)
Z_α	Charge of nucleus α

Greek symbols	
α_V	Volumetric thermal expansion coefficient
β	Thermodynamic beta ($\beta = \frac{1}{k_B T}$)
Γ	Phase space
δ	Delta distribution
ε_0	Vacuum permittivity
θ	Heaviside function
κ_i	Harmonic force constant of umbrella i
Λ	Thermal de Broglie wavelength of a particle with mass m
μ	Chemical potential
σ_i	Spin coordinate of electron i
$\lvert\phi_n\rangle$	Time-independent wave function of energy level E_n

$\|\chi\rangle$	Nuclear wave function of a molecular system
$\|\psi\rangle$	Wave function
$\|\Psi\rangle$	Wave function of a molecular system
$\|\psi^{(e)}\rangle$	Electronic wave function of a molecular system
ω	Frequency
ω_P	Frequency of the harmonic coupling between neighbouring beads in a PIMD simulation with P beads ($\omega_P = \frac{\sqrt{P}}{\beta\hbar}$)

Mathematical symbols	
$\dot{f}$	Time derivative of f
$\langle f \rangle$	Ensemble average of f
$\boldsymbol{\nabla}_\alpha f$	Gradient of f with respect to the position of nucleus α
$\boldsymbol{\nabla}_i f$	Gradient of f with respect to the position of electron i
tr $\hat{A}$	Trace of operator $\hat{A}$

List of Abbreviations

AEI	Aluminophosphate-eighteen
BAS	Brønsted acid site
BDC	1,4-benzenedicarboxylate
BLYP	Becke-Lee-Yang-Parr
CDF	Cumulative distribution function
CHA	Chabazite
CMD	Centroid molecular dynamics
CMM	Center for Molecular Modeling
CN	Coordination number
CV	Collective variable
DFT	Density functional theory
DUT	Dresden University of Technology
FES	Free energy surface
FF	Force field
GC	Grand-canonical
GCMC	Grand-canonical Monte Carlo
GGA	Generalised gradient approximation
GLE	Generalised Langevin equation
HF	Hartree-Fock
INS	Inelastic neutron scattering
IRMOF	Isoreticular MOF
LCD	Largest cavity diameter
LDA	Local density approximation
lp	Large pore
MBIS	Minimal Basis Iterative Stockholder
MC	Monte Carlo
MD	Molecular dynamics
MIL	Matériaux de l'Institut Lavoisier
MLP	Machine learning potential
MMM	Mixed-matrix membrane
MOF	Metal–organic framework
MTD	Metadynamics

MTH	Methanol-to-hydrocarbons
MTTK	Martyna–Tobias–Tuckerman–Klein
NequIP	Neural Equivariant Interatomic Potentials
NGA	Negative gas adsorption
NHC	Nosé–Hoover chain
np	Narrow pore
NPD	Neutron powder diffraction
NQEs	Nuclear quantum effects
PCP	Porous coordination polymer
PBE	Perdew-Burke-Ernzerhof
PES	Potential energy surface
PI	Path integral
PIMD	Path integral molecular dynamics
PLD	Pore-limiting diameter
RDF	Radial distribution function
RPMD	Ring polymer molecular dynamics
SBU	Secondary building unit
SCAN	Strongly constrained and appropriately normed
SI	Système international d'unités
SPC	Soft porous crystal
SSZ	Standard oil synthetic zeolite
TMMC	Transition matrix Monte Carlo
TRPMD	Thermostatted ring polymer molecular dynamics
UFF	Universal force field
UiO	Universitetet i Oslo
US	Umbrella sampling
WHAM	Weighted histogram analysis method
x**MR**	x-membered ring
XC	Exchange-correlation
ZIF	Zeolitic imidazolate framework
ZPE	Zero-point energy
ZSM	Zeolite Socony Mobil

Samenvatting

Eén van de drijvende krachten in technologische vooruitgang is de ontwikkeling van nieuwe materialen. Dankzij het toenemende inzicht in de elementaire opbouw van materie op een atomaire schaal, is de ontdekking van nieuwe materialen niet langer afhankelijk van toevallige ontdekkingen, maar kunnen nieuwe materialen op een doordachte manier worden ontworpen en ontwikkeld. Voor de verschillende uitdagingen in onze huidige samenleving, zoals CO_2-captatie of de duurzame productie van basischemicaliën, vormen nanoporeuze materialen een veelbelovende materiaalklasse in de zoektocht naar technologische oplossingen. In dit doctoraatsonderzoek worden twee types nanoporeuze materialen bestudeerd. Een eerste type zijn de zogenaamde zeolieten, die een essentiële rol vervullen in de petrochemische industrie vanwege hun grote stabiliteit en uitzonderlijke katalytische werking. Deze aluminosilicaten zijn opgebouwd uit SiO_4-tetraëders waarin sommige siliciumatomen vervangen zijn door aluminiumatomen in combinatie met een proton of metaalkation om ladingsneutraliteit te garanderen. Naast hun wijdverspreid gebruik als heterogene katalysatoren in de productie van koolwaterstoffen worden zeolieten ook gebruikt voor het zuiveren van water en het verwijderen van CO_2 uit industriële rookgassen. Een tweede, meer recent type van nanoporeuze materialen zijn de zogenaamde metaalorganische roosters, doorgaans afgekort als MOFs vanwege de Engelse benaming *metal-organic frameworks*, die bestaan uit anorganische metaalclusters die verbonden zijn via organische linkers. Alhoewel deze materialen nog niet gebruikt worden in grootschalige industriële toepassingen, laat de bijna onuitputtelijke mogelijkheid om bouwblokken te combineren toe om hun functionaliteit te optimaliseren voor verschillende toepassingen, gaande van schokabsorptie tot CO_2-captatie en de extractie van water uit de atmosfeer.

Om de ontwerpmogelijkheden van nanoporeuze materialen te verkennen en hun werking te optimaliseren voor gerichte toepassingen is een fundamenteel begrip van het verband tussen de onderliggende structurele opbouw van de materialen en de resulterende materiaaleigenschappen noodzakelijk.

Naast het experimenteel karakteriseren van materialen, kan men dankzij de toenemende computationele rekenkracht ook materialen *in silico* ontwerpen en karakteriseren met behulp van moleculaire modellering. Om betrouwbare voorspellingen te kunnen maken op basis van een computationele beschrijving van een moleculair systeem, moeten nauwkeurige simulatietechnieken gebruikt worden in het modelleerproces. In dit doctoraatsonderzoek wordt daarom gefocust op de impact van de veelgebruikte benadering om atoomkernen te behandelen als klassieke deeltjes, zonder rekening te houden met hun kwantummechanische eigenschappen. In het bijzonder voor lichte atomen (zoals waterstof) op lage temperaturen spelen deze zogenaamde nucleaire kwantumeffecten, doorgaans afgekort als NQEs vanwege de Engelse benaming *nucleair quantum effects*, een uitgesproken rol in het gedrag van atomen. Voor nanoporeuze materialen kunnen NQEs bijvoorbeeld het gedrag van een proton in een zeoliet of de structuur van water in de poriën van een MOF beïnvloeden, twee voorbeelden die uitgebreid aan bod komen in dit doctoraatsonderzoek.

Naast een nauwkeurige kwantummechanische beschrijving van de atoomkernen kunnen ook de elektronen van een moleculair systeem met een grote variatie aan nauwkeurigheid gemodelleerd worden. Aangezien de elektronische Schrödingervergelijking niet exact oplosbaar is voor realistische moleculaire systemen, kunnen er enkel benaderende kwantummechanische oplossingen bekomen worden voor de elektronen, bijvoorbeeld met behulp van dichtheidsfunctionaaltheorie (DFT). Voor grote moleculaire systeem of berekeningen die gepaard gaan met veel verschillende atomaire configuraties wordt een beschrijving met DFT echter vaak onhaalbaar door de grote computationele kost, zodat een effectieve beschrijving van de interatomaire interacties noodzakelijk wordt in de vorm van een zogenaamd krachtveld (*force field*). In conventionele krachtvelden wordt de computationele kost beperkt door het gebruik van fysisch geïnspireerde potentialen met een beperkt aantal parameters, terwijl machine-learning potentialen (MLP's) neurale netwerken gebruiken met miljoenen parameters om een betere overeenstemming te bekomen met kwantummechanische oplossingen, wat deels ten koste gaat van de computationele efficiëntie. Om NQEs in rekening te brengen door middel van padintegraal moleculaire dynamica (PIMD) is een beschrijving met conventionele krachtvelden of MLP's bijna onontkoombaar, aangezien PIMD de computationele kost van de simulaties met minstens één grootteorde doet toenemen in vergelijking met een klassieke behandeling van de atoomkernen.

Bij extreem lage temperaturen, nabij het absolute nulpunt, kan men echter ook statische simulatietechnieken gebruiken in plaats van PIMD, zodat een benaderende kwantummechanische oplossing haalbaar blijft. Via deze aan-

pak werd voor ZIF-8 de rotationele tunneling van methylrotoren onderzocht in de aanwezigheid van argon- en stikstofadsorbaten. Indien er onvoldoende thermische energie beschikbaar is, dan kunnen de methylrotoren in deze MOF de rotationele energiebarrière niet overbruggen, zodat een klassieke draaibeweging uitgesloten is. Vanuit een kwantummechanisch standpunt kunnen de methylrotoren echter nog roteren via het mechanisme van tunneling. Door kwantummechanische berekeningen te combineren met experimentele metingen, uitgevoerd door de groep van prof. J.-C. Tan aan de Universiteit van Oxford, konden wijzigingen in de energieniveaus van de methylrotoren in verband gebracht worden met de bezetting van specifieke adsorptiesites in ZIF-8. Op deze manier kan het kwantummechanische rotationeel tunneleffect dus dienst doen als een gevoelig instrument om de adsorptie van gastmoleculen in MOFs te bestuderen.

Bij eindige temperaturen werd de invloed van NQEs eerst onderzocht voor één van de eerst gesynthetiseerde MOF-structuren, namelijk MOF-5, met behulp van krachtvelden. De structurele eigenschappen van MOF-5 worden echter slechts in beperkte mate beïnvloed door NQEs, net zoals de thermische eigenschappen, die in eerste instantie bepaald worden door een goede beschrijving van anharmonische roostereffecten. De warmtecapaciteit van MOF-5, gevuld met methaanmoleculen, vertoont daarentegen enkel een correcte temperatuursafhankelijkheid wanneer zowel NQEs als anharmonische effecten in rekening worden gebracht door middel van PIMD. Vervolgens werd de invloed van NQEs ook nagegaan voor de *proton hopping*-reactie rond een aluminiumdefect in een zeoliet met een chabazietstructuur. Gegeven de grote afwijking tussen de gerapporteerde experimentele en computationele activeringsenergie van dit proces is het belangrijk om de mogelijke rol van NQEs in deze afwijkende resultaten te bepalen. Om een zo nauwkeurig mogelijke beschrijving te bekomen met een minimum aan benaderingen, werden PIMD-simulaties gebruikt in combinatie met een MLP met DFT-nauwkeurigheid. Verder werden ook de semi-klassieke vrije-energieprofielen van de reactie, die doorgaans gebruikt worden bij PIMD, vervangen door kwantum vrije-energieprofielen door de ontwikkeling van een elegante *sampling*-techniek die toelaat om semi-klassieke vrije-energieprofielen om te zetten in kwantum vrije-energieprofielen. Voor de overdacht van protonen in moleculen werd er aangetoond dat het verschil tussen de semi-klassieke en kwantum beschrijving toeneemt met de hoogte en helling van de vrije-energiebarrière van de reactie. Zelfs op 450 K kunnen NQEs de klassieke vrije-energiebarrière voor een protonoverdacht met ongeveer 60% verlagen. Voor de *proton hopping*-reactie in chabaziet geven NQEs aanleiding tot een activeringsenergie die ongeveer 17% lager ligt dan in een klassieke beschrijving.

Ook bij het modelleren van water in MOFs kunnen NQEs de nauwkeurigheid van de beschrijving verbeteren, niet in het minst voor de watermoleculen, waarvoor de inclusie van NQEs vaak noodzakelijk is. Voor de flexibele MOF MIL-53(Al) werd de relatieve stabiliteit van de twee fasen van deze structuur echter maar in geringe mate beïnvloed door het toevoegen van NQEs aan het krachtveld, zelfs in de aanwezigheid van watermoleculen. Naast NQEs kunnen echter ook *confinement effects* geassocieerd met de beperkte ruimtelijke vrijheid in de nanoporiën van de MOF het gedrag van geadsorbeerde watermoleculen sterk veranderen. In MIL-53(Al) resulteert dit bijvoorbeeld in eendimensionale draden van watermoleculen langsheen de nauwe kanalen van het rooster. In MOF-801 vormen er zich kubische waterclusters in de tetraëdrale poriën die aanleiding geven tot gunstig wateradsorptiegedrag voor de extractie van water uit de atmosfeer. Om het verband tussen het adsorptiegedrag en de structuur van waterclusters beter te begrijpen werd een eenvoudig analytisch model uitgewerkt om de adsorptie van water in een artificiële nanoporie te bestuderen. Door middel van dit model kon aangetoond worden dat een gunstige positionering van primaire adsorptiesites secundaire adsorptiesites kan creëren via gerichte waterstofbruggen, wat een positieve invloed heeft op het adsorptiegedrag van de porie. Op deze manier kan een minutieus ontwerp van de adsorptiesites van een nanoporeus materiaal benut worden om de structuur van het geadsorbeerde water vorm te geven en zo de adsorptie-eigenschappen van MOFs verder te verbeteren voor specifieke toepassingen, zoals de extractie van water uit de atmosfeer in regio's met een aride klimaat.

In hydrofobe MOFs kan de intrusie van water aangewend worden om schokken te absorberen die een hoge snelheid hebben. In waterintrusie-experimenten uitgevoerd aan de Universiteit van Oxford werd een toenemend hysteresiseffect ontdekt in de intrusie-extrusiecyclus van water in ZIF-8 voor schokken met een hogere snelheid die het systeem in staat stellen om 85% van de mechanische impact te absorberen tegenover 17% bij lagere snelheden. Door gebruik te maken van moleculaire modellering kon aangetoond worden dat dit mechanisme verband houdt met het vormen van waterclusters met een zekere kritische grootte. Indien de impact een voldoende lage snelheid heeft, dan kunnen de hydrofobe kooien van ZIF-8 zich geleidelijk vullen met water via de spontane nucleatie van waterclusters, die vanaf een bepaalde kritische grootte verder aangroeien tot de porie gevuld raakt. Indien de snelheid van de impact echter te groot wordt, dan verloopt de spontane nucleatie van waterclusters te traag om de poriën van ZIF-8 te vullen, zodat watermoleculen onder invloed van de externe druk in de hydrofobe poriën worden geduwd, wat gepaard gaat met de dissipatie van energie en zodoende de mechanische impact dempt.

Samenvattend heeft dit doctoraatsonderzoek bijgedragen tot nieuwe inzichten inzake de rol van NQEs in het modelleren van nanoporeuze materialen en de manier waarop de moleculaire structuur van water in nanoporiën het wateradsorptiegedrag van deze materialen beïnvloedt. In het bijzonder voor reacties die gepaard gaan met de overdacht van een proton, een elementaire reactie die in veel chemische processen voorkomt, werd aangetoond dat de inclusie van NQEs essentieel is om een nauwkeurige beschrijving te bekomen. Daarnaast werd ook een nieuw ontwerpprincipe geïntroduceerd om het wateradsorptiegedrag van MOFs verder te verbeteren via een nauwgezette controle van de hydrofiele adsorptiesites in de nanoporiën. Op deze manier zouden MOFs verder geoptimaliseerd kunnen worden voor toepassingen die gebruik maken van wateradsorptie.

Summary

The development of new functional materials is one of the major driving forces in technological advancement. Through the ever increasing fundamental insights into matter at an atomic scale, the historic coincidental discovery of materials has been gradually replaced by the rational design and engineering of materials. In the context of current societal challenges, such as carbon capture or the sustainable production of building-block chemicals, the particular class of nanoporous materials possesses many promising properties in search of technological solutions. In this PhD dissertation, two types of nanoporous materials are considered. A first type are the so-called zeolites, which have become indispensable within the petrochemical industry, due to their high stability and exceptional catalytic performance. The elementary building units of these aluminosilicate materials are SiO_4 tetrahedra, in which some silicon atoms have been substituted by aluminium atoms accompanied by a change-compensating acidic proton or a metal cation. Besides their widespread use as heterogeneous catalysts in the production of hydrocarbons, zeolites can also be used for water purification or the removal of CO_2 from industrial flue gasses. A second, more recent type of nanoporous materials are metal-organic frameworks (MOFs), which consist of inorganic metal clusters connected by organic linkers. Although these materials are yet to reach industrial scale applications, the nearly endless possibilities to combine different building blocks allows to tailor their functionality for many applications, ranging from shock adsorption to carbon capture and atmospheric water harvesting.

To explore the design opportunities of nanoporous materials and optimise their performance for specific applications, a fundamental understanding of the underlying structure–property relations is required. In addition to experimental characterisation techniques, the continuously increasing computational power now also allows for an *in silico* design and characterisation of nanoporous materials by means of various molecular modelling techniques. To obtain reliable predictions from the computational description

of a molecular system, accurate simulation techniques are required to model these systems. Therefore, this PhD dissertation focusses on the impact of the common approximation to treat atomic nuclei as classical particles, in spite of their quantum mechanical nature. Especially for lightweight atoms (such as hydrogen) at low temperatures, these so-called nuclear quantum effects (NQEs) are known to play a decisive role in the description of the molecular behaviour. In nanoporous materials, NQEs could therefore affect the behaviour of an acidic proton on a zeolite or the structural organisation of water molecules confined in the pores of a MOF, two topics which are extensively investigated within this dissertation.

Apart from an accurate quantum mechanical description of the atomic nuclei, also the electrons of the molecular system can be modelled with various levels of accuracy. As the electronic Schrödinger equation cannot be solved exactly for realistic molecular systems, only approximate quantum mechanical solutions can be obtained for the electrons with first-principles methods such as density functional theory (DFT). However, for large molecular systems or calculations which involve many atomic configurations, a DFT description of the system can become computationally too demanding, which necessitates the use of an effective parametrisation of the interatomic interactions by means of a so-called force field. Whereas conventional force fields significantly reduce the computational cost by using physically inspired interaction potentials with a limited number of parameters, machine learning potentials (MLPs) rely on neural networks with millions of parameters to increase the correspondence with first-principles calculations at the expense of a reduction in computational efficiency. When NQEs are taken into account by means of path integral molecular dynamics (PIMD) simulations, a description with conventional force fields or MLPs becomes inevitable, as PIMD increases the computational cost by at least one order of magnitude in comparison with a classical treatment of the nuclei.

At extremely low temperatures, near absolute zero, static simulation methods can be used instead of PIMD, so that a first-principles description of the material remains feasible. In this way, the rotational tunnelling of methyl rotors in ZIF-8 was investigated in the presence of argon and nitrogen adsorbates. In the absence of sufficient thermal energy, the methyl rotors in this MOF are unable to surmount the rotational energy barrier of the rotor, thus preventing a classical rotational movement. Quantum mechanically, the methyl rotors can however still rotate through the mechanism of tunnelling. By combining first-principles calculations with experimental measurements from our collaborators at the University of Oxford, changes in the rotational energy levels of the methyl rotor involved in the tunnelling mechanism could be related to the occupation of specific adsorption sites within ZIF-8. In

this respect, quantum rotational tunnelling can serve as a sensitive atomistic probe for guest adsorption in MOFs.

At finite temperatures, the influence of NQEs was first examined for a force field description of the archetypal MOF-5. The structural properties of the framework exhibit only minor changes due to NQEs, just as the thermal expansion of the framework, which primarily requires a proper description of anharmonicities. For the heat capacity, by contrast, a correct temperature dependence in the presence of methane guest molecules can only be obtained by adequately modelling both NQEs and anharmonicities through PIMD simulations. A second case study of NQEs at finite temperatures focussed on the proton hopping of a Brønsted acid site (BAS) around an aluminium defect in a chabazite zeolite. To exclude the neglect of NQEs within the large discrepancies between experimental and computational activation energies for the proton hopping of the BAS, PIMD simulations were performed with an MLP with DFT accuracy to maximally limit the approximations within the computational description. To this end, the quasi-classical free energy profiles of the reaction, which are most commonly reported for enhanced sampling PIMD simulations, were replaced by proper quantum free energy profiles through the development of an elegant sampling protocol which allows to convert quasi-classical free energy profiles into quantum free energy profiles. For molecular proton transfer reactions, the difference between both approaches was shown to increase with the height and steepness of the free energy barrier of the reaction. Even at 450 K, NQEs can result in a reduction of about 60% of the classical free energy barrier of a molecular proton transfer. For the proton hopping reaction in the chabazite zeolite, NQEs reduced the overall activation energy by about 17% in comparison with a classical description.

Also for the study of water in MOFs, NQEs can improve the accuracy of the system's description, not in the least for the water molecules, which are known to be prone to NQEs. For the flexible MOF MIL-53(Al), the relative stability between its two phases was however observed to be only moderately influenced by NQEs within a force field description, even in the presence of water guest molecules. Apart from NQEs, also the confinement effects associated with the MOF's nanopores can alter the behaviour of the adsorbed water molecules. In MIL-53(Al), for instance, water can form one-dimensional water wires along the framework's narrow pore channels. In MOF-801, the tetrahedral framework pores induce cubic water clusters, which result in suitable water adsorption characteristics for the application of atmospheric water harvesting. To rationalise the adsorption behaviour emerging from particular water clusters that nucleate at hydrophilic framework adsorption sites, an analytical toy model was constructed to probe the adsorption char-

acteristics of a virtual nanopore. With this model, a favourable placement of primary adsorption sites was shown to induce secondary adsorption sites through directional hydrogen bonding, which positively impact the water adsorption behaviour of the nanopore. In this way, the meticulous design of framework adsorption sites can be exploited to template confined water and thus further improve the water adsorption characteristics of MOFs for specific applications, such as atmospheric water harvesting in arid regions.

In hydrophobic MOFs, the intrusion of water can provide a mechanism to absorb high-rate impacts. For ZIF-8, water intrusion experiments performed by our collaborators at the University of Oxford revealed an increased hysteresis in the intrusion-extrusion cycle for high-rate impacts, which allows to absorb 85% of the mechanical impact compared to 17% at low impact rates. Through the use of molecular simulations, this mechanism was shown to originate from the formation of critical-sized water clusters. For sufficiently low impact rates, the sequential filling of the hydrophobic cages of ZIF-8 is triggered by the spontaneous nucleation of water clusters, which can steadily grow to fill a pore of ZIF-8 after reaching a certain critical size. If the impact rate becomes too high, however, the spontaneous organisation of water into clusters is too slow to fill the hydrophobic pores of ZIF-8, so that water molecules are forced into the pores, which involves the dissipation of energy and thus attenuates the mechanical impact.

In conclusion, this PhD dissertation has shed new light on the impact of NQEs in modelling nanoporous materials and the way in which the organisation of nanoconfined water affects the water adsorption behaviour of these materials. In particular for proton transfer reactions, which are omnipresent in chemical processes, an appropiate inclusion of NQEs was shown to be indispensable. Furthermore, through a meticulous control of the hydrophilic adsorption sites within a nanopore, a new design principle was demonstrated to improve their water adsorption, which could be exploited to further optimise MOFs for water adsorption applications.

Part I

A Computational Understanding of Nuclear Quantum Effects and the Structural Organisation of Confined Water in Nanoporous Materials

1

Introduction

All truths are easy to understand once they are discovered; the point is to discover them.

Galileo Galilei[1] (1564–1642)

Throughout history, the discovery of new materials has marked significant advancements within human civilisation, ranging from the systematic improvement of prehistoric tools during the Stone, Bronze, and Iron Ages to the development of computer chips with billions of transistors by means of semiconductor materials in this century. To face the current societal challenges, including climate change, environmental pollution, or a sustainable energy transition, new materials will play a pivotal role in the development of technological solutions. Thanks to the ever increasing understanding of matter at an atomic scale, the search for new materials no longer relies on mere coincidental discovery, but can be guided by rational design strategies. In this respect, functional nanoporous materials have received a great deal of attention during the past few decades, due to their high degree of tunability for a wide range of applications, including carbon capture, the sustainable production of building-block chemicals, and atmospheric water harvesting in arid regions.[2–6] To cleverly guide the design of these materials at the nanoscale, a profound molecular-level understanding of the material's properties in relation to the material's atomic structure is required, which is aided by an unparalleled computing power in this Silicon Age and is further pursued within this PhD dissertation. After introducing the nanoporous materials considered in this work in Section 1.1, the goal and structure of this dissertation are described in more detail in Section 1.2.

1.1 Nanoporous materials

1.1.1 Zeolites

A first class of crystalline nanoporous materials considered in this work are zeolites. These aluminosilicate materials are built up out of corner-sharing TO_4 tetrahedra, where the so-called T-sites are either silicon (Si^{4+}) or aluminium (Al^{3+}) ions. As only pure silica zeolite frameworks are charge-neutral, the charge deficit introduced by aluminium substitutions are compensated by metal cations or protons on the framework (Figure 1.1). Given the different possibilities to connect the TO_4 tetrahedra with one another, various zeolite framework types exist, which can be classified according to their largest pore windows.[7] Up to eight-membered rings (8MR), small-pore zeolites are obtained, whereas large-pore zeolites typically contain twelve-membered or even larger rings. As a consequence, the cages and channels in a zeolite topology can range from nanopores to micropores. Currently, more than 250 unique zeolite frameworks have been catalogued.[8]

Naturally occurring zeolitic minerals were already discovered in 1756 by Axel F. Cronstedt, who coined the name zeolite based on the observation that the material released water vapour upon heating (using the Greek words 'zeo' (to boil) and 'lithos' (stone)).[9, 10] A widespread industrial use of zeolites was however only initiated by the synthetic production of zeolites, as first reported by Richard Barrer in 1948,[11] which allowed to control the composition and size of the zeolite structure to tailor its functions for specific applications. For the past few decades, zeolites have been labelled the workhorses of the petrochemical industry, due to their exceptional performance as heterogeneous catalysts. The acidic character of a charge-compensating proton on the framework, a so-called Brønsted acid site (BAS), results namely in an active catalytic site, whose presence can facilitate many industrially relevant chemical reactions. By means of a judicious choice of the zeolite framework, a reaction can be steered to favour the formation of specific products by exploiting the concept of shape selectivity. For reactants and products of different sizes, the pore windows can act as a molecular sieve, which hinders the diffusion of species larger than the pore window. In this way, reactants can be prevented from reaching the active site, whereas products can be prevented from leaving the zeolite's pores. Furthermore, the overall size of the pores can also exclude specific reaction paths, as the associated reactive complexes cannot be accommodated within the confined space of the zeolite pore.[12, 13]

Although the principle use of zeolites in the petrochemical industry is related to the refinement of oil through catalytic cracking and hydro-cracking, zeo-

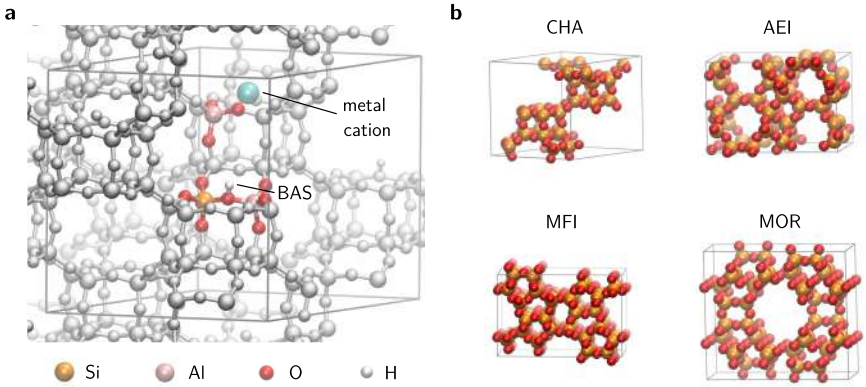

Figure 1.1: **a** Charge-compensating Brønsted acid site (BAS) and metal cation for two aluminium substitutions. **b** Periodic unit cells of four common zeolite topologies.

lites can also be employed in combination with renewable feedstocks such as biomass.[5, 14, 15] Similarly, zeolites also allow to convert molecules with a single carbon atom (such as methanol) into larger hydrocarbons and thus produce building-block chemicals (such as light olefins and aromatics, including propylene) or liquid fuels (such as gasoline) from non-fossil sources.[4] In the case of methanol, this conversion is called the methanol-to-hydrocarbons (MTH) process.

Other non-catalytic applications of zeolites include their use as adsorbent in, for instance, water purification and gas separation.[16] By means of ion exchange with sodium ions (Na^+) present in a zeolite, Ca^{2+} and Mg^{2+} ions can be removed from 'hard water', so that zeolites are commonly used in water softeners or added to washing powders.[17] Also nuclear wastewater can be decontaminated with zeolites, due to their affinity for radioactive isotopes such as ^{137}Cs and ^{90}Sr, which were removed from contaminated seawater after the Fukushima disaster in 2011.[18] To purify industrial flue gasses or feed streams (such as natural gas or biogas), the molecular sieving function of zeolites can be exploited to separate CO_2 from, for instance, CH_4.[19, 20] Furthermore, gas separation in zeolites can also be assisted by the preferential adsorption of CO_2 due to its favourable electrostatic interaction with metal cations on the framework. In **Paper VI** and **Paper XI**, the CO_2 gas separation performance of zeolite-filled mixed-matrix membranes (MMMs) was examined, which consist of zeolite nanoparticles that are incorporated in a polymeric membrane, to combine the polymer's processability and flexibility with the zeolite's separation properties. The results of these studies are discussed in more detail in Section 2.2.6.

1.1.2 Metal-organic frameworks

A second and more recent class of crystalline nanoporous materials are the so-called metal-organic frameworks (MOFs), which are also referred to as porous coordination polymers (PCPs). These materials are composed of inorganic metal clusters, the so-called secondary building units (SBUs), which are connected by organic linkers. Due to the endless possibilities to combine different building units with one another in different topologies, the modular structure of MOFs allows to construct a virtually unlimited number of frameworks. Currently, more than 100 000 MOF structures have been reported.[21, 22] Although the concept of coordination polymers was already explored in the 1960s,[23, 24] the field of MOF research would only start to flourish in the 1990s, as it proved to be particularly challenging to obtain stable porous frameworks which do not collapse in the absence of guest molecules, such as solvents. Only in 1999, Yaghi and co-workers succeeded in successfully synthesising a crystalline MOF with a permanent porosity and a high surface area, called MOF-5.[25] This archetypal cubic framework consists of octahedral $Zn_4O(CO_2)_6$ metal-oxide clusters, which are joined together by 1,4-benzenedicarboxylate (BDC^{2-}) linkers, as shown in Figure 1.2a. Similar MOFs, with the same pcu topology, can be obtained through the concept of isoreticular expansion, using the same SBU in combination with various expanded and functionalised linkers in comparison with MOF-5.[26, 27] This rational design principle of MOF structures by means of reticular synthesis gives rise to a myriad of frameworks, with an exceptional ability to precisely control the pore size and shape, as well as its chemical environment, through a judicious choice of the molecular building blocks, so that their functionalities can be tuned for specific applications.[28]

In spite of their high versatility, the commercialisation of MOFs has been hampered by the limited thermal, mechanical, and chemical stability of many frameworks, which is related to the moderate strength of the coordination bond between the metal nodes and linkers.[29] Some structures, including MOF-5, decompose for instance in the presence of water.[30] Furthermore, the MOF powders obtained within a large-scale MOF synthesis also require a densification procedure into pellets to ensure the processability in practical applications, which implies that the structure must be able to resist pressures up to a few hundreds of MPa.[31] However, in the continued exploration of the vast number of diverse MOF structures, more frameworks endowed with the necessary stability are being identified. The prototypical zirconium MOF UiO-66,[32] for instance, displays an improved stability due to its twelvefold connected $Zr_6O_4(OH)_4$ metal clusters (Figure 1.2b). Besides a good water stability, UiO-66 can also resist moderately acidic or basic solutions, tempe-

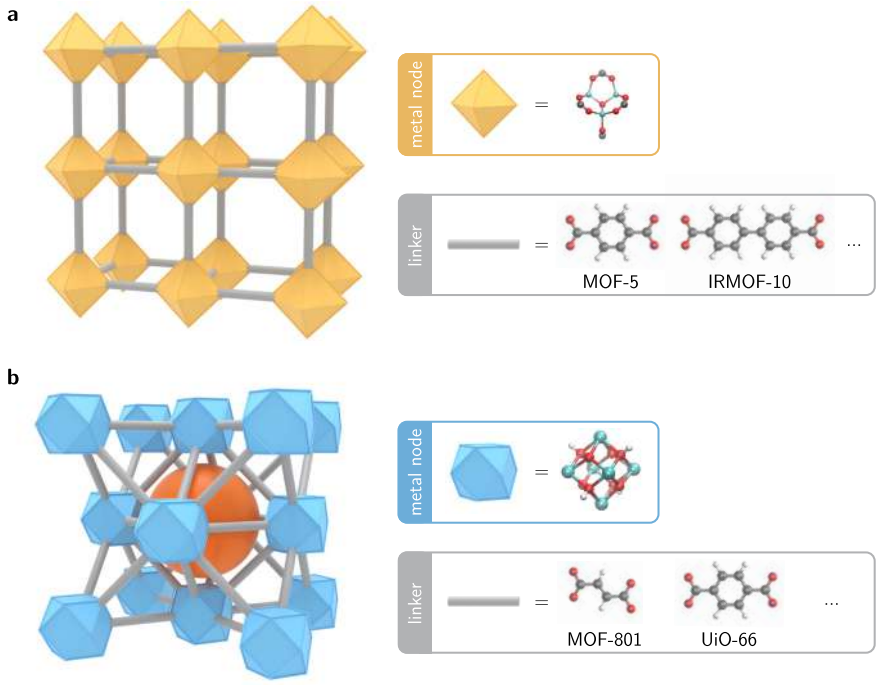

Figure 1.2: **a** Schematic representation of the pcu topology alongside the building blocks of MOF-5 and IRMOF-10. **b** Schematic representation of the fcu topology alongside the building blocks of MOF-801 and UiO-66. The octahedral pore of the framework is indicated with an orange sphere.

ratures above 500 °C, and pressures above 1 GPa.[29, 33]

Another example of a MOF with an excellent thermal, mechanical, and chemical stability is CALF-20, which is ideally suited for carbon dioxide capture.[34] In contrast to many other solid sorbents, the working capacity and selectivity associated with the physisorption of CO_2 in CALF-20 are virtually unaffected by the presence of water. For most adsorbents, the favourable electrostatic interactions with the framework are namely stronger for water molecules than for CO_2 molecules, which are both present in industrial flue gasses, alongside other acid gasses. Under mild regeneration conditions, CALF-20 is however able to obtain a CO_2 purity of 95%. In light of this outstanding performance, the implementation of CALF-20 for carbon capture on an industrial scale is currently further developed in collaboration with the company Svante.

In addition to carbon capture, MOFs can also be used to harvest water from the air. By capturing water at low relative humidities with a MOF, a higher relative humidity can be obtained inside the MOF, which increases

the temperature of the dew point, at which the water vapour can be turned into liquid water.[35] In this way, MOFs can produce liquid water from the air in arid regions, where freshwater sources are scarce. One of the first MOFs used in atmospheric water harvesting is MOF-801, an isoreticular variant of UiO-66 in which the BDC linker is substituted by a fumarate linker (Figure 1.2b). Both passive and active proof-of-concept devices have already been built with MOF-801, relying either on a single day-and-night cycle for the collection of water or on multiple controlled adsorption-desorption cycles for a continuous water production.[36–38]

In the context of heterogeneous catalysis, MOFs can act as single-site catalysts, although they cannot compete with zeolites for reactions in extreme conditions due to the extraordinary stability of zeolites.[39–41] The concept of reticular synthesis does however offer a precise control over the location and distribution of the active sites, in contrast to zeolites, so that active sites can be prevented from interfering with one another. In the context of drug delivery, pharmaceuticals encapsulated in MOFs or MOF composites allow for a more controlled release of the drug molecules, for which a slow or rapid release can positively influence the therapeutic effect, depending on the drug.[42, 43] Besides ordinary diffusion, also the decomposition of the framework in an acidic environment can be used as a release mechanism.

A final set of MOF applications is related to the subclass of the so-called flexible MOFs or soft porous crystals (SPCs), which exhibit a structural transformation in response to external stimuli such as temperature, pressure, guest adsorption, or light.[44–46] In ZIF-8, a zeolitic imidazolate framework (ZIF) with a sodalite topology (Figure 1.3a), both high pressures and the adsorption of guest molecules can trigger a reorientation of the imidazolate linkers, which modulates the opening of the pore windows.[47, 48] In this way, the dynamic gate-opening effect can significantly impact the molecular sieving function of the material. In DUT-49, the flexibility of the linkers gives rise to the phenomenon of negative gas adsorption (NGA), during which the framework is observed to expel guest molecules with an increasing gas pressure, due to a contraction of the framework's pore structure.[49, 50] When a MOF can reversibly switch between two phases with a characteristic difference in pore volume, the structural flexibility is called breathing. In MIL-53, the winerack framework can for instance transition from a narrow pore (np) to a large pore (lp) phase by an increase in temperature or the presence of guest molecules (Figure 1.3b).[51–53] Particular applications related to these types of flexibility are gas separation, sensing (*e.g.* by a reversible colour change upon structural transformation), and shock absorption.[54–56]

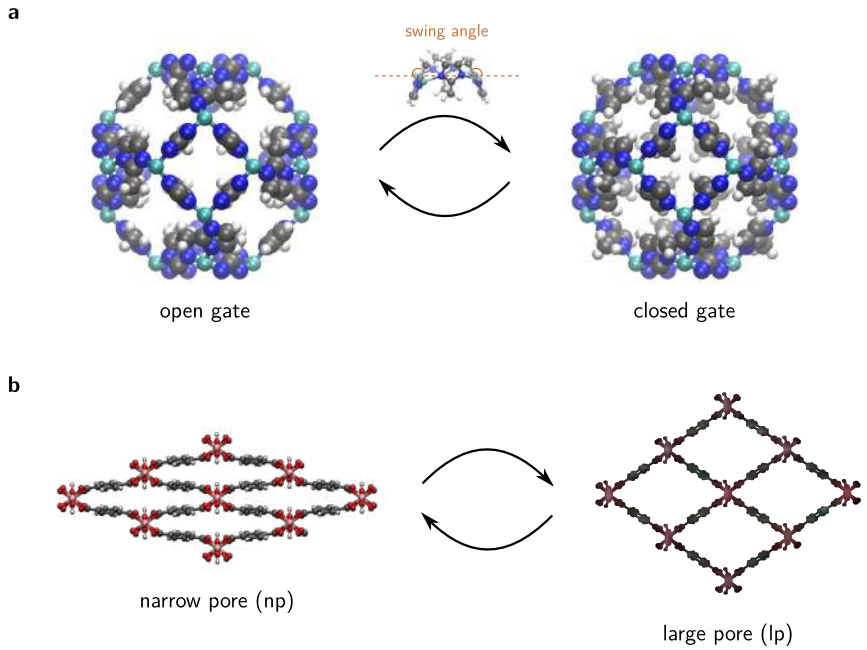

Figure 1.3: **a** Dynamic gate-opening effect in ZIF-8 caused by a reorientation of the methylimidazolate linkers. **b** Breathing transition between the narrow pore (np) and large pore (lp) phases in MIL-53(Al).

1.2 Goal and outline

In this thesis, the functional nanoporous materials introduced in the previous section are investigated using the computational techniques of molecular modelling. During the past few decades, molecular simulations have become a complementary tool to experimental research to explain and predict the characteristic behaviour of molecules and materials. As this theoretical description provides direct access to information at the atomic scale, which cannot always be probed or only indirectly with experiments, it can yield a more fundamental insight into the properties of molecular systems. Furthermore, especially in the particular context of MOFs, computational high-throughput screenings to explore the vast number of (hypothetical) structures can also guide the experimental search towards appropriate functional materials for dedicated applications, without the burdening requirement of synthesis.

This work focusses on the common approximation of neglecting nuclear quantum effects (NQEs) within molecular simulations and its implications for the modelling of nanoporous materials and their adsorbates, water in

particular. For condensed phases of water, the inclusion of NQEs has been shown to significantly improve the agreement between computational and experimental characterisations, as some intrinsically quantum mechanical properties cannot be reproduced with a classical treatment of the nuclei.[57, 58] Especially lightweight atoms, such as hydrogen, are prone to NQEs. Therefore, the impact of NQEs on the acidic protons in zeolites and the lightweight atoms in MOFs should be considered in the continuous pursuit of more accurate models to increase the predictive power of computational simulations. Given the pivotal role of adsorbates within applications of nanoporous materials, this dissertation also studies the behaviour of water confined in MOFs, to rationalise its structural organisation and the related adsorption characteristics in view of applications such as atmospheric water harvesting or shock absorption.

In Chapter 2, the general concepts of molecular modelling are introduced, starting from a fundamental quantum mechanical description. After providing an overview of the different approximations used to model the interatomic interactions, a brief discussion is given of the different techniques to extract properties from molecular simulations. Finally, these computational methods are also extended beyond the classical approximation to account for NQEs. Both the simulation techniques with and without the inclusion of NQEs are illustrated by research results obtained within the frame of collaborations with experimental partners (the group of prof. I. Vankelecom (KU Leuven) and prof. J.-C. Tan (Oxford University)).

In Chapter 3, the influence of NQEs is first examined for the structural and thermal properties of MOFs, focussing on the archetypal MOF-5 framework in combination with methane guest molecules. Next, the concept of quantum free energy calculations is introduced by means of three molecular proton transfer reactions. Subsequently, this computational method is also applied to the hopping of an acidic proton between different framework sites of a chabazite zeolite.

Chapter 4 is entirely devoted to the study of water in MOFs. The specific structural organisation of water confined in the pores of MOFs is investigated for both the flexible MOF MIL-53(Al) and a series of rigid zirconium MOFs (including MOF-801 and UiO-66). To rationalise the observed water motifs, the behaviour of a simplified virtual nanopore with tunable adsorption sites is analysed. Finally, also the mechanism of water intrusion in the hydrophobic ZIF-8 framework is examined to elucidate its ability to attenuate high-rate mechanical impacts.

In Chapter 5, a brief summary of all the results discussed in the previous chapters is given, alongside concluding remarks and a personal perspective regarding the remaining opportunities and challenges in the computational modelling of nanoporous materials and their adsorbates.

2

Computational Methods to Model Nanoporous Materials

It has long been an axiom of mine that the little things are infinitely the most important.

Arthur Conan Doyle[59] (1859–1930)

In this chapter, the general concepts of molecular modelling are introduced, starting from the fundamental theory of quantum mechanics. First, Section 2.1 discusses the different methods that can be used to describe the interatomic interactions (Figure 2.1). Besides approximate solutions to the Schrödinger equation provided by density functional theory (DFT), also force fields are considered, which rely on an effective parametrisation of the interatomic interactions. With the use of machine learning techniques, these interactions can also be represented by a complex neural network, which is able to match the accuracy of the predictions obtained with DFT. After choosing an appropriate model to describe the interatomic interactions, physical and chemical properties of the molecular system can be extracted from static or dynamic simulations, using techniques such as a harmonic approximation, molecular dynamics, or Monte Carlo. An overview of these different sampling techniques is given in Section 2.2, in combination with an illustration of their application to carbon dioxide adsorption in nanoporous materials. Finally, the concept of nuclear quantum effects is introduced in Section 2.3, alongside the computational techniques used to model them. An example of the inclusion of NQEs in static simulations is given for the calculation of the rotational tunnel splitting in the energy levels of the methyl rotors in ZIF-8.

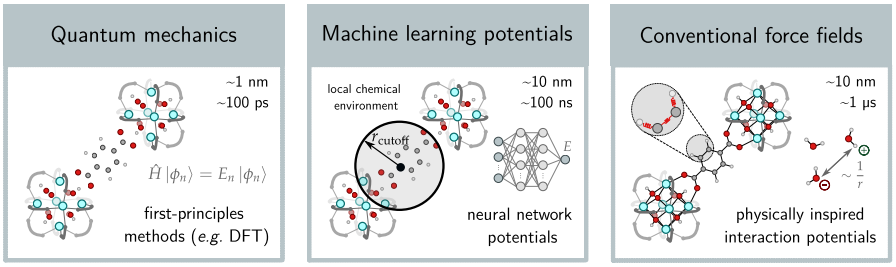

Figure 2.1: Overview of three different methods to describe the interatomic interactions. Figure adapted from Ref. [60] with permission of Elsevier.

2.1 Modelling interatomic interactions

2.1.1 Schrödinger equation

On the atomic scale, the behaviour of particles such as protons or electrons is governed by the laws of quantum mechanics. A fundamental concept within the theory of quantum mechanics is the so-called wave function $|\psi(t)\rangle$, which embodies the Heisenberg uncertainty principle and the wave-particle duality in the form of a probabilistic description of the system. To determine the wave function $|\psi(t)\rangle$, one has to solve the Schrödinger equation

$$i\hbar \frac{\partial}{\partial t} |\psi(t)\rangle = \hat{H} |\psi(t)\rangle \,, \tag{2.1}$$

with $\hbar$ the reduced Planck constant and $\hat{H}$ the Hamiltonian of the quantum mechanical system, which consists of the kinetic and potential energy of the system. From the wave function, all the properties of the quantum mechanical system can be derived, which are consequently also probabilistic in nature. The probability of finding a particle in a volume $\mathrm{d}\boldsymbol{r}$ around the position $\boldsymbol{r}$ at a time between t and $t + \mathrm{d}t$ is for instance given by

$$|\langle \boldsymbol{r}|\psi(t)\rangle|^2 \,\mathrm{d}\boldsymbol{r}\,\mathrm{d}t = |\psi(\boldsymbol{r},t)|^2 \,\mathrm{d}\boldsymbol{r}\,\mathrm{d}t \,. \tag{2.2}$$

In the particular case where the Hamiltonian is not explicitly time-dependent, the time-dependent Schrödinger equation (2.1) can be transformed into the time-independent Schrödinger equation

$$\hat{H} |\phi_n\rangle = E_n |\phi_n\rangle \,, \tag{2.3}$$

with $|\phi_n\rangle$ a stationary eigenstate of the Hamiltonian $\hat{H}$ with energy eigenvalue E_n. An arbitrary wave function $|\psi(t)\rangle$ of this system can then be written as a linear combination of stationary states with a trivial time dependence:

$$|\psi(t)\rangle = \sum_n c_n \, e^{-\frac{i}{\hbar}E_n t} \, |\phi_n\rangle \, . \tag{2.4}$$

This also applies to molecular systems, for which the Hamiltonian (in the absence of external fields) is given by[a]

$$\begin{aligned} \hat{H} &= \hat{T}_n + \hat{V}_{nn} + \hat{T}_e + \hat{V}_{ee} + \hat{V}_{ne} \qquad (2.5) \\ &= \sum_{\alpha=1}^{N_n} \left[-\frac{\hbar^2}{2M_\alpha} \boldsymbol{\nabla}_\alpha^2 + \frac{1}{2} \sum_{\substack{\beta=1 \\ \beta\neq\alpha}}^{N_n} \frac{e^2}{4\pi\varepsilon_0} \frac{Z_\alpha Z_\beta}{|\boldsymbol{R}_\alpha - \boldsymbol{R}_\beta|} \right] \\ &\quad + \sum_{i=1}^{N} \left[-\frac{\hbar^2}{2m_i} \boldsymbol{\nabla}_i^2 + \frac{1}{2} \sum_{\substack{j=1 \\ j\neq i}}^{N} \frac{e^2}{4\pi\varepsilon_0} \frac{1}{|\boldsymbol{r}_i - \boldsymbol{r}_j|} \right] \\ &\quad - \sum_{\alpha=1}^{N_n} \sum_{i=1}^{N} \frac{e^2}{4\pi\varepsilon_0} \frac{Z_\alpha}{|\boldsymbol{r}_i - \boldsymbol{R}_\alpha|}, \qquad (2.6) \end{aligned}$$

with $\hat{T}_n$ the nuclear kinetic energy, $\hat{V}_{nn}$ the repulsive interaction between the nuclei, $\hat{T}_e$ the electronic kinetic energy, $\hat{V}_{ee}$ the repulsive interaction between the electrons, and $\hat{V}_{ne}$ the attractive interaction between the nuclei and the electrons (also called the external potential). The masses, charges, and positions of the N_n nuclei are denoted by respectively M_α, Z_α, and $\boldsymbol{R}_\alpha$, whereas the masses and positions of the N electrons are denoted by respectively m_i and $\boldsymbol{r}_i$. In spite of the apparent simplicity of the time-independent Schrödinger equation, only a limited number of physical problems can be solved analytically (*e.g.* the quantum harmonic oscillator and the hydrogen atom). Other Hamiltonians, such as the molecular Hamiltonian (2.6) with a troublesome electron–electron repulsion, require the use of approximate solution methods, as briefly discussed in the following sections.

2.1.2 Born-Oppenheimer approximation

To solve the time-independent Schrödinger equation for a molecular system, it is commonly assumed that the dynamics of the nuclei and electrons can

a. In this work, the International System of Units (SI) is used.

be decoupled, so that the wave function can be written as[61, 62]

$$\Psi(\boldsymbol{x}_1, \ldots, \boldsymbol{x}_N, \boldsymbol{R}_1, \ldots, \boldsymbol{R}_{N_n}) = \sum_k \psi_k^{(e)}(\boldsymbol{x}_1, \ldots, \boldsymbol{x}_N)\, \chi_k(\boldsymbol{R}_1, \ldots, \boldsymbol{R}_{N_n}), \tag{2.7}$$

with $\boldsymbol{x}_i = (\boldsymbol{r}_i,\ \sigma_i)$ a shorthand notation for the spatial and spin coordinates of electron i. Due to the larger mass of nuclei in comparison with electrons, nuclei move much slower than electrons, so that it can be assumed that the nuclei are approximately fixed in space during the electrons' motion (the so-called clamped nuclei approximation). Within this approximation, the time-independent Schrödinger equation becomes the electronic Schrödinger equation

$$\left[\hat{V}_{nn} + \hat{T}_e + \hat{V}_{ee} + \hat{V}_{ne}\right] \psi_k^{(e)}(\boldsymbol{x}_1, \ldots, \boldsymbol{x}_N) = E_k^{(e)}\, \psi_k^{(e)}(\boldsymbol{x}_1, \ldots, \boldsymbol{x}_N), \tag{2.8}$$

which only depends parametrically on the nuclear coordinates. Given the slow dynamics of the nuclei, the electrons can be assumed to continuously adjust to small changes in the positions of the nuclei. By repeatedly solving the electronic Schrödinger equation for subsequent nuclear coordinates, a potential energy surface (PES) $E_k^{(e)}(\boldsymbol{R}_1, \ldots, \boldsymbol{R}_{N_n})$ is obtained for every electronic energy level k. If the PESs are well separated, the nuclear motion on each surface within the so-called adiabatic approximation is described by

$$\left[\hat{T}_n + E_k^{(e)}(\boldsymbol{R}_1, \ldots, \boldsymbol{R}_{N_n})\right] \chi_{km}(\boldsymbol{R}_1, \ldots, \boldsymbol{R}_{N_n}) = E_m\, \chi_{km}(\boldsymbol{R}_1, \ldots, \boldsymbol{R}_{N_n}), \tag{2.9}$$

which yields the rotational and vibrational energy levels associated with the nuclei. This approximate solution method of the Schrödinger equation for molecular systems is known as the Born-Oppenheimer approximation.

2.1.3 Density functional theory

To solve the electronic Schrödinger equation (2.8), further approximations are necessary due to the correlation introduced by the electron–electron repulsion interaction. As many physical properties of a molecular system are determined by its ground state, the variational principle can be used to find the lowest electronic energy of the system:

$$E_0 = E[\psi_0] = \min_{\psi} \langle \psi |\, \hat{H} - \hat{T}_n \,| \psi \rangle\,. \tag{2.10}$$

It is however impossible to consider all possible wave functions $|\psi\rangle$, so that the ground state is approximated by restricting the variational minimisation

over a subset of wave functions $|\psi_s\rangle$. In the Hartree-Fock method, for instance, the wave function is assumed to be a product of independent one-particle orbitals, represented by a so-called Slater determinant

$$\psi_s(\boldsymbol{x}_1, \boldsymbol{x}_2, \ldots, \boldsymbol{x}_N) = \frac{1}{\sqrt{N!}} \begin{vmatrix} \phi_1(\boldsymbol{x}_1) & \phi_1(\boldsymbol{x}_2) & \ldots & \phi_1(\boldsymbol{x}_N) \\ \phi_2(\boldsymbol{x}_1) & \phi_2(\boldsymbol{x}_2) & \ldots & \phi_2(\boldsymbol{x}_N) \\ \vdots & \vdots & \ddots & \vdots \\ \phi_N(\boldsymbol{x}_1) & \phi_N(\boldsymbol{x}_2) & \ldots & \phi_N(\boldsymbol{x}_N) \end{vmatrix}, \quad (2.11)$$

which possesses the proper antisymmetry upon exchange of any two electrons (as required for fermions). Instead of considering a variational minimisation over the wave function $|\psi\rangle$, which has $4N$ degrees of freedom, it is also possible to determine the ground-state energy from the electron density

$$n(\boldsymbol{r}) = N \int \mathrm{d}\sigma_1 \int \mathrm{d}\boldsymbol{x}_2 \ldots \int \mathrm{d}\boldsymbol{x}_N \, |\psi(\boldsymbol{r}, \sigma_1, \boldsymbol{x}_2 \ldots, \boldsymbol{x}_N)|^2, \quad (2.12)$$

which has only 3 degrees of freedom. As shown by the Hohenberg-Kohn theorems,[63] all properties of a many-electron system are completely determined by its ground-state density $n_0(\boldsymbol{r})$, which minimises the energy functional

$$E_0 = E[n_0(\boldsymbol{r})] = \min_{n(\boldsymbol{r})} E[n(\boldsymbol{r})], \quad (2.13)$$

with the additional constraint that

$$\int \mathrm{d}\boldsymbol{r} \, n(\boldsymbol{r}) = N. \quad (2.14)$$

For an electron density $n(\boldsymbol{r})$, associated with a normalised wave function $\psi(\boldsymbol{r}, \boldsymbol{r}_2 \ldots, \boldsymbol{r}_N)$, the energy functional is given by

$$\begin{aligned} E[n(\boldsymbol{r})] &= \langle\psi| \, \hat{H} - \hat{T}_n \, |\psi\rangle \\ &= T_e[n(\boldsymbol{r})] + V_{ee}[n(\boldsymbol{r})] + \int \mathrm{d}\boldsymbol{r} \, n(\boldsymbol{r}) V_{ne}(\boldsymbol{r}) + V_{nn}, \end{aligned} \quad (2.15)$$

with $F[n(\boldsymbol{r})] = T_e[n(\boldsymbol{r})] + V_{ee}[n(\boldsymbol{r})]$ the so-called universal functional, as it is the same for any N-electron system, independent of the external potential. While the Hohenberg-Kohn theorems prove the existence of such a functional, they do not provide a method to construct the functional. In the approach suggested by Kohn and Sham,[64] an auxiliary independent-particle system is introduced similarly to the Hartree-Fock method. For this non-interacting reference system, characterised by a Slater determinant (2.11), the electron density is given by

$$n(\boldsymbol{r}) = \sum_{i=1}^{N} |\phi_i(\boldsymbol{r})|^2, \quad (2.16)$$

while the kinetic energy $T_e^{(s)}$ and the Hartree energy J are given by

$$T_e^{(s)}[n(\boldsymbol{r})] = \sum_{i=1}^{N} \langle \phi_i | - \frac{\hbar^2}{2m_i} \boldsymbol{\nabla}_i^2 | \phi_i \rangle \tag{2.17}$$

$$J[n(\boldsymbol{r})] = \frac{1}{2} \int \mathrm{d}\boldsymbol{r} \int \mathrm{d}\boldsymbol{r}' \, \frac{e^2}{4\pi\varepsilon_0} \frac{n(\boldsymbol{r}) n(\boldsymbol{r}')}{|\boldsymbol{r} - \boldsymbol{r}'|}. \tag{2.18}$$

Using the auxiliary non-interacting reference system, the energy functional can be rewritten as

$$E[n(\boldsymbol{r})] = T_e^{(s)}[n(\boldsymbol{r})] + J[n(\boldsymbol{r})] + E_{xc}[n(\boldsymbol{r})] + \int \mathrm{d}\boldsymbol{r} \, n(\boldsymbol{r}) V_{ne}(\boldsymbol{r}) + V_{nn}, \tag{2.19}$$

with E_{xc} the exchange-correlation functional, defined as

$$E_{xc}[n(\boldsymbol{r})] = T_e[n(\boldsymbol{r})] - T_e^{(s)}[n(\boldsymbol{r})] + V_{ee}[n(\boldsymbol{r})] - J[n(\boldsymbol{r})]. \tag{2.20}$$

Minimisation of the energy functional $E[n(\boldsymbol{r})]$, under the orthonormality constraint $\langle \phi_i | \phi_j \rangle = \delta_{ij}$, then yields the so-called Kohn-Sham equations

$$\left[-\frac{\hbar^2}{2m_i} \boldsymbol{\nabla}_i^2 + V_{KS}(\boldsymbol{r}) \right] \phi_i(\boldsymbol{r}) = \varepsilon_i \phi_i(\boldsymbol{r}), \tag{2.21}$$

with

$$V_{KS}(\boldsymbol{r}) = V_{ne}(\boldsymbol{r}) + \frac{e^2}{4\pi\varepsilon_0} \int \mathrm{d}\boldsymbol{r}' \, \frac{n(\boldsymbol{r}')}{|\boldsymbol{r} - \boldsymbol{r}'|} + \frac{\delta E_{xc}[n]}{\delta n(\boldsymbol{r})}. \tag{2.22}$$

In Kohn-Sham density functional theory (DFT), the Kohn-Sham equations are solved to determine the ground-state electron density (2.16) from the one-particle Kohn-Sham orbitals $\phi_i(\boldsymbol{r})$ and the corresponding ground-state energy using the energy functional (2.19). In contrast with the Hartree-Fock method, Kohn-Sham DFT yields in principle the exact ground-state density and energy. However, as the exchange-correlation functional E_{xc} is unknown, approximations of the functional have to be devised to solve the Kohn-Sham equations.

The most rudimentary approximation of the exchange-correlation functional is the so-called local density approximation (LDA), which makes use of an exchange-correlation functional that only depends on the electron density. The most common LDA is obtained by assuming that the exchange-correlation functional of the homogeneous electron gas can be used to describe infinitesimal portions of a non-homogeneous electron distribution.[64]

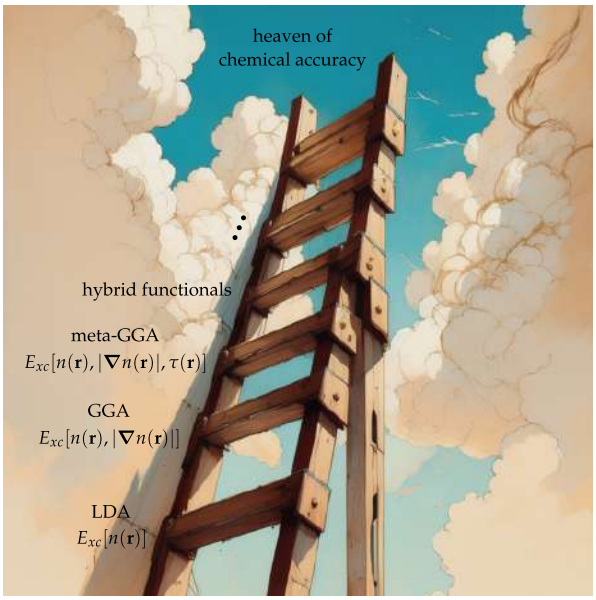

Figure 2.2: Jacob's ladder of successive approximations of the exchange-correlation functional E_{xc} in DFT.

To improve the approximation of the exchange-correlation functional, the so-called generalised-gradient approximation (GGA) is used, which includes a dependency on the gradient of the electron density in the functional. Commonly used GGA functionals are for instance the Perdew-Burke-Ernzerhof (PBE)[65] functional and the Becke-Lee-Yang-Parr (BLYP)[66, 67] functional. Further improvements in the approximation of the exchange-correlation functional can be obtained by including a dependency on the kinetic energy density $\tau(\boldsymbol{r})$ or by including a fraction of Hartree-Fock exchange

$$E_x^{HF} = -\frac{1}{2}\sum_{i=1}^{N}\sum_{j=1}^{N}\frac{e^2}{4\pi\varepsilon_0}\int \mathrm{d}\boldsymbol{r}\int \mathrm{d}\boldsymbol{r}'\ \phi_i^*(\boldsymbol{r})\phi_j^*(\boldsymbol{r}')\,\frac{1}{|\boldsymbol{r}-\boldsymbol{r}'|}\,\phi_i(\boldsymbol{r}')\phi_j(\boldsymbol{r}). \tag{2.23}$$

These improvements result respectively in so-called meta-GGA functionals, such as SCAN[68], or hybrid functionals such as PBE0[69] and B3LYP[70]. The successive refinements of the approximation of the exchange-correlation functional are often depicted as the rungs of Jacob's ladder[71] (Figure 2.2), which extends towards the 'heaven of chemical accuracy' with an exact description of the exchange-correlation functional.

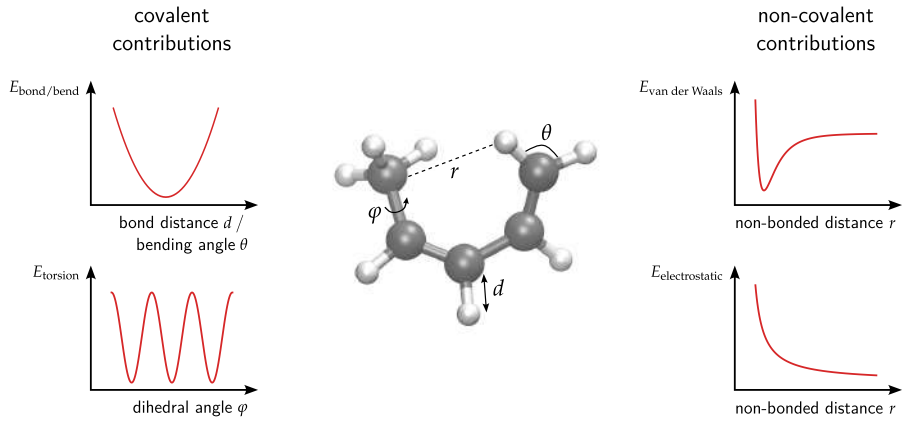

Figure 2.3: Overview of typical force field contributions, illustrated for a pentadiene molecule. The insets show specific bonded (left) and non-bonded (right) contributions. The bonded contributions include a harmonic bond/bend potential and a threefold symmetric torsion potential, whereas the non-bonded contributions include the Coulomb potential for the electrostatic interactions and a Lennard-Jones potential for the van der Waals interactions.

2.1.4 Force fields

For large molecular systems and/or elaborate explorations of the PES, the explicit solution of the electronic Schrödinger equation becomes computationally too demanding. In that case, the PES is approximated by an analytical expression for the interatomic interactions, a so-called force field (FF),[72] which eliminates the explicit description of the electrons. To construct a force field, the interatomic interactions are typically decomposed into different contributions. The covalent or bonded interactions describe the short-range interactions between the nuclei and represent the chemical bonds between them. These interactions can be expressed in terms of internal coordinates, such as bond distances, bending angles, dihedral angles, and out-of-plane distances (Figure 2.3). The non-covalent or non-bonded interactions are described by the long-range electrostatic and van der Waals interactions. Given that force fields do not explicitly model the electrons, every atom in the force field is attributed a charge to effectively reproduce the electrostatic interactions by means of a Coulomb potential. For the van der Waals interactions, typical descriptions include the Lennard-Jones[73, 74] and MM3 Buckingham potential[75].

To parametrise a force field, one can rely both on experimental data and first-principles data obtained from quantum mechanical calculations. In

the case of generic force fields, such as DREIDING or UFF4MOF,[74, 76, 77] the parameters are optimised to reproduce the properties of a wide range of molecular structures. For system-specific force fields, such as MOF-FF or QuickFF,[78–80] the transferability of the force field is traded for a more accurate reproduction of the properties of a single molecular system. In this work, the QuickFF protocol was used to parametrise the force fields of different MOFs. The QuickFF parameters of the covalent interactions are obtained from the DFT equilibrium geometry of the structure and the corresponding Hessian. For the electrostatic interactions, the atomic charges of the framework are determined by partitioning the electron density with the Minimal Basis Iterative Stockholder (MBIS) method.[81] The parameters of the van der Waals interactions are simply taken from the DREIDING or MM3 force field.[74, 82] For smaller guest molecules, such as H_2O or CO_2, well-established force fields from the literature were used (*e.g.* q-TIP4P/f[83] and TraPPE[84]).

2.1.5 Machine learning potentials

A conventional force field description of the PES usually exhibits a high computational efficiency, but a reduced accuracy in comparison with quantum mechanical calculations such as DFT. Moreover, most force fields also do not allow to describe the formation or breakage of bonds, as the topology of the structure is assumed to be fixed in the analytical parametrisation of the force field. Therefore, until recently, chemical reactions could only be modelled quantum mechanically or with dedicated reactive force fields, such as ReaxFF.[85] The recent advent of machine learning potentials (MLPs), however, has opened up the possibility to combine the computational efficiency of conventional force fields with the accuracy of a quantum mechanical description of the PES, including the description of chemical reactions with the formation or breakage of bonds.

In principle, MLPs can be categorised as force fields obtained from first-principles data by means of machine learning techniques.[86] While conventional force fields usually have a few hundreds of parameters, MLPs can have millions of parameters when using neural networks. Furthermore, in contrast to conventional force fields, MLPs do not make use of a predetermined, physically inspired parametrisation of the interatomic interactions, but learn a representation of the PES from first-principles data. Typically, the training data of an MLP consists of a dataset of energies and forces of representative configurations of a molecular system, which can be obtained from (enhanced sampling) molecular dynamics simulations,[87] which are discussed in more detail in Section 2.2. From this dataset, suitable MLP parameters $\boldsymbol{\theta}$ can be

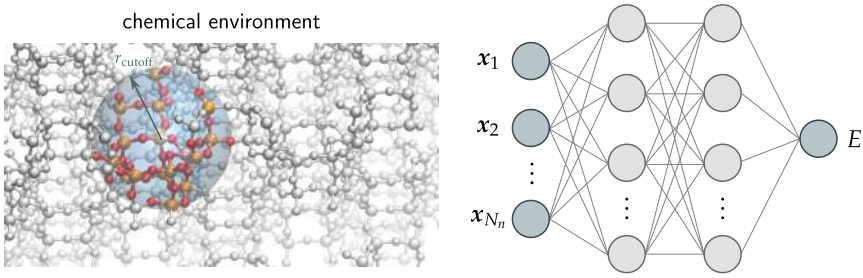

Figure 2.4: Illustration of a chemical environment of a hydrogen atom in a chabazite zeolite, defined by a cutoff radius of 6 Å. From these atomic environments, the atomic feature vectors $\boldsymbol{x}_\alpha$ are automatically learned by a message passing neural network to calculate the energy E of a molecular configuration.

derived by minimising a so-called loss function:

$$\mathcal{L}(\boldsymbol{\theta}) = \lambda_E \left(\frac{E(\boldsymbol{\theta}) - \hat{E}}{N_n} \right)^2 + \frac{\lambda_F}{3N_n} \sum_{\alpha=1}^{N_n} \| \boldsymbol{F}_\alpha(\boldsymbol{\theta}) - \hat{\boldsymbol{F}}_\alpha \|^2, \tag{2.24}$$

with λ_E and λ_F hyperparameters which determine the relative weight of the energies and forces of the configurations in optimising $\boldsymbol{\theta}$, and $\hat{E}$ and $\hat{\boldsymbol{F}}_\alpha$ respectively the reference energies and reference forces on atom α in the first-principles training data that should be reproduced by the MLP. Given that every molecular configuration only possesses a single energy value, but $3N_n$ force components, the use of forces in the MLP training process can significantly reduce the required number of configurations in the training dataset.

In neural network MLPs, the functional form of the PES consists of a sequence of linear combinations and non-linear activation functions, which only require the atomic positions and numbers of a molecular configuration as input. The MLP energy of a configuration on the PES is usually a combination of atomic energy contributions:

$$E = \sum_{\alpha=1}^{N_n} E_\alpha(\boldsymbol{x}_\alpha), \tag{2.25}$$

which depend on the local chemical environment of the atom, represented by a feature vector $\boldsymbol{x}_\alpha$ (Figure 2.4). In message passing neural networks, such as SchNet[88] and NequIP[89], which were used in this dissertation, the atomic

feature vectors $\boldsymbol{x}_\alpha$ are also learned automatically. Through an iterative update procedure, the feature vectors are systematically refined to obtain an adequate description of the chemical environment of each atom. Whereas initially only the immediate neighbourhood around an atom is considered within a certain cutoff radius, a subsequent iteration also takes information from atoms outside the cutoff radius into account as this information was incorporated in the description of neighbouring atoms during the previous iteration. In this way, the concept of message passing results in a larger effective cutoff radius for the interatomic interactions, which increases the accuracy of the description of the PES due to the effective incorporation of long-range interactions.

2.2 Sampling the potential energy surface

For a given description of the interatomic interactions, the prediction of the physical or chemical properties of a molecular system requires information beyond a single point of the potential energy surface (PES) (Figure 2.5). For some purposes, knowledge of the behaviour about the equilibrium configuration(s) at 0 K is sufficient, which can be obtained from so-called static simulations. If also dynamic information is important, simulation techniques such as molecular dynamics or Monte Carlo can be used to model the dynamics of the system at finite temperatures or pressures.

2.2.1 Static simulations

At low temperatures, the characteristics of a molecular system are determined by its (meta)stable configurations, represented by the (local) minima of the PES. Once an equilibrium configuration is obtained by means of a geometry optimisation, the PES is usually approximated by a second-order Taylor expansion in the corresponding minimum:

$$V(\boldsymbol{R}_1,\ldots,\boldsymbol{R}_{N_n}) \approx V(\boldsymbol{R}_1^{(0)},\ldots,\boldsymbol{R}_{N_n}^{(0)}) + \frac{1}{2}\sum_{\alpha,\beta}\boldsymbol{Q}_\alpha^T\mathbf{H}_{\alpha\beta}\boldsymbol{Q}_\beta, \tag{2.26}$$

with $V(\boldsymbol{R}_1,\ldots,\boldsymbol{R}_{N_n}) = E_0^{(e)}(\boldsymbol{R}_1,\ldots,\boldsymbol{R}_{N_n})$ the ground-state PES, $\boldsymbol{Q}_\alpha = \boldsymbol{R}_\alpha - \boldsymbol{R}_\alpha^{(0)}$, $\boldsymbol{R}_\alpha^{(0)}$ the equilibrium position of atom α, and $\mathbf{H}_{\alpha\beta}$ the Hessian for atoms α and β

$$\mathbf{H}_{\alpha\beta} = \frac{\partial^2 V}{\partial\boldsymbol{Q}_\alpha\partial\boldsymbol{Q}_\beta}(\boldsymbol{R}_1^{(0)},\ldots,\boldsymbol{R}_{N_n}^{(0)}). \tag{2.27}$$

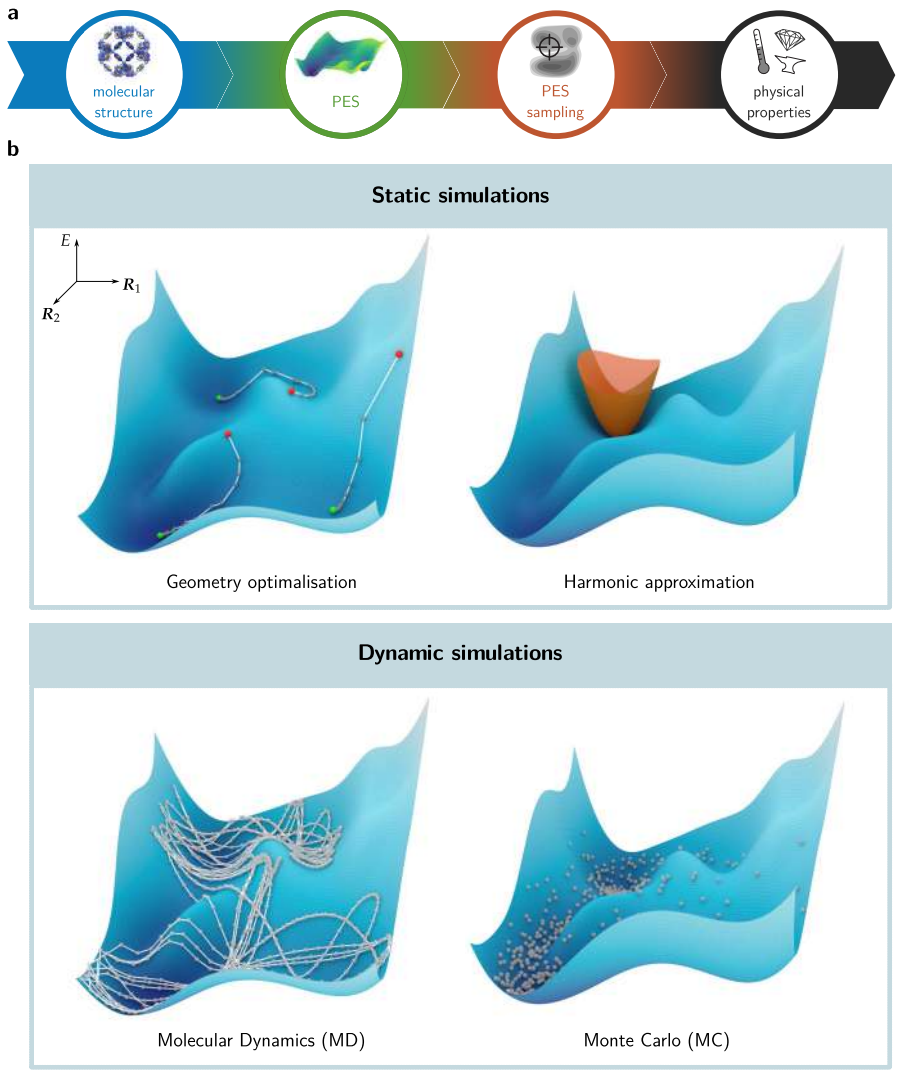

Figure 2.5: a Overview of the different steps in a molecular modelling process. Figure adapted from Ref. [90] with permission of the Royal Society. **b** Schematic illustration of four different PES sampling techniques.

The first-order derivatives in the Taylor expansion are zero, as a PES minimum is considered. By diagonalising the mass-weighted Hessian, the so-called normal modes of the system can be obtained, which allow to represent the system as a set of independent harmonic oscillators for every degree of freedom, with omission of the global translations and rotations (yielding $3N_n - 3$, $3N_n - 5$, or $3N_n - 6$ oscillators for periodic systems, linear

molecules, and non-linear molecules, respectively). Within this harmonic approximation, the thermodynamic properties of a quantum harmonic oscillator can be exploited to characterise the system near the equilibrium configuration, as often done to calculate infrared spectra,[91] elasticity tensors,[87, 92] or heat capacities[93] of crystalline materials.

2.2.2 Molecular dynamics

Although some properties of crystalline materials or molecules are well described by a harmonic approximation of the PES about an equilibrium configuration, other properties, including the flexibility of crystalline frameworks, the diffusion and adsorption of guest molecules, or chemical reactions, require a proper description of the dynamic behaviour of the system at finite temperatures or pressures. In molecular dynamics (MD) simulations, the positions of the atomic nuclei change as a function of time in accordance with Newton's equations of motion:

$$\boldsymbol{F}_\alpha = -\boldsymbol{\nabla}_{\boldsymbol{R}_\alpha} V(\boldsymbol{R}_1, \ldots, \boldsymbol{R}_{N_n}) = M_\alpha \frac{\mathrm{d}^2 \boldsymbol{R}_\alpha}{\mathrm{d}t^2}, \tag{2.28}$$

where the forces $\boldsymbol{F}_\alpha$ ($\alpha \in \{1, \ldots, N_n\}$) acting on the nuclei are obtained from the gradient of the ground-state PES. Numerical integration of these equations, usually performed with the velocity Verlet algorithm,[94, 95] yields a new configuration of the system at every consecutive time step, thus exploring the PES beyond the 0 K equilibrium configuration(s). The time step of the integration is limited by the period of the fastest vibrations in the system, which are typically hydrogen atoms for which a time step of 0.5 fs is advisable.

The properties of the system are extracted from the MD simulation as time averages. Following the assumption of the ergodic hypothesis, these time averages are equal to the corresponding ensemble averages, *i.e.* averages over all microstates of the system that correspond with a certain macrostate and are weighted with their probability of occurrence. When Newton's equations of motion are integrated, a macrostate with a constant number of particles, a constant volume, and a constant energy is implied, so that the microcanonical ensemble is sampled. Other ensembles, such as the canonical or isothermal-isobaric ensemble, can be sampled by modifying the equations of motion, for instance through the introduction of additional degrees of freedom. These fictitious degrees of freedom are associated with so-called thermostats and barostats, which control the temperature or pressure in the simulation, respectively.[94–100]

Due to the use of classical equations of motion, the quantum mechanical nature of the atomic nuclei is completely neglected. To sample the different ensembles quantum mechanically, path integral MD simulations can be used, as explained in Section 2.3. The electrons in an MD simulation, which are only implicitly present through the forces exerted on the nuclei, can be described either quantum mechanically, with first-principles methods such as DFT, or classically, with force fields, depending on the required accuracy, length, and size of the simulation (Figure 2.1).

2.2.3 Monte Carlo

Instead of relying on a natural time evolution of the molecular system on the PES as in MD simulations, the PES can also be sampled stochastically using Monte Carlo (MC) simulations. A completely random sampling of the PES would be very inefficient as, for instance, for the canonical ensemble the statistical weight $e^{-\beta E}$ of many configurations on the PES is negligible, with $\beta = (k_B T)^{-1}$, k_B the Boltzmann constant, and T the temperature. Therefore, configurations in MC simulations are not generated truly randomly, but with a so-called Markov chain in which the probability of each new configuration depends on the previous configuration in the chain.[101] In the Metropolis MC algorithm, a new configuration n is accepted in the Markov chain with a probability

$$\mathrm{acc}(o \to n) = \begin{cases} \dfrac{p(n)}{p(o)} & \text{if } p(n) < p(o) \\ 1 & \text{if } p(n) \geqslant p(o) \end{cases}, \tag{2.29}$$

with o the previous ('old') configuration in the chain and $p(x)$ the probability of configuration x. If the new configuration n is rejected, the chain simply remains in configuration o. The Metropolis acceptance probability satisfies the so-called detailed balance condition

$$p(o)\,\mathrm{acc}(o \to n) = p(n)\,\mathrm{acc}(n \to o), \tag{2.30}$$

which imposes that in equilibrium the average number of accepted moves from an old configuration o to any new configuration n is balanced by the number of reverse moves, thus assuring the sampling of the stationary distribution $p(x)$.[94] More specifically, for the canonical ensemble, the Boltzmann factor $e^{-\beta E}$ is used as probability density, which implies that regions of low energy near equilibrium configurations will be visited more often than high energy regions (Figure 2.5b). In each MC step, a new configuration is generated from the previous one by subjecting it to a translational trial move,

which randomly displaces one of the particles, or to an orientational trial move (in the case of molecules), which randomly rotates one of the molecules. If the new configuration has a lower energy than the previous one, it is always accepted. If the new configuration has a higher energy than the previous one, it is only accepted with a probability $e^{-\beta(E(n)-E(o))}$. To this end, a random number r between 0 and 1 is generated. If $r < e^{-\beta(E(n)-E(o))}$, the new configuration is accepted, otherwise it is rejected and the system remains in the previous configuration. The properties of the system are obtained from an average over all configurations in the Markov chain, which corresponds to an ensemble average. Typically, a few million MC steps are required to converge the properties of nanoporous systems.

In contrast to MD simulations, MC simulations also allow for the simulation of a variable number of particles, so that the grand-canonical (GC) ensemble can be sampled, which fixes the chemical potential μ of the system instead of the number of particles. Therefore, GCMC simulations are ideally suited to model the adsorption of gasses in a material. In addition to the translational and rotational trial moves of the canonical ensemble, insertion and deletion moves of particles are also attempted, for which the acceptance probability uses the probability density

$$p(N) \propto \frac{e^{\beta\mu N}}{\Lambda^{3N} N!}\, e^{-\beta E}, \tag{2.31}$$

with N the number of particles and $\Lambda = \frac{h^2}{2\pi m k_B T}$ the thermal de Broglie wavelength of a particle with mass m. The chemical potential μ can be related to the pressure P of the adsorbed gas through an equation of state, which yields for an ideal monoatomic gas

$$\mu = \frac{1}{\beta}\left[\ln(\Lambda^3) + \ln(\beta P)\right]. \tag{2.32}$$

Similarly to MD simulations, the nuclei in MC simulations are also treated classically. To incorporate their quantum mechanical nature, path integral MC simulations can be used.[102–104] The electrons can be treated in the same way as in MD simulations, as they are also only implicitly present in the energy of each configuration, which can be calculated either quantum mechanically or classically. However, given the large number of MC steps required to obtain converged properties, first-principles techniques are not commonly used in combination with MC, due to their high computational cost.[105, 106]

2.2.4 Transition matrix Monte Carlo

In most GCMC simulations, the adsorbates and adsorbent are usually treated as rigid structures by assuming fixed interatomic distances, which eliminates the structural flexibility. In that case, only translations and rotations of the adsorbates as a whole are accounted for. To include the flexibility of the molecular system for adsorption phenomena, a hybrid MC/MD approach can be used, which interlaces GCMC and MD steps throughout the simulation. In particular for flexible MOFs, a proper description of the framework's flexibility is indispensable to model its adsorption behaviour.[107, 108] Besides a hybrid MC/MD scheme, the transition matrix Monte Carlo (TMMC) method also allows to study adsorption processes in combination with a flexible description of the molecular system.[109, 110] Within TMMC, it suffices to conduct an MD simulation in the canonical ensemble for every relevant number of adsorbates in the absorbent within the pressure range of interest, in combination with virtual adsorbate insertions and deletions. For every virtual insertion and deletion during the MD simulations, the corresponding acceptance probabilities are gathered in the collection matrix $\mathbf{C}$. For a system with N adsorbates, the matrix $\mathbf{C}$ is updated as follows after a virtual insertion:

$$C_{N,N+1} = C_{N,N+1} + \mathrm{acc}(N \to N+1) \tag{2.33}$$

$$C_{N,N} = C_{N,N} + [1 - \mathrm{acc}(N \to N+1)]\,, \tag{2.34}$$

whereas a virtual adsorbate deletion yields the following update rules:

$$C_{N,N-1} = C_{N,N-1} + \mathrm{acc}(N \to N-1) \tag{2.35}$$

$$C_{N,N} = C_{N,N} + [1 - \mathrm{acc}(N \to N-1)]\,, \tag{2.36}$$

where $\mathrm{acc}(N \to N \pm 1)$ are the same acceptance probabilities as the particle insertion and deletion moves in GCMC:

$$\mathrm{acc}(N \to N+1) = \min\left[1, \frac{V}{\Lambda^3(N+1)}\, e^{\beta(\mu - E_{N+1} + E_N)}\right] \tag{2.37}$$

$$\mathrm{acc}(N \to N-1) = \min\left[1, \frac{\Lambda^3 N}{V}\, e^{-\beta(\mu + E_{N-1} - E_N)}\right], \tag{2.38}$$

with E_N the energy of a configuration of the molecular system with N adsorbates. From the collection matrix $\mathbf{C}$, the probability of adsorbing an additional particle or molecule can be calculated as

$$T(N \to N+1) = \frac{C_{N,N+1}}{C_{N,N-1} + C_{N,N} + C_{N,N+1}}. \tag{2.39}$$

Finally, the probability of observing N particles in the system can be obtained from the condition of detailed balance

$$p(N+1) = p(N)\,\frac{T(N \to N+1)}{T(N+1 \to N)}, \tag{2.40}$$

with $p(0)$ a constant that can be determined through normalisation. Remark that in contrast to Eq. (2.31) the probabilities in Eq. (2.40) are no longer dependent on the particle coordinates, as the transition probabilities T are averaged acceptance probabilities of the different configurations visited during the MD simulations. Similarly to GCMC simulations, the TMMC method thus allows to compute the average number of particles adsorbed in a molecular system for a specific chemical potential μ or, equivalently, gas pressure P:

$$\langle N \rangle = \sum_{N} N\, p(N), \tag{2.41}$$

so that an adsorption isotherm can be calculated by considering different gas pressures (or chemical potentials).

2.2.5 Enhanced sampling

For molecular systems characterised by two or more (meta)stable states that are separated by a substantial energy barrier at certain thermodynamic conditions, regular MD or MC simulations are unable to adequately sample the transition between these states. Within a simulation of finite length, the sampling is then no longer ergodic due to the prohibitively small probability of crossing the energy barrier. Therefore, enhanced sampling techniques are required to improve the sampling of all the configurations involved in the rare event of crossing the barrier.

In the canonical ensemble, the equilibrium configurations at a specific temperature and volume minimise the Helmholtz free energy

$$F = E - TS, \tag{2.42}$$

with E the (internal) energy, T the temperature, and S the entropy. Given the strong dependence of the system's equilibrium configurations on the thermodynamic conditions, the energy barriers of the free energy surface (FES) should be considered instead of the intrinsic energy barriers of the PES. At 0 K, the FES coincides with the PES and the static sampling technique of Section 2.2.1 can be used to describe the equilibrium configurations (and intermediate energy maxima). To calculate the FES at finite temperatures,

numerous enhanced sampling methods have been devised, which often rely on one or more so-called collective variables (CVs) to drive an activated process, such as a phase transition, a hindered diffusion process, or a chemical reaction, across the activation barrier(s).[b] CVs can be described as functions of the phase space coordinates which aggregate the relevant degrees of freedom to characterise the rare event in a reduced subspace rather than in the high-dimensional phase space of the system. For a one-dimensional CV $q = Q(\boldsymbol{R}_1, \ldots, \boldsymbol{R}_{N_n})$ the FES is defined as

$$\begin{aligned} F(q) &= -\frac{1}{\beta} \ln\left[p(q)\right] + C = -\frac{1}{\beta} \ln\left[\frac{\int \mathrm{d}\Gamma\, \delta(Q(\boldsymbol{R}^{N_n}) - q)\, e^{-\beta E}}{\int \mathrm{d}\Gamma\, e^{-\beta E}}\right] + C \\ &= -\frac{1}{\beta} \ln\left\langle \delta(Q(\boldsymbol{R}^{N_n}) - q)\right\rangle + C, \end{aligned} \tag{2.43}$$

where $\langle \cdot \rangle$ denotes an ensemble average, C is a normalisation constant, δ represents the delta distribution, Γ is a short-hand notation for the phase space, $\mathrm{d}\Gamma = \mathrm{d}\boldsymbol{R}^{N_n}\,\mathrm{d}\boldsymbol{P}^{N_n} = \mathrm{d}\boldsymbol{R}_1 \ldots \mathrm{d}\boldsymbol{R}_{N_n}\,\mathrm{d}\boldsymbol{P}_1 \ldots \mathrm{d}\boldsymbol{P}_{N_n}$, $\boldsymbol{P}_\alpha$ is the momentum of atom α, and $p(q)$ is the probability density of a configuration with a CV value equal to q. Given that only relative free energy differences are of interest, the constant C can be neglected, since

$$F(q) - F(q') = -\frac{1}{\beta} \ln\left[\frac{p(q)}{p(q')}\right]. \tag{2.44}$$

In the umbrella sampling (US) technique,[95, 111] which is used in this work to construct FESs, a bias potential is introduced to enhance the sampling of all the configurations involved in the rare event. As achieving this with a single bias potential would require *a priori* knowledge of the unknown FES, several bias potentials are used instead to enhance the sampling in different regions of the phase space during independent simulations (Figure 2.6a). Most commonly, a harmonic bias potential is used to restrain the system to a specific range of the CV, so that each US simulation contains a bias potential or umbrella of the form

$$V_i^b(q) = \frac{\kappa_i}{2}(q - q_{i,0})^2, \tag{2.45}$$

with κ_i the umbrella strength and $q_{i,0}$ the equilibrium position of the umbrella. The resulting probability densities of the US simulations are of course biased (Figure 2.6b), given that the statistical weight $e^{-\beta(E+V_i^b)}$ is used

b. In the literature, collective variables are also often referred to as reaction coordinates or order parameters.

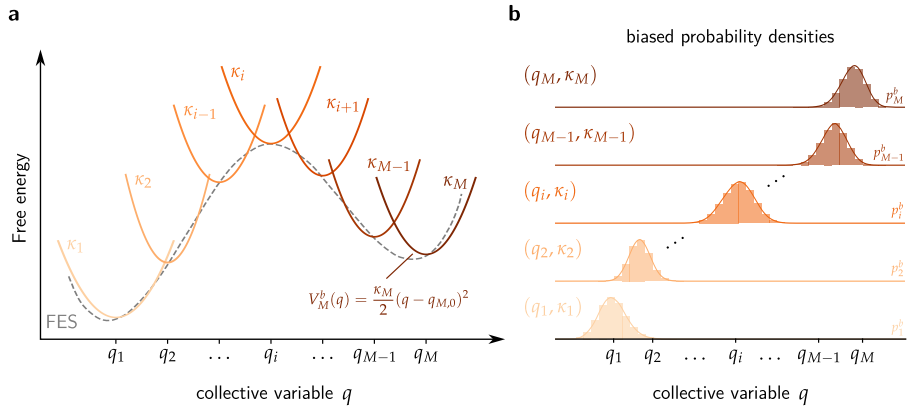

Figure 2.6: **a** Illustration of the harmonic bias potentials used in umbrella sampling simulations to sample a FES as a function of the collective variable q. **b** The biased probability densities obtained from umbrella sampling simulations with the different bias potentials of pane a. By means of the WHAM algorithm, the total unbiased probability density and, hence, the underlying FES can be reconstructed.

instead of the Boltzmann factor $e^{-\beta E}$. Although the relation between the biased and unbiased probability densities is straightforward:

$$\begin{aligned} p_i^b(q) &= \frac{\int \mathrm{d}\Gamma\, \delta(Q(\boldsymbol{R}^{N_n}) - q)\, e^{-\beta(E+V_i^b(q))}}{\int \mathrm{d}\Gamma\, e^{-\beta(E+V_i^b(q))}} \\ &= \frac{\int \mathrm{d}\Gamma\, e^{-\beta E}}{\int \mathrm{d}\Gamma\, e^{-\beta(E+V_i^b(q))}}\, e^{-\beta V_i^b(q)}\, p(q), \end{aligned} \tag{2.46}$$

the reconstruction of the total unbiased probability density from the separate US simulations (covering different CV ranges) is not. By means of the weighted histogram analysis method (WHAM),[112–114] the total unbiased probability density can be reconstructed from a linear combination of the individual unbiased probability densities. An optimal estimate of the total probability density is obtained by minimising the variance of the probability density,[94] which yields the following set of equations:

$$\begin{cases} p(q) &= \dfrac{\sum_{i=1}^{M} h_i(q)}{\sum_{i=1}^{M} n_i f_i\, e^{-\beta V_i^b(q)}} \\ f_i^{-1} &= \displaystyle\int \mathrm{d}q\, p(q) e^{-\beta V_i^b(q)}\,, \\ 1 &= \displaystyle\int \mathrm{d}q\, p(q) \end{cases} \tag{2.47}$$

with M the number of US simulations, $h_i(q)$ the histogram counts of q from simulation i, and n_i the number of samples from simulation i. To solve this set of non-linear equations, a self-consistent iterative procedure can be used, starting from an initial guess of the constants f_i. A proper connection between the individual probability densities can only be ensured if there is sufficient overlap between the probability densities of adjacent CV regions. Therefore, the position $q_{i,0}$ and the force constant κ_i of the umbrellas must be chosen appropriately to attain the required overlap. Through the automated procedure proposed in Ref. 115, these choices can also be iteratively refined to systematically converge the FES.

Besides umbrella sampling, there exist many other enhanced sampling methods, such as metadynamics,[116] variationally enhanced sampling,[117] thermodynamic integration,[94, 118] replica exchange,[119] and transition path sampling.[120] Except for the last two methods, all these techniques also rely on CVs to explore the FES. A major advantage of the US method is its highly efficient parallelisation, given that all umbrellas can be simulated independently from one another. In the particular context of nanoporous materials, Ref. 121 identified US as one of the most computationally efficient methods to construct a FES.

2.2.6 Application to adsorption in nanoporous materials

To illustrate the simulation techniques discussed in the previous paragraphs, we consider the adsorption of CO_2 in two different zeolite topologies. Both of these case studies were initiated by the experimental results obtained by our collaborators from the KU Leuven (the group of prof. Ivo Vankelecom and prof. Michiel Dusselier), who succeeded at successfully synthesising zeolite-filled mixed-matrix membranes (MMMs) with an unprecedented gas separation performance. For Na-SSZ-39, an AEI-type zeolite in which the charge deficit of the aluminium substitutions is compensated by sodium ions (Figure 2.7), the CO_2–CH_4 selectivity and the CO_2 permeability reach values of $>$450 and $\sim$8280 Barrer, respectively, for an MMM with 50 wt% Na-SSZ-39, as detailed in **Paper VI**. In comparison with the empty polymeric membrane (Matrimid 5218), these values represent a $\sim$10-fold and $\sim$1000-fold increase of the selectivity and permeability, respectively, thereby outperforming existing polymer-based membranes and even most zeolite-only membranes.

The adsorption properties of the zeolite filler play a decisive role in the gas-separation performance of the MMM. In addition to experimental measurements on the zeolite crystal, simulations can provide a molecular-level insight into the adsorption phenomena. From GCMC simulations, both the single-gas isotherms of CO_2 and CH_4 can be obtained as well as the mixed-gas

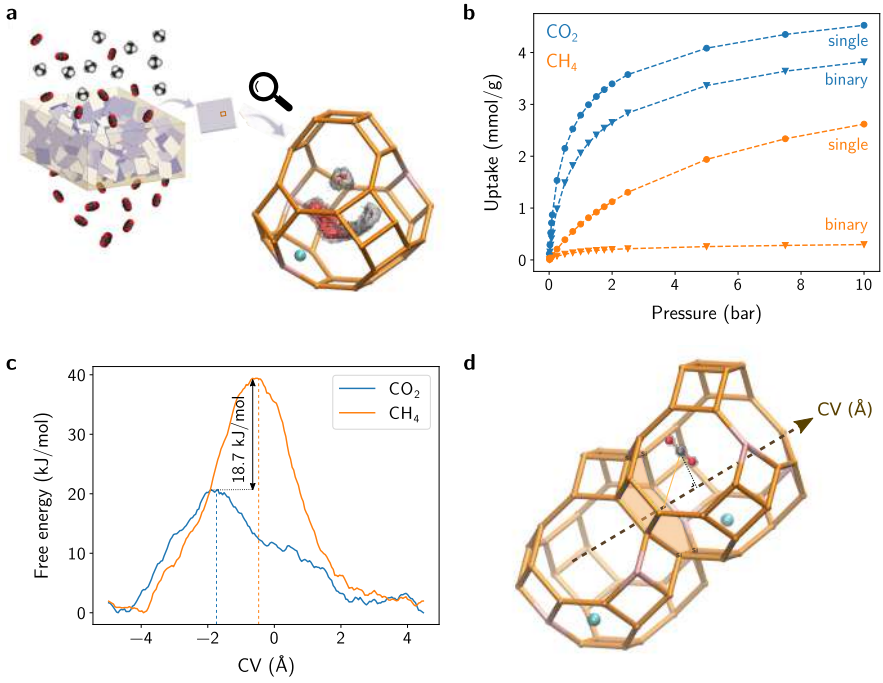

Figure 2.7: **a** Schematic representation of the molecular sieving of CH_4 and the CO_2 permeation through an Na-SSZ-39 MMM with a quasi-continuous phase of zeolite platelets. The zoom inset shows two density isosurfaces in an Na-SSZ-39 supercage, obtained from GCMC simulations at 298 K and 0.1 bar (red) or 1 bar (gray). Al sites are coloured pink, Na^+ ions are cyan, and O atoms are omitted. **b** Single-gas and equimolar binary-gas CO_2/CH_4 adsorption isotherms of Na-SSZ-39 at 298 K obtained from GCMC simulations. **c** Free energy profiles of a single CO_2 or CH_4 molecule diffusing through an eight-membered ring in Na-SSZ-39, obtained from umbrella sampling simulations at 298 K. **d** Illustration of the CV used to construct the free energy profiles in pane c. Figures adapted from Ref. [19] with permission of the American Association for the Advancement of Science.

isotherms. Using a simple force field parametrisation of the non-bonding electrostatic and van der Waals interactions of the zeolite and the adsorbates, a good qualitative agreement can be found between the experimental and computational single-gas adsorption isotherms. Due to the strong electrostatic interaction between the sodium ions and CO_2, the AEI zeolite exhibits a much higher CO_2 uptake than CH_4 uptake. At low pressures, the sodium ions are the preferential CO_2 adsorption sites, as shown in Figure 2.7a. When both CO_2 and CH_4 are adsorbed simultaneously from an equimolar gas mixture,

the CH_4 uptake drastically reduces, while the CO_2 uptake only shows a modest decrease (Figure 2.7b), so that the zeolite possesses a good CO_2–CH_4 selectivity.

Besides the favourable interaction between CO_2 and the zeolite framework, as confirmed by the experimental and computational adsorption enthalpies (-35.1 and -31.6 kJ/mol, respectively), the adsorption behaviour of CO_2 and CH_4 in Na-SSZ-39 is also affected by the molecular sieving function of the zeolite's pore windows. To probe the diffusion of both molecules through an eight-membered ring connecting two zeolite cages, the free energy barrier along this diffusion path can be determined using umbrella sampling simulations. In each umbrella, the CV restricts the adsorbate to move in a plane parallel to the eight-membered ring, as shown in Figure 2.7d. In contrast with the GCMC simulations, these enhanced sampling simulations are performed at a higher level of theory, using a first-principles description of the PES with the PBE-D3(BJ)[65, 122, 123] functional. For CO_2, a free energy barrier of 20.7 kJ/mol is obtained (Figure 2.7c), whereas for CH_4 the free energy barrier is about twice as high (39.4 kJ/mol). By relying on transition state theory, the free energy profiles also allow to compute the associated rate constants, which are proportional to the self-diffusion coefficients:[124]

$$\frac{D_{\mathrm{CO2}}}{D_{\mathrm{CH4}}} \approx \frac{k_{\mathrm{CO2}}}{k_{\mathrm{CH4}}} = \frac{A_{\mathrm{CO2}}\, e^{-\beta F_{\mathrm{CO2}}(q^\ddagger)}}{\int_{-\infty}^{q^\ddagger} \mathrm{d}q\, e^{-\beta F_{\mathrm{CO2}}(q)}} \frac{\int_{-\infty}^{q^\ddagger} \mathrm{d}q\, e^{-\beta F_{\mathrm{CH4}}(q)}}{A_{\mathrm{CH4}}\, e^{-\beta F_{\mathrm{CH4}}(q^\ddagger)}} \approx 1587, \tag{2.48}$$

with $q^\ddagger$ the transition state and

$$A = \sqrt{\frac{k_B T}{2\pi}} \left\langle \sqrt{\sum_{\alpha=1}^{N} \sum_{i=1}^{3} \frac{1}{M_\alpha} \left(\frac{\partial q}{\partial R_{\alpha,i}} \right)^2} \right\rangle_{q=q^\ddagger}. \tag{2.49}$$

As a consequence, CH_4 permeates more difficultly through the AEI zeolite in comparison with CO_2, because of its larger kinetic diameter.

In a second case study, outlined in **Paper XI**, the AEI zeolite is replaced by the CHA zeolite, which is already commercially available. Given the exceptional performance of Na-SSZ-39 with one sodium atom in every cage, the influence of different sodium loadings, or equivalently Si/Al ratios, is investigated for the CHA zeolite Na-SSZ-13. The resulting CO_2 permeability and CO_2–CH_4 selectivity are shown in Figure 2.8a for an MMM with 50 wt% Na-SSZ-13 and Si/Al ratios of 2, 5, 10, or $+\infty$ (*i.e.* pure Si-CHA) or equivalently about 4, 2, 1, or 0 sodium atoms in every cage. The best performing MMM is obtained

with a single sodium atom in every cage (*i.e.* Na-CHA-10), yielding a CO_2–CH_4 selectivity >230 and a CO_2 permeability >2100 Barrer. With decreasing sodium content, a lower selectivity is observed, whereas an increasing sodium content reduces both the selectivity and permeability.

To explain the selectivity and permeability trends, we can again rely on GCMC and umbrella sampling simulations, just as for the AEI zeolite. However, given the more challenging description of the zeolites with a low Si/Al ratio, the classical force field description is replaced by an MLP to also perform GCMC simulations with a first-principles accuracy. The largest CO_2 uptake is obtained for a Si/Al ratio of 11, which can be rationalised by the trade-off between an increasing heat of adsorption and a decreasing pore volume as a function of lower Si/Al ratios (Figure 2.8b and c). Furthermore, the number of viable gas diffusion pathways also decreases when a cage contains more than two sodium atoms, as the diffusion through some of the eight-membered rings is hindered by the presence of the sodium atoms. The strong CO_2–Na^+ interaction also results in an overall increase of the free energy barrier for the diffusion between cages with a higher sodium content, as shown in Figure 2.8d. Although the umbrella sampling simulations are performed with a similar one-dimensional CV as for the AEI zeolite, three-dimensional free energy profiles are reported to ease the interpretation of the results. To transform the one-dimensional free energy profile $F(q)$ into a three-dimensional free energy profile $F(x,y,z)$, the following formula can be used:

$$F(x,y,z) = -\frac{1}{\beta}\ln\left[\int \mathrm{d}q \;\; p_b(x,y,z|q)\, e^{-\beta F(q)}\right] + C, \qquad (2.50)$$

with C a constant and $p_b(x,y,z|q)$ the conditional probability that the three-dimensional CV takes the value (x,y,z) in a simulation with a time-independent bias when the one-dimensional CV has a value q. Therefore, it suffices to keep track of the Cartesian coordinates of the CO_2 molecule during the umbrella sampling simulations to expand the one-dimensional free energy profile into a three-dimensional free energy profile.

For a Si/Al ratio of 11, the regions of low free energy are located near the sodium ions, so that a CO_2 molecule is more likely to reside in this region. Given the energy penalty associated with leaving the proximity of a sodium ion, the preferential diffusion pathways connect sodium ions along eight-membered rings, which is always possible at a Si/Al ratio of 11. For lower Si/Al ratios, the strong CO_2 affinity of the sodium ions reduces the mobility of the molecules, as the diffusion pathways with a low free energy barrier are eliminated, which explains the distinctive decrease in permeability for the CHA-MMMs.

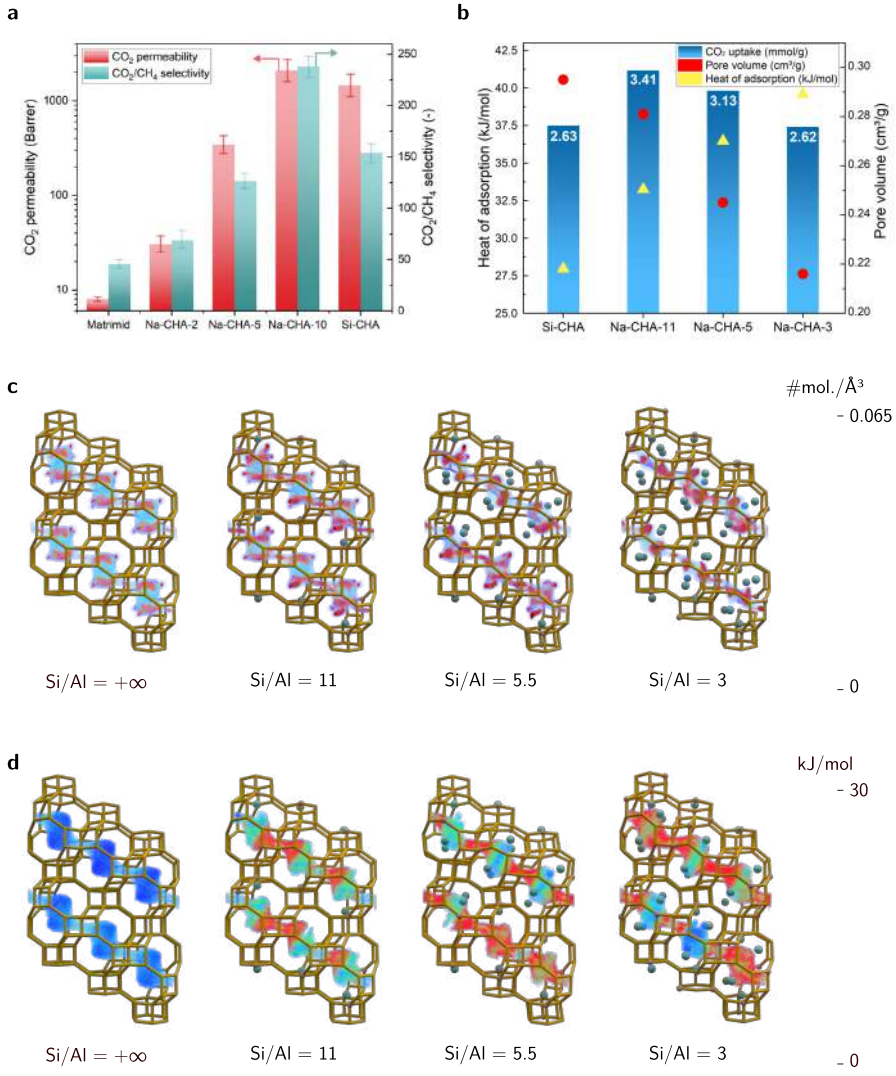

Figure 2.8: **a** CO_2 permeability and CO_2–CH_4 selectivity of a 50 wt% Na-SSZ-13 MMM at 298 K and 2 bar (for an equimolar CO_2/CH_4 gas mixture). **b** CO_2 gas uptake, heat of adsorption, and pore volume of Na-SSZ-13 obtained from GCMC simulations at 298 K and 1 bar. **c** CO_2 density in Na-SSZ-13 obtained from GCMC simulations at 298 K and 1 bar. **d** Free energy of a single CO_2 molecule in Na-SSZ-13 obtained from umbrella sampling simulations at 298 K.

In contrast to conventional gas separation technologies, which are often very energy-intensive, MMMs offer a more sustainable alternative for applications such as carbon capture and natural gas or biogas purification due to their low energy consumption.[125] As demonstrated for the CHA-MMMs, the selectivity and permeability of the zeolite fillers can be tuned by changing the Si/Al ratio of the structure. Furthermore, also different charge-compensating ions can be used to optimise the zeolite's performance for specific separations. By embedding these zeolite particles in a flexible polymer matrix, an easy processable material is obtained which holds great promise for large-scale industrial applications, especially given the commercial availability of both CHA and the Matrimid polymer.

2.3 Modelling nuclear quantum effects

In most atomistic simulations, the Born-Oppenheimer approximation (see Section 2.1.2) is used to separate the electronic and nuclear degrees of freedom from one another. By assuming a continuous adaptation of the electrons to changes in the nuclear coordinates, the nuclear motion can be approximated by a sequence of configurations on the electronic PES. In regular MD (and also MC) simulations, an additional approximation is made by treating the atomic nuclei as classical particles when sampling the PES, thus completely neglecting their quantum mechanical nature. Especially for lightweight atoms (such as hydrogen) at low temperatures, high pressures, or high densities, the classical approximation is unable to provide an accurate description of the molecular system. Therefore, a proper modelling of these systems requires the inclusion of nuclear quantum effects (NQEs), which give rise to, for instance, a quantisation of the energy levels (*i.e.* rotational and vibrational energy levels), the presence of zero-point energy (ZPE),[c] the possibility of tunnelling,[d] and isotope effects.[126] These NQEs can affect for instance the stability of crystalline polymorphs,[127] result in the delocalisation and tunnelling of protons in enzymes,[128] yield a proper temperature dependence for the heat capacity of crystals,[93] or improve the calculation of reaction rates.[129] Even at higher temperatures, NQEs can still play an important role, as the ZPE of many chemical bonds exceeds the thermal energy in a wide temperature range. In water, for example, an O–H stretch (with a frequency $\omega \approx 3600\ \mathrm{cm}^{-1}$) possesses a ZPE ($\sim \frac{\hbar\omega}{2}$) of about 21

c. The ZPE is the minimal energy present in a quantum mechanical system, even at 0 K.

d. The non-zero probability of a particle to pass through a potential energy barrier is referred to as tunnelling. Classically, the particle is unable to cross the barrier as it does not possess sufficient energy to surmount the barrier.

kJ/mol, whereas the thermal energy ($\sim k_B T$) at room temperature is only of the order of 2.5 kJ/mol.[58]

2.3.1 Static simulations

In static simulations, the harmonic approximation of the PES around equilibrium configurations (see Section 2.2.1) allows to exploit the properties of quantum harmonic oscillators. From the analytical solutions of the Schrödinger equation, one can easily derive the thermodynamic properties of a set of quantum harmonic oscillators, including for instance the isochoric heat capacity[e]

$$C_V = k_B \sum_{\omega} \frac{(\beta\hbar\omega)^2 \, e^{-\beta\hbar\omega}}{(1 - e^{-\beta\hbar\omega})^2}. \tag{2.52}$$

In the high-temperature limit for $\hbar\omega \ll k_B T$, the classical Dulong-Petit law is retrieved,[130, 131] yielding a constant value of $N_\omega k_B$, with N_ω the number of harmonic oscillators or, equivalently, the number of degrees of freedom.

When information beyond the harmonic approximation of the PES is required, for instance to calculate the energy levels of a rotational energy barrier, other simulation techniques are required. In **Paper IX**, the Schrödinger equation was solved numerically to determine the rotational energy levels of a methyl top (*i.e.* a $-CH_3$ rotor) in ZIF-8. In the presence of guest molecules, ZIF-8 exhibits a so-called dynamic gate opening effect, in which the 2-methylimidazolate linkers of the framework change their inclination and thus close or open the pore windows of the framework (Figures 1.3 and 2.9a). To monitor this transition, our experimental collaborators from Oxford University (the group of prof. J.-C. Tan) measured the structural changes of ZIF-8 during the adsorption of argon and nitrogen gas using inelastic neutron scattering (INS) spectra and neutron powder diffraction (NPD) patterns. These measurements were performed at 3 K and complemented by adsorption isotherms measured at 77 K. Near absolute zero, the methyl rotors possess insufficient thermal energy to surmount the rotational energy barrier, which excludes the classical rotational motion. The methyl top can however still rotate through the quantum mechanism of tunnelling. At this low temperature, only the librational ground state of the methyl rotor is populated, which consists of a symmetric singlet state $|A\rangle$ and a

e. The heat capacity is defined as the amount of heat required to increase the temperature of the system by one unit:

$$C = \frac{\delta Q}{\mathrm{d}T}. \tag{2.51}$$

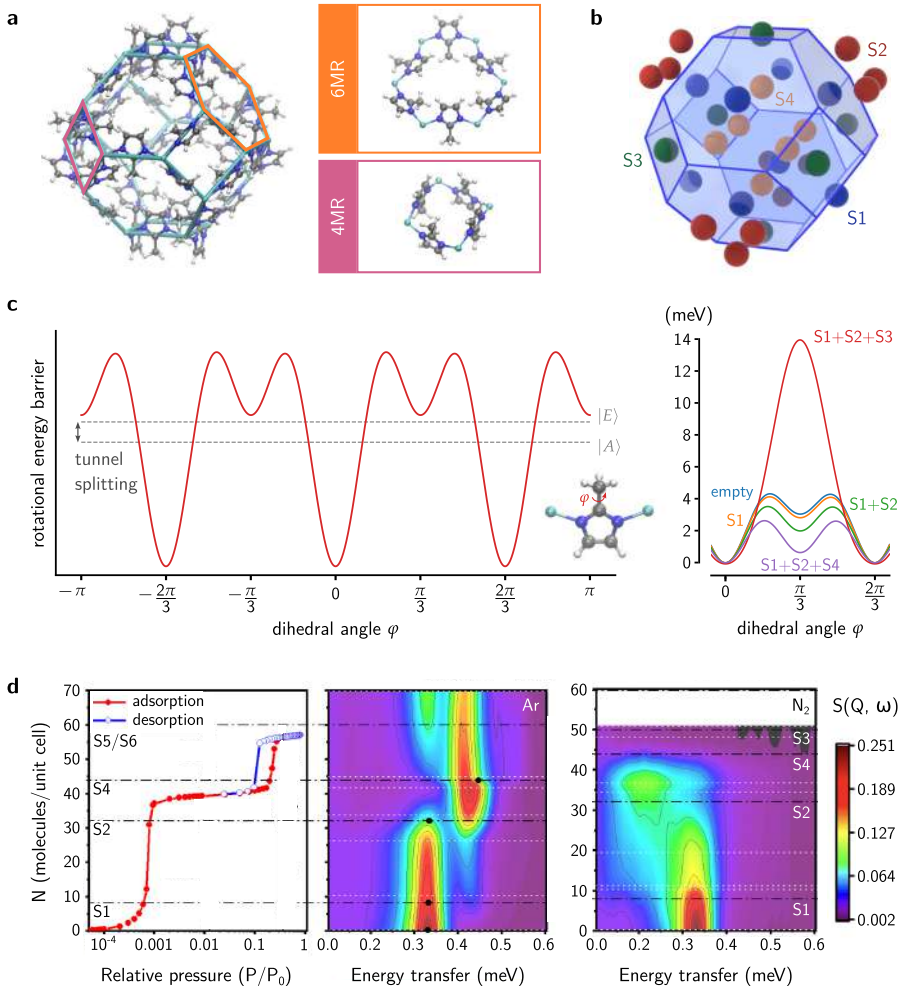

Figure 2.9: **a** Sodalite cage of a ZIF-8 unit cell with its constituent six-membered rings (6MRs) and four-membered rings (4MRs). **b** Four (out of six) adsorption sites for argon and nitrogen in ZIF-8, as identified in Ref. [132]. **c** Schematic representation (left) of the rotational energy barrier of a methyl top in ZIF-8, with a threefold symmetry. The lowest energy levels, corresponding to a symmetric singlet state $|A\rangle$ and an antisymmetric doublet state $|E\rangle$, are indicated with a dashed line. The right pane shows the rotational energy barrier for a sequential filling of ZIF-8 with argon according to the adsorption sites in pane b. For every adsorption site, all equivalent adsorption positions are occupied simultaneously. **d** Adsorption isotherm of argon measured at 77 K and interpolated INS spectra of both argon and nitrogen measured at 3 K. The ZIF-8 powder was dosed with gases at 77 K for the INS experiments. Panes b and d are adapted from Ref. [133] with permission of the American Physical Society.

twofold degenerate antisymmetric doublet state $|E\rangle$, in agreement with the C_3 symmetry of the rotor (Figure 2.9c).[134, 135] With INS, the energy difference between these two states, the so-called tunnel splitting, can be measured for different gas loadings in ZIF-8 (Figure 2.9d). Computationally, the rotational energy barrier of a methyl top can be calculated using a first-principles method such as DFT. Subsequently, this barrier can be used to numerically solve the Schrödinger equation of the methyl rotor to obtain the rotational energy levels and infer the tunnel splitting.

For both argon and nitrogen gas in ZIF-8, a good qualitative agreement is obtained between experiment and simulation. By sequentially filling the known adsorption sites within ZIF-8 (Figure 2.9b), the simulations reveal a successive occupation of the S1, S2, and S4 sites for both gasses. When more gas molecules are adsorbed in ZIF-8, the argon molecules occupy the S5 and S6 sites of the framework, without any adsorption on the S3 sites, as the tunnel splitting would disappear in that case due to a substantial increase in the rotational energy barrier (Figure 2.9c). For nitrogen, on the contrary, the S3 sites are occupied once the S4 sites are filled, as the scattering signal of the tunnel splitting disappears in the INS measurements (Figure 2.9d). This computationally predicted filling sequence is also in good agreement with the changes in the experimental adsorption isotherms as a function of the gas loading. In this way, quantum rotational tunnelling can provide important complementary insights into the adsorption behaviour in certain nanoporous materials in combination with adsorption isotherms.

2.3.2 Path integral molecular dynamics

To account for NQEs at finite temperatures and pressures, while also including the anharmonicities of the PES, path integral molecular dynamics (PIMD) simulations can be used. The path integral formulation of quantum mechanics was first introduced by Richard Feynman in 1948 as an alternative but equivalent description of the time evolution of a wave function $\psi(\boldsymbol{r}, t)$.[136] Instead of relying on the Schrödinger equation to determine the time evolution of $\psi(\boldsymbol{r}, t)$ to a new state $\psi(\boldsymbol{r}', t')$ through the operator $e^{-\frac{i}{\hbar}\hat{H}(t'-t)}$, this time evolution can also be expressed as a sum over all the possible paths starting at time t in $\boldsymbol{r}$ and ending at time t' in $\boldsymbol{r}'$, with every path weighted by a phase factor which equals the classical action of the path (in units of $\hbar$).

Similarly, this concept can also be applied to the Boltzmann factor, which is given by $e^{-\beta\hat{H}}$ in a quantum description. By introducing an imaginary time $t = -i\beta\hbar$, the time propagator $e^{-\frac{i}{\hbar}\hat{H}t}$ can be transformed into $e^{-\beta\hat{H}}$, which is therefore also called the imaginary-time propagator. Using a Trotter

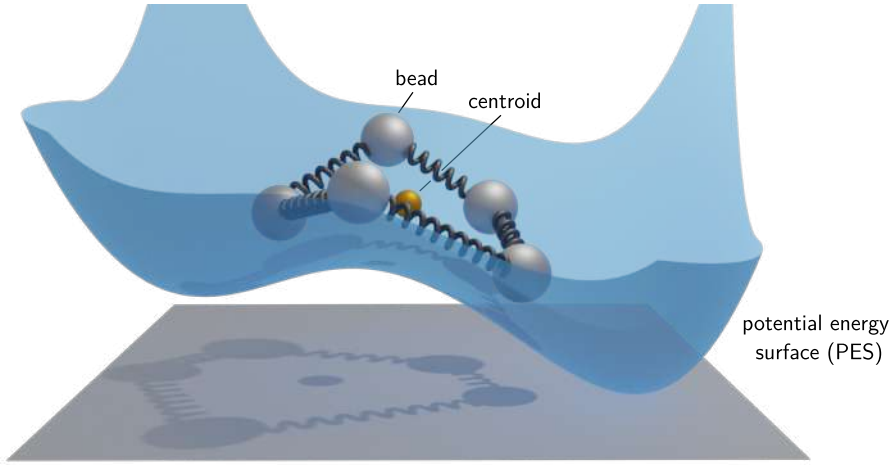

Figure 2.10: Schematic representation of a path integral ring polymer with five beads on a PES. The quasi-classical path centroid (Eq. (2.60)) is indicated in yellow. Figure reproduced from Ref. [137] with permission of the American Chemical Society.

expansion, the Boltzmann factor can be rewritten as

$$e^{-\beta\hat{H}} = \lim_{P\to\infty}\left[e^{-\frac{\beta}{2P}\hat{V}}e^{-\frac{\beta}{P}\hat{T}_n}e^{-\frac{\beta}{2P}\hat{V}}\right]^P, \tag{2.53}$$

with $\hat{T}_n$ the nuclear kinetic energy and $\hat{V}$ the ground-state PES of the nuclei. Through the insertion of completeness relations between all the exponential factors in Eq. (2.53),[95] a statistical weight $e^{-\beta H_P} = e^{-\beta(H_P^0+V_P)}$ is obtained, with

$$H_P^0 = \sum_{k=1}^{P}\sum_{\alpha=1}^{N_n}\left[\frac{\boldsymbol{P}_\alpha^{(k)2}}{2M_\alpha} + \frac{1}{2}M_\alpha\omega_P^2\left(\boldsymbol{R}_\alpha^{(k+1)} - \boldsymbol{R}_\alpha^{(k)}\right)^2\right] \tag{2.54}$$

$$V_P = \frac{1}{P}\sum_{k=1}^{P} V(\boldsymbol{R}_1^{(k)},\ldots,\boldsymbol{R}_{N_n}^{(k)}), \tag{2.55}$$

where $\omega_P = \frac{\sqrt{P}}{\beta\hbar}$ and $\boldsymbol{R}_\alpha^{(P+1)} = \boldsymbol{R}_\alpha^{(1)}$. Therefore, the quantum statistical weight $e^{-\beta\hat{H}}$ can be replaced by a classical Boltzmann factor $e^{-\beta H_P}$, with a classical Hamiltonian H_P, which describes a ring polymer with P beads that interact with one another through a harmonic nearest-neighbour coupling with angular frequency ω_P (Figure 2.10). This so-called classical isomorphism

thus allows to describe the quantum nature of the nuclei by means of a classical system in an extended phase space, which is exploited in PIMD simulations. Given that this classical isomorphism only replicates the appropriate quantum statistics of molecular configurations, imaginary-time PIMD only allows for the calculation of static properties, as the sampling dynamics remain classical and thus neglect the quantum mechanical time evolution of the system.[126, 138] A more elaborate mathematical derivation of the path integral formalism can be found in the Supporting Information of **Paper I**.

In the limit of an infinite number of beads ($P \to \infty$), exact quantum statistics are obtained. PIMD simulations are of course limited to a finite a number of beads, for which a converged value strongly depends on the property of interest and the thermodynamic conditions. For most properties at room temperature, a total of 16 to 64 beads is usually sufficient. In comparison with a regular MD simulation, the computational cost of a PIMD simulation is P times higher, as P replicas of the system are simulated in parallel. To reduce this computational cost, several acceleration techniques have been devised to lower the number of beads.[126] The harmonic NQEs can for instance be mimicked by a coloured-noise thermostat,[139, 140] which uses the generalised Langevin equation (GLE) to impose a frequency-dependent effective temperature for every harmonic mode in accordance with their quantum statistical weight. A more accurate factorisation of the Boltzmann weight $e^{-\beta\hat{H}}$ instead of the second-order Trotter factorisation (Eq. (2.53)) can also improve the bead convergence. An example of such a high-order path integral method is the fourth-order Suzuki-Chin method, which approximates the Boltzmann weight as

$$e^{-\beta\hat{H}} = \left[e^{-\frac{\beta}{P}\hat{H}}\right]^P = \left[e^{-\frac{\beta}{P}\frac{\hat{V}_e}{3}} e^{-\frac{\beta}{P}\hat{T}_n} e^{-\frac{\beta}{P}\frac{4\hat{V}_o}{3}} e^{-\frac{\beta}{P}\hat{T}_n} e^{-\frac{\beta}{P}\frac{\hat{V}_e}{3}}\right]^{\frac{P}{2}} + \mathcal{O}\left(P^{-5}\right), \tag{2.56}$$

with

$$\hat{V}_e = \hat{V} + \frac{\alpha}{6}\left(\frac{\beta}{P}\right)^2 [\hat{V}, [\hat{T}_n, \hat{V}]] \quad \text{and} \quad \hat{V}_o = \hat{V} + \frac{1-\alpha}{12}\left(\frac{\beta}{P}\right)^2 [\hat{V}, [\hat{T}_n, \hat{V}]], \tag{2.57}$$

where $\hat{V}_e$ represents the potential energy of the even beads, $\hat{V}_o$ the potential energy of the odd beads, $[\hat{T}_n, \hat{V}]$ the commutator between the nuclear kinetic energy and the ground-state PES of the nuclei, and $\alpha \in [0, 1]$ is an arbitrary parameter. In the classical isomorphism, the potential of the ring polymer is

then given by

$$V_P = \frac{1}{P}\sum_{k=1}^{\frac{P}{2}}\left[\frac{2}{3}\,V(\boldsymbol{R}_1^{(2k-1)},\ldots,\boldsymbol{R}_{N_n}^{(2k-1)}) + \frac{\alpha}{9\omega_P^2}\sum_{\mu=1}^{N_n}\frac{\left|\boldsymbol{F}_\mu^{(2k-1)}\right|^2}{M_\mu} + \right.$$
$$\left.\frac{4}{3}\,V(\boldsymbol{R}_1^{(2k)},\ldots,\boldsymbol{R}_{N_n}^{(2k)}) + \frac{1-\alpha}{9\omega_P^2}\sum_{\mu=1}^{N_n}\frac{\left|\boldsymbol{F}_\mu^{(2k)}\right|^2}{M_\mu}\right], \qquad (2.58)$$

with $\boldsymbol{F}_\mu^{(k)} = -\frac{\partial V(\boldsymbol{R}_1^{(k)},\ldots,\boldsymbol{R}_{N_n}^{(k)})}{\partial \boldsymbol{R}_\mu^{(k)}}$ the force on bead k of atom μ. These high-order path integrals were used in **Paper II**, which is further discussed in Chapter 3.

Similarly to classical MD simulations, the electronic PES in PIMD simulations can be described either quantum mechanically, using first-principles methods, or classically, using force fields. However, empirical force fields that are parametrised on experimental data are not suitable for PIMD simulations, as the inherent presence of NQEs in experimental measurements implies an effective inclusion of NQEs in the force field parameters (up to a certain extent), which leads to a double counting of NQEs in PIMD simulations.[83] Therefore, only first-principles-based force fields can be used or empirical force fields which have been refitted for PIMD simulations, such as q-TIP4P/f[83].

2.3.3 Ring polymer molecular dynamics

As mentioned in the previous section, imaginary-time PIMD simulations can only be used to calculate time-independent equilibrium properties, as it is merely a sampling technique for the quantum Boltzmann distribution $e^{-\beta\hat{H}}$. To obtain quantum dynamics, the time propagator $e^{-\frac{i}{\hbar}\hat{H}t}$ should be taken into account, either by solving the time-dependent Schrödinger equation or by means of real-time Feynman path integrals. However, in the limit of short-time scales, the classical ring polymer isomorphism can also provide a heuristic method to approximate quantum dynamics. In particular for condensed phase systems, which often display a rapid quantum decoherence, these approximations have already been proven to yield reasonable results.[126, 141, 142] Using the ring polymer Hamiltonian introduced in the previous section, it is therefore also possible to calculate real-time correlation functions, by means of the so-called Kubo-transformed correlation function[141, 142]

$$c_{AB}(t) = \frac{1}{\beta}\frac{\int_0^\beta \mathrm{d}\lambda\ \mathrm{tr}\left[e^{-(\beta-\lambda)\hat{H}}\hat{A}(0)e^{-\lambda\hat{H}}\hat{B}(t)\right]}{\mathrm{tr}\left[e^{-\beta\hat{H}}\right]}, \qquad (2.59)$$

with $\mathrm{tr}[\cdot]$ the trace of the operator. This method is referred to as ring polymer molecular dynamics (RPMD) and allows for instance to compute diffusion coefficients, reaction rates, and infrared spectra. In the limit of high temperatures ($\beta \to 0$), zero time ($t \to 0$), and a harmonic potential, RPMD can be shown to reproduce the exact quantum correlation function for both linear and non-linear operators.[138] In **Paper VIII**, the RPMD method was used to calculate quantum rate constants, as discussed in Section 3.2.2.

Besides RPMD, another frequently used ring polymer approximation to quantum dynamics is centroid molecular dynamics (CMD),[143, 144] in which the so-called path centroid (Figure 2.10), defined as the geometrical average of all the ring polymer beads

$$\boldsymbol{R}_\alpha^{(c)} = \frac{1}{P} \sum_{\alpha=1}^{P} \boldsymbol{R}_\alpha^{(k)}, \tag{2.60}$$

is propagated on an effective centroid potential. Similarly to RPMD, CMD satisfies the same limits for the exact quantum correlation functions, but only for linear operators. Heuristically, both methods could therefore be regarded as interpolating between these limits, while conserving the quantum Boltzmann distribution.[138] Each method has its own distinct advantages and disadvantages. CMD predicts for instance an infrared spectrum of liquid water that is in close agreement with experimental results at room temperature.[145] At lower temperatures, however, the so-called curvature problem results in an artificial redshift and broadening of the spectral peaks, because an angular spread of the ring polymer (*e.g.* for a delocalised proton) artificially shortens the centroid bond length and thus softens the bond stretch mode.[138, 146, 147] RPMD, by contrast, can accurately estimate the rates of tunnelling reactions,[148] but produces spurious resonances in the infrared spectra due to a coupling with internal ring polymer modes. To mitigate the spurious resonances within RPMD, thermostatted RPMD (TRPMD) can be used, which thermostats the internal ring polymer modes to dampen the resonances and conceptually holds the middle ground between CMD and RPMD.[146]

3

Nuclear Quantum Effects in Metal–Organic Frameworks and Zeolites

Nature isn't classical, dammit, and if
you want to make a simulation of nature,
you'd better make it quantum mechanical.

Richard P. Feynman[149] (1918–1988)

With the use of the modelling techniques introduced in the previous chapter, this chapter discusses the importance of nuclear quantum effects (NQEs) in modelling nanoporous materials. In Section 2.3.1, a nuclear quantum description was already applied to the methyl rotors in ZIF-8 to calculate the rotational tunnelling splitting near absolute zero. In the following sections, the influence of NQEs at finite temperatures is considered for different properties and materials. In Section 3.1, the structural and thermal properties of the archetypal MOF-5 are discussed, both in the absence and presence of guest molecules. Besides NQEs, also the role played by anharmonicities is assessed. In Section 3.2, the concept of quantum free energy profiles is introduced together with an elegant procedure to construct these profiles, as proposed in **Paper VII**. After illustrating the concept for molecular proton transfer reactions, it is applied to the proton hopping of a Brønsted acid site (BAS) in the chabazite zeolite.

3.1 Interplay between NQEs and anharmonicities

As mentioned in Section 2.3.2, PIMD simulations can be used to model NQEs and anharmonicities at finite temperatures and pressures. To assess their importance in predicting the properties of MOFs, the archetypal MOF-5 framework was simulated with both classical and quantum nuclei in **Paper I** and **Paper II**, in collaboration with the group of prof. M. Ceriotti at the EPFL. The role of anharmonicities is evaluated by considering both a static (harmonic) and dynamic sampling of the PES. Furthermore, the anharmonic description of the PES itself is also analysed by considering two different force field parametrisations: (i) a 'harmonic' force field with quadratic bond and bend potentials and (ii) an 'anharmonic' force field with higher-order polynomial bond and bend potentials.

Within a temperature range of 100–500 K, the average bond lengths of the framework are virtually unaffected by the inclusion of NQEs. The bond length fluctuations do however increase, with a more substantial increase for bonds characterised by a high frequency, as the lightweight atoms involved in these bonds are more susceptible to NQEs. The temperature dependence of these bond fluctuations is also modified by NQEs, due to the dominant contribution of the ZPE. The high-frequency C–H stretch of the BDC linkers in MOF-5 ($\omega > 3000$ cm^{-1}), for instance, is observed to be more or less temperature independent below 500 K, due to its high ZPE ($\approx \frac{\hbar\omega}{2}$) in comparison with the thermal energy $k_B T$. Therefore, the C–H stretch is not yet thermally active within this temperature range, in contrast to the classical description.

The volume of the framework is affected by both anharmonicities and NQEs, as shown in Figure 3.1a. When adopting an anharmonic parametrisation of the bonds for the PES, larger equilibrium bond lengths are obtained as higher vibrational energy levels are occupied (Figure 3.1b). The additional increase in volume upon inclusion of NQEs can be related to the large volume-dependent ZPE of the structure. For an anharmonic PES, this effect is perceivable over a wide volume range and as a consequence, also over a wide temperature range, since the increase in ZPE is about one order of magnitude larger than the corresponding thermal energy (*i.e.* 41.2 kJ/mol versus 4 kJ/mol). For a PES with harmonic bond contributions, the ZPE effect remains limited to the lowest temperatures. The volumetric thermal expansion coefficient of MOF-5, defined as the relative change in volume with respect to temperature at constant pressure:

$$\alpha_V = \frac{1}{V}\left(\frac{\partial V}{\partial T}\right)_P, \tag{3.1}$$

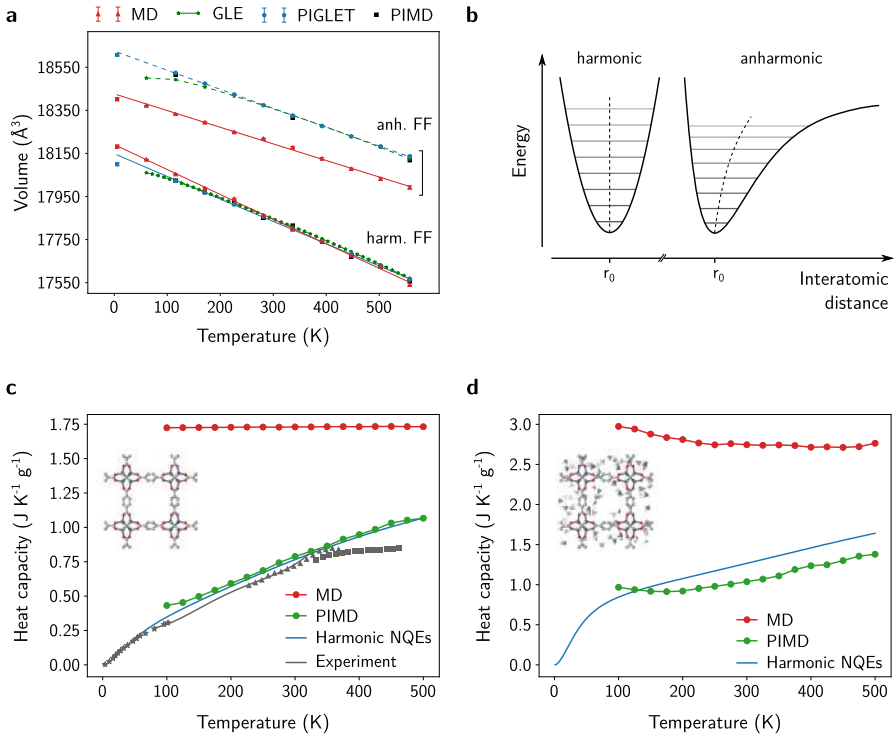

Figure 3.1: **a** Volume of MOF-5 as a function of temperature, calculated with (PI)MD simulations using the harmonic ('harm. FF', bottom curves) and anharmonic ('anh. FF', top curves) force field of MOF-5. The data points at 0 K were obtained from geometry optimisations. **b** Schematic representation of the quantum mechanical energy levels of a harmonic potential (left) and an anharmonic Morse potential (right). The expectation value of the position is represented by the dashed line. **c** Heat capacity of MOF-5 as a function of temperature, calculated with (PI)MD simulations and a harmonic approximation (Eq. (2.52)) or measured experimentally (indicated with squares,[150] stars,[151] and triangles[152]). **d** Heat capacity of MOF-5 loaded with 100 methane molecules as a function of temperature, calculated with (PI)MD simulations and a harmonic approximation (Eq. (2.52)). Panes a and b are adapted from Ref. [153] with permission of the American Institute of Physics. Panes c and d are adapted from Ref. [93] with permission of the American Chemical Society.

is primarily determined by the description of the anharmonicities. Only when the PES properly accounts for anharmonicities, one retrieves a thermal expansion coefficient in line with experimental measurements. The inclusion of NQEs merely plays a secondary role.

In view of the use of MOFs in gas storage and gas separation applications, the response of the MOF to thermal fluctuations induced by the adsorption and desorption processes constitutes an elemental material property.[154] To probe the ability of a material to cope with thermal fluctuations, the heat capacity, as defined in Section 2.3.1, can be used. Classical MD simulations yield a nearly constant heat capacity (Figure 3.1c), in line with the Dulong-Petit law, which predicts a heat capacity contribution of k_B for every degree of freedom. A proper temperature dependence of the heat capacity is obtained both with PIMD simulations and a simple harmonic description of the NQEs (as introduced in Section 2.3.1). As both quantum descriptions agree well with the experimental results, the influence of an adequate anharmonic sampling is small for the heat capacity of the MOF framework. Therefore, the use of the simple harmonic approximation is preferred for this purpose, as the PIMD simulations require at least 64 beads to converge the heat capacity, even in combination with a fourth-order Suzuki-Chin path integral method.

When the MOF-5 framework is loaded with methane molecules, NQEs continue to play a minor role in the prediction of the structural properties of the system, just as for the empty framework. For the heat capacity, the inclusion of NQEs remains crucial, but in contrast to the empty framework, the harmonic approximation no longer yields the same results as PIMD simulations. Due to the mobility of the adsorbates, a dynamic sampling is required, which accounts for the low-frequency anharmonic motions of the adsorbates. Even within classical MD simulations, the anharmonicities associated with the methane guest molecules give rise to a temperature dependent heat capacity. As the adsorbates are primarily affected by anharmonicities, while the description of the framework itself is most susceptible to NQEs, the heat capacity of the methane-loaded framework can be determined in good approximation by combining a harmonic quantum description of the framework with an anharmonic description of the guest–guest and guest–host interactions. Especially within the context of high-throughput screenings, this approximation can be of interest due to its limited computational cost.

3.2 Quantum free energy profiles

To simulate activated processes within PIMD, classical enhanced sampling techniques are most often applied to the ring polymer centroids, which contract the beads of the ring polymer to a single particle (Figure 2.10). The resulting free energy profile is then given by

$$F_{\text{centroid}}(q_{cl}^{(c)}) = -\frac{1}{\beta} \ln \left\langle \delta(Q(\boldsymbol{R}^{(c)^{Nn}}) - q_{cl}^{(c)}) \right\rangle , \tag{3.2}$$

with $\boldsymbol{R}_i^{(c)} = \frac{1}{P}\sum_{P=1}^{N} \boldsymbol{R}_i^{(k)}$ and $q_{cl}^{(c)}$ a CV that only depends on the centroid positions. However, this centroid free energy profile provides only a quasi-classical approximation to the quantum free energy profile, as only the ring polymer beads adequately sample the appropriate quantum statistics.[155, 156] Therefore, a quantum free energy profile relies on a CV that explicitly depends on the positions of the beads:

$$F_{\text{quantum}}(q) = -\frac{1}{\beta}\ln\left\langle \frac{1}{P}\sum_{k=1}^{P}\delta(Q(\boldsymbol{R}^{(k)^{N_n}}) - q)\right\rangle, \tag{3.3}$$

where an average is taken over all the beads to improve the statistical convergence, as is commonly done for thermodynamic quantities in PIMD. Due to the equivalence of the beads, the quantum free energy profile can in principle be determined by performing enhanced sampling simulations in which the rare event is sampled by biasing a single bead. However, this is most likely to result in a deficient sampling, in particular around free energy maxima. When restraining a single bead around a free energy maximum, the ring polymer namely possesses the freedom to orient itself toward either side of the barrier, so that only one side of the barrier will be sampled for maxima with a certain height and steepness. In this respect, applying a bias to the centroid is more convenient to circumvent these sampling difficulties, similar to the calculation of rate constants (see Section 3.2.2).[148] Given the implicit dependence of the centroid coordinates on the positions of the beads, **Paper VII** demonstrated that the quantum free energy profile can be obtained from the centroid free energy profile by means of a transformation of the CV:

$$F_{\text{quantum}}(q) = -\frac{1}{\beta}\ln\left[\frac{1}{P}\sum_{k=1}^{P}\int \mathrm{d}q_{cl}^{(c)}\; p_b(q^{(k)}|q_{cl}^{(c)})\, e^{-\beta F_{\text{centroid}}(q_{cl}^{(c)})}\right] + C, \tag{3.4}$$

with C is a negligible constant and $p_b(q^{(k)}|q_{cl}^{(c)})$ the conditional probability that the CV takes the value q for bead k when the centroid CV has a value $q_{cl}^{(c)}$ in a simulation with a time-independent bias. As a consequence, the quantum free energy profile of a rare event can be calculated by driving the system across the free energy barrier with a centroid CV, followed by a post-processing step in which the centroid CV is transformed into a bead CV. To construct the conditional probability $p_b(q^{(k)}|q_{cl}^{(c)})$, it suffices to keep track of the correspondence between $q^{(k)}$ and $q_{cl}^{(c)}$ throughout the biased simulations.

By relying on the equivalence of the beads, the quantum free energy profile can also be obtained by averaging the free energy profiles of all the beads:

$$F_{\text{quantum}}(q) = \frac{1}{P}\sum_{k=1}^{P} F^{(k)}(q) = -\frac{1}{P\beta}\sum_{k=1}^{P} \ln\left\langle \delta(Q(\boldsymbol{R}^{(k)^{N_n}}) - q)\right\rangle \tag{3.5}$$
$$= -\frac{1}{P\beta}\sum_{k=1}^{P} \ln\left[\int \mathrm{d}q_{cl}^{(c)}\; p_b(q^{(k)}|q_{cl}^{(c)})\, e^{-\beta F_{\text{centroid}}(q_{cl}^{(c)})}\right] + C.$$

Theoretically, both expressions of the quantum free energy (Eqs. (3.4) and (3.5)) are equivalent, but mathematically, Eq. (3.4) is more sensitive to inequivalences in the sampling of the beads, as illustrated in Section 3.2.1. Therefore, Eq. (3.5) is the preferred transformation approach.

3.2.1 Molecular proton transfers

To assess the importance of NQEs in free energies and the difference between quasi-classical centroid free energy profiles and proper quantum free energy profiles, three molecular proton transfers were examined in **Paper VII**. Aside from the ubiquitous nature of proton transfer reactions in chemical processes, these reactions are specifically chosen because of the NQEs associated with the low mass of the proton and the wide variety in shape and height of the free energy barriers (ranging from about 25–275 kJ/mol). To obtain a truly quantum free energy profile, both the electrons and nuclei have to be described quantum mechanically. Given the required 64 beads (or more at lower temperatures) to converge the energy, the computational cost of PIMD simulations in combination with umbrella sampling is still substantial, even for small molecular systems. Therefore, these simulations were performed with neural network MLPs to model the PES of the reactions at a PBE0 level of theory.

In Figure 3.2, the three proton transfer reactions are depicted alongside the corresponding free energy profiles. The first reaction is the concerted double proton transfer in the formic acid dimer. This simultaneous proton transfer can be elicited by means of a CV that uses a difference in coordination numbers (Figure 3.2a):

$$\mathrm{CV}_1 = \mathrm{CN}_{\mathrm{O}_1,\mathrm{H}_1} - \mathrm{CN}_{\mathrm{O}_2,\mathrm{H}_1} - \mathrm{CN}_{\mathrm{O}_3,\mathrm{H}_2} + \mathrm{CN}_{\mathrm{O}_4,\mathrm{H}_2}, \tag{3.6}$$

with

$$\mathrm{CN}_{i,j} = \frac{1 - \left(\frac{\boldsymbol{r}_{ij}}{\boldsymbol{r}_0}\right)^6}{1 - \left(\frac{\boldsymbol{r}_{ij}}{\boldsymbol{r}_0}\right)^{12}}, \tag{3.7}$$

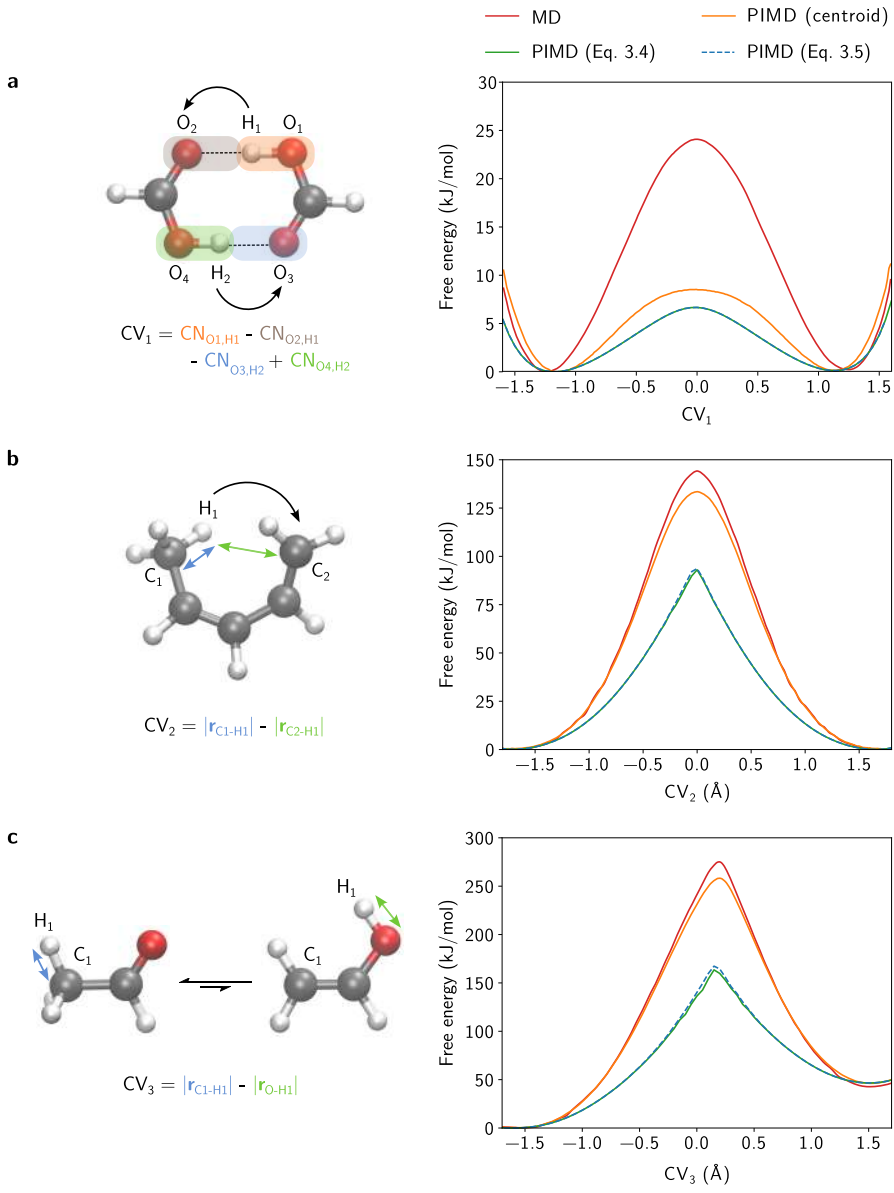

Figure 3.2: Free energy profiles and corresponding CV definitions of **a** the double proton transfer in a formic acid dimer at 200 K, **b** a sigmatropic proton rearrangement in pentadiene at 450 K, and **c** the tautomerization of acetaldehyde to vinyl alcohol at 450 K. For each proton transfer, both the classical free energy (MD) and the quantum free energy (PIMD) are reported. The PIMD (centroid) profile represents the free energy that is directly obtained when sampling along the centroid CV, before applying the appropriate transformation of Eq. (3.4) or (3.5). Figure adapted from Ref. [137] with permission of the American Chemical Society.

where $\boldsymbol{r}_{ij}$ is the interatomic distance between atoms i and j, and $\boldsymbol{r}_0 = 1.4$ Å. Classically, a free energy barrier of 24.1 kJ/mol is obtained at 200 K. When accounting for NQEs, the barrier height reduces to 7.3 kJ/mol, which only differs marginally from the centroid free energy barrier height of 8.5 kJ/mol. The second reaction is a sigmatropic proton rearrangement in pentadiene (Figure 3.2b), which can be instigated by a CV that uses a difference in interatomic distances:

$$\mathrm{CV}_2 = |\boldsymbol{r}_{\mathrm{C}_1-\mathrm{H}_1}| - |\boldsymbol{r}_{\mathrm{C}_2-\mathrm{H}_1}|\,. \tag{3.8}$$

By exchanging a classical description for a quasi-classical centroid description, the free energy barrier decreases by about 11 kJ/mol (from 144.2 to 133.5 kJ/mol at 450 K). A subsequent transformation to a bead CV further lowers the barrier to 93 kJ/mol, resulting in a total reduction of 35% with respect to the classical description. The final reaction is the tautomerization of acetaldehyde to vinyl alcohol (Figure 3.2c), which can also be steered by a CV based on interatomic distances:

$$\mathrm{CV}_3 = |\boldsymbol{r}_{\mathrm{C}_1-\mathrm{H}_1}| - |\boldsymbol{r}_{\mathrm{O}-\mathrm{H}_1}|\,. \tag{3.9}$$

Due to the higher and steeper classical free energy barrier (275.1 kJ/mol at 450 K), the difference with the centroid free energy further increases to about 17 kJ/mol at the maximum value. For the bead free energy profile, the effect is even more pronounced, as the barrier height drops to 163.5 kJ/mol, a diminution of 40% with respect to the classical barrier. This distinct difference between the free energy profiles obtained for the centroid and the beads can be explained by the spatial extension of the path integral ring polymer of the transitioning proton(s). In Figure 3.3, the probability density of the radius of gyration r_{gyr} and the maximal extent r_{max} of the proton ring polymer are shown as a function of the CV for each of the three reactions, with

$$r_{gyr} = \sqrt{\frac{1}{P}\sum_{k=1}^{P} \left|\boldsymbol{r}_H^{(k)} - \boldsymbol{r}_H^{(c)}\right|^2} \tag{3.10}$$

$$r_{max} = \max_{k\in\{1,\dots,P\}} \left|\boldsymbol{r}_H^{(k)} - \boldsymbol{r}_H^{(c)}\right|. \tag{3.11}$$

Around the free energy maximum, the probability densities are observed to become sparser and possess a larger average value. This implies that the ring polymer of the proton is stretched around the transition state, so that the individual beads experience a lower free energy than the centroid when it is fixed to the free energy maximum. For higher and more sharply peaked free

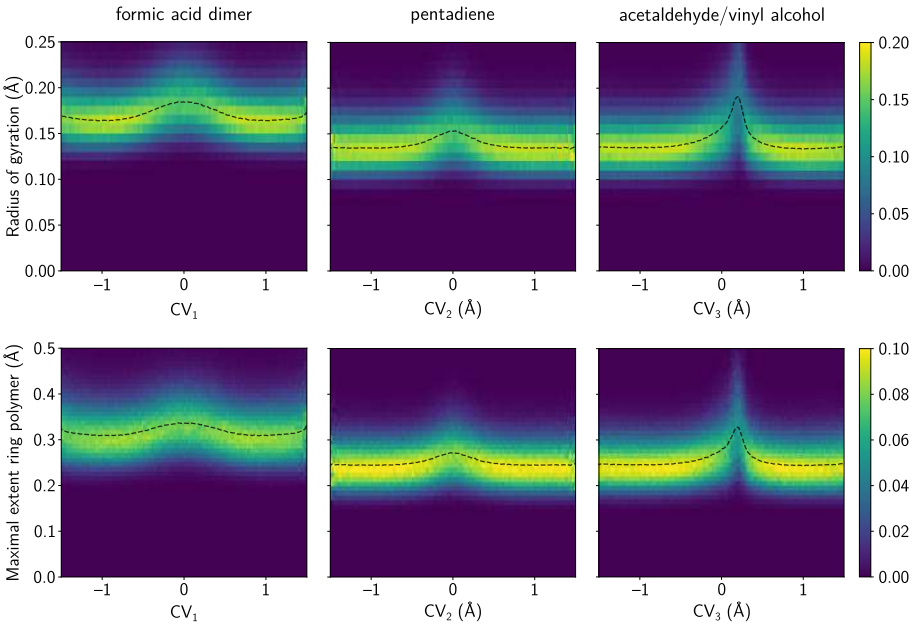

Figure 3.3: The conditional probability density $p(r_{gyr/max}|\mathrm{CV}_i)$ of the radius of gyration (*top row*) and maximal ring polymer extent (*bottom row*) (Eqs. (3.10) and (3.11)) of the transitioning proton(s) in formic acid, pentadiene, and acetaldehyde/vinyl alcohol as a function of the CV. The average of the probability density as a function of the CV is indicated by a dashed black line. Figure reproduced from Ref. [137] with permission of the American Chemical Society.

energy barriers, the ring polymer of the proton is further extended, thereby increasing the dissimilarity between the centroid and the beads.

The theoretically equivalent transformations for the quantum free energy profile, given by Eqs. (3.4) and (3.5), are in excellent agreement for the proton transfers in the formic acid dimer and pentadiene (Figure 3.2). For acetaldehyde, however, a small deviation of the order of 5 kJ/mol is present in the transition state region. To put the equivalence between both transformations further to the test, the role of NQEs is enhanced by decreasing the temperature from 450 K to 100 K for the proton transfer in pentadiene. From 200 K onwards, the required number of beads in the PIMD simulations is doubled to 128 to converge the energy. The resulting free energy profiles are reported in Figure 3.4a. Classically, the free energy barriers vary only by about 5 kJ/mol across the temperature range between 100 K and 450 K. The centroid free energy profiles, by contrast, exhibit a reduction in the free en-

ergy barrier of almost 50% (or 62.5 kJ/mol) and display a systematic flattening with decreasing temperatures. After applying transformation (3.5), the shape of the free energy barrier is again preserved as a function of temperature for the bead free energy profiles. Besides an overall reduction in the height of the free energy barrier, a similar temperature effect is observed as for the centroid (*i.e.* a decrease from 94 kJ/mol to 45 kJ/mol). When using transformation (3.4), large deviations occur at lower temperatures in comparison with transformation (3.5), yielding an irregularly jagged profile with large error bars (Figure 3.4b), which indicates a lack of convergence. Given that both profiles are constructed with the same underlying data, this discrepancy must be related to the specific form of both transformation formulas. To this end, Figure 3.4c shows the integral figuring in both transformations as a function of the bead CV for every bead in PIMD simulations at 100 K. Notwithstanding the apparent similarity of the integral for all beads, the inset of Figure 3.4c reveals that the region of low probability around the transition state actually spans several orders of magnitude. As a consequence, every outlier will heavily influence the average value of the integral, resulting in an outcome that is very sensitive to inequivalences in the sampling of the beads. If, however, one first takes the logarithm and then an average over the beads (as in Eq. (3.5)), normal distributions are averaged (Figure 3.4d) and the average becomes more robust with respect to inequivalences in the sampling of the beads. Therefore, Eq. (3.5) is the preferred transformation approach.

To rationalise the flattening of the centroid free energy profiles with decreasing temperatures, the spatial extension of the ring polymer of the transitioning proton must be considered. As shown in Figure 3.4e, the prominent NQEs at lower temperatures significantly increase the radius of gyration in a large region around the transition state (from about 0.15 Å at 450 K to about 0.6 Å at 100 K). As the ring polymer is maximally stretched out for a broader range of CV values around the transition state at low temperatures, the free energy barrier is flattened across the same CV range.

3.2.2 Zeolite proton hopping

Also in the field of zeolite catalysis, proton transfer reactions play an essential role. One the most fundamental proton transfer reactions, the so-called proton hopping reaction, consists of an exchange of the Brønsted acid site (BAS) between the oxygen atoms neighbouring an Al^{3+} substitution in the zeolite. In spite of the apparent simplicity of this reaction, both experimentally and computationally reported activation energies for proton hopping of the BAS exhibit a large spread.[157, 158] For the CHA zeolite, experimental activation energies obtained with infrared spectroscopy cover a range of about 15–25

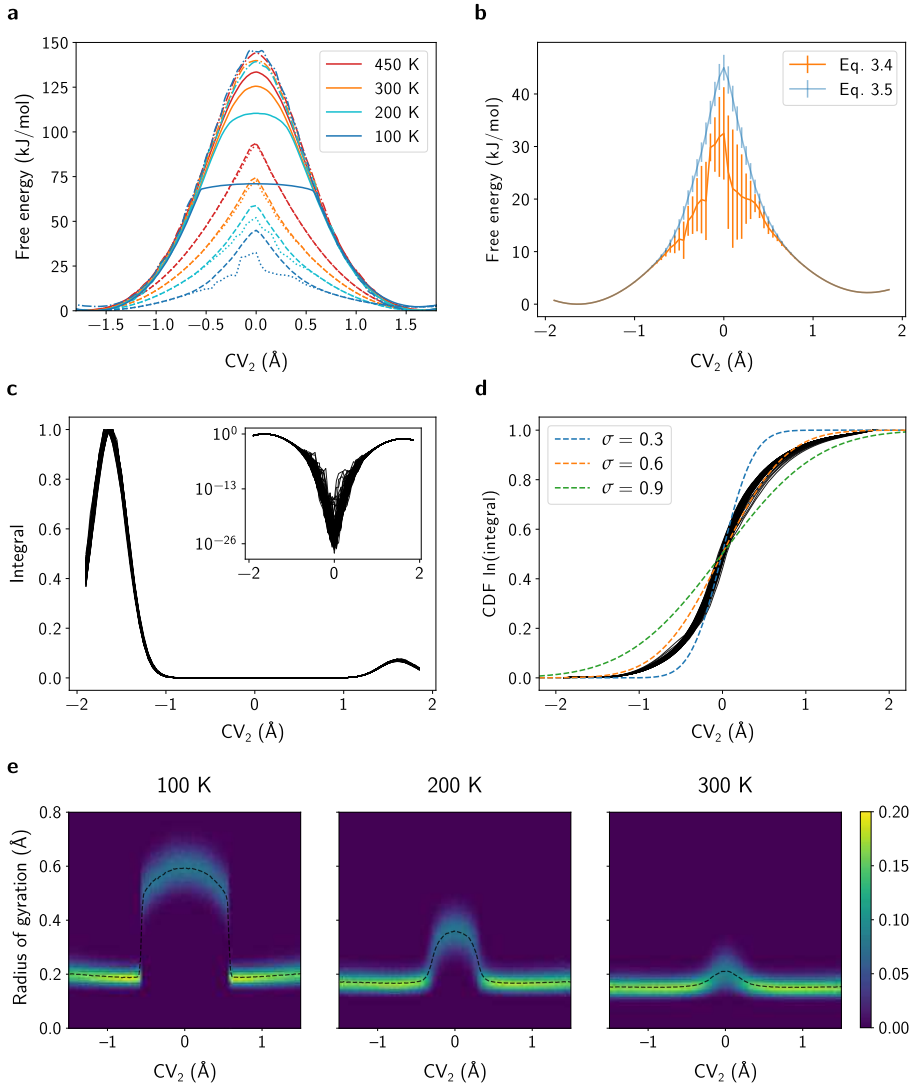

Figure 3.4: **a** Classical (dash-dotted line), centroid (solid line), and quantum (dotted Eq. (3.4) or dashed Eq. (3.5) lines) free energy profiles of a sigmatropic proton rearrangement in pentadiene at different temperatures. **b** Quantum free energy profiles of pentadiene at 100 K, with 2σ error bars obtained via bootstapping with random subsets of 16 beads. **c-d** Integral (c) and cumulative distribution function (CDF) of the normalised integral (d) from Eqs. (3.4) and (3.5) from umbrella sampling PIMD simulations at 100 K. The coloured curves in pane d represent CDFs of normal distributions (with zero mean and standard deviation σ). **e** Conditional probability density $p(r_{gyr/max}|\mathrm{CV}_2)$ of the radius of gyration of the transitioning proton in pentadiene as a function of the CV and temperature. The average of the probability density is indicated by a dashed black line. Figures reproduced from Ref. [137] with permission of the American Chemical Society.

kJ/mol (for a wide temperature range), whereas computational activation energies are situated in the range of about 65–80 kJ/mol. Possible explanations for this discrepancy include the residual presence of water or extra-framework aluminium species in the experimental samples, which are known to alter the behaviour of the BAS. Furthermore, computational characterisations of the proton hopping reaction usually neglect the NQEs associated with the BAS or only approximately take them into account. To elucidate the impact of NQEs on the proton hopping reaction, **Paper VIII** investigated the proton hopping around an isolated aluminium substitution in H-CHA (H-SSZ-13), with a rigorous treatment of the NQEs using PIMD. This work was performed in collaboration with my colleagues Massimo Bocus and Ruben Goeminne at the CMM. Just as for the molecular proton transfer reactions, a neural network MLP was required to keep the computational cost of the PIMD simulations tractable in combination with a revPBE-D3[159, 160] level of theory and umbrella sampling at different temperatures.

In Figure 3.5a, the free energy profiles between two of the four oxygen atoms neighbouring the aluminium substitution are shown for a temperature of 273 and 573 K. In comparison with a classical treatment of the nuclei, both the centroid and quantum free energy barrier show a substantial reduction at 273 K (from 74.6 kJ/mol to 64.5 or 55.1 kJ/mol, respectively). At 573 K, the influence of the NQEs diminishes, but still remains present with a ~ 5 kJ/mol difference for the centroid and a ~ 9 kJ/mol difference for the beads.

From these free energy profiles, the rate constant of the proton hopping can be calculated for each pair of oxygen atoms around the aluminium defect (Figure 3.5b). To go beyond the transition state approximation and take the possibility of barrier recrossings into account, the long-time limit of the time-dependent rate constant is used,[94, 161] which is given by

$$\begin{aligned} k &= \lim_{t\to+\infty} k(t) = \lim_{t\to+\infty} \frac{\int \mathrm{d}^{N_n}\boldsymbol{P} \int \mathrm{d}^{N_n}\boldsymbol{R}\, e^{-\beta H}\, \delta(q-q^\ddagger)\, \dot{q}\, \theta(q(t)-q^\ddagger)}{\int \mathrm{d}^{N_n}\boldsymbol{P} \int \mathrm{d}^{N_n}\boldsymbol{R}\, e^{-\beta H}\, \theta(q^\ddagger - q)} \\ &= \lim_{t\to+\infty} \left\langle \dot{q}(0)\, \theta(q(t)-q^\ddagger) \right\rangle_{q(0)=q^\ddagger} \frac{e^{-\beta F(q^\ddagger)}}{\int_{-\infty}^{q^\ddagger} \mathrm{d}q\, e^{-\beta F(q)}}, \end{aligned} \tag{3.12}$$

with $\dot{q}$ the time derivative of the CV, $\delta(q)$ the delta distribution, and $\theta(q)$ the Heaviside function. Using this expression, the classical rate constant can be obtained from a series of short MD simulations in which the system is initialised in the transition state $q^\ddagger$. Only the simulations which end up in the product state (defined as $q > q^\ddagger$) contribute to the ensemble average, which

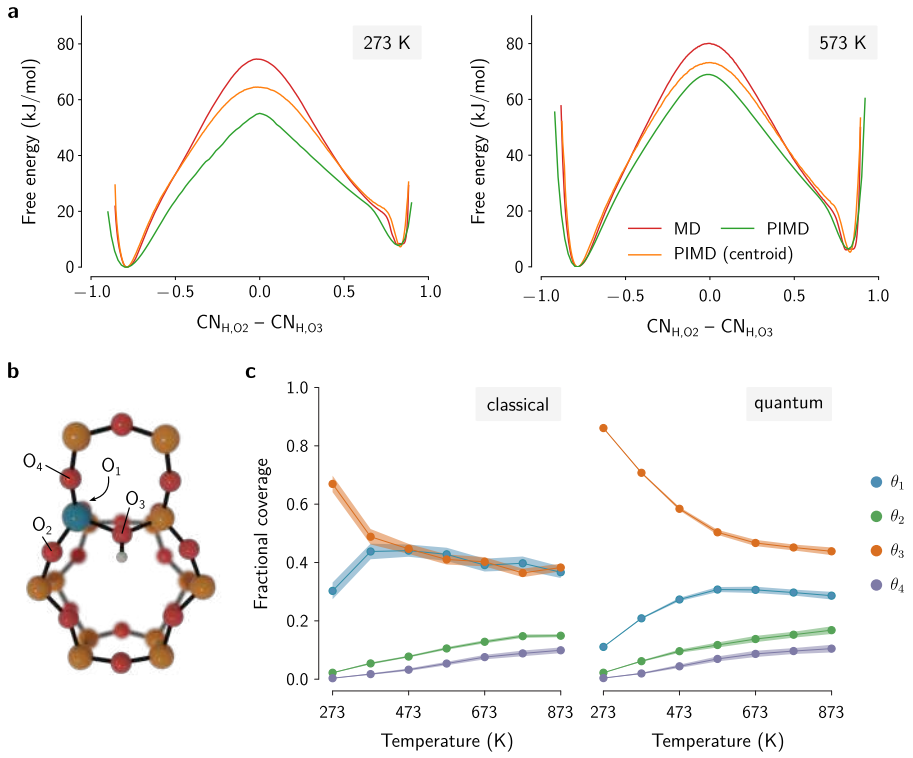

Figure 3.5: **a** Classical, centroid, and quantum free energy profiles for proton hopping between two oxygen atoms (O_2 and O_3, see pane (b)) neighbouring an aluminium defect in H-CHA, calculated with (PI)MD umbrella sampling simulations at 273 and 573 K. The PIMD simulations were performed with 16 beads. **b** Molecular representation of a part of the H-CHA framework around the aluminium defect (blue), labelling the neighbouring oxygen atoms. **c** Equilibrium coverages of the four oxygen atoms surrounding the aluminium defect as a function of temperature, calculated from the classical (MD) or quantum (RPMD) rate constants. Figures adapted from Ref. [157] with permission of Springer Nature.

thus establishes a correlation between the initial velocity at the transition state $\dot{q}(0)$ and the probability of reaching the product state. Given the fast convergence of the time-dependent rate constant for substantial free energy barriers, only short MD simulations are required of about 50 ps.

To obtain a quantum rate constant, the approximate quantum dynamics of RPMD are used, as explained in Section 2.3.3. Similarly to the calculation of free energy profiles, either the ring polymer centroid or one of the beads can be initialised in the transition state for the rate calculation. Due to the

large conformational freedom of the ring polymer with only one of beads located in transition state, the convergence of the rate constant using a bead CV is very challenging and requires at least a few hundred thousand RPMD trajectories. Just as for free energy profiles, the use of a centroid CV allows for a more efficient sampling, as conformations in which the ring polymer is entirely oriented towards either side of the transition state are avoided. Furthermore, as rate constants are independent of the CV used to sample the free energy, the bead and centroid CV can be shown to yield the same rate constant,[148] so that the quantum rate constant is given by

$$k_{\mathrm{q}} = \lim_{t\to\infty} \left\langle \dot{q}^{(c)}(0)\, \theta(q^{(c)}(t) - q^{(c)\ddagger}) \right\rangle_{q^{(c)}(0)=q^{(c)\ddagger}} \frac{e^{-\beta F(q^{(c)\ddagger})}}{\displaystyle\int_{-\infty}^{q^{(c)\ddagger}} \mathrm{d}q^{(c)}\, e^{-\beta F(q^{(c)})}}. \tag{3.13}$$

To combine the rate constants of the six possible proton hopping paths in H-CHA, a total rate constant r can be defined:

$$r = \sum_{i=1}^{4} \sum_{\substack{j=1 \\ j\neq i}}^{4} k_{ij} \nu_i, \tag{3.14}$$

with ν_i the equilibrium coverage of oxygen atom i, so that

$$\frac{\mathrm{d}\nu_i}{\mathrm{d}t} = 0 \qquad \text{and} \qquad \sum_{i=1}^{4} \nu_i = 1. \tag{3.15}$$

The classical and quantum equilibrium coverages in H-CHA are shown in Figure 3.5c for a temperature range of 273–873 K. Classically, the O_3 site is most probable at the lowest temperature of 273 K, while for all other temperatures the O_1 and O_3 sites are equally probable to carry the BAS. When including NQEs, the O_3 site distinctly becomes the most probable location for the BAS across the entire temperature range, which appears to be related to a strengthening of the weak interactions between the proton and non-adjacent oxygen atoms of the zeolite framework. The resulting overall hopping rate (3.14) is reported in Figure 3.6a using an Arrhenius plot. From the slope of the curves, a classical activation energy of 67.1 kJ/mol is obtained and a quantum activation energy of 55.8 kJ/mol, so that NQEs reduce the activation energy by about 11 kJ/mol or 17%. At 273 K, the reaction proceeds 65 times faster in the presence of NQEs (Figure 3.6b), whereas at 473 K, a 7-fold speed-up of the proton hopping still remains noticeable.

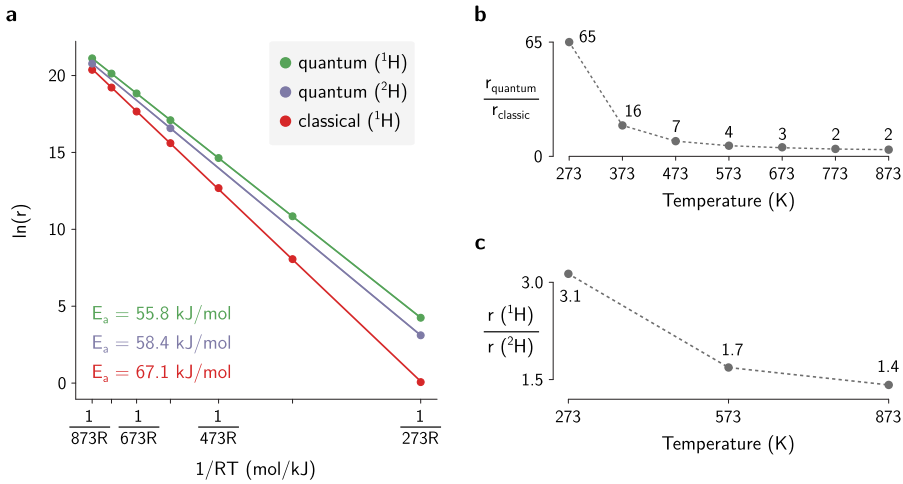

Figure 3.6: **a** Arrhenius plot of the overall hopping rate (Eq. (3.14)) as a function of 1/RT. **b** Speed-up of the overall hopping rate due to the inclusion of NQEs as a function of temperature. **c** Kinetic isotope effect for protium versus deuterium as a function of temperature. Figures adapted from Ref. [157] with permission of Springer Nature.

Finally, the RPMD simulations also allow to study the kinetic isotope effect of the proton transfer by replacing the hydrogen atom by deuterium, which is a commonly used experimental technique to probe the impact of NQEs. Compared to protium, the quantum activation energy only increases by 2.6 kJ/mol, so that the increase in mass is insufficient to retrieve a classical behaviour. At 273 K, the reaction progresses three times slower for the heavier isotope, whereas at 573 K the difference in reaction speed is already halved and steadily fades away as the temperature further increases.

4

Water Confined in Metal–Organic Frameworks

Nature uses only the longest threads to weave her patterns, so each small piece of her fabric reveals the organization of the entire tapestry.

Richard P. Feynman[162] (1918–1988)

As mentioned in Chapter 1, many of the potential applications of metal-organic frameworks (MOFs) involve the adsorption of guest molecules in the nanopores of the framework. For water-stable MOFs, these applications also include atmospheric water harvesting, [6, 38, 163] water purification,[164–166] shock adsorption,[167] and adsorbent-based heat-pumps and chillers with water as a green working fluid.[168–171] In comparison with bulk water, nanoconfined water exhibits many deviating properties, due to the strong disruption of the intricate hydrogen bond network. For both carbon nanotubes and MOFs, highly ordered water structures have been observed, which are reminiscent of ice, but remain stable at various (moderate) thermodynamic conditions.[172–177] In addition to the dimensions of the nanopore, the combination of hydrophilic and hydrophobic sites in many MOFs further shapes the confined water and decisively determines the adsorption behaviour of the material. The initial adsorption of water typically occurs at hydrophilic adsorption sites such as open metal sites or hydroxyl groups, during the so-called seeding stage of the adsorption process.[178] Subsequently, additional water molecules can be adsorbed at these seeds, so that they steadily grow

into water clusters. After the clustering stage, the successive adsorption of water molecules will eventually lead to the coalescence of clusters into an extended hydrogen-bonded network during the networking stage. This adsorption mechanism is present in many MOFs, including MOF-303,[178] CAU-10-H,[177], MOF-801,[168, 179, 180] MIL-101,[181], and Co_2Cl_2BTDD.[182] For MOF-303, the specific location and strength of the adsorption sites give rise to an ideal adsorption behaviour for the application of atmospheric water harvesting.

In the first section of this chapter, the water network in different zirconium MOFs, such as MOF-801 and UiO-66, is examined to gain insight into the way in which a framework templates confined water. From the primary and secondary adsorption sites identified in these materials, the interplay between these sites and the resulting adsorption isotherms are studied by means of a virtual nanopore with precisely controlled adsorption sites. In particular within the context of atmospheric water harvesting, cleverly engineered adsorption sites have the potential to further enhance the performance of MOF adsorbents. In Section 4.2, the mechanism of water intrusion in the hydrophobic pores of ZIF-8 is investigated, in view of its potential application to absorb mechanical impacts.

4.1 Framework-induced water motifs

4.1.1 Structural response to water adsorbates

When water molecules are adsorbed in the nanopores of a MOF, the framework is observed to adapt to their presence. In the case of rigid MOFs with nanopores that can host at least a few water molecules, such as the zirconium MOFs considered in the following paragraphs (including MOF-801, UiO-66, UiO-67, and MOF-808), the structural response of the framework is limited to a small volume contraction which increases with the water loading until a reduction of about 1–2% is reached. A further increase of the water loading causes the framework to expand, so that the material can eventually exceed the initial volume of the empty framework.

For flexible MOFs, such as MIL-53(Al), the presence of water adsorbates influences the relative stability of the (meta-)stable phases of the framework. As the transition between the narrow-pore (np) and large-pore (lp) phases of MIL-53(Al) is well described using the volume as a CV, the relative stability of both phases can be assessed by constructing free energy profiles as a function of the volume for different water loadings, as done in **Paper III**. In Figure 4.1a, the classical and quantum free energy profiles of the empty framework are reported. Given that the volume does not explicitly depend on the atomic

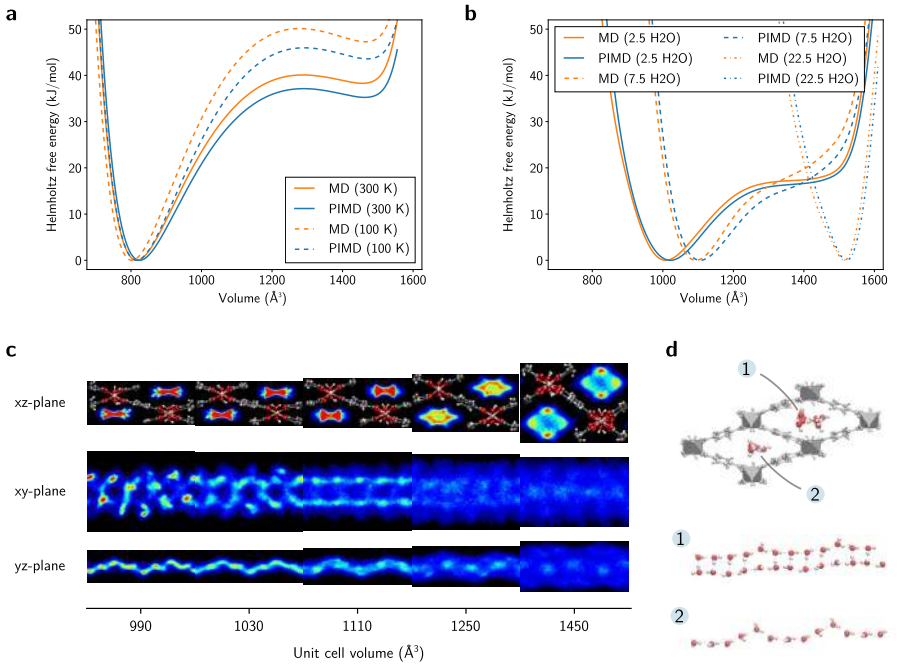

Figure 4.1: **a** Free energy profile of MIL-53(Al) as a function of volume at 100 and 300 K, calculated with both MD and PIMD umbrella sampling simulations. **b** Free energy profile of MIL-53(Al) as a function of volume at 300 K for water loadings of 2.5, 7.5, and 22.5 water molecules per conventional unit cell, calculated with both MD and PIMD umbrella sampling simulations. **c** Water density in MIL-53(Al) projected onto the xz-, xy-, and yz-plane for 7.5 water molecules per unit cell at different volumes. The densities are symmetrised using the space group of the framework. For the xy- and yz-planes, only the upper half of the simulation cell is shown, as the bottom half is its symmetrical equivalent. **d** Illustration of the one-dimensional water wires formed in MIL-53(Al). Figures a–c reproduced from Ref. [183] with permission of the Royal Society of Chemistry.

positions, there is no distinction to be made between the centroid and bead free energy profiles, so that also the quantum free energy profile is readily obtained from PIMD umbrella sampling simulations which bias the volume. Both at a temperature of 100 and 300 K, the impact of NQEs on the relative phase stability is very modest as it only amounts to about 3–4 kJ/mol. This minor influence on the phase stability can be ascribed to the small quantum effects associated with low-frequency modes (*i.e.* below 100 cm^{-1}), which dominate the lp-to-np transition.[52]

Also for water-loaded frameworks, the contribution of NQEs in the free energy remains small (Figure 4.1b). For the lowest loading (2.5 H_2O/unit cell), the free energy profile roughly preserves the shape obtained in the absence of water, but it is shifted towards higher equilibrium volumes by about 200 $Å^3$ and the lp phase is no longer a stable phase. For intermediate and high water loadings (7.5 and 22.5 H_2O/unit cell, respectively), the profile continues to shift towards larger equilibrium volumes while the former lp minimum gradually disappears until a profile with a sharp single minimum is obtained.

4.1.2 Water organisation in nanoconfinement

Depending on the pore size of the channels of the flexible MIL-53(Al) framework, different water organisations can be discerned. At smaller volumes, one-dimensional water wires are formed along the channels (Figure 4.1c–d).[184, 185] As the volume of the channels increases, the water molecules take advantage of the additional spatial freedom in the pores and are less organised, yielding a more dilute density profile.

In the cage-type pores of the zirconium MOFs investigated in **Paper X**, three-dimensionally templated water clusters are encountered. To systematically probe the influence of nanoconfinement on the formation of water clusters in the presence of hydrophilic adsorption sites, seven different zirconium MOFs were considered to maximally vary the topology and pore size for similar chemical building bricks: MOF-801, UiO-66, UiO-67, MOF-808, UiO-68, MOF-841, and NU-1000 (Figure 4.2). For the clarity of discussion, the ensuing paragraphs will however only focus on the first four frameworks.

To characterise the structure of nanoconfined water, one can start by analysing the connectivity of the hydrogen bond network. For bulk liquid water, every water molecule tends to engage in 2 to 4 hydrogen bonds, resulting in an average of 2.7 hydrogen bonds per molecule, as shown in Figure 4.3. In nanoconfinement, the compartmentalisation of the water molecules imposed by the framework strongly alters the opportunities for hydrogen bonding, especially in smaller pores. At low water loadings, the formation of hydrogen bonds is limited by the limited presence of water molecules, which skews the hydrogen bond distribution towards 0 or 1 hydrogen bond per molecule. At higher water loadings, only frameworks which primarily consist of large pores (with a diameter > 10 Å, such as UiO-67 and MOF-808) approach the hydrogen bond distribution of bulk water. For frameworks with smaller pore sizes, a disrupted hydrogen bond network also persists at the highest water loadings (cf. UiO-66 and MOF-801).

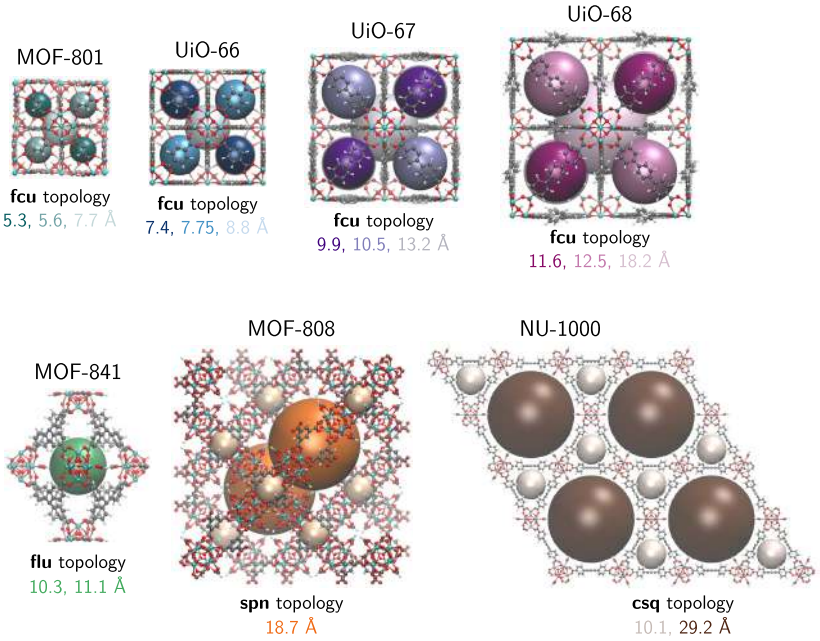

Figure 4.2: Overview of the structures of the zirconium MOFs investigated in this work. The pores of each framework are indicated with coloured spheres and the corresponding pore diameters are listed below the figure. Note that the structure of NU-1000 is rescaled with a factor of 0.65 compared to the other structures.

The water structure beyond the first hydrogen-bonded neighbours can be probed with radial distribution functions (RDFs). The first RDF peak represents the hydrogen bonds across the water network, which are only minorly affected by confinement given the good resemblance with the RDF of bulk liquid water, apart from a modulation in the peak intensity (Figure 4.4). From the first RDF minimum onwards, significant deviations from the structure in bulk water are observed for the smaller UiO-66 and MOF-801 frameworks. The second solvation shell, represented by the second RDF peak, is for instance shifted to larger distances by 0.4–0.5 Å and comprises a smaller range of interatomic distances. In UiO-67 and MOF-808, just as for the hydrogen bond distributions, the larger pores allow to retrieve a bulk-like organisation of water, with only small shifts in the RDF peak positions.

To explain the deviating water structure in MOF-801 and UiO-66, the water density in the frameworks is examined in Figure 4.5, to discern the preferential adsorption sites and the water structures that emerge from it. Both MOF-801 and the UiO-type MOFs have an fcu topology, which gives rise to an

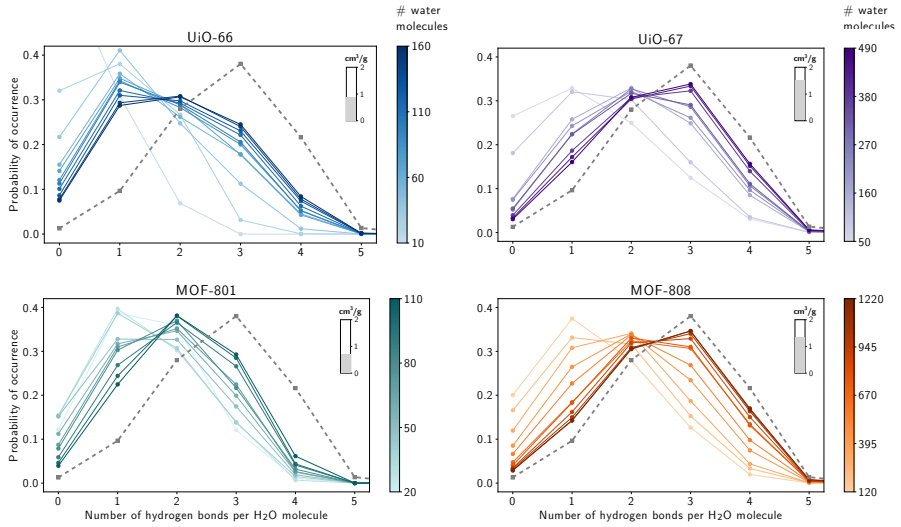

Figure 4.3: Probability distribution of the number of hydrogen bonds per water molecule for confinement in four different MOFs, obtained from PIMD simulations at 300 K with 32 beads. For each framework, a gradient colour scale is used to indicate the water loading in the unit cell. The highest water loading was determined from GCMC simulations at 1 bar. The hydrogen bond distribution of bulk water is indicated with a grey dashed line. The specific volume of each framework is indicated in the upper right corner of every pane.

octahedral pore and two types of tetrahedral pores in their unit cell. The first tetrahedral pore, labelled T1 in Figure 4.5, is characterised by the presence of μ-OH moieties on the zirconium bricks, which constitute the corners of the tetrahedron. In the T1 pores of MOF-801 and UiO-66, cubic water clusters are formed, which nucleate at the μ-OH groups. After the initial adsorption of water molecules at the four μ-OH groups in the corners of the pore (site 1 in Figure 4.5), these molecules serve as seeds for the additional adsorption of four more water molecules (site 2 in Figure 4.5), which complete the cubic cluster. In their turn, the water molecules at site 2 can further expand the cluster by means of a hydrogen bond that connects the tetrahedral cage with the octahedral cage (site 3 in Figure 4.5).

The second tetrahedral pore, labelled T2 in Figure 4.5, contains μ-O instead of μ-OH groups on the cornering metal nodes. In UiO-66, these pores give rise to a different density pattern compared to the T1 pores. Due to a different interaction with the μ-O groups, the primary adsorption sites in the corners of the pore are displaced, thereby misaligning the anchoring points for a cubic water cluster. In the absence of an optimal pore-filling water cluster, the

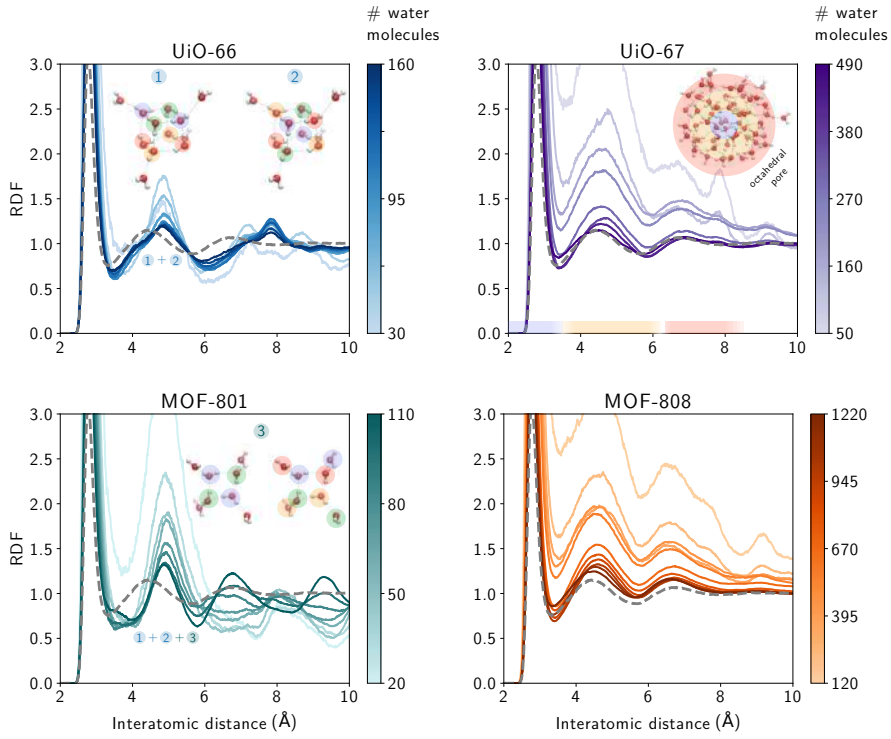

Figure 4.4: Radial distribution functions (RDFs) between the oxygen atoms of the water molecules in four different MOFs. For each framework, a gradient colour scale is used to indicate the water loading in the unit cell. The O–O RDF of bulk water is indicated with a grey dashed line. The insets for UiO-66 and MOF-801 (labelled 1–3) show the contributions of representative O–O pairs to the second peak of the RDF. The inset for UiO-67 shows the bulk-like shell structure in the octahedral pore.

hydrogen bond network freely changes its configuration in the pore, resulting in a sparser density around the primary adsorption sites. In MOF-801, the cubic water clusters do occur in the T2 pores, as they can be stabilised by the smaller pore size in comparison with UiO-66 (whose tetrahedral pores have a diameter that is about 2 Å larger). Experimentally, these water clusters have also been resolved in MOF-801 through X-ray diffraction,[179] but could not be directly connected with the specific terminations of the cornering metal nodes.

When further increasing the pore size by going from UiO-66 to UiO-67, the water density is further attenuated by the additional spatial freedom in the pores (Figure 4.5). The primary μ-OH adsorption sites in the T1 pores continue to branch out cubically, but no longer yield a unique pore-

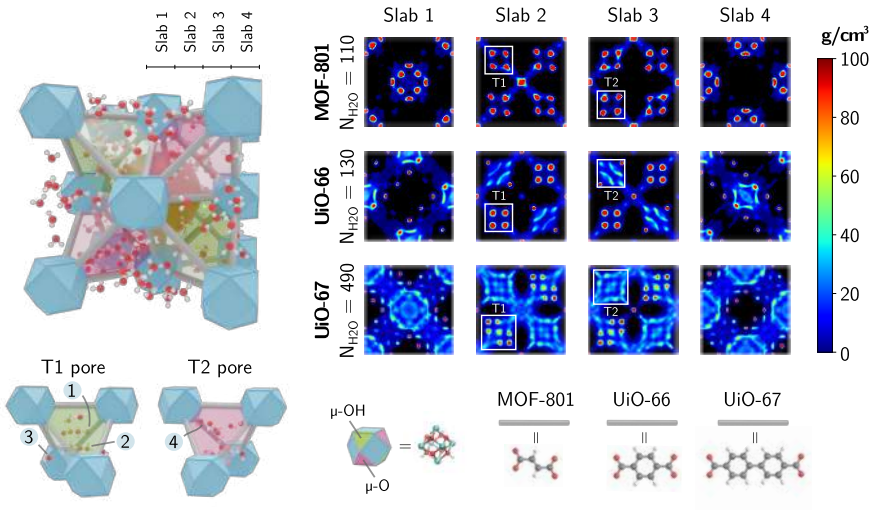

Figure 4.5: Density plots of water molecules confined in three different MOFs, alongside a schematic representation of a water-filled MOF with an fcu topology. Two exemplary water clusters, present in the T1 and T2 pore, are shown at the bottom of the figure, with the following labelled adsorption sites: (1) adsorbed at a μ-OH group of the metal node, (2) hydrogen bonded to sites 1, (3) connecting tetrahedral and octahedral pores, and (4) adsorbed at a μ-O group of the metal node. Densities lower than 0.001 g/cm^3 are attributed the colour black. The densities of the MOFs are symmetrised using the space group of the framework, so that only four slabs of one half of the framework are shown.

filling cluster. In the T2 pores, the dilution of the density is even higher, although some of the framework induced structure remains present. For the even larger pores of UiO-68, the thinning trend of the density continues and the MOF framework no longer provides a strong template for the water organisation in the pores.

4.1.3 Adsorption site arrangements and water isotherms

As demonstrated in the previous section for MOF-801 and UiO-66, the presence of hydrophilic adsorption sites plays a pivotal role in shaping the structure of nanoconfined water. During the pore filling process, the water structure induced by the framework will also decisively determine its adsorption properties. For MOF-303, which possesses ideal adsorption characteris-

tics for atmospheric water harvesting, experimental isotherm measurements showed a decrease in water uptake at low pressures when the pyrazole linkers of the framework are substituted by less hydrophilic furan (MOF-333)[178] or thiopene (CAU-23)[186] linkers, due to the altered primary adsorption sites. Similarly, the water uptake at low pressures in UiO-66 can also be enhanced or reduced by the incorporation of hydrophilic or hydrophobic linker functionalisations.[187, 188]

To rationalise the water structures observed in MOF-801 and UiO-66, and disentangle the effects of confinement and hydrophilic adsorption sites, a virtual cubic nanopore is considered, as depicted in Figure 4.6. For this repulsive cubic box, the pore parameters, such as the pore size and the location of the adsorption sites, can be precisely controlled and varied, which allows for a systematic exploration of their impact on the resulting water structures and adsorption isotherms.

In the absence of adsorption sites, an ordered water structure can only be imposed by very small box sizes (with a side length below 6 Å), which are unlikely to contain sufficient water molecules to form a cubic cluster. Starting from a box length of 6 Å, the water molecules move freely within the box and eventually yield a spherically symmetric density, as shown in Figure 4.6a. When introducing tetrahedrally arranged adsorption sites in the pore, a cubic water cluster can be formed for box lengths varying from 6 to 10 Å, if the primary adsorption sites outline a cube with a side of about 3 Å. In that case, the primary adsorption sites induce secondary adsorption sites on the remaining, 'empty' corners of the cube, as they are located within a hydrogen bond distance from the primary adsorption sites. With this configuration of tetrahedral adsorption sites, the virtual pore can thus mimic the adsorption behaviour of the T1 pore in MOF-801 and UiO-66. When the tetrahedral adsorption sites are placed further apart, the adsorption pattern of the T2 pore in UiO-66 can be reproduced. Due to the absence of unique secondary adsorption sites, the additional water molecules can now hydrogen bond to the primary adsorption sites in a wider region around each site, yielding a more distributed density. If the tetrahedral adsorption sites are replaced by a cubic arrangement of primary adsorption sites, the cubic water clusters can be stabilised over a broader range of intersite distances (*i.e.* cubes with a side of 3–4 Å) for lower adsorption energies.

The connection between the location of the adsorption sites and the resulting adsorption behaviour as a function of pressure is investigated by constructing water isotherms using the TMMC methodology (Section 2.2.4). In Figure 4.6b, the water isotherms of a repulsive box with a side of 6 Å and tetrahedrally arranged adsorption sites with a strength of 35 kJ/mol are reported for three different locations of the adsorption sites. When focussing on the particular

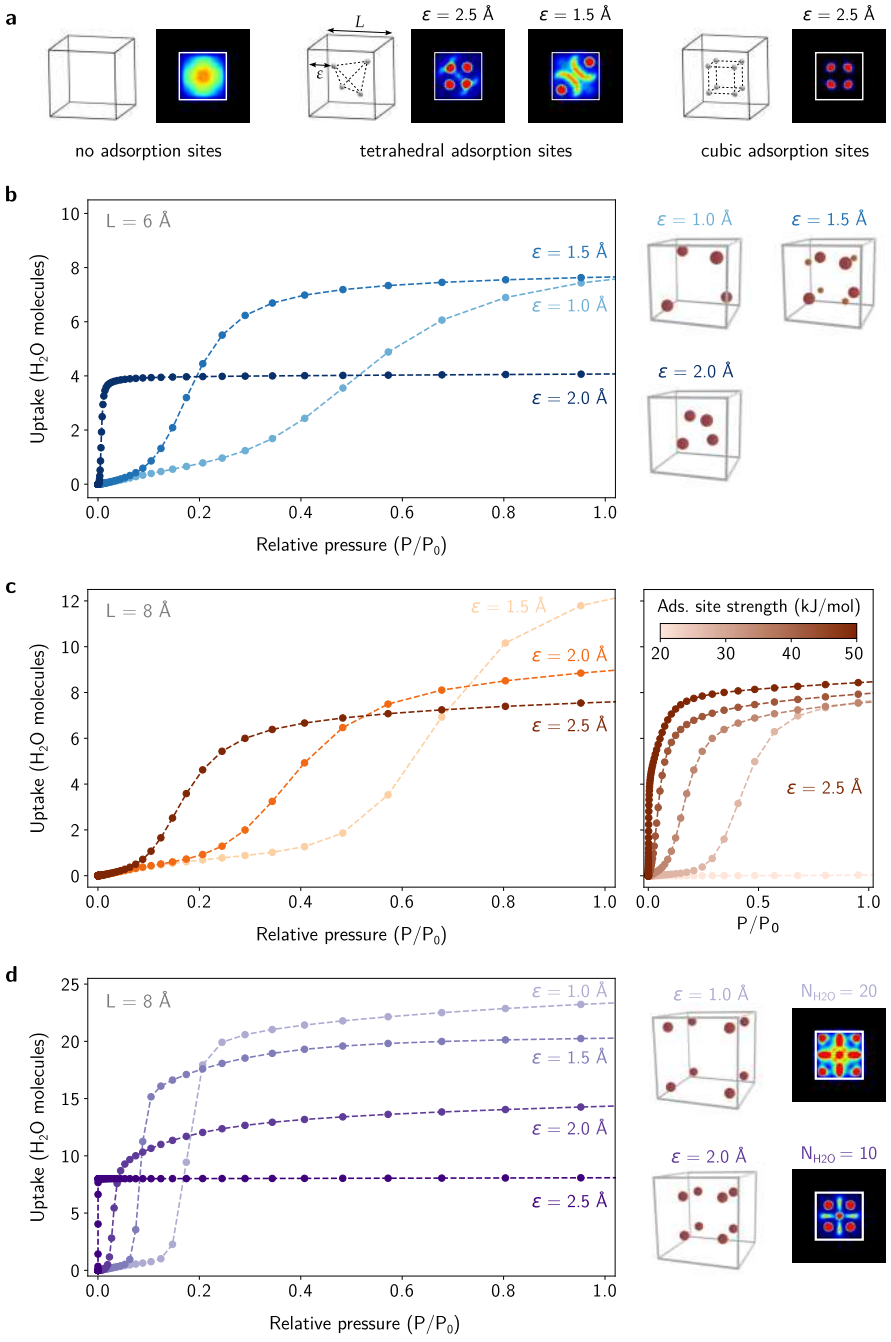

Figure 4.6: **a** Symmetrised density of eight water molecules in a repulsive cubic box with a side of 8 Å and differently placed adsorption sites of 20 kJ/mol. **b** Water adsorption isotherms for a repulsive cubic box with a side of 6 Å and tetrahedrally arranged primary adsorption sites with a strength of 35 kJ/mol (indicated in red). **c–d** Water adsorption isotherms for a repulsive cubic box with a side of 8 Å and tetrahedrally (c) or cubically (d) arranged adsorption sites with a strength of 35 kJ/mol. In pane c the influence of the adsorption site strength is also shown.

context of atmospheric water harvesting, the ideal adsorption behaviour is characterised by a step-shaped isotherm with a steep uptake at a relative pressure P/P_0 between 0.1 and 0.3. In that way, water can be easily adsorbed at low pressures, while retaining moderate regeneration conditions.[6, 36] For the tetrahedrally arranged adsorption sites in the virtual pore, this behaviour is only obtained for ε = 1.5 Å, when the primary adsorption sites induce a cubic structure with secondary adsorption sites through hydrogen bonding. When the adsorption sites are placed further apart, in the corners of the box (ε = 1.0 Å), the isotherm is flattened across a wide pressure range due to the absence of localised secondary adsorption sites and a lack of cooperative adsorption among the sites, which limits the working capacity associated with the pore. Similarly, a closer spacing of the adsorption sites (ε = 2.0 Å) also reduces the working capacity of the pore, as the total uptake of the pore decreases and the adsorption at very low pressures implies that these molecules cannot be desorbed at moderate conditions.

For a larger repulsive box, with a side of 8 Å (Figure 4.6c), a comparable trend is observed for the isotherms and the underlying structure of the adsorption sites. The preferred adsorption behaviour is again obtained in the presence of secondary adsorption sites (ε = 2.5 Å), whereas a larger spacing between the adsorption sites (ε < 2.5 Å) decreases the steepness of the isotherm and shifts it towards higher pressures, thus reducing the working capacity of the pore.

To consider the effect of a higher number of adsorption sites, the tetragonal configuration is replaced by a cubic arrangement of adsorption sites (Figure 4.6d). In contrast to the tetrahedral arrangement, placing the eight primary adsorption sites at a hydrogen bond distance from one another (ε = 2.5 Å) results in an immediate occupation of the sites at the lowest pressures. The four additional primary adsorption sites yield a too strong cooperative interaction in comparison with the secondary adsorption sites in the tetrahedral arrangement. For larger spacings between the adsorption sites (ε < 2.0 Å), the suitable isotherm shape for atmospheric water harvesting can be retrieved. The most beneficial arrangement of the adsorption sites is obtained when they are located in the corners of the box, so that the volume of the pore can be maximally exploited, which increases the water uptake. In particular for ε = 1.0 Å, where the distance between the adsorption sites equals two hydrogen bond lengths, the adsorption of water molecules in between the primary adsorption sites has a favourable effect on the uptake (Figure 4.6d), similar to the secondary adsorption sites in the case of tetrahedrally arranged adsorption sites. Therefore, larger pores can be more efficiently filled with a higher number of adsorption sites located near the edges of the pore, than with a small cubic water cluster stabilised in the centre of the pore.

As demonstrated by the different arrangements of hydrophilic adsorption sites in the virtual nanopore, the precise location of these sites and the interplay between them give rise to a specific water organisation, which determines the adsorption characteristics of the pore. For certain configurations of the primary adsorption sites, secondary adsorption sites emerge in between these sites through the completion of the hydrogen bond network. In particular for the application of atmospheric water harvesting, the presence of secondary adsorption sites can have a favourable influence on the water adsorption isotherm, as these sites can improve the adsorption capacity of the pore while maintaining modest desorption energies. Therefore, the water structure induced by a MOF framework constitutes an important design parameter in the further development of MOFs with an enhanced efficiency for atmospheric water harvesting.

4.2 Shock absorption through water intrusion

Besides different types of polymeric foams, which rely on mechanisms such as plastic deformation, elastic buckling, or viscoelastic dissipation to absorb the energy of a mechanical impact,[189] also hydrophobic nanoporous materials can be used for this purpose. Through the forced intrusion of liquid water or aqueous solutions in these hydrophobic materials, their resistance against water intrusion can be harnessed to attenuate a mechanical impact. For the hydrophobic ZIF-8 framework, the water intrusion and extrusion at different strain rates were experimentally measured by our collaborators at the University of Oxford (the group of prof. J.-C. Tan). The resulting stress-strain curves are reported in Figure 4.7. Initially, the combined system of ZIF-8 and the surrounding water displays an elastic compression, with a linear decrease in volume as a function of increasing pressure. Next, the water starts to intrude the hydrophobic cages of ZIF-8 and the pressure remains constant while the volume of the system further decreases. After filling the accessible pores of the framework with water, the system again shows an elastic compression. The unloading of ZIF-8 follows a similar pattern, but with an extrusion pressure that is lower than the intrusion pressure, so that energy is dissipated during each intrusion-extrusion cycle.

Using a dedicated experimental setup, the influence of different strain rates ranging from 10^{-3} to 10^{3} s^{-1} were examined in **Paper IV**, to approach realistic strain rates for impact-attenuating materials. As the strain rate increases, the hysteresis of the intrusion-extrusion cycle also strongly increases, due to a significantly higher intrusion pressure (which almost triples from 25 MPa to 70 MPa) and a lower extrusion pressure. As a consequence, the energy ab-

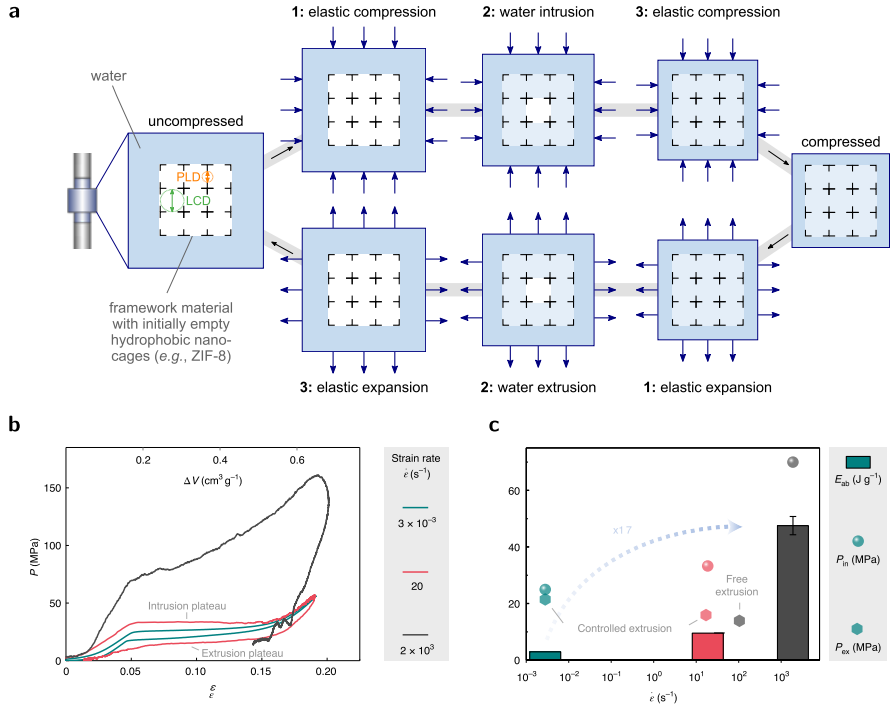

Figure 4.7: a Schematic overview of the different stages during the compression (top) and expansion (bottom) of a hydrophobic nanoporous material in a water intrusion/extrusion experiment. **b** Compressive stress–strain curves for water intrusion/extrusion in ZIF-8 at three different strain rates. The unloading part of the high-rate experiment is uncontrolled (that is, without external driving force), so only part of the extrusion plateau can be recorded. **c** Intrusion pressure, extrusion pressure, and energy absorption density as a function of the intrusion and extrusion strain rates. The error bar represents the uncertainty due to the incomplete unloading curve at high strain rate. Figures reproduced from Ref. [167] with permission of Springer Nature.

sorption capacity of the material is also strongly enhanced (Figure 4.7c): from about 3 J/g at quasi-static conditions to about 47 J/g at high-rate impacts, which correspond with 17% and 85% of the mechanical energy, respectively. Furthermore, in contrast to a mechanism such as plastic deformation which can only attenuate a single impact, the ZIF-8 system can withstand multiple impact cycles, as the applied mechanical pressure is below the amorphisation pressure.

To deduce the molecular origin of this intrusion phenomenon, MC and MD simulations were performed for different water distributions. At low

water loadings, canonical MC simulations indicate that the water molecules preferentially occupy the regions near the six- (6MR) and four-membered (4MR) rings (*i.e.* sites S2 and S4 in Figure 2.9c). At higher water loadings, the water molecules tend to cluster around the centre of the ZIF-8 cages, as the formation of a hydrogen-bonded network is energetically more favourable than interacting with the hydrophobic framework. Furthermore, MD simulations at these high loadings also reveal that the dynamic gate opening effect of the ZIF-8 structure is not at the basis of the intrusion phenomenon, as the gate is observed to further close in the presence of the water molecules. To gain insight into the water mobility in ZIF-8 and the associated cage filling process, the spontaneous diffusion of water is monitored for a saturation loading of 42 water molecules in a single cage (cage 1 in Figure 4.8a). During the first 0.45 ns of the simulation, the water gradient between the cages leads to the diffusion of water molecules to the neighbouring cages 2 and 3. Subsequently, the cluster of six water molecules in cage 2 continues to grow throughout the simulation, whereas the two water molecules in cage 3 are insufficiently stabilised and rejoin the larger water cluster in cage 1. The timescale associated with the spontaneous nucleation and growth process of a stable water cluster in cage 2 is of the order of nanoseconds, as inferred from the exponential fit to the water occupation of cage 2 in Figure 4.8a.

Using umbrella sampling MD simulations, the free energy barrier of the nucleation process of a water cluster can be quantified as a function of the water distribution. To bias the simulations, the same CV can be used as in Section 2.2.6, which restrains the transitioning water molecule to move in a plane parallel to the 6MR between the cages (Figure 4.8b). Starting from a critical-sized cluster of five water molecules in cage 1, with an additional transitioning water molecule, and an empty cage 2, a free energy difference ΔF_1 of about 15 kJ/mol is obtained between the two cages. As more water molecules are added to cage 2, the free energy difference between the cages starts to decrease and eventually disappears for a cluster of four water molecules. Also for a larger number of water molecules in cage 2, the free energy difference between the cages remains negligible. When the critical-sized cluster in cage 1 is replaced by a supercritical cluster of thirty water molecules, similar results are obtained. Therefore, in line with the spontaneous diffusion process considered in Figure 4.8a, the free energy profiles confirm the pivotal role played by critical-sized water clusters to fill the hydrophobic cages of ZIF-8.

For sufficiently low strain rates, the water intrusion process in ZIF-8 will thus occur through the spontaneous nucleation of critical-sized water clusters in cages neighbouring already filled cages. As the strain rate associated with the impact increases, the diffusion process eventually becomes too slow to

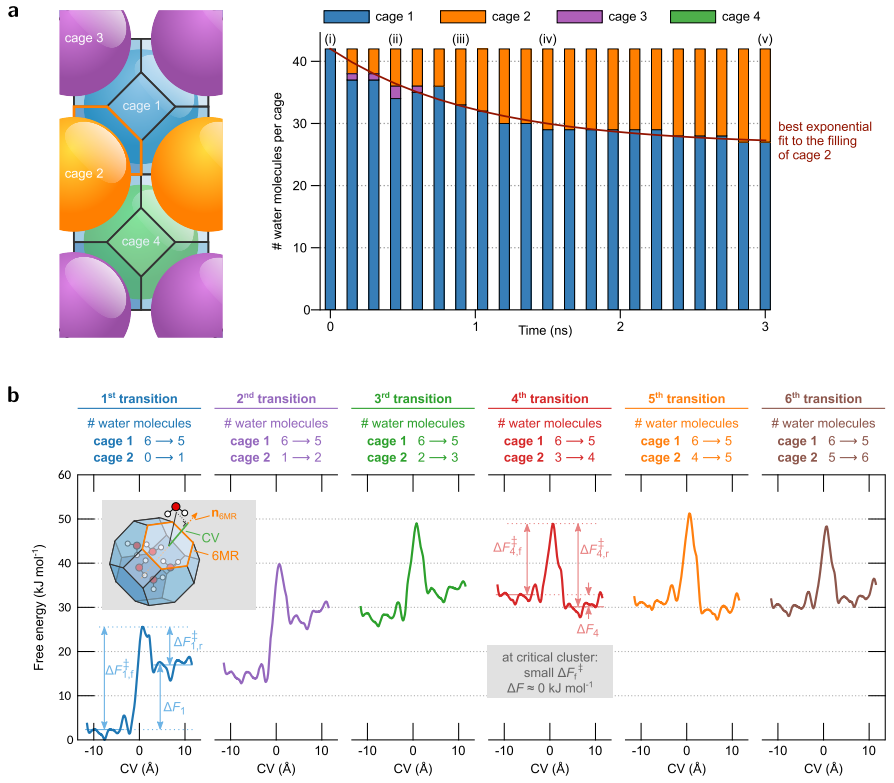

Figure 4.8: **a** Evolution of the number of water molecules in a ZIF-8 supercell with four inequivalent cages (at 300 K and 0 MPa). In the initial configuration, cage 1 contains 42 water molecules and all other cages are empty. The best exponential fit of $a(1 - e^{-t/\tau})$ to the filling of cage 2 (red line) yields a time constant $\tau \approx 1$ ns. **b** Free energy profiles for the transition of a water molecule from cage 1, containing a critical-sized water cluster of five additional molecules, to cage 2, containing zero (first transition) to five (sixth transition) water molecules. The CV (inset) used to bias the umbrella sampling simulations is similar to the one used in Section 2.2.6. Figures reproduced from Ref. [167] with permission of Springer Nature.

form critical-sized water clusters and the water molecules are forced into the neighbouring hydrophobic cages, thereby dissipating the energy of the impact to overcome the free energy barrier between the cages.

Apart from ZIF-8, this rate dependent behaviour of water intrusion is also present in other hydrophobic ZIFs, such as ZIF-67 and ZIF-71. In ZIF-7 and ZIF-9, by contrast, a strong hysteresis effect is absent as water molecules

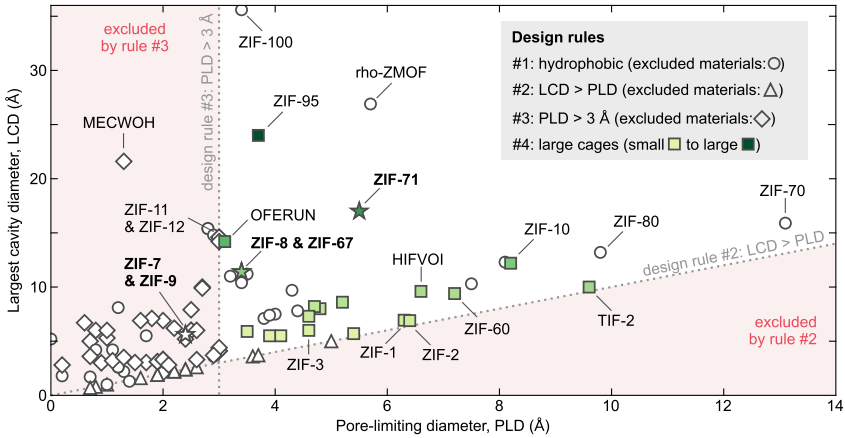

Figure 4.9: Identification of promising high-rate impact-attenuating materials among the 105 ZIFs tabulated in Ref. 190, using four design rules. The eligible materials are attributed a colour according to their pore size. The uncoloured materials are excluded because they are not hydrophobic (as determined by their linkers, shown with circles), not cage-type (triangles), or have a too small PLD (diamonds). Experimentally validated materials are bold-faced (stars). Figure reproduced from Ref. [167] with permission of Springer Nature.

remain trapped in the framework, due to their small pore-limiting diameters (PLDs). Also for zeolites such as ZSM-5, zeolite-β, and mordenite, the rate dependence of the intrusion-extrusion cycle is small, due the higher mobility of water inside the channels of the zeolites. Based on these experimental observations, four design rules can be proposed to identify promising materials for high-rate impact attenuation through water intrusion. First, a hydrophobic material is required. Second, the material should possess a structure of nanocages, with a largest cavity diameter (LCD) that is strictly larger than the PLD. Third, the pore windows should be sufficiently large to allow for a spontaneous diffusion of water between the cages of the framework during extrusion. Otherwise, the shock absorber is not reusable. Finally, for materials with larger cages, a higher energy absorption density can be achieved, as the pores can accommodate larger water clusters. In Figure 4.9, these design rules are applied to a set of 105 ZIF-like materials, which reveals an additional 17 eligible materials for high-rate shock absorption through water intrusion.

5

Conclusions and Perspectives

We can only see a short distance ahead, but
we can see plenty there that needs to be done.

Alan Turing[191] (1912–1954)

Through the rational design of functional nanoporous materials, their performance can be optimised for many different applications, ranging from carbon capture or the sustainable production of building-block chemicals to shock absorption and atmospheric water harvesting. To cleverly guide this design at the nanoscale, a profound molecular-level understanding of the material's fundamental properties and their influence on the various physical or chemical processes of interest is required. While experimental characterisation techniques can easily study the overall functional behaviour of these materials, the underlying molecular mechanisms can often only be probed indirectly with, for instance, spectroscopic techniques. A theoretical description of these materials through molecular modelling, by contrast, offers both direct access to an atomic-scale resolution and a precise control over their molecular design. In this PhD dissertation, computational modelling was used to examine the properties of two classes of nanoporous materials: zeolites and metal-organic frameworks (MOFs). Due to their high stability and exceptional catalytic performance, zeolites are widely used within the petrochemical industry and can play an important role in future technologies such as biomass conversion. Furthermore, these porous aluminosilicate structures have also emerged in many commercial applications,

ranging from cat litter to water purification or gas separation. The more recent material class of MOFs is yet to reach industrial scale applications, but holds great promise to contribute to solutions for current societal challenges, as exemplified by proof-of-concepts for carbon dioxide capture from flue gasses or atmospheric water harvesting in arid regions. To explore the nearly endless possibilities to create MOF structures, by combining different organic linkers with various metal clusters in search of optimal functional materials, molecular modelling can offer guidance through high-throughput screenings and fundamental insights into structure–property relations which can serve as material design principles. A prerequisite for reliable computational predictions is the use of accurate simulation techniques to model molecular systems. Therefore, this dissertation focussed on the impact of the common approximation to treat atomic nuclei as classical particles, in spite of their quantum mechanical nature. As lightweight atoms are most susceptible to these so-called nuclear quantum effects (NQEs), the behaviour of an acidic proton on a zeolite framework (Chapter 3) or the structural organisation of water molecules confined in the pores of a MOF (Chapter 4) are of particular interest.

In each molecular simulation, approximations in the computational description of the system are inevitable, due to the impossibility of exactly solving the quantum mechanical Schrödinger equation for realistic molecular systems. Using the Born-Oppenheimer approximation, the electronic and nuclear degrees freedom can be separated from one another and can subsequently be described at various levels of accuracy, as outlined in Chapter 2. Approximate quantum mechanical solutions for the electrons can be obtained with density functional theory (DFT), whereas force fields rely on an effective parametrisation of the interatomic interactions to reduce the computational cost of the simulations. In conventional force fields, a limited number of parameters is used in combination with physically inspired interaction potentials, whereas machine learning potentials (MLPs) use neural networks with millions of parameters to increase the correspondence with quantum mechanical electronic structure calculations. Irrespective of the description of the electronic degrees of freedom, the nuclei in a molecular system are most often treated as classical particles. For quite some molecular systems, this is a perfectly reasonable approximation within a certain range of thermodynamic conditions. In **Paper VI** and **Paper XI**, classical simulation techniques were used to model the adsorption and diffusion of carbon dioxide and methane in zeolite frameworks containing sodium ions. The molecular insights obtained from these simulations contributed in explaining the performance of the zeolite-filled mixed-matrix membranes synthesised by our experimental collaborators at the KU Leuven (the group of prof. I.

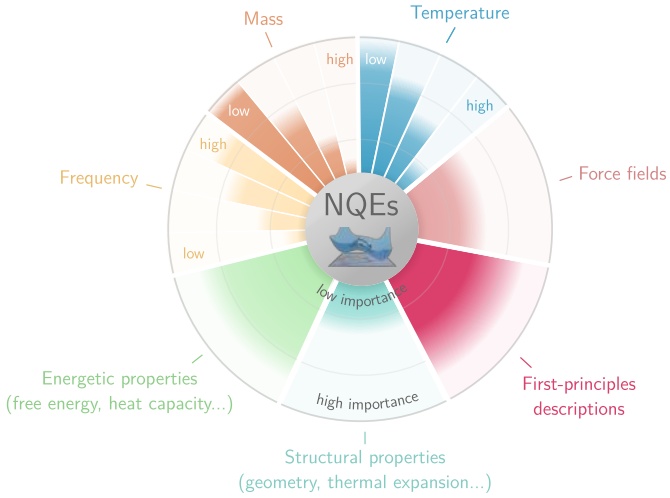

Figure 5.1: Schematic representation of the importance of including nuclear quantum effects (NQEs) in a molecular simulation for different parameters, properties, and methods.

Vankelecom), including the molecular sieving of carbon dioxide and the optimal sodium content associated with a high carbon dioxide permeability. For other molecular systems, a classical description of the nuclei is insufficient and NQEs have to be taken into account, in particular for processes that involve light atoms or occur at low temperatures (Figure 5.1). A first example which necessitates the inclusion of NQEs is the study of the rotational tunnelling of methyl rotors in ZIF-8, as tunnelling is a purely quantum mechanical phenomenon without classical analogue. For both argon and nitrogen adsorption in ZIF-8, experimental measurements at 3 K revealed a change in the tunnel splitting of the rotational energy levels as a function of the number of adsorbates. To explain these experimental observations of our collaborators at the University of Oxford (the group of prof. J.-C. Tan), a computational description combining DFT and NQEs related the different tunnel splittings to the occupation of specific adsorption sites in ZIF-8, as discussed in **Paper IX**. In this way, quantum rotational tunnelling can be used as a sensitive atomistic probe for guest adsorption in MOFs.

In Chapter 3, the influence of NQEs in MOFs and zeolites was examined at higher temperatures, corresponding with realistic operating conditions. For the archetypal MOF-5 framework, studied in **Paper I** and **Paper II**, only minor influences were perceivable in the structural properties of the material. To accurately reproduce its negative thermal expansion, a proper inclusion of anharmonicities in the force field proved to be of primary im-

portance, whereas NQEs only play a secondary role. The main effect of accounting for the quantum mechanical zero-point energy is a change in the absolute volume of the framework when using a proper anharmonic description. In the estimation of the heat capacity, by contrast, NQEs are essential to reproduce the correct temperature dependence. While harmonic NQEs are sufficient to yield a satisfactory agreement with experiments for the framework itself, the presence of methane guest molecules also requires the inclusion of anharmonicities, for which path integral molecular dynamics (PIMD) simulations can be used. Within PIMD, the quantum statistics of the nuclei are mimicked by simultaneously simulating multiple replicas of the molecular system. The quantum mechanical properties of the system are then obtained by averaging over the different replicas of each nucleus. However, in most enhanced sampling techniques, which are used to simulate activated processes and calculate free energy barriers between (meta)stable configurations of the molecular system, a quasi-classical approach is commonly used to derive properties from the so-called path integral centroids, which geometrically average the different replicas of every atom. Depending on the activated process under investigation, **Paper VII** demonstrated that this quasi-classical characterisation of a free energy barrier can significantly deviate from the purely quantum mechanical description. By means of an elegant sampling protocol devised in **Paper VII**, both quantum and quasi-classical centroid free energy profiles can be obtained from a single set of simulations by making use of a post-processing transformation. For the three molecular proton transfer reactions used as case studies to assess the difference between both approaches, higher and steeper free energy barriers are observed to be more prone to NQEs, which increases the discrepancy between both descriptions. For the proton transfer with the highest free energy barrier, the appropriate quantum method yields a reduction of about 60% of the classical free energy barrier at 450 K, whereas the centroid method only yields a reduction of about 6%. As the free energy barrier grows higher and becomes more sharply peaked, the inequivalence between the PIMD replicas and centroid becomes more pronounced, resulting in larger quantum corrections, which also affect the overall shape of the free energy profile.

In **Paper VIII**, this protocol was applied to the proton hopping reaction of a Brønsted acid site (BAS) around an aluminium defect in a chabazite zeolite. As large deviations between experimental and computational activation energies have been reported for the proton hopping of the BAS, it is instructive to evaluate the impact of a rigorous treatment of NQEs for this reaction. To maximally limit the approximations within the computational description, the electronic degrees of freedom are preferably described by means of DFT. Given the size of the molecular system in combination with numerous

enhanced sampling simulations employing the computationally costly PIMD technique, DFT accuracy can only be obtained by training an MLP to DFT reference data of a feasible number of system configurations. With this MLP, both classical and quantum free energy profiles and reaction rate constants can be determined at different temperatures, to extract the activation energy of the hopping reaction and the equilibrium occupation of the BAS on the oxygen atoms neighbouring the aluminium defect. In the presence of NQEs, the simulation results displayed a different preferential oxygen occupation and a reduction of the activation energy of the hopping by about 11 kJ/mol (or 17%) in comparison with a classical description. Furthermore, the MLP also allows to calculate kinetic isotope effects, for which a substitution with deuterium yields the expected moderation of the NQEs due its heavier mass.

Within the context of accurate simulation techniques, water is a prominently researched molecular system, as its many anomalous properties over a large range of thermodynamic conditions turn out to be very complex to reproduce accurately with a single model or common level of theory. In this respect, also NQEs can contribute to a more accurate modelling of water, which initiated the study of water in MOFs outlined in Chapter 4. For water confined in the flexible MOF MIL-53(Al), the inclusion of NQEs was however observed to have a very modest impact on the relative stability of the two phases of MIL-53(Al) within a force field description, as discussed in **Paper III**. In particular near room temperature, competing NQEs can weaken the impact on the intricate hydrogen bond network of water and thus also reduce its effect on water properties. Apart from NQEs, the confinement effects associated with the MOF's nanopores have a decisive impact on the behaviour of the adsorbed water molecules. In MIL-53(Al), for instance, water can form one-dimensional water wires along the framework's pore channels. Furthermore, in **Paper X**, zirconium MOFs with moderate pore sizes were shown to shape water through a beneficial positioning of hydrophilic adsorption sites. One of these MOFs, MOF-801, exhibits suitable water adsorption characteristics for the application of atmospheric water harvesting, which can be related to the formation of cubic water clusters. By means of an analytical toy model, the favourable influence of an advantageous placement of water adsorption sites was demonstrated to positively impact the adsorption behaviour of water through the cooperative formation of secondary adsorption sites via directional hydrogen bonds. By exploiting this templating mechanism of water in nanopores, involving a meticulous design of primary adsorption sites and secondary induced adsorption sites, one can imagine a further improvement and tailoring of the water adsorption characteristics of new MOFs towards specific applications, such as atmospheric water harvesting.

Besides hydrophilic adsorption sites, also hydrophobic frameworks can direct

the organisation of water at the nanoscale. For ZIF-8, examined in **Paper IV**, high-rate water intrusion experiments performed by our collaborators at the University of Oxford revealed a strong hysteresis in the intrusion-extrusion cycle, which results in a seventeenfold increase of the energy absorption capacity, so that 85% of the mechanical energy is dissipated (compared to 17% at low impact rates). The molecular origin of this high-rate impact attenuation can be traced back to the formation of critical-sized water clusters. For sufficiently low impact rates, the hydrophobic cages of ZIF-8 can be sequentially filled through the spontaneous nucleation of water clusters, which can steadily grow to fill a pore of ZIF-8 after reaching a certain critical size. If the impact rate becomes too high, however, the spontaneous organisation of water into clusters is too slow to fill the hydrophobic pores of ZIF-8, so that water molecules are forced into the pores, which involves crossing a free energy barrier, so that the energy of the impact is dissipated. In addition to ZIF-8, the design rules extracted from this case study also revealed 17 other ZIF materials that could be eligible for high-rate shock absorption through water intrusion.

In summary, NQEs have been shown to be indispensable in modelling proton transfer reactions over a wide range temperatures. Through the simulation approach proposed in **Paper VII**, the impact of NQEs on the free energy barriers of these reactions can be made explicit by constructing quantum free energy profiles instead of quasi-classical centroid free energy profiles. However, given the significant increase in computational cost to include NQEs by means of PIMD simulations (which are at least one order of magnitude more costly than a classical treatment of the nuclei), MLPs play a crucial role in making PIMD simulations with a first-principles accuracy affordable, especially for large molecular structures and in combination with enhanced sampling techniques to calculate free energy barriers. Within a force field description of MOFs, NQEs appear to only have a moderate influence on most structural and thermal properties, except for the heat capacity (Figure 5.1). A proper anharmonic description of MOFs and their adsorbates is often more important than the inclusion of NQEs, even in the presence of water. The properties of water confined in the pores of a MOF can however be distinctly different, due to the altered shape of the hydrogen bond network imposed by the framework. As demonstrated by the analytical toy model devised in **Paper X**, the specific structure of water clusters that nucleate at hydrophilic adsorption sites strongly determines the material's water adsorption behaviour. Through a more fundamental understanding of this structure–property relation, including the role of secondary induced adsorption sites, the water adsorption characteristics of MOFs can be further tuned for water applications such as atmospheric water harvesting.

In the ceaseless quest for more accurate and reliable modelling techniques, the inclusion of NQEs is destined to become a standard molecular modelling approach for certain material properties in the near future. This evolution will be further driven by the continued increase in computational power and the advances in MLPs, which keep the computational cost of a first-principles description in combination with techniques such as PIMD affordable, while also allowing for the simulation of reactive events. In addition to NQEs, a further improvement of the description of physical and chemical processes, such as proton transfers, will also require the use of more accurate first-principles methods within the training of the MLP, as different DFT exchange-correlation functionals can yield a large spread on the free energy barriers of these reactions.[192]

Similarly, the development of MLPs based on accurate first-principles data can also improve the description of the adsorption of water in MOFs.[193] To obtain a closer agreement with the experimental water adsorption studies, the perfect and infinite MOF crystals within simulations should be replaced by crystals of finite size which contain defects. For MOF-801, defect-rich crystals were shown to exhibit a different water uptake in comparison to single crystals, due to the adsorption of water on defects such as open metal sites and the interparticle condensation of water in the bulk material.[180] Through this continuous pursuit of more realistic computational models described with a higher accuracy, the remaining gap between experimental and computational material characterisation can be further reduced to attain a more complete understanding of these materials and advance their rational design in view of new technological applications.

Part II

Published Papers

A

Publications in International Peer-Reviewed Journals

Paper I **On the importance of anharmonicities and nuclear quantum effects in modelling the structural properties and thermal expansion of MOF-5**

A. Lamaire, J. Wieme, S.M.J. Rogge, M. Waroquier, V. Van Speybroeck

Journal of Chemical Physics, **2019**, *150* (9), 094503

Paper II **Modeling the structural and thermal properties of loaded metal-organic frameworks. An interplay of quantum and anharmonic fluctuations**

V. Kapil, J. Wieme, S. Vandenbrande, A. Lamaire, V. Van Speybroeck, M. Ceriotti

Journal of Chemical Theory and Computation, **2019**, *15* (5), 3237–3249

Paper III **Atomistic insight in the flexibility and heat transport properties of the stimuli-responsive metal-organic framework MIL-53(Al) for water-adsorption applications using molecular simulations**

A. Lamaire, J. Wieme, A.E.J. Hoffman, V. Van Speybroeck

Faraday Discussions, **2021**, *225*, 301–323

Paper IV **High rate nanofluidic energy absorption in porous zeolitic frameworks**
Y. Sun, S.M.J. Rogge, A. Lamaire, S. Vandenbrande, J. Wieme, C.R. Siviour, V. Van Speybroeck, J.-C. Tan
Nature Materials, **2021**, *20* (7), 1015–1023

Paper V **Correlating MOF-808 parameters with mixed-matrix membrane (MMM) CO_2 permeation for a more rational MMM design**
R. Thür, D. Van Havere, N. Van Velthoven, S. Smolders, A. Lamaire, J. Wieme, V. Van Speybroeck, D. De Vos, I. Vankelecom
Journal of Materials Chemistry A, **2021**, *9* (21), 12782–12796

Paper VI **Truly combining the advantages of polymeric and zeolite membranes for gas separations**
X. Tan, S. Robijns, R. Thür, Q. Ke, N. De Witte, A. Lamaire, Y. Li, I. Aslam, D. Van Havere, T. Donckels, T. Van Assche, V. Van Speybroeck, M. Dusselier, I. Vankelecom
Science, **2022**, *378* (6625), 1189–1194

Paper VII **Quantum free energy profiles for molecular proton transfers**
A. Lamaire, M. Cools-Ceuppens, M. Bocus, T. Verstraelen, V. Van Speybroeck
Journal of Chemical Theory and Computation, **2023**, *19* (1), 18–24

Paper VIII **Nuclear quantum effects on zeolite proton hopping kinetics explored with machine learning potentials and path integral molecular dynamics**
M. Bocus, R. Goeminne, A. Lamaire, M. Cools-Ceuppens, T. Verstraelen, V. Van Speybroeck
Nature Communications, **2023**, *14* (1), 1008

Paper IX **Quantum tunneling rotor as a sensitive atomistic probe of guests in a metal-organic framework**
K. Titov, M.R. Ryder, A. Lamaire, Z. Zeng, A.K. Chaudhari, J. Taylor, E.M. Mahdi, S.M.J. Rogge, S. Mukhopadhyay, S. Rudić, V. Van Speybroeck, F. Fernandez-Alonso, and J.-C. Tan
Physical Review Materials, **2023**, *7* (7), 073402

Paper X **Water motifs in zirconium metal-organic frameworks induced by nanoconfinement and hydrophilic adsorption sites**

A. Lamaire, J. Wieme, S. Vandenhaute, R. Goeminne, S.M.J. Rogge, V. Van Speybroeck

In revision

Paper XI **Design of a tunable mixed matrix membrane platform for high-performance gas separations**

X. Tan, S. Robijns, A. Lamaire, R. Goeminne, N. De Witte, M. Dickmann, R. Verbeke, T. Van der Donck, D. Van Havere, R. de Oliveira Silva, Q. Ke, Y. Li, R. Thür, I. Aslam, C. Van Goethem, T. Donckels, D. Sakellariou, V. Van Speybroeck, T. Van Assche, M. Dusselier, I. Vankelecom

In revision

Paper I

On the importance of anharmonicities and nuclear quantum effects in modelling the structural properties and thermal expansion of MOF-5

A. Lamaire, J. Wieme, S.M.J. Rogge, M. Waroquier, V. Van Speybroeck

Journal of Chemical Physics, **2019**, *150* (9), 094503

A. Lamaire performed the research and wrote the manuscript with contributions from all authors.

The Journal of Chemical Physics ARTICLE scitation.org/journal/jcp

On the importance of anharmonicities and nuclear quantum effects in modelling the structural properties and thermal expansion of MOF-5

Cite as: J. Chem. Phys. 150, 094503 (2019); doi: 10.1063/1.5085649
Submitted: 13 December 2018 • Accepted: 6 February 2019 •
Published Online: 4 March 2019

Aran Lamaire, Jelle Wieme, Sven M. J. Rogge, Michel Waroquier, and Veronique Van Speybroeck[a]

AFFILIATIONS

Center for Molecular Modeling (CMM), Ghent University, Technologiepark 46, 9052 Zwijnaarde, Belgium

[a]Electronic mail: Veronique.VanSpeybroeck@UGent.be

ABSTRACT

In this article, we investigate the influence of anharmonicities and nuclear quantum effects (NQEs) in modelling the structural properties and thermal expansion of the empty MOF-5 metal-organic framework. To introduce NQEs in classical molecular dynamics simulations, two different methodologies are considered, comparing the approximate, but computationally cheap, method of generalised Langevin equation thermostatting to the more advanced, computationally demanding path integral molecular dynamics technique. For both methodologies, similar results were obtained for all the properties under investigation. The structural properties of MOF-5, probed by means of radial distribution functions (RDFs), show some distinct differences with respect to a classical description. Besides a broadening of the RDF peaks under the influence of quantum fluctuations, a different temperature dependence is also observed due to a dominant zero-point energy (ZPE) contribution. For the thermal expansion of MOF-5, by contrast, NQEs appear to be only of secondary importance with respect to an adequate modelling of the anharmonicities of the potential energy surface (PES), as demonstrated by the use of two differently parametrised force fields. Despite the small effect in the temperature dependence of the volume of MOF-5, NQEs do however significantly affect the absolute volume of MOF-5, in which the ZPE resulting from the intertwining of NQEs and anharmonicities plays a crucial role. A sufficiently accurate description of the PES is therefore prerequisite when modelling NQEs.

I. INTRODUCTION

Within the past few decades, the field of atomistic computer simulations has established itself as an important and complementary tool to experimental research in the characterisation of various types of materials. This computational approach does not only provide information about the fundamental molecular features underlying the material's properties but also allows for a large scale screening of potentially interesting materials, where new material designs can be assessed without the burdening requirement of synthesis that precedes experimental characterisation.[1] For metal-organic frameworks (MOFs),[2–4] in particular, a screening by means of atomistic simulations is recommended as these crystalline materials are built up out of inorganic building blocks that are connected to one another through organic linkers, giving rise to a virtually unlimited number of possible frameworks that can be constructed out of the vast amount of building blocks.[5–7] The designer aspect of MOFs along with the versatility in properties of the different MOF structures makes this class of nanoporous materials most attractive for industrial applications,[8] ranging from

The Journal of Chemical Physics ARTICLE scitation.org/journal/jcp

gas storage and gas separation[9,10] over heterogeneous catalysis[11] to shock absorption for the more flexible framework materials.[12]

Computationally, material properties can be obtained from molecular dynamics (MD) simulations as time averaged quantities by integrating the equations of motion throughout time. By relying on the Born-Oppenheimer approximation, as is usually done in MD simulations, one can separate the dynamics of the nuclei from the dynamics of the electronic structure of the system. Depending on the required length of the simulation and the size of the molecular system, the potential energy surface (PES) is then described *ab initio*, typically by means of density functional theory (DFT), or analytically, using force fields. However, irrespective of the description of the PES, a vast majority of the MD simulations treats the atomic nuclei as classical particles, in spite of their quantum mechanical nature. For sufficiently heavy atoms at sufficiently high temperatures, subjected to moderate interatomic interactions, this approximation is expected to be reasonable. Lighter atoms at lower temperatures or atoms subjected to strong interatomic interactions on the contrary cannot be described as classical particles, but have to be treated quantum mechanically as nuclear quantum effects (NQEs) such as zero-point energy (ZPE) and tunnelling can induce significant deviations from the classical behaviour. For water, a prototypical case study within the context of NQEs, the importance of NQEs has been demonstrated for ample of aspects,[13,14] including the occurrence of transient autoprotolysis events in liquid water[15] and a proper description of the heat capacity of both liquid water and ice.[16] Given the large ZPE of about 21 kJ/mol per O—H stretch,[13] which is in sharp contrast with the classical contribution to the kinetic energy of only 3.7 kJ/mol at 300 K (as predicted by the equipartition law), the importance of NQEs in water is abundantly clear.

Within the context of MOFs, NQEs are hardly ever taken into account, despite the presence of many light framework atoms, such as hydrogen and carbon. Only when studying water molecules confined in the pores of a framework, NQEs have been included to some extent.[17,18] In this work, the importance of NQEs in the structural and thermal properties of the empty framework of MOF-5[19] is assessed by means of MD simulations. In this way, the NQEs inherent to the MOF itself are investigated rather than the NQEs associated with water present in its pores, using MOF-5 as a prototypical rigid framework (Fig. 1). The structural properties of MOF-5 are probed by means of radial distribution functions (RDFs), which yield information about the interatomic equilibrium distances and the thermal activation of bond stretches of different atom pairs. The thermal property under review is the well-known negative thermal expansion of MOF-5,[20–25] for which a delicate interplay between the modelling of anharmonicities and NQEs is demonstrated.

For each of these properties, the importance of NQEs is assessed by comparing ordinary, classical MD simulations to MD simulations including NQEs, where the quantum mechanical description of the nuclei is pursued using two different methodologies. The first method is the so-called generalised

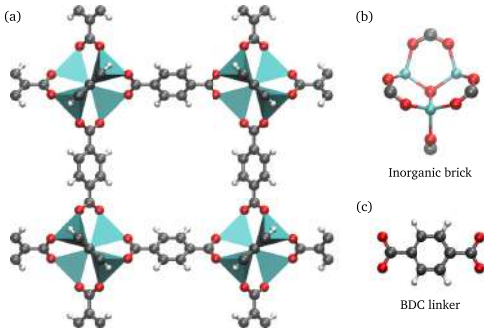

FIG. 1. (a) Conventional unit cell of MOF-5, with the ZnO_4 tetrahedra indicated in light blue. (b) $Zn_4O(CO_2)_6$ metal oxide cluster. (c) 1,4-benzenedicarboxylate (BDC) linker.

Langevin equation (GLE) quantum thermostat,[26] which allows us to include harmonic NQEs at virtually no additional computational cost. The second method that will be considered is the more advanced technique of path integral MD (PIMD),[27,28] which entails a more rigorous description of both harmonic and anharmonic NQEs, at a sometimes considerable additional computational expense. By combining both methods, the computational cost of PIMD simulations can however be reduced by a factor of about four[29,30] and therefore, this synergistic approach will also be considered, alongside the GLE quantum thermostat and regular PIMD, as explained in Sec. II.

II. METHODOLOGY: MODELLING NUCLEAR QUANTUM EFFECTS

A. GLE quantum thermostat

A first, but approximate technique to include NQEs in MD simulations is the so-called generalised Langevin equation (GLE) quantum thermostat.[26] Just as any other thermostat, the GLE thermostat imposes a sampling of the canonical ensemble instead of the microcanonical ensemble by adapting Hamilton's equations of motion, to allow for an exchange of heat with the system's surroundings

$$\dot{q}(t) = p(t), \tag{1}$$

$$\dot{p}(t) = -\frac{dV(q)}{dq} - \int_{-\infty}^{t} K(t-\tau)p(\tau)\,d\tau + \zeta(t), \tag{2}$$

with q the generalised coordinate describing the position of a particle with a unit mass, p the conjugate momentum, $V(q)$ the potential energy, $K(t)$ the memory kernel of the GLE, and $\zeta(t)$ a random Gaussian distributed force. To impose a canonical sampling, the time correlation function $H(t) = \langle\zeta(t)\zeta(0)\rangle$ of the random force $\zeta(t)$ has to be related to the memory kernel $K(t)$ by means of the fluctuation-dissipation theorem[31,32]

$$H(\omega) = k_B T K(\omega), \tag{3}$$

The Journal of Chemical Physics ARTICLE scitation.org/journal/jcp

with k_B the Boltzmann constant, T the temperature, and $H(\omega)$ and $K(\omega)$ the Fourier transforms of, respectively, $H(t)$ and $K(t)$. However, if one wants to turn the GLE thermostat into a GLE quantum thermostat, which can be used as a tool to introduce NQEs in MD simulations, the constraint imposed by the fluctuation-dissipation theorem has to be relaxed to provide the necessary freedom to include harmonic NQEs. To that end, an effective temperature $T^\star$, given by

$$T^\star = \frac{\hbar\omega}{2k_B}\coth\left(\frac{\hbar\omega}{2k_BT}\right), \tag{4}$$

is introduced in order to match the probability distribution ρ of the displacement q of a classical harmonic oscillator with frequency ω and mass m,

$$\rho(q) \propto \exp\left(-\frac{m\omega^2q^2}{2k_BT}\right), \tag{5}$$

to the quantum mechanical probability distribution of the displacement (see Sec. S1), which is proportional to

$$\rho(q) \propto \exp\left[-\frac{1}{2}m\omega^2q^2\frac{1}{\frac{\hbar\omega}{2}\coth\left(\frac{\hbar\omega}{2k_BT}\right)}\right]. \tag{6}$$

In this way, the classical canonical sampling imposed by the Boltzmann distribution [Eq. (5)] can be transformed into a quantum mechanical sampling that is in accordance with the probability distribution of the quantum harmonic oscillator [Eq. (6)] and as a consequence introduces a sampling of the harmonic NQEs. Therefore, one should picture the GLE quantum thermostat as a thermostat that excites every vibrational mode present in a molecular system to an effective temperature $T^\star$, which is the temperature the mode is supposed to have according to the probability distribution of the quantum harmonic oscillator.

The appropriate canonical sampling is then once again obtained by imposing the fluctuation-dissipation theorem, where the effective, frequency-dependent temperature $T^\star$ now takes the role of the physical temperature T so that

$$H(\omega) = k_BT^\star K(\omega). \tag{7}$$

However, since the GLE quantum thermostat is a so-called non-equilibrium thermostat that violates the fluctuation-dissipation theorem (i.e., the fluctuation-dissipation theorem for the physical temperature T), one now also needs to explicitly impose the equipartition theorem, as this cannot longer be taken for granted for a non-equilibrium thermostat. In view of an adequate modelling of harmonic NQEs, one therefore also has to satisfy the equipartition theorem for the quantum harmonic oscillator, which requires that

$$\langle p^2\rangle = m^2\omega^2\langle q^2\rangle = \frac{\hbar m\omega}{2}\coth\left(\frac{\hbar\omega}{2k_BT}\right). \tag{8}$$

The only difference between an ordinary GLE thermostat and the GLE quantum thermostat is hence the way in which the memory kernel $K(t)$ and the random force $\zeta(t)$ are related to one another so that the GLE thermostat allows us to include harmonic NQEs in MD simulations without almost any additional computational cost. For a more detailed discussion of the GLE quantum thermostat, the reader is referred to Refs. 26, 33, and 34

B. Second order path integral MD

A more rigorous method to model NQEs in MD simulations is given by the path integral MD formalism.[35] In this formalism, which can be traced back to Feynman's path integral formulation of quantum mechanics,[36] NQEs are evoked by replacing every atom of the molecular structure by a so-called ring polymer that consists of P atom replicas, called beads, that interact with one another via a harmonic nearest-neighbour interaction, as depicted schematically in Fig. 2.

For an N-atom molecular system characterised by the Hamiltonian

$$H = \sum_{i=1}^{N}\frac{\mathbf{p}_i^2}{2m_i} + V(\mathbf{r}_1,\ldots,\mathbf{r}_N), \tag{9}$$

with $\mathbf{p}_i$ and $\mathbf{r}_i$, respectively, the momentum and position of the ith particle and $V(\mathbf{r}_1, \ldots, \mathbf{r}_N)$ the potential energy, this more rigorous introduction of NQEs can be readily obtained by means of a Trotter factorisation of the quantum mechanical canonical partition function $Z = \mathrm{Tr}[e^{-\beta\hat{H}}]$, expanding the canonical density matrix $e^{-\beta\hat{H}}$ as follows:

$$e^{-\beta\hat{H}} = \left[e^{-\frac{\beta}{2P}\hat{V}}e^{-\frac{\beta}{P}\sum_{i=1}^{N}\frac{\hat{\mathbf{p}}_i^2}{2m_i}}e^{-\frac{\beta}{2P}\hat{V}}\right]^P + \mathcal{O}(P^{-2}), \tag{10}$$

with $\beta = (k_BT)^{-1}$ the inverse temperature and P the number of beads. The resulting expression for the quantum mechanical canonical partition function Z then becomes (see Sec. S2)

$$Z_P = \prod_{k=1}^{P}\prod_{i=1}^{N}\int d\mathbf{p}_i^{(k)}\int d\mathbf{r}_i^{(k)}\,e^{-\beta H_P}, \tag{11}$$

where the Hamiltonian of the N-atom system is replaced by the Hamiltonian of an extended molecular system given by

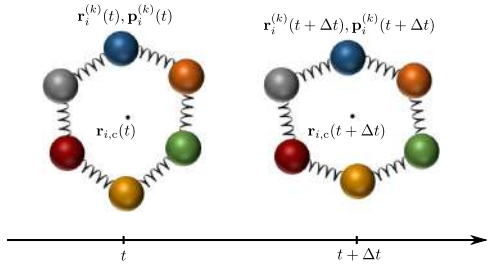

FIG. 2. Schematic representation of the time evolution of a 6 bead ring polymer with centroid $\mathbf{r}_{i,c}$.

The Journal of Chemical Physics ARTICLE scitation.org/journal/jcp

$$H_P = H_P^0 + V_P, \tag{12}$$

with

$$H_P^0 = \sum_{k=1}^{P}\sum_{i=1}^{N}\left[\frac{\mathbf{p}_i^{(k)^2}}{2m_i} + \frac{1}{2}m_i\omega_P^2\left(\mathbf{r}_i^{(k+1)} - \mathbf{r}_i^{(k)}\right)^2\right] \tag{13}$$

and

$$V_P = \frac{1}{P}\sum_{k=1}^{P} V(\mathbf{r}_1^{(k)}, \ldots, \mathbf{r}_N^{(k)}), \tag{14}$$

with $\mathbf{r}_i^{(k)}$ and $\mathbf{p}_i^{(k)}$, respectively, the position and momentum of the kth bead of the ith particle, $\omega_P = \frac{\sqrt{P}}{\beta\hbar}$ the angular frequency of the harmonic interaction between the neighbouring beads of the ring polymer, and $\mathbf{r}_i^{(P+1)} = \mathbf{r}_i^{(1)}$.

The higher the number of beads P, the smaller the error in the Trotter factorisation of Eq. (10), yielding quantum mechanically exact results in the limit of an infinite number of beads. PIMD is therefore not only more accurate than the GLE quantum thermostat, as it takes both harmonic and anharmonic NQEs into account, but it also allows us to systematically increase the accuracy with which NQEs are modelled by increasing the number of beads, a desirable feature that is lacking for the GLE quantum thermostat.

The major downside of PIMD when compared to the GLE quantum thermostat is the considerable computational overhead that is induced by substituting every atom in the system by multiple bead replicas. Given the efficiency of the GLE quantum thermostat in modelling harmonic NQEs, it is however possible to develop a hybrid PI + GLE scheme,[29,30] combining PIMD with a GLE quantum thermostat in order to reduce the number of beads required to converge PIMD simulations. In the so-called PIGLET thermostatting scheme,[30] the potential and kinetic energy of the system are enforced to match the harmonic quantum limit by subjecting the path centroid, defined as

$$\mathbf{r}_{i,c} = \frac{1}{P}\sum_{k=1}^{P}\mathbf{r}_i^{(k)}, \tag{15}$$

to classical thermostatting, while the individual beads are subjected to a GLE quantum thermostat. As a consequence, the required number of beads to converge the energy is reduced by a factor of about four since the GLE quantum thermostat already takes care of the harmonic NQEs so that higher bead multiples are only necessary to converge the remaining anharmonic NQEs.[13]

Besides PIGLET thermostatting, there also exist other cost reducing techniques for PIMD,[37] such as multiple time stepping (MTS),[38] ring polymer contraction (RPC),[28,39] and perturbed path integrals (PPI).[40,41] In the MTS algorithm, an algorithm first devised for classical MD, a more efficient force evaluation is obtained by separating the slowly varying long-range interactions from the rapidly varying short-range interactions. Given their different characteristic time scales, the long-range interactions only need to be evaluated at fixed time multiples of the short-range interactions, which are calculated at every time step. A similar splitting of the interaction is used in RPC, where the long-range part of the potential is evaluated on a contracted ring polymer containing fewer than P beads. In the limit of contraction to a single bead, the classical long-range force evaluation is retrieved. A different approach is used in PPI, where the theory of Feynman path integrals is combined with quantum mechanical perturbation theory to reduce the required number of beads by means of an *a posteriori* correction to the canonical partition function [Eq. (11)].

Finally, the convergence of PIMD simulations can also be accelerated by so-called high-order PI schemes, which rely on a more accurate decomposition of the canonical density matrix than the second-order Trotter factorisation [Eq. (10)]. A more accurate decomposition scheme such as the Suzuki-Chin (SC) scheme[42,43] then reduces the error to $\mathcal{O}(P^{-4})$, which also reduces the required number of beads to reach convergence. The force evaluation in SC PIMD is, however, more expensive than in Trotter PIMD,[44] as the equivalent of Eq. (14) not only depends on the physical potential energy, but also on the derivative of the physical potential energy. Nonetheless, SC PIMD becomes very advantageous at low temperatures or when a high accuracy is required. Therefore, this technique is used to validate our results, as outlined in Sec. IV.

III. COMPUTATIONAL DETAILS

As already mentioned in the Introduction, the importance of NQEs in MOF-5 will be assessed within this work by comparing ordinary, classical MD simulations to MD simulations including NQEs, using either a GLE quantum thermostat or PIMD. Given the rather large conventional unit cell of MOF-5, containing 424 atoms, an *ab initio* description of the PES is to be viewed as computationally too expensive, especially in combination with PIMD, so that all MD simulations within this work are performed using an in-house developed force field, generated from *ab initio* data using the in-house developed software package `QuickFF`.[45,46] In view of recent publications exemplifying a delicate interplay between a correct description of anharmonic force field contributions and NQEs,[14,47–49] the bond and bend contributions in the force field of MOF-5 are parametrised both by harmonic potentials, resulting in a "harmonic" force field, and by higher order polynomials, resulting in an "anharmonic" force field (see Sec. S3). For both types of force fields, the simulation results are discussed in Sec. IV.

All MD simulations are furthermore conducted in the NPT ensemble at a pressure of 1 bar, using a cut-off radius of 15 Å for the long-range interactions. For the classical and GLE quantum thermostatted MD simulations, the in-house MD code `Yaff`[50] is used in combination with `LAMMPS`,[51] which allows us to speed up the evaluation of the non-covalent force field contributions. The PIMD simulations on the other hand are performed with the iPI software package,[52,53] delegating the force evaluation to `Yaff`.

In the classical MD simulations, temperature and pressure are, respectively, controlled by a three bead Nosé-Hoover

The Journal of Chemical Physics ARTICLE scitation.org/journal/jcp

chain (NHC) thermostat[54–56] and a Martyna-Tuckerman-Tobias-Klein (MTTK) barostat.[57,58] For the GLE quantum thermostatted MD simulations, a Langevin barostat is employed, whereas the PIMD simulations use white noise Langevin[27] or PIGLET thermostatting[30] in combination with a Bussi-Zykova-Parrinello barostat.[52] The relaxation times of the different thermostats and barostats are set to, respectively, 0.1 ps and 1 ps.[59] For all simulations, except for the ordinary PIMD simulations using a white noise Langevin thermostat, an MD integration step of 0.5 fs is used. The ordinary PIMD simulations require a smaller integration step of 0.25 fs due to the presence of artificial high-frequency modes introduced by the harmonic nearest neighbour coupling.[28] The total simulation time of all PIMD simulations is 1.25 ns, whereas the classical and GLE quantum thermostatted simulations have a total simulation time of 3 ns. The equilibration time is set to 150 ps.

Finally, to fix the number of replicas in the PIMD simulations, the convergence of the volume was tested as function of the number of beads (Fig. S1), reaching convergence at, respectively, 8 beads for PIGLET thermostatted PIMD simulations and 32 beads for ordinary PIMD simulations.

IV. RESULTS AND DISCUSSION

A. Structural properties: RDFs

To evaluate the influence of NQEs upon the structural properties of MOF-5, a series of radial distribution functions (RDFs) is constructed, focussing on two different atom pairs. On the one hand, we consider C—H pairs of atoms, as the C—H bonds in MOF-5 have the highest characteristic frequency, i.e., about 3195 cm^{-1}, as obtained from a normal mode analysis performed with TAMkin.[60] On the other hand, we also consider Zn—O pairs of atoms, as the Zn—O bond in MOF-5 is characterised by a much lower characteristic frequency of about 450 cm^{-1} and the low-frequency modes involving ZnO_4 tetrahedra are believed to contribute to the negative thermal expansion of MOF-5.[20] Based on their characteristic frequency, these bonds can also be attributed a so-called characteristic temperature or Debye temperature

$$\Theta_D = \frac{\hbar\omega}{k_B}, \tag{16}$$

which can be used as a measure to quantify the importance of NQEs, as it represents the temperature at which the quantum mechanical energy quantum $\hbar\omega$ equals the thermal energy quantum k_BT and NQEs are only expected to be of importance for temperatures $T \ll \Theta_D$. For the C—H and Zn—O bonds in MOF-5, the characteristic temperatures are, respectively, given by 4600 K and 650 K.

For both types of atom pairs, the RDFs are shown in Fig. 3, comparing classical MD simulations to MD simulations including NQEs at different temperatures, using the anharmonic force field of MOF-5. The first peak of each RDF is always located at the equilibrium bond distance of the atom pair in MOF-5. The atom pairs contributing to the other RDF peaks are indicated on Fig. S2. For the C—H pairs of atoms, the equilibrium bond length is observed to increase by an amount of about 0.02 Å when including NQEs (see Table S2 and Fig. S6), shifting the first RDF peak towards slightly higher equilibrium distances. This shift is also present for the more distant RDF peaks, indicating that the molecular structure as a whole is affected by the presence of NQEs. Furthermore, the RDF peaks are also observed to be much broader when modelled quantum mechanically instead of classically, yielding widths that are more than twice as large (see Fig. S3). In addition, the quantum mechanical widths appear to be more or less temperature independent so that, in contrast to the classical description, the C—H stretch is not yet thermally active at temperatures below 500 K. Quantum mechanically, the behaviour of the C—H stretch is therefore dominated by the ZPE it possesses, as it is significantly larger than the thermal energy up to temperatures as high as $\Theta_D/2$ = 2300 K (within a harmonic approximation).

For the Zn—O pairs of atoms, the differences between the RDFs with and without NQEs are less pronounced, but nevertheless still present. Given the much lower characteristic temperature of the Zn—O stretch in comparison with the C—H stretch, the ZPE associated with the Zn—O bond only dominates the thermal energy up to a temperature of about 300 K. Contrary to the C—H pairs of atoms, the first RDF peak of the Zn—O pairs of atoms shows no appreciable shift when including NQEs (see Table S3 and Fig. S6), as it is comprised of two overlapping RDF peaks corresponding to the $Zn—O_1$ and $Zn—O_2$ bonds [see Fig. 4(a)], limiting the peak's resolution. If the probability distribution of the $Zn—O_1$ bond is however isolated, as done in Fig. 4(b), one does observe a minor shift in the equilibrium bond length, just as for the C—H atom pairs. The different RDF peaks are furthermore also observed to broaden under the influence of NQEs, albeit by less than half their classical width (see Fig. S4).

When comparing the RDFs obtained using different methods to model NQEs, as shown for GLE quantum thermostatted MD simulations and PIGLET thermostatted PIMD simulations in the right column of Fig. 3, the different methods are found to agree well with one another. For the Zn—O pairs of atoms, there is almost no observable difference between the RDFs, whereas for the C—H pairs of atoms only minor differences are present, which are limited to the first RDF peak. The GLE quantum thermostat therefore performs remarkably well in comparison with PIMD, given its approximate nature and low computational cost. In order to benchmark the accuracy of the PIGLET thermostatted PIMD simulations, a 16 bead SC PIMD simulation was performed at 300 K,[44] confirming the validity of the results obtained with PIGLET thermostatting, as shown in Fig. S5.

Performing the above mentioned simulations with a harmonic force field of MOF-5 instead of an anharmonic force field leads to similar results (see Sec. S5). The inclusion of anharmonic contributions in the force field mainly causes the RDF peaks to shift towards larger interatomic distances, as the equilibrium bond lengths are larger for anharmonic potentials with the same force constant, as illustrated by Fig. 5. When including NQEs, this effect becomes even more pronounced for the bonds with a high characteristic frequency.

The Journal of Chemical Physics ARTICLE scitation.org/journal/jcp

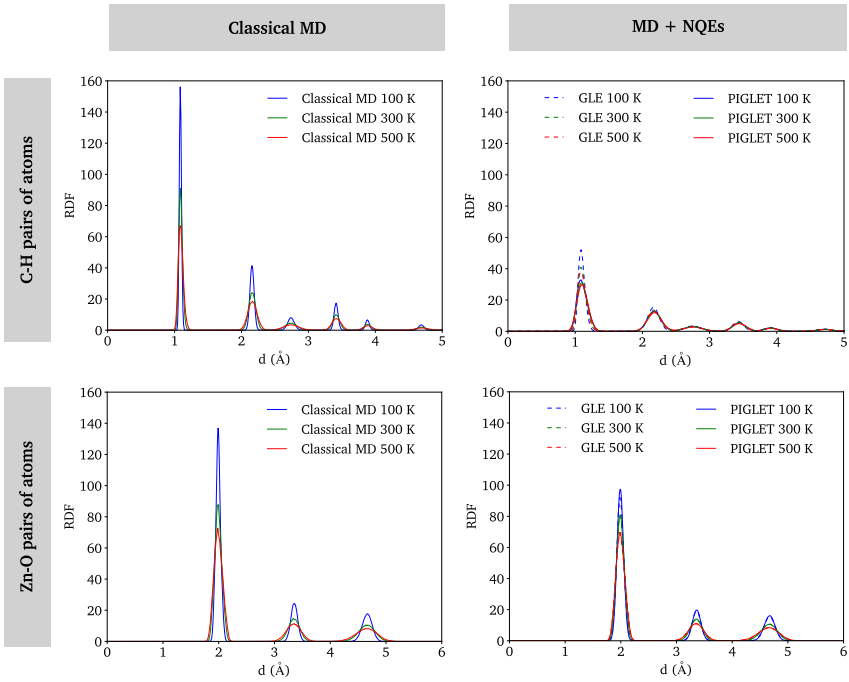

FIG. 3. RDFs of C—H pairs of atoms (top row) and Zn—O pairs of atoms (bottom row) of MOF-5 as obtained using classical MD simulations (left column) and MD simulations including NQEs (right column) at different temperatures, using the anharmonic force field of MOF-5.

For the Zn—O RDFs, there is no additional shift due to NQEs, as a consequence of the low characteristic temperature of the Zn—O stretch (Table S3). For the C—H RDFs, by contrast, the difference in peak positions is about 0.02 Å for the first peak at 100 K, a value that further increases both with the peak number and the temperature, reaching a value of 0.06 Å for the sixth peak at 500 K (Table S2), a value that is two times larger than in classical simulations. This correlated effect between the inclusion of anharmonicities in the bond description and an adequate modelling of NQEs can be inferred from the quantum mechanical description of an anharmonic potential such as the well-known Morse potential. In comparison with a harmonic potential, the anharmonic potential systematically yields a larger equilibrium bond distance, even at the lowest vibrational energy level, where the bond only possesses a ZPE (Fig. 5). As higher vibrational energy levels of the anharmonic potential are occupied, the equilibrium bond distance increases up to a point where the occupation of additional vibrational energy levels no longer affects the equilibrium bond distance, explaining the observed temperature dependence of the RDF peak shifts. The more distinct differences for the C—H RDFs can be related to the higher characteristic frequency of the C—H bond, resulting in a larger ZPE and a larger separation between the vibrational energy levels. The higher the peak number, the larger the peak shift due to the accumulated effect of increased equilibrium bond lengths for the intermediate atoms. This coupling between the description of anharmonicities and NQEs will also prove to be important in an accurate description of the negative thermal expansion of MOF-5, as explained in Sec. IV B.

Apart from RDFs, the structural properties of MOF-5 can also be characterised by other means such as probability distributions of internal coordinates including (dihedral) angles, X-ray diffraction (XRD) patterns, or pore volume sizes. An example of an interesting internal coordinate is the $C_1—C_2—C_2$ angle [Fig. 4(d)], which can be viewed as a measure for the transverse translational motion of the benzene ring, an important motion in the negative thermal expansion of MOF-5.[20] Just as for atomic bonds, the probability distribution of the

The Journal of Chemical Physics ARTICLE scitation.org/journal/jcp

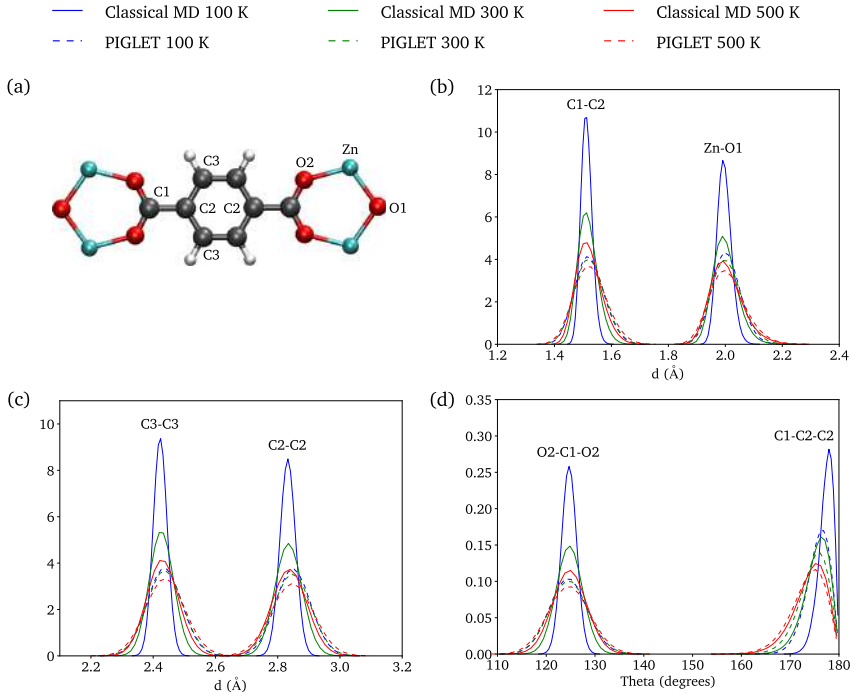

FIG. 4. (a) Labelling convention of the atoms in MOF-5. (b) Probability distribution of C_1-C_2 and $Zn-O_1$ distances. (c) Probability distribution of C_2-C_2 and C_3-C_3 distances. (d) Probability distribution of $O_2-C_1-O_2$ and $C_1-C_2-C_2$ angles. Solid lines indicate classical MD results, whereas dotted lines indicate PIGLET thermostatted PIMD results.

angle is observed to have a different mean value and to become noticeably broader when including NQEs, especially at lower temperatures. The XRD pattern by contrast shows no appreciable differences (Fig. S7), as its resolution is less adequate to identify smaller structural changes. Similarly, also the pore volume of MOF-5 is observed to change only marginally when including NQEs.

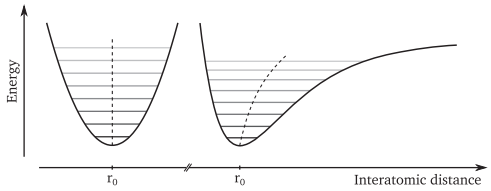

FIG. 5. Schematic representation of the energy levels of a harmonic potential (left) and an anharmonic Morse potential (right). The expectation value of the position is represented by the dashed black line.

B. Thermal expansion

The second property of MOF-5 for which the importance of NQEs is examined is the negative thermal expansion of MOF-5.[20–25] Quantitatively, the thermal expansion can be characterised by the volumetric thermal expansion coefficient α_V, defined as the relative change in volume with respect to temperature at constant pressure, that is,

$$\alpha_V = \frac{1}{V}\left(\frac{\partial V}{\partial T}\right)_p = \left(\frac{\partial \ln V}{\partial T}\right)_p. \quad (17)$$

Within first order, the volumetric thermal expansion coefficient α_V is then obtained as the slope of a linear fit to the logarithm of the volume as a function of temperature. For periodic framework materials such as MOF-5, one can also define a lattice thermal expansion coefficient α_a, which is related

The Journal of Chemical Physics ARTICLE scitation.org/journal/jcp

to the volumetric thermal expansion coefficient by $\alpha_V = 3\alpha_a$, assuming an isotropic thermal expansion.

In Fig. 6, the temperature dependence of the volume of MOF-5 is shown for (PI)MD simulations performed with both the harmonic and anharmonic force fields, for which the corresponding lattice thermal expansion coefficients are listed in Table I. As all the thermal expansion coefficients calculated with the anharmonic force field lie within the experimental range, including the value derived from classical MD simulations, NQEs appear to be only of secondary importance in modelling the thermal expansion of MOF-5. A proper description of the anharmonicities of the underlying PES is observed to be far more important, as evidenced by the simulation results obtained with the harmonic force field of MOF-5. Also in the harmonic case, NQEs only yield small corrections to the classically obtained results, which does however partly correct for the overestimation of the lattice thermal expansion coefficient in comparison with experimental values (see Table I and Fig. S11). As a consequence, more accurate MD simulations accounting for NQEs are only useful if the PES is modelled sufficiently accurately, as the most decisive contribution to the thermal expansion stems from an adequate modelling of the anharmonicities, reducing the thermal expansion coefficient by about 20%–30% for MOF-5.

The absolute volume on the other hand is significantly affected by the presence of NQEs in an anharmonic description of the atomic bonds, yielding differences of the order of 150 Å^3 with respect to the classically predicted volume, an effect which is completely absent within a harmonic description of the atomic bonds (Fig. 6). To explain this interplay between NQEs and anharmonicities, the equilibrium volume at 0 K is determined by means of a series of fixed volume geometry optimisations, as shown in Fig. 7. NQEs are then only accounted for within the harmonic limit, yielding a ZPE contribution of $\sum_k \frac{\hbar\omega_k}{2}$, with ω_k the normal mode frequencies as determined with TAMkin. The resulting equilibrium volumes, with and without NQEs, are indicated in Fig. 6 and are observed to agree well with the extrapolated (PI)MD simulation data so that the explanation for the difference in volumes is to be found within the phenomenon of ZPE.

In the harmonic limit, the ZPE only depends on the normal mode frequencies of the structure so that it is instructive to determine how those frequencies depend on the volume of the structure. For a harmonic potential, the normal mode frequencies as given by the second order positional derivative of the potential are volume independent, yielding a constant ZPE contribution as a function of volume (see Sec. S6). An anharmonic potential by contrast has a second order positional derivative that depends on the position, due to the presence of higher order polynomial contributions to the potential, and is hence characterised by a set of volume dependent normal mode frequencies. As a consequence,

TABLE I. Lattice thermal expansion coefficient of MOF-5. (PI)MD simulations performed with the harmonic force field of MOF-5 are indicated by "harm. FF," whereas the anharmonic force field simulations are indicated by "anh. FF."

	α_a (10^{-6} K^{-1})
Classical MD (harm. FF)	−21.5
GLE (harm. FF)	−19.1
PIGLET PIMD (harm. FF)	−19.5
PIMD (harm. FF)	−19.9
Classical MD (anh. FF)	−14.2
GLE (anh. FF)	−15.3
PIGLET PIMD (anh. FF)	−16.0
PIMD (anh. FF)	−16.4
Literature[21,61]	[−13.3, −5.3]
Experimental (Ref. 24)	[−16, −10]
Experimental (Ref. 20)	−13.1(1)

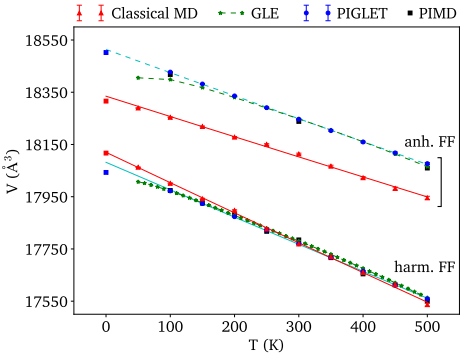

FIG. 6. Volume of MOF-5 as a function of temperature as obtained from (PI)MD simulations using the harmonic ("harm. FF," bottom curves) and anharmonic ("anh. FF," top curves) force field of MOF-5. The data points at 0 K were obtained from geometry optimisations with `Yaff`.

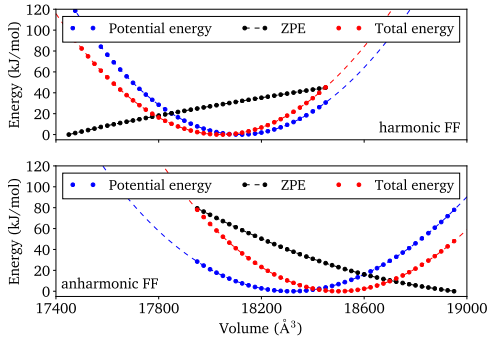

FIG. 7. Potential energy, ZPE, and the sum of both energies as a function of the volume of MOF-5, obtained using `Yaff` geometry optimisations with the harmonic (top figure) and anharmonic (bottom figure) force fields of MOF-5.

The Journal of Chemical Physics ARTICLE scitation.org/journal/jcp

also the ZPE becomes volume dependent, which translates into a temperature dependence within the context of thermal expansion. With decreasing volumes, the normal mode frequencies of MOF-5 are observed to increase up to 30 cm^{-1} (Fig. S8), resulting in an increase of the corresponding ZPE contributions. As the total increase in ZPE is about one order of magnitude larger than the corresponding increase in thermal energy (i.e., 41.2 kJ/mol versus 4.0 kJ/mol), the difference in volume due to the presence of NQEs is perceived within a wide temperature range. Only at very high temperatures, classical and quantum mechanical volumes can be observed to converge to one another (Fig. S10).

The volume dependence of the ZPE of MOF-5 in the harmonic force field (Fig. 7) is to be attributed to other energy contributions in the force field that have an anharmonic character, such as the non-covalent electrostatic and van der Waals contributions. With decreasing volume, or equivalently increasing temperature, the normal mode frequencies are now observed to decrease (Fig. S8) so that also the ZPE decreases with temperature and the thermal energy becomes the dominant energy contribution. The difference in volume due to the presence of NQEs is therefore only noticeable in a relatively small low temperature range, in contrast with the anharmonic case.

To conclude, we also evaluate the different methodologies used to model NQEs in the thermal expansion of MOF-5. Just as for the RDFs, the GLE quantum thermostat performs well when compared to the more demanding PIMD simulations, yielding similar absolute volumes and a matching volumetric temperature dependence. Only at the lowest temperatures, below 100 K, the GLE quantum thermostat predicts a deviating behaviour from the PIMD results, as for the GLE thermostat the volume is observed to saturate. Given the approximate nature of the GLE quantum thermostat, modelling only harmonic NQEs, this saturation of the crystal volume can be understood as an artefact of the constant harmonic ZPE, which causes the bond length fluctuations to become constant and thus saturates the crystal volume.

V. CONCLUSIONS

In this article, we examined the influence of anharmonicities and NQEs upon an accurate modelling of the structural and thermal properties of MOF-5. The structural properties, probed by means of RDFs, were shown to be significantly affected by the presence of NQEs. Under the influence of quantum fluctuations, the RDF peaks tend to broaden and show furthermore a small shift towards larger interatomic distances, due to a coupling between NQEs and the anharmonicities of the PES. Also for the temperature dependence of the RDFs and hence, the structure itself, a different picture emerges. At lower temperatures, the ZPE becomes the most dominant energy contribution and as a consequence, reduces the importance of the thermal energy. For the highest characteristic frequencies in MOF-5, this effect is perceivable up to very high temperatures, making the C—H bond virtually temperature independent below 500 K. For the negative thermal expansion of MOF-5, by contrast, the inclusion of NQEs appears to be only of secondary importance with respect to a proper modelling of the anharmonicities of the PES, as it yields only small corrections to the thermal expansion coefficient. The interplay between NQEs and anharmonicities does however affect the absolute volume, as volume dependent characteristic frequencies lead to a volume dependent ZPE, resulting in a different equilibrium volume. A sufficiently accurate description of the PES is therefore prerequisite when modelling NQEs.

A comparison of different methodologies capable of modelling NQEs furthermore showed an excellent agreement between the approximate technique of GLE thermostatting and the more rigorous framework of PIMD, at least for the structural properties and the negative thermal expansion of MOF-5. Therefore, the inclusion of NQEs in MD simulations of MOF-5 can be achieved most efficiently by means of a GLE thermostat, which produces almost no computational overhead.

SUPPLEMENTARY MATERIAL

In the supplementary material, a more elaborate discussion of the GLE quantum thermostat and PIMD can be found, as well as additional information concerning the RDFs and thermal expansion of MOF-5. Also the convergence of the PIMD simulations and the force field parametrisation are addressed, providing a force field parameter input file for MOF-5.

ACKNOWLEDGMENTS

This work was supported by the Fund for Scientific Research Flanders (FWO), the Research Board of Ghent University, and the European Union's Horizon 2020 research and innovation programme [consolidator ERC Grant Agreement No. 647755-DYNPOR (2015–2020)]. The computational resources and services used in this work were provided by the VSC (Flemish Supercomputer Center), funded by the Research Foundation—Flanders (FWO) and the Flemish Government—department EWI. We would also like to thank Michele Ceriotti (COSMO, EPFL) for his valuable input and his help in improving this manuscript.

REFERENCES

[1] S. Curtarolo, G. L. W. Hart, M. B. Nardelli, N. Mingo, S. Sanvito, and O. Levy, "The high-throughput highway to computational materials design," Nat. Mater. **12**, 191–201 (2013).
[2] H. Furukawa, K. E. Cordova, M. O'Keeffe, and O. M. Yaghi, "The chemistry and applications of metal-organic frameworks," Science **341**, 1230444 (2013).
[3] S. Kitagawa, "Future porous materials," Acc. Chem. Res. **50**, 514–516 (2017).
[4] G. Maurin, C. Serre, A. Cooper, and G. Férey, "The new age of MOFs and of their porous-related solids," Chem. Soc. Rev. **46**, 3104–3107 (2017).
[5] M. Eddaoudi, D. B. Moler, H. Li, B. Chen, T. M. Reineke, M. O'Keeffe, and O. M. Yaghi, "Modular chemistry: Secondary building units as a basis for the

The Journal of Chemical Physics ARTICLE scitation.org/journal/jcp

design of highly porous and robust metal-organic carboxylate frameworks," Acc. Chem. Res. **34**, 319–330 (2001).
[6]C. E. Wilmer, M. Leaf, C. Y. Lee, O. K. Farha, B. G. Hauser, J. T. Hupp, and R. Q. Snurr, "Large-scale screening of hypothetical metal-organic frameworks," Nat. Chem. **4**, 83 (2011).
[7]P. Z. Moghadam, A. Li, S. B. Wiggin, A. Tao, A. G. P. Maloney, P. A. Wood, S. C. Ward, and D. Fairen-Jimenez, "Development of a Cambridge structural database subset: A collection of metal-organic frameworks for past, present, and future," Chem. Mater. **29**, 2618–2625 (2017).
[8]P. Silva, S. M. F. Vilela, J. P. C. Tomé, and F. A. Almeida Paz, "Multifunctional metal-organic frameworks: From academia to industrial applications," Chem. Soc. Rev. **44**, 6774–6803 (2015).
[9]J. A. Mason, J. Oktawiec, M. K. Taylor, M. R. Hudson, J. Rodriguez, J. E. Bachman, M. I. Gonzalez, A. Cervellino, A. Guagliardi, C. M. Brown, P. L. Llewellyn, N. Masciocchi, and J. R. Long, "Methane storage in flexible metal-organic frameworks with intrinsic thermal management," Nature **527**, 357–361 (2015).
[10]E. J. Carrington, C. A. McAnally, A. J. Fletcher, S. P. Thompson, M. Warren, and L. Brammer, "Solvent-switchable continuous-breathing behaviour in a diamondoid metal-organic framework and its influence on CO_2 versus CH_4 selectivity," Nat. Chem. **9**, 882–889 (2017).
[11]S. M. J. Rogge, A. Bavykina, J. Hajek, H. Garcia, A. I. Olivos-Suarez, A. Sepúlveda-Escribano, A. Vimont, G. Clet, P. Bazin, F. Kapteijn, M. Daturi, E. V. Ramos-Fernandez, F. X. Llabrés i Xamena, V. Van Speybroeck, and J. Gascon, "Metal-organic and covalent organic frameworks as single-site catalysts," Chem. Soc. Rev. **46**, 3134–3184 (2017).
[12]L. Vanduyfhuys, S. M. J. Rogge, J. Wieme, S. Vandenbrande, G. Maurin, M. Waroquier, and V. Van Speybroeck, "Thermodynamic insight into stimuli-responsive behaviour of soft porous crystals," Nat. Commun. **9**, 204 (2018).
[13]M. Ceriotti, W. Fang, P. G. Kusalik, R. H. McKenzie, A. Michaelides, M. A. Morales, and T. E. Markland, "Nuclear quantum effects in water and aqueous systems: Experiment, theory, and current challenges," Chem. Rev. **116**, 7529–7550 (2016).
[14]S. Habershon, T. E. Markland, and D. E. Manolopoulos, "Competing quantum effects in the dynamics of a flexible water model," J. Chem. Phys. **131**, 024501 (2009).
[15]M. Ceriotti, J. Cuny, M. Parrinello, and D. E. Manolopoulos, "Nuclear quantum effects and hydrogen bond fluctuations in water," Proc. Natl. Acad. Sci. U. S. A. **110**, 15591–15596 (2013).
[16]C. Vega, M. M. Conde, C. McBride, J. L. F. Abascal, E. G. Noya, R. Ramirez, and L. M. Sesé, "Heat capacity of water: A signature of nuclear quantum effects," J. Chem. Phys. **132**, 046101 (2010).
[17]F. Paesani, "Water in metal-organic frameworks: Structure and diffusion of H_2O in MIL-53(Cr) from quantum simulations," Mol. Simul. **38**, 631–641 (2012).
[18]D. D. Borges, R. Semino, S. Devautour-Vinot, H. Jobic, F. Paesani, and G. Maurin, "Computational exploration of the water concentration dependence of the proton transport in the porous UiO-66(Zr)-$(CO_2H)_2$ metal-organic framework," Chem. Mater. **29**, 1569–1576 (2017).
[19]H. Li, M. Eddaoudi, M. O'Keeffe, and O. M. Yaghi, "Design and synthesis of an exceptionally stable and highly porous metal-organic framework," Nature **402**, 276–279 (1999).
[20]N. Lock, Y. Wu, M. Christensen, L. J. Cameron, V. K. Peterson, A. J. Bridgeman, C. J. Kepert, and B. B. Iversen, "Elucidating negative thermal expansion in MOF-5," J. Phys. Chem. C **114**, 16181–16186 (2010).
[21]D. Dubbeldam, K. Walton, D. Ellis, and R. Snurr, "Exceptional negative thermal expansion in isoreticular metal-organic frameworks," Angew. Chem. **119**, 4580–4583 (2007).
[22]S. S. Han and W. A. Goddard, "Metal-organic frameworks provide large negative thermal expansion behavior," J. Phys. Chem. C **111**, 15185–15191 (2007).
[23]J. L. C. Rowsell, E. C. Spencer, J. Eckert, J. A. K. Howard, and O. M. Yaghi, "Gas adsorption sites in a large-pore metal-organic framework," Science **309**, 1350–1354 (2005).
[24]W. Zhou, H. Wu, T. Yildirim, J. R. Simpson, and A. R. H. Walker, "Origin of the exceptional negative thermal expansion in metal-organic framework-5 Zn_4O(1,4–benzenedicarboxylate)3," Phys. Rev. B **78**, 054114 (2008).
[25]L. H. N. Rimmer, M. T. Dove, A. L. Goodwin, and D. C. Palmer, "Acoustic phonons and negative thermal expansion in MOF-5," Phys. Chem. Chem. Phys. **16**, 21144–21152 (2014).
[26]M. Ceriotti, G. Bussi, and M. Parrinello, "Colored-noise thermostats à la carte," J. Chem. Theory Comput. **6**, 1170–1180 (2010).
[27]M. Ceriotti, M. Parrinello, T. E. Markland, and D. E. Manolopoulos, "Efficient stochastic thermostatting of path integral molecular dynamics," J. Chem. Phys. **133**, 124104 (2010).
[28]S. Habershon, D. E. Manolopoulos, T. E. Markland, and T. F. Miller III, "Ring-polymer molecular dynamics: Quantum effects in chemical dynamics from classical trajectories in an extended phase space," Annu. Rev. Phys. Chem. **64**, 387–413 (2013).
[29]M. Ceriotti, D. E. Manolopoulos, and M. Parrinello, "Accelerating the convergence of path integral dynamics with a generalized Langevin equation," J. Chem. Phys. **134**, 084104 (2011).
[30]M. Ceriotti and D. E. Manolopoulos, "Efficient first-principles calculation of the quantum kinetic energy and momentum distribution of nuclei," Phys. Rev. Lett. **109**, 100604 (2012).
[31]R. Zwanzig, "Memory effects in irreversible thermodynamics," Phys. Rev. **124**, 983–992 (1961).
[32]R. Zwanzig, *Nonequilibrium Statistical Mechanics* (Oxford University Press, 2001).
[33]M. Ceriotti, G. Bussi, and M. Parrinello, "Langevin equation with colored noise for constant-temperature molecular dynamics simulations," Phys. Rev. Lett. **102**, 020601 (2009).
[34]M. Ceriotti, G. Bussi, and M. Parrinello, "Nuclear quantum effects in solids using a colored-noise thermostat," Phys. Rev. Lett. **103**, 030603 (2009).
[35]M. E. Tuckerman, *Statistical Mechanics: Theory and Molecular Simulation* (OUP, Oxford, 2010).
[36]R. P. Feynman, "Space-time approach to non-relativistic quantum mechanics," Rev. Mod. Phys. **20**, 367–387 (1948).
[37]T. E. Markland and M. Ceriotti, "Nuclear quantum effects enter the mainstream," Nat. Rev. Chem. **2**, 0109 (2018).
[38]V. Kapil, J. VandeVondele, and M. Ceriotti, "Accurate molecular dynamics and nuclear quantum effects at low cost by multiple steps in real and imaginary time: Using density functional theory to accelerate wavefunction methods," J. Chem. Phys. **144**, 054111 (2016).
[39]T. E. Markland and D. E. Manolopoulos, "An efficient ring polymer contraction scheme for imaginary time path integral simulations," J. Chem. Phys. **129**, 024105 (2008).
[40]I. Poltavsky and A. Tkatchenko, "Modeling quantum nuclei with perturbed path integral molecular dynamics," Chem. Sci. **7**, 1368–1372 (2016).
[41]I. Poltavsky, R. A. DiStasio, Jr., and A. Tkatchenko, "Perturbed path integrals in imaginary time: Efficiently modeling nuclear quantum effects in molecules and materials," J. Chem. Phys. **148**, 102325 (2018).
[42]M. Suzuki, "Hybrid exponential product formulas for unbounded operators with possible applications to Monte Carlo simulations," Phys. Lett. A **201**, 425–428 (1995).
[43]S. A. Chin, "Symplectic integrators from composite operator factorizations," Phys. Lett. A **226**, 344–348 (1997).
[44]V. Kapil, J. Behler, and M. Ceriotti, "High order path integrals made easy," J. Chem. Phys. **145**, 234103 (2016).
[45]L. Vanduyfhuys, S. Vandenbrande, T. Verstraelen, R. Schmid, M. Waroquier, and V. Van Speybroeck, "QuickFF: A program for a quick and easy derivation of force fields for metal-organic frameworks from *ab initio* input," J. Comput. Chem. **36**, 1015–1027 (2015).
[46]L. Vanduyfhuys, S. Vandenbrande, J. Wieme, M. Waroquier, T. Verstraelen, and V. Van Speybroeck, "Extension of the QuickFF force field protocol

The Journal of Chemical Physics ARTICLE scitation.org/journal/jcp

for an improved accuracy of structural, vibrational, mechanical and thermal properties of metal-organic frameworks," J. Comput. Chem. **39**, 999–1011 (2018).
[47]T. E. Markland and B. J. Berne, "Unraveling quantum mechanical effects in water using isotopic fractionation," Proc. Natl. Acad. Sci. U. S. A. **109**, 7988–7991 (2012).
[48]M. Rossi, P. Gasparotto, and M. Ceriotti, "Anharmonic and quantum fluctuations in molecular crystals: A first-principles study of the stability of paracetamol," Phys. Rev. Lett. **117**, 115702 (2016).
[49]H.-Y. Ko, R. A. DiStasio, B. Santra, and R. Car, "Thermal expansion in dispersion-bound molecular crystals," Phys. Rev. Mater. **2**, 055603 (2018).
[50]T. Verstraelen, L. Vanduyfhuys, and S. Vandenbrande, Yaff, yet another force field, 2011, http://molmod.ugent.be/software/.
[51]S. Plimpton, "Fast parallel algorithms for short-range molecular dynamics," J. Comput. Phys. **117**, 1–19 (1995).
[52]M. Ceriotti, J. More, and D. E. Manolopoulos, "i-PI: A Python interface for *ab initio* path integral molecular dynamics simulations," Comput. Phys. Commun. **185**, 1019–1026 (2014).
[53]V. Kapil, M. Rossi, O. Marsalek, R. Petraglia, Y. Litman, T. Spura, B. Cheng, A. Cuzzocrea, R. H. Meißner, D. M. Wilkins, P. Juda, S. P. Bienvenue, W. Fang, J. Kessler, I. Poltavsky, S. Vandenbrande, J. Wieme, C. Corminboeuf, T. D. Kühne, D. E. Manolopoulos, T. E. Markland, J. O. Richardson, A. Tkatchenko, G. A. Tribello, V. Van Speybroeck, and M. Ceriotti, "i-PI 2.0: A universal force engine for advanced molecular simulations," Comput. Phys. Commun. **236**, 214–223 (2018).
[54]S. Nosé, "A molecular dynamics method for simulations in the canonical ensemble," Mol. Phys. **52**, 255–268 (1984).
[55]W. G. Hoover, "Canonical dynamics: Equilibrium phase-space distributions," Phys. Rev. A **31**, 1695–1697 (1985).
[56]G. J. Martyna, M. L. Klein, and M. Tuckerman, "Nosé-Hoover chains: The canonical ensemble via continuous dynamics," J. Chem. Phys. **97**, 2635–2643 (1992).
[57]G. J. Martyna, D. J. Tobias, and M. L. Klein, "Constant pressure molecular dynamics algorithms," J. Chem. Phys. **101**, 4177–4189 (1994).
[58]G. J. Martyna, M. E. Tuckerman, D. J. Tobias, and M. L. Klein, "Explicit reversible integrators for extended systems dynamics," Mol. Phys. **87**, 1117–1157 (1996).
[59]S. M. J. Rogge, L. Vanduyfhuys, A. Ghysels, M. Waroquier, T. Verstraelen, G. Maurin, and V. Van Speybroeck, "A comparison of barostats for the mechanical characterization of metal-organic frameworks," J. Chem. Theory Comput. **11**, 5583–5597 (2015).
[60]A. Ghysels, T. Verstraelen, K. Hemelsoet, M. Waroquier, and V. Van Speybroeck, "TAMkin: A versatile package for vibrational analysis and chemical kinetics," J. Chem. Inf. Model. **50**, 1736–1750 (2010).
[61]J. K. Bristow, D. Tiana, and A. Walsh, "Transferable force field for metal-organic frameworks from first-principles: BTW-FF," J. Chem. Theory Comput. **10**, 4644–4652 (2014).

Supporting Information for

On the importance of anharmonicities and nuclear quantum effects in modelling the structural properties and thermal expansion of MOF-5

Aran Lamaire, Jelle Wieme, Sven M. J. Rogge, Michel Waroquier, and Veronique Van Speybroeck

Center for Molecular Modeling (CMM), Ghent University, Technologiepark 46, 9052 Zwijnaarde, Belgium

S1 GLE quantum thermostat

Starting from the coordinate representation of the canonical density matrix $\rho(q,q')$ of a quantum harmonic oscillator with mass m and frequency ω, which can be derived within the path integral formalism of quantum mechanics[1] and is given by

$$\rho(q,q') = \left[\frac{m\omega}{2\pi\hbar\sinh(\beta\hbar\omega)}\right]^{1/2} \exp\left[-\frac{m\omega}{2\hbar\sinh(\beta\hbar\omega)}\left((q^2+q'^2)\cosh(\beta\hbar\omega) - 2qq'\right)\right], \tag{S1.1}$$

the quantum mechanical probability distribution of the displacement q of the harmonic oscillator can be determined as $\rho(q) = \rho(q,q)$. From Equation (S1.1), it then follows that

$$\begin{aligned}
\rho(q) &= \left[\frac{m\omega}{2\pi\hbar\sinh(\beta\hbar\omega)}\right]^{1/2} \exp\left[-\frac{m\omega q^2}{\hbar\sinh(\beta\hbar\omega)}\Big(\cosh(\beta\hbar\omega) - 1\Big)\right] \\
&= \left[\frac{m\omega}{2\pi\hbar\sinh(\beta\hbar\omega)}\right]^{1/2} \exp\left[\frac{m\omega q^2}{i\hbar\sin(i\beta\hbar\omega)}\Big(\cos(i\beta\hbar\omega) - 1\Big)\right] \\
&= \left[\frac{m\omega}{2\pi\hbar\sinh(\beta\hbar\omega)}\right]^{1/2} \exp\left[-\frac{m\omega q^2}{i\hbar}\frac{2\sin^2\left(\frac{i\beta\hbar\omega}{2}\right)}{2\sin\left(\frac{i\beta\hbar\omega}{2}\right)\cos\left(\frac{i\beta\hbar\omega}{2}\right)}\right] \\
&= \left[\frac{m\omega}{2\pi\hbar\sinh(\beta\hbar\omega)}\right]^{1/2} \exp\left[-\frac{m\omega q^2}{\hbar\coth\left(\frac{\beta\hbar\omega}{2}\right)}\right] \\
&= \left[\frac{m\omega^2}{2\pi\hbar\sinh(\beta\hbar\omega)}\right]^{1/2} \exp\left[-\frac{1}{2}m\omega^2q^2\frac{1}{\frac{\hbar\omega}{2}\coth\left(\frac{\beta\hbar\omega}{2}\right)}\right].
\end{aligned} \tag{S1.2}$$

As the corresponding classical probability distribution is proportional to a Boltzmann factor:

$$\rho(q) \propto \exp\left(-\frac{\omega^2q^2}{2k_BT}\right), \tag{S1.3}$$

both probability distributions can be related to one another by defining an effective, ω-dependent temperature $T^\star$ given by

$$T^\star = \frac{\hbar\omega}{2k_B}\coth\left(\frac{\hbar\omega}{2k_BT}\right), \tag{S1.4}$$

which allows to transform the classical Boltzmann distribution into the corresponding quantum mechanical distribution.

S2 Path integral MD

S2.1 Real time path integrals

For a single particle, restricted to move in one dimension, the path integral formulation of quantum mechanics can be derived straightforwardly from the well-known Schrödinger formulation of quantum mechanics[1]. In the Schrödinger formulation, the wave function $\psi(x,t)$ of the particle satisfies the time-dependent Schrödinger equation

$$i\hbar\frac{\partial\psi}{\partial t} = \hat{H}\psi, \tag{S2.1}$$

with $\hat{H}$ the Hamiltonian given by

$$\hat{H} = \frac{\hat{p}^2}{2m} + V(\hat{x}), \tag{S2.2}$$

with p and x respectively the momentum and position of the particle and $V(x)$ the potential energy. A formal solution to the Schrödinger equation is then given by

$$|\psi(t)\rangle = e^{-\frac{i}{\hbar}\hat{H}(t-t')}\,|\psi(t')\rangle = \mathcal{U}(t,t')\,|\psi(t')\rangle\,, \tag{S2.3}$$

with $\mathcal{U}(t,t') = e^{-\frac{i}{\hbar}\hat{H}(t-t')}$ the so-called time evolution operator or quantum propagator. In the coordinate representation, this equation can be rewritten in the following way by making use of a completeness relation $\hat{I} = \int \mathrm{d}x'\,|x'\rangle\,\langle x'|$:

$$\begin{aligned}\psi(x,t) &= \langle x|\psi(t)\rangle = \langle x|\,e^{-\frac{i}{\hbar}\hat{H}(t-t')}\,|\psi(t')\rangle \\ &= \int \mathrm{d}x'\,\langle x|\,e^{-\frac{i}{\hbar}\hat{H}(t-t')}\,|x'\rangle\,\langle x'|\psi(t')\rangle \\ &= \int \mathrm{d}x'\mathcal{U}(x,t;x',t')\,\psi(x',t'),\end{aligned} \tag{S2.4}$$

with $\mathcal{U}(x,t;x',t') = \langle x|\,e^{-\frac{i}{\hbar}\hat{H}(t-t')}\,|x'\rangle$ a matrix element that represents the probability amplitude of finding the particle initially in x' at time t', in x at time t. In the path integral formulation of quantum mechanics, this probability amplitude can be shown to equal a sum over all the possible paths starting at time t' in x' and ending at time t in x, where every path is weighted by a phase factor whose phase is given by the classical action in units of $\hbar$. To prove this statement, we expand the time evolution operator into a Trotter factorisation, yielding

$$e^{-\frac{i}{\hbar}\hat{H}t} = \lim_{P\to\infty}\left[e^{-\frac{i\hat{V}t}{2\hbar P}}e^{-\frac{i\hat{p}^2t}{2m\hbar P}}e^{-\frac{i\hat{V}t}{2\hbar P}}\right]^P, \tag{S2.5}$$

where t' was taken to be zero, since the time evolution operator only depends on the time difference between the initial and final state. If we then insert a completeness relation between every factor of the Trotter factorisation, the probability amplitude $\mathcal{U}(x,t;x',0)$ can be rewritten as

$$\mathcal{U}(x,t;x',0) = \langle x|\,e^{-\frac{i}{\hbar}\hat{H}t}\,|x'\rangle = \lim_{P\to\infty}\langle x|\left[e^{-\frac{i\hat{V}t}{2\hbar P}}e^{-\frac{i\hat{p}^2t}{2m\hbar P}}e^{-\frac{i\hat{V}t}{2\hbar P}}\right]^P|x'\rangle$$

$$= \lim_{P\to\infty} \int \mathrm{d}x_2 \ldots \mathrm{d}x_P \, \langle x| \, e^{-\frac{i\hat{V}t}{2\hbar P}} e^{-\frac{i\hat{p}^2 t}{2m\hbar P}} e^{-\frac{i\hat{V}t}{2\hbar P}} \, |x_P\rangle \, \langle x_P| \ldots |x_{P-1}\rangle$$
$$\langle x_{P-1}| \ldots |x_2\rangle \, \langle x_2| \, e^{-\frac{i\hat{V}t}{2\hbar P}} e^{-\frac{i\hat{p}^2 t}{2m\hbar P}} e^{-\frac{i\hat{V}t}{2\hbar P}} \, |x'\rangle \,, \tag{S2.6}$$

with

$$\langle x_{k+1}| \, e^{-\frac{i\hat{V}t}{2\hbar P}} e^{-\frac{i\hat{p}^2 t}{2m\hbar P}} e^{-\frac{i\hat{V}t}{2\hbar P}} \, |x_k\rangle = \langle x_{k+1}| \, e^{-\frac{i\hat{p}^2 t}{2m\hbar P}} \, |x_k\rangle \, e^{-\frac{it}{2\hbar P}(V(x_k)+V(x_{k+1}))}, \tag{S2.7}$$

since $V(\hat{x}) \, |x_k\rangle = V(x_k) \, |x_k\rangle$. The only remaining matrix element, involving the kinetic energy $\frac{\hat{p}^2}{2m}$, can subsequently be evaluated by switching to the momentum representation:

$$\begin{aligned} \langle x_{k+1}| \, e^{-\frac{i\hat{p}^2 t}{2m\hbar P}} \, |x_k\rangle &= \int \mathrm{d}p \, \langle x_{k+1}| \, e^{-\frac{i\hat{p}^2 t}{2m\hbar P}} \, |p\rangle \, \langle p|x_k\rangle \\ &= \int \mathrm{d}p \, \langle x_{k+1}|p\rangle \, \langle p|x_k\rangle \, e^{-\frac{ip^2 t}{2m\hbar P}} \\ &= \frac{1}{2\pi\hbar} \int \mathrm{d}p \, e^{\frac{ip(x_{k+1}-x_k)}{\hbar}} e^{-\frac{ip^2 t}{2m\hbar P}}, \end{aligned} \tag{S2.8}$$

with

$$\langle x|p\rangle = \frac{1}{\sqrt{2\pi\hbar}} e^{\frac{ipx}{\hbar}}, \tag{S2.9}$$

which yields an integration that can be performed analytically by making use of the following Gaussian integral

$$\int_{-\infty}^{+\infty} \mathrm{d}y e^{-ay^2+by} = \sqrt{\frac{\pi}{a}} \, e^{\frac{b^2}{4a}}, \tag{S2.10}$$

with $a = \frac{it}{2m\hbar P}$ and $b = \frac{i(x_{k+1}-x_k)}{\hbar}$, so that the matrix element is given by

$$\begin{aligned} \langle x_{k+1}| \, e^{-\frac{i\hat{p}^2 t}{2m\hbar P}} \, |x_k\rangle &= \frac{1}{2\pi\hbar} \sqrt{\frac{2m\pi\hbar P}{it}} \, \exp\left[-\frac{2m\hbar P}{4i\hbar^2 t}(x_{k+1}-x_k)^2\right] \\ &= \sqrt{\frac{mP}{2\pi i\hbar t}} \, \exp\left[-\frac{mP}{2i\hbar t}(x_{k+1}-x_k)^2\right]. \end{aligned} \tag{S2.11}$$

By setting $x_1 = x'$ and $x_{P+1} = x$, the probability amplitude $\mathcal{U}(x,t;x',0)$ of finding the particle initially in x', in x at time t can finally be written as

$$\mathcal{U}(x,t;x',0) = \lim_{P\to\infty} \left(\frac{mP}{2\pi i\hbar t}\right)^{\frac{P}{2}} \int \mathrm{d}x_2 \ldots \mathrm{d}x_P \exp\left\{-\sum_{k=1}^{P}\left[\frac{mP}{2i\hbar t}(x_{k+1}-x_k)^2 + \frac{it}{2\hbar P}\left(V(x_k)+V(x_{k+1})\right)\right]\right\}. \tag{S2.12}$$

To investigate the formal limit of this expression for $P \to \infty$, we introduce a parameter $\epsilon = \frac{t}{P}$, that allows us to rewrite the equation as

$$\mathcal{U}(x,t;x',0) = \lim_{\substack{P\to\infty \\ \epsilon\to 0}} \left(\frac{m}{2\pi i\hbar\epsilon}\right)^{\frac{P}{2}} \int \mathrm{d}x_2 \ldots \mathrm{d}x_P \exp\left\{\frac{i\epsilon}{\hbar}\sum_{k=1}^{P}\left[\frac{m}{2}\left(\frac{x_{k+1}-x_k}{\epsilon}\right)^2 - \frac{V(x_k)+V(x_{k+1})}{2}\right]\right\}. \tag{S2.13}$$

By letting P approach infinity and, equivalently, ϵ approach zero, the time interval separating the space

points $x_1, ..., x_{P+1}$ becomes infinitely small and the number of points discretising the interval $[x_{P+1}, x_1]$ becomes infinite, so that the position of the particle can be described as a continuous function of time $x(\tau)$, with $x(0) = x'$ and $x(t) = x$. The same reasoning also allows to identify $\frac{x_{k+1}-x_k}{\epsilon}$ as the velocity of the particle,

$$\lim_{\epsilon\to 0}\left(\frac{x_{k+1}-x_k}{\epsilon}\right) = \frac{\mathrm{d}x}{\mathrm{d}\tau} = \dot{x}(\tau), \tag{S2.14}$$

so that the argument of the exponential in equation (S2.13) contains the classical action $S[x]$ of the particle in a Riemann sum integral representation:

$$\lim_{\epsilon\to 0}\epsilon\sum_{k=1}^{P}\left[\frac{m}{2}\left(\frac{x_{k+1}-x_k}{\epsilon}\right)^2 - \frac{V(x_k)+V(x_{k+1})}{2}\right] = \int_0^t \mathrm{d}\tau\left[\frac{1}{2}m\dot{x}^2(\tau) - V(x(\tau))\right] = S[x]. \tag{S2.15}$$

Finally, as the the number of points discretising the interval $[x_{P+1}, x_1]$ becomes infinite, the integration over $x_2, ..., x_P$ is to be regarded as an integration over all the possible functions $x(\tau)$ starting in x' at $\tau = 0$ and ending in x at $\tau = t$, since all the points of the function $x(\tau)$ are being varied except for the endpoints x and x', a type of integration that is also known as functional integration. The integration measure is then symbolically written as

$$\lim_{\substack{P\to\infty\\ \epsilon\to 0}}\left(\frac{m}{2\pi i\hbar\epsilon}\right)^{\frac{P}{2}}\mathrm{d}x_2\ldots\mathrm{d}x_P \equiv \mathcal{D}x(\tau), \tag{S2.16}$$

so that the continuous limit or functional integral representation of the time evolution operator in the coordinate space is given by

$$\mathcal{U}(x,t;x',0) = \int_{x(0)=x'}^{x(t)=x}\mathcal{D}x(\tau)\,\exp\left\{\frac{i}{\hbar}\int_0^t \mathrm{d}\tau\left[\frac{1}{2}m\dot{x}^2(\tau) - V(x(\tau))\right]\right\} = \int_{x'}^{x}\mathcal{D}x\, e^{\frac{i}{\hbar}S[x]}, \tag{S2.17}$$

proving the earlier statement that the probability amplitude $\mathcal{U}(x,t;x',0)$ can be written as a sum over paths starting in x' at time 0 and ending in x at time t, where every path is weighted by a phase factor whose phase is the classical action in units of $\hbar$.

S2.2 Imaginary time path integrals

From the real time path integral formulation of the time evolution operator $\hat{\mathcal{U}}(t) = e^{-\frac{i}{\hbar}\hat{H}t}$, the imaginary time path integral formulation of the canonical density matrix $\hat{\rho}(\beta) = e^{-\beta\hat{H}}$ can be straightforwardly derived by means of a Wick rotation, according to which

$$\hat{\rho}(\beta) = \hat{\mathcal{U}}(-i\beta\hbar) \qquad \text{and} \qquad \hat{\mathcal{U}}(t) = \hat{\rho}\left(\frac{it}{\hbar}\right). \tag{S2.18}$$

The canonical density matrix can hence be obtained from the time evolution operator by evaluating $\hat{\mathcal{U}}$ at an imaginary time $t = -i\beta\hbar$. Conversely, the time evolution operator can be obtained from the canonical density matrix by evaluating $\hat{\rho}$ at an imaginary inverse temperature $\beta = \frac{it}{\hbar}$, a transformation which can be graphically depicted as a rotation between the real and imaginary axis of the plane spanned by the

complex variable $\theta = t + i\beta\hbar$[1]. The resulting path integral representation of the canonical density matrix is then given by

$$\rho(x, x'; \beta) = \lim_{P\to\infty} \left(\frac{mP}{2\pi\beta\hbar^2}\right)^{\frac{P}{2}} \int \mathrm{d}x_2 \ldots \mathrm{d}x_P \, \exp\left\{-\beta \sum_{k=1}^{P} \left[\frac{1}{2} m\omega_P^2 (x_{k+1} - x_k)^2 + \frac{1}{2P}\left(V(x_k) + V(x_{k+1})\right)\right]\right\}, \tag{S2.19}$$

with $x' = x_1$, $x = x_{P+1}$, and $\omega_P = \frac{\sqrt{P}}{\beta\hbar}$ the angular frequency of the harmonic nearest-neighbour coupling between the points along the path. The corresponding expression of the quantum mechanical canonical partition function is given by

$$\begin{aligned} Z &= \mathrm{Tr}\left[e^{-\beta\hat{H}}\right] = \int \mathrm{d}x \, \langle x| \, e^{-\beta\hat{H}} \, |x\rangle = \int \mathrm{d}x \rho(x, x; \beta) \\ &= \lim_{P\to\infty} \left(\frac{mP}{2\pi\beta\hbar^2}\right)^{\frac{P}{2}} \int \mathrm{d}x_1 \ldots \mathrm{d}x_P \, \exp\left\{-\beta \sum_{k=1}^{P} \left[\frac{1}{2} m\omega_P^2 (x_{k+1} - x_k)^2 + \frac{1}{P} V(x_k)\right]\right\}\Bigg|_{x_{P+1}=x_1}, \end{aligned} \tag{S2.20}$$

where we made use of the cyclic boundary condition, which requires that $x = x'$ (or equivalently $x_{P+1} = x_1$), so that

$$\frac{1}{2P} \sum_{k=1}^{P} (V(x_k) + V(x_{k+1})) = \frac{1}{P} \sum_{k=1}^{P} V(x_k). \tag{S2.21}$$

If we then rewrite the prefactor in equation (S2.20) as a product of Gaussian integrals:

$$\left(\frac{mP}{2\pi\beta\hbar^2}\right)^{\frac{P}{2}} = \int \mathrm{d}p_1 \ldots \mathrm{d}p_P \exp\left\{-\sum_{k=1}^{P} \frac{2\pi^2\beta\hbar^2 p_k^2}{mP}\right\}, \tag{S2.22}$$

a set of conjugate momenta variables $p_1, ..., p_P$ can be introduced in the partition function, so that

$$Z = \int \mathrm{d}p_1 \ldots \mathrm{d}p_P \int \mathrm{d}x_1 \ldots \mathrm{d}x_P \, \exp\left\{-\beta \sum_{k=1}^{P} \left[\frac{p_k^2}{2\tilde{m}} + \frac{1}{2} m\omega_P^2 (x_{k+1} - x_k)^2 + \frac{1}{P} V(x_k)\right]\right\}\Bigg|_{x_{P+1}=x_1}, \tag{S2.23}$$

with $\tilde{m} = \frac{mP}{(2\pi\hbar)^2}$. In this way, it becomes possible to use the imaginary time path integral formulation in MD simulations (PIMD), as the quantum mechanical partition function Z can now be mapped onto a classical partition function, that describes the system by means of a fictitious necklace of P system replicas, called beads, that interact with one another via a harmonic nearest-neighbour coupling with frequency ω_P (Figure 2). This mapping is also known as the classical isomorphism. The Hamiltonian of the simulated system is then given by

$$H_P = \sum_{k=1}^{P} \left[\frac{p_k^2}{2\tilde{m}} + \frac{1}{2} m\omega_P^2 (x_{k+1} - x_k)^2 + \frac{1}{P} V(x_k)\right]\Bigg|_{x_{P+1}=x_1}, \tag{S2.24}$$

an expression which can straightforwardly be generalised to a collection of N distinguishable particles in

3 dimensions:

$$H_P = \sum_{k=1}^{P} \left[\sum_{i=1}^{N} \frac{\mathbf{p}_i^{(k)^2}}{2\tilde{m}_i} + \sum_{i=1}^{N} \frac{1}{2} m_i \omega_P^2 \left(\mathbf{r}_i^{(k+1)} - \mathbf{r}_i^{(k)} \right)^2 + \frac{1}{P} V(\mathbf{r}_1^{(k)}, ..., \mathbf{r}_N^{(k)}) \right]. \tag{S2.25}$$

S3 Force field parametrisation

All the force fields used within this work were derived from *ab initio* data, using our in-house developed software package `QuickFF`[2,3]. The force field parameters are provided in `Yaff` input format in Table S1. The atom types defined in the force field are the same as the ones used in Ref. 2. The covalent part of the force field, which describes the interactions between chemically bonded pairs of atoms, is parametrised in the following way

$$\begin{aligned} V_{cov}^{FF} &= V_{bond} + V_{bend} + V_{torsion} + V_{oopdist} + V_{cross} \qquad \text{(S3.1)} \\ &= V_{bond} + V_{bend} + \sum_i \frac{K_{d,i}}{2}(d_i - d_{i,0})^2 + \sum_i \frac{K_{\phi,i}}{2}[1 - \cos(m_{\phi,i}(\phi_i - \phi_{i,0}))] + \sum_{\substack{i,j \\ (i \neq j)}} K_{i,j}^{rr}(r_i - r_{i,0})(r_j - r_{j,0}), \end{aligned}$$

with V_{bond}, V_{bend}, $V_{torsion}$, $V_{oopdist}$, and V_{cross} the force field contributions of the bonds, bends, torsion angles, out-of-plane distances (oopdist), and cross terms respectively. Each of these contributions is parametrised as a function of the appropriate internal coordinates, including the bond distances r_i, the bend angles θ_i (*vide infra*), the out-of-plane distances d_i, and the dihedral angles ϕ_i. The rest values of these internal coordinates are denoted by $r_{i,0}$, $\theta_{i,0}$, $d_{i,0}$, and $\phi_{i,0}$. The multiplicity of the dihedral angles is denoted by $m_{\phi,i}$ and the force constants are labelled $K_{r,i}$, $K_{\theta,i}$, $K_{d,i}$, $K_{\phi,i}$, and $K_{i,j}^{rr}$. In the so-called 'harmonic' MOF-5 force field, the bonds and bends are parametrised by

$$V_{bond} = \sum_i \frac{K_{r,i}}{2}(r_i - r_{i,0})^2 \tag{S3.2}$$

$$V_{bend} = \sum_i \frac{K_{\theta,i}}{2}(\theta_i - \theta_{i,0})^2, \tag{S3.3}$$

whereas the 'anharmonic' MOF-5 force field makes use of the following definitions

$$V_{bond} = \sum_i \frac{K_{r,i}}{2}(r_i - r_{i,0})^2 \left[1 - 2.55\,(r_i - r_{i,0}) + \frac{7}{12}\left(2.55\,(r_i - r_{i,0})\right)^2 \right] \tag{S3.4}$$

$$V_{bend} = \sum_i \frac{K_{\theta,i}}{2}(\theta_i - \theta_{i,0})^2 \left[1 - 0.14\,(\theta_i - \theta_{i,0}) + 5.6 \cdot 10^{-5}(\theta_i - \theta_{i,0})^2 - 7 \cdot 10^{-7}(\theta_i - \theta_{i,0})^3 + 2.2 \cdot 10^{-8}(\theta_i - \theta_{i,0})^4 \right]. \tag{S3.5}$$

The non-covalent part of the force field consists of the electrostatic and van der Waals contributions, which describe the Coulomb interaction between the Gaussian distributed charge densities, the Pauli repulsion, and the dispersion interaction. Using the MM3 Buckingham potential for the description of the van der

Waals interactions, the non-covalent part of the force field takes the following form

$$V_{noncov}^{FF} = \frac{1}{2} \sum_{\substack{i,j \\ (i \neq j)}} \frac{q_i q_j}{4\pi\varepsilon_0 r_{ij}} \operatorname{erf}\left(\frac{r_{ij}}{d_{ij}}\right) + \frac{1}{2} \sum_{\substack{i,j \\ (i \neq j)}} \varepsilon_{ij} \left[1.84 \cdot 10^5 \, e^{-12\frac{r_{ij}}{\sigma_{ij}}} - 2.25 \left(\frac{\sigma_{ij}}{r_{ij}}\right)^6\right], \tag{S3.6}$$

with q_i the charge of atom i, r_{ij} the distance between atoms i and j, $d_{ij} = \sqrt{d_i^2 + d_j^2}$ a mixed charge radius derived from the individual Gaussian charge distribution radii d_i and d_j, erf the error function, σ_{ij} the equilibrium distance of the MM3 potential, and ε_{ij} the well depth of the MM3 potential. Just as for the Lennard-Jones potential, empirical mixing rules are used for the interaction between atoms i and j, given by $\sigma_{ij} = \sigma_i + \sigma_j$ and $\varepsilon_{ij} = \sqrt{\varepsilon_i \varepsilon_j}$, as tabulated in Ref. 4.

S4 Convergence of the PIMD simulations

In order to obtain fully converged RDFs and thermal expansion coefficients including NQEs, 8 beads were used for the PIGLET thermostatted PIMD simulations, whereas 32 beads were used for the regular PIMD simulations to assure convergence of the volume of MOF-5, as shown in Figure S1.

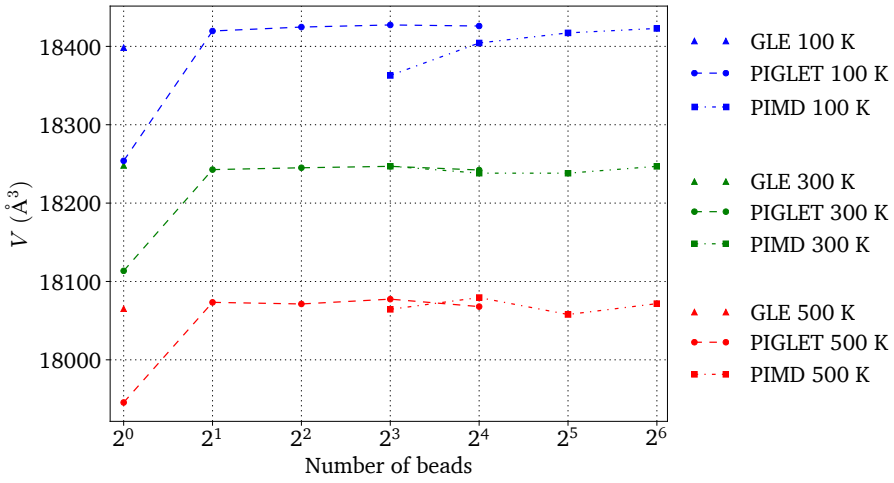

Figure S1: Convergence of the volume of MOF-5 as a function of the number of beads, comparing GLE thermostatted MD simulations and PIGLET thermostatted PIMD simulations (8 beads) to ordinary, Langevin thermostatted PIMD simulations (32 beads).

Table S1: Force field parameters of the anharmonic MOF-5 force field in `Yaff` input format.

```
# MM3QUART
#---------
MM3QUART:UNIT  K kjmol/A**2
MM3QUART:UNIT  R0 A

MM3QUART:PARS      C_ph      C_ph  4.0235900412e+03  1.3930859155e+00
MM3QUART:PARS      C_ph      H_ph  3.4057330879e+03  1.0847740222e+00
MM3QUART:PARS      O_ce        Zn  8.9239440814e+02  2.0347161610e+00
MM3QUART:PARS      O_ca        Zn  9.7852145881e+02  1.9169097752e+00
MM3QUART:PARS      C_ca      O_ca  5.6935698009e+03  1.2739271271e+00
MM3QUART:PARS      C_ca      C_pc  2.8198115487e+03  1.4961158143e+00
MM3QUART:PARS      C_pc      C_ph  3.8832500884e+03  1.4001340079e+00


# MM3BENDA
#----------
MM3BENDA:UNIT  K kjmol/rad**2
MM3BENDA:UNIT  THETA0 deg

MM3BENDA:PARS      C_ph      C_ph      H_ph  2.9053440775e+02  1.2013974500e+02
MM3BENDA:PARS      C_ph      C_ph      C_ph  6.1864845083e+02  1.1996439539e+02
MM3BENDA:PARS      O_ca        Zn      O_ca  3.6359512585e+01  1.3438117178e+02
MM3BENDA:PARS        Zn      O_ce        Zn  1.7593552737e+02  1.0946606702e+02
MM3BENDA:PARS      C_ca      O_ca        Zn  1.1700257032e+02  1.3918065078e+02
MM3BENDA:PARS      O_ca      C_ca      O_ca  7.3935359520e+02  1.2272556049e+02
MM3BENDA:PARS      C_pc      C_ca      O_ca  6.6190055195e+02  1.1860003768e+02
MM3BENDA:PARS      C_pc      C_ph      C_ph  5.8816132569e+02  1.2031868523e+02
MM3BENDA:PARS      C_pc      C_ph      H_ph  3.0051887407e+02  1.1908053083e+02
MM3BENDA:PARS      C_ca      C_pc      C_ph  3.9260965985e+02  1.2020872432e+02
MM3BENDA:PARS      C_ph      C_pc      C_ph  5.6358621584e+02  1.1953360720e+02


# TORSION
#--------
TORSION:UNIT  A kjmol
TORSION:UNIT  PHI0 deg

TORSION:PARS      C_ph      C_pc      C_ph      C_ph  2 3.0928632221e+01  0.0000000000e+00
TORSION:PARS      C_ph      C_ph      C_ph      H_ph  2 3.1967987548e+01  0.0000000000e+00
TORSION:PARS      C_ph      C_ph      C_ph      C_ph  2 3.2165172488e+01  0.0000000000e+00
TORSION:PARS      C_ca      C_pc      C_ph      C_ph  2 4.5636248064e+01  0.0000000000e+00
TORSION:PARS      C_pc      C_ca      O_ca        Zn  2 1.3791713490e+01  0.0000000000e+00
TORSION:PARS      C_ph      C_pc      C_ca      O_ca  2 2.7501306061e+00  0.0000000000e+00
TORSION:PARS      C_pc      C_ph      C_ph      H_ph  2 3.1096578757e+01  0.0000000000e+00
TORSION:PARS      C_ph      C_pc      C_ph      H_ph  2 3.1835635613e+01  0.0000000000e+00
TORSION:PARS      C_ca      C_pc      C_ph      H_ph  2 1.5445488413e+01  0.0000000000e+00
TORSION:PARS      H_ph      C_ph      C_ph      H_ph  2 1.3292476591e+01  0.0000000000e+00
TORSION:PARS      C_pc      C_ph      C_ph      C_ph  2 2.8105763227e+01  0.0000000000e+00


# OOPDIST
#--------
OOPDIST:UNIT  K kjmol/A**2
OOPDIST:UNIT  D0 A

OOPDIST:PARS      C_ca      C_ph      C_ph      C_pc  2.5088068557e+02  0.0000000000e+00
OOPDIST:PARS      C_ph      C_ph      H_ph      C_ph  2.5888197721e+02  0.0000000000e+00
OOPDIST:PARS      C_pc      C_ph      H_ph      C_ph  3.1677202316e+02  0.0000000000e+00
OOPDIST:PARS      C_pc      O_ca      O_ca      C_ca  1.7360630145e+03  0.0000000000e+00
```

```
# Cross
#-----
Cross:UNIT  KSS kjmol/angstrom**2
Cross:UNIT  KBS0 kjmol/(angstrom*rad)
Cross:UNIT  KBS1 kjmol/(angstrom*rad)
Cross:UNIT  R0 angstrom
Cross:UNIT  R1 angstrom
Cross:UNIT  THETA0 deg

Cross:PARS      C_ph      H_ph  1.2582197724e+02  6.8368846208e+01  1.3495301523e+02  1.3930933518e+00  1.0846841574e+00  1.2006351464e+02
Cross:PARS      C_ph      C_ph  6.1178391874e+02  1.8939388736e+01  1.8939388736e+01  1.3930933518e+00  1.3930933518e+00  1.2008192322e+02
Cross:PARS      O_ca        Zn  6.0187326594e+01  3.0261783813e+01 -3.4924361665e-01  1.9298847320e+00  2.0073075041e+00  1.0909580185e+02
Cross:PARS      O_ca        Zn  1.0084268259e+02  1.4116583794e+02  1.4116583794e+02  1.9298847320e+00  1.9298847320e+00  1.1123073832e+02
Cross:PARS        Zn      O_ce  1.4951011505e+02  4.7274913074e+01  4.7274913074e+01  2.0073075041e+00  2.0073075041e+00  1.0947390099e+02
Cross:PARS      C_ca        Zn  3.1063225866e+02  5.6855620578e+01  3.9411352643e+01  1.2739873187e+00  1.9298847320e+00  1.3516256863e+02
Cross:PARS      O_ca      C_ca  8.1849232460e+02  4.0391681762e+02  4.0391681762e+02  1.2739873187e+00  1.2739873187e+00  1.2287973459e+02
Cross:PARS      C_pc      C_ca  4.2359055463e+02  2.0963288396e+02  4.3311486298e+02  1.5016213206e+00  1.2739873187e+00  1.1851074064e+02
Cross:PARS      C_pc      C_ph  5.6854609424e+02  1.2596413203e+01 -9.9363445283e+00  1.4010006112e+00  1.3930933518e+00  1.2024412712e+02
Cross:PARS      C_pc      H_ph  1.0949541401e+02  5.7209441149e+01  1.3464065713e+02  1.4010006112e+00  1.0846841574e+00  1.1925421962e+02
Cross:PARS      C_ca      C_ph  3.1209435721e+02  1.6304918842e+02  3.2787664031e+01  1.5016213206e+00  1.4010006112e+00  1.2035163672e+02
Cross:PARS      C_ph      C_ph  6.1864214058e+02  9.4681250011e+00  9.4681250011e+00  1.4010006112e+00  1.4010006112e+00  1.1930792564e+02
```

```
#Fixed charges
#---------------

FIXQ:UNIT Q0 e
FIXQ:UNIT P e
FIXQ:UNIT R angstrom
FIXQ:SCALE 1 1.0
FIXQ:SCALE 2 1.0
FIXQ:SCALE 3 1.0
FIXQ:DIELECTRIC 1.0

# Atomic parameters
# ----------------------------------------------------
# KEY        label  Q_0A              R_A
# ----------------------------------------------------
FIXQ:ATOM       Zn  0.0000000000  2.0730000000
FIXQ:ATOM     H_ph  0.0000000000  0.7240000000
FIXQ:ATOM     C_ca  0.0000000000  1.1630000000
FIXQ:ATOM     C_pc  0.0000000000  1.1630000000
FIXQ:ATOM     O_ca  0.0000000000  1.1180000000
FIXQ:ATOM     C_ph  0.0000000000  1.1630000000
FIXQ:ATOM     O_ce  0.0000000000  1.1180000000
# Bond parameters
# ----------------------------------------------------
# KEY         label0   label1           P_AB
# ----------------------------------------------------
FIXQ:BOND      C_ph      C_ph  -0.0000000000
FIXQ:BOND      C_ca      C_pc  -0.1800000000
FIXQ:BOND      O_ce        Zn  -0.4450000000
FIXQ:BOND      C_ph      H_ph  -0.1200000000
FIXQ:BOND      C_ca      O_ca   0.3950000000
FIXQ:BOND      C_pc      C_ph  -0.0000000000
FIXQ:BOND      O_ca        Zn  -0.3250000000


# van der Waals
#==============

# The following mathemetical form is supported:
#  - MM3:   EPSILON*(1.84e5*exp(-12*r/SIGMA)-2.25*(SIGMA/r)^6)
#  - LJ:    4.0*EPSILON*((SIGMA/r)^12 - (SIGMA/r)^6)
#
# Remark:
#  In MM3, if ONLYPAULI=1 then only the pauli term will be used.
#  If ONLYPAULI=0, the full MM3 expression is used with 12.

MM3:UNIT SIGMA angstrom
MM3:UNIT EPSILON kcalmol
MM3:SCALE 1 0.0
MM3:SCALE 2 0.0
MM3:SCALE 3 1.0

# ---------------------------------------------
# KEY      ffatype  SIGMA  EPSILON  ONLYPAULI
# ---------------------------------------------

MM3:PARS       Zn     2.290   0.276      0
MM3:PARS     O_ce     1.820   0.059      0
MM3:PARS     O_ca     1.820   0.059      0
MM3:PARS     C_ca     1.940   0.056      0
MM3:PARS     C_pc     1.960   0.056      0
MM3:PARS     C_ph     1.960   0.056      0
MM3:PARS     H_ph     1.620   0.020      0
```

S5 RDFs and XRD patterns

In Figure S2, the atom pairs contributing to the different RDF peaks are indicated for both Zn–O pairs of atoms and C–H pairs of atoms. For each RDF peak, the peak position and peak width obtained from (PI)MD simulations with the harmonic and anharmonic force field of MOF-5 are compared to one another in Tables S2–S3 and Figures S3-S4. A more detailed visual comparison between the first RDF peak as obtained from MD and PIMD simulations is given in Figure S6 for the anharmonic force field.

In Figure S5, the accuracy of the PIGLET thermostatted PIMD simulations is verified by comparing the C–H and Zn–O RDFs of the 8 bead PIGLET thermostatted PIMD simulations to 16 bead Suzuki-Chin PIMD simulations. As both simulation techniques yield identical results, the efficient PIGLET thermostatting scheme can be used without any loss of accuracy.

The XRD pattern of MOF-5 obtained from classical MD simulations and GLE thermostatted MD simulations at 300 K is shown in Figure S7. As there are no major alterations in the crystal structure of MOF-5 when accounting for NQEs, there are no appreciable differences between both XRD patterns. The differences that are observed in the RDFs are simply too small to be noticeable at the resolution scale of the XRD pattern.

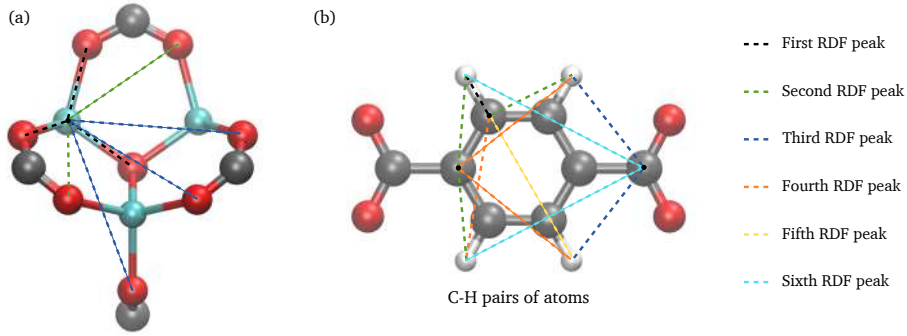

Figure S2: Schematic overview of the atom pairs contributing to the different RDF peaks for (a) the Zn–O pairs of atoms and (b) the C–H pairs of atoms.

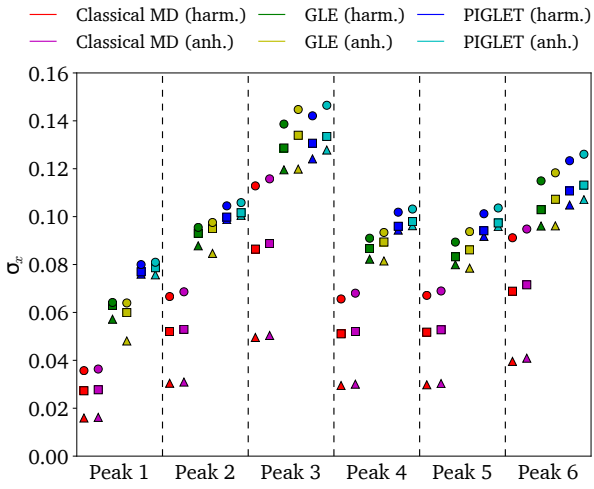

Figure S3: Gaussian peak width σ_x of the first six C–H RDF peaks in MOF-5, comparing different methodologies (classical MD, GLE thermostatted MD, and 8 bead PIGLET thermostatted PIMD) for three different temperatures (△ = 100 K, □ = 300 K, and ○ = 500 K). The results obtained with the harmonic force field of MOF-5 are indicated by harm., whereas the results obtained with the anharmonic force field are indicated by anh.

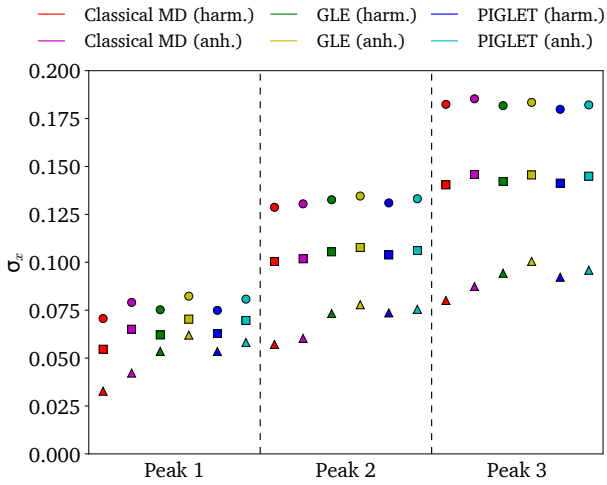

Figure S4: Gaussian peak width σ_x of the first three Zn–O RDF peaks in MOF-5, comparing different methodologies (classical MD, GLE thermostatted MD, and 8 bead PIGLET thermostatted PIMD) for three different temperatures (△ = 100 K, □ = 300 K, and ○ = 500 K). The results obtained with the harmonic force field of MOF-5 are indicated by harm., whereas the results obtained with the anharmonic force field are indicated by anh.

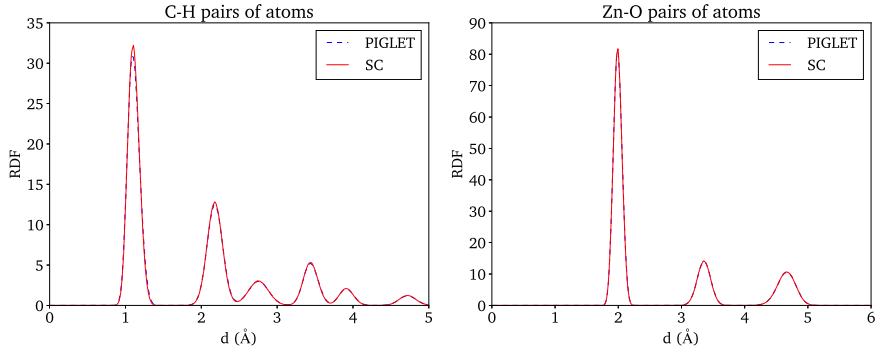

Figure S5: RDFs of the C–H pairs of atoms (left) and Zn–O pairs of atoms (right) of MOF-5 at 300 K, comparing 8 bead PIGLET thermostatted PIMD simulations to 16 bead Suzuki-Chin (SC) PIMD simulations.

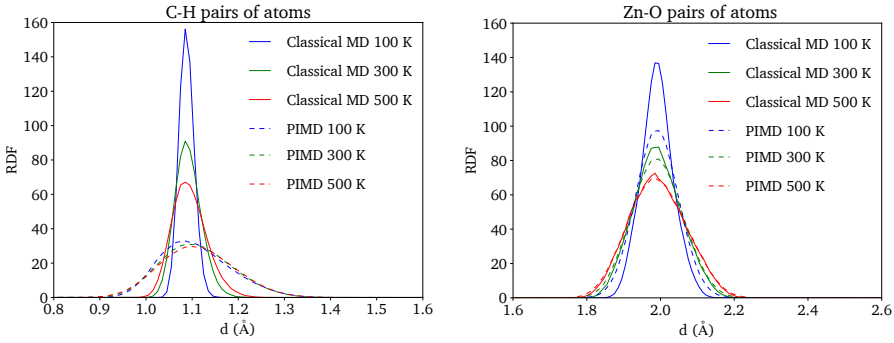

Figure S6: First RDF peak of the C–H pairs of atoms (left) and Zn–O pairs of atoms (right) of MOF-5 at different temperatures, comparing classical MD simulations to 8 bead PIGLET thermostatted PIMD simulations.

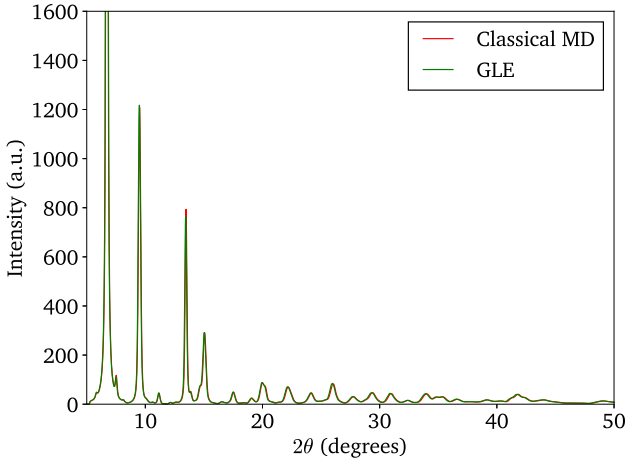

Figure S7: XRD pattern of MOF-5 obtained from classical MD simulations and GLE thermostatted MD simulations at 300 K using the anharmonic force field of MOF-5.

Table S2: Peak position (in Å) of the first six C–H RDF peaks of MOF-5 obtained from classical MD simulations, GLE thermostatted MD simulations, and 8 bead PIGLET thermostatted PIMD simulations. The results obtained with the anharmonic force field of MOF-5 are indicated by anh.

T (K)	**NHC**	**NHC anh.**	**GLE**	**GLE anh.**	**PIGLET**	**PIGLET anh.**
100	1.086	1.087	1.084	1.093	1.079	1.098
	2.155	2.158	2.147	2.166	2.145	2.176
	2.737	2.740	2.727	2.748	2.728	2.755
	3.409	3.413	3.398	3.425	3.397	3.438
	3.877	3.882	3.865	3.894	3.864	3.908
	4.680	4.687	4.669	4.706	4.668	4.719
300	1.086	1.089	1.083	1.096	1.079	1.104
	2.154	2.161	2.145	2.170	2.145	2.179
	2.731	2.741	2.725	2.749	2.725	2.754
	3.406	3.416	3.397	3.431	3.396	3.441
	3.873	3.885	3.864	3.901	3.863	3.913
	4.674	4.691	4.666	4.712	4.665	4.721
500	1.086	1.090	1.083	1.096	1.078	1.107
	2.152	2.163	2.145	2.172	2.144	2.180
	2.727	2.742	2.723	2.748	2.723	2.753
	3.402	3.419	3.396	3.432	3.394	3.443
	3.869	3.888	3.862	3.902	3.860	3.914
	4.669	4.696	4.663	4.714	4.662	4.722

Table S3: Peak position (in Å) of the first three Zn–O RDF peaks of MOF-5 obtained from classical MD simulations, GLE thermostatted MD simulations, and 8 bead PIGLET thermostatted PIMD simulations. The results obtained with the anharmonic force field of MOF-5 are indicated by anh.

T (K)	**NHC**	**NHC anh.**	**GLE**	**GLE anh.**	**PIGLET**	**PIGLET anh.**
100	1.973	1.990	1.971	1.989	1.971	1.990
	3.338	3.355	3.335	3.360	3.336	3.362
	4.637	4.664	4.634	4.671	4.635	4.672
300	1.972	1.990	1.971	1.990	1.971	1.990
	3.329	3.350	3.328	3.354	3.328	3.356
	4.624	4.658	4.624	4.662	4.623	4.663
500	1.970	1.989	1.970	1.990	1.970	1.990
	3.320	3.345	3.319	3.349	3.319	3.350
	4.610	4.651	4.611	4.656	4.611	4.656

S6 Thermal expansion

In Figure S8, the 1200 lowest normal modes of MOF-5 with wavenumbers up to about 1750 cm^{-1} are shown for different volumes, optimised with the harmonic or anharmonic force field of MOF-5. For each force field, the volumes were chosen around the minimum and maximum equilibrium volume of MOF-5 between 0 and 500 K, to represent the volume range that is encountered in the investigation of the thermal expansion (Figure 6). For the harmonic force field, the normal mode frequencies of the different volumes are observed to only differ for the lowest wavenumbers, with about 40 modes showing differences larger than 15 cm^{-1}. For the anharmonic force field, the normal mode frequencies are affected more significantly, as the differences in frequency are now present over the entire frequency range, with about 240 modes that differ more than 15 cm^{-1} between the two volumes. As a consequence, the harmonic ZPE,

$$E_{ZPE} = \frac{1}{2}\sum_k \hbar\omega_k, \tag{S6.1}$$

also changes as a function of the volume of MOF-5. For the harmonic force field, the volume dependence of the normal mode frequencies is very small, as the atomic bonds are described by harmonic potentials (S3.2), which are characterised by volume independent normal mode frequencies ω_i:

$$\frac{\partial^2 V_{bond}}{\partial r_i^2} = K_{r,i} = m_i\omega_i^2, \tag{S6.2}$$

with $K_{r,i}$ the force constant of the atomic bond and m_i the reduced mass of the atom pair. Any volume dependence of the normal mode frequencies is therefore the result of other anharmonic contributions to the force field, such as the non-covalent electrostatic and van der Waals interactions. For the anharmonic force field, by contrast, the anharmonic potentials (S3.4) describing the atomic bonds do result in volume dependent normal mode frequencies $\tilde{\omega}_i$, since

$$\frac{\partial^2 V_{bond}}{\partial r_i^2} = K_{r,i}\left[1 - 7.65\,(r_i - r_{i,0}) + \frac{7}{2}\,(2.55\,(r_i - r_{i,0}))^2\right] = m_i\tilde{\omega}_i^2, \tag{S6.3}$$

with $\tilde{\omega}_i$ a function of $r_i - r_{i,0}$. In the anharmonic description, the ZPE is therefore also position or volume dependent, which translates into a temperature dependence within the context of thermal expansion (Figure 6).

From the normal mode frequencies, calculated at different volumes, a so-called quasi-harmonic approximation of the free energy profile of MOF-5 can be constructed for both the harmonic and anharmonic force field. In this approximation, the material is represented by a collection of N decoupled quantum harmonic oscillators with frequencies ω_i. As the partition function of a quantum harmonic oscillator can be calculated analytically, the quasi-harmonic approximation allows for an analytical description of the

free energy of the material:

$$F(T) = \sum_{i=1}^{N} \left(\frac{\hbar\omega_i}{2} + k_B T \ln[1 - \exp(-\beta\hbar\omega_i)] \right). \tag{S6.4}$$

In this way, temperature related information concerning the material's behaviour can be obtained without performing (PI)MD simulations. By calculating, for different temperatures, the volume at which the quasi-harmonic free energy profile of MOF-5 reaches its minimum, the thermal expansion coefficient of MOF-5 can be estimated from the slope of a linear fit to the logarithm of the volume as a function of temperature (see Section IV B). In Figure S9, the temperature dependence of the volume of MOF-5, as predicted by the quasi-harmonic approximation, is shown for both the harmonic and anharmonic force field of MOF-5. The resulting thermal expansion coefficients of the respective force fields are $-20 \cdot 10^{-6}$ K^{-1} and $-51 \cdot 10^{-7}$ K^{-1}. Compared to the thermal expansion coefficients predicted by (PI)MD simulations (see Table I), the quasi-harmonic approximation seems to perform rather well for the harmonic force field, whereas for the anharmonic force field the thermal expansion coefficient is severely underestimated. For the harmonic force field, there is however a fairly large uncertainty on the value of the thermal expansion coefficient, since the quasi-harmonic approximation already breaks down at temperatures as low as 200 K, at which the free energy profile no longer exhibits a minimum within the relevant volume range. Given the complexity of the motions associated with the negative thermal expansion of MOF-5, a proper dynamical sampling of the structure by means of (PI)MD is required to accurately reproduce the negative thermal expansion, as outlined in Section IV B.

In Figure S10, the temperature dependence of the volume of MOF-5 is shown for MD and PIMD simulations for temperatures up to 3000 K. In this high temperature limit, the MD and PIMD results are observed to converge to one another, as the ZPE of the nuclei becomes less important than their thermal energy, so that the classical and quantum mechanical description of the nuclei start coinciding. A comparison with experimental results is given in Figure S11. The anharmonic force field results are observed to yield a temperature dependent slope, and hence a thermal expansion coefficient, that is in line with the experimental results, as discussed in Section IV B. The absolute value of the density/volume exhibits however a difference of about 5 % with respect to experiment. This difference can be traced back to the overestimation of bond lengths by the B3LYP functional[5], which was used to generate the necessary *ab initio* data for the construction of the force field.

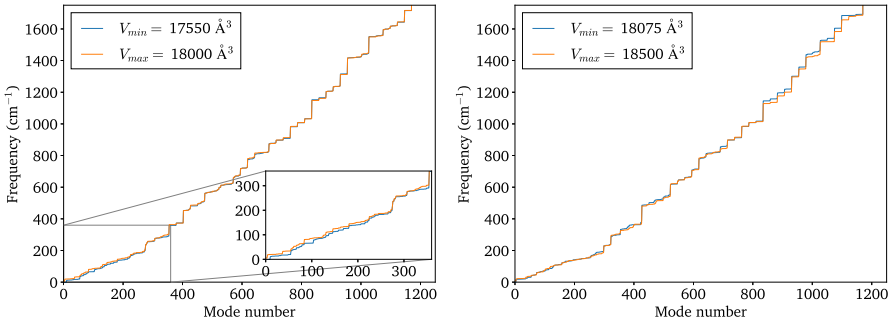

Figure S8: Normal mode frequencies for different volumes of MOF-5, optimised with the harmonic force field (left) and anharmonic force field (right).

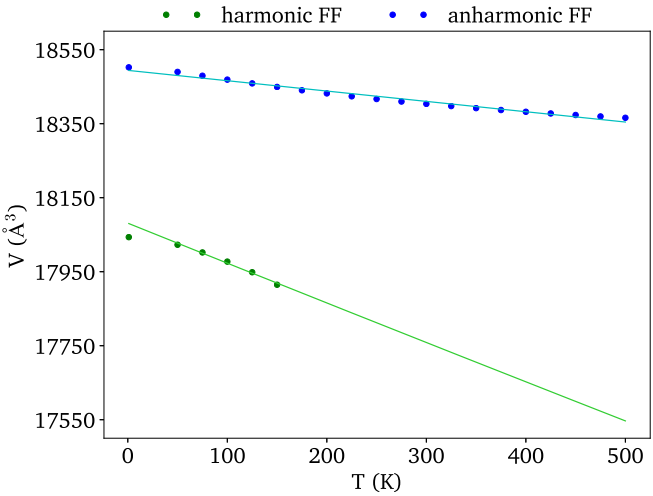

Figure S9: Volume of MOF-5 as a function of temperature as obtained from the static quasi-harmonic approximation using both the harmonic and anharmonic force field.

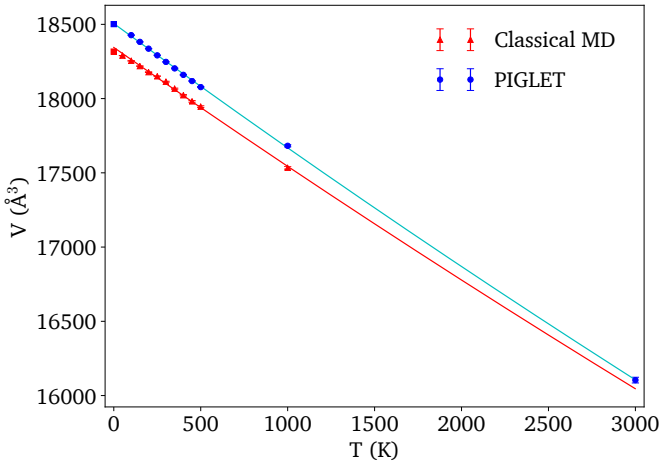

Figure S10: Volume of MOF-5 as a function of temperature as obtained from (PI)MD simulations using the anharmonic force field. The data points at 0 K were obtained from geometry optimisations with `Yaff`.

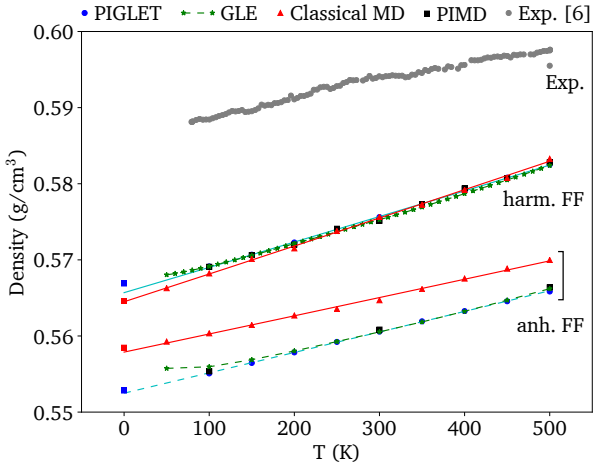

Figure S11: Density of MOF-5 as a function of temperature as obtained from (PI)MD simulations using the harmonic ('harm. FF') and anharmonic ('anh. FF') force field of MOF-5. The data points at 0 K were obtained from geometry optimisations with `Yaff`. The experimental data was obtained from Ref. 6.

References

(1) Tuckerman, M. E. *Statistical Mechanics: Theory and Molecular Simulation*; OUP Oxford, 2010.

(2) Vanduyfhuys, L.; Vandenbrande, S.; Verstraelen, T.; Schmid, R.; Waroquier, M.; Van Speybroeck, V. QuickFF: A program for a quick and easy derivation of force fields for metal-organic frameworks from ab initio input. *J. Comput. Chem.* **2015**, *36*, 1015–1027.

(3) Vanduyfhuys, L.; Vandenbrande, S.; Wieme, J.; Waroquier, M.; Verstraelen, T.; Van Speybroeck, V. Extension of the QuickFF force field protocol for an improved accuracy of structural, vibrational, mechanical and thermal properties of metal-organic frameworks. *J. Comput. Chem.* **2018**, *39*, 999–1011.

(4) Molecular mechanics parameters. *Journal of Molecular Structure: THEOCHEM* **1994**, *312*, 69 – 83.

(5) Tafipolsky, M.; Amirjalayer, S.; Schmid, R. Ab initio parametrized MM3 force field for the metal-organic framework MOF-5. *J. Comput. Chem.* **2007**, *28*, 1169–1176.

(6) Lock, N.; Wu, Y.; Christensen, M.; Cameron, L. J.; Peterson, V. K.; Bridgeman, A. J.; Kepert, C. J.; Iversen, B. B. Elucidating Negative Thermal Expansion in MOF-5. *J. Phys. Chem. C* **2010**, *114*, 16181–16186.

Paper II

Modeling the structural and thermal properties of loaded metal-organic frameworks. An interplay of quantum and anharmonic fluctuations

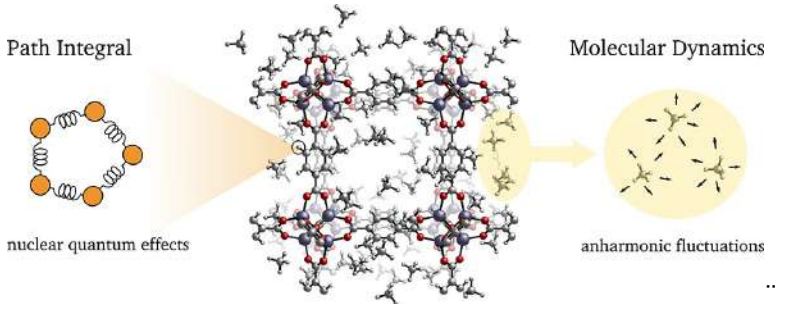

V. Kapil‡, J. Wieme‡, S. Vandenbrande, A. Lamaire,
V. Van Speybroeck, M. Ceriotti

Journal of Chemical Theory and Computation, **2019**, 15 (5), 3237–3249

A. Lamaire contributed to the interpretation of the results and the preparation of the manuscript.

JCTC Journal of Chemical Theory and Computation
Article
Cite This: J. Chem. Theory Comput. 2019, 15, 3237−3249
pubs.acs.org/JCTC

Modeling the Structural and Thermal Properties of Loaded Metal−Organic Frameworks. An Interplay of Quantum and Anharmonic Fluctuations

Venkat Kapil,*[,†,¶] Jelle Wieme,[‡,¶] Steven Vandenbrande,[‡] Aran Lamaire,[‡] Veronique Van Speybroeck,[‡] and Michele Ceriotti[†]

[†]Laboratory of Computational Science and Modelling, Institute of Materials, Ecole Polytechnique Fédérale de Lausanne, CH-1015 Lausanne, Switzerland

[‡]Center for Molecular Modeling, Ghent University, Tech Lane Ghent Science Park Campus A, Technologiepark 46, 9052 Zwijnaarde, Belgium

Supporting Information

ABSTRACT: Metal−organic frameworks show both fundamental interest and great promise for applications in adsorption-based technologies, such as the separation and storage of gases. The flexibility and complexity of the molecular scaffold pose a considerable challenge to atomistic modeling, especially when also considering the presence of guest molecules. We investigate the role played by quantum and anharmonic fluctuations in the archetypical case of MOF-5, comparing the material at various levels of methane loading. Accurate path integral simulations of such effects are made affordable by the introduction of an accelerated simulation scheme and the use of an optimized force field based on first-principles reference calculations. We find that the level of statistical treatment that is required for predictive modeling depends significantly on the property of interest. The thermal properties of the lattice are generally well described by a quantum harmonic treatment, with the adsorbate behaving in a classical but strongly anharmonic manner. The heat capacity of the loaded framework−which plays an important role in the characterization of the framework and in determining its stability to thermal fluctuations during adsorption/desorption cycles−requires, however, a full quantum and anharmonic treatment, either by path integral methods or by a simple but approximate scheme. We also present molecular-level insight into the nanoscopic interactions contributing to the material's properties and suggest design principles to optimize them.

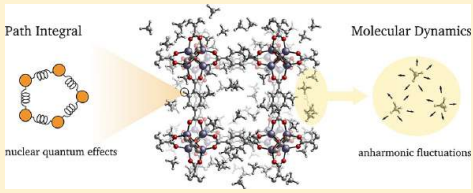

1. INTRODUCTION

Tailor-made porous materials[1] like metal−organic frameworks (MOFs)[2] are at the core of emerging technologies due to their exceptional physical and chemical properties, such as a high tunable porosity and an associated large gas storage capacity. Therefore, they have been proposed for applications such as adsorbed natural gas (ANG) storage in vehicles,[3,4] adsorption-driven heat pumps,[5,6] and carbon capture and sequestration (CCS).[7,8] While a lot of work still needs to be done to optimize the crucial adsorption and storage properties of these porous materials,[9] studies on other critical requirements such as heat management are gaining interest.[10] For instance, the heat capacity, i.e., the amount of energy required to increase the material's temperature, is a fundamental thermodynamic property of interest in these applications which involve large thermal fluctuations, as adsorption and desorption processes imply the release or consumption of energy. Moreover, the heat capacity of the MOF affects the energy penalty to regenerate the adsorbent in, for example, CCS.[11] To date, however, information on the heat capacity is lacking for most MOFs,[12,13] and the influence of adsorbed guest molecules on the heat capacity has not yet been investigated, in contrast to other thermal properties such as the thermal expansion behavior and the thermal conductivity.[14,15]

Within this context, an efficient and accurate simulation protocol to tackle the structural and thermal properties of MOFs including all the relevant physical effects could facilitate a better understanding of the structure−property relations and suggest design principles for materials with improved properties. Due to the importance of finite-temperature effects, anharmonicity, and nuclear quantum effects (NQEs), the modeling of the thermophysics of MOFs is generally not a trivial exercise. The first two effects have already been the subject of many investigations and were included in our protocol to characterize the thermodynamics of MOFs.[16,17] Furthermore, very recently, some of the present authors highlighted the necessity of an accurate theoretical framework for the design of thermoresponsive MOFs.[18] However, the impact of NQEs has so far received far less attention within the

Received: December 23, 2018
Published: April 19, 2019

DOI: 10.1021/acs.jctc.8b01297
J. Chem. Theory Comput. 2019, 15, 3237−3249

Journal of Chemical Theory and Computation Article

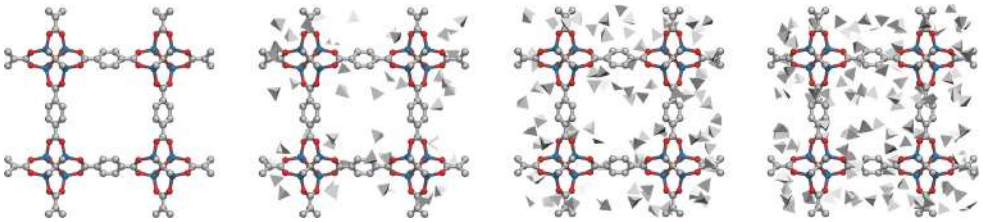

Figure 1. Structure of MOF-5 with a gas loading x of 0, 50, 100, and 150 molecules of methane (left to right) in the conventional unit cell $(8(Zn_4O(CO_2)_6)\cdot xCH_4)$. The oxygen, carbon, and zinc atoms are shown in red, silver, and blue, respectively. For the sake of aesthetics, the hydrogen atoms are not included. The methane molecules are represented by silver tetrahedra.

MOF community, despite the many light atoms contained in the crystal structure and present inside the pores.[19−21]

In this regard, path integral molecular dynamics (PIMD)[22] provides an ideal reference framework for the evaluation of thermodynamic averages, as it seamlessly captures both NQEs and the anharmonic motion of nuclei. The statistics of distinguishable quantum particles can be obtained through the equivalence between the thermodynamics of a quantum system and a classical ring polymer containing P replicas of the system.[23] In the limit of large P values, NQEs can then be systematically accounted for. The major downside of this technique is the associated high computational cost, i.e., P times the corresponding cost of a classical molecular dynamics (MD) simulation. However, several methodological advances[24−29] that enable a reduction of the computational cost have made it a mainstream technique for material modeling.[30]

An additional difficulty arises from the fact that most experiments and practical applications are performed in isothermal−isobaric conditions, while the vast majority of atomistic simulations are performed with a fixed unit cell, corresponding to isochoric conditions. As most solid materials have a very small compressibility, the difference between the two ensembles is often negligible. For MOFs on the contrary—particularly when loaded with a gas—the behavior in isobaric and isochoric conditions can be very different. Some of us emphasized the importance of taking into account the variations of the cell shape to simulate properties of flexible MOFs.[16] While algorithms for performing path integral simulations at constant pressure conditions exist,[31,32] an accurate evaluation of the thermophysical properties requires a very large number of replicas to reach convergence. In this Article, we introduce a method, based on a recently developed implementation of high-order path integral factorizations,[26] to greatly accelerate the convergence of these simulations.

This method, in combination with a first-principles-based force field,[17,33,34] makes it possible to characterize the structural and thermophysical properties of complex molecular systems such as guest-loaded MOFs. We investigate the archetypical case of the well-known MOF-5[35,36] in the presence and absence of methane in its pores (see Figure 1). Evaluating and understanding the impact of methane adsorption on the properties of MOFs is especially important as they have been proposed as potential adsorbents for natural gas storage applications.[3,4,9] We demonstrate the crucial role of a complete statistical-mechanical treatment of the quantum and anharmonic fluctuations in MOFs for a correct description of the structural properties and the heat capacity of guest-loaded MOFs. By meticulously disentangling anharmonic and nuclear quantum effects for both the lattice and the guest molecules, we are able to propose an efficient empirical calculation scheme which may be used to screen MOFs for beneficial thermal properties on a larger scale.

2. METHODOLOGY

2.1. Materials. The materials that are considered in this theoretical work are pristine and methane-loaded MOF-5 scaffolds.[35] This framework consists of $Zn_4O(CO_2)_6$ inorganic nodes connected through 1,4-benzenedicarboxylate (bdc) linkers. The unit cell is cubic and contains eight inorganic nodes, as shown in Figure 1. We consider three different loadings x of 50, 100, and 150 methane molecules in the conventional unit cell $(8(Zn_4O(CO_2)_6)\cdot xCH_4)$, which encompass both the low- and high-adsorption regime.[3,37] At 100 bar and room temperature, for example, approximately 120 methane molecules are present per conventional unit cell, as experimentally measured by Mason et al.[3] (see SI Figure S2). Our force field underestimates the high-pressure saturation loading at various temperatures (see SI Figure S3), which is a property that is extremely sensitive to the underlying potential energy surface.[38] It is also important to note that experimentally the chemical potential is controlled and not the number of guest molecules and that the experimental loading is highly dependent on the temperature. For computational convenience, we performed all our molecular dynamics simulations at a fixed number of particles. The purpose of comparing multiple loadings is only to provide qualitative insight into the interplay between temperature, framework, and guest molecules rather than to compare directly with experiment.

2.2. First-Principles-Derived Force Fields. The molecular simulations are performed using newly developed force fields for MOF-5 and methane. They are constructed with `QuickFF`,[33,34] a software package developed to derive force fields for MOFs in an easy yet accurate way based on information obtained from first-principles input data. Isolated cluster models were used to generate the required first-principles input data, which includes the equilibrium geometry and Hessian together with the atomic charges. Within the `QuickFF` protocol, the quantum mechanical potential energy surface (PES) is approximated by a sum of analytical functions of the nuclear coordinates that describe the covalent and noncovalent interactions. The covalent interactions, which mimic the chemical bonds between the atoms, are approximated by different terms as a function of the internal coordinates (bonds, bends, out-of-plane distances, and dihedrals). The noncovalent interactions are composed of

DOI: 10.1021/acs.jctc.8b01297
J. Chem. Theory Comput. 2019, 15, 3237−3249

electrostatic and van der Waals interactions. The guest−host interactions between MOF-5 and methane only include noncovalent terms. A detailed discussion of the force field energy expression and derivation is provided in the Supporting Information (see SI Section S4).

2.3. Thermodynamic Ensembles. In order to study the classical and quantum isobaric heat capacity of the guest-loaded MOF scaffold, the classical and quantum isothermal−isobaric thermodynamic ensembles−as defined in ref 16−are respectively used. For a system with N particles, subject to an external mechanical stress $\boldsymbol{\sigma} = \mathcal{P}\boldsymbol{I} + \boldsymbol{\sigma}_a$, with $\mathcal{P}$ the hydrostatic pressure and $\boldsymbol{\sigma}_a$ the deviatoric stress, the classical ($\square$ = cl) and quantum ($\square$ = qn) isothermal−isobaric ensembles at temperature $k_B T = \beta^{-1}$ and fixed normalized cell tensor $\boldsymbol{h}_0$ are described by the partition functions

$$\Delta_{\square}(N, \mathcal{P}(\boldsymbol{h}_0), T) \propto \int \mathrm{d}\mathcal{V} e^{-\beta \mathcal{P} \mathcal{V}} Z_{\square}(N, \mathcal{V}(\boldsymbol{h}_0), T) \tag{1}$$

where $Z_{\square}(N, \mathcal{V}(\boldsymbol{h}_0), T)$ are the corresponding canonical partition functions at volume $\mathcal{V}$, normalized cell tensor $\boldsymbol{h}_0$, and temperature T. Similarly, the flexible $N\mathcal{P}(\boldsymbol{\sigma}_a = \boldsymbol{0})T$ partition functions, which allow the cell shape to change, are defined by the partition functions:[39]

$$\Delta_{\square}(N, \mathcal{P}(\boldsymbol{\sigma}_a = \boldsymbol{0}), T) \propto \int \mathrm{d}\mathcal{V} e^{-\beta \mathcal{P} \mathcal{V}} \int \mathrm{d}\boldsymbol{h}_0 \delta(\det(\boldsymbol{h}_0) - 1) Z_{\square}(N, \mathcal{V}(\boldsymbol{h}_0), T) \tag{2}$$

The classical ensembles are sampled by classical molecular dynamics, whereas the quantum ensembles are sampled using path integral molecular dynamics.[22] The latter maps the quantum partition function of a system onto that of a classical ring polymer Hamiltonian made of P replicas of the system.[23] Formally, exact results can be obtained in the limit of $P \to \infty$. Unfortunately, the requisite value of P to calculate structural properties rises rapidly with decreasing temperature, and for properties such as heat capacity[40] the increase in P is even greater. This makes the standard scheme prohibitively expensive.

2.4. Accelerated Simulation Scheme. To remedy this problem, we present an accelerated scheme based on a constant pressure integrator for the high-order path integral method.[24] The quantum statistics of distinguishable particles arises from the noncommutative nature of the potential and kinetic energy operators. In standard (second-order) path integral schemes, an approximate factorization of the high-temperature Boltzmann operator is introduced, that leads to an error that decreases as $O(1/P^2)$. High-order techniques use an alternative splitting of the Boltzmann operator,[41,42] leading to an alternative ring polymer Hamiltonian with a faster, $O(1/P^4)$ convergence to the exact quantum limit. This makes it possible to reduce the number of replicas and hence the computational cost.[24] While many high-order schemes exist,[29,41] here we focus on the specific case[43] of a fourth-order Suzuki-Chin (SC) splitting,[42,44] which yields a so-called SC Hamiltonian $H_P^{\mathrm{sc}}(\mathbf{p}, \mathbf{q})$. Considering for simplicity the case of a single particle in an external potential, the SC Hamiltonian takes the form

$$H_P^{\mathrm{sc}}(\mathbf{p}, \mathbf{q}) = H_P^0(\mathbf{p}, \mathbf{q}) + V_P^{\mathrm{sc}}(\mathbf{q}) \tag{3}$$

where

$$H_P^0(\mathbf{p}, \mathbf{q}) = \sum_{j=1}^{P} \frac{[\mathbf{p}^{(j)}]^2}{2m} + \sum_{j=1}^{P} \frac{1}{2} m \omega_P^2 [\mathbf{q}^{(j)} - \mathbf{q}^{(j+1)}]^2$$

is the ring polymer Hamiltonian of a free particle, subjected to cyclic boundary conditions ($j + P = j$), and

$$V_P^{\mathrm{sc}}(\mathbf{q}) = \sum_{j=1}^{P/2} \left[\frac{2}{3} V(\mathbf{q}^{(2j-1)}) + \frac{4}{3} V(\mathbf{q}^{(2j)}) + \frac{1}{9} \tilde{V}(\mathbf{q}^{(2j)}) \right] \tag{4}$$

Note that the odd and even replicas feel the physical potential $V(\mathbf{q}^{(j)})$ scaled by factors of 2/3 and 4/3 respectively and that the high-order term $\tilde{V}(\mathbf{q}^{(j)}) = \omega_P^{-2} m^{-1} |\mathbf{f}^{(j)}|^2$, that depends on the modulus of the force $\mathbf{f}^{(j)} \equiv -\partial V(\mathbf{q}^{(j)})/\partial \mathbf{q}^{(j)}$, only acts on the even replicas.

The improved efficiency of the high-order scheme is demonstrated by studying the convergence of the total energy and its temperature derivative for a harmonic model of MOF-5−obtained by computing the dynamical matrix associated with the first-principles-derived force field described in Section 2.2−with respect to the number of replicas. The analysis is done analytically at two different temperatures: T = 100 and 300 K, as described in ref 45. As shown in Figure 2, the high-order scheme improves the convergence of both the energy and the heat capacity by a factor of 2 at room temperature. In the low temperature or high accuracy regime where quantum effects dominate, the efficiency of the high-order scheme is even more significant.

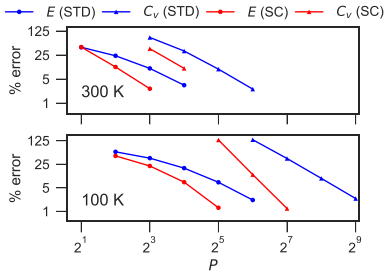

Figure 2. Fractional error in the standard (blue) and Suzuki-Chin (red) path integral estimators of the energy (circles) and the heat capacity (triangles) of the empty MOF-5 modeled by the corresponding Debye crystal potential, as a function of the number of beads P at 100 K (bottom) and 300 K (top). The values of the energy and the heat capacity were obtained analytically.[45]

The high accuracy afforded by the SC scheme makes it particularly useful to compute the heat capacity. Thus far, however, it has only been successfully applied to relatively simple systems,[46] and heat capacities in particular have only been reported for small clusters of molecules and constant-volume conditions.[47] The difficulty in applying fourth-order schemes to complex materials can be understood by considering the fact that the force and virial contain derivatives of $\tilde{V}$ with respect to the atomic positions and the cell parameters

$$\tilde{\mathbf{f}}^{(j)} \equiv -\frac{\partial \tilde{V}(\mathbf{q}^{(j)})}{\partial \mathbf{q}^{(j)}}, \qquad \tilde{\Xi}^{(j)} \equiv \frac{\mathrm{d}\tilde{V}(\mathbf{q}^{(j)})}{\mathrm{d}\boldsymbol{h}} \boldsymbol{h}^T \tag{5}$$

DOI: 10.1021/acs.jctc.8b01297
J. Chem. Theory Comput. 2019, 15, 3237−3249

Given that $\tilde{V}(\mathbf{q}^{(j)})$ already contains first-order derivatives of the physical potential, the computation of the forces and the virial, required to sample the isothermal−isobaric ensemble by means of path integral dynamics, also demands the evaluation of higher-order derivatives of the potential, which is often cumbersome and computationally prohibitive. Much of the work on the practical implementation of high-order path integrals has therefore focused on avoiding the calculation of these terms, by sampling the standard path integral Hamiltonian and introducing fourth-order statistics by reweighting.[24,46] Unfortunately, reweighting schemes have poor statistical performance for large systems,[24,48] so the application of the SC scheme has until now been limited to small systems and to constant-volume sampling.

To circumvent these limitations, we evaluate the virial using a finite-difference scheme that has recently been introduced by some of the present authors, to sample the SC canonical partition function directly. We discuss the essential ingredients of this scheme in Appendix A and report a detailed derivation in the SI. Direct access to the instantaneous force and virial allows us to develop an integration scheme that samples the quantum isothermal−isobaric ensemble. This scheme can be regarded as an extension of the second-order scheme introduced in the pioneering work of Martyna and co-workers.[31] The rather cumbersome derivation and the equations of motion are given in the SI. It should be noted that our implementation in `i-PI`[49] is also fully compatible with multiple time stepping[28,50] and stochastic thermostatting, extending the integrators introduced in ref 51 to the isothermal−isobaric ensemble.

By using the finite-difference expressions, only $P/2$ additional force evaluations are needed instead of $P/2$ Hessians. It is also useful to note that these components have a P^{-2} prefactor, which means that they become small and slowly varying for typical values of P used in SC simulations.[26] This facilitates the use of a long time step for integrating the high-order forces and virials, enabling us to sample the ensemble while evaluating the expensive terms rather infrequently.

To further reduce the computational effort, we combine this scheme with other accelerated PIMD methods that rely on the separation of the total potential into a cheap short-ranged term and an expensive long-ranged term, which is the case in our study, as discussed in Subsection 2.2. We consider in particular ring polymer contraction (RPC)[27] and multiple time stepping (MTS).[50] Within the first method, the long-ranged components can be computed separately on a smaller ring polymer of P' beads, which are subsequently, without loss of accuracy, extrapolated to the case of P beads. The second method reduces the frequency at which the long-ranged interactions are computed by the use of a longer time step for the integration. The two methods can also be used together to achieve substantial computational savings[28] and can be seamlessly combined with our high-order constant pressure scheme.

2.5. Calculation of Thermodynamic Observables. Within the SC scheme, the thermodynamic averages of all structural observables A are estimated by an ensemble average over the odd replicas

$$\mathcal{A}^{\mathrm{OP}} = \frac{2}{P}\left\langle \sum_{j=1}^{P/2} A(\mathbf{q}^{(2j-1)}) \right\rangle \tag{6}$$

as first demonstrated by Jang and Voth.[24] These estimators are commonly referred to as "operator" (OP) estimators, as opposed to the "thermodynamic" estimators obtained by derivation of the path integral partition function, that often have pathological statistical behavior. The simplicity of OP estimators makes the SC scheme very appealing in comparison to other high-order schemes, in which *ad hoc* estimators need to be constructed for simple structural observables.[46,52] The OP estimators for the total energy ($\mathcal{E}$) and enthalpy ($\mathcal{H}$) are listed in Appendix B. Since the standard estimators for the heat capacity in path integral methods tend to be very complex and exhibit a large variance, we derive an OP double-virial estimator for the isobaric (and isochoric) heat capacity $C_P = \frac{\partial \mathcal{H}}{\partial T}$. The derivation is presented in the SI (Section S3.2), and the resulting expression is given in Appendix B, where it is also shown that this estimator has very good statistical properties and outperforms existing heat capacity estimators.[47] However, in this study we computed thermophysical properties over a broad range of temperatures and found it more convenient to estimate C_P by means of a finite difference approximation to the temperature derivative of the enthalpy:

$$C_p(T) = \frac{\partial \mathcal{H}}{\partial T} \approx \frac{\mathcal{H}|_{T+\Delta T} - \mathcal{H}|_{T-\Delta T}}{2\Delta T} \tag{7}$$

A dedicated estimator will prove useful in simulations that are targeted at a single, specific temperature.

3. COMPUTATIONAL DETAILS

The required first-principles cluster data for the determination of the covalent terms in the force field are generated with `Gaussian 16`[53] using the B3LYP[54] exchange-correlation functional. A 6-311G(d,p) basis set[55] is used for the C, O, and H atoms, together with the LanL2DZ basis set for Zn.[56] The atomic charges are derived with the Minimal Basis Iterative Stockholder (MBIS) partitioning scheme.[57] The atomic charges of the MOF-5 clusters are obtained from the PBE[58] electron density computed with `GPAW`.[59] For methane, the atomic charges are derived from the B3LYP all-electron density obtained with `Gaussian 16`. The parameters of the van der Waals interactions are taken from the MM3 force field.[60,61] The van der Waals interactions are calculated up to a cutoff of 15 Å, and a tail correction is added to the potential and its derivatives.[62] The initial configurations of the methane molecules are generated using `RASPA`[63] by inserting methane molecules at random positions, while ensuring that only realistic intermolecular distances are retained. Afterward a canonical Monte Carlo algorithm was used to equilibrate the positions.

For MOF-5 with and without methane, we perform classical and path integral MD simulations at a mechanical pressure of 1 bar and at different temperatures in the range of 100 to 500 K. The classical MD simulations of both loaded and pristine MOF-5 are performed using `Yaff` in the $N\mathcal{P}(\sigma_a = 0)T$ ensemble, i.e. without constraints on the unit cell.[16] While the covalent interactions are calculated by `Yaff`, the expensive long-range interactions are computed by `lammps`[64] in a computationally efficient manner. The equations of motion are updated via a Verlet scheme, with a time step of 0.5 fs. The temperature is controlled via a single Nosé−Hoover chain consisting of three beads, with a relaxation time of 100 fs.[65−67] A Martyna-Tobias-Klein barostat with a relaxation time of

DOI: 10.1021/acs.jctc.8b01297
J. Chem. Theory Comput. 2019, 15, 3237−3249

Journal of Chemical Theory and Computation Article

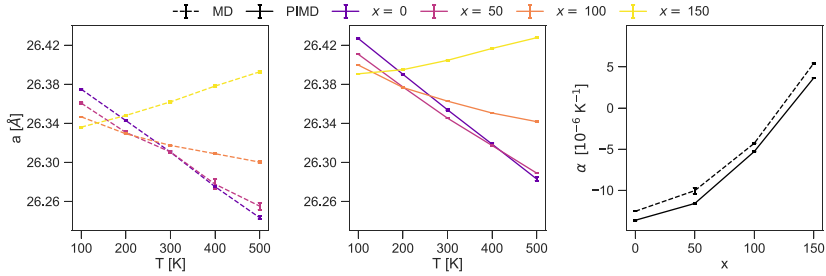

Figure 3. Panels (a) and (b) show the lattice parameter a of MOF-5 with x = 0, 50, 100, and 150 molecules of methane as a function of temperature (T), obtained from classical MD and PIMD, respectively. Panel (c) shows the linear thermal expansion coefficient (α) as a function of x. The classical and quantum estimates are respectively shown with dashed and solid lines. Error bars indicate statistical uncertainty.

1000 fs is used to control the pressure.[16,39,68] We performed five independent runs of 500 ps, starting from a different random seed and from different methane positions. For the empty MOF-5, a single trajectory of 500 ps was used. An equilibration time of 100 ps was considered.

The PIMD simulations are performed with the universal force engine `i-PI`[49] in the $N\mathcal{P}(\boldsymbol{h}_0)T$ ensemble, in which the cubic symmetry is kept fixed. As shown in the SI (see Section S6.2), the results obtained in the classical limit (P = 1) agree perfectly with those obtained in the classical $N\mathcal{P}(\boldsymbol{\sigma}_a = \mathbf{0})T$ ensemble. This indicates that the effect of cell shape sampling on the heat capacity is negligible for this rigid MOF and thus isotropic barostatting suffices for our PIMD simulations. The evaluation of the forces is carried out by `Yaff` and `lammps`, similar to the classical MD simulations, while the time evolution of the nuclei to sample the appropriate thermodynamic ensemble is done with `i-PI`. To control the temperature, a PILE-L thermostat[69] is applied to the system, and a white noise Langevin thermostat[70] is applied to the cell. To control the pressure, a path-integral version of the Bussi-Zykova-Parinello (BZP) barostat,[32,71] adapted to the SC scheme, is used. The time constants for the thermostats and the barostats are the same as the ones used in the classical simulations. A *BAOAB* type[51] MTS scheme[50] (see SI Section S2.3) is used to integrate the equations of motion. The computationally cheap short-range terms of the force field are computed on 64 replicas and integrated with a time step of 0.25 fs. The remainder of the interactions, i.e. the expensive long-range interactions, are computed on 8 replicas using RPC and integrated with a time step of 1 fs. As discussed above, a finite differences strategy is adopted to determine the heat capacity from the enthalpy with a temperature interval of 25 K. We performed 30 independent runs of 50 ps, starting from a different random seed and from different methane positions. For the empty MOF-5, five independent trajectories of 125 ps were used. An equilibration time of 25 ps was considered.

4. RESULTS

Having developed an accelerated integration scheme for the quantum isothermal−isobaric ensemble, we now focus on the structural and thermal properties of methane-loaded MOF-5. Extensions toward other MOFs and adsorbates will be the topic of future studies. The importance of the inclusion of NQEs and anharmonicities in the modeling of the heat capacity is probed by comparing the results with other methods such as classical MD, which neglects NQEs, and the harmonic approximation, which neglects anharmonicity. We discuss the accuracy of these commonly adopted approximations and provide empirical relations, which might resolve the general lack of knowledge of the heat capacity of this class of materials.

4.1. Structural Properties. To unravel the influence of adsorbates on the framework and finally on the heat capacity, we start by investigating the structural response of MOF-5 for various loadings and temperatures. Here, one could already expect to observe significant NQEs, as zero-point effects were recently found to substantially increase the volume of MOF-5 when comparing classical MD with PIMD.[21] Additionally, NQEs have previously been observed to change the volume of bulk alkanes by about 10%.[72−74] A comparison of Figures 3(a) and (b) indeed reveals that the inclusion of NQEs increases the volume by almost 1% for all loadings and temperatures. Horizontally, this shift corresponds to a substantial temperature reduction of about 100 K.

Interestingly, the qualitative changes in the volume as a function of loading at different temperatures do not change appreciably with or without the inclusion of NQEs. At low temperatures, the material slightly shrinks in the presence of methane. The observed adsorption-induced deformation can be understood by attractive van der Waals interactions between the framework and the adsorbed methane.[75,76] At higher temperatures, by contrast, the empty framework has the lowest volume, as entropic and kinetic effects start dominating and the adsorbed molecules increase the internal pressure, which leads to a volumetric expansion when increasing the loading. The main effect of NQEs on the volume of the guest-loaded system is thus an upward volume shift,[21] which is to a large extent independent of the number of guest molecules and the temperature.

Varying the concentration and the type of adsorbates in the framework was suggested by Calero and co-workers[15] as a way to control and tune the thermal expansion of a system based on classical MD simulations. We confirm that with methane it is possible to go from the well-known negative thermal expansion behavior of the empty framework[77−79] toward positive thermal expansion. A proper inclusion of NQEs in our molecular dynamics simulations does not influence the predictions in this temperature window,[21] and this conclusion still holds with methane in the pores, as shown in Figure 3(c).

A more surprising picture emerges when looking at the distribution of methane inside MOF-5. Recent PIMD

DOI: 10.1021/acs.jctc.8b01297
J. Chem. Theory Comput. 2019, 15, 3237−3249

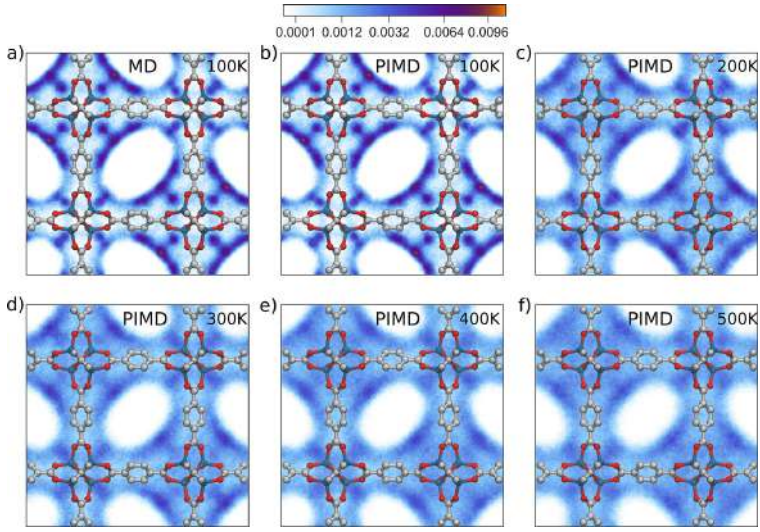

Figure 4. Methane distribution in the pores of MOF-5 at different temperatures as obtained from PIMD simulations. Orange spots indicate high probability adsorption sites. Other colors show the distribution of the low probability methane positions in the conventional unit cell and visualize the probability representation (from very high (orange), to high (dark blue), to low (white) probability). The results are displayed for a loading x of 100 methane molecules per conventional unit cell ($8(Zn_4O(CO_2)_6)$).

simulations[73] of bulk methane (at 110 K) have shown that NQEs lead to significant changes in the structure of methane at low temperature, corresponding to an overall softening of the structure and an increase in the intermolecular distance by about 0.1 Å. In contrast, in our study of methane confined in the pores of MOF-5, even at 100 K—where NQEs are expected to be the greatest—there is no appreciable difference between the shape of the classical and quantum distribution functions of methane, as shown in Figure 4. This can be understood by the fact that the change in the structure of bulk methane comes entirely from the isotropic expansion of the gas.[80] In the case of methane molecules confined in the pores, the low compressibility of the framework makes the expansion as observed in bulk methane when including NQEs impossible.

This discussion shows that the structural response of MOF-5 to a varying number of methane molecules and temperature is largely unaffected by NQEs, except for the zero-point lattice fluctuations. Our observations also corroborate the common practice of ignoring NQEs when studying the loading of porous materials by Grand Canonical Monte Carlo simulations.[63] Nevertheless, this conclusion cannot be generalized to other adsorbates, especially those possessing stronger intermolecular interactions such as hydrogen bonding.

4.2. Heat Capacity. MOF-5 has been the subject of a few experimental heat capacity studies[12,13,81,82] which have shown that the material has a low specific (or molar) heat capacity, about 0.7 J/g·K at room temperature, even when compared to other MOFs. Depending on the type of the application, a large (e.g., for ANG to limit temperature fluctuations) or a small (e.g., for CCS to limit the energy penalty) heat capacity is sought after. It is thus important to understand how this property changes at different levels of loading and temperature and to determine the factors influencing the heat capacity, which is now possible using our high-order PIMD scheme.

In the previous section, it has been shown that classical MD can—at least qualitatively—be used to model the structural response of MOF-5 in the presence of methane at various temperatures. This approach is however expected to fail for the description of the heat capacity since the heat capacity of most solids is dominated by NQEs at room temperature, as evidenced by experimental deviations from the classical Dulong-Petit law. The most common way of including NQEs for solids is the static harmonic approximation, using Einstein or Debye harmonic model for solids, which is usually able to reproduce the heat capacity semi-quantitatively and will therefore also be used for comparison.

We begin by presenting the estimates of the temperature dependence of the isobaric heat capacity of the empty MOF-5 framework. As shown in Figure 5, the classical MD estimates (dashed line) are in agreement with the Dulong-Petit law. The simulations yield an almost constant value of 3 k_B per degree of freedom, which indeed results in large deviations from the experimental values.[12,13,81,82] Upon inclusion of NQEs with our PIMD scheme (solid line), we find that the results follow the experimental measurements reasonably well up to almost 400 K. This agreement is remarkable, as these measurements are typically carried out on the as-synthesized sample, which possibly includes solvents[12] and differs from the perfect crystal that we have simulated.

Figure 5 also reveals that the results obtained using the simple and computationally inexpensive harmonic approximation (dotted line) are in good agreement with the exact values computed with PIMD. This implies that anharmonic quantum contributions to the heat capacity and the effect of an adequate anharmonic sampling are small for the empty MOF. Moreover,

DOI: 10.1021/acs.jctc.8b01297
J. Chem. Theory Comput. 2019, 15, 3237−3249

Journal of Chemical Theory and Computation Article

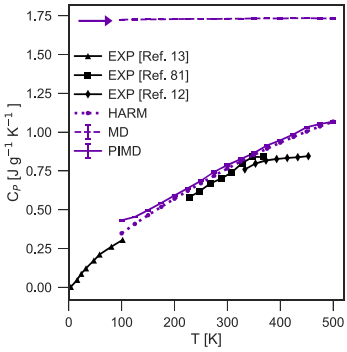

Figure 5. Heat capacity C_P of the empty MOF-5 as a function of temperature (T) computed using classical MD (dashed), PIMD (solid), and the harmonic approximation (dotted). The right pointing arrow shows the Dulong-Petit limit. Different experimental results are shown in black using triangular,[13] square,[81] and diamond[12] markers. Error bars indicate statistical uncertainty.

the harmonic approximation using the UFF4MOF force field[83] yields largely similar results (see SI Section S6.1), so that a less accurate and generic model for the potential energy surface is capable of reproducing the heat capacity of the empty framework.

Another notable detail of our calculations is that the harmonic approximation was used to estimate the isochoric heat capacity instead of the isobaric one. As the isobaric and isochoric heat capacities are almost the same, the MOF behaves like a regular solid, despite its large negative thermal expansion coefficient. The harmonic approximation could therefore serve as an efficient procedure to accurately estimate the heat capacity of the empty framework in the increasing number of high-throughput MOF screenings.[9,84]

In order to study the effect of adsorbates, we start by considering the case of a loading x of 100 methane molecules per conventional unit cell ($8(Zn_4O(CO_2)_6)\cdot 100CH_4$). Contrary to the case of the empty framework, we could not find published experimental data for the heat capacity of the guest-loaded framework. Although a high-level PIMD strategy might not be required to estimate the heat capacity of the empty MOF host, PIMD proves to be crucial to capture the correct temperature dependence of the loaded system, as can be seen in the left panel of Figure 6. Here, anharmonic effects become important as we observe differences between the PIMD results and the harmonic approximation. The discrepancy in the qualitative behavior of the heat capacity between both techniques can be understood through the mobility of the guest molecules in the large pores of the framework, which cannot be adequately captured by a harmonic approximation.[85] These low-frequency anharmonic motions explain why we find at the classical MD level a similar low-temperature dependence as in PIMD, but only PIMD simulations include both anharmonic and nuclear quantum effects correctly. Interestingly, the combination of both effects yields a heat capacity that does not change monotonically but exhibits a minimum at about 200 K.

Extending toward other loadings of methane in the middle panel of Figure 6, it becomes clear that the heat-capacity minimum as a function of temperature depends strongly on the number of guests and becomes more pronounced at higher loadings. Even when expressing the heat capacity normalized to the total mass of the system, one can see that at a fixed temperature C_P increases almost linearly with the loading (see Figure 6(c) at 300 K). For the volumetric heat capacity, i.e., the heat capacity per unit of volume of the system, similar results are obtained (see SI Section S6.4).

To rationalize the origin of the nonmonotonic temperature dependence of the heat capacity, we determine which interactions give the most substantial contribution to C_P. To this end, the force-field energy contributions are decomposed in terms of the host, host−guest, and guest−guest interactions (see SI Section S6.3). Figure 7 displays the most important results of this analysis. The host and guest−guest contributions to the specific heat capacity are visualized in panels (a) and (c). The shape of the different host curves appears to be independent of the loading. In fact, when rescaled to the mass of the empty MOF, the curves coincide with one another and with the curve obtained within the harmonic approximation. This demonstrates that the degrees of freedom of the MOF-5 framework, which are more strongly quantized, are predominantly harmonic and do not change significantly due to the interaction with methane. Their contribution to the total heat capacity per unit mass, however, decreases with the loading

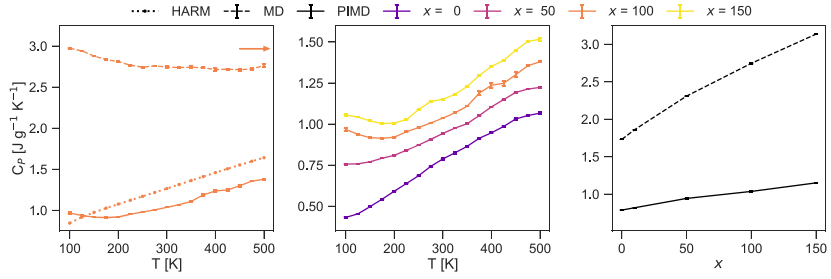

Figure 6. Panel (a) shows the comparison of the classical (dashed), quantum (solid), and harmonic estimates (dotted) of the isobaric heat capacity C_P of MOF-5 with 100 molecules of methane, as a function of the temperature T. Panel (b) shows the temperature dependence of the quantum isobaric heat capacity of MOF-5 with x molecules of methane. Panel (c) shows the quantum isobaric heat capacity of the MOF with x molecules of methane as a function of x at 300 K. Error bars indicate statistical uncertainty.

DOI: 10.1021/acs.jctc.8b01297
J. Chem. Theory Comput. 2019, 15, 3237−3249

Journal of Chemical Theory and Computation Article

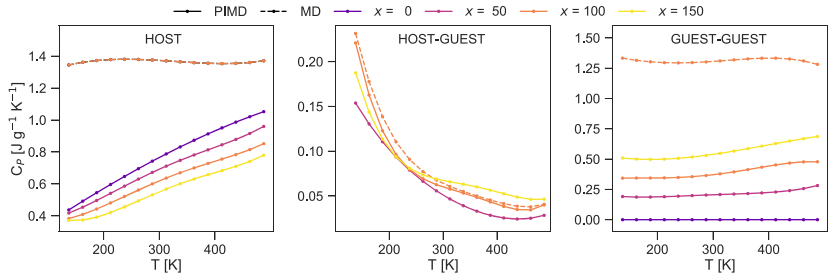

Figure 7. Panels (a), (b), and (c) respectively show the decomposition of the specific heat capacity of the MOF and the adsorbate system into host, host−guest, and guest−guest contributions for different gas loadings (x). The curves were obtained by deriving a polynomial fit to the energy as a function of temperature.

due to a change in the mass balance. The guest−guest interactions, on the other hand, are relatively constant and only show a small increase when going from 100 to 500 K, due to the activation of high-frequency vibrational modes. The most interesting contribution arises from the host−guest interactions, which explains the nonmonotonic behavior of the specific heat capacity of the guest-loaded system. The contribution of these interactions decreases with a sharp temperature dependence when sufficient guest molecules are present inside the pores. The large heat capacity at temperatures lower than 100 K originates from the known first-order structural phase transition of methane in MOF-5 at 60 K,[86,87] from which we observe the decreasing tail. Since the methane molecules are more localized at low temperatures, the attractive host−guest interactions allow for efficiently storing thermal energy. At higher temperatures, from 250 to 500 K, the host−guest contributions become negligible as the confined guests become more mobile and less bound to the framework, so that the increase in thermal energy can no longer be stored in the physical interactions between the methane guests and the MOF-5 host.

Another decomposition of the force-field energy in terms of the covalent, electrostatic, and van der Waals interactions shows that the short-range covalent interactions and thus the network of chemical bonds (Figure 8) dominates the contributions to the heat capacity. For the empty MOF-5 framework, the noncovalent interactions are negligible (see SI Section S6.3). This confirms that the heat capacity of empty MOF-5 can be approximated by considering only contributions from the separate molecular fragments of the material[12] and suggests why the harmonic approximation works well for this material. For the loaded framework, the noncovalent part starts to play a role, which is especially true for the host−guest interactions. Not surprisingly, in the case of nonpolar methane molecules, these interactions are dominated by the van der Waals terms in the force field (see SI Section S6.3). This suggests that the use of different, more polar, guests in which electrostatic interactions play a more prominent role (e.g., CO_2) could give rise to other interesting phenomena. However, care must be taken in interpreting these different terms, as a separation is not unambiguously defined and might be force-field dependent. Nevertheless, simulations using a different force-field model for the guest−host and guest−guest interactions display the same qualitative behavior (see SI Section S6.5), suggesting that our conclusions are rather robust.

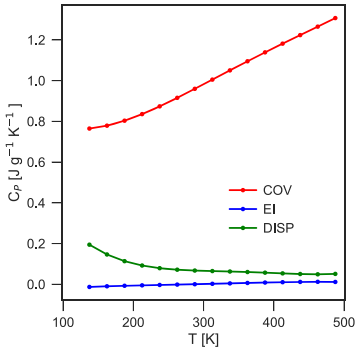

Figure 8. Decomposition of the total heat capacity of MOF-5 with 100 methane molecules per unit cell into covalent (COV), electrostatic (EI), and van der Waals (DISP) contributions. The curves were obtained by deriving a polynomial fit to the energy as a function of temperature.

4.3. The Interplay of Gas Loading, Anharmonicities, and Quantum Effects. Our analysis of the structural and thermal properties of methane-loaded MOF-5 shows that the total system does not always need a full treatment of anharmonicities and NQEs. This suggests that a full path integral sampling of the entire system may not be necessary, especially if qualitative trends are to be studied. Hence, inspired by our results, we propose an empirical formula for the volume and the heat capacity in which the most important effects, i.e., anharmonicities and/or NQEs, are captured and which might prove to be beneficial for future studies of guest-loaded MOFs.

As discussed above, the main difference between the volume with or without NQEs comes from zero-point effects in the lattice.[21] The correct volume can therefore be estimated as follows

$$\mathcal{V} \approx \mathcal{V}^{\mathrm{anh}}_{\mathrm{qn}}[\text{MOF-5}] - \mathcal{V}^{\mathrm{anh}}_{\mathrm{cl}}[\text{MOF-5}] + \mathcal{V}^{\mathrm{anh}}_{\mathrm{cl}}[\text{MOF-5} + \mathrm{CH_4}]$$

where anh stands for the inclusion of anharmonicities with MD, and cl and qn denote the use of classical or path integral MD, respectively. The left most panel of Figure 9 indicates that this approximate volume agrees very well with the exact results obtained from PIMD simulations. A more stringent test is the

DOI: 10.1021/acs.jctc.8b01297
J. Chem. Theory Comput. 2019, 15, 3237−3249

Journal of Chemical Theory and Computation Article

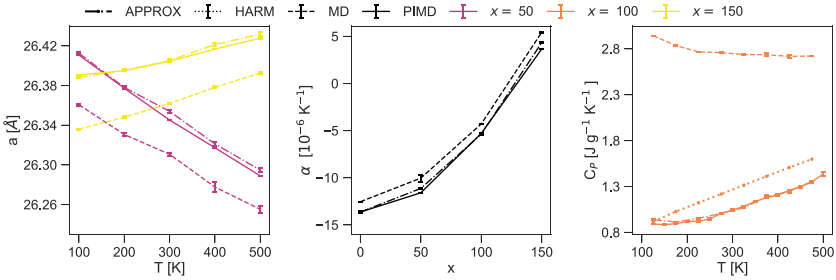

Figure 9. Panels (a), (b), and (c) respectively show the temperature dependence of the cell parameter (a) for MOF-5 with 50 and 150 molecules of methane, the linear thermal expansion coefficient α of MOF-5 as a function of methane loading x, and the isobaric heat capacity C_P of MOF-5 with 100 molecules of methane, obtained with classical MD (dashed), PIMD (solid), and the approximation introduced in the work (dot-dashed). Error bars indicate statistical uncertainty.

thermal expansion coefficient, which is—as shown in Figure 9(b)—also in excellent agreement with the PIMD results. For systems where a first-principles treatment of the potential energy surface is required and PIMD simulations are too expensive, other approximate techniques such as the quasi-harmonic approximation or classical MD with a quantum thermostat could be used to estimate the zero-point effects.[21]

In contrast, we observed in the previous section that the heat capacity of the framework could be estimated with a harmonic approximation, while the guest–host interactions are dominated by anharmonicities. For that reason, we propose

$$C \approx (C_{qn}^{har} - C_{cl}^{har} + C_{cl}^{anh})[\text{MOF-5} + \text{CH}_4]$$

in which the high frequency modes of adsorbate and the MOF are treated in a harmonic fashion and the host–guest interactions are treated classically. For C_{cl}^{har}, the Dulong-Petit law can be used. The proposed relation is analogous to similar corrections that are routinely used to compare the heat capacity obtained from classical simulations with experimental data.[88] As shown in the rightmost panel of Figure 9, this approximation works really well for this system and is even able to qualitatively reproduce the heat capacity minimum for a loading of 100 methane molecules. Beyond 200 K, the agreement between the empirical expression and the exact PIMD becomes quantitatively correct. This method could thus be an inexpensive route to estimate the heat capacity of guest-loaded MOFs.

5. CONCLUSIONS

To summarize, we developed an efficient and accurate methodology to calculate the isobaric thermophysical properties of materials, that is generally applicable and therefore ideally suited to the study of guest-loaded MOFs. For this purpose, we derived and implemented the necessary algorithms in `i-PI`[49] to perform simulations in the quantum isothermal–isobaric ensemble using the Suzuki-Chin path integral molecular dynamics framework. The method is rigorous and can be seamlessly combined with other cost-reduction techniques, which facilitates a huge reduction of the computational cost compared to standard techniques.

We demonstrated the applicability of our approach by investigating the heat capacity of the prototypical MOF-5 loaded with different numbers of methane molecules. We observed that the level of statistical sampling that is needed to achieve quantitative accuracy depends on the property of interest. For all the cases we considered, we found the framework to behave in a strongly quantized manner but to be largely amenable to a harmonic treatment. The adsorbates, on the other hand, show only mild quantum effects in their intermolecular interactions but require a full anharmonic description. The heat capacity shows a particularly subtle interplay of quantum and anharmonic fluctuations, that results in a nonmonotonic temperature dependence of the heat capacity, with a minimum around 200 K.

Through a decomposition of the heat capacity into molecular interactions, we find that the host–guest interactions are responsible for this behavior, as their contribution to the total heat capacity decreases with temperature. By comparing the behavior of different classes of framework materials and guest molecules, this may reveal new design rules to optimize the thermal behavior of a storage material over a broad range of temperatures and levels of loading. Our approach provides an affordable route to perform benchmark studies and approximation strategies to carry out the high-throughput studies that are needed to obtain a complete understanding of the interplay between framework, adsorbate, and quantum mechanical and anharmonic fluctuations that determine the thermophysical properties of MOFs.

APPENDIX A: SUZUKI-CHIN FORCES AND VIRIALS

Recently, some of the present authors showed that the high-order force can be estimated in a finite difference fashion,[26] without computing the full Hessian (see SI Section S1.5)

$$\begin{aligned}\tilde{\mathbf{f}}^{(2j)} &= \omega_P^{-2} m^{-1} \frac{\partial}{\partial \mathbf{q}^{(2j)}} |\mathbf{f}^{(2j)}|^2 \\ &= -2\omega_P^{-2} \lim_{\epsilon \to 0} \frac{1}{\epsilon\delta} \left(\mathbf{f}^{(2j)}|_{\mathbf{q}^{(2j)} + \epsilon\delta \mathbf{u}^{(2j)}} - \mathbf{f}^{(2j)} \right)\end{aligned} \tag{8}$$

where $\mathbf{u}^{(2j)} = \mathbf{f}^{(2j)}/m$ and $\delta = \left[(3NP)^{-1} \sum_{j=1}^{P} \mathbf{u}^{(j)} \cdot \mathbf{u}^{(j)} \right]^{-1/2}$ is a normalization factor, so that ϵ represents the root-mean-square displacement applied to each atom. This avoids the explicit calculation of the Hessian and allows for the direct sampling of the Suzuki-Chin canonical ensemble. Following a similar strategy (see SI Section S1.6), we show that the high-order component of the virial can be estimated as

DOI: 10.1021/acs.jctc.8b01297
J. Chem. Theory Comput. 2019, 15, 3237–3249

$$\tilde{\Xi}^{(2j)} = \left[-\sum_{j=1}^{N} \mathbf{q}_i^{(2j)} \otimes \tilde{\mathbf{f}}_i^{(2j)} + \frac{\partial \tilde{V}(\mathbf{q}^{(2j)})}{\partial \boldsymbol{h}} \boldsymbol{h}^T \right]$$
$$= -2\omega_P^{-2} \left[\sum_{j=1}^{N} \mathbf{f}_i^{(2j)} \otimes \mathbf{f}_i^{(2j)}/m + \lim_{\epsilon \to 0} \frac{1}{\epsilon\delta} (\Xi^{(2j)}|_{\mathbf{q}+\epsilon\delta\mathbf{u}^{(2j)}} - \Xi^{(2j)}) \right] \quad (9)$$

APPENDIX B: SUZUKI-CHIN ESTIMATORS

The operator (OP) and thermodynamic (TD) estimators of the energy for Suzuki-Chin isothermal−isobaric PIMD simulations of a single particle system, described in Section 2.4, are given by

$$\mathcal{E}^{\mathrm{OP}} = \frac{3}{2\beta} + \frac{2}{P} \sum_{j=1}^{P/2} \left\langle -\frac{1}{2} (\mathbf{q}^{(2j-1)} - \bar{\mathbf{q}}) \cdot \mathbf{f}^{(2j-1)} \right\rangle + \frac{2}{P} \sum_{j=1}^{P/2} \langle V(\mathbf{q}^{(2j-1)}) \rangle \quad (10)$$

$$\mathcal{E}^{\mathrm{TD}} = \frac{3}{2\beta} + \frac{1}{P} \sum_{j=1}^{P} \left\langle -\frac{1}{2} (\mathbf{q}^{(j)} - \bar{\mathbf{q}}) \cdot \mathbf{f}^{\mathrm{sc}(j)} \right\rangle + \frac{1}{P} \sum_{j=1}^{P/2} \left\langle \frac{3}{9} \tilde{V}(\mathbf{q}^{(2j)}) \right\rangle + \frac{1}{P} \sum_{j=1}^{P} \langle w_j V(\mathbf{q}^{(j)}) \rangle \quad (11)$$

where $\bar{\mathbf{q}} \equiv \frac{1}{P} \sum_{j=1}^{P} \mathbf{q}^{(j)}$ is the position of the centroid, $\mathbf{f}^{\mathrm{sc}(j)} \equiv -\partial V^{\mathrm{sc}}(\mathbf{q}^{(j)})/\partial \mathbf{q}^{(j)}$ is the total Suzuki-Chin force, and $\langle \cdot \rangle$ denotes a thermodynamic average over the quantum isothermal−isobaric ensemble. The generalization to a many particle system is straightforward. The □ = OP or □ = TD estimators of the enthalpy are obtained through the simple expression:

$$\mathcal{H}^{\square} = \mathcal{E}^{\square} + \mathcal{P}\langle \mathcal{V} \rangle \quad (12)$$

The □ = OP or □ = TD (that we will refer to as the Yamamoto estimator[47]) double virial estimators of the heat capacity take the following form

$$\frac{C_P^{\square}}{k_B \beta^2} = \mathrm{Cov}[\mathcal{H}^{\square}, \mathcal{H}^{\mathrm{TD}}] + \mathcal{E}^{\square\prime} \quad (13)$$

where $\mathcal{E}^{\square\prime}$ for □ = TD is given in ref 47 and

$$\mathcal{E}^{\mathrm{OP}\prime} = \frac{3N}{2\beta^2} + \frac{1}{\beta P} \sum_{j=1}^{P/2} \langle (\mathbf{q}^{(2j-1)} - \bar{\mathbf{q}}) \cdot \mathbf{f}_{\mathrm{dcv}}^{(2j-1)} \rangle \quad (14)$$

The double virial force $\mathbf{f}_{\mathrm{dcv}}^{(2j-1)}$, which depends on the Hessian of the physical potential, can be estimated in a computationally efficient way by finite differences:

$$\mathbf{f}_{\mathrm{dcv}}^{(j)} = \frac{3}{2} \mathbf{f}^{(j)} + \lim_{\epsilon \to 0} \frac{1}{2\epsilon} [\mathbf{f}^{(j)}|_{\mathbf{q}^{(j)} + \epsilon(\mathbf{q}^{(j)} - \bar{\mathbf{q}})} - \mathbf{f}^{(j)}] \quad (15)$$

We tested this estimator on the well-known isobaric heat capacity of liquid water which is 1 cal mol^{-1} K^{-1} or 9 k_B per molecule at 300 K. The water molecules are modeled with the q-TIP4P/f force field,[89] and the heat capacity is estimated with SC PIMD using the aforementioned estimators. As shown in Figure 10, both estimators converge to the same value and are in excellent agreement with the experiments. More importantly, however, the variance of the computationally expensive $\mathcal{E}^{\square\prime}$ term with the OP method is almost two orders of magnitude smaller than with the Yamamoto estimator. The OP estimator also only requires one-fourth of the number of force evaluations than its Yamamoto counterpart and should therefore always be preferred.

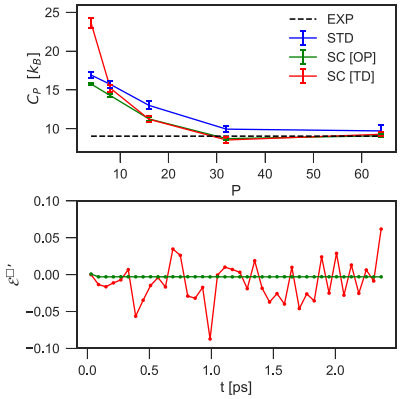

Figure 10. Top panel shows the convergence of the isobaric heat capacity of liquid water at 300 K, modeled by the q-TIP4P/f potential, as a function of the number of replicas. The blue curve was obtained from standard PIMD using the Yamamoto estimator, while the red and green curves were obtained from SC PIMD using the Yamamoto (TD) and OP estimator, respectively. The dashed black line represents the experimental result. Error bars indicate statistical uncertainty. The bottom panel shows instantaneous values of the computationally expensive $\mathcal{E}^{\square\prime}$ term when computed with the OP and the Yamamoto (TD) estimator.

ASSOCIATED CONTENT

Supporting Information

The Supporting Information is available free of charge on the ACS Publications website at DOI: 10.1021/acs.jctc.8b01297.

Derivation of Suzuki-Chin partition functions, forces, virials, and total stress; equations of motion and integration schemes for sampling isothermal−isobaric ensemble; derivation of heat capacity estimators; details of generation and validation of first-principles force field; temperature dependence of adsorption isotherms for methane; formula of the harmonic heat capacity; comparison of different barostats; decomposition of total heat capacity into contributions from different physical interactions; temperature dependence of volumetric heat capacity and comparison of host−guest interactions for a different force field (PDF)

AUTHOR INFORMATION

Corresponding Author

*E-mail: venkat.kapil@epfl.ch.

ORCID

Venkat Kapil: 0000-0003-0324-2198
Jelle Wieme: 0000-0002-4841-2608
Veronique Van Speybroeck: 0000-0003-2206-178X
Michele Ceriotti: 0000-0003-2571-2832

DOI: 10.1021/acs.jctc.8b01297
J. Chem. Theory Comput. 2019, 15, 3237−3249

Journal of Chemical Theory and Computation Article

Author Contributions

[¶]V.K. and J.W. contributed equally to this work.

Funding

We acknowledge financial support by the Swiss National Science Foundation (project ID 200021-159896), the Fund for Scientific Research Flanders (FWO), the Research Board of Ghent University, and the European Union's Horizon 2020 research and innovation programme (consolidator ERC grant agreement No. 647755-DYNPOR (2015-2020)). The computational resources and services used in this work were provided by VSC (Flemish Supercomputer Center), funded by Ghent University, FWO, and the Flemish Government department EWI.

Notes

The authors declare no competing financial interest.

■ ACKNOWLEDGMENTS

We also want to acknowledge F. Giberti, R. Semino, S. M. J. Rogge, and L. Vanduyfhuys for their valuable input and discussions.

■ REFERENCES

(1) Slater, A. G.; Cooper, A. I. Function-led design of new porous materials. *Science* **2015**, *348*, aaa8075.

(2) Furukawa, H.; Cordova, K. E.; O'Keeffe, M.; Yaghi, O. M. The chemistry and applications of metal-organic frameworks. *Science* **2013**, *341*, 1230444.

(3) Mason, J. A.; Veenstra, M.; Long, J. R. Evaluating metal-organic frameworks for natural gas storage. *Chem. Sci.* **2014**, *5*, 32−51.

(4) He, Y.; Chen, F.; Li, B.; Qian, G.; Zhou, W.; Chen, B. Porous metal-organic frameworks for fuel storage. *Coord. Chem. Rev.* **2018**, *373*, 167−198.

(5) de Lange, M. F.; Verouden, K. J. F. M.; Vlugt, T. J. H.; Gascon, J.; Kapteijn, F. Adsorption-Driven Heat Pumps: The Potential of Metal-Organic Frameworks. *Chem. Rev.* **2015**, *115*, 12205−12250.

(6) Wang, S.; Lee, J. S.; Wahiduzzaman, M.; Park, J.; Muschi, M.; Martineau-Corcos, C.; Tissot, A.; Cho, K. H.; Marrot, J.; Shepard, W.; Maurin, G.; Chang, J.-S.; Serre, C. A robust large-pore zirconium carboxylate metal-organic framework for energy-efficient water-sorption-driven refrigeration. *Nat. Energy* **2018**, *3*, 985−993.

(7) Sumida, K.; Rogow, D. L.; Mason, J. A.; McDonald, T. M.; Bloch, E. D.; Herm, Z. R.; Bae, T.-H.; Long, J. R. Carbon Dioxide Capture in Metal-Organic Frameworks. *Chem. Rev.* **2012**, *112*, 724−781.

(8) Trickett, C. A.; Helal, A.; Al-Maythalony, B. A.; Yamani, Z. H.; Cordova, K. E.; Yaghi, O. M. The chemistry of metal-organic frameworks for CO_2 capture, regeneration and conversion. *Nat. Rev. Mater.* **2017**, *2*, 17045.

(9) Simon, C. M.; Kim, J.; Gomez-Gualdron, D. A.; Camp, J. S.; Chung, Y. G.; Martin, R. L.; Mercado, R.; Deem, M. W.; Gunter, D.; Haranczyk, M.; Sholl, D. S.; Snurr, R. Q.; Smit, B. The materials genome in action: identifying the performance limits for methane storage. *Energy Environ. Sci.* **2015**, *8*, 1190−1199.

(10) Mason, J. A.; Oktawiec, J.; Taylor, M. K.; Hudson, M. R.; Rodriguez, J.; Bachman, J. E.; Gonzalez, M. I.; Cervellino, A.; Guagliardi, A.; Brown, C. M.; Llewellyn, P. L.; Masciocchi, N.; Long, J. R. Methane storage in flexible metal-organic frameworks with intrinsic thermal management. *Nature* **2015**, *527*, 357−361.

(11) Huck, J. M.; Lin, L.-C.; Berger, A. H.; Shahrak, M. N.; Martin, R. L.; Bhown, A. S.; Haranczyk, M.; Reuter, K.; Smit, B. Evaluating different classes of porous materials for carbon capture. *Energy Environ. Sci.* **2014**, *7*, 4132−4146.

(12) Mu, B.; Walton, K. S. Thermal Analysis and Heat Capacity Study of Metal-Organic Frameworks. *J. Phys. Chem. C* **2011**, *115*, 22748−22754.

(13) Kloutse, F. A.; Zacharia, R.; Cossement, D.; Chahine, R. Specific heat capacities of MOF-5, Cu-BTC, Fe-BTC, MOF-177 and MIL-53(Al) over wide temperature ranges: Measurements and application of empirical group contribution method. *Microporous Mesoporous Mater.* **2015**, *217*, 1−5.

(14) Babaei, H.; Wilmer, C. E. Mechanisms of Heat Transfer in Porous Crystals Containing Adsorbed Gases: Applications to Metal-Organic Frameworks. *Phys. Rev. Lett.* **2016**, *116*, 025902.

(15) Balestra, S. R. G.; Bueno-Perez, R.; Hamad, S.; Dubbeldam, D.; Ruiz-Salvador, A. R.; Calero, S. Controlling Thermal Expansion: A Metal-Organic Frameworks Route. *Chem. Mater.* **2016**, *28*, 8296−8304.

(16) Rogge, S. M. J.; Vanduyfhuys, L.; Ghysels, A.; Waroquier, M.; Verstraelen, T.; Maurin, G.; Van Speybroeck, V. A Comparison of Barostats for the Mechanical Characterization of Metal-Organic Frameworks. *J. Chem. Theory Comput.* **2015**, *11*, 5583−5597.

(17) Vanduyfhuys, L.; Rogge, S. M. J.; Wieme, J.; Vandenbrande, S.; Maurin, G.; Waroquier, M.; Van Speybroeck, V. Thermodynamic insight into stimuli-responsive behaviour of soft porous crystals. *Nat. Commun.* **2018**, *9*, 204.

(18) Wieme, J.; Lejaeghere, K.; Kresse, G.; Van Speybroeck, V. Tuning the balance between dispersion and entropy to design temperature-responsive flexible metal-organic frameworks. *Nat. Commun.* **2018**, *9*, 4899.

(19) Paesani, F. Water in metal-organic frameworks: structure and diffusion of H_2O in MIL-53(Cr) from quantum simulations. *Mol. Simul.* **2012**, *38*, 631−641.

(20) Borges, D. D.; Semino, R.; Devautour-Vinot, S.; Jobic, H.; Paesani, F.; Maurin, G. Computational Exploration of the Water Concentration Dependence of the Proton Transport in the Porous UiO-66(Zr)-$(CO_2H)_2$ Metal-Organic Framework. *Chem. Mater.* **2017**, *29*, 1569−1576.

(21) Lamaire, A.; Wieme, J.; Rogge, S. M. J.; Waroquier, M.; Van Speybroeck, V. On the importance of anharmonicities and nuclear quantum effects in modelling the structural properties and thermal expansion in MOF-5. *J. Chem. Phys.* **2019**, *150*, 094503.

(22) Parrinello, M.; Rahman, A. Study of an F center in molten KCl. *J. Chem. Phys.* **1984**, *80*, 860.

(23) Chandler, D.; Wolynes, P. G. Exploiting the isomorphism between quantum theory and classical statistical mechanics of polyatomic fluids. *J. Chem. Phys.* **1981**, *74*, 4078−4095.

(24) Jang, S.; Jang, S.; Voth, G. A. Applications of higher order composite factorization schemes in imaginary time path integral simulations. *J. Chem. Phys.* **2001**, *115*, 7832−7842.

(25) Ceriotti, M.; Manolopoulos, D. E. Efficient First-Principles Calculation of the Quantum Kinetic Energy and Momentum Distribution of Nuclei. *Phys. Rev. Lett.* **2012**, *109*, 100604.

(26) Kapil, V.; Behler, J.; Ceriotti, M. High order path integrals made easy. *J. Chem. Phys.* **2016**, *145*, 234103.

(27) Markland, T. E.; Manolopoulos, D. E. An efficient ring polymer contraction scheme for imaginary time path integral simulations. *J. Chem. Phys.* **2008**, *129*, 024105.

(28) Kapil, V.; VandeVondele, J.; Ceriotti, M. Accurate molecular dynamics and nuclear quantum effects at low cost by multiple steps in real and imaginary time: Using density functional theory to accelerate wavefunction methods. *J. Chem. Phys.* **2016**, *144*, 054111.

(29) Poltavsky, I.; Tkatchenko, A. Modeling quantum nuclei with perturbed path integral molecular dynamics. *Chem. Sci.* **2016**, *7*, 1368−1372.

(30) Markland, T. E.; Ceriotti, M. Nuclear quantum effects enter the mainstream. *Nat. Rev. Chem.* **2018**, *2*, 0109.

(31) Martyna, G. J.; Hughes, A.; Tuckerman, M. E. Molecular dynamics algorithms for path integrals at constant pressure. *J. Chem. Phys.* **1999**, *110*, 3275.

(32) Ceriotti, M.; More, J.; Manolopoulos, D. E. i-PI: A Python interface for ab initio path integral molecular dynamics simulations. *Comput. Phys. Commun.* **2014**, *185*, 1019−1026.

(33) Vanduyfhuys, L.; Vandenbrande, S.; Verstraelen, T.; Schmid, R.; Waroquier, M.; Van Speybroeck, V. QuickFF: A program for a

DOI: 10.1021/acs.jctc.8b01297
J. Chem. Theory Comput. 2019, 15, 3237−3249

quick and easy derivation of force fields for metal-organic frameworks from ab initio input. *J. Comput. Chem.* **2015**, *36*, 1015−1027.
(34) Vanduyfhuys, L.; Vandenbrande, S.; Wieme, J.; Waroquier, M.; Verstraelen, T.; Van Speybroeck, V. Extension of the QuickFF force field protocol for an improved accuracy of structural, vibrational, mechanical and thermal properties of metal-organic frameworks. *J. Comput. Chem.* **2018**, *39*, 999−1011.
(35) Li, H.; Eddaoudi, M.; O'Keeffe, M.; Yaghi, O. M. Design and synthesis of an exceptionally stable and highly porous metal-organic framework. *Nature* **1999**, *402*, 276−279.
(36) Eddaoudi, M.; Kim, J.; Rosi, N.; Vodak, D.; Wachter, J.; O'Keeffe, M.; Yaghi, O. M. Systematic design of pore size and functionality in isoreticular MOFs and their application in methane storage. *Science* **2002**, *295*, 469−472.
(37) Zhou, W.; Wu, H.; Hartman, M. R.; Yildirim, T. Hydrogen and methane adsorption in metal-organic frameworks: A high-pressure volumetric study. *J. Phys. Chem. C* **2007**, *111*, 16131−16137.
(38) Vandenbrande, S.; Verstraelen, T.; Gutiérrez-Sevillano, J. J.; Waroquier, M.; Van Speybroeck, V. Methane adsorption in Zr-based MOFs: Comparison and critical evaluation of force fields. *J. Phys. Chem. C* **2017**, *121*, 25309−25322.
(39) Martyna, G. J.; Tobias, D. J.; Klein, M. L. Constant pressure molecular dynamics algorithms. *J. Chem. Phys.* **1994**, *101*, 4177.
(40) Shiga, M.; Shinoda, W. Calculation of heat capacities of light and heavy water by path-integral molecular dynamics. *J. Chem. Phys.* **2005**, *123*, 134502.
(41) Takahashi, M.; Imada, M. Monte Carlo calculation of quantum systems. II. Higher order correction. *J. Phys. Soc. Jpn.* **1984**, *53*, 3765−3769.
(42) Chin, S. A. Symplectic integrators from composite operator factorizations. *Phys. Lett. A* **1997**, *226*, 344−348.
(43) The standard fourth-order Suzuki-Chin Splitting contains an *alpha* parameter which can be used to share the high order term between odd and even beads. In this case we have set it to zero so that the high order term is evaluated only on the even beads reducing the computational cost by a factor of 2.
(44) Suzuki, M. Hybrid exponential product formulas for unbounded operators with possible applications to Monte Carlo simulations. *Phys. Lett. A* **1995**, *201*, 425−428.
(45) Brain, G. *Higher Order Propagators in Path Integral Molecular Dynamics*. Ph.D. thesis, Part II Chemistry Thesis, Oxford University, 2011.
(46) Pérez, A.; Tuckerman, M. E. Improving the convergence of closed and open path integral molecular dynamics via higher order Trotter factorization schemes. *J. Chem. Phys.* **2011**, *135*, 064104.
(47) Yamamoto, T. M. Path-integral virial estimator based on the scaling of fluctuation coordinates: Application to quantum clusters with fourth-order propagators. *J. Chem. Phys.* **2005**, *123*, 104101.
(48) Ceriotti, M.; Brain, G. A. R.; Riordan, O.; Manolopoulos, D. E. The inefficiency of re-weighted sampling and the curse of system size in high order path integration. *Proc. R. Soc. London, Ser. A* **2012**, *468*, 2−17.
(49) Kapil, V.; Rossi, M.; Marsalek, O.; Petraglia, R.; Litman, Y.; Spura, T.; Cheng, B.; Cuzzocrea, A.; Meißner, R. H.; Wilkins, D. M.; Juda, P.; Bienvenue, S. P.; Fang, W.; Kessler, J.; Poltavsky, I.; Vandenbrande, S.; Wieme, J.; Corminboeuf, C.; Kühne, T. D.; Manolopoulos, D. E.; Markland, T. E.; Richardson, J. O.; Tkatchenko, A.; Tribello, G. A.; Speybroeck, V. V.; Ceriotti, M. i-PI 2.0: A universal force engine for advanced molecular simulations. *Comput. Phys. Commun.* **2019**, *236*, 214−223.
(50) Tuckerman, M.; Berne, B. J.; Martyna, G. J. Reversible multiple time scale molecular dynamics. *J. Chem. Phys.* **1992**, *97*, 1990.
(51) Leimkuhler, B.; Matthews, C. Robust and efficient configurational molecular sampling via Langevin dynamics. *J. Chem. Phys.* **2013**, *138*, 174102.
(52) Poltavsky, I.; DiStasio, R. A., Jr.; Tkatchenko, A. Perturbed path integrals in imaginary time: Efficiently modeling nuclear quantum effects in molecules and materials. *J. Chem. Phys.* **2018**, *148*, 102325.
(53) Frisch, M. J.; Trucks, G. W.; Schlegel, H. B.; Scuseria, G. E.; Robb, M. A.; Cheeseman, J. R.; Scalmani, G.; Barone, V.; Petersson, G. A.; Nakatsuji, H.; Li, X.; Caricato, M.; Marenich, A. V.; Bloino, J.; Janesko, B. G.; Gomperts, R.; Mennucci, B.; Hratchian, H. P.; Ortiz, J. V.; Izmaylov, A. F.; Sonnenberg, J. L.; Williams-Young, D.; Ding, F.; Lipparini, F.; Egidi, F.; Goings, J.; Peng, B.; Petrone, A.; Henderson, T.; Ranasinghe, D.; Zakrzewski, V. G.; Gao, J.; Rega, N.; Zheng, G.; Liang, W.; Hada, M.; Ehara, M.; Toyota, K.; Fukuda, R.; Hasegawa, J.; Ishida, M.; Nakajima, T.; Honda, Y.; Kitao, O.; Nakai, H.; Vreven, T.; Throssell, K.; Montgomery, J. A., Jr.; Peralta, J. E.; Ogliaro, F.; Bearpark, M. J.; Heyd, J. J.; Brothers, E. N.; Kudin, K. N.; Staroverov, V. N.; Keith, T. A.; Kobayashi, R.; Normand, J.; Raghavachari, K.; Rendell, A. P.; Burant, J. C.; Iyengar, S. S.; Tomasi, J.; Cossi, M.; Millam, J. M.; Klene, M.; Adamo, C.; Cammi, R.; Ochterski, J. W.; Martin, R. L.; Morokuma, K.; Farkas, O.; Foresman, J. B.; Fox, D. J. *Gaussian16*, Revision B.01; Gaussian Inc.: Wallingford, CT, 2016.
(54) Becke, A. D. Density-Functional Thermochemistry. III. The Role of Exact Exchange. *J. Chem. Phys.* **1993**, *98*, 5648−5652.
(55) Krishnan, R.; Binkley, J. S.; Seeger, R.; Pople, J. A. Self-Consistent Molecular Orbital Methods. 20. Basis Set for Correlated wave-Functions. *J. Chem. Phys.* **1980**, *72*, 650−654.
(56) Hay, P. J.; Wadt, W. R. Ab initio effective core potentials for molecular calculations. Potentials for the transition metal atoms Sc to Hg. *J. Chem. Phys.* **1985**, *82*, 270.
(57) Verstraelen, T.; Vandenbrande, S.; Heidar-Zadeh, F.; Vanduyfhuys, L.; Van Speybroeck, V.; Waroquier, M.; Ayers, P. W. Minimal Basis Iterative Stockholder: Atoms in molecules for force-field development. *J. Chem. Theory Comput.* **2016**, *12*, 3894−3912.
(58) Perdew, J. P.; Burke, K.; Ernzerhof, M. Generalized Gradient Approximation Made Simple. *Phys. Rev. Lett.* **1996**, *77*, 3865.
(59) Mortensen, J. J.; Hansen, L. B.; Jacobsen, K. W. Real-space grid implementation of the projector augmented wave method. *Phys. Rev. B: Condens. Matter Mater. Phys.* **2005**, *71*, 035109.
(60) Lii, J. H.; Allinger, N. L. Molecular mechanics. The MM3 force field for hydrocarbons. 3. The van der Waals Potentials and crystal data for aliphatic and aromatic hydrocarbons. *J. Am. Chem. Soc.* **1989**, *111*, 8576−8582.
(61) Allinger, N. L.; Zhou, X.; Bergsma, J. Molecular mechanics parameters. *J. Mol. Struct.: THEOCHEM* **1994**, *312*, 69−83.
(62) Sun, H. COMPASS: An ab initio force-field optimized for condensed-phase applications - Overview with details on alkane and benzene compounds. *J. Phys. Chem. B* **1998**, *102*, 7338−7364.
(63) Dubbeldam, D.; Calero, S.; Ellis, D. E.; Snurr, R. Q. RASPA: molecular simulation software for adsorption and diffusion in flexible nanoporous materials. *Mol. Simul.* **2016**, *42*, 81−101.
(64) Plimpton, S. Fast Parallel Algorithms for Short-Range Molecular Dynamics. *J. Comput. Phys.* **1995**, *117*, 1−19.
(65) Nosé, S. A molecular dynamics method for simulations in the canonical ensemble. *Mol. Phys.* **1984**, *52*, 255−268.
(66) Hoover, W. G. Canonical Dynamics: Equilibrium Phase-Space Distributions. *Phys. Rev. A: At., Mol., Opt. Phys.* **1985**, *31*, 1695−1697.
(67) Martyna, G. J.; Klein, M. L.; Tuckerman, M. Nose-Hoover Chains - the Canonical Ensemble Via Continuous Dynamics. *J. Chem. Phys.* **1992**, *97*, 2635−2643.
(68) Martyna, G. J.; Tuckerman, M. E.; Tobias, D. J.; Klein, M. L. Explicit reversible integrators for extended systems dynamics. *Mol. Phys.* **1996**, *87*, 1117−1157.
(69) Ceriotti, M.; Parrinello, M.; Markland, T. E.; Manolopoulos, D. E. Efficient stochastic thermostatting of path integral molecular dynamics. *J. Chem. Phys.* **2010**, *133*, 124104.
(70) Bussi, G.; Parrinello, M. Accurate sampling using Langevin dynamics. *Phys. Rev. E* **2007**, *75*, 56707.
(71) Bussi, G.; Zykova-Timan, T.; Parrinello, M. Isothermal-isobaric molecular dynamics using stochastic velocity rescaling. *J. Chem. Phys.* **2009**, *130*, 074101.
(72) Balog, E.; Hughes, A. L.; Martyna, G. J. Constant pressure path integral molecular dynamics studies of quantum effects in the liquid state properties of n-alkanes. *J. Chem. Phys.* **2000**, *112*, 870−880.

DOI: 10.1021/acs.jctc.8b01297
J. Chem. Theory Comput. 2019, 15, 3237−3249

(73) Pereyaslavets, L.; Kurnikov, I.; Kamath, G.; Butin, O.; Illarionov, A.; Leontyev, I.; Olevanov, M.; Levitt, M.; Kornberg, R. D.; Fain, B. On the importance of accounting for nuclear quantum effects in ab initio calibrated force fields in biological simulations. *Proc. Natl. Acad. Sci. U. S. A.* **2018**, *115*, 8878−8882.
(74) Veit, M.; Jain, S. K.; Bonakala, S.; Rudra, I.; Hohl, D.; Csányi, G. Equation of state of fluid methane from first principles with machine learning potentials. *J. Chem. Theory Comput.* **2019**, *15*, 2574−2586.
(75) Ravikovitch, P. I.; Neimark, A. V. Density Functional Theory Model of Adsorption Deformation. *Langmuir* **2006**, *22*, 10864−10868.
(76) Joo, J.; Kim, H.; Han, S. S. Volume shrinkage of a metal-organic framework host induced by the dispersive attraction of guest gas molecules. *Phys. Chem. Chem. Phys.* **2013**, *15*, 18822−18826.
(77) Zhou, W.; Wu, H.; Yildirim, T.; Simpson, J. R.; Hight Walker, A. R. Origin of the exceptional negative thermal expansion in metal-organic framework-5 $Zn_4O(1,4\text{-benzenedicarboxylate})_3$. *Phys. Rev. B: Condens. Matter Mater. Phys.* **2008**, *78*, 054114.
(78) Lock, N.; Wu, Y.; Christensen, M.; Cameron, L. J.; Peterson, V. K.; Bridgeman, A. J.; Kepert, C. J.; Iversen, B. B. Elucidating Negative Thermal Expansion in MOF-5. *J. Phys. Chem. C* **2010**, *114*, 16181−16186.
(79) Lock, N.; Christensen, M.; Wu, Y.; Peterson, V. K.; Thomsen, M. K.; Plitz, R. O.; Ramirez-Cuesta, A. J.; McIntyre, G. J.; Norén, K.; Kutteh, R.; Kepert, C. J.; Kearley, G. J.; Iversen, B. B. Scrutinizing negative thermal expansion in MOF-5 by scattering techniques and ab initio calculations. *Dalton Trans* **2013**, *42*, 1996−2007.
(80) A 10% increase in volume due to NQEs, assuming the molecules to be spherical, is associated with a $(1.10)^{1/3}$ times increase in the effective radius. The classical "radius" is close to 4 Å, and thus the increase in the intermolecular distance due to NQEs coming from the isotropic expansion of the gas is $(1.10)^{1/3}*4 - 4 \approx 0.13$ Å.
(81) Ming, Y.; Purewal, J.; Liu, D.; Sudik, A.; Xu, C.; Yang, J.; Veenstra, M.; Rhodes, K.; Soltis, R.; Warner, J.; Gaab, M.; Müller, U.; Siegel, D. J. Thermophysical properties of MOF-5 powders. *Microporous Mesoporous Mater.* **2014**, *185*, 235−244.
(82) Liu, D.; Purewal, J. J.; Yang, J.; Sudik, A.; Maurer, S.; Müller, U.; Ni, J.; Siegel, D. J. MOF-5 composites exhibiting improved thermal conductivity. *Int. J. Hydrogen Energy* **2012**, *37*, 6109−6117.
(83) Addicoat, M. A.; Vankova, N.; Akter, I. F.; Heine, T. Extension of the Universal Force Field to metal-organic frameworks. *J. Chem. Theory Comput.* **2014**, *10*, 880−891.
(84) Tabor, D. P.; Roch, L. M.; Saikin, S. K.; Kreisbeck, C.; Sheberla, D.; Montoya, J. H.; Dwaraknath, S.; Aykol, M.; Ortiz, C.; Tribukait, H.; Amador-Bedolla, C.; Brabec, C. J.; Maruyama, B.; Persson, K. A.; Aspuru-Guzik, A. Accelerating the discovery of materials for clean energy in the era of smart automation. *Nat. Rev. Mater.* **2018**, *3*, 5−20.
(85) Tsivion, E.; Head-Gordon, M. Methane storage: molecular mechanisms underlying room-temperature adsorption in $Zn_4O(BDC)_3$ (MOF-5). *J. Phys. Chem. C* **2017**, *121*, 12091−12100.
(86) Wu, H.; Zhou, W.; Yildirim, T. Methane sorption in nanoporous metal-organic frameworks and first-order phase transition of confined methane. *J. Phys. Chem. C* **2009**, *113*, 3029−3035.
(87) Kuchta, B.; Dundar, E.; Formalik, F.; Llewellyn, P. L.; Firlej, L. Adsorption-Induced Structural Phase Transformation in Nanopores. *Angew. Chem., Int. Ed.* **2017**, *56*, 16243−16246.
(88) Levitt, M.; Hirshberg, M.; Sharon, R.; Laidig, K. E.; Daggett, V. Calibration and Testing of a Water Model for Simulation of the Molecular Dynamics of Proteins and Nucleic Acids in Solution. *J. Phys. Chem. B* **1997**, *101*, 5051−5061.
(89) Habershon, S.; Markland, T. E.; Manolopoulos, D. E. Competing quantum effects in the dynamics of a flexible water model. *J. Chem. Phys.* **2009**, *131*, 024501.

DOI: 10.1021/acs.jctc.8b01297
J. Chem. Theory Comput. 2019, 15, 3237−3249

Paper III

Atomistic insight in the flexibility and heat transport properties of the stimuli-responsive metal-organic framework MIL-53(Al) for water-adsorption applications using molecular simulations

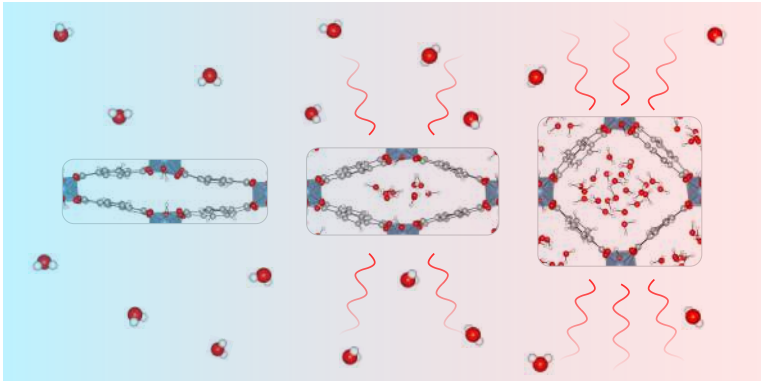

A. Lamaire‡, J. Wieme‡, A.E.J. Hoffman, V. Van Speybroeck

Faraday Discussions, **2021**, 225, 301–323

A. Lamaire and J. Wieme performed the research and wrote the manuscript with contributions from all authors. The free energy calculations were performed by A. Lamaire, whereas the thermal conductivity simulations were performed by J. Wieme.

Faraday Discussions
Cite this: *Faraday Discuss.*, 2021, **225**, 301

PAPER

Atomistic insight in the flexibility and heat transport properties of the stimuli-responsive metal–organic framework MIL-53(Al) for water-adsorption applications using molecular simulations†

Aran Lamaire, ‡ Jelle Wieme, ‡ Alexander E. J. Hoffman and Veronique Van Speybroeck *

Received 23rd February 2020, Accepted 12th March 2020
DOI: 10.1039/d0fd00025f

To exploit the full potential of metal–organic frameworks as solid adsorbents in water-adsorption applications, many challenges remain to be solved. A more fundamental insight into the properties of the host material and the influence that water exerts on them can be obtained by performing molecular simulations. In this work, the prototypical flexible MIL-53(Al) framework is modelled using advanced molecular dynamics simulations. For different water loadings, the presence of water is shown to affect the relative stability of MIL-53(Al), triggering a phase transition from the narrow-pore to the large-pore phase at the highest considered loading. Furthermore, the effect of confinement on the structural organisation of the water molecules is also examined for different pore volumes of MIL-53(Al). For the framework itself, we focus on the thermal conductivity, as this property plays a decisive role in the efficiency of adsorption-based technologies, due to the energy-intensive adsorption and desorption cycles. To this end, the heat transfer characteristics of both phases of MIL-53(Al) are studied, demonstrating a strong directional dependence for the thermal conductivity.

1 Introduction

For more than two decades, metal–organic frameworks (MOFs) have been investigated for their exceptional adsorption properties. Today, these porous, hybrid inorganic–organic crystalline frameworks still hold a lot of potential for a wide range of adsorption technologies in fields related to sustainable energy storage and the reduction of the greenhouse effect.[1–4] Water-adsorption

Center for Molecular Modeling, Ghent University, Tech Lane Ghent Science Park Campus A, Technologiepark 46, 9052 Zwijnaarde, Belgium. E-mail: Veronique.VanSpeybroeck@UGent.be

† Electronic supplementary information (ESI) available: Additional information on the force field and extra figures regarding the molecular dynamics simulations. See DOI: 10.1039/d0fd00025f

‡ Both authors contributed equally to this work.

applications are one of the many promising possibilities for the use of MOFs as advanced solid adsorbents.[5–9] Water-stable MOFs could, for instance, find use in adsorption-driven heat pumps or chillers,[10–15] and in atmospheric water harvesting.[16–19]

However, just as for all applications involving repeated adsorption processes, the heat management in water-adsorption applications poses an important engineering challenge. Insight into the thermal transport characteristics of MOFs is therefore essential, as their efficiency as adsorbents is strongly reduced when the temperature of the system increases, thus requiring proper control over the heat released by adsorption. This not only holds for storage tanks, in which the slow dissipation of heat could hinder the tank-filling cycles, but also for heat pumps, in which heat should be transferred rapidly to the surroundings. External heat exchangers or more conductive MOF composites could be developed to meet these requirements, but this comes at a cost.[20–23] As the thermal conductivity of MOFs is very complicated to measure accurately,[24–28] relatively few experimental studies have discussed the importance of the intrinsic heat dissipation in MOFs, so that mainly computational investigations have provided explanations for their low thermal conductivities.[29–36] Nevertheless, for most MOFs, reference data is still lacking in the literature.[28,36] In this work, the thermal conductivity of MIL-53(Al) was simulated,[37] a bistable material that possesses a narrow-pore (np) and a large-pore (lp) phase (Fig. 1) and is known for its anisotropic mechanical and thermal properties.[38,39] For practical applications, quantification of the anisotropy in the heat transfer is required as it can affect the design and operation of certain devices.[40] In this proof-of-principle study for the flexible MIL-53(Al) framework, we show that the intrinsic thermal conductivity of the framework differs between its (meta)stable states, which might be exploited in nanoscale applications that require precise control over the thermal conductivity *via* external stimuli, such as temperature and pressure.[41–43]

These stimuli, alongside guest adsorption, can trigger the intrinsic flexibility of MIL-53(Al), resulting in a reversible structural transformation[44–47] that can contribute to the internal heat management during the adsorption process, as the heat of adsorption is partially used to overcome the energetic barrier between the different phases.[48,49] In other words, by carefully selecting a MOF exhibiting a reversible phase transition in the desired adsorption range, it becomes possible

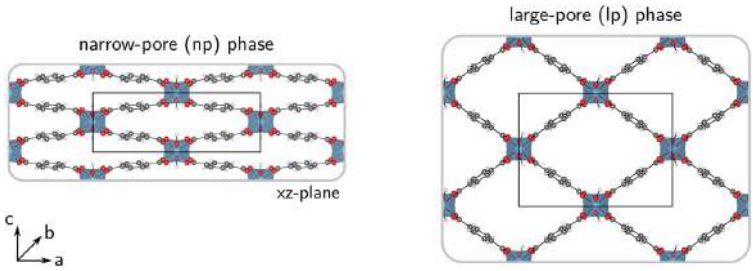

Fig. 1 Molecular representations of the narrow-pore (np) and the large-pore (lp) phases of MIL-53(Al). The *a*-, *b*- and *c*-directions are indicated together with the conventional unit cells in the *ac*-plane.

to lower the overall amount of heat released in the adsorption process in comparison to a material without a phase transition.

However, designing a MOF with a reversible phase transition in the relevant adsorption window is a nontrivial task. Experimentally, this is accompanied by a high degree of trial and error, as the underlying thermodynamic potential cannot be directly accessed.[46] Despite the abundance of adsorption studies in MOFs, only a limited number of theoretical studies have investigated the critical effect that guest molecules can have on the phase stability.[46,50,51] Some of the present authors recently demonstrated that standard computational considerations typically do not suffice for these complex materials, as long-range dispersion interactions and correlated atomic motion might play an important qualitative and quantitative role in the description of these stimuli-responsive MOFs.[52,53] In this work, the validity of another typical approximation – *i.e.* the neglect of nuclear quantum effects in the simulations[54] – is tested for the modelling of guest-induced phase transitions.

We chose the rather extreme case of water in MIL-53(Al), where large nuclear quantum effects could be expected.[55] This particular framework is known to be moderately stable with respect to water[56,57] and the presence of water in MIL-53 materials has already been computationally explored in the past.[51,58–61] Furthermore, MIL-53(Al) variants with different organic linkers (*e.g.* MOF-303 and A520) have been investigated specifically for water-adsorption applications.[11,19] In this contribution, the phase stability of MIL-53(Al) in the presence of water is discussed, alongside the possible influence of neglecting nuclear quantum effects. Finally, we also try to obtain molecular-level insight into the water structure inside the pores, which is currently an active field of research for water-stable MOFs.[58,60,62–65]

Using advanced molecular simulation tools on the prototypical flexible material MIL-53(Al), this work thus considers two important fundamental issues strongly related to water-adsorption applications of MOFs: (1) the phase stability and the water structure inside the pores of a stimuli-responsive MOF and (2) the anisotropic thermal conductivity properties of the adsorbent.

2 Methodology

2.1 Force field

To model the potential energy surface of MIL-53(Al), a force field is used, as the computational cost of first-principles methods is currently too high to extract the properties under investigation. This force field was generated with our in-house developed QuickFF protocol for deriving force fields from first-principles input.[66,67] In this way, we approximate the quantum mechanical potential energy surface in the neighbourhood of the equilibrium structure – which is defined by the optimized geometry and the Hessian at the PBE+D3(BJ) level of theory[68–70] – using a combination of analytical covalent, electrostatic, and van der Waals force field terms. The covalent interactions are written in terms of bonds, bends, out-of-plane distances, and dihedral angles, and contain both anharmonic terms and cross terms. Minimal Basis Iterative Stockholder (MBIS) charges are used to describe the electrostatic potential between Gaussian charge distributions centered on the nuclei.[71] The van der Waals interactions were modelled by the MM3-Buckingham model[72] up to a finite cutoff of 12 Å and were supplemented with tail corrections.[73] This particular force field was specifically constructed to

accurately model structural, vibrational, mechanical, and thermal properties, and corresponds with the MCAM force field discussed in ref. 67. More details regarding the force field energy expression can be found in the ESI (Section S1†).

For the simulations of MIL-53(Al) including water, the q-TIP4P/F[74] force field was used to describe the water molecules. This force field was derived by Habershon *et al.* from the well-known TIP4P/2005 model[75] and extended to include both flexibility and anharmonicity. The O–H stretch is described by a quartic potential, whereas the H–O–H bond angle is described by a harmonic potential (see ESI Section S1†). Similar to the rigid TIP4P/2005 model, the non-covalent interactions are modelled using four interaction sites, assigning an additional interaction site M to every water molecule, which is located at the bisector of the H–O–H angle. For the van der Waals interactions, described by a Lennard-Jones potential, only the oxygen atoms yield a non-zero contribution. The interactions between the water molecules and the framework can also be modelled by a Lennard-Jones potential, using the Lorentz–Berthelot mixing rules for the rescaled MM3 parameters of the framework: $\sigma_{LJ} = 2^{5/6}\sigma_{MM3}$, which ensures that the minima of both potentials occur at the same internuclear distance.

Complementary to the van der Waals interactions, only the H atoms and M sites of the water molecules yield contributions to the electrostatic interactions, as the oxygen atoms do not bear a charge. By placing the negative charge on the M site rather than on the oxygen atom, a better mean-field description of the polarization of the water molecules can be obtained. Although a more rigorous inclusion of electronic polarization might enhance the description of the interactions between the framework and the guest molecules, especially when making the framework polarizable as shown by Cirera *et al.*,[59] it is by no means trivial to make the extension to fully polarizable force fields. Therefore, explicit electronic polarization is commonly not taken into account when studying water in confinement.[62,63] In spite of these limitations of a mean-field description of the polarization, this water model does allow us to describe hydrogen bonding effects, as discussed in the ESI (Section S1†).

Finally, the q-TIP4P/F force field was also tailored for use in quantum simulations, making use of path integral molecular dynamics (PIMD)[54] instead of classical molecular dynamics (MD), thereby exchanging the classical treatment of the atomic nuclei with a quantum mechanical one. Given the importance of an accurate description of the low mass protons, as they play a pivotal role in the behaviour of water, a proper inclusion of nuclear quantum effects (NQEs), such as the zero-point energy of the nuclei, is required.

2.2 Construction of the Helmholtz free energy profiles

The flexibility of MIL-53(Al) is investigated using the thermodynamic protocol discussed in ref. 46, starting from MD simulations in the (N, V, $\boldsymbol{\sigma}_a = \mathbf{0}$, T) ensemble for a set of volumes. From these simulations, which were carried out at temperatures of 100 K and 300 K, the pressure profile $P(V)$ is extracted (Fig. S2†), from which the Helmholtz free energy profile $F(V)$ can be obtained as a function of the volume V for each temperature *via* thermodynamic integration.

The classical MD simulations are performed with Yaff,[76] using a Verlet time step of 0.5 fs. The temperature is controlled by a Nosé–Hoover chain thermostat[77–79] containing three beads with a relaxation time of 0.1 ps, while the pressure

is controlled by a Martyna–Tuckerman–Tobias–Klein barostat[80,81] using a relaxation time of 1 ps.

To examine the influence of nuclear quantum effects (NQEs), PIMD simulations[54] are performed on the same volume grid and for the same temperatures. Applying PIMD on large structures such as MOFs is challenging due to the large computational cost that is associated with it, but it is necessary for a correct quantitative description of different properties, such as the thermal expansion and the heat capacity.[82,83] The PIMD simulations were performed with i-PI,[84,85] which delegates the evaluation of the forces to external codes. In this case, the covalent interactions are computed by Yaff[76] and the long-range interactions are evaluated using LAMMPS for ring-polymers containing 32 beads.[86] To control the temperature, a PILE-L thermostat[87] is applied to the system and a white noise Langevin thermostat[88] is applied to the cell. To control the pressure, a modified path-integral version of the Raiteri–Gale–Bussi barostat[84,89] is used to sample the $(N, V, \boldsymbol{\sigma}_a = \mathbf{0}, T)$ ensemble. The time constants of the thermostats and the barostats are respectively 0.1 and 0.25 ps. A BAOAB type[90] scheme is used to integrate the equations of motion.

Both classical and path integral MD simulations were performed with and without water in the pores, considering three different loadings, *i.e.* 2.5, 7.5, and 22.5 water molecules per conventional unit cell. All the simulations related to the calculation of Helmholtz free energy profiles were performed on a $1 \times 2 \times 1$ supercell, containing 152 framework atoms including 8 aluminium atoms.

2.3 Thermal conductivity

The Green–Kubo approach[91,92] was used in combination with classical MD simulations to determine the thermal conductivity. This formalism is based on the fluctuation–dissipation theorem and states that the thermal conductivity κ can be computed by integrating the heat current autocorrelation function (HCACF) over time:

$$\kappa_{ii} = \frac{1}{k_B V T^2} \int_0^{+\infty} \mathrm{d}t \, \langle J_i(t) J_i(0) \rangle. \quad (1)$$

An advantage of this method is that the heat current J_i ($i = x, y,$ or z) – and thus κ_{ii} – can be simultaneously extracted in all directions from one set of simulations.

This method has been used previously by some of the present authors to compute the thermal conductivity of various well-known MOFs, such as UiO-66, HKUST-1, and MOF-5, at their equilibrium volume.[36] In this work, we computed the thermal conductivity of MIL-53(Al) for different unit cell volumes ranging from 750 Å^3 to 1500 Å^3 in steps of 50 Å^3. To this end, a series of one hundred independent simulations per volume point were conducted. First, a hundred starting structures were extracted from MD snapshots taken every 5 ps from an equilibrated classical MD simulation in the $(N, V, \boldsymbol{\sigma}_a = \mathbf{0}, T)$ ensemble at 300 K using a $1 \times 2 \times 1$ supercell (*i.e.* a conventional cell elongated along the Al(OH) chain) in Yaff.[76] These structures were subsequently converted to $7 \times 8 \times 7$ supercells containing 29 792 atoms, as this is necessary to limit finite size effects.[93] Finally, classical MD simulations are performed with LAMMPS[86] to equilibrate the supercells at 300 K for 375 ps in the $(N, V, \boldsymbol{h}_0, T)$ ensemble and for 125 ps in the (N, V, E) ensemble. The HCACF is thereafter collected

during one hundred 6 ns runs in the microcanonical ensemble. The heat flux is computed every 4 fs and the HCACF is averaged in blocks of 200 ps, of which an example is shown in Fig. S6.† All classical MD simulations were performed using a 0.5 fs timestep, except for the ones in the (N, V, E) ensemble which used a 1 fs timestep. The system's temperature was also verified to be 300 K at the end of the *NVE* simulations.

Afterwards, the thermal conductivity was computed by integrating the HCACF over time (Fig. S6†). As the resulting thermal conductivity can be substantially influenced by slow oscillations in the HCACF, it is necessary to integrate over a sufficiently long time interval.[93] These slow oscillations in the tail of the auto-correlation function mix with numerical noise, which contaminates the HCACF and cumulates a considerable integration error for the thermal conductivity.[94,95] For some simulations, this resulted in a slight deviation from zero for the HCACF's tail, which we removed after fitting.[94] Methods that take care of this in a systematic way are to the best of our knowledge not directly applicable to complex systems like MOFs due to a non-monotonic HCACF.[96] Finally, we determined the thermal conductivity by taking the running average of the last 25 ps, similar to previous work.[29,36,96]

An error bar was estimated using bootstrapping. This is done by resampling the thermal conductivity results of the hundred independent trajectories. We find errors between 0.02 and 0.1 W m^{-1} K^{-1}. Note that this error bar only captures sampling effects and does not take into account limitations of the force field and the simulation method.

2.4 Vibrational analysis

To understand the influence of NQEs on the Helmholtz free energy profile of MIL-53(Al), the vibrational frequency spectrum of MIL-53(Al) is also investigated.[97,98] The normal modes and the corresponding frequencies of the np and lp phases are determined *via* diagonalization of the mass-weighted Hessian, obtained from *ab initio* calculations. For more details about the computational settings, we refer to previous work.[98]

These lattice vibrations are furthermore also known to have an impact on the thermal properties of a material. For the specific case of MOFs, it was shown that vibrational modes can be linked with the direction of the heat transfer within the system.[30] The effect of the lattice vibrations on the thermal conductivity can be assessed by constructing the so-called vibrational density of states (VDOS):[30]

$$\mathrm{VDOS}(\sigma) = \int \mathrm{d}t\ \gamma(t)\ \exp\ (-2\pi i\sigma t), \tag{2}$$

which corresponds with the Fourier transform of the velocity autocorrelation function, $\gamma(t)$, defined as

$$\gamma(t) = \frac{\left\langle \sum_i \boldsymbol{v}_i(0)\cdot\boldsymbol{v}_i(t) \right\rangle}{\left\langle \sum_i \boldsymbol{v}_i(0)\cdot\boldsymbol{v}_i(0) \right\rangle}. \tag{3}$$

The VDOS spectra of the different atom types in MIL-53(Al) can be calculated from the classical MD simulations on the $1 \times 2 \times 1$ supercells. The integration in the VDOS expression is then reduced to a sum, resulting in a discrete Fourier transform that is evaluated using Yaff.[76]

3 Results and discussion

3.1 Flexibility of MIL-53(Al)

As the relative stability of the narrow-pore (np) and large-pore (lp) phases of MIL-53(Al) has already been demonstrated to depend critically on the description of long-range dispersion interactions[52,99] and is altered by the presence of additional metastable phases of coexisting lp and np layers at a mesoscale level,[53,100] we now revert our attention to the influence of NQEs on the phase stability. Given the intention to examine the presence of water molecules in the MIL-53 framework, the archetypal molecules investigated within the context of NQEs, we first assess the effect of including NQEs for the empty framework. Following the thermodynamic protocol outlined in Section 2.2, Helmholtz free energy profiles of MIL-53(Al) are constructed at 100 and 300 K, using both classical MD and PIMD, for which the results are depicted in Fig. 2a. At 300 K, classical MD predicts an lp–np Helmholtz free energy difference of 38.3 kJ mol^{-1}, whereas PIMD yields a difference of 35.2 kJ mol^{-1}. At 100 K, the Helmholtz free energy differences obtained from classical MD and PIMD are respectively 47.3 kJ mol^{-1} and 43.6 kJ mol^{-1}. These moderate differences of about 3 to 4 kJ mol^{-1} in the relative lp–np stability can be explained by considering the vibrational frequencies characterizing the np and lp phases (Fig. 3), obtained from an *ab initio* normal mode analysis of the

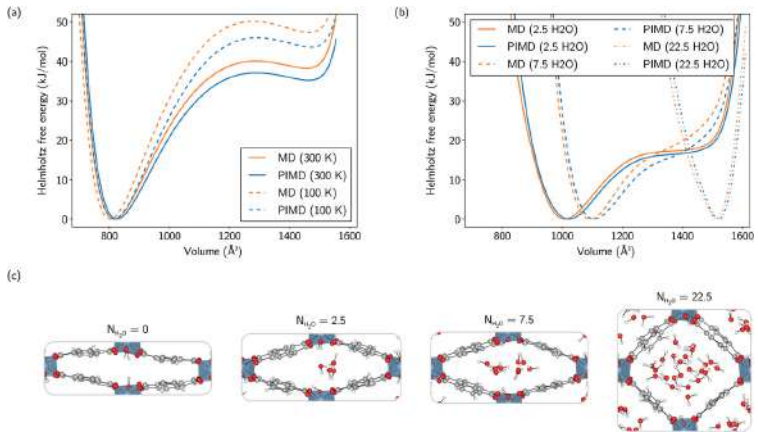

Fig. 2 (a) Helmholtz free energy profiles of MIL-53(Al) as a function of volume at 100 K and 300 K, as calculated using both MD and PIMD simulations. (b) Helmholtz free energy profiles of MIL-53(Al) as a function of volume at 300 K for water loadings of 2.5, 7.5, and 22.5 water molecules per conventional unit cell, as calculated using both MD and PIMD simulations. (c) Molecular representations of an MD snapshot at the equilibrium volume with 0, 2.5, 7.5, and 22.5 water molecules in the pores. All simulations were performed with a $1 \times 2 \times 1$ supercell.

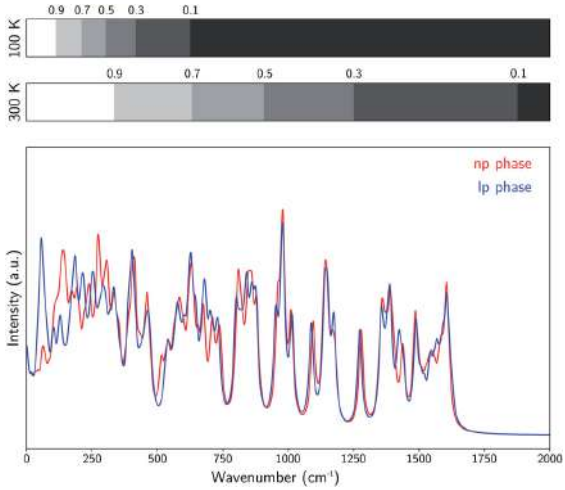

Fig. 3 Visualization of the *ab initio* vibrational frequencies of the np and lp phases of MIL-53(Al). At each vibrational frequency, a Lorentzian curve was generated with a full-width-at-half-maximum of 10 cm^{-1}. The bars on top indicate the wavenumber regions for which the ratio of the quantum mechanical and classical partition functions is larger than respectively 0.9, 0.7, 0.5, 0.3, and 0.1, both at 100 K and 300 K.

structures.[98] From these vibrational frequencies, the classical and quantum mechanical partition functions can be calculated using a harmonic approximation. The ratio of both partition functions for a specific set of modes is then to be viewed as a measure of the degree of quantumness of these modes:

$$\frac{Z_{\text{quantum}}}{Z_{\text{classical}}} = \prod_{i=1}^{N} \frac{\exp\left(-\frac{\hbar\omega_i}{2k_B T}\right)}{1-\exp\left(-\frac{\hbar\omega_i}{k_B T}\right)} \prod_{i=1}^{N} \frac{\hbar\omega_i}{k_B T}, \tag{4}$$

where ω_i is the angular frequency of the mode, T is the temperature, and k_B is the Boltzmann constant. As shown in Fig. 3, a quantum mechanical description of the modes is particularly important within a higher frequency range. The lower the temperature, the lower the frequency at which modes start to yield a significant quantum mechanical contribution to the partition function. Since the modes associated with the lp-to-np transition are predominantly located within the low frequency region (*i.e.* below 100 cm^{-1}),[98] the difference in the relative lp–np stability due to the quantum mechanical nature of the atomic nuclei is expected to be relatively moderate, as observed in Fig. 2a. However, the fact that there is a small difference in the relative lp–np stability clearly indicates that the np and lp phases are affected differently by NQEs.

3.2 Water in the pores of MIL-53(Al)

Although a substantial number of MOFs possess poor stability with respect to hydration, the MIL-53 family of soft porous crystals is known to have stable

hydrated phases, which have been investigated both experimentally and computationally, focusing mainly on the chromium- and gallium-based variants.[51,58–61,101–108]

Here, the influence of the presence of water on the Helmholtz free energy profile of MIL-53(Al) is investigated, closely monitoring the changes in behaviour of the adsorbed species along the profile. Three different water loadings are considered: 2.5, 7.5, and 22.5 water molecules per conventional unit cell, varying from a ratio of less than one molecule per aluminium atom to almost six molecules per aluminium atom. For the lowest loading, the metastable lp phase disappears, while the Helmholtz free energy profile retains a shape similar to the profile of the empty framework, but shifted to an equilibrium volume that is about 200 $Å^3$ larger, thereby stabilizing an intermediate state with a volume in between those of the np and lp phases of the empty framework. On increasing the water loading up to 7.5 molecules per unit cell, the equilibrium volume is further shifted by an additional 85 $Å^3$ and the Helmholtz free energy profile is no longer reminiscent of the bistable empty material. At the highest water loading, representing a 'superhydrated' state, the Helmholtz free energy profile possesses a sharp minimum which is only shifted towards higher volumes by about 55 $Å^3$ with respect to the lp equilibrium volume.

The differences between the classically and quantum-mechanically calculated Helmholtz free energy profiles are similar to the ones observed for the empty framework, resulting in a Helmholtz free energy difference of the same order of magnitude, *i.e.* generally smaller than about 3 kJ mol^{-1}, at larger volumes.

From these simulations, one can also infer the average adsorption enthalpy by simply conducting one additional simulation on a single water molecule. The average adsorption enthalpy ΔH_{ads} of the sequential adsorption of N gas phase water molecules into the empty framework is then given by

$$\Delta H_{ads}(0 \rightarrow N; T) = \Delta U(0 \rightarrow N; T) + P\Delta V(0 \rightarrow N; T) - N(U_{H_2O} + k_B T), \quad (5)$$

where $\Delta U(0 \rightarrow N)$ and $\Delta V(0 \rightarrow N)$ are respectively the change in internal energy and volume of the system on adsorbing N water molecules and U_{H_2O} is the internal energy of a single water molecule in the gas phase. A derivation of this formula can be found in the ESI of ref. 36. The values of the adsorption enthalpy for the different water loadings, calculated using both MD and PIMD, are reported in Table 1 and are of the same order of magnitude as the experimental isosteric heat of adsorption mentioned in ref. 19 and 28 for other aluminium-based frameworks such as MIL-160(Al) and MOF-303. The differences related to the inclusion of NQEs are once more limited to about 2–3 kJ mol^{-1}. As more water molecules are

Table 1 Average adsorption enthalpy $\Delta H_{ads}/N$ per H_2O molecule at 300 K and 1 bar (in kJ mol^{-1}) for different water loadings of MIL-53(Al) at the equilibrium volume

	$N_{H_2O} = 2.5$	$N_{H_2O} = 7.5$	$N_{H_2O} = 22.5$
Classical MD	−26.9	−45.1	−48.5
PIMD	−24.2	−42.9	−46.6

added to the framework, the increase in the magnitude of the adsorption energy decreases, as demonstrated by the small difference in adsorption enthalpy for 7.5 and 22.5 water molecules per unit cell. This also implies that the adsorption process of water within MIL-53(Al) cannot be described by means of a simplified mean-field model, which is of course related to the more complex nature of directional hydrogen bonding interactions that are essential in the description of water.

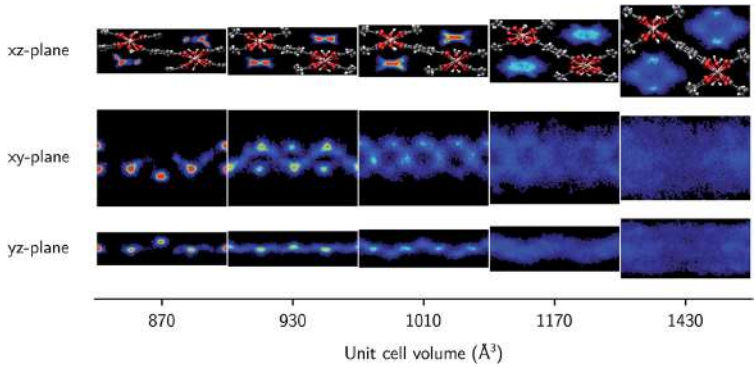

Fig. 4 Symmetrised water density in MIL-53(Al) projected onto the *xz*-plane (perpendicular to the *b*-axis), the *xy*-plane (perpendicular to the *c*-axis), and the *yz*-plane (perpendicular to the *a*-axis) for 2.5 water molecules per unit cell at different volumes. In each figure, a 1 × 2 × 1 supercell is shown, containing 5 water molecules. For the *xy*- and *yz*-planes, only the upper half of the simulation cell is shown, as the bottom half is its symmetrical equivalent.

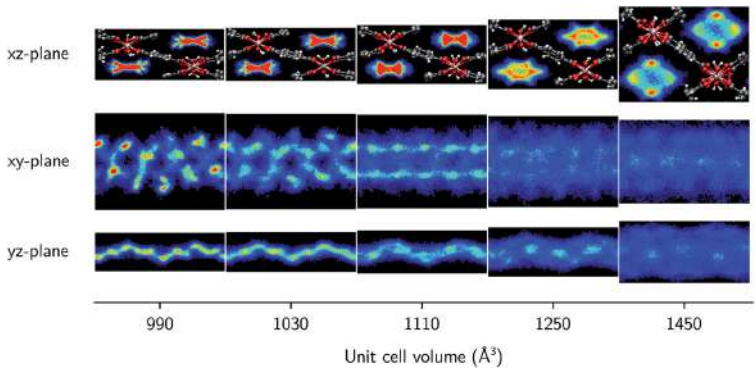

Fig. 5 Symmetrised water density in MIL-53(Al) projected onto the *xz*-plane (perpendicular to the *b*-axis), the *xy*-plane (perpendicular to the *c*-axis), and the *yz*-plane (perpendicular to the *a*-axis) for 7.5 water molecules per unit cell at different volumes. In each figure, a 1 × 2 × 1 supercell is shown, containing 15 water molecules. For the *xy*- and *yz*-planes, only the upper half of the simulation cell is shown, as the bottom half is its symmetrical equivalent.

Finally, the molecular organization of the water molecules within the MIL-53 framework can also be considered by means of density plots of the guest molecules, thereby visualizing their spatial probability distribution. These densities are shown in Fig. 4 and 5 for different volumes and for both 2.5 and 7.5 water molecules per unit cell, considering the projections onto the planes perpendicular to each of the three cell axes. The density plots for the case of 22.5 water molecules per unit cell can be found in the ESI (Fig. S3†). While no clear preferential hydrogen bonding is observed with the hydroxyl framework groups, which is most likely related to the lack of an explicit force field description of hydrogen bonding or polarization,[59] Medders *et al.*[104] also reported a disruption of these preferential hydrogen bonds for water loadings exceeding the number of hydroxyl framework groups. Hydrogen bonds are however formed with the oxygen atoms of the carboxylate groups of the linkers of the framework (see ESI Fig. S4†). Furthermore, the typical 1D water wires in the direction of the aluminium-oxide chains, which have been observed in previous studies of MIL-53-type frameworks,[58,102,104] are also present in our simulations at lower volumes (within the np region). At higher volumes, the water molecules take advantage of the additional motional freedom gained through the increase in pore size, leading to a more diffuse picture when compared to the np region. Given that the larger densities are located near the edges of the pore, the presence of the framework is clearly also felt at higher volumes.

3.3 Thermal conductivity

After having investigated the organization of water molecules within the framework of MIL-53(Al), as well as their impact on the flexibility, we now focus again on the framework itself, instead of on the host–guest and guest–guest effects. Insight into the intrinsic heat transfer characteristics of the adsorbent is also essential for a molecular-level understanding of water-adsorption applications. The influence of guest molecules on the thermal conductivity of MOFs is still

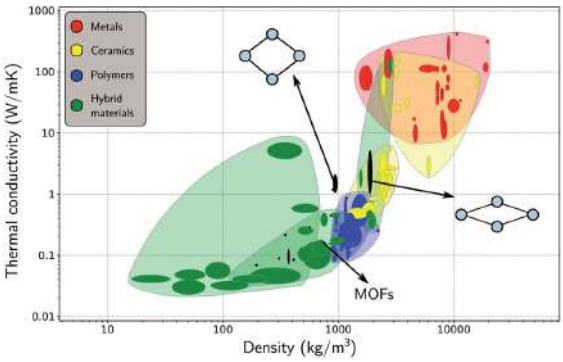

Fig. 6 Materials property chart displaying the thermal conductivity and the density of MOFs alongside other material classes, namely, metals (and alloys), ceramics (glasses and (non-)technical ceramics), polymers, and hybrid materials (composites, foams, and natural materials). The thermal conductivities of the lp and the np phases are indicated with black ovals. Figure adapted from ref. 36 with permission of the American Chemical Society.

a topic of debate, but lies beyond the scope of the current study.[26,32,109,110] Some studies have suggested that guest molecules improve the heat transfer (*i.e.* the thermal conductivity increases with the loading), while others have reported the opposite.

In general, MOFs are poor heat conductors, especially in comparison with other materials (Fig. 6),[36] which can pose a major technological barrier for practical applications. Therefore, both experimental and theoretical in-depth investigations are required to address this problem. However, apart from an already established relationship between the difficult heat dissipation in MOFs and their inherent porosity,[29,30,33,36,109] the directional dependence of the thermal conductivity has barely been investigated.[31,33,40] Given that flexible MOFs can have a very anisotropic response to different stimuli,[38,111] the heat transfer is also expected to show a directional dependence. For a set of idealized MOFs, Wilmer and coworkers studied the anisotropy of the thermal conductivity,[33] considering frameworks with a simple cubic structure, a triangular-channel structure, and a hexagonal-channel structure, and discussed how the pore shape and size affect the thermal conductivity in different directions. Their study indicated that MOFs with smaller pores are likely to have a better thermal performance, *i.e.* a higher thermal conductivity, which was also demonstrated for the IRMOF series.[36,109]

3.3.1 Volume dependence of the thermal conductivity. As MIL-53(Al) has lozenge-shaped channels (Fig. 1), which differ in size and shape for the np and lp phases, we computed the thermal conductivity along the *a*-, *b*- and *c*-directions as a function of the volume of the conventional unit cell. The results are shown in Fig. 7. In the region where MIL-53(Al) is mechanically unstable (Fig. S2†),[46] a separation of lp and np volume states was observed in agreement with recent findings of Rogge *et al.*[53] These long-range correlation effects impeded an accurate estimation of the thermal conductivity in between the (meta)stable lp and the np phases, as the obtained volume distribution depends on the size of the simulation cell. A snapshot of a structure containing different volume states is displayed in Fig. S7,† together with its volume distribution which shows two distinct maxima. Interestingly, no transitions were observed between the different volume states during the microcanonical simulations used to compute the heat current autocorrelation function. After the equilibration run at 300 K in the canonical ensemble, in which a separation between the lp and np volume states occurs spontaneously, the individual cells remain frozen in the acquired volume states. While local energy fluctuations are still possible in the microcanonical ensemble, transitions between different volume states are expected to be extremely unlikely in a $7 \times 8 \times 7$ supercell, as the energy of the total system is kept constant. These spatially disordered phenomena in flexible materials will have to be taken into account in future heat transfer studies and pose an additional difficulty for the already challenging modelling of these flexible systems.

In the lp region (Fig. 7), the thermal conductivity in the *a*-direction is clearly higher than the thermal conductivity in the *c*-direction. In these directions, the heat is transferred along the bonds of the organic linkers, which are more aligned with the *a*-direction than with the *c*-direction (Fig. 1). As the angle between the organic linkers and the *a*-direction increases from approximately 30 to 40 degrees in the lp region, the alignment with the *a*-direction decreases at larger volumes and so does the thermal conductivity. Consequently, the opposite trend is found

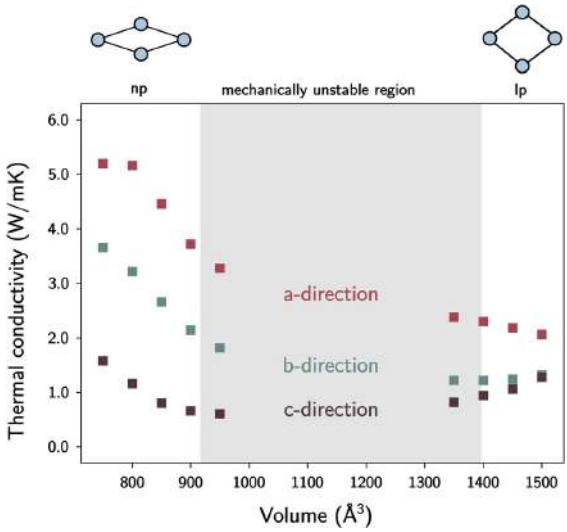

Fig. 7 The thermal conductivity of MIL-53(Al) as a function of the volume at room temperature. The volumes in between the lp and the np phases are mechanically unstable.

for the *c*-direction. For the one-dimensional Al(OH) chains (*i.e.* the *b*-direction), the heat conduction is also observed to be worse than for the *a*-direction.

The trends in the np region are less intuitive. The thermal conductivity along the *a*-direction generally increases when the volume decreases (Fig. 7). At the lowest volumes, the organic linkers are nearly parallel with this direction due to the knee-cap configuration of MIL-53(Al), and the dominant thermal resistance

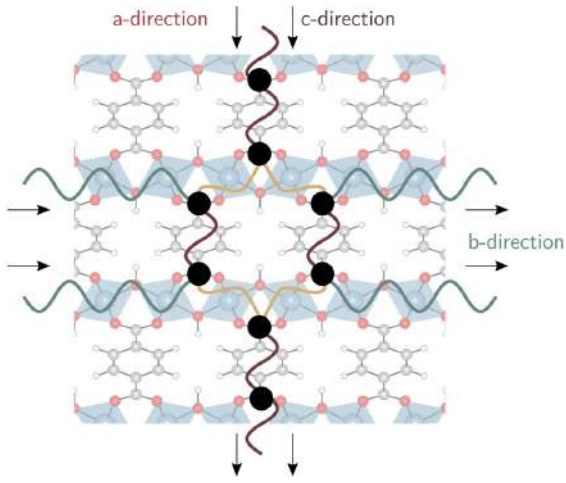

Fig. 8 Schematic illustration of the energy carriers along the *a*-, *b*- and *c*-directions.

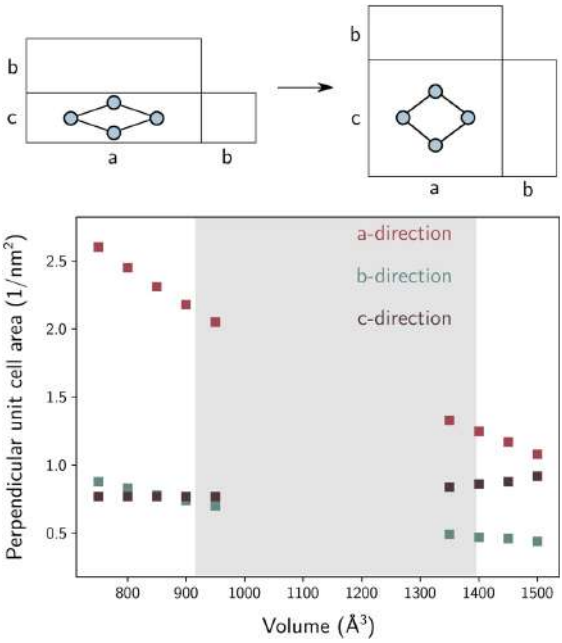

Fig. 9 Inverse of the cross-sectional area in the unit cell perpendicular to the indicated lattice direction as a function of the volume. A schematic representation of the cross-sectional area in the three directions is shown on top.

along this direction will reside in the organic–inorganic connections in between connecting linkers (Fig. 8). A very strong increase in the thermal conductivity along the *c*-direction is absent, which shows that although the organic linkers are stacked very closely, not a lot of heat is transported along the pore vacuum.

The thermal conductivity in the *b*-direction strongly increases at the lowest volumes. However, note that the thermal conductivity in a certain direction is defined as the ability of a material with unit length thickness along this direction to transfer heat per unit of cross-sectional surface area in the perpendicular direction (Fig. S5†). In MIL-53(Al), the unit cell surface area perpendicular to the *b*-direction increases substantially during the phase transition towards increasing volume, while the lattice parameter *b* does not, as schematically illustrated in Fig. 9. Hence, the thermal conductivity along this direction follows to some extent the trend in the inverse of the area as a function of the volume (Fig. 9). In other words, per unit of surface area, fewer conducting Al(OH) chains are present, causing the thermal conductivity to decrease. The same reasoning holds for the number of stacked organic linkers in the surface area perpendicular to the *a*-direction.

Furthermore, the sharp increase in the thermal conductivity along the *b*-direction at the lowest volumes is believed to be connected to another phenomenon. As the interchain thermal resistance is heavily reduced by both the close approach of the Al(OH) chains (in the *c*-direction) and the almost parallel stacking

of the organic linkers, the heat dissipated along the direction of the Al(OH) chain can spread more easily over multiple chains. This might also explain why the volume dependence of the thermal conductivity in the *a*- and *b*-directions roughly follows the same trend.

3.3.2 Specific *vs.* absolute thermal conductivity. When comparing the values of the thermal conductivity near the equilibrium np and lp volumes of MIL-53(Al) (Table 2) to those of other MOFs reported in the literature (Table 3), the lp phase is found to yield a thermal conductivity of the same order of magnitude as other MOFs with a similar mass density (*e.g.* MOF-505 and UiO-66).[36] For the np phase, on the other hand, the thermal conductivity has a much higher value than for other MOFs, especially along the *a*- and *b*-directions. However, given that its mass density is almost doubled with respect to the lp phase and the thermal conductivity strongly correlates with the mass density (Fig. 6), this is to be expected.

Although these values for the specific thermal conductivity seem to imply that heat is conducted much easier in the np phase than in the lp phase, a fair comparison should also take the difference in cell shape of the two phases into account. For practical MOF applications, the required amount of material will play an important role and is expected to remain constant throughout the

Table 2 Thermal conductivity of MIL-53(Al) in both phases ($V_{np} = 800$ Å^3, $V_{lp} = 1500$ Å^3) at room temperature. The absolute thermal conductivity is given per conventional unit cell. More information regarding the error bars is given in the Methodology section

	lp	np
κ_{aa} (W m^{-1} K^{-1})	2.06 ± 0.02	5.16 ± 0.08
κ_{bb} (W m^{-1} K^{-1})	1.32 ± 0.02	3.22 ± 0.06
κ_{cc} (W m^{-1} K^{-1})	1.28 ± 0.02	1.16 ± 0.02
ρ (kg m^{-3})	922	1727
κ_{aa}^{abs} (nW K^{-1})	1.2	1.0
κ_{bb}^{abs} (nW K^{-1})	4.4	5.8
κ_{cc}^{abs} (nW K^{-1})	1.0	2.4

Table 3 Overview of the thermal conductivities of MOFs published in the literature

	κ (W m^{-1} K^{-1})	
MOF	Experiment	Simulations
Al-soc-MOF-1	—	0.22 (ref. 36)
HKUST-1	0.27–0.39 (ref. 25 and 27)	0.45–0.58 (ref. 25 and 36)
IRMOF-10	—	0.02–0.09 (ref. 36 and 109)
IRMOF-16	—	0.07 (ref. 36)
MIL-160	0.06 (ref. 28)	—
MOF-5	0.34 (ref. 24)	0.12–0.31 (ref. 25, 29, 36 and 109)
MOF-177	—	0.08–0.09 (ref. 36)
MOF-505	—	1.16–1.26 (ref. 36)
UiO-66	0.11 (ref. 27)	0.87 (ref. 36)
UiO-67	0.19 (ref. 27)	—
UMCM-1	—	0.07–0.13 (ref. 36)
ZIF-8	0.33 (ref. 26)	0.17 (ref. 30 and 110)

operation of the device. Therefore, it is instructive to determine the absolute thermal conductivity κ^{abs}, which is an extensive property (with units W K^{-1}):

$$\kappa_{ii}^{abs} = \frac{A}{d}\,\kappa_{ii}, \tag{6}$$

where A is the cross-sectional area perpendicular to the path of the heat flow (i-direction), d is the thickness along the path of the heat flow, and κ is the thermal conductivity along the path of the heat flow (Fig. S5†). This quantity can be used to compare the heat transfer characteristics of the lp and the np phases for the same amount of matter, correcting for their different physical dimensions. The tabulated values for κ^{abs} (Table 2) indicate that the heat transfer in the a- and b-directions for a given temperature difference is not as different for the lp and np phases as the specific thermal conductivities suggest. The thermal conductivity in the b-direction does, however, slightly increase, which might be related to a decrease in the interchain thermal resistance, as suggested in the previous section. In Fig. S8,† the absolute thermal conductivity is shown as a function of volume for a single unit cell.

A possible strategy to exploit the anisotropy of the thermal conductivity of MOFs was suggested by Wilmer *et al.*[33] Given that structures with large channels are known to be beneficial for rapid gas adsorption, but also give rise to ultra-low thermal conductivities, MOFs could be designed to rapidly dissipate heat along the channel direction to remedy the problem of heat conduction. For MIL-53(Al), the heat transfer per unit cell was shown to behave anisotropically (Table 2), with heat dissipating more easily along the one-dimensional aluminium-oxide chains following the b-direction. This result is in line with the good thermal conductivity of aluminium oxide (Al_2O_3, $\kappa \approx 30$ W m^{-1} K^{-1}).

3.3.3 Vibrational density of states. The difference in heat transfer along the organic linkers (a- and c-directions) and the inorganic chain (b-direction) is also reflected in the overlap of the vibrational density of states (VDOS). A low overlap

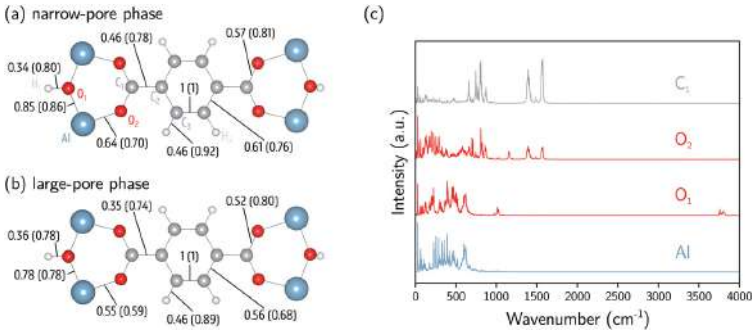

Fig. 10 Analysis of the atomic vibrational density of states (VDOS). (a) The similarity index calculated at 0–4000 cm^{-1} (0–700 cm^{-1}) for the np phase (800 $Å^3$). (b) The similarity index calculated at 0–4000 cm^{-1} (0–700 cm^{-1}) for the lp phase (1500 $Å^3$). (c) The atomic VDOS for Al, O_1, O_2, and C_1. The atomic VDOS for other atoms is reported in the ESI (Fig. S9 and S10†). The intensities have been rescaled by dividing the complete spectrum by the square root of the integral of the square of the spectrum.

between the VDOS of neighbouring interfaces, such as a solid–liquid or solid–solid interface, implies a high thermal resistance.[112–114] For ZIF-8, Zhang and Jiang demonstrated that there is little overlap between the atomic VDOS of the main energy carriers (Zn and N) in the framework.[30,110] For MIL-53(Al), we quantified the overlap in VDOS along all atomic bonds using a similarity index:[97]

$$\text{similarity index} = \frac{\int \mathrm{d}\sigma\, f(\sigma)\, g(\sigma)}{\sqrt{\int \mathrm{d}\sigma\, f^2(\sigma) \int \mathrm{d}\sigma\, g^2(\sigma)}}. \quad (7)$$

It is a measure of the correlation between two spectra $f(\sigma)$ and $g(\sigma)$ in a certain frequency range. We determined this similarity index for all chemically bonded atom pairs by computing the overlap between the VDOS of both atoms in the frequency range 0–4000 cm^{-1} and in the low-frequency range 0–700 cm^{-1}. Using this approach, a large overlap in the VDOS along the aluminium-oxide chain is found, as displayed in Fig. 10. This similarity index is especially large when compared to the similarity indices of the Al–O_2, O_2–C_1, and C_1–C_2 bonds along which the heat needs to transfer for the *a*- and *c*-directions (Fig. 8), so that the similarity index corroborates the absolute thermal conductivity results. Finally, the results in Fig. 10 also show that the overlap is systematically larger in the np phase, which again agrees well with Table 2.

4 Conclusions

Within the past few years, MOFs have gradually gained a more established reputation as promising solid adsorbents in the field of water-adsorption applications. To obtain a more fundamental understanding of their potential performance and shed light on current barriers, such as the slow heat transfer of MOFs, molecular simulations can be performed to theoretically investigate the framework properties and the interactions with water. In this work, the flexible MIL-53(Al) framework was analysed, focusing on the influence of water on the phase stability and the structural properties, as well as on the thermal conductivity of the framework.

To assess the flexibility of the framework, an adequate modelling technique is required, such as the thermodynamic protocol in ref. 46, which allows the construction of Helmholtz free energy profiles to identify the (meta)stable states of the system as a function of the loading. Several studies have already highlighted the importance of the weak dispersion forces[36,99] and structural disorder[53,100] in the description of the flexibility of MIL-53(Al), but the quantum nature of the atoms has not yet been taken into account. However, as evidenced by this study of MIL-53(Al) with and without water in the pores, nuclear quantum effects do not seem to play a major role in the relative phase stability of the material. Both classical and path integral molecular dynamics simulations indicate that the volume of the np phase continuously increases with the water loading until the lp phase becomes the only stable state at a very high loading. For all the considered water loadings, the adsorbed molecules are observed to engage in ordered hydrogen bonded structures resembling 1D water wires along the aluminium-oxide chains for volume states located around the equilibrium volume. If the pore volume, on the contrary, substantially deviates from the

equilibrium volume, the water molecules spread more freely inside the pores, although they remain predominantly located near the edges of the pores due to their interaction with the framework.

Furthermore, the thermal conductivity of the framework was also calculated in the three crystal directions as a function of the volume, which allows us to compare the thermal performance of the np and lp phases. To capture the influence of long-range spatial disorder present in experimental samples, new simulation strategies will have to be developed. In this work, the thermal conductivity of MIL-53(Al) was found to be strongly linked to the geometry of the unit cell, and in absolute numbers the heat transfer in the np phase was shown to be more efficient. The aluminium-oxide chain was thereby identified as the best conducting fragment of the material, as confirmed by the overlap in the vibrational density of states of the aluminium and oxygen atoms.

These findings clearly demonstrate that molecular simulations can offer useful insights into the fundamental properties relevant for water-adsorption applications. Promising water-adsorption materials pointed out by experimental studies will be further explored in future studies.

Conflicts of interest

There are no conflicts to declare.

Note added after first publication

This article replaces the version published on 29 October 2020, which contained a formatting error in section 2.3 and an error in eqn (3).

Acknowledgements

This work is supported by the Fund for Scientific Research Flanders (FWO, grant no. 11D2220N). V. V. S. acknowledges funding from the European Union's Horizon 2020 Research and Innovation Program (consolidator ERC grant agreement No. 647755 - DYNPOR (2015–2020)). The work is furthermore supported by the Research Board of Ghent University (BOF). The computational resources and services used in this work were provided by VSC (Flemish Supercomputer Center), funded by Ghent University, FWO, and the Flemish Government department EWI.

Notes and references

1 A. Schoedel, Z. Ji and O. M. Yaghi, *Nat. Energy*, 2016, **1**, 16034.
2 Y. He, F. Chen, B. Li, G. Qian, W. Zhou and B. Chen, *Coord. Chem. Rev.*, 2018, **373**, 167–198.
3 H. Li, K. Wang, Y. Sun, C. T. Lollar, J. Li and H.-C. Zhou, *Mater. Today*, 2018, **21**, 108–121.
4 M. Ding, R. W. Flaig, H.-L. Jiang and O. M. Yaghi, *Chem. Soc. Rev.*, 2019, **48**, 2783–2828.
5 N. C. Burtch, H. Jasuja and K. S. Walton, *Chem. Rev.*, 2014, **114**, 10575–10612.
6 J. Carnivet, A. Fateeva, Y. Guo, B. Coasne and D. Farrusseng, *Chem. Soc. Rev.*, 2014, **43**, 5594–5617.

7 H. Furukawa, F. Gándara, Y.-B. Zhang, J. Jiang, W. L. Queen, M. R. Hudson and O. M. Yaghi, *J. Am. Chem. Soc.*, 2014, **136**, 4369–4381.

8 C. Wang, X. Liu, N. K. Demir, P. J. Chen and K. Li, *Chem. Soc. Rev.*, 2016, **45**, 5107–5134.

9 J. Duan, W. Jin and S. Kitagawa, *Coord. Chem. Rev.*, 2017, **332**, 48–74.

10 J. Ehrenmann, S. K. Henninger and C. Janiak, *Chem.–Eur. J.*, 2011, **2011**, 471–474.

11 F. Jeremias, D. Fröhlich, C. Janiak and S. K. Henninger, *RSC Adv.*, 2014, **4**, 24076–24082.

12 A. Cadiau, J. S. Lee, D. B. Borges, P. Fabry, T. Devic, M. T. Wharmby, C. Martineau, D. Foucher, F. Taulelle, C.-H. Jun, Y. K. Hwang, N. Stock, M. F. De Lange, F. Kapteijn, J. Gascon, G. Maurin, J.-S. Chang and C. Serre, *Adv. Mater.*, 2015, **27**, 4775–4780.

13 M. F. de Lange, K. J. F. M. Verouden, T. J. H. Vlugt, J. Gascon and F. Kapteijn, *Chem. Rev.*, 2015, **115**, 12205–12250.

14 S. Wang, J. S. Lee, M. Wahiduzzaman, J. Park, M. Muschi, C. Martineau-Corcos, A. Tissot, K. H. Cho, J. Marrot, W. Shepard, G. Maurin, J.-S. Chang and C. Serre, *Nat. Energy*, 2018, **3**, 985–993.

15 D. Lenzen, J. Zhao, S.-J. Ernst, M. Wahiduzzaman, A. K. Inge, D. Fröhlich, H. Xu, H.-J. Bart, C. Janiak, S. Henninger, G. Maurin, X. Zou and N. Stock, *Nat. Commun.*, 2019, **10**, 3025.

16 H. Kim, S. Yang, S. R. Rao, S. Narayanan, E. A. Kapustin, H. Furukawa, A. S. Umans, O. M. Yaghi and E. N. Wang, *Science*, 2017, **356**, 430–434.

17 A. J. Rieth, S. Yang, E. N. Wang and M. Dinca, *ACS Cent. Sci.*, 2017, **3**, 668–672.

18 M. J. Kalmutzki, C. S. Diercks and O. M. Yaghi, *Adv. Mater.*, 2018, **30**, 1704304.

19 N. Hanikel, M. S. Prévot, F. Fathieh, E. A. Kapustin, H. Lyu, H. Wang, N. J. Diercks, G. T. Glover and O. M. Yaghi, *ACS Cent. Sci.*, 2019, **5**, 1699–1706.

20 J. J. Purewal, D. Liu, J. Yang, A. Sudik, D. J. Siegel, S. Maurer and U. Müller, *Int. J. Hydrogen Energy*, 2012, **37**, 2723–2727.

21 J. Purewal, D. Liu, A. Sudik, M. Veenstra, J. Yang, S. Maurer, U. Müller and D. J. Siegel, *J. Phys. Chem. C*, 2012, **116**, 20199–20212.

22 D. Liu, J. J. Purewal, J. Yang, A. Sudik, S. Maurer, U. Müller, J. Ni and D. J. Siegel, *Int. J. Hydrogen Energy*, 2012, **37**, 6109–6117.

23 Y. Ming, J. Purewal, D. Liu, A. Sudik, C. Xu, J. Yang, M. Veenstra, K. Rhodes, R. Soltis, J. Warner, M. Gaab, U. Müller and D. J. Siegel, *Microporous Mesoporous Mater.*, 2014, **185**, 235–244.

24 B. L. Huang, Z. Ni, A. Millward, A. J. H. McGaughey, C. Uher, M. Kaviany and O. M. Yaghi, *Int. J. Heat Mass Transfer*, 2007, **50**, 405–411.

25 K. J. Erickson, F. Léonard, V. Stavila, M. E. Foster, C. D. Spataru, R. E. Jones, B. M. Foley, P. E. Hopkins, M. D. Allendorf and A. A. Talin, *Adv. Mater.*, 2015, **27**, 3453–3459.

26 B. Cui, C. O. Audu, Y. Liao, S. T. Nguyen, O. K. Farha, J. T. Hupp and M. Grayson, *ACS Appl. Mater. Interfaces*, 2017, **9**, 28139–28143.

27 J. Huang, X. Xia, X. Hu, S. Li and K. Liu, *Int. J. Heat Mass Transfer*, 2019, **138**, 11–16.

28 S. Cui, A. Marandi, G. Lebourleux, M. Thimon, M. Bourdon, C. Chen, M. I. Severino, V. Steggles, F. Nouar and C. Serre, *Appl. Therm. Eng.*, 2019, **161**, 114135.

29 B. L. Huang, A. J. H. McGaughey and M. Kaviany, *Int. J. Heat Mass Transfer*, 2007, **50**, 393–404.
30 X. Zhang and J. Jiang, *J. Phys. Chem. C*, 2013, **117**, 18441–18447.
31 X. Wang, R. Guo, D. Xu, J. Chung, M. Kaviany and B. Huang, *J. Phys. Chem. C*, 2015, **119**, 26000–26008.
32 H. Babaei and C. E. Wilmer, *Phys. Rev. Lett.*, 2016, **116**, 025902.
33 H. Babaei, A. J. H. McGaughey and C. E. Wilmer, *Chem. Sci.*, 2017, **8**, 583–589.
34 H. Babaei, A. J. H. McGaughey and C. E. Wilmer, *ACS Appl. Mater. Interfaces*, 2018, **10**, 2400–2406.
35 K. B. Sezginel, P. A. Asinger, H. Babaei and C. E. Wilmer, *Chem. Mater.*, 2018, **30**, 2281–2286.
36 J. Wieme, S. Vandenbrande, A. Lamaire, V. Kapil, L. Vanduyfhuys and V. Van Speybroeck, *ACS Appl. Mater. Interfaces*, 2019, **11**, 38697–38707.
37 T. Loiseau, C. Serre, C. Huguenard, G. Fink, F. Taulelle, M. Henry, T. Bataille and G. Férey, *Chem.–Eur. J.*, 2004, **10**, 1373–1382.
38 A. U. Ortiz, A. Boutin, A. H. Fuchs and F.-X. Coudert, *Phys. Rev. Lett.*, 2012, **109**, 195502.
39 C. Nanthamathee, S. Ling, B. Slater and M. P. Attfield, *Chem. Mater.*, 2015, **27**, 85–95.
40 Y. Ming, H. Chi, R. Blaser, C. Xu, J. Yang, M. Veenstra, M. Gaab, U. Müller, C. Uher and D. J. Siegel, *Int. J. Heat Mass Transfer*, 2015, **82**, 250–258.
41 P. D. Shima and J. Philip, *J. Phys. Chem. C*, 2011, **115**, 20097–20104.
42 G. Zhu, J. Liu, Q. Zheng, R. Zhang, D. Li, D. Banerjee and D. G. Cahill, *Nat. Commun.*, 2016, **7**, 13211.
43 J. Shin, J. Sung, M. Kang, X. Xie, B. Lee, K. M. Lee, T. J. White, C. Leal, N. R. Sottos, P. V. Braun and D. G. Cahill, *Proc. Natl. Acad. Sci. U. S. A.*, 2019, **116**, 5973–5978.
44 S. Horike, S. Shimomura and S. Kitagawa, *Nat. Chem.*, 2009, **1**, 695–704.
45 A. Schneemann, I. Schwedler, I. Senkovska, S. Kaskel and R. A. Fischer, *Chem. Soc. Rev.*, 2014, **43**, 6062–6096.
46 L. Vanduyfhuys, S. M. J. Rogge, J. Wieme, S. Vandenbrande, G. Maurin, M. Waroquier and V. Van Speybroeck, *Nat. Commun.*, 2018, **9**, 204.
47 J. H. Lee, S. Jeoung, Y. G. Chung and H. R. Moon, *Coord. Chem. Rev.*, 2019, **389**, 161–188.
48 J. A. Mason, J. Oktawiec, M. K. Taylor, M. R. Hudson, J. Rodriguez, J. E. Bachman, M. I. Gonzalez, A. Cervellino, A. Guagliardi, C. M. Brown, P. L. Llewellyn, N. Masciocchi and J. R. Long, *Nature*, 2015, **527**, 357–361.
49 S. Hiraide, H. Tanaka, N. Ishikawa and M. T. Miyahara, *ACS Appl. Mater. Interfaces*, 2017, **9**, 41066–41077.
50 J. S. Grosch and F. Paesani, *J. Am. Chem. Soc.*, 2012, **134**, 4207–4215.
51 F.-X. Coudert, A. U. Ortiz, V. Haigis, D. Bousquet, A. H. Fuchs, A. Ballandras, G. Weber, I. Bezverkhyy, N. Geoffroy, J.-P. Bellat, G. Ortiz, G. Chaplais, J. Patarin and A. Boutin, *J. Phys. Chem. C*, 2014, **118**, 5397–5405.
52 J. Wieme, K. Lejaeghere, G. Kresse and V. Van Speybroeck, *Nat. Commun.*, 2018, **9**, 4899.
53 S. M. J. Rogge, M. Waroquier and V. Van Speybroeck, *Nat. Commun.*, 2019, **10**, 4842.
54 T. M. Markland and M. Ceriotti, *Nat. Rev. Chem.*, 2018, **2**, 0109.

55 M. Ceriotti, W. Fang, P. G. Kusalik, R. H. McKenzie, A. Michealides, M. A. Morales and T. E. Markland, *Chem. Rev.*, 2016, **116**, 7529.
56 I. J. Kang, N. A. Khan, E. Haque and S. H. Jhung, *Chem.–Eur. J.*, 2011, **17**, 6437–6442.
57 I. Bezverkhyy, G. Ortiz, G. Chaplais, C. Marichal, G. Weber and J.-P. Bellat, *Microporous Mesoporous Mater.*, 2014, **183**, 156–161.
58 F. Paesani, *Mol. Simul.*, 2012, **38**, 631–641.
59 J. Cirera, J. C. Sung, P. B. Howland and F. Paesani, *J. Chem. Phys.*, 2012, **137**, 054704.
60 F. Paesani, *J. Phys. Chem. C*, 2013, **117**, 19508–19516.
61 J. M. Salazar, G. Weber, J. M. Simon, I. Bezverkhyy and J. P. Bellat, *J. Chem. Phys.*, 2015, **142**, 124702.
62 D. D. Borges, R. Semino, S. Devautour-Vinot, H. Jobic, F. Paesani and G. Maurin, *Chem. Mater.*, 2017, **29**, 1569–1576.
63 A. J. Rieth, K. M. Hunter, M. Dinca and F. Paesani, *Nat. Commun.*, 2019, **10**, 4771.
64 T. Ichii, T. Arikawa, K. Omoto, N. Hosono, H. Sato, S. Kitagawa and K. Tanaka, *Commun. Chem.*, 2020, **3**, 16.
65 N. C. Burtch, I. M. Walton, J. T. Hungerford, C. R. Morelock, Y. Jiao, J. Heinen, Y.-S. Chen, A. A. Yakovenko, W. Xu, D. Dubbeldam and K. S. Walton, *Nat. Chem.*, 2020, **12**, 186–192.
66 L. Vanduyfhuys, S. Vandenbrande, T. Verstraelen, R. Schmid, M. Waroquier and V. Van Speybroeck, *J. Comput. Chem.*, 2015, **36**, 1015–1027.
67 L. Vanduyfhuys, S. Vandenbrande, J. Wieme, M. Waroquier, T. Verstraelen and V. Van Speybroeck, *J. Comput. Chem.*, 2018, **39**, 999–1011.
68 J. P. Perdew, K. Burke and M. Ernzerhof, *Phys. Rev. Lett.*, 1996, **77**, 3865–3868.
69 S. Grimme, J. Antony, S. Ehrlich and H. Krieg, *J. Chem. Phys.*, 2010, **132**, 154104.
70 S. Grimme, S. Ehrlich and L. Goerigk, *J. Comput. Chem.*, 2011, **32**, 1456–1465.
71 T. Verstraelen, S. Vandenbrande, F. Heidar-Zadeh, L. Vanduyfhuys, V. Van Speybroeck, M. Waroquier and P. W. Ayers, *J. Chem. Theory Comput.*, 2016, **12**, 3894–3912.
72 J. H. Lii and N. L. Allinger, *J. Am. Chem. Soc.*, 1989, **111**, 8576–8582.
73 H. Sun, *J. Phys. Chem. B*, 1998, **102**, 7338–7364.
74 S. Habershon, T. E. Markland and D. E. Manolopoulos, *J. Chem. Phys.*, 2009, **131**, 024501.
75 J. L. F. Abascal and C. Vega, *J. Chem. Phys.*, 2005, **123**, 234505.
76 T. Verstraelen, L. Vanduyfhuys, S. Vandenbrande and S. M. J. Rogge, *Yaff 1.4.2*, 2017, http://molmod.github.io/yaff/index.html.
77 W. G. Hoover, *Phys. Rev. A: At., Mol., Opt. Phys.*, 1985, **31**, 1695–1697.
78 S. Nosé, *Mol. Phys.*, 1986, **57**, 187–191.
79 G. J. Martyna, M. L. Klein and M. E. Tuckerman, *J. Chem. Phys.*, 1992, **97**, 2635–2643.
80 G. J. Martyna, D. J. Tobias and M. L. Klein, *J. Chem. Phys.*, 1994, **101**, 4177–4189.
81 G. J. Martyna, M. E. Tuckerman, D. J. Tobias and M. L. Klein, *Mol. Phys.*, 1996, **87**, 1117–1157.
82 A. Lamaire, J. Wieme, S. M. J. Rogge, M. Waroquier and V. Van Speybroeck, *J. Chem. Phys.*, 2019, **150**, 094503.

83 V. Kapil, J. Wieme, S. Vandenbrande, A. Lamaire, V. Van Speybroeck and M. Ceriotti, *J. Chem. Theory Comput.*, 2019, **15**, 3237–3249.

84 M. Ceriotti, J. More and D. E. Manolopoulos, *Comput. Phys. Commun.*, 2014, **185**, 1019–1026.

85 V. Kapil, M. Rossi, O. Marsalek, R. Petraglia, Y. Litman, T. Spura, B. Cheng, A. Cuzzocrea, R. H. Meißner, D. M. Wilkins, P. Juda, S. P. Bienvenue, W. Fang, J. Kessler, I. Poltavsky, S. Vandenbrande, J. Wieme, C. Corminboeuf, T. D. Kühne, D. E. Manolopoulos, T. E. Markland, J. O. Richardson, A. Tkatchenko, G. A. Tribello, V. Van Speybroeck and M. Ceriotti, *Comput. Phys. Commun.*, 2019, **236**, 214–223.

86 S. Plimpton, *J. Comput. Phys.*, 1995, **117**, 1–19.

87 M. Ceriotti, M. Parrinello, T. E. Markland and D. E. Manolopoulos, *J. Chem. Phys.*, 2010, **133**, 124104.

88 G. Bussi and M. Parrinello, *Phys. Rev. E: Stat., Nonlinear, Soft Matter Phys.*, 2007, **75**, 56707.

89 P. Raiteri, J. D. Gale and G. Bussi, *J. Phys.: Condens. Matter*, 2011, **23**, 334213.

90 B. Leimkuhler and C. Matthews, *J. Chem. Phys.*, 2013, **138**, 174102.

91 M. S. Green, *J. Chem. Phys.*, 1954, **22**, 398–413.

92 R. Kubo, *J. Phys. Soc. Jpn.*, 1957, **12**, 570–586.

93 P. K. Schelling, S. R. Phillpot and P. Keblinski, *Phys. Rev. B: Condens. Matter Mater. Phys.*, 2002, **65**, 144306.

94 J. Chen, G. Zhang and B. Li, *Phys. Lett. A*, 2010, **374**, 2392–2396.

95 L. de Sousa Oliveira and A. P. Greaney, *Phys. Rev. E*, 2017, **95**, 023308.

96 A. J. H. McGaughey and M. Kaviany, *Int. J. Heat Mass Transfer*, 2004, **47**, 1799–1816.

97 A. E. J. Hoffman, L. Vanduyfhuys, I. Nevjestic, J. Wieme, S. M. J. Rogge, H. Depauw, P. Van Der Voort, H. Vrielinck and V. Van Speybroeck, *J. Phys. Chem. C*, 2018, **122**, 2734–2746.

98 A. E. J. Hoffman, J. Wieme, S. M. J. Rogge, L. Vanduyfhuys and V. Van Speybroeck, *Z. Kristallogr. - Cryst. Mater.*, 2019, **234**, 529–545.

99 A. M. Walker, B. Civalleri, B. Slater, C. Mellot-Draznieks, F. Corá, C. M. Zicovich-Wilson, G. Román-Pérez, J. M. Soler and J. D. Gale, *Angew. Chem., Int. Ed.*, 2010, **49**, 7501–7503.

100 J. Keupp and R. Schmid, *Adv. Theory Simul.*, 2019, **2**, 1900117.

101 F. Salles, S. Bourrelly, H. Jobic, T. Devic, V. Guillerm, P. LLewellyn, C. Serre, G. Férey and G. Maurin, *J. Phys. Chem. C*, 2011, **115**, 10764–10776.

102 N. Guillou, F. Millange and R. I. Walton, *Chem. Commun.*, 2011, **47**, 713–715.

103 V. Haigis, F.-X. Coudert, R. Vuilleurmier and A. Boutin, *Phys. Chem. Chem. Phys.*, 2013, **15**, 19049–19056.

104 G. R. Medders and F. Paesani, *J. Phys. Chem. Lett.*, 2014, **5**, 2897–2902.

105 V. Haigis, F.-X. Coudert, R. Vuilleumier, A. Boutin and A. H. Fuchs, *J. Phys. Chem. Lett.*, 2015, **6**, 4365–4370.

106 G. Weber, I. Bezverkhyy, J.-P. Bellat, A. Ballandras, G. Ortiz, G. Chaplais, J. Patarin, F.-X. Coudert, A. H. Fuchs and A. Boutin, *Microporous Mesoporous Mater.*, 2016, **222**, 145–152.

107 L. R. Parent, H. C. Pham, J. P. Patterson, M. S. J. Denny, S. M. Cohen, N. C. Gianneschi and F. Paesani, *J. Am. Chem. Soc.*, 2017, **139**, 13973–13976.

108 E. Cockayne, *Powder Diffr.*, 2019, **34**, 227–232.

109 L. Han, M. Budge and A. P. Greaney, *Comput. Mater. Sci.*, 2014, **94**, 292–297.

110 W. Wei, J. Huang, W. Li, H. Peng and S. Li, *J. Phys. Chem. C*, 2019, **123**, 27369–27374.
111 S. Henke, A. Schneemann and R. A. Fischer, *Adv. Funct. Mater.*, 2013, **23**, 5990–5996.
112 E. T. Swartz and R. O. Pohl, *Rev. Mod. Phys.*, 1989, **61**, 605.
113 M. Hu, Y. Jing and X. Zhang, *Phys. Rev. B: Condens. Matter Mater. Phys.*, 2015, **91**, 155408.
114 A. Giri and P. E. Hopkins, *Adv. Funct. Mater.*, 2019, 1903857.

Paper IV

High rate nanofluidic energy absorption in porous zeolitic frameworks

Y. Sun‡, S.M.J. Rogge‡, A. Lamaire, S. Vandenbrande, J. Wieme, C.R. Siviour, V. Van Speybroeck, J.-C. Tan

Nature Materials, **2021**, 20 (7), 1015–1023

A. Lamaire performed the *ab initio* and umbrella sampling MD simulations, and contributed in the analysis, discussion, and interpretation of the results.

nature materials

ARTICLES

https://doi.org/10.1038/s41563-021-00977-6

High-rate nanofluidic energy absorption in porous zeolitic frameworks

Yueting Sun[1,2,4]✉, Sven M. J. Rogge[3,4]✉, Aran Lamaire[3], Steven Vandenbrande[3], Jelle Wieme[3], Clive R. Siviour[1], Veronique Van Speybroeck[3]✉ and Jin-Chong Tan[1]✉

Optimal mechanical impact absorbers are reusable and exhibit high specific energy absorption. The forced intrusion of liquid water in hydrophobic nanoporous materials, such as zeolitic imidazolate frameworks (ZIFs), presents an attractive pathway to engineer such systems. However, to harness their full potential, it is crucial to understand the underlying water intrusion and extrusion mechanisms under realistic, high-rate deformation conditions. Here, we report a critical increase of the energy absorption capacity of confined water-ZIF systems at elevated strain rates. Starting from ZIF-8 as proof-of-concept, we demonstrate that this attractive rate dependence is generally applicable to cage-type ZIFs but disappears for channel-containing zeolites. Molecular simulations reveal that this phenomenon originates from the intrinsic nanosecond timescale needed for critical-sized water clusters to nucleate inside the nanocages, expediting water transport through the framework. Harnessing this fundamental understanding, design rules are formulated to construct effective, tailorable and reusable impact energy absorbers for challenging new applications.

Energy absorption during mechanical impact plays a crucial role in modern society, from injury prevention and safety measures in industrial settings to cushioning systems that increase user comfort[1]. As current state-of-the-art energy absorption materials rely on processes such as extensive plastic deformation, cell buckling and viscoelastic dissipation[2,3], a major dilemma is the conflict between the required high energy density and the desire for reusability, to afford protection from multiple impacts. This challenge motivates the development of efficient energy-absorbing systems that are intrinsically recoverable, which requires one to identify and leverage fundamentally new energy absorption mechanisms.

In this regard, the pressurized intrusion of liquid water and aqueous solutions in hydrophobic nanoporous materials such as zeolites and metal-organic frameworks (MOFs) has emerged as a promising mechanism to yield high-performance energy-absorbing systems[4–6]. In this process, a hydrostatic pressure forces water to intrude into the hydrophobic nanopores, thereby converting mechanical work into interfacial energy. Given the exceedingly large surface area of MOFs (typically 1,000–10,000 $m^2 g^{-1}$) combined with their highly tuneable framework architecture and chemical composition[7], MOFs are emerging as an attractive platform for nanofluidic energy absorption. Hitherto, among the huge family of MOFs[8], a few materials have been identified for this application[9–13], mainly hydrothermally stable zeolitic imidazolate frameworks (ZIFs) consisting of hydrophobic nanocages[14–16]. However, current research has focused only on their performance under quasi-static loading conditions, that is, through slow intrusion and extrusion processes with typical strain rates of 10^{-5}–10^{-3} s^{-1} (refs. [4,17]). Some studies have started to investigate the influence of loading speed[10,18,19], but remain far from realistic strain rates, which can exceed 10^3 s^{-1} for impact-attenuating materials.

Herein, we systematically investigate the response of various promising impact-attenuating MOFs, namely ZIF-8, ZIF-7, ZIF-9, ZIF-67 and ZIF-71, under practically relevant strain rates of up to 10^3 s^{-1}. Hereto, dynamic water intrusion–extrusion experiments using the dedicated high-rate experimental platform depicted in Fig. 1a–c were conducted. The energy absorption densities of the investigated ZIF materials improve substantially on increasing strain rate. Molecular dynamics (MD) simulations demonstrate that this beneficial effect originates from the intrinsic nanosecond timescale necessary for water molecules to cluster in the ZIFs' hydrophobic nanocages and to facilitate transport across nanocages. This fundamental timescale, which increases the water intrusion pressure and energy absorption density at higher strain rates, depends on the cage-type geometry of the framework materials and is absent in channel-containing zeolites (ZSM-5, zeolite-β, mordenite). On the basis of these findings, four rules are formulated to design efficient and reusable energy-absorbing materials for high-rate mechanical impacts via the pressurized liquid intrusion mechanism, identifying ZIFs as a unique class of energy-absorbing materials. These generally applicable design rules are important to further the development of nanofluidics, which has become a flourishing field over the last decade[20].

Rate-dependent water intrusion of ZIF-8

We started our investigation with ZIF-8 (ref. [21]), which is arguably the best-known ZIF for liquid intrusion studies[9,17,18,22,23]. ZIF-8 adopts the sodalite topology with relatively narrow apertures comprising six-membered rings (6MR) (aperture size roughly 3.40 Å) connecting larger internal cages (roughly 11.6 Å, Fig. 1d and Supplementary Fig. 1)[15]. These two geometrical parameters correspond with the pore-limiting diameter (PLD) and the largest cavity diameter (LCD), respectively.

Figure 2b shows the water intrusion and extrusion of ZIF-8 at different strain rates, $\dot{\varepsilon}$, encompassing six orders of magnitude from 10^{-3} s^{-1} to 10^3 s^{-1}. As schematically indicated in Fig. 2a, three stages can be identified during loading. Initially and up to a strain, ε, of about 0.05 (equivalent to a specific volume change ΔV of roughly

[1]Department of Engineering Science, University of Oxford, Oxford, UK. [2]School of Engineering, University of Birmingham, Edgbaston, Birmingham, UK. [3]Center for Molecular Modeling (CMM), Ghent University, Zwijnaarde, Belgium. [4]These authors contributed equally: Yueting Sun, Sven M. J. Rogge. ✉e-mail: Y.Sun.9@bham.ac.uk; Sven.Rogge@UGent.be; Veronique.VanSpeybroeck@UGent.be; jin-chong.tan@eng.ox.ac.uk

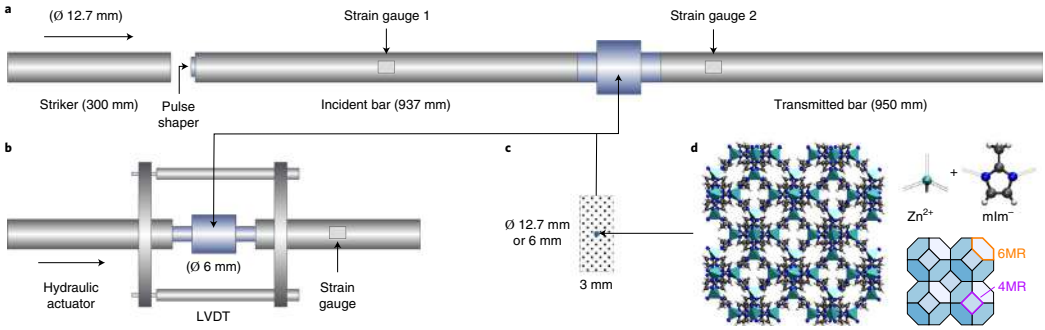

Fig. 1 | Experimental setup. a, SHPB setup for high-rate experiments ($10^3\,s^{-1}$). **b**, Hydraulic compression setup for medium-rate experiments ($1–10^2\,s^{-1}$), with a pair of LVDTs for displacement measurement. **c**, Water suspension of ZIF-8, which is sealed in stainless-steel chambers each with a pair of pistons (shown in **a**,**b**). **d**, Nanoporous framework structure, building blocks and sodalite topology of ZIF-8 with indication of the 4MR and 6MR apertures. Low-rate experiments (up to $0.1\,s^{-1}$) are performed on a commercial screw-driven testing machine (Instron 5582) using the stainless-steel chamber shown in **b**.

$0.17\,cm^3\,g^{-1}$), the pressure increases linearly with the reduction in system volume. This is attributed to the elastic compression of the {ZIF-8 + water} system, without any pore intrusion owing to ZIF-8's hydrophobicity. Next, the intrusion of water in the ZIF-8 nanocages gives rise to a plateau at the intrusion pressure P_{in}, until water molecules occupy the entire accessible pore volume. Afterwards, a linear reduction in system volume with increasing pressure is again observed. Similarly, the unloading curve shows an extrusion plateau, albeit at a lower extrusion pressure, P_{ex}, than the intrusion pressure, during which water escapes from the ZIF-8 cages.

As shown in Fig. 2c, the strain rate strongly affects the intrusion pressure, which almost triples from 25 MPa during the quasi-static compression to 70 MPa during the high-rate experiment. In contrast, the extrusion pressure experiences a drop with increasing strain rate. This yet-unidentified behaviour substantially increases the hysteresis and hence absorption capacity at the high loading rate compared to the quasi-static behaviour, eventually absorbing 85% of the mechanical energy stored during the intrusion process compared to only 17% at quasi-static conditions. Consequently, the energy absorption density, E_{ab}, is enhanced 17-fold, from roughly $3\,J\,g^{-1}$ under quasi-static compression to roughly $47\,J\,g^{-1}$ under high-rate loading representative of impact events. In contrast to other size-dependent MOF phenomena[24,25], this enhanced absorption density can be obtained with different crystal sizes (Supplementary Figs. 20–21).

To use this promising {ZIF-8 + water} system as a reusable shock absorber, the intruded water molecules should eventually extrude from the framework. Figure 2d presents five consecutive high-rate experiments, which exhibit a consistent performance subject to multiple impact cycles. Since the applied mechanical pressure is not yet high enough to cause structural amorphization[26], the molecular structure of ZIF-8 remains intact, as evidenced from the X-ray diffraction patterns (Supplementary Fig. 4). Figure 2e demonstrates that even when considering 1,000 loading–unloading cycles (at a strain rate of $0.03\,s^{-1}$), the performance reveals only a slight initial drop in the intrusion and extrusion pressure in cyclic loading. Furthermore, Fig. 2e shows that the system can be fully recovered after a 24 h relaxation (that is, with mechanical pressure removed), indicating that all water molecules extrude from ZIF-8 given sufficient relaxation time. To further confirm the material stability and reusability, Supplementary Fig. 18 demonstrates that ZIF-8 is stable after 20 high-rate intrusion–extrusion cycles or after being immersed in water for over a week.

While the water intrusion rate during these experiments as well as its extrusion rate in the low-rate and medium-rate experiments are externally controlled through the displacement rate, the high-rate split-Hopkinson-pressure-bar (SHPB) setup of Fig. 1a leads to a free water extrusion process that represents the performance under realistic impact and reveals the intrinsic timescale of water mobility in ZIF-8. Figure 2c reveals that this intrinsic water extrusion occurs at a much lower rate than its externally driven intrusion process ($10^2\,s^{-1}$ versus $10^3\,s^{-1}$, see also Supplementary Fig. 12), corroborating the earlier observation that some water molecules remain in the structure when the system is not allowed to relax sufficiently between different cycles. High-rate experiments with different loading pulses indicate that water extrusion starts at a higher rate, which then gradually decreases, indicating a higher water mobility when more water is present inside the framework (Supplementary Fig. 13).

Intrinsic water mobility revealed by MD simulations

These experiments unveil a highly interesting mechanism, in which the ZIF-8 energy absorption capacity critically increases with increasing strain rate. While this is expected to be related to the mobility and reorganization of water in the nanocages, it is necessary to understand the nanoscale origin of this phenomenon to fully explore the potential of the rate-dependent intrusion–extrusion performance and generalize it towards other materials. To this end, MD simulations were conducted using a fully flexible and ab initio derived ZIF-8 force field. This force field is validated in the Supplementary Information and complemented by the flexible TIP4P/2005f water model[27], given its agreement with experimental adsorption isotherms[16,28,29].

First, grand canonical Monte Carlo (GCMC) simulations were performed, revealing that water saturation in ZIF-8 is obtained at roughly 80 molecules per unit cell (Supplementary Fig. 23) or, equivalently, roughly 40 molecules per cage, in excellent agreement with previous studies[16,28,29]. Subsequently, snapshots at different water loadings were extracted to start separate canonical Monte Carlo simulations. Figure 3a reveals the distribution of these water molecules in ZIF-8 for the different cross-sections defined in Fig. 3b. At low water loading, distinct crystallographic adsorption sites are detected, which can be compared to the experimental argon adsorption sites by Hobday et al.[30]. For water, the most favourable adsorption sites are located between the four-membered ring (4MR) and 6MR apertures (site Ar-2 in ref. [30]) and near the 4MR apertures (site

NATURE MATERIALS ARTICLES

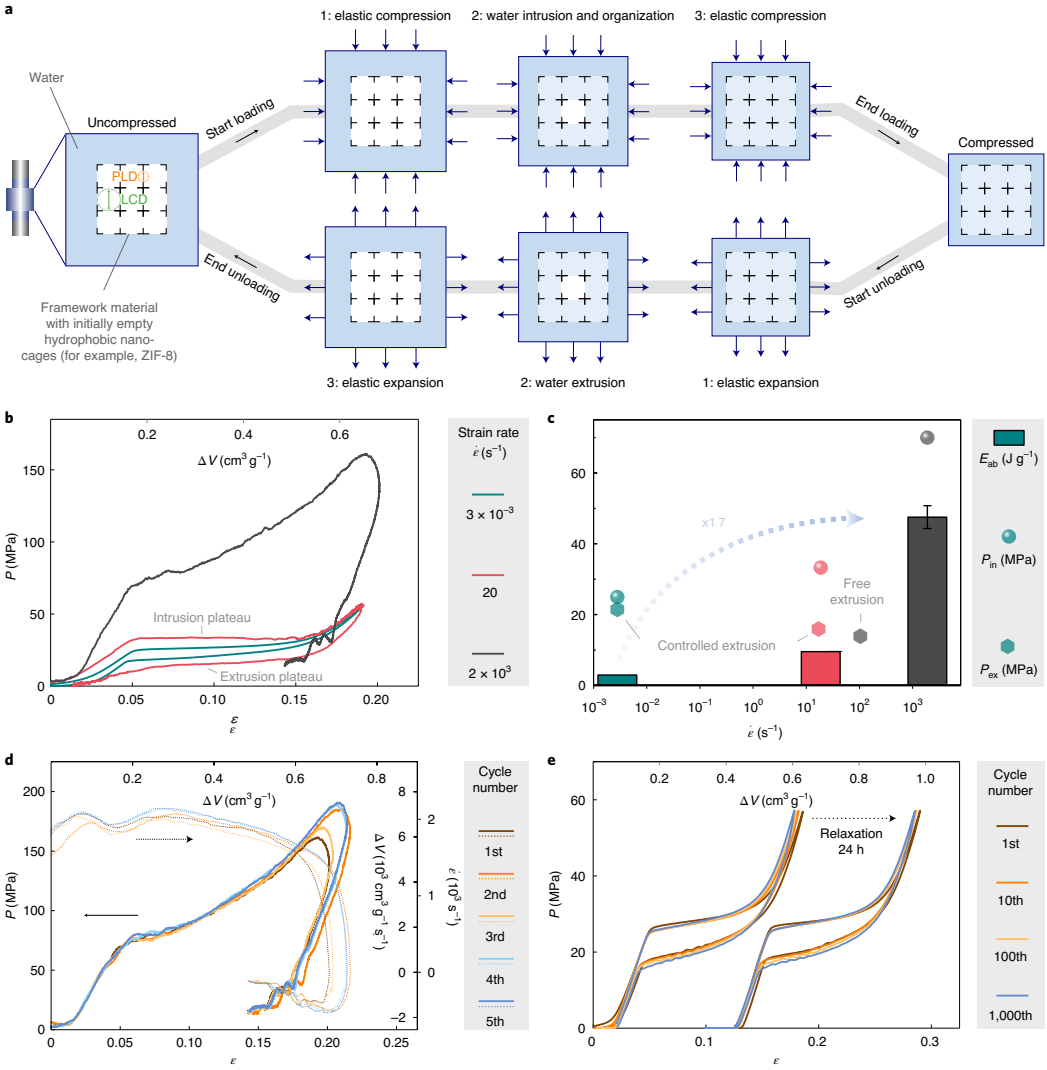

Fig. 2 | Water intrusion and extrusion of ZIF-8 at low-rate, medium-rate and high-rate loading conditions. a, Schematic overview of the different processes during compression (top) and expansion (bottom), including the water intrusion/extrusion processes that give rise to distinct plateaus and indication of the PLD and LCD of the nanoporous material. **b**, Compressive stress–strain curves at three different strain rates corresponding to a specific volume change rate $\Delta\dot{V}$ of 1×10^{-2}, 70 and 7×10^{3} cm^3 g^{-1} s^{-1}, respectively. The unloading part of the high-rate experiment is uncontrolled (that is, without external driving force), so only part of the extrusion plateau can be recorded. **c**, Intrusion pressure, extrusion pressure and energy absorption density under three different loading conditions, plotted as a function of the intrusion and extrusion strain rates measured by the SHPB technique (see also Supplementary Fig. 12). The error bar represents the uncertainty due to the incomplete unloading curve at high strain rate. **d**, Five consecutive high-rate experiments (roughly 6 min interval between each cycle), showing consistent performance against multiple impacts. The small variation in their responses can be attributed to the strain rate history shown as the dashed lines in the graph. **e**, 1,000 intrusion–extrusion cycles at a strain rate of 0.03 s^{-1} (or 0.1 cm^3 g^{-1} s^{-1}), confirming the durability of the system. After 24 h relaxation, during which the sample was kept under no mechanical pressure, another set of 1,000 cycles was recorded. The intrusion–extrusion cycles after relaxation are horizontally offset by a value of 0.12 for clarity.

Ar-4 in ref. [30]). Notably, no water is adsorbed directly inside either the 4MR or 6MR apertures, although the 6MR apertures are the most favourable adsorption sites for argon[30]. At high water loadings, the water molecules agglomerate around the cage centre due to ZIF-8's hydrophobicity, partaking in a hydrogen-bonded cluster that provides more favourable interactions than the ZIF-8 framework.

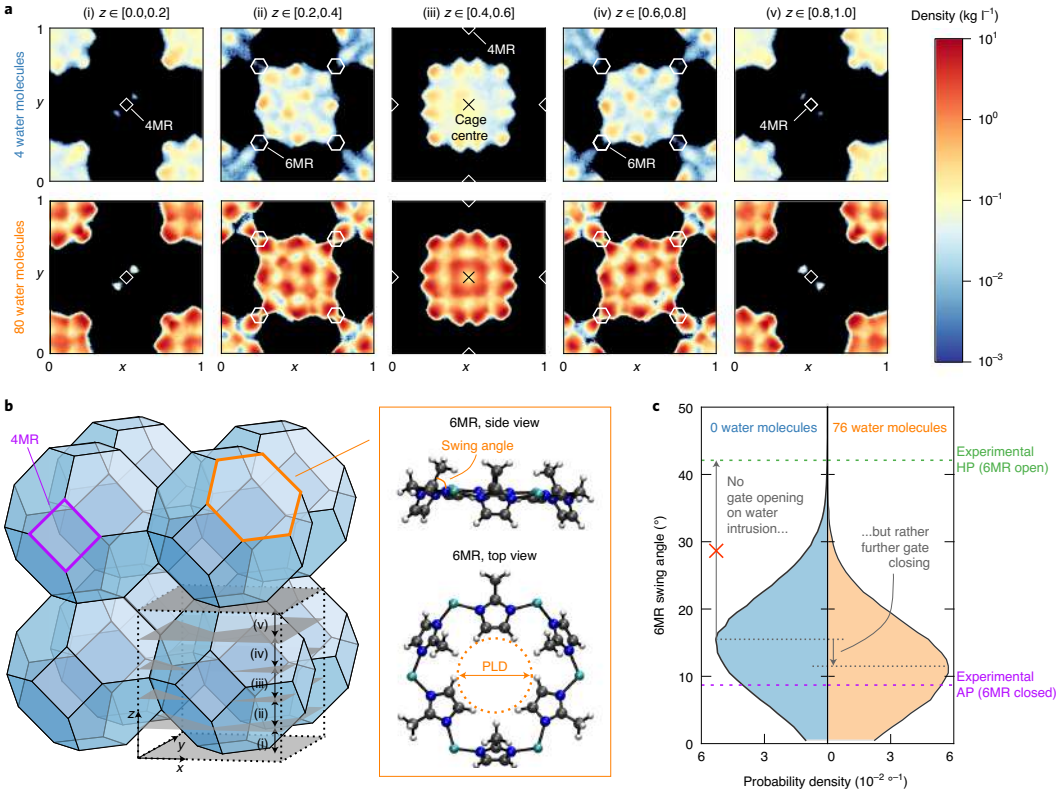

Fig. 3 | Simulated water distribution in ZIF-8 and its effect on gate opening. a, Symmetrized water density from a 2×2×2 ZIF-8 simulation cell as obtained from canonical Monte Carlo simulations at 298 K with either 4 or 80 water molecules per unit cell in the ambient-pressure (AP) phase. The axes are defined in fractional coordinates and the unit cell is sliced in five equal slabs for clarity (**b**). The 4MR and 6MR apertures connecting the cages are denoted by (truncated) diamonds and hexagons, respectively. Other water loadings are shown in Supplementary Figs. 24–26. **b**, The ZIF-8 topology with the cross-sections used for the density plots in **a** as well as the 4MR and 6MR apertures. Atomistic representation of the 6MR aperture, showing in orange the PLD and 6MR swing angle. **c**, Probability density of the 6MR dihedral swing angle of ZIF-8 during a 5 ns MD simulation at 300 K and 0 MPa with either 0 or 76 water molecules per ZIF-8 unit cell. Experimental ambient- and high-pressure (HP) phases are indicated in purple and green, respectively[39]. Swing angle distributions and X-ray diffraction patterns at other water loadings and increased mechanical pressures along with the swing angle distributions obtained through ab initio MD simulations at various temperatures are all shown in Supplementary Figs. 27–37.

Subsequently, 300 K MD simulations of fully flexible ZIF-8 structures were performed, confirming that water avoids the 6MR apertures irrespective of the applied pressure (Supplementary Figs. 38–48). As a result, without a driving force, water molecules seldom hop between ZIF-8 cages. However, an increasing water loading facilitates hopping and hence enables water transport (Supplementary Figs. 49–51). This agrees well with the higher water mobility at the onset of the extrusion experiments, when more water is present in the cages (Supplementary Fig. 13). To understand whether this water mobility can be attributed to structural effects such as gate opening, the swing angle defining the 6MR aperture and the associated PLD (Fig. 3b) are monitored[31]. As shown in Fig. 3c and ref. [23], higher water loadings do not lead to the anticipated gate opening but rather close the 6MR aperture even further.

Fig. 4 | Determining the intrinsic timescale for water mobility in the ZIF-8 nanocages by non-equilibrium MD simulations. a, A 1×1×2 ZIF-8 supercell with four inequivalent cages connected through 6MR apertures. **b**, Evolution of the number of water molecules per cage at 300 K and 0 MPa when starting from 42 water molecules in cage 1 while all other cages are initially empty. The best exponential fit of $a\left(1-e^{-t/\tau}\right)$ to the filling of cage 2 (red line) yields a time constant $\tau \cong 1$ ns (see the statistical analysis in Supplementary Fig. 65). **c**, Visualization of water-filled ZIF-8 structures at five representative points during the simulation; a full water cluster analysis is provided in Supplementary Fig. 87. **d**, Free energy profiles associated with a water molecule transitioning from cage 1, containing a critical-sized water cluster of five additional molecules, to cage 2, initially containing between zero (first transition) and five (sixth transition) water molecules. Results obtained through six independent sets of umbrella sampling (US) simulations using a similar CV (inset) as in ref. [40]. Additional US simulations are reported in Supplementary Figs. 84–85.

NATURE MATERIALS ARTICLES

To mimic water mobility more closely, an inhomogeneous water distribution inside a 1×1×2 supercell of ZIF-8 was created, which only contains 42 water molecules in cage 1, as shown in Fig. 4a. During the MD simulation, this water gradient steers the molecules from cage 1 towards the neighbouring cages 2 and 3 through the 6MR apertures, despite their hydrophobicity (Fig. 4b). After 0.45 ns,

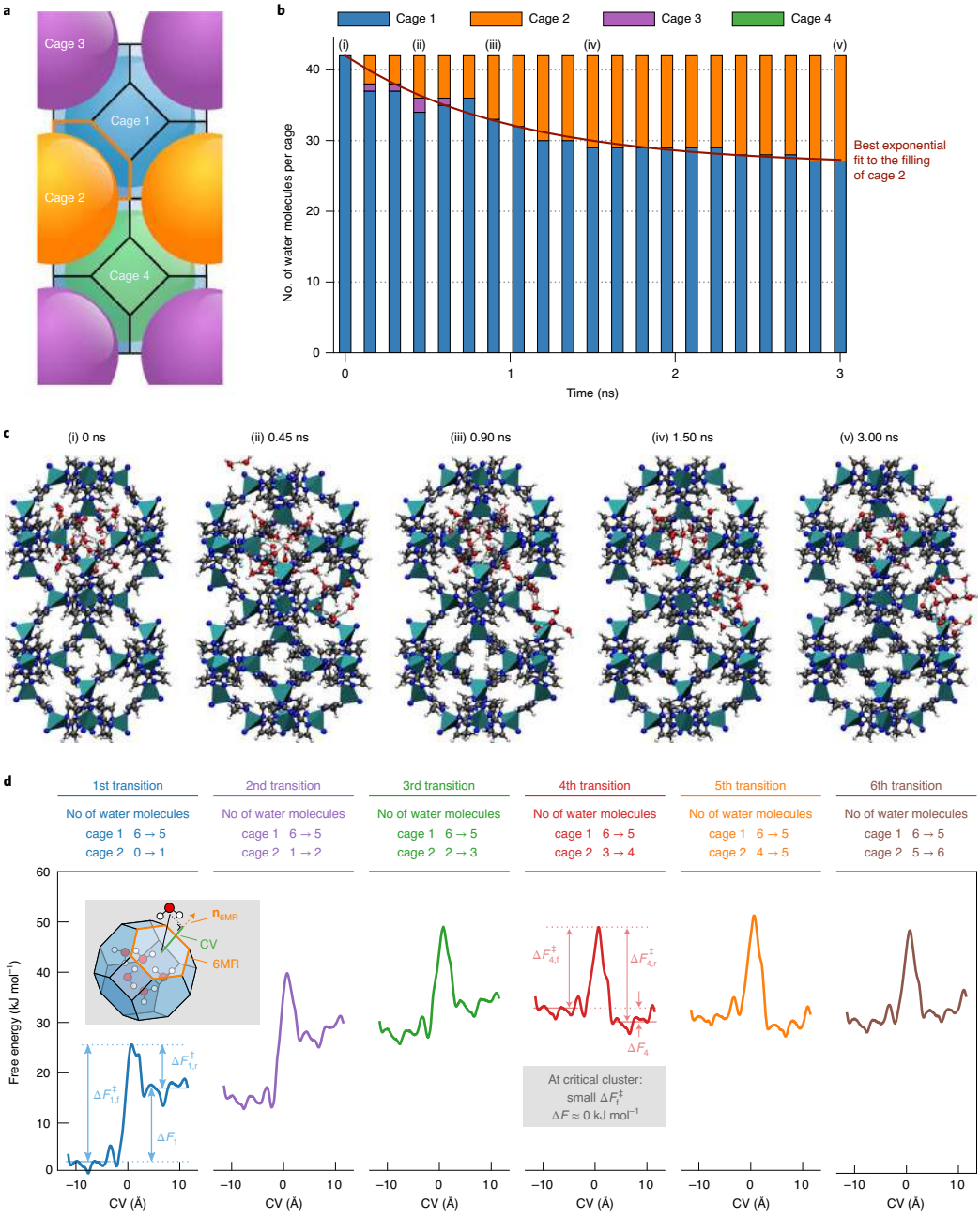

six and two water molecules have diffused to cages 2 and 3, respectively (Fig. 4c(ii)). While the six water molecules in cage 2 form a stable hydrogen-bonded cluster, the two molecules in cage 3 are insufficiently stabilized and diffuse back into cage 1—against the water gradient. The water cluster inside cage 2 continues to grow as the existing cluster facilitates further hopping from cage 1 to 2. An exponential fit to the number of water molecules in cage 2 reveals that this nucleation process occurs on a nanosecond timescale (Fig. 4b), independent of the cages in which the cluster nucleates and the ZIF-8 model size (Supplementary Figs. 63–80).

To further quantify the free energy barrier of the nucleation process, the umbrella sampling free energy profiles associated with a water molecule transitioning from cage 1 to 2 are shown in Fig. 4d and Supplementary Figs. 84–85. Herein, besides the water molecule that undergoes the transition, cage 1 contained a critical-sized cluster of five water molecules while cage 2 contained in between zero and five water molecules. Figure 4d and Supplementary Table 3 indicate that, while the empty cage 2 (collective variable (CV) > 0 Å) is substantially less favourable than cage 1 (CV < 0 Å), with free energy differences ΔF up to 15 kJ mol^{-1}, the transition of additional water molecules is facilitated once a critical-sized cluster of about four water molecules is present in cage 2. Figure 4d therefore confirms that the slow nucleation of such critical-sized water clusters is crucial to facilitate water diffusion through ZIF-8's hydrophobic cages, in agreement with Fig. 4b.

This observation also explains the substantial increase in intrusion pressure and energy absorption density at higher strain rates in Fig. 2c. Since the intrinsic intrusion process is predicted to occur through the nucleation of critical-sized water clusters, the timescale for nucleation can be associated with an intrinsic strain rate (Supplementary Information). If the externally applied strain rate is lower than this intrinsic rate, critical-sized water clusters will spontaneously nucleate in cages neighbouring already filled cages, facilitating the further intrusion process. However, if the strain rate exceeds this intrinsic rate, critical-sized water clusters cannot organize in time and additional work needs to be exerted—through an increased input pressure—to help overcome the free energy barrier of the 6MR aperture. This also indicates that water molecules remaining in the ZIF-8 cages during the extrusion process due to insufficient relaxation will facilitate the subsequent intrusion process and lower the intrusion pressure, as confirmed by Fig. 2e.

Generalization of the rate effect and design rules

The here-established water intrusion mechanism for ZIF-8 suggests that other materials that are constructed from nanocages connected through hydrophobic narrow apertures could also exhibit the rate-dependent water intrusion behaviour. To derive generally applicable design rules, we repeated the water intrusion experiments on a group of hydrophobic ZIFs, namely ZIF-67, ZIF-7, ZIF-9 and ZIF-71 (Supplementary Fig. 1), leading to the energy absorption densities and intrusion pressures shown in Fig. 5a and Supplementary Fig. 14.

Figure 5b,d and Supplementary Fig. 16 demonstrate that ZIF-67 and ZIF-71 exhibit the attractive rate dependence and reusability, confirming the ZIF-8 as proof-of-concept. For ZIF-71, a very high intrusion pressure, exceeding 150 MPa, under a loading rate of roughly 2,000 s^{-1} is expected (Supplementary Fig. 15). However, for ZIF-7 and ZIF-9, water is permanently trapped inside (Fig. 5c). This is probably due to their smaller PLDs, as their hydrophobic apertures are narrower than the size of water molecules[12]. Therefore, ZIF-7 and ZIF-9 can only be reused after evacuating the intruded water molecules by heat treatment to regain the original porosity[12], in contrast to ZIF-8, ZIF-67 and ZIF-71, which can be directly reused to absorb multiple impacts. Finally, the comparison between the structural analogues, ZIF-8 versus ZIF-67 (Fig. 5d) and ZIF-7 versus ZIF-9 (Fig. 5c), suggests that the influence of the chemical moieties is very limited.

On the basis of these experimental observations, four general rules emerge that can be used to design mechanical impact absorbers leveraging the high-rate water intrusion mechanism. First, the material should be hydrophobic. Second, the material should consist of nanocages, that is, LCD > PLD. Third, the apertures connecting the nanocages should be sufficiently large to ensure reusability. On the basis of our experimental observations on ZIF-11 and ZIF-12 (Supplementary Fig. 17), the PLD threshold value is roughly 3 Å for water intrusion systems. Finally, larger nanocages can accommodate larger water clusters and hence increase the energy absorption density at high strain rates.

In Fig. 5e and Supplementary Tables 5–8, the 105 ZIF-like materials tabulated in ref. [32] are tested against these design rules. Figure 5e demonstrates that, besides the here-validated ZIF-8, ZIF-67 and ZIF-71, our design rules identify an additional 17 materials as potential high-performance impact-attenuating materials via the high-rate water intrusion mechanism depicted in Fig. 2a. These design rules can furthermore be generalized to other porous zeolite frameworks, as validated for chabazite in Supplementary Fig. 19.

Contrasting against channel-containing frameworks

To further test our hypothesis that the cage-type structure is essential for the rate-dependent intrusion–extrusion phenomenon of ZIFs (design rule no. 2), we performed water intrusion experiments for several typical channel-containing zeolites, namely ZSM-5, zeolite-β and mordenite (Supplementary Fig. 2). Supporting our hypothesis, Fig. 6a reveals that the rate dependence of their intrusion pressure is considerably weaker than for ZIFs. The same is true for their extrusion pressure, which is always located near the magnitude of the intrusion pressure, leading to a hysteresis area and energy absorption density that are not substantially enhanced by high loading rates (Fig. 6d and Supplementary Figs. 88–90).

Explicitly contrasting ZSM-5 and ZIF-8 in Fig. 6c,d reveals a much higher spontaneous extrusion rate in the former. Furthermore, ZIF-8 exhibits a slight increase of the gradient with the intrusion rate (Fig. 2b), which is absent for ZSM-5 (Fig. 6b). Both observations indicate that the water flow inside channel-containing structures experiences a much lower transport resistance, in agreement with previous reports observing enhanced flow in small channels[33–38]. This suggests the advantage under high-rate mechanical impact of cage-type structures, which can be made into efficient and reusable energy absorbers thanks to the intrinsic nanosecond timescale for water organization, over more frequently used channel-containing structures, which perform as non-linear springs with a very limited rate dependence.

Discussion

Developing efficient impact-attenuating materials is an important societal challenge for a wide variety of applications, with current state-of-the-art energy absorption materials often showing a poor efficiency or recoverability in cyclic loading. Herein, we discovered a promising approach to mitigate mechanical impact under industrially relevant impact conditions and associated high strain rates. We revealed that the energy absorption density associated with the forced intrusion of liquid water in framework materials containing nanocages separated by hydrophobic apertures critically depends on the strain rate. On the basis of this concept, {ZIF + water} systems are effective as high-rate nanofluidic energy absorbers for mitigating mechanical impacts at realistic strain rates of 10^3 s^{-1}.

The ZIF-8 material serves as a proof-of-concept, for which we observed a sharp rise in energy absorption density with elevating strain rates, stemming from the major enhancement of the hysteresis bound by the water intrusion–extrusion curves. The fundamental process underpinning this rate-dependent water intrusion did not depend on the gate-opening mechanism that dominates its gas

NATURE MATERIALS ARTICLES

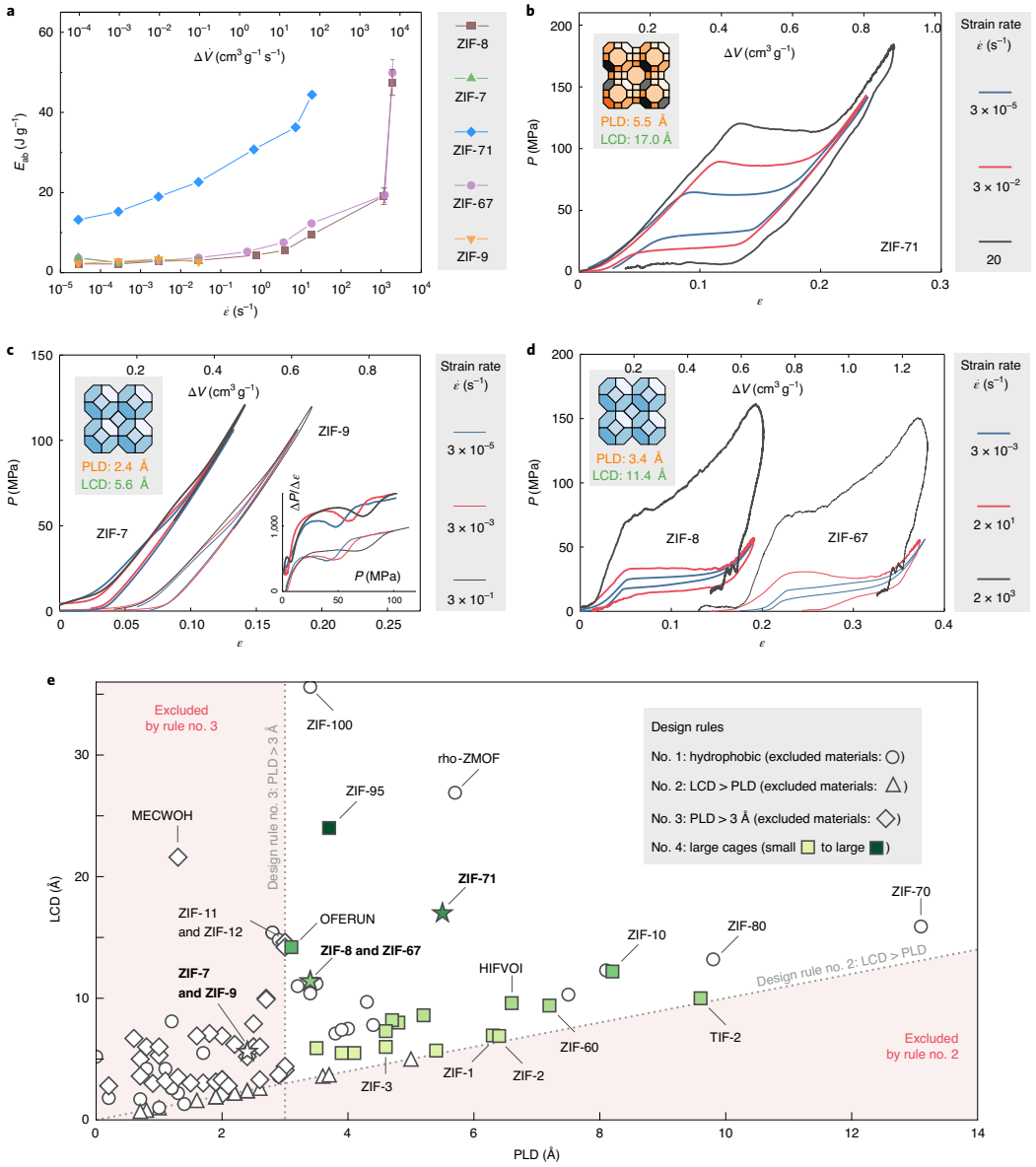

Fig. 5 | Generalization of the design rules. a, Energy absorption densities of various hydrophobic cage-type ZIFs as a function of the strain rate. The error bars represent the uncertainty due to the incomplete unloading curves. **b**, Water intrusion and extrusion of ZIF-71 at three different strain rates, which correspond to a specific volume change rate $\Delta\dot{V}$ of 1×10^{-4}, 1×10^{-1} and 80 cm^3 g^{-1} s^{-1}, respectively. **c**, Water intrusion of ZIF-7 and ZIF-9 at three different strain rates, which correspond to $\Delta\dot{V}$ of 1×10^{-4}, 1×10^{-2} and 1 cm^3 g^{-1} s^{-1}, respectively. Their intrusion pressures, which can be identified from the $\Delta P/\Delta\varepsilon$ during loading process (inset), increase with the strain rate as design rule no. 2 is satisfied, although design rule no. 3 is violated. **d**, Water intrusion and extrusion of ZIF-8 and ZIF-67 at three different strain rates, which correspond to $\Delta\dot{V}$ of 1×10^{-2}, 70 and 7×10^{3} cm^3 g^{-1} s^{-1}, respectively. Plots in **c** and **d** are offset horizontally for clarity. **e**, Materials selection map of the 105 ZIFs tabulated in ref. [32] and Supplementary Tables 5–8 according to their PLD and LCD, showing 20 promising materials fulfilling our design rules (□ to ■); others are either not hydrophobic (as determined by their linkers, shown with circles), not cage-type (triangles) or have too small a PLD (diamonds). Experimentally validated materials are bold-faced (stars).

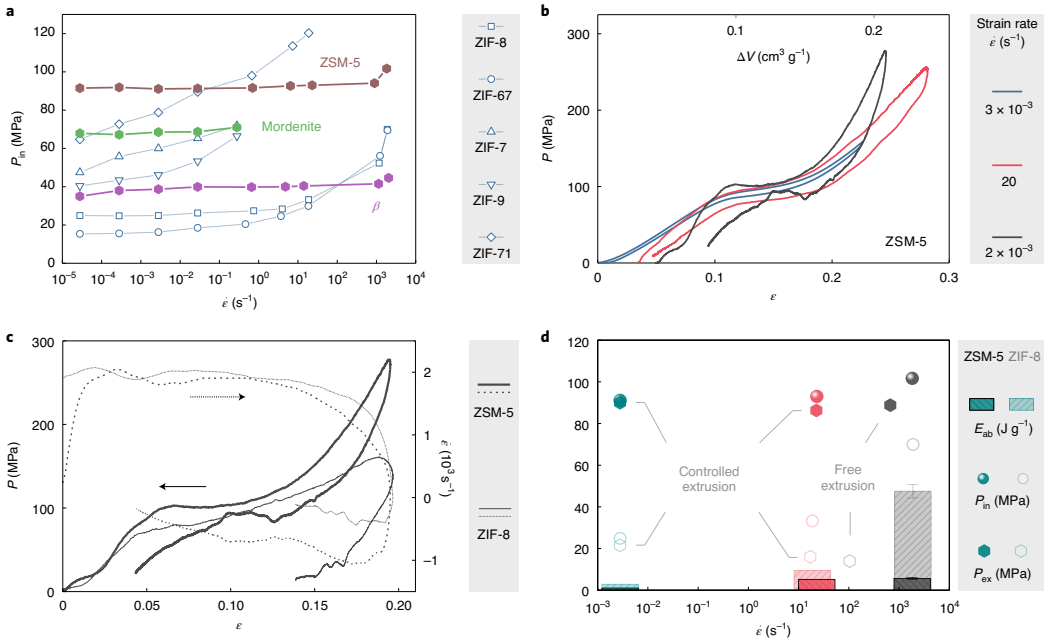

Fig. 6 | Water intrusion and extrusion of channel-containing zeolites at different conditions. a, Water intrusion pressure as a function of strain rate, comparing the behaviour of channel-containing zeolites against cage-type ZIFs. Owing to the limited pore volume of mordenite, its intrusion pressure at higher loading rate is not available. **b**, Water intrusion and extrusion of ZSM-5 at three different strain rates, which correspond to a specific volume change rate $\Delta\dot{V}$ of 2×10^{-3}, 20 and 2×10^{3} cm^3 g^{-1} s^{-1}, respectively. **c**, Comparison between ZIF-8 and ZSM-5 under high-rate deformation. **d**, Intrusion pressure, extrusion pressure and energy absorption density of ZSM-5 (dark colour and filled symbols) at the three different conditions, compared with ZIF-8 (light colour and open symbols). The error bars represent the uncertainty due to the incomplete unloading curves at high strain rates.

adsorption behaviour. Instead, we established that the unique rate dependence is controlled by the intrinsic timescale to form critically sized and stable hydrogen-bonded clusters in the hydrophobic cages, as they facilitate the inefficient water transport through the hydrophobic apertures separating adjacent cages. Because externally controlling the water intrusion beyond this intrinsic timescale requires substantially higher intrusion pressures, we observed a substantial rise in energy absorption density at higher strain rates. We showed that this ZIF-8 proof-of-concept can be generalized to several other cage-type ZIFs, whereas it is absent for channel-containing zeolites. Four design rules were formulated, based on these theoretical and experimental observations, to construct high-rate energy absorption materials, thereby identifying 17 more potential candidate materials. These generally applicable design rules shed light on the synergistic role played by the framework architecture and hydrophobicity during forced water intrusion, which are key to the design and tuning of nanoporous materials such as ZIFs towards practical and reusable impact-attenuating materials.

Online content

Any methods, additional references, Nature Research reporting summaries, source data, extended data, supplementary information, acknowledgements, peer review information; details of author contributions and competing interests; and statements of data and code availability are available at https://doi.org/10.1038/s41563-021-00977-6.

Received: 28 June 2020; Accepted: 3 March 2021;
Published online: 22 April 2021

References

1. Lu, G. & Yu, T. *Energy Absorption of Structures and Materials* (Woodhead, 2003). .
2. Gibson, L. J. & Ashby, M. F. *Cellular Solids: Structure and Properties* 2nd edn (Cambridge Univ. Press, 1997).
3. Clough, E. C. et al. Elastomeric microlattice impact attenuators. *Matter* **1**, 1519–1531 (2019).
4. Fraux, G., Coudert, F. X., Boutin, A. & Fuchs, A. H. Forced intrusion of water and aqueous solutions in microporous materials: from fundamental thermodynamics to energy storage devices. *Chem. Soc. Rev.* **46**, 7421–7437 (2017).
5. Eroshenko, V., Regis, R.-C., Soulard, M. & Patarin, J. Energetics: a new field of applications for hydrophobic zeolites. *J. Am. Chem. Soc.* **123**, 8129–8130 (2001).
6. Tinti, A., Giacomello, A., Grosu, Y. & Casciola, C. M. Intrusion and extrusion of water in hydrophobic nanopores. *Proc. Natl Acad. Sci. USA* **114**, E10266–E10273 (2017).
7. Furukawa, H., Cordova, K. E., O'Keeffe, M. & Yaghi, O. M. The chemistry and applications of metal-organic frameworks. *Science* **341**, 1230444 (2013).
8. Moghadam, P. Z. et al. Development of a Cambridge Structural Database subset: a collection of metal–organic frameworks for past, present, and future. *Chem. Mater.* **29**, 2618–2625 (2017).
9. Ortiz, G., Nouali, H., Marichal, C., Chaplais, G. & Patarin, J. Energetic performances of the metal–organic framework ZIF-8 obtained using high pressure water intrusion–extrusion experiments. *Phys. Chem. Chem. Phys.* **15**, 4888–4891 (2013).
10. Grosu, Y. et al. Stability of zeolitic imidazolate frameworks: effect of forced water intrusion and framework flexibility dynamics. *RSC Adv.* **5**, 89498–89502 (2015).

11. Ortiz, G., Nouali, H., Marichal, C., Chaplais, G. & Patarin, J. L. Energetic performances of 'ZIF-71-aqueous solution' systems: a perfect shock-absorber with water. *J. Phys. Chem. C.* **118**, 21316–21322 (2014).
12. Sun, Y., Li, Y. & Tan, J. C. Liquid intrusion into zeolitic imidazolate framework-7 nanocrystals: exposing the roles of phase transition and gate opening to enable energy absorption applications. *ACS Appl. Mater. Interfaces* **10**, 41831–41838 (2018).
13. Grosu, Y. et al. A highly stable nonhysteretic {Cu_3(tebpz) MOF + water} molecular spring. *Chem. Phys. Chem.* **17**, 3359–3364 (2016).
14. Park, K. S. et al. Exceptional chemical and thermal stability of zeolitic imidazolate frameworks. *Proc. Natl Acad. Sci. USA* **103**, 10186–10191 (2006).
15. Banerjee, R. et al. High-throughput synthesis of zeolitic imidazolate frameworks and application to CO_2 capture. *Science* **319**, 939–943 (2008).
16. Ortiz, A. U., Freitas, A. P., Boutin, A., Fuchs, A. H. & Coudert, F.-X. What makes zeolitic imidazolate frameworks hydrophobic or hydrophilic? The impact of geometry and functionalization on water adsorption. *Phys. Chem. Chem. Phys.* **16**, 9940–9949 (2014).
17. Khay, I. et al. Assessment of the energetic performances of various ZIFs with SOD or RHO topology using high pressure water intrusion-extrusion experiments. *Dalton Trans.* **45**, 4392–4400 (2016).
18. Sun, Y., Li, Y. & Tan, J. C. Framework flexibility of ZIF-8 under liquid intrusion: discovering time-dependent mechanical response and structural relaxation. *Phys. Chem. Chem. Phys.* **20**, 10108–10113 (2018).
19. Lowe, A. et al. Effect of flexibility and nanotriboelectrification on the dynamic reversibility of water intrusion into nanopores: pressure-transmitting fluid with frequency-dependent dissipation capability. *ACS Appl. Mater. Interfaces* **11**, 40842–40849 (2019).
20. Bocquet, L. Nanofluidics coming of age. *Nat. Mater.* **19**, 254–256 (2020).
21. Huang, X. C., Lin, Y. Y., Zhang, J. P. & Chen, X. M. Ligand-directed strategy for zeolite-type metal-organic frameworks: zinc(II) imidazolates with unusual zeolitic topologies. *Angew. Chem. Int. Ed.* **45**, 1557–1559 (2006).
22. Khay, I., Chaplais, G., Nouali, H., Marichal, C. & Patarin, J. Water intrusion–extrusion experiments in ZIF-8: impacts of the shape and particle size on the energetic performances. *RSC Adv.* **5**, 31514–31518 (2015).
23. Fraux, G., Boutin, A., Fuchs, A. H. & Coudert, F.-X. Structure, dynamics, and thermodynamics of intruded electrolytes in ZIF-8. *J. Phys. Chem. C.* **123**, 15589–15598 (2019).
24. Sakata, Y. et al. Shape-memory nanopores induced in coordination frameworks by crystal downsizing. *Science* **339**, 193–196 (2013).
25. Krause, S. et al. The effect of crystallite size on pressure amplification in switchable porous solids. *Nat. Commun.* **9**, 1573 (2018).
26. Bennett, T. D. & Cheetham, A. K. Amorphous metal-organic frameworks. *Acc. Chem. Res.* **47**, 1555–1562 (2014).
27. Gonzalez, M. A. & Abascal, J. L. A flexible model for water based on TIP4P/2005. *J. Chem. Phys.* **135**, 224516 (2011).
28. Ghosh, P., Kim, K. C. & Snurr, R. Q. Modeling water and ammonia adsorption in hydrophobic metal-organic frameworks: single components and mixtures. *J. Phys. Chem. C.* **118**, 1102–1110 (2014).
29. Zhang, H. & Snurr, R. Q. Computational study of water adsorption in the hydrophobic metal-organic framework ZIF-8: adsorption mechanism and acceleration of the simulations. *J. Phys. Chem. C* **121**, 24000–24010 (2017).
30. Hobday, C. L. et al. Understanding the adsorption process in ZIF-8 using high pressure crystallography and computational modelling. *Nat. Commun.* **9**, 1429 (2018).
31. Durholt, J. P., Fraux, G., Coudert, F. X. & Schmid, R. Ab initio derived force fields for zeolitic imidazolate frameworks: MOF-FF for ZIFs. *J. Chem. Theory Comput.* **15**, 2420–2432 (2019).
32. Phan, A. et al. Synthesis, structure, and carbon dioxide capture properties of zeolitic imidazolate frameworks. *Acc. Chem. Res.* **43**, 58–67 (2010).
33. Majumder, M., Chopra, N., Andrews, R. & Hinds, B. J. Enhanced flow in carbon nanotubes. *Nature* **438**, 44 (2005).
34. Holt, J. K. et al. Fast mass transport through sub-2-nanometer carbon nanotubes. *Science* **312**, 1034–1037 (2006).
35. Secchi, E. et al. Massive radius-dependent flow slippage in carbon nanotubes. *Nature* **537**, 210–213 (2016).
36. Radha, B. et al. Molecular transport through capillaries made with atomic-scale precision. *Nature* **538**, 222–225 (2016).
37. Tunuguntla, R. H. et al. Enhanced water permeability and tunable ion selectivity in subnanometer carbon nanotube porins. *Science* **357**, 792–796 (2017).
38. Keerthi, A. et al. Ballistic molecular transport through two-dimensional channels. *Nature* **558**, 420–424 (2018).
39. Moggach, S. A., Bennett, T. D. & Cheetham, A. K. The effect of pressure on ZIF-8: increasing pore size with pressure and the formation of a high-pressure phase at 1.47 GPa. *Angew. Chem. Int. Ed.* **48**, 7087–7089 (2009).
40. Cnudde, P. et al. Light olefin diffusion during the MTO process on H-SAPO-34: a complex interplay of molecular factors. *J. Am. Chem. Soc.* **142**, 6007–6017 (2020).

Methods

Material synthesis and characterization. ZIF-8 was purchased from Aldrich Sigma (Basolite Z1200). Other ZIFs were synthesized using chemical compounds without further purification following the protocols outlined in the Supplementary Information. Zeolites ZSM-5, zeolite-β and mordenite were purchased from Alfa Aesar (45883, 45875, 45877 respectively). All of them were heated at 1,000 °C for 3 h and cooled in air, to obtain higher hydrophobicity before use. The chabazite was obtained from Johnson–Matthey (1318-02-1 22:1 CHA) and was heated at 950 °C for 3 h before use. This heat treatment procedure can increase the Si/Al ratio through dealumination, and therefore has been established as an efficient way to enhance the hydrophobicity of zeolites[41,42]. The effect of different heat treatment conditions on their water intrusion behaviours is shown in Supplementary Fig. 93. Microscopy imaging and X-ray diffraction of the synthesized samples were performed, and results are also shown in the Supplementary Information.

Sample fabrication. The obtained ZIFs and deionized water were combined and sealed in a stainless-steel chamber by precisely fitting sealing rings. As shown in Fig. 1, the thickness of the sample is always 3 mm. In the low-rate Instron experiments and medium-rate hydraulic experiments, we adjusted the diameter of the sample to 6 mm, which includes 25 mg of ZIF material. In the SHPB experiments, we scaled the sample up to 12.7 mm in diameter, which includes 112 mg of ZIF material. As such, the pistons of the sealing chamber have the same diameter as the bars of SHPB, which means they can be impedance matched to avoid reflection of stress waves at the piston-bar interface.

Because of the relatively lower pore volume of zeolites compared to ZIFs, a higher amount of zeolite was used per sample, so that the lengths of water intrusion and extrusion plateaus are comparable to those of the ZIFs. This allows better identification of the corresponding pressures from the pressure–volume curves. Using a different amount of zeolite does not affect our observations, as shown in Supplementary Fig. 92. To fabricate a sample of 6 mm in diameter, we adopted 100 mg for ZSM-5, 50 mg for zeolite-β and 50 mg for mordenite. For the larger sample, 12.7 mm in diameter, we used 448 mg for ZSM-5, 224 mg for zeolite-β and 224 mg for mordenite.

Liquid intrusion experiments. Our liquid intrusion experimental platform is shown in Fig. 1. It is composed of a sealing chamber of the sample (Fig. 1c) and three different mechanical loading apparatus that provide appropriate driving force for water intrusion at different loading rates and allow the corresponding stress–strain measurement. The loading apparatus includes a commercial screw-driven load frame (Instron 5582) for low-rate experiments (up to 0.1 s^{-1}), an in-house hydraulic compression machine for medium-rate experiments (1–10^2 s^{-1}) and the SHPB setup for high-rate experiments (10^3 s^{-1}). By using this experimental platform, pressure–volume change ($P-\Delta V$) curves or stress–strain curves along the water intrusion and extrusion process are obtained over a wide range of strain rates (10^{-5}–10^3 s^{-1}).

The efficacy of the low-rate experimental method has been reported in our recent work[12,18]. We applied a constant crosshead displacement rate, corresponding to a certain strain rate in the sample. Then, at a peak pressure at which water molecules have filled the framework porosity (for example, 56 MPa for ZIF-8), we reversed the crosshead direction to obtain the extrusion behaviour at the same displacement rate. The Instron records the force and displacement history during the loading and unloading cycles.

Medium-rate experiments were conducted on a hydraulic compression machine (Fig. 1b), consisting of a hydraulic actuator, a strain-gauge based force transducer and a pair of linear variable differential transformers (LVDTs) for displacement measurement. An appropriate peak displacement is preset, at which water molecules have filled up the framework porosity. We used the same strain rate for the loading and unloading process, which is controlled by the hydraulic actuator and measured by the displacement signals from the LVDTs.

High-rate experiments were carried out on a SHPB setup driven by a gas gun. In the experiment, the impact of a striker onto the incident bar produces an incident stress wave that propagates through the sample, with a certain amount being reflected, into the transmitted bar. The wave profiles recorded by the strain gauges on the incident and transmitted bars are used to calculate the forces and displacements at the specimen-bar interfaces and hence produce stress–strain curves using standard calculations[43]. The strain rate was also recorded using the reflected wave throughout the loading and unloading process. Stress equilibrium inside the sample during the impact is checked for each experiment, by confirming that the forces at the two interfaces have the same magnitude. All bars, including the piston of the sealing chamber, are made of the same material and have the same diameter, so as to match the impedances. Tungsten is selected as the bar material, to provide sufficient impact energy to drive the water intrusion process and allowing us to obtain experimental data at higher strain rates. Pulse shapers are used to achieve a constant strain rate during the loading process. The unloading process of the sample is uncontrolled, which means that the strain rate during the unloading process is not constant and can be different from that of the loading process. The unloading data were recorded and used to reveal the intrinsic extrusion behaviour of water from the nanoporous framework. This procedure is different from the low- and medium-rate experiments, where the unloading process is still displacement-controlled by the compression head and the unloading rate is set to be the same as the loading rate. Unfortunately, without any driving force, the SHPB technique does not allow us to capture a complete unloading curve, unless extremely long bars are used, which are not available. The uncontrolled free water extrusion process in high-rate experiments represents the performance of {ZIF + water} systems under realistic impact loading conditions, and the difference in the unloading setting for experiments at different strain rates does not affect our discussion on the rate-dependent energy absorption phenomenon (Supplementary Information).

On the basis of the obtained $P-\Delta V$ or stress–strain curves, the intrusion pressure P_{in} is determined as the onset of the intrusion plateau, while the extrusion pressure P_{ex} is determined as the midpoint of the extrusion plateau. For the incomplete extrusion plateaus in high-rate experiments, P_{ex} is taken from the last data point. The plateaus of ZIF-7, ZIF-9 and mordenite are short; therefore, their P_{in} and P_{ex} are determined on the basis of the gradient of the plot. The intrusion and extrusion rates are taken from the value of the selected data point of P_{in} and P_{ex}. The strain rate history during the intrusion and extrusion is perfectly constant in the low-rate experiments but has some oscillations in the medium-rate and high-rate experiments. Energy absorption is defined as the hysteresis area enclosed by the loading and unloading curve, which is a certain percentage of the mechanical energy stored during the loading process.

Periodic ab initio simulations. Here, 0 K density functional theory (DFT) calculations were performed with the Vienna Ab initio Simulation Package (VASP)[44] using the projector-augmented wave method[45]. The computational unit cell contained a total of 276 atoms, 12 of which are zinc atoms. The Perdew–Burke–Ernzerhof (PBE) exchange-correlation functional[46] was combined with the DFT-D3 dispersion scheme using Becke–Johnson damping[47,48]. The recommended GW PBE projector-augmented wave potentials were used for all elements and functionals (v.5.4). For the zinc atoms, the 3*s*, 3*p*, 3*d* and 4*s* electrons were included explicitly. For the carbon and nitrogen atoms, the 2*s* and 2*p* electrons were considered as valence electrons. For the hydrogen atoms, the 1*s* electron was treated as a valence electron. These DFT calculations were performed with a plane-wave kinetic-energy cut-off of 800 eV and using Gaussian smearing with a smearing width of 0.05 eV. Projection operators were evaluated in reciprocal space. A Γ-point *k*-grid was used for all volumes. The real-space fast Fourier transfer grid was used to describe wave vectors up to twice the maximum wave vector present in the basis set. An augmentation grid that is twice as large was used to avoid wrap-around errors to obtain accurate forces. The electronic (ionic) convergence criterion was set to 10^{-9} (10^{-8}) eV. The resulting energy equation of state, reported in Supplementary Fig. 22, was constructed by fixed volume relaxations in which the positions and cell shape were optimized[49]. Subsequently, the dynamical matrix was determined using 0.015 Å displacements for all atomic coordinates with respect to the equilibrium structure.

To probe the influence of temperature on the ZIF-8 swing angle, an additional set of $(N, P, \sigma_a = 0, T)$ ab initio MD simulations[50] was performed at temperatures of 100, 200 and 300 K and at 0 MPa using the CP2K software package[51,52]. In these calculations, the PBE-D3(BJ)[46–48] level of theory was used in combination with Gaussian TZVP-MOLOPT basis sets[53], a plane-wave basis set with a cut-off of 800 Ry and a relative cut-off of 60 Ry, and Goedecker–Teter–Hutter pseudopotentials[54]. The temperature of the simulations was controlled with a Nosé–Hoover chain thermostat consisting of three beads and with a time constant of 0.1 ps (refs. [55–58]). The pressure was controlled with a Martyna–Tobias–Klein barostat with a time constant of 1 ps (refs. [59,60]). These parameters were validated before to correctly capture the flexibility of MOFs[50]. The MD time step was set to 0.5 fs. The total simulation time for the ab initio MD simulations comprised 11 ps, of which the first picosecond was discarded for equilibration.

Force-field derivation. From the dynamical matrix determined above, a flexible and ab initio-based force field for the empty ZIF-8 structure was derived. The covalent part of the force field, which contains diagonal terms that describe bonds, bends, out-of-plane distances and torsion angles as well as cross terms, was derived using the in-house QuickFF software package[61,62]. The Lennard–Jones parameters were obtained from the Dreiding force field[63], whereas the electrostatics were modelled as Coulomb interactions between Gaussian charge distributions[64] with the atomic charges computed using the Minimal Basis Iterative Stockholder partitioning method[65]. More details about the ZIF-8 force-field derivation are provided in the Supplementary Information.

To describe the interactions between the different adsorbed water molecules and between the water molecules and the framework, a Lennard–Jones potential and point-charge electrostatics were used. The water molecules were described with the TIP4P/2005f model[27]. This model was chosen given its agreement with experimental water adsorption isotherms[16,28,29], although the rigid TIP4P/2005 model does underestimate the vapour pressure[66].

Force-field-based Monte Carlo simulations. Canonical Monte Carlo and GCMC simulations were performed using the RASPA2 software package[67] to extract the water density plots in the ZIF-8 framework. To this end, we first performed a series of GCMC simulations at a temperature of 298 K and a water pressure

that varied from 300 Pa to 6.6 kPa over the different simulations, using the Peng–Robinson equation of state to relate the water pressure and the chemical potential[68]. From these GCMC results, the saturation limit was determined and initial {ZIF-8 + water} snapshots were extracted at water loadings of 4, 8, 20, 40, 60 and 80 water molecules. These snapshots were then used as the starting point for separate canonical Monte Carlo simulations, in which the water loading was kept constant and at a temperature of 298 K. In these canonical Monte Carlo simulations, the average density of the centres of mass of the water molecules was averaged over at least 2 million Monte Carlo cycles. The framework structures for the open- and closed-gate configurations of ZIF-8 were obtained from ref. [39] (identifiers TUDHUW and TUDJOS in the Cambridge Crystallographic Database for the ambient- and high-pressure phases, respectively) and the simulations were performed in a 2×2×2 supercell. During these Monte Carlo simulations, the framework and the internal coordinates of the water molecules were kept rigid. The Lennard–Jones interactions were truncated at 12 Å with analytical tail corrections to correct for the finite cut-off. Electrostatic interactions were treated using the Ewald summation method[69].

Force-field-based MD simulations. On the basis of the GCMC determined saturation limit of 80 water molecules per unit cell, 21 initial ZIF-8 structures were generated with 0, 4, 8, …, 80 water molecules per unit cell by varying the chemical potential during the GCMC simulations. To create an inhomogeneous water distribution, the initial structure with 80 water molecules was doubled along one of the crystal axes and all water molecules except for those in one out of four cages were removed (Fig. 4). For each water loading, 11 simulations were run at pressures spaced equally between 0 and 100 MPa.

For each of these structures and pressures, an $(N, P, \sigma_a = 0, T)$ MD simulation[50] has been performed using our in-house developed software code Yaff[70] for a total simulation time of 3 ns (inhomogeneous water distribution) or 5 ns (homogeneous water distribution). Furthermore, for the longer simulations and the larger ZIF-8 models discussed in the Supplementary Information, the Yaff software package was interfaced with LAMMPS to calculate the long-range interactions more efficiently[71]. During these $(N, P, \sigma_a = 0, T)$ MD simulations, the temperature was controlled to be on average 300 K using a Nosé–Hoover chain thermostat consisting of three beads and with a time constant of 0.1 ps (refs. [55–58]). The pressure was controlled with a Martyna–Tobias–Klein barostat with a time constant of 1 ps (refs. [59,60]). The integration time step was limited to 0.5 fs to ensure energy conservation when using the velocity Verlet scheme. The long-range van der Waals interactions were cut off at a radius of 12 Å, which was compensated by tail corrections. The electrostatic interactions were efficiently calculated using an Ewald summation with a real-space cut-off of 12 Å, a splitting parameter α of 0.213 $Å^{-1}$ and a reciprocal space cut-off of 0.32 $Å^{-1}$ (ref. [69]). The snapshots in Fig. 4c were generated using VMD[72], while the PLD and LCDs were calculated with Zeo++ (ref. [73]).

Force-field-based umbrella sampling simulations. To quantify the free energy associated with the hopping of a water molecule from one cage to an adjacent cage in ZIF-8, umbrella sampling simulations were performed using our in-house developed software code Yaff[70,74]. A 2×2×2 ZIF-8 supercell was adopted to avoid potential, spurious interactions between periodic images of the water molecules. From the 16 cages in this supercell, 14 cages were kept empty, leaving only two adjacent cages that were potentially filled, named cage 1 and cage 2. The CV used in these umbrella sampling simulations is based on earlier diffusion work in related zeolite materials and is defined as follows[40]. First, the relative vector between the centroid of the selected water molecule that undergoes the hopping and the centre of the 6MR aperture separating cages 1 and 2 is determined. The CV is then defined as the oriented, perpendicular projection of this relative vector on the outwards normal of this 6MR aperture as observed from cage 1. Hence, CV = 0 Å corresponds to the water molecule being in the 6MR aperture, while CV < 0 Å and CV > 0 Å correspond to the molecule being in cages 1 and 2, respectively.

For each of the 20 different transitions (vide infra), the CV was divided into 47 equidistant windows centred with CV values between −11.5 Å and 11.5 Å. To restrict the simulation to each individual window, a harmonic bias potential at the centres of these equidistant windows was applied with a force constant of 25 kJ mol^{-1} $Å^{-2}$. Each of these umbrella sampling simulations was run for 2.25 ns, including 10 ps of equilibration time. After this, the free energy profile for each of the transitions was obtained from the sampling distribution in each window by the weighted histogram analysis method (WHAM)[75,76]. To prevent the other water molecules from escaping from their respective cages, an additional harmonic bias potential with a force constant of 100 kJ mol^{-1} $Å^{-2}$ was applied to each of those other water molecules whenever the centroid of the molecule was at least at a distance of 9 Å from the respective cage centre; this bias potential disappeared as long as the water molecules remained within a radius of 9 Å from their respective cage centres. This bias was also applied to the water molecule that undergoes the transition, but only when the molecule was sufficiently far from the 6MR aperture and hence sufficiently committed to one cage (|CV| ≥ 3 Å). In this case, the additional spherical bias, which adds to the harmonic bias defined by the umbrella sampling, does not influence the transition through the 6MR aperture that is used in the definition of the CV, but prevents the water molecule from leaving the cage through a different 6MR aperture, similar to the effect of the spherical bias on the spectator water molecules.

The above procedure was followed for 20 different transitions. In the first set of ten transitions, besides the biased water molecule, cage 1 was filled with a critical cluster of five water molecules, while cage 2 was filled with in between zero (first transition) and nine (tenth transition) water molecules. The results of the first six of these simulations are shown in Fig. 4d. In the second set of ten transitions, this procedure was repeated but with a supercritical cluster of 30 molecules instead of a critical cluster of five water molecules in cage 1 to quantify the effect of supersaturation. All results are discussed in Supplementary Figs. 84–85.

Data availability

Source data for the main paper figures are provided with this paper. Additional experimental data generated during the current study are available from the authors upon request. Relevant configurations for the optimizations and MD simulations are available through Zenodo[77]. Additional computational data supporting the results of this work are available from the online GitHub repository at https://github.com/SvenRogge/supporting-info or upon request from the authors.

Code availability

The Yaff software used to perform the MD simulations in this paper is freely accessible via https://molmod.ugent.be/software/yaff. Representative input and processing scripts are available at https://github.com/SvenRogge/supporting-info.

References

41. Sun, Y. et al. Experimental study on energy dissipation characteristics of ZSM-5 zeolite/water system. *Adv. Eng. Mater.* **15**, 740–746 (2013).
42. Sun, Y. et al. A candidate of mechanical energy mitigation system: dynamic and quasi-static behaviors and mechanisms of zeolite β/water system. *Mater. Des.* **66**, 545–551 (2015).
43. Gray, G. T. III Classic split Hopkinson pressure bar testing. *ASM Handb.* **8**, 462–476 (2000).
44. Kresse, G. & Furthmüller, J. Efficient iterative schemes for ab initio total-energy calculations using a plane-wave basis set. *Phys. Rev. B* **54**, 11169–11186 (1996).
45. Kresse, G. & Joubert, D. From ultrasoft pseudopotentials to the projector augmented-wave method. *Phys. Rev. B.* **59**, 1758–1775 (1999).
46. Perdew, J. P., Burke, K. & Ernzerhof, M. Generalized gradient approximation made simple. *Phys. Rev. Lett.* **77**, 3865–3868 (1996).
47. Grimme, S., Antony, J., Ehrlich, S. & Krieg, H. A consistent and accurate ab initio parametrization of density functional dispersion correction (DFT-D) for the 94 elements H-Pu. *J. Chem. Phys.* **132**, 154104 (2010).
48. Grimme, S., Ehrlich, S. & Goerigk, L. Effect of the damping function in dispersion corrected density functional theory. *J. Comput. Chem.* **32**, 1456–1465 (2011).
49. Vanpoucke, D. E. P., Lejaeghere, K., Van Speybroeck, V., Waroquier, M. & Ghysels, A. Mechanical properties from periodic plane wave quantum mechanical codes: the challenge of the flexible nanoporous MIL-47(V) framework. *J. Phys. Chem. C* **119**, 23752–23766 (2015).
50. Rogge, S. M. J. et al. A comparison of barostats for the mechanical characterization of metal-organic frameworks. *J. Chem. Theory Comput.* **11**, 5583–5597 (2015).
51. VandeVondele, J. et al. Quickstep: fast and accurate density functional calculations using a mixed Gaussian and plane waves approach. *Comput. Phys. Commun.* **167**, 103–128 (2005).
52. Hutter, J., Iannuzzi, M., Schiffmann, F. & VandeVondele, J. CP2K: atomistic simulations of condensed matter systems. *Wiley Interdiscip. Rev. Comput. Mol. Sci.* **4**, 15–25 (2014).
53. VandeVondele, J. & Hutter, J. Gaussian basis sets for accurate calculations on molecular systems in gas and condensed phases. *J. Chem. Phys.* **127**, 114105 (2007).
54. Goedecker, S., Teter, M. & Hutter, J. Separable dual-space Gaussian pseudopotentials. *Phys. Rev. B* **54**, 1703–1710 (1996).
55. Nosé, S. A molecular dynamics method for simulations in the canonical ensemble. *Mol. Phys.* **52**, 255–268 (1984).
56. Nosé, S. A unified formulation of the constant temperature molecular dynamics methods. *J. Chem. Phys.* **81**, 511–519 (1984).
57. Hoover, W. G. Canonical dynamics: equilibrium phase-space distributions. *Phys. Rev. A* **31**, 1695–1697 (1985).
58. Martyna, G. J., Klein, M. L. & Tuckerman, M. Nosé–Hoover chains: the canonical ensemble via continuous dynamics. *J. Chem. Phys.* **97**, 2635–2643 (1992).
59. Martyna, G. J., Tobias, D. J. & Klein, M. L. Constant pressure molecular dynamics algorithms. *J. Chem. Phys.* **101**, 4177–4189 (1994).
60. Martyna, G. J., Tuckerman, M. E., Tobias, D. J. & Klein, M. L. Explicit reversible integrators for extended systems dynamics. *Mol. Phys.* **87**, 1117–1157 (1996).

61. Vanduyfhuys, L. et al. Extension of the QuickFF force field protocol for an improved accuracy of structural, vibrational, mechanical and thermal properties of metal-organic frameworks. *J. Comput. Chem.* **39**, 999–1011 (2018).
62. Vanduyfhuys, L. et al. QuickFF: a program for a quick and easy derivation of force fields for metal-organic frameworks from ab initio input. *J. Comput. Chem.* **36**, 1015–1027 (2015).
63. Mayo, S. L., Olafson, B. D. & Goddard, W. A. DREIDING: a generic force field for molecular simulations. *J. Phys. Chem.* **94**, 8897–8909 (1990).
64. Chen, J. & Martínez, T. J. QTPIE: charge transfer with polarization current equalization. A fluctuating charge model with correct asymptotics. *Chem. Phys. Lett.* **438**, 315–320 (2007).
65. Verstraelen, T. et al. Minimal basis iterative stockholder: atoms in molecules for force-field development. *J. Chem. Theory Comput.* **12**, 3894–3912 (2016).
66. Chen, J. L., Xue, B., Mahesh, K. & Siepmann, J. I. Molecular simulations probing the thermophysical properties of homogeneously stretched and bubbly water systems. *J. Chem. Eng. Data* **64**, 3755–3771 (2019).
67. Dubbeldam, D., Calero, S., Ellis, D. E. & Snurr, R. Q. RASPA: molecular simulation software for adsorption and diffusion in flexible nanoporous materials. *Mol. Simul.* **42**, 81–101 (2015).
68. Peng, D.-Y. & Robinson, D. B. A new two-constant equation of state. *Ind. Eng. Chem. Fundam.* **15**, 59–64 (1976).
69. Ewald, P. P. Die Berechnung optischer und elektrostatischer Gitterpotentiale. *Ann. der Phys.* **369**, 253–287 (1921).
70. Yaff, Yet Another Force Field, v.1.4.2 (Center for Molecular Modeling, 2019); http://molmod.github.io/yaff/index.html
71. Plimpton, S. Fast parallel algorithms for short-range molecular dynamics. *J. Comput. Phys.* **117**, 1–19 (1995).
72. Humphrey, W., Dalke, A. & Schulten, K. VMD: visual molecular dynamics. *J. Mol. Graph.* **14**, 33–38 (1996).
73. Willems, T. F., Rycroft, C. H., Kazi, M., Meza, J. C. & Haranczyk, M. Algorithms and tools for high-throughput geometry-based analysis of crystalline porous materials. *Micropor. Mesopor. Mat.* **149**, 134–141 (2012).
74. Torrie, G. M. & Valleau, J. P. Nonphysical sampling distributions in Monte Carlo free-energy estimation: umbrella sampling. *J. Comput. Phys.* **23**, 187–199 (1977).
75. Kumar, S., Rosenberg, J. M., Bouzida, D., Swendsen, R. H. & Kollman, P. A. The weighted histogram analysis method for free-energy calculations on biomolecules. I. The method. *J. Comput. Chem.* **13**, 1011–1021 (1992).
76. Souaille, M. & Roux, B. Extension to the weighted histogram analysis method: combining umbrella sampling with free energy calculations. *Comput. Phys. Commun.* **135**, 40–57 (2001).
77. Rogge, S. M. J. Supporting molecular data for high rate nanofluidic energy absorption in porous zeolitic frameworks. *Zenodo* https://doi.org/10.5281/zenodo.4534252 (2021).

Acknowledgements

Y.S. and J.-C.T. thank the K.C. Wong Fellowship (Y.S.) and the European Research Council (ERC) Consolidator grant (under the grant agreement no. 771575 PROMOFS (J.-C.T.)) for funding the research. Y.S. also thanks the University of Birmingham for startup funds. S.M.J.R., A.L., S.V. and J.W. thank the Fund for Scientific Research Flanders (FWO, grant nos. 12T3519N (S.M.J.R.), 11D2220N (A.L.), 11U1914N (S.V.) and 1103618N (J.W.)) and the Research Board of Ghent University (BOF). Funding was also received from the European Union's Horizon 2020 Research and Innovation Programme (ERC Consolidator grant agreement no. 647755—DYNPOR (2015–2020) (V.V.S.)). We thank the Research Complex at Harwell for access to the materials characterization facilities and T. Johnson at Johnson–Matthey Technology Centre for providing the chabazite material. The computational resources (Stevin Supercomputer Infrastructure) and services used in this work were provided by the VSC (Flemish Supercomputer Centre), funded by Ghent University, the FWO and the Flemish Government—department EWI.

Author contributions

Y.S. conceived and performed all experiments, with guidance from C.R.S. and J.-C.T. S.M.J.R. performed the force-field-based MD simulations. A.L. performed the ab initio and umbrella sampling MD simulations. S.V. performed the GCMC and canonical Monte Carlo simulations. J.W. derived the ZIF-8 covalent force field, all under the guidance of V.V.S. Y.S., S.M.J.R., J.-C.T. and V.V.S wrote the paper with contributions from all authors.

Competing interests

The authors declare no competing interests.

Additional information

Supplementary information The online version contains supplementary material available at https://doi.org/10.1038/s41563-021-00977-6.

Correspondence and requests for materials should be addressed to Y.S., S.M.J.R., V.V.S. or J.-C.T.

Peer review information *Nature Materials* thanks Len Barbour, Joern Ilja Siepmann and Dan Zhao for their contribution to the peer review of this work.

Paper V

Correlating MOF-808 parameters with mixed-matrix membrane (MMM) CO_2 permeation for a more rational MMM design

R. Thür, D. Van Havere, N. Van Velthoven, S. Smolders, A. Lamaire, J. Wieme, V. Van Speybroeck, D. De Vos, I. Vankelecom

Journal of Materials Chemistry A, **2021**, 9 (21), 12782–12796

A. Lamaire performed the GCMC simulations and contributed to the interpretation of the results and the writing of the manuscript.

Journal of Materials Chemistry A

ROYAL SOCIETY OF CHEMISTRY

PAPER

View Article Online
View Journal | View Issue

Cite this: J. Mater. Chem. A, 2021, 9, 12782

Correlating MOF-808 parameters with mixed-matrix membrane (MMM) CO_2 permeation for a more rational MMM development†

Raymond Thür,[a] Daan Van Havere,[a] Niels Van Velthoven,[a] Simon Smolders,[a] Aran Lamaire,[b] Jelle Wieme,[b] Veronique Van Speybroeck,[b] Dirk De Vos[a] and Ivo F. J. Vankelecom *[a]

Consistent structure–performance relationships for the design of MOF (metal–organic framework)-based mixed-matrix membranes (MMMs) for gas separation are currently scarce in MMM literature. An important step in establishing such relationships could be to correlate intrinsic MOF parameters, such as CO_2 uptake and the CO_2 adsorption enthalpy (Q_{st}), with the separation performance indicators of the MMM (*i.e.* separation factor and permeability). Such a study presumes the availability of a platform MOF, which allows systematic comparison of the relevant MOF parameters. MOF-808 can take up the role of such a platform MOF, owing to its unique cluster coordination and subsequent ease of introducing additional functional molecules. For this purpose, formic acid (FA) modulated MOF-808 (MOF–FA) was post-synthetically functionalized with five different ligands (histidine (His), benzoic acid (BA), glycolic acid (GA), lithium sulfate (Li_2SO_4) and trifluoroacetic acid (TFA)) to create a series of isostructural MOFs with varying affinity/diffusivity properties but as constant as possible remaining properties (*e.g.* particles size distribution). CO_2 uptake and CO_2 adsorption enthalpy of the MOFs were determined with CO_2 sorption experiments and Clausius–Clapeyron analysis. These MOF properties were subsequently linked to the CO_2/N_2 separation factor and CO_2 permeability of the corresponding MMM. Unlike what is often assumed in literature, MOF-808 CO_2 uptake proved to be a poor indicator for MMM performance. In contrast, a strong correlation was observed between Q_{st} at high CO_2 loadings on one hand and CO_2 permeability under varying feed conditions on the other hand. Furthermore, correlation coefficients of $Q_{st,15}$ and $Q_{st,30}$ (Q_{st} at 15 and 30 cm^3 (STP) g^{-1}) with the separation factor were significantly better than those calculated for CO_2 uptake. The surprising lack of correlation between membrane performance and CO_2 uptake and the strong correlation with Q_{st} opens possibilities to rationally design MMMs and stresses the need for more fundamental research focused on finding consistent relationships between filler properties and the final membrane performance.

Received 19th October 2020
Accepted 11th May 2021

DOI: 10.1039/d0ta10207e

rsc.li/materials-a

1 Introduction

Mixed-matrix membranes (MMMs) consist of a continuous polymer matrix containing dispersed nanoparticles (so-called fillers).[1,2] While polymeric membranes show good processability but rather moderate gas separation performance,[3,4] purely inorganic membranes can reach high selectivity/permeance combinations due to their particular size sieving abilities or strong affinity for the target component.[5] However, inorganic membranes are often uneconomical to produce as they are brittle, making it challenging to prepare up-scaled membranes with large specific surface.[6] MMMs are believed to profit from the best of both worlds, having improved separation capacity due to nanoparticle addition while maintaining the good film-forming properties of the polymer. Much research has been dedicated in the past 10 years to find better combinations of polymers and MOFs with enhanced performance compared to the state-of-the-art.[2,7–13] A lot of these literature reports focus on the use and modification of conventional MOFs, frequently employing a trial-and-error approach for developing novel MMMs. Although the membrane performance can indeed often be boosted by incorporation of MOFs in terms of higher permeability or gas pair selectivity, the theoretical understanding behind the MMM concept remains rather poor and consistent structure–performance relationships for the

[a]Centre for Membrane Separations, Adsorption, Catalysis and Spectroscopy for Sustainable Solutions (cMACS), KU Leuven, Celestijnenlaan 200F, Box 2454, Heverlee, 3001, Belgium

[b]Center for Molecular Modeling, Ghent University, Tech Lane Ghent Science, Park Campus A, Technologiepark 46, Zwijnaarde, 9052, Belgium. E-mail: ivo.vankelecom@kuleuven.be; Tel: +32 16 32 15 94

† Electronic supplementary information (ESI) available. See DOI: 10.1039/d0ta10207e

View Article Online
Paper Journal of Materials Chemistry A

design of MMMs are currently very scarce.[14,15] A first step towards finding such structure–performance relationships could be the linking of intrinsic MOF parameters to the gas permeation behavior of the MMM (thus determining indicators for the MMM separation performance based on MOF parameters). For example, Seoane and co-workers proposed a method to quantify polymer-MOF compatibility based on the Hansen solubility parameters of MOF and polymer.[1] With respect to the membrane selectivity and permeability, MOF parameters such as pore volume and CO_2 uptake are often identified as key drivers in the ultimate MMM performance, where good MMM separation performance goes hand in hand with high pore volume and CO_2 uptake.[16–21] However, no study has been devoted so far to the systematic correlation between MOF and MMM parameters for a series of isostructural MOFs. This is understandable since such a study presumes the availability of a platform MOF, which allows systematic comparison of the relevant MOF parameters. Furthermore, the overall gas permeation through the MMM is the result of a subtle interplay between polymer and MOF-related factors, which complicates the identification of one-on-one correlations and causalities between parameters.

MOF-808, consisting of the same $Zr_6O_4(OH)_4$ cluster as UiO-66 but linked through six 1,3,5-benzenetricarboxylate (BTC^{3-}) linkers, can take up the role of such a platform MOF since it can be simply modified to change intrinsic MOF properties while preserving the same MOF structure and topology.[10] Next to the six BTC^{3-} linkers occupying the binding sites (at opposing vertices of the cluster), the six equatorial binding sites can theoretically be occupied by up to six modulator or ligand molecules[22] (Fig. 1), which can be easily attached *via* solvent-assisted ligand exchange.[23] As shown in previous work, it is possible to create isostructural MOF-808 derivatives with subtly altered BET surface area, pore volume, CO_2 uptake and CO_2 affinity.[10] Moreover, other appealing features of MOF-808 include its excellent thermal, chemical and mechanical stability, following from the strong interaction of the Zr_6-cluster and the carboxylate ligands, and the easy up-scaling of the synthesis in non-toxic solvents such as water.[24]

In this work, post-synthetic functionalization of MOF-808 was applied to create a series of isostructural MOF-808 with systematically varying characteristics, such as pore volume, surface area, CO_2 uptake and CO_2 adsorption enthalpy (Q_{st}). For this purpose, a single batch of MOF–FA was produced to guarantee a uniform starting material for all functionalizations, hence avoiding differences in MOF morphology or particle size due to batch variations. Five different functional molecules (histidine (His), benzoic acid (BA), glycolic acid (GA), lithium sulfate (Li_2SO_4) and trifluoroacetic acid (TFA)) were selected based on their anticipated interaction with CO_2. The polyimide Matrimid 5218 (Matrimid) was used as polymer matrix as it is regarded as a benchmark polymer for membrane gas separation tests in academic research.[1,25–27] The obtained MOF characteristics were correlated with the MMM performance parameters (CO_2/N_2 separation factor, pure gas permeability (PGP) and mixed-gas permeability) in an attempt to identify the MOF

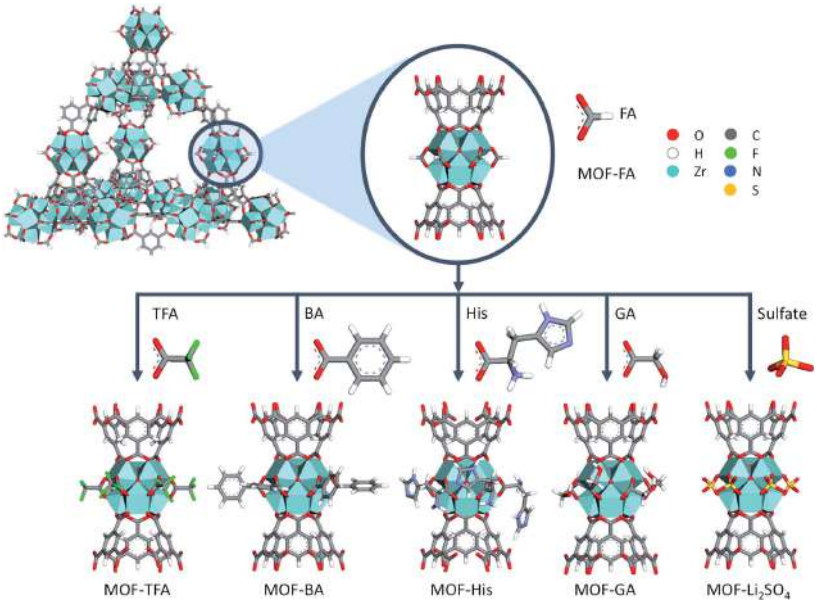

Fig. 1 Overview of MOF-808 functionalization strategy. FA = formic acid, TFA = trifluoroacetic acid, BA = benzoic acid, His = histidine, GA = glycolic acid. For clarity, lithium ions are not shown.

View Article Online
Journal of Materials Chemistry A Paper

parameters that are best suited to use as predictors for the MMM permeation behavior.

2 Experimental and methodology section

2.1 Chemicals

Polyimide (Matrimid 5218) was kindly provided by Huntsman (Switzerland). Sulfuric acid (99.9%), $Li_2SO_4 \cdot H_2O$ (>98.5%), BA (>99.5%), GA (99%) and histidine (L, >99%) were purchased from Sigma-Aldrich. TFA (99%) was acquired from Merck-Schuchardt. FA (99%), tetrahydrofuran (THF, >99%), dimethylsulfoxide (DMSO, 99%) acetone (technical grade) and ethanol (pure) were supplied by Acros. Zirconylchloride octahydrate ($ZrOCl_2 \cdot 8H_2O$) was acquired from Abcr GmbH and BTC from J & K Chemicals. CO_2 (>99.999%) and N_2 (>99.999%) were purchased from Air Liquide and used as delivered.

2.2 MOF synthesis

The different MOF-808 samples are denoted as MOF-*x*, with *x* being the ligand type, *e.g.* MOF-808 functionalized with BA is denoted as MOF–BA. A single batch of MOF–FA was prepared (yield 12.6 g) to prevent differences between samples due to batch variations. All functionalized MOFs were synthesized using MOF–FA as starting material.

2.2.1 Synthesis of MOF–FA. The MOF synthesis recipe used in previous work[10] was adapted for using FA as modulator and subsequently scaled up. 5.08 g (24.2 mmol) BTC and 23.4 g (72.8 mmol) $ZrOCl_2 \cdot 8H_2O$ were dissolved in 182 mL H_2O in a 500 mL round-bottom flask. Subsequently, 26.8 mL FA (712 mmol) was added and the mixture was thoroughly stirred for 15 min. The reaction mixture was then heated to 100 °C under reflux for 5 h in an oil bath. The formed MOF sludge was transferred into Falcon tubes and washed with distilled water (30 mL). After 8 h, the MOF samples were centrifuged (4000 rpm, 30 min) and the supernatant was decanted. This was repeated 4 times with distilled water and 3 times with ethanol. After the last washing step, a clean, white powder (12.6 g) was obtained by drying in a vacuum oven at 70 °C overnight.

2.2.2 Synthesis of MOF–BA. MOF–BA was functionalized according to the method developed by Baek *et al.*[28] 250 mg of MOF–FA was suspended in a 50 mL DMSO solution with 1.12 g (9.251 mmol) BA in a 100 mL Schott bottle. The bottle was then placed in an oil bath at 100 °C under constant stirring. After 24 h, the reaction was stopped and the reaction mixture poured into Falcon tubes and washed with DMSO (3 times, 30 mL) and acetone (3 times, 30 mL), similar to the washing procedure of MOF–FA. After washing, the MOF was dried at 70 °C and stored for further use.

2.2.3 Synthesis of MOF–His, MOF–TFA and MOF–GA. MOF–FA (250 mg) was suspended in a 50 mL aqueous solution of 0.005 mol ligand (0.78 g histidine, 0.57 g TFA, 0.38 g GA) in a 100 mL Schott bottle. The bottle was placed on a stirring plate for 24 h at room temperature. Afterwards, the functionalized MOFs were washed 3 times with water and 3 times with acetone, similar to the washing procedure of MOF–FA. Finally, the MOFs were dried at 70 °C and stored for further use.

2.2.4 Synthesis of MOF–Li_2SO_4. An aqueous solution of sulfuric acid (0.1 M, 50 mL) was prepared in a 100 mL Schott bottle by mixing 0.268 mL sulfuric acid with 49.732 mL water, in which 250 mg of MOF–FA was suspended to form MOF–SO_4. The mixture was stirred for 24 h at room temperature. Next, MOF–SO_4 was washed with water and acetone, dried and re-suspended in a 50 mL aqueous solution containing 0.64 g (0.005 mol) $Li_2SO_4 \cdot H_2O$ for 24 h under continuous stirring. The resulting MOF was washed with water (3 times) and with acetone (3 times), dried at 70 °C and stored for further use.

2.3 Membrane synthesis

The different Matrimid MMMs are denoted as MMM-*x*, with *x* being the ligand type. For example, the Matrimid MMM containing MOF–TFA is denoted as MMM–TFA.

2.3.1 Preparation of pristine Matrimid membranes. Matrimid membranes were prepared by dissolving 0.42 g of polymer in 5.58 g THF. After stirring overnight, the polymer solution was poured into a Teflon Petri dish (d = 6 cm) in a nitrogen bag. Evaporation of the solvent was slowed down by placing a plastic funnel over the Petri dish. Once the membrane had solidified due to solvent evaporation, the polymer film was removed from the Petri dish and annealed in a muffle oven by heating from room temperature to 110 °C at 5 °C min^{-1}. The membrane remained at this temperature for 2 h. Next, the membrane was heated at 5 °C min^{-1} to 180 °C for 6 h. Subsequently, the membranes were allowed to cool down naturally.

2.3.2 Mixed-matrix membrane synthesis. 10 wt% MMMs were prepared by dispersing 0.047 g of dried MOF in 5.58 g THF. The dispersion was then thoroughly sonicated for 15 min. Following an adapted priming protocol,[20] 0.42 g polymer was added to the dispersion in three steps (0.14 g per turn). All samples were continuously stirred on a magnetic stirring plate. Before and after polymer addition, the samples were sonicated for 15 min. After the final polymer addition, the polymer/MOF dispersion was stirred overnight and cast into a Petri dish (d = 6 cm) in a nitrogen bag. Evaporation of the solvent was slowed down by placing a plastic funnel over the Petri dish. Once the membrane had solidified due to solvent evaporation, the polymer film was removed from the Petri dish and annealed in a muffle oven by heating from room temperature to 110 °C at 5 °C min^{-1}. The membrane remained at this temperature for 2 h. Next, the membrane was heated at 5 °C min^{-1} to 180 °C for 6 h. The membranes were finally allowed to cool down naturally. Filler loading was determined with the following equation:

$$\text{Filler loading (wt\%)} = 100 \times \left(\frac{m_{\text{filler}}}{m_{\text{filler}} + m_{\text{polymer}}}\right) \quad (1)$$

with m_{filler} and m_{polymer} the weight of the filler and polymer, respectively.

2.4 Characterization

2.4.1 X-ray diffraction. MOF crystallinity was analyzed with X-ray diffraction (XRD). XRD diffractograms were measured by

View Article Online
Paper Journal of Materials Chemistry A

a Malvern PANanlytical Empyrean diffractometer in transmission mode over a 1.3–45° 2θ range. A PIXcel3D solid-state detector and Cu anode (Cu Kα1: 1.5406 Å; Cu Kα2: 1.5444 Å) were used for detection and X-ray generation.

2.4.2 Nuclear magnetic resonance. Proton and fluorine nuclear magnetic resonance (^{1}H and ^{19}F NMR) measurements were carried out to determine the average number of functionalizer molecules per Zr_6 cluster. First, 3 mg MOF-808 was dispersed in 600 μL deuterated DMSO. Next, 25 μL of a 40 wt% hydrofluoric acid (HF) solution was added for MOF digestion. For ^{19}F NMR, 10 μL fluorobenzene was added to the mixture as an internal standard. NMR spectra were recorded on a Bruker AMX-300 spectrometer at 300 MHz for ^{1}H NMR and at 400 MHz for ^{19}F NMR (16 scans). A recycle delay time of 30 s was applied for ^{19}F NMR. The output was analyzed with SpinWorks 4.2 software.

2.4.3 Scanning electron microscopy. Particle morphology was examined with scanning electron microscopy (SEM, Philips XL30 FEG). To avoid sample charging, all samples were coated with a layer of gold/palladium. Particle size distribution was analyzed with ImageJ and statistical analysis (one-way ANOVA) to determine whether differences in size occurred between the MOFs.

2.4.4 Attenuated total reflectance-Fourier transform infrared spectroscopy. Attenuated total reflectance-Fourier transform infrared spectroscopy (ATR-FTIR) measurements on MOF and MMM samples were conducted to identify functional groups. All samples were dried prior to the measurement. A Varian 670 FTIR imaging spectrometer was used, containing a diamond ATR crystal and a Single Point MCT detector. 32 scans were recorded at a resolution of 2 cm^{-1}.

2.4.5 N_2 and CO_2 physisorption. N_2 and CO_2 physisorption experiments were performed with a Micromeritics 3Flex surface analyzer. Prior to the measurement, all MOFs were activated under vacuum at 100 °C for 16 h. N_2 physisorption was conducted at −196 °C. Surface areas were calculated *via* the multipoint BET method applied to the isotherm adsorption branch, taking into account surface area criteria as given by Rouquerol[29] and the consistency criteria described by Walton and Snurr.[30] CO_2 sorption was measured at three different temperatures (273 K, 293 K, 313 K) to allow determination of the CO_2 Q_{st} of the different MOFs with the Clausius–Clapeyron equation (eqn (2)):[31]

$$\frac{\partial \ln(p)}{\partial\left(\frac{1}{T}\right)} = \frac{-Q_{st}}{R} \tag{2}$$

with p the equilibrium pressure (mbar), T the temperature (K), R the universal gas constant (J mol^{-1} K^{-1}).

The sorption data were first fitted with the dual-site Langmuir model (eqn (3)):[31]

$$N = N_{m,A} \times \frac{b_A \times p}{1 + b_A \times p} + N_{m,B} \times \frac{b_B \times p}{1 + b_B \times p} \tag{3}$$

with N the amount of adsorbed gas (cm^3 (STP) g^{-1}), $N_{m,A}$ and $N_{m,B}$ the amount of adsorbed gas at saturation for sorption site A and B respectively (cm^3 (STP) g^{-1}), b_A and b_B the adsorption equilibrium constants for respectively sorption site A and B and p the pressure (mbar).

The Clausius–Clapeyron data points were then interpolated based on the fit values. Next, for a range of different CO_2 loadings, Q_{st} can be calculated from the slope of a $\ln(p)$ *vs.* $1/T$ plot, according to eqn (2).

2.4.6 Membrane gas sorption. Sorption of N_2 and CO_2 was measured at 30 °C up to pressures of 15 bar for all membranes. A Rubotherm series IsoSORP© instrument was used to conduct the measurements. First, helium pycnometry was carried out on all membranes to determine the membrane weight and volume. The additional weight resulting from gas sorption in the membrane over time was determined with a magnetically suspended balance. The buoyancy of the measurement gases was taken into account to calculate the correct weight of the sample (eqn (4)):

$$m_{corrected} = m_{measured} + \rho_{gas} \times V_{sample} \tag{4}$$

with $m_{corrected}$ the corrected weight (g), $m_{measured}$ the measured weight (g), ρ_{gas} the measuring gas density (g cm^{-3}) and V_{sample} the sample volume (cm^3).

The N_2 and CO_2 solubility in the membranes can be calculated with eqn (5):

$$S = \frac{C}{p} \tag{5}$$

with S the gas solubility (cm^3 (STP) cm^{-3} cmHg), C the quantity of adsorbed gas (cm^3 (STP) cm^{-3}) and p the pressure (cmHg).

2.4.7 Grand canonical Monte Carlo (GCMC) simulation of CO_2 adsorption behavior in MOF-808. The input structures for the GCMC simulations were obtained by optimizing the primitive unit cell of the different MOF-808 structures using CP2K.[32] The optimizations were performed at the PBE-D3(BJ)[33–35] level of theory, combined with Gaussian TZVP-MOLOPT[36] basis sets, a plane wave basis set with a cut-off of 800 Ry and a relative cut-off of 60 Ry, and Goedecker–Teter–Hutter (GTH) pseudopotentials,[37] allowing for a relaxation of both the atomic positions and the unit cell. The GCMC simulations were performed with RASPA,[38] using a fixed framework and rigid CO_2 and N_2 adsorbate molecules described by the TraPPE force field.[39] The atomic framework charges were derived from cluster calculations using the Minimal Basis Iterative Stockholder (MBIS) partitioning scheme[40] (see ESI† for more details), while the Lennard-Jones interaction parameters are taken from the DREIDING model[41] (except for zirconium, which was taken from UFF).[42,43] The temperature was set to 300 K. Each GCMC simulation consists of 10^7 cycles, with equal probabilities for translation, rotation, and (re)insertion moves. The first 10^5 cycles are regarded as equilibration steps and are not taken into account in any analysis.

The CO_2 enthalpy of adsorption can be determined from the GCMC simulations using eqn (6):

$$\Delta H_{ads} = \frac{\langle UN\rangle_\mu - \langle U\rangle_\mu \langle N\rangle_\mu}{\langle N^2\rangle_\mu - \langle N\rangle_\mu^2} - \langle U_{host}\rangle - \langle U_{guest}\rangle - k_B T \tag{6}$$

with U the total energy of the host framework and the adsorbed molecules, N the number of adsorbed molecules, $\langle U_{host}\rangle$ the average energy of the adsorbent, $\langle U_{guest}\rangle$ the average energy of the adsorbate molecule in the gas phase, k_B the Boltzmann constant, and T the absolute temperature.

$\langle\ldots\rangle_\mu$ denotes an average in the grand-canonical ensemble. As the host framework and the adsorbed molecules are described as rigid molecular systems, $\langle U_{host}\rangle = \langle U_{guest}\rangle = 0$.

The mixed-gas CO_2/N_2 selectivities of MOF–FA and MOF–TFA were determined from a separate set of GCMC simulations in which both CO_2 and N_2 molecules can be inserted or deleted. The mole fractions were set to 0.5, so that the selectivity can be calculated from the ratio of the number of adsorbed CO_2 molecules to the number of adsorbed N_2 molecules.

2.4.8 Gas permeation. Our in-house developed high-throughput gas separation set-up (HTGS) was used to examine the gas permeation behavior of the synthesized membranes. A detailed set-up description is given elsewhere.[44–46] HTGS allows simultaneous pure gas and mixed-gas testing of 16 membrane coupons at varying membrane temperatures and feed pressures. The active membrane area is 1.91 cm^2. CO_2 pure gas permeability and the CO_2/N_2 mixed-gas permeability and separation factor were measured for all membranes.

CO_2/N_2 mixed-gas separation factors (α^*) were measured by a GC analysis of the permeate composition. The ratio of the feed and permeate mole fraction of CO_2 and N_2 then renders the separation factor (eqn (7)):

$$\alpha^*_{CO_2/N_2} = \frac{y_{CO_2}/y_{N_2}}{x_{CO_2}/x_{N_2}} \quad (7)$$

where y_{CO_2} and y_{N_2} are the mole fractions of CO_2 and N_2 in the permeate, x_{CO_2} and x_{N_2} the mole fractions of gas CO_2 and N_2 in the feed. The ratio y_{CO_2}/y_{N_2} is determined from chromatogram peak areas of the permeate, while x_{CO_2}/x_{N_2} is determined by the feed settings.

Determination of the pure gas and mixed-gas permeabilities of CO_2 and N_2 was performed with a constant-volume–varying-pressure method. A pressure sensor (MKS Baratron) measures the change in pressure in a 75 cm^3 measuring cylinder while permeate gas is accumulated in the cylinder. The change in pressure as a function of time (dp/dt) is then used to calculated the permeability P (Barrer) with eqn (8). For pure gas measurements, the mole fraction of the gas in permeate and feed is 1.

$$P_{CO_2} = 10^{10} \times \frac{y_{CO_2} \times V \times V_m \times L}{x_{CO_2} \times p_{up} \times A \times R \times T} \times \frac{dp}{dt} \quad (8)$$

with P_i the gas permeability (Barrer), y_i the mole fraction of the component in the permeate, x_i the mole fraction of the component in the feed, V the downstream volume (cm^3), V_m the molar volume (22.414 L mol^{-1}), A the membrane permeation area (1.91 cm^2), L the membrane thickness (μm), T the operating temperature (K), p_{up} the upstream pressure (bar), R the gas constant (0.082 L atm mol^{-1} K^{-1}) and dp/dt the pressure increase (torr s^{-1}).

3 Results and discussion

3.1 Characterization of MOFs and membranes

Functionalization of the starting material MOF–FA does not change the crystal structure of the MOF since all its functionalized derivatives show a high degree of crystallinity (Fig. S1†), in good agreement with literature.[10,23,28] The variation in relative intensity between the large diffraction peak at 4.3° and the two smaller peaks at 8.3° and 8.7° can be attributed to the varying pore filling of the different MOFs.[47–49] Furthermore, post-synthetic functionalization does not affect the particle size nor morphology as confirmed by SEM (Fig. S2†). All MOFs have the same, lumped octahedral shape and a uniform, average MOF size of around 350 nm, originating from the starting material. A one-way analysis of variance (ANOVA) suggested no statistical difference in particle size between the MOFs (Tables S1 and S2†).

ATR-FTIR was used to further confirm the presence of the different ligands in the MOFs (Fig. 2). In all spectra, peaks situated at 453 cm^{-1} (Zr-μ_3-OH stretch) and 660 cm^{-1} (Zr-μ_3-O stretch) are associated with the Zr-oxide cluster.[20] Likewise, clearly distinguishable peaks are observed at 760 cm^{-1}, 1385 cm^{-1}, 1572 cm^{-1} and 1620 cm^{-1}, corresponding to vibrations of the BTC linker.[50] No signal was found between 1715–1750 cm^{-1}, which corresponds with the C=O stretch of uncoordinated ligands or BTC, hence indicating that the MOF pores do not contain physisorbed ligands.[50] Specific peaks belonging to the ligand were found for all samples. Additional bands for MOF–His are visible at 822 cm^{-1} and 1067 cm^{-1},

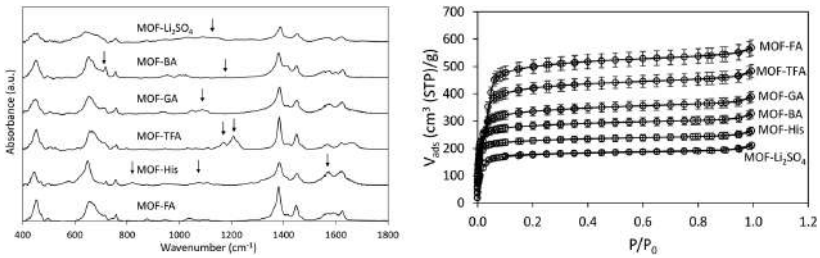

Fig. 2 ATR-FTIR spectrum (left) and N_2 adsorption isotherms at 77 K (right) of all MOFs.

View Article Online
Paper Journal of Materials Chemistry A

resulting from mixed $-NH_3^+$ and –CH bending. Together with the higher relative absorbance of the signal at 1574 cm^{-1} ($-NH_3^+$ deformation), these absorptions suggests that histidine is present in its (partially) protonated form.[51–53] Specific absorption bands for MOF–TFA were recorded at 1170 and 1208 cm^{-1}, attributed to –CF symmetrical and anti-symmetrical stretch, respectively.[10] Signals for MOF–BA and MOF–GA were less pronounced as their characteristic bands mostly coincide with linker peaks. For MOF–BA, the signal at 718 cm^{-1} has a higher absorbance (associated with an increased out-of-plane –CH stretching of the benzene ring) while a new peak occurs at 1178 cm^{-1} (–CH bending ring).[54] MOF–GA shows a weak signal increase at 1000–1075 cm^{-1} (C–O stretch) but, most importantly, a broad signal at 3300 cm^{-1} due to –OH stretch (from GA, ethanol or water).[52] Finally, an enhanced absorbance intensity in the 900–1200 cm^{-1} region has previously been associated with effective SO_4 functionalization of MOF-808.[55]

Further confirmation of successful post-synthetic functionalization was performed with ^1H NMR and ^{19}F NMR (Fig. S4†). A higher ligand loading on the cluster was detected in the following order: MOF–TFA = MOF–His (3.3) > MOF–BA (3.2) > MOF–GA (2.3) > MOF–FA (2.2), as can be seen in Table 1. The difference in loading seems to roughly increase with decreasing pK_a of the carboxylic acid functional group (in water): TFA (0.23) > His (1.78) > GA (3.83) ~ FA (3.75).[56,57] A lower pK_a results in a larger concentration of deprotonated ligand at equal pH and thus a higher probability of incorporation in the MOF framework. MOF–BA deviates from this trend as it has the highest pK_a (4.20) but, at the same time, a loading of 3.2 BA per Zr_6 cluster. Due to the limited solubility of BA in water, BA functionalization took place in DMSO, whereas the other functionalizations were water-based, making it difficult to draw conclusions with regard to BA. None of the functional ligands had a cluster loading equal to the theoretical maximum of six, indicating that the remaining vacant sites were occupied by other charge compensating moieties (*i.e.* $-OH^-$, $-Cl^-$).[28]

CO_2 and N_2 physisorption experiments were conducted to determine characteristic MOF-808 parameters, such as pore volume and diameter, BET value and CO_2 uptake (Table 1). N_2 adsorption isotherms are given in Fig. 2. Substantial differences in BET surface area and pore volume exist between the functionalized MOFs. For the starting material MOF–FA, BET and pore volume correspond well with literature.[10,24,58] The BET surface area, pore volume and pore diameter (Fig. S5†) all decrease with increasing size of the ligand (MOF–TFA > MOF–GA > MOF–BA > MOF–His). Although Li_2SO_4 is considerably smaller in size than histidine and BA, MOF–Li_2SO_4 denotes the lowest BET and pore volume measured. As MOF–Li_2SO_4 retained its crystalline structure after functionalization, the low BET and pore volume suggest that the MOF pores might be partially blocked by salt deposition.

Furthermore, functionalization strongly affects the CO_2 uptake of the different MOFs as well (Fig. S6†). At 1000 mbar and 273 K, the MOF–FA starting material displays the highest uptake (65.9 cm^3 (STP) g^{-1}), indicating that functionalization reduced the uptake capacity of the MOFs. The CO_2 uptake follows a decreasing trend from MOF–FA > MOF–His > MOF–TFA > MOF–GA > MOF–BA > MOF–Li_2SO_4. However, only small differences in uptake (ranging from 48.1–55.2 cm^3 (STP) g^{-1}) are observed between the functionalized MOFs, except for MOF–Li_2SO_4, which loses more than 40% of uptake capacity compared to MOF–FA, further pointing towards the deposition of Li_2SO_4, blocking adsorption sites.[59] Besides the total CO_2 uptake capacity of the MOF, the initial slope of the CO_2 adsorption isotherm in the low-pressure region also reveals qualitative information about the MOF CO_2-philicity as it is governed by the sorption equilibrium constant (*b*-value).[60–63] Hence, adsorption in this pressure region is expected to correlate primarily with the MOF–CO_2 binding strength rather than with the specific surface area or pore volume. The slope in the lower pressure region (0–100 mbar, Fig. S7†) increases in the order MOF–BA < MOF–Li_2SO_4 < MOF–GA < MOF–FA ≈ MOF–His < MOF–TFA, which was further confirmed by the *b*-values obtained from the dual-site Langmuir model (Table S3†). The observed trends in CO_2 uptake and initial slope (*b*-value) indicate that MOF–TFA has the highest affinity for CO_2, although this is eventually not reflected in the highest total CO_2 uptake since the MOF starting material (*i.e.* MOF–FA) can adsorb up to 28% more CO_2. While this observation seems to contradict at first sight, it can be explained by the larger pore volume and surface area of MOF–FA. Furthermore, an almost linear CO_2 adsorption isotherm is observed for MOF–BA in the low-pressure region, which has previously been associated with a lack of high-affinity bindings sites in the MOF.[63,64] At higher pressures, the difference between the isotherms of the other MOFs is less pronounced (Fig. S6†).

Table 1 Average number of ligand molecules per Zr_6 cluster, pore volume (cm^3), pore diameter (Å), BET value (m^2 g^{-1}) and CO_2 uptake (cm^3 (STP) g^{-1}) at 273 K and 1000 mbar for all MOFs

	Ligands per Zr_6 cluster[a]	Pore volume (cm^3)	Pore diameter (Å)	BET value (m^2 g^{-1})	CO_2 uptake[b] (cm^3 (STP) g^{-1})
MOF–FA	2.2	0.76	18.4	2304	65.9
MOF–TFA	3.3	0.68	17.7	1946	51.2
MOF–GA	2.3	0.55	15.6	1421	50.9
MOF–BA	3.2	0.46	13.8	1119	48.1
MOF–His	3.4	0.37	10.9	901	55.2
MOF–Li_2SO_4	—	0.28	15.6	727	37.2

[a] As determined by NMR. [b] At 273 K and 1000 mbar.

View Article Online
Journal of Materials Chemistry A Paper

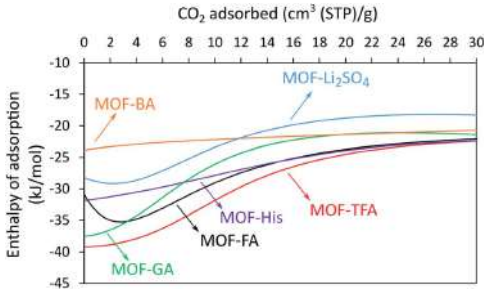

Fig. 3 Experimental CO_2 adsorption enthalpies as a function of CO_2 loading for all MOFs.

To obtain a more accurate and quantitative measure of the effect of functionalization on the MOF CO_2 affinity, the loading-dependent CO_2 Q_{st} was calculated for each MOF with the Clausius–Clapeyron method based on a dual-site Langmuir model (Fig. 3). Table S4† gives the MOF Q_{st} values at different loadings. At zero coverage, the diverse functionalizations result in a difference of ~15 kJ mol^{-1} between the highest Q_{st} (MOF–TFA, 39.2 kJ mol^{-1}) and the lowest Q_{st} (MOF–BA, 23.9 kJ mol^{-1}). The curve of the graphs of MOF–FA, MOF–TFA, MOF–GA, MOF–Li_2SO_4 and (to a lesser extent) MOF–His all display a substantial Q_{st} reduction with increasing coverage. Comparable behavior has been associated with the saturation of high-affinity gas binding sites inside the MOF.[65,66] The minima in Q_{st} observed for MOF–FA and MOF–Li_2SO_4 are believed to be an artefact of the model's limited number of temperature data points. For the higher coverages, the Q_{st} appears to approach a pseudo-constant value of roughly 21–22 kJ mol^{-1}, with only small differences in the adsorption enthalpy between the MOFs, corresponding with the occupation of the low-affinity adsorption sites in the isostructural MOFs.[66] The change in Q_{st} of MOF–BA remains rather limited, suggesting a larger binding site homogeneity (as was also concluded from the CO_2 adsorption isotherm). CO_2 Q_{st} values in this work are comparable to the Q_{st} values reported in literature for similar MOFs. Plonka *et al.* found a Q_{st} of 32 kJ mol^{-1} for FA modulated MOF-808, well in line with our findings.[67] Very similar values were reported for perfluoroalkane functionalized NU-1000 (which contains the same Zr_6 cluster as MOF-808) with $Q_{st,0}$ between 20 and 34 kJ mol^{-1} while the pristine NU-1000 gave a CO_2 $Q_{st,0}$ of 17 kJ mol^{-1}.[66,68] For UiO-66, CO_2 adsorption enthalpies at zero coverage vary between 26 and 38 kJ mol^{-1}, depending on the type of functionalization.[69,70] The highest Q_{st} in this work was noted for MOF–TFA over the entire range of CO_2 loading.

SEM cross-sections of the MMMs show that the different MOFs are homogeneously incorporated in the polymer matrix, without noticeable differences between the samples (Fig. S12 and S13†). TGA measurements revealed that thermal stability of the membranes after incorporation of the MOF remained at the same level for all MOFs (Fig. S14†). In addition, all MMMs contained between 8 and 10 wt% MOF. An enhanced T_g was observed for all MMMs compared to the unfilled Matrimid membrane (T_g = 312 °C), indicating polymer rigidification at the polymer/particle interphase to a certain extent (Fig. S15†). Only small variations in T_g can be observed between the MMMs, suggesting a very similar degree of polymer rigidification for the different MMMs. All MMMs have a T_g between 320 and 322 °C with an exception of MMM–FA (T_g = 324 °C). This is most probably a result of the slightly higher weight percentage of MOF–FA in the membrane as can be observed from TGA data. Finally, N_2 and CO_2 sorption were measured for all membranes (Fig. 4) and the corresponding solubility values were calculated in Table S5.† With increasing pressure, CO_2 sorption in the membranes clearly increases from Matrimid < MMM–GA < MMM–His < MMM–BA < MMM–FA < MMM–Li_2SO_4 < MMM–TFA. On the other hand, the N_2 sorption data are more difficult to analyze as only small differences between the samples can be

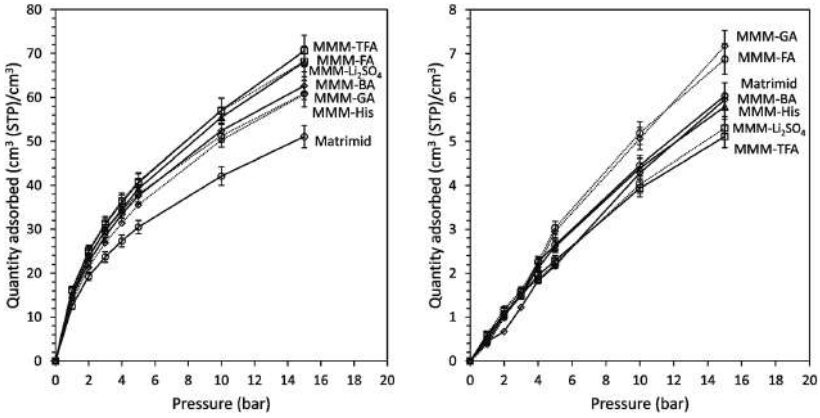

Fig. 4 CO_2 (left) and N_2 (right) sorption in the Matrimid reference membrane and all MMMs.

View Article Online
Paper Journal of Materials Chemistry A

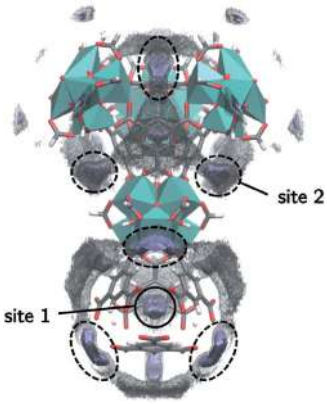

Fig. 5 Two isosurfaces of the density of MOF–FA from GCMC simulations at 2 bar. The high density isosurface of sites 1 and 2 is shown in iceblue and a lower density isosurface is shown to encapsulate the metal cluster.

noticed. In general, a strong improvement in solubility selectivity is observed for FA, BA, TFA and Li_2SO_4 functionalized MOF-808 compared to the pristine Matrimid membrane while MOF–GA and MOF–His only modestly affect the CO_2/N_2 solubility selectivity. At 5 bar, the highest solubility selectivities are measured for MOF–TFA (17.8) and MOF–Li_2SO_4 (18.4), which represent an 54% and 59% increase compared to Matrimid, respectively.

3.2 Computational MOF characterization

GCMC simulations were applied on MOF–FA and MOF–TFA to acquire the MOF CO_2 adsorption sites, adsorption enthalpy and mixed-gas CO_2/N_2 adsorption selectivity. Additionally, the CO_2 adsorption isotherms were simulated and are available in Fig. S9.†

The adsorption densities of the CO_2 molecules at different pressure for MOF–FA are displayed in Fig. 6, in which the primitive unit cell was expanded to the conventional cubic cell for ease of interpretation (Fig. S10†). At low pressures, the CO_2 molecules are primarily located within the cages formed by the four benzene rings of the linker, yielding a square grid of adsorption sites when viewing MOF-808 along the *c*-axis (marked as site 1 in Fig. 5 and 6). A second type of adsorption

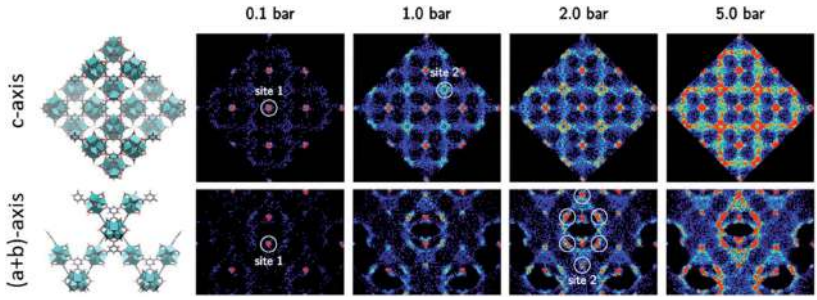

Fig. 6 Density of the adsorbed CO_2 molecules in MOF–FA at 300 K projected on a plane orthogonal to the c-axis and the (*a* + *b*)-axis of the conventional unit cell. The CO_2 molecules are represented by the positions of the carbon atoms.

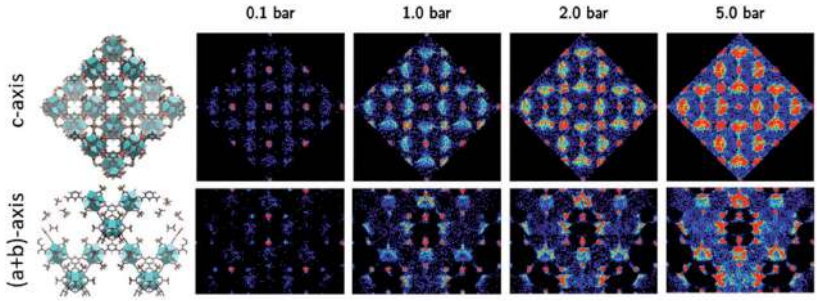

Fig. 7 Density of the adsorbed CO_2 molecules in MOF–TFA at 300 K projected on a plane orthogonal to the *c*-axis and the (*a* + *b*)-axis of the conventional unit cell. The CO_2 molecules are represented by the positions of the carbon atoms.

View Article Online
Journal of Materials Chemistry A Paper

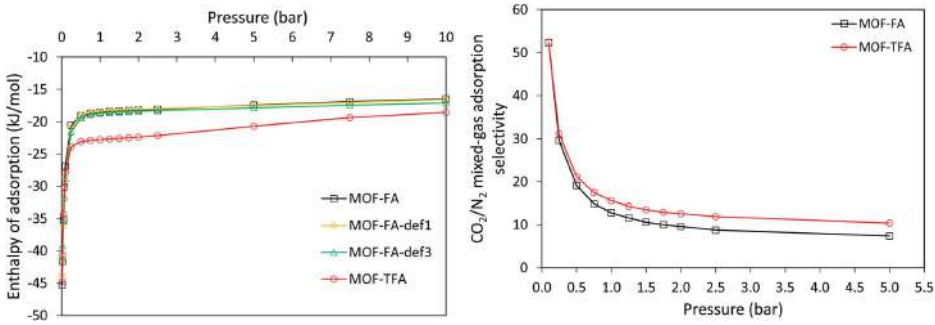

Fig. 8 Simulated CO_2 adsorption enthalpies for MOF–FA, MOF–TFA and MOF–FA with 1 and 3 defects, respectively (left). Simulated mixed-gas adsorption CO_2/N_2 selectivities for MOF–FA and MOF–TFA (right).

sites that gain importance with increasing pressure are located in between the zirconium clusters, covering the open sides of the linkers (marked as site 2 in Fig. 5 and 6).[67] At higher pressures, the linkers eventually become fully encapsulated by CO_2 with increasing pressure.

Although the adsorption sites for MOF–TFA are similar, the filling pattern is different due to the presence of the TFA functional groups, which results in a higher degree of localization of the adsorbed CO_2 molecules (Fig. 7). After filling the tetragonal cages at the lowest pressures, the CO_2 molecules further adsorb onto the linkers. In contrast to MOF–FA, the adsorption sites located above the benzene rings of the linkers are also significantly occupied for mid-range pressures, implying that the surrounding TFA functionalizations enhance the adsorption energy of these sites (more negative adsorption enthalpy).

This is also confirmed by the calculated enthalpies of CO_2 adsorption for both MOFs (Fig. 8, also Table S6†). At the lowest pressures, the enthalpy of adsorption is completely dominated by the host–adsorbate interaction. Initially, the enthalpy values for MOF–FA and MOF–TFA are hence very similar as CO_2 first adsorbs in the tetragonal cages (site 1). Once adsorption sites on the linker molecules (site 2) become relevant, MOF–TFA shows significantly lower adsorption enthalpies (stronger host–adsorbate interaction), in good agreement with the experimentally determined isosteric CO_2 adsorption enthalpy. A more moderate difference is observed at higher pressures as the adsorbate–adsorbate interactions also start to contribute to the adsorption enthalpy. Eventually, this is reflected in higher mixed-gas CO_2/N_2 selectivities for MOF–TFA, confirming the experimental trends. Finally, the influence of open metal site defects (*i.e.* as a result of missing modulators) on the enthalpy of adsorption was also investigated for MOF–FA, by creation of a MOF–FA structure with 1 defect (MOF–FA-def1) and 3 defects (MOF–FA-def3), respectively (Fig. S11 and Table S6†). As can be seen in Fig. 8, no difference in CO_2 adsorption enthalpy is observed between MOF–FA and MOF–FA-def1 while the CO_2 adsorption enthalpy of MOF–FA-def3 is slightly lower than that of MOF–FA but still significantly higher than the adsorption enthalpy of MOF–TFA, indicating that the sole effect of defects on the CO_2 adsorption is rather limited in MOF–FA.

3.3 Gas permeation

CO_2 permeability of the mixed-gas experiments with 15%/85% v/v and 50%/50% v/v CO_2/N_2 feed compositions and of the CO_2 pure gas experiment is given in Fig. 9. All MMMs show a significantly higher CO_2 permeability for all feed compositions compared to the pristine Matrimid membrane, owing to the incorporation of

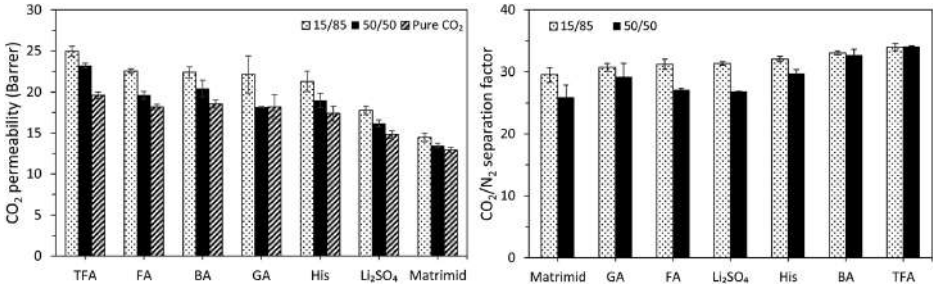

Fig. 9 CO_2 permeability (left) and CO_2/N_2 separation factor (right) for the 15%/85% v/v and 50%/50% v/v mixed-gas CO_2/N_2 experiment and the CO_2 pure gas experiment of all membranes. Gas filtrations were performed at 30 °C and 5 bar feed pressure. All MMMs contain 10 wt% MOF.

View Article Online
Paper Journal of Materials Chemistry A

Table 2 Correlation coefficients between MOF-808 parameters (CO_2 uptake at 50 and 1000 mbar and Q_{st} at a coverage of 0, 15, 30 cm^3 (STP) g^{-1}) and the corresponding MMM parameters (α^* at 15%/85% v/v and 50%/50% v/v CO_2/N_2 feed, and CO_2 permeabilities for 15%/85% v/v and 50%/50% v/v CO_2/N_2 feed and the pure CO_2 feed ($P_{100/0}$)). Strong correlations are indicated in bold and weak correlations in italics. Intermediate correlations have no special markings

	CO_2 uptake (50 mbar)	CO_2 uptake (1000 mbar)	BET surface area	Pore volume	$Q_{st,0}$	$Q_{st,15}$	$Q_{st,30}$
$\alpha^*_{15/85}$	*0.079*	*0.053*	*0.123*	*0.173*	*0.056*	0.414	*0.291*
$\alpha^*_{50/50}$	*0.010*	*0.106*	*0.126*	*0.230*	*0.222*	0.368	0.423
$P_{15/85}$	0.431	0.658	0.722	**0.800**	0.513	0.756	**0.834**
$P_{50/50}$	0.532	0.558	0.681	0.733	0.473	**0.844**	0.793
$P_{100/0}$	0.352	0.665	0.622	0.716	0.433	0.715	**0.866**

the MOF.[71,72] For the 15%/85% v/v CO_2/N_2, the 50%/50% v/v CO_2/N_2 and the pure CO_2 data, respectively, the smallest permeability increase was observed for MMM–Li_2SO_4 (+23%, +20%, +15%) while the most substantial increase was recorded for MMMs containing MOF–TFA (+52%, +72%, +72%) as a result of a substantially increased CO_2 solubility upon incorporation of the TFA functionalized MOF (+33%). The low MMM–Li_2SO_4 permeability can be linked to the above-mentioned pore blockage by Li_2SO_4 deposition. Furthermore, a similar trend can be seen for the various feed conditions with the CO_2 permeability increasing in the order Matrimid < MMM–Li_2SO_4 < MMM–His ≈ MMM–GA ≈ MMM–BA ≈ MMM–FA < MMM–TFA. Finally, the CO_2 permeability is reduced when the CO_2 content in the feed is increased from 15% to 50% and eventually to 100%. A similar trend was observed for UiO-66-NH_2 MMMs based on various fluorinated polyimides.[11,19,73] These observations are in line with the dual-mode sorption model, which predicts saturation of polymer excess free volume elements at elevated CO_2 pressure, resulting in a lowered CO_2 solubility.[74,75]

The CO_2/N_2 separation factors of Matrimid (Fig. 9) for the 15%/85% v/v (29.5) and the 50%/50% v/v feed (25.9) are similar to literature.[76,77] In general, incorporation of the functionalized MOFs leads to a small enhancement in CO_2/N_2 separation factor for both feed mixtures compared to the pristine Matrimid membrane, but only small differences can be noticed between the MMMs. DSC measurements confirmed a similar increase in T_g for all MMMs. This indicates a certain (and similar) degree of polymer rigidification at the polymer/particle interface, thus (partially) explaining the elevated MMM separation factor. In addition, since no differences in particle morphology or particle size were observed with SEM (all MOFs were synthesized starting from the same MOF–FA batch), it is reasonable to assume that polymer rigidification is comparable for all MMMs. Similar to the permeability measurements, MOF–TFA causes the largest improvement of the separation factor of all MOFs, while MOF–GA, MOF–Li_2SO_4 and MOF–FA do not significantly affect the 15%/85% v/v and 50%/50% v/v separation factor. Functionalization with TFA (+9%, +25%) results in the best performance (compared to MMM–FA), which can be explained by the improved CO_2/N_2 selectivity for MOF–TFA (as was confirmed by the GCMC simulations) and the resulting increasing in solubility selectivity for MMM–TFA. As mentioned earlier, it is believed that the strongly polarized C–F bonds in MOF–TFA and the consequent higher CO_2 affinity are at the base of the good separation factor for MMM–TFA.[10] This was confirmed by both experimental and simulated CO_2 adsorption enthalpies, which were significantly lower (stronger MOF–CO_2 interaction) upon functionalization with TFA and eventually resulted in an enhanced CO_2/N_2 mixed-gas adsorption selectivity for MOF–TFA compared to MOF–FA (Fig. 8). For the BA functionalized MOF, MMM–BA probably profits from enhanced π–π interaction between phenyl groups at the MOF surface and aromatic moieties of the polymer chains, which has previously been reported to improve polymer–MOF compatibility and, as a result, the separation factor.[78] It can be hypothesized that a higher CO_2 Q_{st} might lead to a higher selectivity for the MMM based on MOF–TFA, but observations for MOF–BA (with the lowest $Q_{st,0}$ but second highest α^*) contradict this. Finally, a lowered CO_2/N_2 selectivity for the 50%/50% v/v feed is expected based on the dual-sorption model as the N_2 partial pressure is reduced (higher N_2 permeability), while the CO_2 partial pressure is enhanced (lower CO_2 permeability).[75]

3.4 Correlation of MOF parameters with membrane CO_2 permeation

Overall, the effect of ligand type on the MMM CO_2 permeability and CO_2/N_2 separation factor strongly varies when compared to the MOF–FA starting material. Only functionalization with TFA and Li_2SO_4 causes the MMM permeability to change significantly while improved separation factors with respect to MOF–FA are only observed for BA and TFA functionalization. To quantify the relationship between the examined MOF properties and the MMM permeation behavior, correlation coefficients between these parameters have been calculated in Table 2. Results were interpreted based on statistic guidelines defined by Ross *et al.*[79] Correlation coefficients lower than 0.30 are considered as weak correlations, between 0.30 and 0.80 as moderate and higher than 0.80 as strong.

The conventional MOF parameters (BET surface area and pore volume) display a moderate linear correlation with the obtained permeabilities. This seems reasonable, owing to the positive relationship between gas diffusivity and MMM free volume.[75] In addition, a weak correlation is observed between these parameters and the CO_2/N_2 separation factor. Unexpectedly, also CO_2 uptake in both the low (at 50 mbar) and high (at 1000 mbar) pressure region correlates very poorly with both separation factors, while only moderate correlations were noted

View Article Online
Journal of Materials Chemistry A Paper

with permeability in 15%/85%, 50%/50% v/v and pure CO_2 feed. This strongly contrasts with literature, where a high CO_2 uptake is very frequently used to explain MMM permeation observations.[27,80] The correlation of Q_{st} on one hand with CO_2 permeability and CO_2/N_2 separation factor on the other hand is less straightforward to interpret. The adsorption enthalpy at zero coverage ($Q_{st,0}$) shows moderate correlation with the CO_2 permeabilities, comparable to the CO_2 uptake values. Similarly, only weak correlations are observed for $Q_{st,0}$ and the different separation factors. Interestingly, strong correlations are observed between $Q_{st,15}$ and $Q_{st,30}$ on one hand and $P_{15/85}$, $P_{50/50}$ and $P_{100/0}$ on the other hand while correlation coefficients of $Q_{st,15}$ and $Q_{st,30}$ with the $\alpha^*_{15/85}$ and $\alpha^*_{50/50}$ are higher than for CO_2 uptake but are still considered only moderate. As such, Q_{st} can be considered as the most effective predictor for MMM CO_2 permeability amongst all MOF parameters.

A possible explanation for the difference in correlation strength of the Q_{st} at low loading and the ones at high loading might be found in the existence of mobile and immobile gas species in the membrane.[81] $Q_{st,0}$ represents the adsorption enthalpy of the high affinity sorption sites in the MOF and can possibly be linked to the tetragonal cages, which are the primary CO_2 sorption sites (marked as site 1 in Fig. 6 and 7) at very low CO_2 pressure. These sites correspond with highly negative CO_2 adsorption enthalpies (very strong MOF–CO_2 interaction) and the highest CO_2/N_2 mixed-gas adsorption selectivity values observed (up to 60, Fig. 8). Moreover, they are present in both MOF–FA and MOF–TFA (and, by extension, in all functionalized MOF-808 samples), explaining the very similar enthalpy and selectivity values for both MOFs at low CO_2 pressures. At relatively higher CO_2 pressures (starting from 0.25 bar in Fig. 8), the GCMC simulations show substantial differences in adsorption enthalpy and CO_2/N_2 adsorption selectivities between MOF–FA and MOF–TFA caused by the increased influence of the second type of adsorption sites (marked as site 2 in Fig. 6 and 7). It can thus be hypothesized that these sites (partially) immobilize gas molecules through (too) strong binding interaction[26] and thus do not (or to a lesser extent) contribute to gas permeation through the membrane. Although this hypothesis should be proven by performing time-lag experiments, it would explain the observed difference in correlation coefficients for $Q_{st,0}$ and $Q_{st,30}$.[81]

As the overall gas permeability through the MMM is a net result of both MOF and polymer properties and their mutual interactions, it is not unexpected that none of the MOF parameters can predict the trends in MMM permeability one-on-one. Nonetheless, the unanticipated lack of correlation for CO_2 permeability with CO_2 uptake and its strong correlation with $Q_{st,15}$ and $Q_{st,30}$ once more underline the difficulty to formulate strong and general guidelines to steer MMM design and, more importantly, the need for more research aiming at finding consistent relationships between MOF and MMM structures and ultimate membrane performance.

4 Conclusions

An attempt was made to fundamentally correlate MOF-808 parameters with the CO_2/N_2 separation performance indicators of the corresponding MMMs. More specifically, MOF CO_2 uptake, CO_2 Q_{st} at different CO_2 loading, pore volume and BET surface area were correlated with the MMM CO_2/N_2 separation factor and CO_2 permeability under varying feed conditions. Post-synthetic functionalization of FA modulated MOF-808 with different ligands (*i.e.* TFA, BA, GA, histidine and Li_2SO_4) proved to be a successful tool to influence this set of MOF parameters, leading to a broad range of systematically varying parameter values for BET surface area, pore volume, CO_2 uptake and CO_2 Q_{st}. For the different MOF-808 MMMs tested in this work, MOF CO_2 uptake was a poor predictor for MMM performance, showing a very weak correlation with CO_2/N_2 separation factor and only moderate correlation with CO_2 permeability. This is in contrast to literature where CO_2 uptake is one of the dominant factors used to explain MMM separation behavior. The loading-dependent CO_2 Q_{st} correlates substantially better with the membrane performance indicators than the CO_2 uptake. Correlation coefficients of $Q_{st,15}$ and $Q_{st,30}$ with the separation factor were higher than for CO_2 uptake, but were still considered only moderate. A strong correlation was however found between $Q_{st,15}$ and $Q_{st,30}$ on one hand and $P_{15/85}$, $P_{50/50}$ and $P_{0/100}$ on the other hand, indicating that Q_{st} can be considered as the most effective predictor for MMM CO_2 permeability amongst the MOF parameters. Interestingly, Q_{st} at zero coverage failed to show a strong correlation with the MMM performance indicators. GCMC simulations on MOF–FA and MOF–TFA revealed the existence of 2 types of adsorption sites in MOF-808. The first type of adsorption type is independent of cluster functionalization (*e.g.* TFA instead of FA) and corresponds with the tetragonal 'linker' cage, resulting in very strong MOF–CO_2 interaction (highly negative adsorption enthalpies) even at low CO_2 pressures while the second type of adsorption site was shown to be susceptible to TFA functionalization. Finally, the existence of different adsorption sites with varying adsorption enthalpies was linked to the observed difference in correlation coefficients for $Q_{st,0}$ and $Q_{st,30}$ with CO_2 permeability.

Conflicts of interest

There are no conflicts to declare.

Acknowledgements

R. T., N. V. V. and A. L. acknowledge the FWO for their support through a(n) (SB-)PhD fellowship (1S63317N, 1S32917N and 11D2220N). A. L. and V. V. S. would also like to thank the Research Board of Ghent University (BOF) for their support and the European Union's Horizon 2020 Research and Innovation Programme [ERC Consolidator Grant Agreement 647755 – DYNPOR (2015–2020)] for the received funding. The computational resources (Stevin Supercomputer Infrastructure) and services used in this work were provided by the VSC (Flemish Supercomputer Center), funded by Ghent University, FWO and the Flemish Government – Department EWI.

View Article Online
Paper Journal of Materials Chemistry A

References

1 B. Seoane, J. Coronas, I. Gascon, M. E. Benavides, O. Karvan, J. Caro, F. Kapteijn and J. Gascon, Metal–Organic Framework Based Mixed Matrix Membranes: A Solution for Highly Efficient CO_2 Capture?, *Chem. Soc. Rev.*, 2015, **44**, 2421–2454, DOI: 10.1039/C4CS00437J.

2 M. Rezakazemi, A. Ebadi Amooghin, M. M. Montazer-Rahmati, A. F. Ismail and T. Matsuura, State-of-the-Art Membrane Based CO_2 separation Using Mixed Matrix Membranes (MMMs): An Overview on Current Status and Future Directions, *Prog. Polym. Sci.*, 2014, **39**(5), 817–861, DOI: 10.1016/j.progpolymsci.2014.01.003.

3 K. Vanherck, G. Koeckelberghs and I. F. J. Vankelecom, Crosslinking Polyimides for Membrane Applications: A Review, *Prog. Polym. Sci.*, 2013, **38**(6), 874–896, DOI: 10.1016/j.progpolymsci.2012.11.001.

4 C. Z. Liang, T.-S. Chung and J.-Y. Lai, A Review of Polymeric Composite Membranes for Gas Separation and Energy Production, *Prog. Polym. Sci.*, 2019, **97**, 101141, DOI: 10.1016/j.progpolymsci.2019.06.001.

5 H. Li, K. Haas-Santo, U. Schygulla and R. Dittmeyer, Inorganic Microporous Membranes for H_2 and CO_2 Separation—Review of Experimental and Modeling Progress, *Chem. Eng. Sci.*, 2015, **127**, 401–417, DOI: 10.1016/j.ces.2015.01.022.

6 M. Tsapatsis, Toward High-Throughput Zeolite Membranes, *Science*, 2011, **334**(November), 767–769, DOI: 10.1126/science.1205957.

7 Q. Qian, W. S. Chi, G. Han and Z. P. Smith, Impact of Post-Synthetic Modification Routes on Filler Structure and Performance in Metal–Organic Framework-Based Mixed-Matrix Membranes, *Ind. Eng. Chem. Res.*, 2020, **59**, 5432–5438, DOI: 10.1021/acs.iecr.9b04820.

8 W. S. Chi, B. J. Sundell, K. Zhang, D. J. Harrigan, S. C. Hayden and Z. P. Smith, Mixed-Matrix Membranes Formed from Multi-Dimensional Metal–Organic Frameworks for Enhanced Gas Transport and Plasticization Resistance, *ChemSusChem*, 2019, **02139**, 2355–2360, DOI: 10.1002/cssc.201900623.

9 S. Shahid and K. Nijmeijer, Performance and Plasticization Behavior of Polymer–MOF Membranes for Gas Separation at Elevated Pressures, *J. Membr. Sci.*, 2014, **470**, 166–177, DOI: 10.1016/j.memsci.2014.07.034.

10 R. Thür, N. Van Velthoven, V. Lemmens, M. Bastin, S. Smolders, D. De Vos and I. F. J. Vankelecom, Modulator-Mediated Functionalization of MOF-808 as a Platform Tool to Create High-Performance Mixed-Matrix Membranes, *ACS Appl. Mater. Interfaces*, 2019, **11**, 44792–44801, DOI: 10.1021/acsami.9b19774.

11 M. Z. Ahmad, T. A. Peters, N. M. Konnertz, T. Visser, C. Téllez, J. Coronas, V. Fila, W. M. de Vos and N. E. Benes, High-Pressure CO_2/CH_4 Separation of Zr-MOFs Based Mixed Matrix Membranes, *Sep. Purif. Technol.*, 2020, **230**(June 2019), 115858, DOI: 10.1016/j.seppur.2019.115858.

12 G. Dong, H. Li and V. Chen, Challenges and Opportunities for Mixed-Matrix Membranes for Gas Separation, *J. Mater. Chem. A*, 2013, **1**(15), 4610–4630, DOI: 10.1039/C3TA00927K.

13 M. Van Essen, E. Montrée, M. Houben, Z. Borneman and K. Nijmeijer, Magnetically Aligned and Enriched Pathways of Zeolitic Imidazolate Framework 8 in Matrimid Mixed Matrix Membranes for Enhanced CO_2 Permeability, *Membranes*, 2020, **10**(7), 155.

14 T. Rodenas, M. Van Dalen, E. García-Pérez, P. Serra-Crespo, B. Zornoza, F. Kapteijn and J. Gascon, Visualizing MOF Mixed Matrix Membranes at the Nanoscale: Towards Structure–Performance Relationships in CO_2/CH_4 Separation Over NH2-MIL-53(Al)@PI, *Adv. Funct. Mater.*, 2014, **24**, 249–256, DOI: 10.1002/adfm.201203462.

15 A. Ozcan, R. Semino, G. Maurin and A. O. Yazaydin, Modeling of Gas Transport through Polymer/MOF Interfaces: A Microsecond-Scale Concentration Gradient-Driven Molecular Dynamics Study, *Chem. Mater.*, 2020, **32**, 1288–1296, DOI: 10.1021/acs.chemmater.9b04907.

16 Z. Kang, Y. Peng, Z. Hu, Y. Qian, C. Chi, L. Y. Yeo, L. Tee and D. Zhao, Mixed Matrix Membranes Composed of Two-Dimensional Metal–Organic Framework Nanosheets for Pre-Combustion CO_2 Capture: A Relationship Study of Filler Morphology versus Membrane, *J. Mater. Chem. A*, 2015, **3**, 20801–20810, DOI: 10.1039/c5ta03739e.

17 K. Chen, K. Xu, L. Xiang, X. Dong, Y. Han, C. Wang, L. Sun and Y. Pan, Enhanced CO_2/CH_4 Separation Performance of Mixed-Matrix Membranes through Dispersion of Sorption-Selective MOF Nanocrystals, *J. Membr. Sci.*, 2018, **563**(March), 360–370, DOI: 10.1016/j.memsci.2018.06.007.

18 Y. Cheng, Y. Ying, L. Zhai, G. Liu, J. Dong, Y. Wang, M. P. Christopher, S. Long, Y. Wang and D. Zhao, Mixed Matrix Membranes Containing MOF@COF Hybrid Fillers for Efficient CO_2/CH_4 Separation, *J. Membr. Sci.*, 2019, **573**(November 2018), 97–106, DOI: 10.1016/j.memsci.2018.11.060.

19 Q. Qian, A. X. Wu, W. S. Chi, P. A. Asinger, S. Lin, A. Hypsher and Z. P. Smith, Mixed-Matrix Membranes Formed from Imide-Functionalized UiO-66-NH2 for Improved Interfacial Compatibility, *ACS Appl. Mater. Interfaces*, 2019, **11**, 31257–31269, DOI: 10.1021/acsami.9b07500.

20 R. Thür, N. Van Velthoven, S. Slootmaekers, J. Didden, R. Verbeke, S. Smolders, W. Egger, M. Dickmann, D. De Vos and I. F. Vankelecom, J. Bipyridine-Based UiO-67 as Novel Filler in Mixed-Matrix Membranes for CO_2-Selective Gas Separation, *J. Membr. Sci.*, 2019, **576**(15 April 2019), 78–87, DOI: 10.1016/j.memsci.2019.01.016.

21 G. Yu, Y. Li, Z. Wang, T. Xiaoteng, G. Zhu and X. Zou, Mixed Matrix Membranes Derived from Nanoscale Porous Organic Frameworks for Permeable and Selective CO_2 Separation, *J. Membr. Sci.*, 2019, **591**(August), 117343, DOI: 10.1016/j.memsci.2019.117343.

22 C. Jia, F. G. Cirujano, B. Bueken, B. Claes, D. Jonckheere, K. M. Van Geem and D. De Vos, Geminal Coordinatively Unsaturated Sites on MOF-808 for the Selective Uptake of Phenolics from a Real Bio-Oil Mixture, *ChemSusChem*, 2019, **101**, 1256–1266, DOI: 10.1002/cssc.201802692.

23 N. Van Velthoven, M. Henrion, J. Dallenes, A. Krajnc, A. L. Bugaev, P. Liu, S. Bals, A. V. Soldatov and D. E. De Vos, S,O-Functionalized Metal–Organic Frameworks as Heterogeneous Single-Site Catalysts for the Oxidative Alkenylation of Arenes via C–H Activation, *ACS Catal.*, 2020, **10**, 5077–5085, DOI: 10.1021/acscatal.0c00801.

24 H. Reinsch, S. Waitschat, S. M. Chavan, K. P. Lillerud and N. Stock, A Facile "Green" Route for Scalable Batch Production and Continuous Synthesis of Zirconium MOFs, *Eur. J. Inorg. Chem.*, 2016, **2016**(27), 4490–4498, DOI: 10.1002/ejic.201600295.

25 D. F. Sanders, Z. P. Smith, R. Guo, L. M. Robeson, J. E. McGrath, D. R. Paul and B. D. Freeman, Energy-Efficient Polymeric Gas Separation Membranes for a Sustainable Future: A Review, *Polymer*, 2013, **54**(18), 4729–4761, DOI: 10.1016/j.polymer.2013.05.075.

26 M. Galizia, W. S. Chi, Z. P. Smith, T. C. Merkel, R. W. Baker and B. D. Freeman, Polymers and Mixed Matrix Membranes for Gas and Vapor Separation: A Review and Prospective Opportunities, *Macromolecules*, 2017, **50**, 7809–7843, DOI: 10.1021/acs.macromol.7b01718.

27 Q. Qian, P. A. Asinger, M. J. Lee, G. Han, K. M. Rodriguez, S. Lin, F. M. Benedetti, A. X. Wu, W. S. Chi and Z. P. Smith, MOF-Based Membranes for Gas Separations, *Chem. Rev.*, 2020, **120**(16), 8161, DOI: 10.1021/acs.chemrev.0c00119.

28 J. Baek, B. Rungtaweevoranit, X. Pei, M. Park, S. C. Fakra, Y.-S. Liu, R. Matheu, S. A. Alshmimri, S. Alshehri, C. A. Trickett, *et al.*, Bioinspired Metal–Organic Framework Catalysts for Selective Methane Oxidation to Methanol, *J. Am. Chem. Soc.*, 2018, **140**, 18208–18216, DOI: 10.1021/jacs.8b11525.

29 F. Rouquerol, J. Rouquerol and K. Sing, *Adsorption by Powders and Porous Solids*, Academic Press, San Diego, 11th edn, 1999.

30 K. S. Walton and R. Q. Snurr, Applicability of the BET Method for Determining Surface Areas of Microporous Metal–Organic Frameworks, *J. Am. Chem. Soc.*, 2007, **129**(27), 8552–8556, DOI: 10.1021/ja071174k.

31 H. J. Park and M. P. Suh, Enhanced Isosteric Heat, Selectivity and Uptake Capacity of CO_2 Adsorption in a Metal–Organic Framework by Impregnated Metal Ions, *Chem. Sci.*, 2013, **4**(3), 685–690, DOI: 10.1039/c2sc21253f.

32 J. Hutter, M. Iannuzzi, F. Schiffmann and J. Vande Vondele, Cp2k: Atomistic Simulations of Condensed Matter Systems, *Wiley Interdiscip. Rev.: Comput. Mol. Sci.*, 2013, **4**(1), 15–25.

33 J. P. Perdew, K. Burke and M. Ernzerhof, Generalized Gradient Approximation Made Simple, *Phys. Rev. Lett.*, 1996, **77**(3), 3865–3868.

34 S. Grimme, J. Antony, S. Ehrlich and H. Krieg, A Consistent and Accurate Ab Initio Parametrization of Density Functional Dispersion Correction (DFT-D) for the 94 Elements H-Pu, *J. Phys. Chem.*, 2010, **132**, 154104.

35 S. Grimme, S. Ehrlich and L. Goerigk, Effect of the Damping Function in Dispersion Corrected Density Functional Theory, *J. Comput. Chem.*, 2011, **32**(7), 1456–1465.

36 J. Vande Vondele and J. Hutter, Gaussian Basis Sets for Accurate Calculations on Molecular Systems in Gas and Condensed Phases, *J. Chem. Phys.*, 2007, **127**(11), 114105.

37 S. Goedecker, M. Teter and J. Hutter, Separable Dual-Space Gaussian Pseudopotentials, *Phys. Rev. B: Condens. Matter Mater. Phys.*, 1996, **54**, 1703–1710.

38 D. Dubbeldam, S. Calero, D. E. Ellis and R. Q. Snurr, RASPA: Molecular Simulation Software for Adsorption and Diffusion in Flexible Nanoporous Materials, *Mol. Simul.*, 2016, **42**(2), 81–101.

39 J. J. Potoff and J. I. Siepmann, Vapor–Liquid Equilibria of Mixtures Containing Alkanes, Carbon Dioxide, and Nitrogen, *AIChE J.*, 2004, **47**(7), 1676–1682.

40 T. Verstraelen, S. Vandenbrande, F. Heidar-Zadeh, L. Vanduyfhuys, V. Van Speybroeck, M. Waroquier and P. W. Ayers, Minimal Basis Iterative Stockholder: Atoms in Molecules for Force-Field Development, *J. Chem. Theory Comput.*, 2016, **12**, 3894–3912, DOI: 10.1021/acs.jctc.6b00456.

41 S. L. Mayo, B. D. Olafson and W. A. Goddard, DREIDING: A Generic Force Field for Molecular Simulations, *J. Phys. Chem.*, 1990, **94**(26), 8897–8909.

42 S. Vandenbrande, T. Verstraelen, J. J. Gutiérrez-Sevillano, M. Waroquier and V. Van. Van Speybroeck, Methane Adsorption in Zr-Based MOFs: Comparison and Critical Evaluation of Force Fields, *J. Phys. Chem. C*, 2017, **121**(45), 25309–25322, DOI: 10.1021/acs.jpcc.7b08971.

43 A. K. Rappe, C. J. Casewit, K. S. Colwell, W. A. Goddard III and W. M. Skiff, UFF, a Full Periodic Table Force Field for Molecular Mechanics and Molecular Dynamics Simulations, *J. Am. Chem. Soc.*, 1992, **114**(25), 10024–10035.

44 A. L. Khan, S. Basu, A. Cano-odena and I. F. J. Vankelecom, Novel High Throughput Equipment for Membrane-Based Gas Separations, *J. Membr. Sci.*, 2010, **354**(1–2), 32–39, DOI: 10.1016/j.memsci.2010.02.069.

45 J. Didden, R. Thür, A. Volodin and I. F. J. Vankelecom, Blending PPO-Based Molecules with Pebax MH 1657 in Membranes for Gas Separation, *J. Appl. Polym. Sci.*, 2018, **135**, 46433, DOI: 10.1002/app.46433.

46 R. Thür, V. Lemmens, D. Van Havere, M. van Essen, K. Nijmeijer and I. F. J. Vankelecom, Tuning 6FDA-DABA Membrane Performance for CO_2 Removal by Physical Densification and Decarboxylation Cross-Linking during Simple Thermal Treatment, *J. Membr. Sci.*, 2020, **610**, 118195, DOI: 10.1016/j.memsci.2020.118195.

47 J. Hafizovic, M. Bjørgen, U. Olsbye, P. D. C. Dietzel, S. Bordiga, C. Prestipino, C. Lamberti and K. P. Lillerud, The Inconsistency in Adsorption Properties and Powder XRD Data of MOF-5 Is Rationalized by Framework Interpenetration and the Presence of Organic and Inorganic Species in the Nanocavities, *J. Am. Chem. Soc.*, 2007, (No. 7), 3612–3620, DOI: 10.1021/ja0675447.

48 S. Øien-ØDegaard, G. C. Shearer, D. S. Wragg and K. P. Lillerud, Pitfalls in Metal–Organic Framework Crystallography: Towards More Accurate, *Chem. Soc. Rev.*, 2017, **46**, 4867–4876, DOI: 10.1039/c6cs00533k.

49 B. Chen, X. Wang, Q. Zhang, X. Xi, J. Cai, H. Qi, S. Shi, J. Wang, D. Yuan and M. Fang, Synthesis and Characterization of the Interpenetrated MOF-5, *J. Mater. Chem.*, 2010, **20**, 3758–3767, DOI: 10.1039/b922528e.

50 K. Xuan, Y. Pu, F. Li, J. Luo, N. Zhao and F. Xiao, Metal–Organic Frameworks MOF-808-X as Highly Efficient Catalysts for Direct Synthesis of Dimethyl Carbonate from CO2 and Methanol, *Chin. J. Catal.*, 2019, **40**, 533–566, DOI: 10.1016/S1872-2067(19)63291-2.

51 Y. Jiang, C. Liu, J. Caro and A. Huang, A New UiO-66-NH2 Based Mixed-Matrix Membranes with High CO_2/CH_4 Separation Performance, *Microporous Mesoporous Mater.*, 2019, **274**(July 2018), 203–211, DOI: 10.1016/j.micromeso.2018.08.003.

52 B. C. Smith, *Infrared Spectral Interpretation: A Systematic Approach*, CRC Press LLC, 1998.

53 S. Kumar, A. K. Rai, S. B. Rai and D. K. Rai, Infrared and Raman Spectra of Histidine: An Ab Initio DFT Calculations of Histidine Molecule and Its Different Protonated Forms, *Indian J. Phys.*, 2010, **84**, 563–573, DOI: 10.1007/s12648-010-0039-6.

54 S. G. Stepanian, I. D. Reva, E. D. Radchenko and G. G. Sheina, Infrared Spectra of Benzoic Acid Monomers and Dimers in Argon Matrix, *Vib. Spectrosc.*, 1996, **11**, 123–133, DOI: 10.1016/0924-2031(95)00068-2.

55 J. Jiang, F. Gándara, Y.-B. Zhang, K. Na, O. M. Yaghi and W. G. Klemperer, Superacidity in Sulfated Metal-Organic Framework-808, *J. Am. Chem. Soc.*, 2014, **136**, 12844–12847, DOI: 10.1021/ja507119n.

56 R. Williams, W. P. Jencks and F. H. Westheimer, *pK_a Data Compiled by R. Williams*, 2011, https://www.chem.wisc.edu/areas/reich/pkatable/pKa_compilation-1-Williams.pdf, accessed Mar 19, 2020.

57 G. Fan, Y. Liu and H. Wang, Identification of Thermophilic Proteins by Incorporating Evolutionary and Acid Dissociation Information into Chou's General Pseudo Amino Acid Composition, *J. Theor. Biol.*, 2016, **407**, 138–142, DOI: 10.1016/j.jtbi.2016.07.010.

58 J. Xu, J. Liu, X. Wang, Y. Xu, S. Chen and X. Wang, Optimized Synthesis of Zr(IV) Metal Organic Frameworks (MOFs-808) for Efficient Hydrogen Storage, *New J. Chem.*, 2019, **43**(2), 4092–4099, DOI: 10.1039/c8nj06362a.

59 S. Wendy and L. Queen, An Experimental and Computational Study of CO2 Adsorption in the Sodalite-Type M-BTT (M^{I}_{4}Cr,Mn,Fe,Cu) Metal–Organic Frameworks Featuring Open Metal Sites, *Chem. Sci.*, 2018, **9**, 4579, DOI: 10.1039/c8sc00971f.

60 D.-X. Xue, A. J. Cairns, Y. Belmabkhout, L. Wojtas, Y. Liu, M. H. Alkordi and M. Eddaoudi, Tunable Rare-Earth Fcu-MOFs: A Platform for Systematic Enhancement of CO_2 Adsorption Energetics and Uptake, *J. Am. Chem. Soc.*, 2013, **135**, 7660–7667, DOI: 10.1021/ja401429x.

61 H.-Y. Cho, D.-A. Yang, J. Kim, S.-Y. Jeong and W.-S. Ahn, CO_2 Adsorption and Catalytic Application of Co-MOF-74 Synthesized by Microwave Heating, *Catal. Today*, 2012, **185**(1), 35–40, DOI: 10.1016/j.cattod.2011.08.019.

62 B. Arstad, H. Fjellvåg, K. O. Kongshaug, O. Swang and R. Blom, Amine Functionalised Metal Organic Frameworks (MOFs) as Adsorbents for Carbon Dioxide, *Adsorption*, 2008, **14**, 755–762, DOI: 10.1007/s10450-008-9137-6.

63 J. A. Mason, K. Sumida, Z. R. Herm, R. Krishna and J. R. Long, Evaluating Metal–Organic Frameworks for Post-Combustion Carbon Dioxide Capture via Temperature Swing Adsorption, *Energy Environ. Sci.*, 2011, **4**, 3030–3040, DOI: 10.1039/c1ee01720a.

64 M. I. Hossain, J. D. Cunningham, T. M. Becker, B. E. Grabicka, K. S. Walton, B. D. Rabideau and T. G. Glover, Impact of MOF Defects on the Binary Adsorption of CO2 and Water in UiO-66, *Chem. Eng. Sci.*, 2019, **203**, 146–357, DOI: 10.1016/j.ces.2019.03.053.

65 A. Koutsianos, E. Kazimierska, A. R. Barron, M. Taddei and E. Andreoli, A New Approach to Enhancing the CO_2 Capture Performance of Defective UiO-66 *via* Post-Synthetic Defect Exchange, *Dalton Trans.*, 2019, **48**, 3349–3359, DOI: 10.1039/c9dt00154a.

66 P. Deria, J. E. Mondloch, E. Tylianakis, P. Ghosh, W. Bury, R. Q. Snurr, J. T. Hupp and O. K. Farha, Perfluoroalkane Functionalization of NU-1000 via Solvent-Assisted Ligand Incorporation: Synthesis and CO_2 Adsorption Studies, *J. Am. Chem. Soc.*, 2013, **14**, 16801–16804, DOI: 10.1021/ja408959g.

67 A. M. Plonka, T. G. Grissom, D. G. Musaev, A. Balboa, W. O. Gordon, D. L. Collins-Wildman, S. K. Ghose, Y. Tian, A. M. Ebrahim, M. B. Mitchell, *et al.*, Effect of Carbon Dioxide on the Degradation of Chemical Warfare Agent Simulant in the Presence of Zr Metal Organic Framework MOF-808, *Chem. Mater.*, 2019, **31**, 9904–9914, DOI: 10.1021/acs.chemmater.9b04565.

68 L. Luconi, G. Mercuri, T. Islamoglu, A. Fermi, G. Bergamini, G. Giambastiani and A. Rossin, Benzothiazolium-Functionalized NU-1000: A Versatile Material for Carbon Dioxide Adsorption and Cyanide Luminescence Sensing, *J. Mater. Chem. C*, 2020, **8**, 7492–7500, DOI: 10.1039/d0tc01436b.

69 T. G. Grissom, D. M. Driscoll, D. Troya, N. S. Sapienza, P. M. Usov, A. J. Morris and J. R. Morris, Molecular-Level Insight into CO_2 Adsorption on the Zirconium-Based Metal–Organic Framework, UiO-66: A Combined Spectroscopic and Computational Approach, *J. Phys. Chem. C*, 2019, **123**, 13731–13738, DOI: 10.1021/acs.jpcc.9b02513.

70 C. H. Lau, R. Babarao and M. R. Hill, A Route to Drastic Increase of CO_2 Uptake in Zr Metal Organic Framework UiO-66, *Chem. Commun.*, 2013, **49**(207890), 3634–3637, DOI: 10.1039/c3cc40470f.

71 T. S. Chung, L. Y. Jiang, Y. Li and S. Kulprathipanja, Mixed Matrix Membranes (MMMs) Comprising Organic Polymers with Dispersed Inorganic Fillers for Gas Separation, *Prog. Polym. Sci.*, 2007, **32**(4), 483–507, DOI: 10.1016/j.progpolymsci.2007.01.008.

72 J. Ahn, W. J. Chung, I. Pinnau, J. Song, N. Du, G. P. Robertson and M. D. Guiver, Gas Transport Behavior of Mixed-Matrix Membranes Composed of Silica Nanoparticles in

a Polymer of Intrinsic Microporosity (PIM-1), *J. Membr. Sci.*, 2010, **346**(2), 280–287, DOI: 10.1016/j.memsci.2009.09.047.

73 C. Ma and J. J. Urban, Enhanced CO_2 Capture and Hydrogen Purification by Hydroxy Metal–Organic Framework/Polyimide Mixed Matrix Membranes, *ChemSusChem*, 2019, **12**, 1–8, DOI: 10.1002/cssc.201902248.

74 J. G. H. Wijmans and R. W. Baker, *The Solution-Diffusion Model: A Unified Approach to Membrane Permeation*, 2006. DOI: 10.1002/047002903X.ch5.

75 S. Matteucci, Y. Yampolskii, B. D. Freeman and I. Pinnau, Transport of Gases and Vapors in Glassy and Rubbery Polymers, in *Materials Science of Membranes for Gas and Vapor Separation*, 2006, pp. 1–48.

76 T. Dingel, M. Tessema, S. R. Venna, G. Dahe, D. P. Hopkinson, H. M. El-kaderi and A. K. Sekizkardes, Incorporation of Benzimidazole Linked Polymers into Matrimid to Yield Mixed Matrix Membranes with Enhanced CO_2/N_2 Selectivity, *J. Membr. Sci.*, 2018, **554**(January), 90–96, DOI: 10.1016/j.memsci.2018.02.054.

77 M. Shan, B. Seoane, A. Pustovarenko, X. Wang and X. Liu, Benzimidazole Linked Polymers (BILPs) in Mixed-Matrix Membranes: Influence of Filler Porosity on the CO_2/N_2 Separation Performance, *J. Membr. Sci.*, 2018, **566**(May), 213–222, DOI: 10.1016/j.memsci.2018.08.023.

78 S. R. Venna, M. Lartey, T. Li, A. Spore, S. Kumar, H. B. Nulwala, D. R. Luebke, L. Rosi and E. Albenze, Fabrication of MMMs with Improved Gas Separation Properties Using Externally-Functionalized MOF Particles, *J. Mater. Chem. A*, 2015, **3**, 5014–5022, DOI: 10.1039/C4TA05225K.

79 S. Ross, *Introduction to Probability and Statistics for Engineers and Scientists*, 4th edn, 2009.

80 M. Vinoba, M. Bhagiyalakshmi, Y. Alqaheem, A. A. Alomair, A. Pérez and M. S. Rana, Recent Progress of Fillers in Mixed Matrix Membranes for CO_2 Separation: A Review, *Sep. Purif. Technol.*, 2017, **188**, 431–450, DOI: 10.1016/j.seppur.2017.07.051.

81 D. R. Paul and W. J. Koros, Effect of Partially Immobilizing Sorption on Permeability and the Diffusion Time Lag, *J. Polym. Sci.*, 1976, **14**, 675–685.

Paper VI

Truly combining the advantages of polymeric and zeolite membranes for gas separations

X. Tan, S. Robijns, R. Thür, Q. Ke, N. De Witte, A. Lamaire, Y. Li, I. Aslam, D. Van Havere, T. Donckels, T. Van Assche, V. Van Speybroeck, M. Dusselier, I. Vankelecom

Science, **2022**, 378 (6625), 1189–1194

A. Lamaire was responsible for the computational contribution to this work, performed the GCMC simulations and the *ab initio* free energy calculations, and contributed to the interpretation of the results and the preparation of the manuscript.

RESEARCH ARTICLE

MEMBRANES

Truly combining the advantages of polymeric and zeolite membranes for gas separations

Xiaoyu Tan[1], Sven Robijns[2], Raymond Thür[1]†, Quanli Ke[2]‡, Niels De Witte[3], Aran Lamaire[4], Yun Li[1], Imran Aslam[1], Daan Van Havere[1], Thibaut Donckels[2], Tom Van Assche[3], Veronique Van Speybroeck[4], Michiel Dusselier[2]*, Ivo Vankelecom[1]*

Mixed-matrix membranes (MMMs) have been investigated to render energy-intensive separations more efficiently by combining the selectivity and permeability performance, robustness, and nonaging properties of the filler with the easy processing, handling, and scaling up of the polymer. However, truly combining all in one single material has proven very challenging. In this work, we filled a commercial polyimide with ultrahigh loadings of a high–aspect ratio, CO_2-philic Na-SSZ-39 zeolite with a three-dimensional channel system that precisely separates gas molecules. By carefully designing both zeolite and MMM synthesis, we created a gas-percolation highway across a flexible and aging-resistant (more than 1 year) membrane. The combination of a CO_2-CH_4 mixed-gas selectivity of ~423 and a CO_2 permeability of ~8300 Barrer outperformed all existing polymer-based membranes and even most zeolite-only membranes.

Over the past decades, membrane technology has matured into an established technology for many energy-intensive separations (*1*–*3*). Compared with conventional technologies, membrane technology offers a more sustainable alternative, owing to its low energy consumption, small footprint, and modular design, making it possible to retrofit membranes in existing plants (*2*, *3*). Membranes are already in use for gas separations—for example, natural gas purification, syngas treatment, and air separation (*4*–*7*)—and are becoming part of the toolbox for CO_2 removal (*5*–*10*). Whereas conventional polymeric membranes are cheap and processable, they often suffer from aging issues or an intrinsic permeability-selectivity trade-off, which makes it challenging to obtain high permeability together with sufficient selectivity (*11*–*16*). On the other hand, inorganic membranes prepared from zeolites or other crystalline microporous materials, such as metal-organic frameworks (MOFs), typically display better separation performances but tend to be brittle and more expensive and possess poor processability and scalability (*17*–*21*). Mixed-matrix membranes (MMMs), which consist of fillers embedded in a polymeric matrix, aim at combining the intrinsic advantages of a polymeric membrane with the filler's superior gas separation properties (*22*–*27*).

Zeolites are of particular interest for MMM development because they have well-defined, rigid pores and outstanding thermal and chemical stability. Because the intrinsically low selectivity and high permeability of rubbery polymers (such as polydimethylsiloxane) neutralize the benefits of the zeolite, rigid glassy polymers are key for the development of high-performance zeolite-filled MMMs (*28*–*32*). However, the poor adhesion between zeolites and glassy polymers typically results in nonselective interfacial voids (*31*, *32*). Consequently, obtaining high zeolite loadings (≥50 wt %) while guaranteeing a defect-free polymer-zeolite interface in combination with a highly selective zeolite and appropriate glassy polymer matrix is essential to the creation of high-performance MMMs for a variety of the most critical separation challenges. In this work, a platelet-shaped, CO_2-philic, small-pore (eight-membered ring) AEI-type zeolite (SSZ-39) (*33*–*36*), possessing a long-range ordered three-dimensional (3D)–channel system and gas-selective windows, was incorporated in a poly(3,3′-4,4′-benzophenone tetracarboxylic-dianhydride diaminophenylindane) (Matrimid 5218) polymer. Because of the combination of well-designed zeolite and MMM syntheses, we obtained a high zeolite loading with a quasi-continuous zeolite phase across a self-standing membrane.

[1]Centre for Membrane Separations, Adsorption, Catalysis and Spectroscopy for Sustainable Solutions (cMACS), KU Leuven, Celestijnenlaan 200F, 3001 Leuven, Belgium. [2]Center for Sustainable Catalysis and Engineering, KU Leuven, Celestijnenlaan 200F, 3001 Leuven, Belgium. [3]Department of Chemical Engineering, Vrije Universiteit Brussel, Pleinlaan 2, 1050 Brussels, Belgium. [4]Center for Molecular Modeling, Ghent University, Tech Lane Ghent Science Park, Technologiepark 46, 9052 Zwijnaarde, Belgium.
*Corresponding author. Email: ivo.vankelecom@kuleuven.be (I.V.); michiel.dusselier@kuleuven.be (M.D.)
†Present address: Agfa-Gevaert NV, Septestraat 27, 2640 Mortsel, Belgium.
‡Present address: Institute of Catalytic Reaction Engineering, Zhejiang University of Technology, Hangzhou 310014, China.

Result and discussion

Zeolite characterization

SSZ-39 zeolites were synthesized according to modified literature recipes (*33*–*35*). X-ray diffraction (XRD) of the samples confirmed the highly crystalline, pure AEI type zeolite (fig. S9). N_2 physisorption demonstrated a micropore volume of ~0.3 cm^3/g (fig. S11), which is close to the theoretical accessible volume of the AEI framework (*37*), suggesting a nearly perfect 3D-connected channel system, which allows fast gas transport. Transmission electron microscopy (TEM) images showed platelet-shaped SSZ-39 particles (Fig. 1A) of ~150 nm thickness and ~1.8 by 1.8 μm in size (fig. S48), the average aspect ratio thus reaching ~12. The random packing of the high–aspect ratio zeolite platelets (fig. S49) results in a low bulk density of ~15 mg/cm^3 (fig. S12), and elemental analysis of the as-synthesized SSZ-39 indicated a Si/Al molar ratio of ~11 (table S3).

CO_2, CH_4, and N_2 uptake and isosteric adsorption enthalpies (Q_{st}) were determined for both calcined SSZ-39 (Na/Al ratio ≈ 0.12) and Na^+-exchanged SSZ-39 (Na-SSZ-39; Na/Al ratio ≈ 0.93) (table S3). The adsorption isotherms of CO_2, CH_4, and N_2 at 10°C are shown in Fig. 1D for a pressure range of 0 to 8 bar. The theoretical maximum CO_2 uptake of Na-SSZ-39 reached ~7.0 mmol/g (~11.0 $mmol/cm^3$) at 10°C, and the steric heat of adsorption for CO_2 at zero coverage was −35.1 kJ/mol, reflecting a desired strong physical adsorption for membrane applications. For both SSZ-39 and Na-SSZ-39, the gas uptake decreases in the order $CO_2 \gg CH_4 > N_2$. The isosteric adsorption enthalpy of CO_2 in Na-SSZ-39 was far larger than that of CH_4 (−21.4 kJ/mol) and N_2 (−19.4 kJ/mol) as a result of the large polarizability and quadrupole moment of CO_2 (*38*). A more negative CO_2 adsorption enthalpy was obtained on Na-SSZ-39 compared with SSZ-39 (table S19). Additionally, the pronounced difference in CO_2 adsorption in the low-pressure region of the isotherms (Fig. 1D) suggests that Na^+ exchange resulted in an increased CO_2-philicity (*38*).

To better understand these findings at a molecular level, the pure-gas and mixed-gas adsorption behaviors in Na-SSZ-39 were modeled by using grand canonical Monte Carlo (GCMC) simulations. The pure-gas adsorption simulations show a good qualitative resemblance with the experimental data (fig. S37), and the enthalpies of adsorption are in good agreement (at 2 bar, GCMC yields −31.6 kJ/mol for CO_2, −18.5 kJ/mol for CH_4, and −15.8 kJ/mol for N_2). The 3D density isosurfaces for CO_2 adsorption (Fig. 1C) show that CO_2 molecules preferentially interact with the Na^+ (especially at low CO_2 pressures), whereas the windows of Na-SSZ-39 remain open for gas transport. This tendency corroborates the enhanced CO_2-philicity through Na^+ exchange, improving CO_2 adsorption and transport in Na-SSZ-39. The Si/Al molar ratio of 11 implies that on average, one aluminum site (fully counted) and thus one sodium ion exists per cage (*37*). Furthermore,

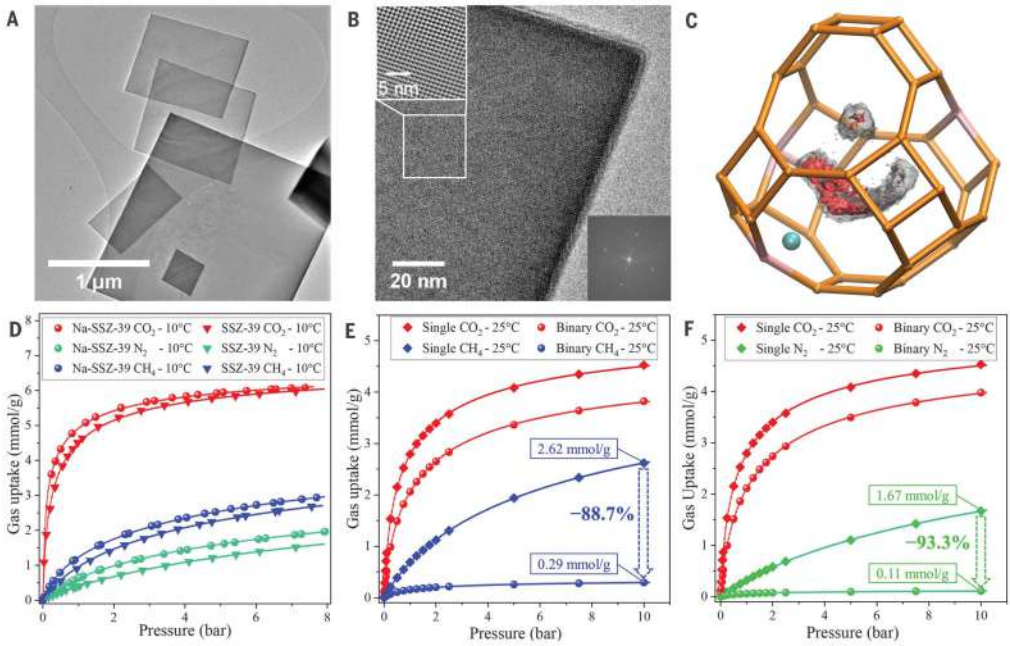

Fig. 1. SSZ-39 zeolite. (**A** and **B**). TEM images of (A) Na-SSZ-39 platelet and (B) its base-face. (Insets) (top left) A Fourier-filtered image from the selected area and (bottom right) the Fourier-transform of this image, proving that the base face refers to the [001] crystal plane of the AEI-type framework (fig. S47). (**C**) 3D density isosurface for CO_2 adsorption in a Na-SSZ-39 cage at 0.1 bar (red) and 1 bar (gray) under 25°C [by means of GCMC, where (3 × 1/3) Al sites are pink, Na^+ is cyan, and O is omitted], indicating that the Na^+ is a preferential adsorption site, particularly at lower pressures. At higher pressures, additional molecules are adsorbed, occupying the remaining space of the cage. (**D**) Experimental CO_2, CH_4, and N_2 adsorption isotherms of SZZ-39 and Na-SSZ-39 zeolites at 10°C. (**E**) Single-gas and equimolar mixed-gas CO_2-CH_4 adsorption isotherms of Na-SSZ-39 zeolite at 25°C (by means of GCMC). (**F**) Single-gas and equimolar mixed-gas CO_2-N_2 adsorption isotherms of Na-SSZ-39 zeolite at 25°C (by means of GCMC) (supplementary materials).

the CO_2-CH_4 and CO_2-N_2 mixed-gas sorption simulations demonstrate the competitive sorption of CO_2 at the expense of CH_4 and N_2 (movie S1). This strong competitive sorption behavior drastically reduces the uptake of CH_4 and N_2. For example, compared with the single-gas adsorption, the CH_4 uptake from an equimolar CO_2-CH_4 mixture was reduced by 88.7% (for N_2, 93.3%) at 10 bar/25°C (Fig. 1, E and F). In addition, ab initio free-energy barrier calculations [by using enhanced sampling molecular dynamics (MD) simulations] for the diffusion inside the zeolite confirmed the molecular sieving behavior of Na-SSZ-39 (fig. S41). The biggest (static) aperture of Na-SSZ-39 predicts diffusion of molecules with a diameter of 3.84 Å, which is close to the kinetic diameter of CH_4 (3.80 Å) but prominently larger than that of CO_2 (3.30 Å). Consequently, the free-energy barrier for CH_4 permeation through the eight-membered ring in Na-SSZ-39 is far higher than for CO_2 (a 18.7 kJ/mol difference). Therefore, the self-diffusion coefficient for CO_2 is ~1000-fold greater than for CH_4. Consequently, in a CO_2-CH_4 mixture, CH_4 is prevented from entering the zeolite by a geometric restriction supplemented by a competitive advantage in CO_2 adsorption. By combining the results of MD and GCMC simulations, the theoretical equimolar CO_2-CH_4 mixed-gas selectivity in Na-SSZ-39 zeolite mounted to >10,000 (at 25°C), thus pointing toward a substantial potential for further improving membrane performance on the basis of this zeolite platform (supplementary materials).

MMM characterization

Self-standing MMMs were prepared, with Na-SSZ-39 reaching extremely high loadings of up to 55 wt %. XRD confirmed the preservation of zeolite crystallinity in MMMs after all synthesis steps (fig. S13). Scanning electron microscopy (SEM) membrane cross sections (Fig. 2A) show that the zeolite platelets are positioned in the polymer matrix in a random, nonaligned packing. This homogeneous distribution of zeolite platelets at high loading was realized through a subtle and carefully optimized interplay between zeolite and casting solution during MMM synthesis. More specifically, favorable molecular interactions between zeolite and the Matrimid-chloroform solution were combined with a small density difference between zeolite and solvent (~1.55 g/cm^3 and ~1.49 g/cm^3, respectively), the high–aspect ratio of the filler, a high viscosity of the casting solution, dedicated evaporation control of the solvent, and thermal annealing. After membrane solidification, remaining interfacial defects were eliminated by means of a tuned annealing protocol, which had a profound impact on the final MMM performance (fig. S59). The 180°C annealing program resulted in slightly more permeable membranes than those of the 260°C program, but the 260°C program induced a far higher CO_2-CH_4 selectivity [for 50 wt % Na-SSZ-39 MMM, the selectivity increased from ~200 to >420 (table S5)], whereas the 350°C program resulted in fragile and brittle

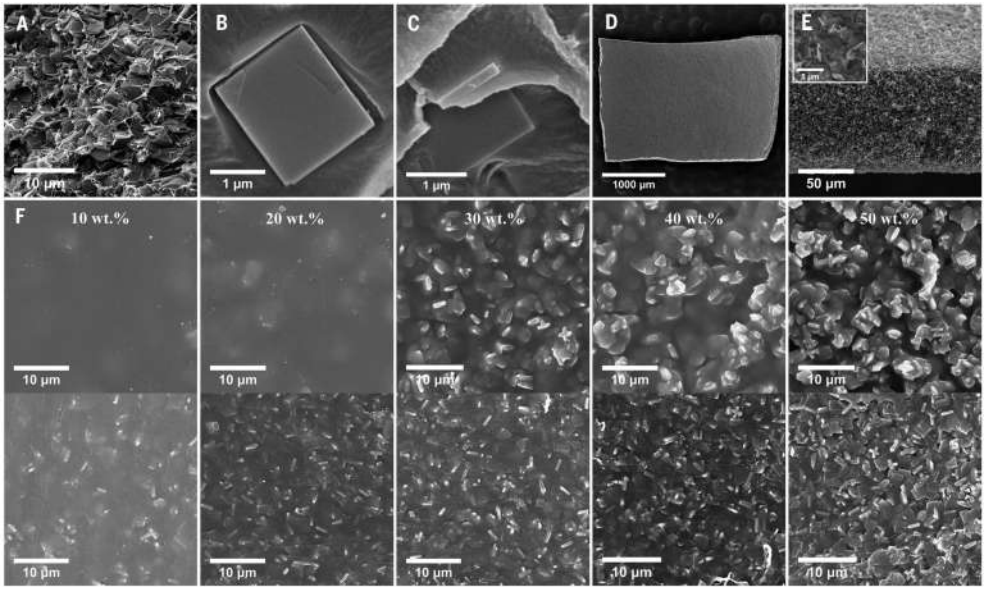

Fig. 2. SEM images of the platelet-shaped Na-SSZ-39 MMMs. (**A**) Cross section of the 40 wt % Na-SSZ-39 MMM after 260°C annealing. (**B** and **C**) Cross section of 20 wt % Na-SSZ-39 MMM (B) before and (C) after annealing. (**D**) Top view and (**E**) cross section of the 30 wt % Na-SSZ-39 MMM after 800°C oxidative treatment, burning off the polymer (figs. S51 to S53). (**F**) (Top) Top view and (bottom) bottom view of membranes with 10 to 50 wt % platelet-shaped zeolite loading (supplementary materials).

carbonized membranes. As shown in Fig. 2C, 260°C-annealed membranes did not show sieve-in-a-cage morphology, which traditionally is a major issue for zeolite MMMs (*31*). Compared with its nonannealed counterparts (Fig. 2B), a much better zeolite-polymer adhesion can be observed (figs. S54 and S55). Full removal of the polymer by means of oxidative treatment at 800°C (fig. S51) led to a stable zeolite-only film (Fig. 2, D and E, and figs. S51 to S53), confirming the high zeolite loading in a random packing. This nearly continuous zeolite phase across the MMM thus creates a "percolation highway" to allow ultrafast permeation of the selected gas molecules.

As anticipated, neither Fourier transform infrared nor Raman microspectroscopy could find evidence for a covalent interaction between polymer and zeolite after annealing (figs. S18 and S61 to S66). Differential scanning calorimetry analysis indicated very good polymer-zeolite interactions in the MMM: With the Na-SSZ-39 loading, the glass transition temperature increased from 314°C (for Matrimid) to 325°C (for annealed Na-SSZ-39 MMMs), pointing toward "wrapping" of the zeolite by the polymer and rigidification of the polymer chains at the interface (fig. S17). We performed CO_2, CH_4, and N_2 sorption experiments on the 260°C annealed Matrimid membrane and the 50 wt % Na-SSZ-39 MMM to quantify their respective gas uptake. A substantially higher gas uptake was noted for the MMM (fig. S30).

Membrane gas separation performance

The mixed-gas selectivities of Na-SSZ-39 MMMs (table S5) were clearly higher than those of their ideal-gas selectivities (table S8) because of the competitive sorption of CO_2 in the Na-SSZ-39 zeolite. For example, for the 50 wt % Na-SSZ-39 MMM, the CO_2-CH_4 ideal-gas selectivity was ~336 (1 bar/25°C), whereas the equimolar CO_2-CH_4 mixed-gas selectivity reached >420 (2 bar/25°C—1 bar CO_2 and CH_4 partial pressures). Likewise, the CO_2-N_2 ideal-gas selectivity at 1 bar/25°C was ~32, whereas its mixed-gas selectivity at 2 bar/25°C increased to ~60. Once the stronger adsorbing CO_2 occupied the adsorption sites, the zeolite channels become partly inaccessible for the other gas, thus inhibiting permeation of CH_4 and N_2.

On the basis of the physisorption and ideal-gas permeation results, gas solubility and diffusivity values were calculated for the unfilled Matrimid membrane and 50 wt % Na-SSZ-39 MMM (table S20). With respect to the unfilled membrane, the MMM displayed a 4.6-times greater CO_2 solubility, whereas the CH_4 and N_2 solubility increased by 7.5 and 3.4 times, respectively. A 220-fold increase in CO_2 diffusivity was denoted for the MMM compared with that of the unfilled Matrimid membrane, whereas CH_4 and N_2 diffusivity only increased 14 and 148 times, respectively. The enhancement of CO_2-CH_4 diffusivity selectivity thus explains the strong improvement of the MMM gas separation capability (table S21). This results from the sharp size-sieving effect of Na-SSZ-39 for the CO_2-CH_4 pair. The increase in diffusivity selectivity for CO_2-N_2 is less pronounced because N_2 possesses a smaller kinetic diameter. The notable difference in separation factor for CO_2-CH_4 and CO_2-N_2 confirms the central role of the highly accurate size-sieving mechanism for the strong selectivities of Na-SSZ-39 MMMs.

Mixed-gas CO_2-CH_4 and CO_2-N_2 separation performances are presented in Fig. 3. For CO_2-CH_4, we observed a continuous increase in separation factor with increasing Na-SSZ-39 loading. Whereas the unfilled Matrimid membrane denotes a CO_2-CH_4 separation factor of ~45 and CO_2 permeability ~8 Barrer, we obtained the best MMM performance with the 50 wt % Na-SSZ-39 loading, which obtained a selectivity of >420 at 2 bar/25°C (~10-fold increase) at a simultaneous extreme CO_2 permeability of ~8280 Barrer (~1037-fold increase). We obtained similar results for the CO_2-N_2 separation performance in which the 50 wt %

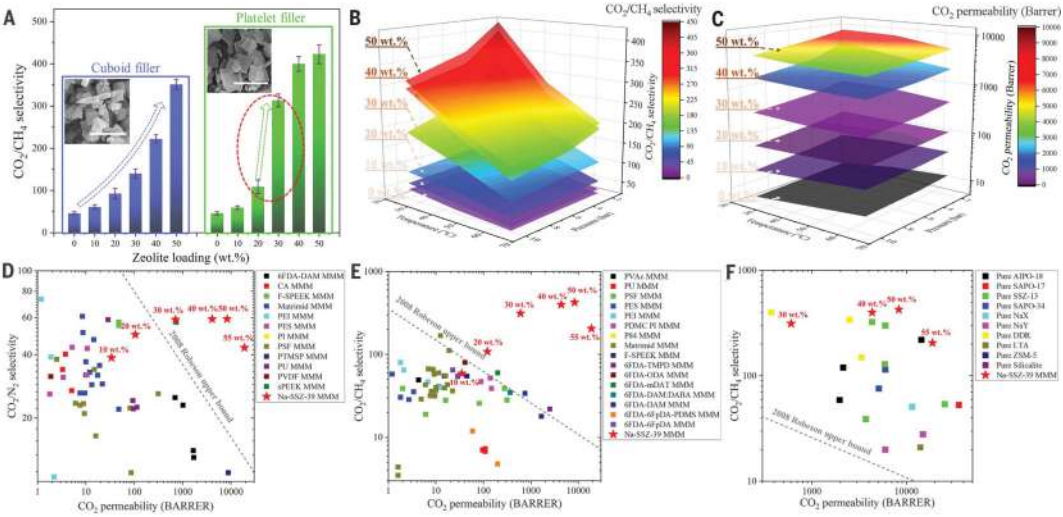

Fig. 3. The gas separation performances of Na-SSZ-39 MMMs. (**A**) The selectivity difference between cuboid-shaped and platelet-shaped Na-SSZ-39 MMMs. (Inset) SEM images show the morphology difference of two zeolites. (**B** and **C**) The temperature and pressure dependence of CO_2-CH_4 selectivity and CO_2 permeability. Nine points constitute a plane. (**D** and **E**) The performance of zeolite-filled MMMs from literature are shown in CO_2-N_2 and CO_2-CH_4 2008 Robeson plots. The red stars indicate the platelet-shaped Na-SSZ-39 MMMs. (**F**) The pure zeolite membranes from literature compared with the Na-SSZ-39 MMMs (≥30 wt %) and 2008 CO_2-CH_4 Robeson plot (full datasets are available in the supplementary materials).

MMM combined a CO_2 permeability of >8300 Barrer with a CO_2-N_2 separation factor of ~60 (versus ~8 and ~35 for unfilled Matrimid). The temperature and pressure dependency of the membrane performance are shown in Fig. 3, B and C, with different zeolite loadings. With increasing temperature, the CO_2 adsorption in the zeolite obviously decreased (fig. S27), resulting in lowered CO_2 permeability and CO_2-CH_4 selectivity. We observed similar behavior with rising feed pressure: Both CO_2 permeability and CO_2-CH_4 selectivity reduced. Because of its high CO_2-philicity, Na-SSZ-39 is already saturated with CO_2 molecules at low feed pressure. Further increased pressures thus contribute less to CO_2 permeation. For the same reason, the Na-SSZ-39 MMMs exhibit enhanced performance in feeds with lower CO_2 partial pressures (table S6). For example, the 50 wt % Na-SSZ-39 MMM gave a CO_2 permeability of >10,000 Barrer and a CO_2-CH_4 selectivity >460 for a 20 vol % CO_2/80 vol % CH_4 feed (figs. S23 and S24), which is close to the compositions of industrial feed streams, such as certain biogas and natural gas sources (*39*, *40*).

When depicted on selectivity-permeability trade-off plots, the Na-SSZ-39 MMMs already surpass the 2008 Robeson upper bound (*11*) from 30 wt % loading onward for CO_2-N_2 (Fig. 3D) and even from 20 wt % for CO_2-CH_4 (Fig. 3E). Ultimately, they realize an unprecedented jump toward the upper-right corner of the Robeson plot, ending up even beyond the performance area that is dominated by zeolite-only membranes (Fig. 3F). Outperforming most existing zeolite-only membranes can be related to the properties of the Na-SSZ-39 filler as well as the membrane morphology. Moreover, compared with the zeolite-only membranes, the Na-SSZ-39 MMMs (Fig. 4B) additionally keep their flexibility because of the presence of the polymer matrix (Fig. 4A and movie S2). Furthermore, because of the stability of the Na-SSZ-39 filler and the thermal annealing protocol, the Na-SSZ-39 MMMs (Fig. 4B) possess antiaging properties. Although the aging characteristics may vary with film thickness, the self-standing 50 wt % Na-SSZ-39 MMM shows comparable CO_2-CH_4 selectivity and CO_2 permeability even 360 days after preparation (table S5). From an application point of view in the frame of CO_2 removal, this antiaging, high-flux, and high-selectivity membrane can allow substantial reductions in both operational and capital costs because a simplified and more energy-efficient operation scheme with less recycling and milder compression and recompression stages can be applied, in combination with reduced membrane areas and less replacement (*2*, *3*).

The gas-separation performance of the Na-SSZ-39 MMMs can thus be explained by a combination of three factors.

First, the selection of the Na-SSZ-39 zeolite as membrane filler is critical. Because of its accurate molecular size-sieving effect and strong CO_2-philicity, Na-SSZ-39 possesses enormous diffusivity and solubility selectivities, thus promoting ultrahigh mixed-gas selectivity. Moreover, the noncentrosymmetric AEI-type framework allows preparation of high–aspect ratio platelets. In contrast to many high–aspect ratio porous materials that possess 1D channels perpendicular to their base face (*41*, *42*), the SSZ-39 platelet is equipped with a 3D channel system, with 3.84-Å windows in its lateral face (Fig. 1B). Therefore, regardless of the platelet's orientation inside the membrane, the SSZ-39 pore system always allows unhindered gas flow (Fig. 4, D and E).

Second, the sudden jump in CO_2-CH_4 separation factor at 20 to 30 wt % loading suggests a percolation effect (Fig. 3A); from this loading onward, gas permeation through the membrane is predominantly going through the zeolite phase. The reason for this shift in phase dominance should be sought in the practical ability to incorporate ultrahigh loadings of the high–aspect ratio filler in the polymer. This creates a membrane morphology, which consists of a quasi-continuous zeolite phase across the membrane starting from only 20 to 30 wt % loading (Fig. 4D) and allows for percolation of the gas molecules with minimal influence of the less permeable polymer phase. The top and bottom views (Fig. 2F) of the MMMs show that the zeolite platelets pile up from the bottom

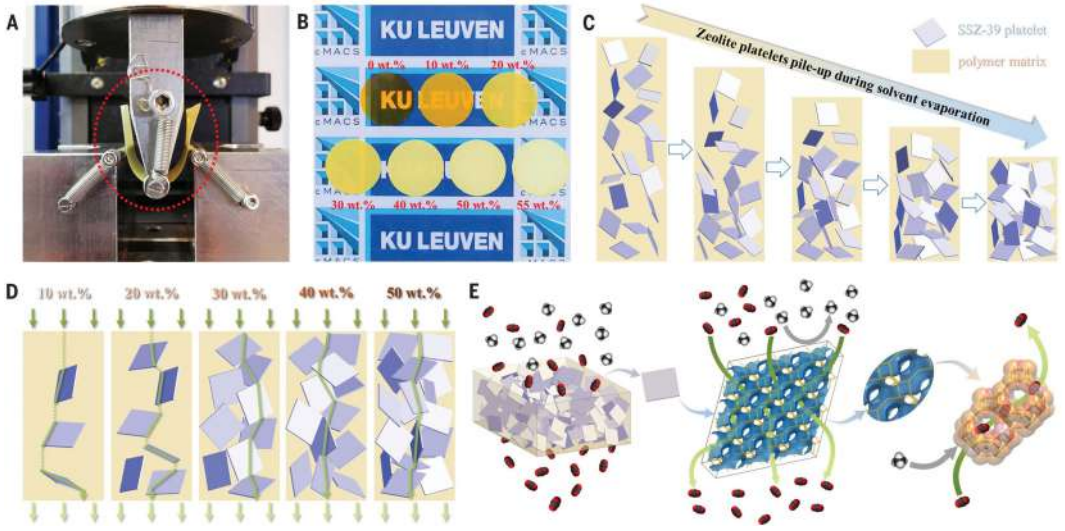

Fig. 4. Characterization and illustrations of platelet-shaped Na-SSZ-39 MMM. (**A**) The flexibility test (three-points bending) for 50 wt % Na-SSZ-39 MMM (table S4). (**B**) Visual appearance of 0 to 55 wt % Na-SSZ-39 MMMs. (**C**) Illustration of the solidification process of the platelet-shaped Na-SSZ-13 MMM, which results in a quasi-continuous zeolite phase across the membrane. (**D**) Illustration of the nonaligned zeolite platelet distribution in the polymer matrix with different zeolite loading. The preferential gas permeation pathways are indicated with the green arrows. (**E**) Schematic illustration of a MMM with (left) quasi-continuous zeolite phase and the unhindered CO_2 permeation (indicated with green arrows) through the (middle) 3D-channel system of platelet-shaped Na-SSZ-39 filler regardless of its orientation, as well as (right) the precise molecular sieving behavior that excludes CH_4 from CO_2 through the zeolite window.

and appear at the top of membrane when the zeolite loading reaches 30 wt % (Fig. 4C). In this context, the nonaligned, randomly oriented Na-SSZ-39 platelet distribution, which leads to a selective gas permeation highway, is a key driver and prerequisite for the membrane's extraordinary performance. This was also confirmed by comparing the platelet-shaped Na-SSZ-39 filler with a cuboid-shaped one [with similar properties except the aspect ratio (supplementary materials)]. As Fig. 3A shows, the sudden increment in CO_2-CH_4 selectivity was only observed for the platelet-shaped Na-SSZ-39 MMMs. Furthermore, although the cuboid-shaped Na-SSZ-39 MMMs also show great performances, the platelet-shaped Na-SSZ-39 MMMs exhibited far better CO_2-CH_4 selectivity and CO_2 permeability (tables S5 to S13), thus further confirming the morphology benefits of platelet-shaped Na-SSZ-39 MMMs.

Last, because the overall gas transport through the MMM is a net result of the properties of both zeolite and polymer, as well as of their mutual interactions, it is crucial to obtain a defect-free zeolite-polymer interface. Although rubbery polymers, such as polydimethylsiloxane (PDMS), facilitate creation of a defect-free interface (fig. S60), their intrinsically low selectivity and high permeability neutralize the beneficial contribution of the zeolite (table S15). The well-designed membrane preparation strategy minimizes the occurrence of unselective voids at the zeolite-Matrimid interface (figs. S54, S55, S58, and S59), allowing for ultrahigh zeolite loadings of >50 wt % without chemical modification of zeolite or polymer nor use of additives. Even at these high loadings, the Na-SSZ-39 MMMs still maintain desired flexibility (Fig. 4A), thus also creating excellent opportunities for module construction and upscaling.

Conclusions

We developed an ultrahigh-performance zeolite-filled MMM for CO_2 separations that shows unprecedented CO_2 removal performance, not only greater than that of any existing polymeric membrane or MMM but even surpassing that of most zeolite-only membranes. By circumventing the traditional incompatibility between zeolite filler and glassy polymer matrix, we prepared a flexible, defect-free zeolite-polyimide MMM with ultrahigh (>50 wt %) zeolite loadings. Na-SSZ-39 zeolite was discovered to be a superior filler because of its outstanding CO_2-philicity, precise molecular-sieving windows, strong competitive sorption behavior, and excellent stability, promoting strong, nonaging CO_2-separation performances. Because of the high–aspect ratio and 3D-channel system of the filler, a percolating gas permeation highway was created across the membrane, thus drastically enhancing the membrane's performance.

We used a scalable method to prepare defect-free zeolite-filled membranes with a commercially available glassy polymer, thus opening the door to developing well-processable, robust, and economical high-performance zeolite-filled MMMs for a variety of gas and liquid separations. It is especially beneficial for those zeolites that are difficult to be engineered into defect-free zeolite-only films.

REFERENCES AND NOTES

1. D. S. Sholl, R. P. Lively, *Nature* **532**, 435–437 (2016).
2. R. W. Baker, *Membrane Technology and Applications* (Wiley, ed. 3, 2012).
3. S. P. Nunes, K.-V. Peinemann, *Membrane Technology: In the Chemical Industry* (Wiley-VCH, ed. 2, 2006).
4. P. Bernardo, E. Drioli, G. Golemme, *Ind. Eng. Chem. Res.* **48**, 4638–4663 (2009).
5. R. W. Baker, B. T. Low, *Macromolecules* **47**, 6999–7013 (2014).
6. C. A. Scholes, G. W. Stevens, S. E. Kentish, *Fuel* **96**, 15–28 (2012).
7. S. Basu, A. L. Khan, A. Cano-Odena, C. Liu, I. F. J. Vankelecom, *Chem. Soc. Rev.* **39**, 750–768 (2010).
8. S. K. Simons, K. Nijmeijer, M. Wessling, *J. Membr. Sci.* **340**, 214–220 (2009).
9. G. He *et al.*, *Energy Environ. Sci.* **12**, 3305–3312 (2019).
10. M. E. Boot-Handford *et al.*, *Energy Environ. Sci.* **7**, 130–189 (2014).
11. L. M. Robeson, *J. Membr. Sci.* **320**, 390–400 (2008).
12. H. B. Park, J. Kamcev, L. M. Robeson, M. Elimelech, B. D. Freeman, *Science* **356**, eaab0530 (2017).
13. B. Comesaña-Gándara *et al.*, *Energy Environ. Sci.* **12**, 2733–2740 (2019).
14. N. Du *et al.*, *Nat. Mater.* **10**, 372–375 (2011).

15. M. Carta *et al*., *Science* **339**, 303–307 (2013).
16. H. W. H. Lai *et al*., *Science* **375**, 1390–1392 (2022).
17. Z. Lai *et al*., *Science* **300**, 456–460 (2003).
18. N. Rangnekar, N. Mittal, B. Elyassi, J. Caro, M. Tsapatsis, *Chem. Soc. Rev.* **44**, 7128–7154 (2015).
19. M. Y. Jeon *et al*., *Nature* **543**, 690–694 (2017).
20. X. Ma *et al*., *Science* **361**, 1008–1011 (2018).
21. N. Kosinov, J. Gascon, F. Kapteijn, E. J. M. Hensen, *J. Membr. Sci.* **499**, 65–79 (2016).
22. W. J. Koros, C. Zhang, *Nat. Mater.* **16**, 289–297 (2017).
23. S. Wang *et al*., *Energy Environ. Sci.* **9**, 1863–1890 (2016).
24. J. E. Bachman, Z. P. Smith, T. Li, T. Xu, J. R. Long, *Nat. Mater.* **15**, 845–849 (2016).
25. A. Kertik *et al*., *Energy Environ. Sci.* **10**, 2342–2351 (2017).
26. B. Wang *et al*., *Adv. Mater.* **32**, e1907701 (2020).
27. B. Seoane *et al*., *Chem. Soc. Rev.* **44**, 2421–2454 (2015).
28. J. Dechnik, J. Gascon, C. J. Doonan, C. Janiak, C. J. Sumby, *Angew. Chem. Int. Ed.* **56**, 9292–9310 (2017).
29. M. Galizia *et al*., *Macromolecules* **50**, 7809–7843 (2017).
30. I. F. Vankelecom, E. Scheppers, R. Heus, J. B. Uytterhoeven, *J. Phys. Chem.* **98**, 12390–12396 (1994).
31. R. Mahajan, R. Burns, M. Schaeffer, W. J. Koros, *J. Appl. Polym. Sci.* **86**, 881–890 (2002).
32. D. Bastani, N. Esmaeili, M. Asadollahi, *J. Ind. Eng. Chem.* **19**, 375–393 (2013).
33. S. I. Zones, Y. Nakagawa, S. T. Evans, G. S. Lee, US patent 5,958,370A (1999).
34. N. Nakazawa, S. Inagaki, Y. Kubota, *Chem. Lett.* **45**, 919–921 (2016).
35. M. Dusselier *et al*., *Chem. Mater.* **27**, 2695–2702 (2015).
36. M. Dusselier, M. E. Davis, *Chem. Rev.* **118**, 5265–5329 (2018).
37. Ch. Baerlocher, L. B. McCusker, Database of zeolite structures (2017); http://www.iza-structure.org/databases.
38. T. D. Pham, Q. Liu, R. F. Lobo, *Langmuir* **29**, 832–839 (2013).
39. S. Faramawy, T. Zaki, A. A. E. Sakr, *J. Nat. Gas Sci. Eng.* **34**, 34–54 (2016).
40. Y. Li *et al*., *Environ. Sci. Technol.* **53**, 11569–11579 (2019).
41. T. Rodenas *et al*., *Nat. Mater.* **14**, 48–55 (2015).
42. S. J. Datta *et al*., *Science* **376**, 1080–1087 (2022).

ACKNOWLEDGMENTS

We thank M. Roeffaers (KU Leuven, cMACS) for providing the Raman Spectromicroscopy measurement, M. Bastin for density measurement, and K. Yan for illustration drawing. This work was supported by the Fund for Scientific Research Flanders (FWO) and the Research Board of Ghent University (BOF). The computational resources (Stevin Supercomputer Infrastructure) and services used in this work were provided by the VSC (Flemish Supercomputer Center), funded by Ghent University, FWO, and the Flemish Government–department EWI. **Funding:** This work was supported by the Strategic Basic Research, Research Foundation–Flanders "SBOFWO" Biogas-Mambo S003721N (X.T. and I.V.); VlaioCataSPC moonrise HBC.2020.2612 (X.T. and I.V.); Research Foundation–Flanders "FWO" scholarships 1241822N, 12X7319N, and 1SB8821N (R.T., Y.L., and D.V.H.); Research Foundation–Flanders "FWO" G085220N (S.R., N.D.W., T.V.A., and M.D.); and Hercules fund AKUL/13/19 (I.V.) **Author contributions:** Conceptualization: X.T., Q.K., and I.V. Methodology: X.T., S.R., Q.K., R.T., M.D., and I.V. Investigation: X.T., S.R., Q.K., N.D.W., A.L., Y.L., I.A., D.V.H., and T.D. Visualization: X.T., S.R., A.L., and N.D.W. Funding acquisition: I.V., M.D., T.V.A., and V.V.S. Project administration: X.T. and I.V. Supervision: I.V. Writing – original draft: X.T. and R.T. Writing – review and editing: All authors. **Competing interests:** The authors declare that they have no competing interests. X.T., I.V., M.D., S.R., and R.T. submitted patent application EP22170367.1 by KU Leuven, which is based on this invention. **Data and materials availability:** All data are available in the main text or the supplementary materials.

SUPPLEMENTARY MATERIALS

Submitted 27 July 2022; accepted 16 November 2022
10.1126/science.ade1411

Paper VII

Quantum free energy profiles for molecular proton transfers

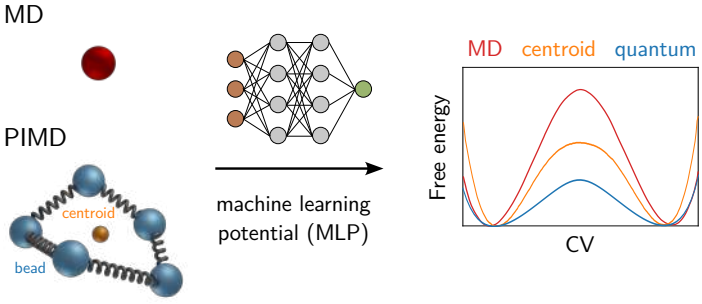

A. Lamaire, M. Cools-Ceuppens, M. Bocus, T. Verstraelen, V. Van Speybroeck

Journal of Chemical Theory and Computation, **2023**, 19 (1), 18–24

A. Lamaire performed the research and wrote the manuscript with contributions from all authors.

JCTC Journal of Chemical Theory and Computation

pubs.acs.org/JCTC Letter

Quantum Free Energy Profiles for Molecular Proton Transfers

Aran Lamaire, Maarten Cools-Ceuppens, Massimo Bocus, Toon Verstraelen, and Veronique Van Speybroeck*

Cite This: *J. Chem. Theory Comput.* 2023, 19, 18–24 Read Online

ACCESS | Metrics & More | Article Recommendations | Supporting Information

ABSTRACT: Although many molecular dynamics simulations treat the atomic nuclei as classical particles, an adequate description of nuclear quantum effects (NQEs) is indispensable when studying proton transfer reactions. Herein, quantum free energy profiles are constructed for three typical proton transfers, which properly take NQEs into account using the path integral formalism. The computational cost of the simulations is kept tractable by deriving machine learning potentials. It is shown that the classical and quasi-classical centroid free energy profiles of the proton transfers deviate substantially from the exact quantum free energy profile.

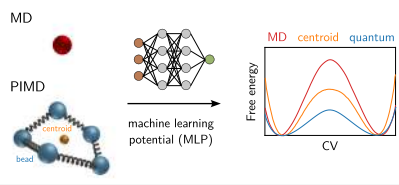

For many molecular systems, a quantum mechanical description of the electronic potential energy surface (PES) is the preferred simulation technique to properly model the interparticle interactions. Using the appropriate thermodynamic ensemble, the properties of these systems can then be derived at realistic temperatures and pressures by means of molecular dynamics (MD) simulations. While the underlying PES is hereby quantum mechanically determined by solving the electronic structure problem, the nuclear motion on the PES is most often described classically by Newtonian dynamics. As a consequence, nuclear quantum effects (NQEs) such as zero-point energy, the quantization of energy levels, or tunnelling are completely neglected, in spite of their importance in many chemical and biological processes.[1] In particular, at low temperatures and for light-weighted atoms such as hydrogen, NQEs can significantly alter the atomic behavior. To include the quantum mechanical nature of the nuclei in MD simulations, one can use path integral MD (PIMD) simulations, which rely on Feynman's path integral formulation of quantum mechanics.[2] Notwithstanding the substantial computational overhead of *ab initio* PIMD, describing both electrons and nuclei quantum mechanically, the ever improving performance of computing resources alongside the development of machine learning potentials (MLPs) with an *ab initio* accuracy is steadily establishing the technique as a common modeling approach.[3−7]

For activated processes, both classical and quantum MD simulations require the use of enhanced sampling methods to sample all the configurations involved in the rare event of crossing the energy barrier between two (meta)stable states. For classical MD, numerous enhanced sampling protocols have been devised to calculate free energy profiles, including umbrella sampling,[8] metadynamics,[9] thermodynamic integration, and variationally enhanced sampling.[10] Apart from a few dedicated path integral analogues, such as path integral metadynamics,[11] many classical enhanced sampling techniques are also applied to PIMD using the path centroid, which contracts the beads of the path integral ring polymer to a single atom (Figure 1). However, this only provides a quasi-classical

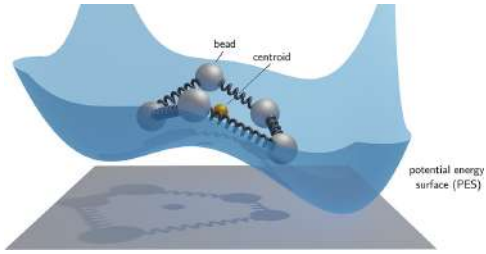

Figure 1. Schematic representation of a path integral ring polymer with five beads on a potential energy surface (PES). The path centroid is indicated in yellow.

approximation to the quantum free energy profile, as the beads of the path integral ring polymer rather than the averaged path centroids are subjected to the actual quantum free energy profile, as also pointed out by refs 6 and 12. The quantum free energy profile is thus obtained by treating both the electrons and nuclei quantum mechanically and expressed as a function of bead related quantities. Nevertheless, the path centroids can

Received: August 25, 2022
Published: December 23, 2022

https://doi.org/10.1021/acs.jctc.2c00874
J. Chem. Theory Comput. 2023, 19, 18–24

Journal of Chemical Theory and Computation pubs.acs.org/JCTC Letter

still be used to bias a PIMD simulation and surmount the free energy barrier, just as for the classical counterpart, if the free energy profile of the centroid is afterward transformed to a profile for the beads.

In this work, the influence of both NQEs and a proper description of the quantum free energy profile is examined for three molecular proton transfers: (1) the concerted proton transfer in the formic acid dimer, (2) the sigmatropic proton rearrangement in pentadiene, and (3) the tautomerization of acetaldehyde to vinyl alcohol. These reactions, aside from being ubiquitous reaction types within organic synthesis, are specifically selected to illustrate the impact of the different free energy descriptions on processes with different free energy barrier shapes and heights (ranging from about 25−275 kJ/mol). Furthermore, as the importance of NQEs is known to increase with decreasing temperature,[1] a temperature range of 200−450 K is considered.

METHODS

Path Integral Molecular Dynamics (PIMD). To include the quantum mechanical nature of the atomic nuclei in a molecular dynamics (MD) simulation, one can rely on Feynman's path integral formulation of quantum mechanics. Using the Born−Oppenheimer approximation, the electronic and nuclear degrees of freedom in an MD simulation can be decoupled to obtain an electronic potential energy surface (PES) that is only parametrically dependent on the nuclear coordinates. Depending on the system that is to be studied, the PES can be described by classical force fields, machine learning potentials (MLPs), or *ab initio* solutions of the Schrödinger equation. For the nuclei, however, one generally adopts a classical treatment, sampling the classical canonical ensemble with statistical weights proportional to $e^{-\beta H}$, with $\beta = \frac{1}{k_B T}$ the inverse temperature and H the Hamiltonian of the nuclear subsystem. To sample the corresponding quantum ensemble, the Hamiltonian is replaced by the appropriate quantum mechanical operator $\hat{H}$, for which the statistical weight can be cast into the following form using a Trotter expansion[13]

$$e^{-\beta\hat{H}} \approx [e^{-\frac{\beta}{2P}\hat{V}}\, e^{-\frac{\beta}{P}\hat{T}}\, e^{-\frac{\beta}{2P}\hat{V}}]^P \tag{1}$$

with $\hat{V}$ the potential energy operator and $\hat{T}$ the kinetic energy operator. In the limit of $P \to \infty$, this expansion yields exact results. By means of the path integral technique, the quantum canonical partition function can then be transformed into a classical equivalent by using an extended phase space in which every atom i is replaced by P harmonically coupled beads, that is

$$Z_P \propto \prod_{k=1}^{P}\prod_{i=1}^{N} \int \mathrm{d}\mathbf{p}_i^{(k)} \int \mathrm{d}\mathbf{r}_i^{(k)}\, e^{-\beta H_P} \tag{2}$$

with

$$H_P = \sum_{k=1}^{P}\sum_{i=1}^{N}\left[\frac{\mathbf{p}_i^{(k)2}}{2m_i} + \frac{1}{2}m_i\omega_P^2(\mathbf{r}_i^{(k+1)} - \mathbf{r}_i^{(k)})^2\right] + \frac{1}{P}\sum_{k=1}^{P} V(\mathbf{r}_1^{(k)}, ..., \mathbf{r}_N^{(k)}) \tag{3}$$

where $\mathbf{r}_i^{(k)}$ and $\mathbf{p}_i^{(k)}$ are respectively the position and momentum of the k-th bead of the i-th particle, m_i is the mass of particle i, $\omega_P = \frac{\sqrt{P}}{\beta\hbar}$ is the angular frequency of the harmonic nearest-neighbor interaction, and $\mathbf{r}_i^{(P+1)} = \mathbf{r}_i^{(1)}$.

Quantum Free Energy Profiles. To derive a free energy profile of a reaction using enhanced sampling techniques such as umbrella sampling, metadynamics, or variationally enhanced sampling, one starts by constructing a suitable collective variable q, described by a function $Q(\mathbf{r}^N)$, that allows to drive the reaction across the activation barrier.[14] In classical statistical physics, the free energy as a function of the variable q is then defined as

$$\begin{aligned} F_{\mathrm{cl}}(q) &= -\frac{1}{\beta}\ln\frac{\int \mathrm{d}\Gamma\, \delta(Q(\mathbf{r}^N) - q)\, e^{-\beta H}}{\int \mathrm{d}\Gamma\, e^{-\beta H}} \\ &= -\frac{1}{\beta}\ln\langle\delta(Q(\mathbf{r}^N) - q)\rangle \end{aligned} \tag{4}$$

where H denotes the classical Hamiltonian, Γ is the entire phase space, and $\mathrm{d}\Gamma = \mathrm{d}\mathbf{r}^N\, \mathrm{d}\mathbf{p}^N$. In the path integral formalism, however, every atom is replaced by a set of harmonically coupled beads, so that thermodynamic quantities are determined by averaging over the beads. Therefore, the quantum free energy is defined as[6,13]

$$F_{\mathrm{quantum}}(q) = -\frac{1}{\beta}\ln\left\langle \frac{1}{P}\sum_{k=1}^{P}\delta(Q(\mathbf{r}^{(k)^N}) - q)\right\rangle \tag{5}$$

where the ensemble average $\langle\cdot\rangle$ uses the Hamiltonian H_P of the classical isomorphism (eq 3). Although the collective variable q now depends on bead quantities, it is possible to calculate the quantum free energy profile by applying a bias in a collective variable $q_{cl}^{(c)}$ that only depends on centroid quantities, in which the beads are contracted to a single atom. The position of the centroid of atom i is for instance given by

$$\mathbf{r}_i^{(c)} = \frac{1}{P}\sum_{P=1}^{N}\mathbf{r}_i^{(k)} \tag{6}$$

The resulting free energy profile $F_{\mathrm{centroid}}(q_{cl}^{(c)})$, given by

$$F_{\mathrm{centroid}}(q_{cl}^{(c)}) = -\frac{1}{\beta}\ln\langle\delta(Q(\mathbf{r}^{(c)^N}) - q_{cl}^{(c)})\rangle \tag{7}$$

can subsequently be converted into $F_{\mathrm{quantum}}(q)$ by means of a transformation of the collective variable (see Supporting Information S1)

$$\begin{aligned} F_{\mathrm{quantum}}(q) &= -\frac{1}{\beta}\ln\left[\frac{1}{P}\sum_{k=1}^{P}\langle\delta(Q(\mathbf{r}^{(k)^N}) - q)\rangle\right] \\ &= -\frac{1}{\beta}\ln\left[\frac{1}{P}\sum_{k=1}^{P}\int \mathrm{d}q_{cl}^{(c)}\, p_b(q^{(k)}|q_{cl}^{(c)})\, e^{-\beta F_{\mathrm{centroid}}(q_{cl}^{(c)})}\right] + C \end{aligned} \tag{8}$$

where C is a negligible constant, and $p_b(q^{(k)}|q_{cl}^{(c)})$ is the conditional probability that the collective variable takes the value q for bead k in a biased simulation when the centroid collective variable has a value $q_{cl}^{(c)}$. Hence, by simply tracking the values of $q^{(k)}$ and $q_{cl}^{(c)}$ throughout the enhanced sampling simulations in the centroid collective variable $q_{cl}^{(c)}$, the conditional probability $p_b(q^{(k)}|q_{cl}^{(c)})$ can be constructed, and $F_{\mathrm{centroid}}(q_{cl}^{(c)})$ can be converted into $F_{\mathrm{quantum}}(q)$. Remark that this transformation approach can be shown to be equivalent to the method proposed in ref 6 by Tuckerman *et al.* (see Supporting Information S1).

https://doi.org/10.1021/acs.jctc.2c00874
J. Chem. Theory Comput. 2023, 19, 18−24

Journal of Chemical Theory and Computation pubs.acs.org/JCTC Letter

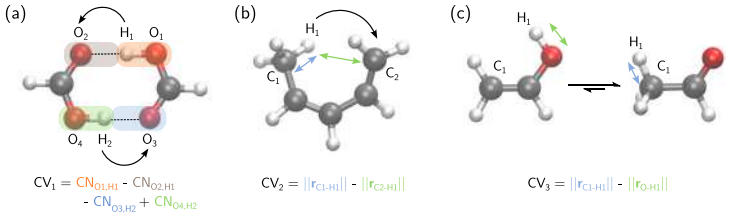

Figure 2. Molecular representation of (a) a double proton transfer in a formic acid dimer, (b) a sigmatropic proton rearrangement in pentadiene, and (c) the tautomerization of vinyl alcohol to acetaldehyde. The collective variable (CV) used to sample the proton transfer reaction is indicated below each representation, where $CN_{i,j}$ denotes a coordination number (see eq 12).

Furthermore, given that all the beads of an atom are in principle equivalent, the quantum free energy is also given by

$$F_{\text{quantum}}(q) = \frac{1}{P}\sum_{k=1}^{P} F^{(k)}(q) = -\frac{1}{P\beta}\sum_{k=1}^{P} \ln\langle\delta(Q(\mathbf{r}^{(k)^N}) - q)\rangle \tag{9}$$

which can also be obtained by biasing the ring polymer's centroid in an enhanced PIMD simulation through a similar transformation as in eq 8:

$$\begin{aligned} F_{\text{quantum}}(q) &= -\frac{1}{P\beta}\sum_{k=1}^{P} \ln\langle\delta(Q(\mathbf{r}^{(k)^N}) - q)\rangle \\ &= -\frac{1}{P\beta}\sum_{k=1}^{P} \ln\left[\int \mathrm{d}q_{cl}^{(c)}\, p_b(q^{(k)}|q_{cl}^{(c)})\, e^{-\beta F_{\text{centroid}}(q_{cl}^{(c)})}\right] + C \end{aligned} \tag{10}$$

Both formulas of the quantum free energy (eqs 8 and 10) should in principle yield the same result, as they are theoretically equivalent. Discrepancies between these different methods of calculating the quantum free energy can however arise due to the sensitivity of eq 8 to inequivalences in the sampling of the beads. In particular at lower temperatures, these bead inequivalences tend to become more prominent (see Supporting Information S10). Therefore, eq 10 is the preferred transformation approach, as it is more robust with respect to bead inequivalences. If one does not rely on centroid biased simulations, eq 9 implies that every bead should be biased separately, which would make the calculation of the quantum free energy profile P times more expensive. Strictly speaking, the equivalence of the beads also allows to bias only a single bead, although this reduces the sampling efficiency and is most likely to yield sampling difficulties, similar to the issues known for the calculation of rate constants (which can be calculated from both centroid or quantum free energy profiles).[15] More specifically, when a single bead is restrained around the top of a free energy barrier, the ring polymer possesses the freedom to orient ifself toward either side of the barrier. For a steep free energy barrier, the ring polymer is most likely to sample only one side of the barrier, which hampers a proper sampling. However, by optimizing the time constant of the PILE[16] thermostat as a function of the force constant of the umbrella bias potential, Bishop *et al.*[12] showed that it is possible to obtain converged quantum free energy profiles by biasing only a single bead. As their study only included dimers, which give rise to free energy profiles with a Lennard-Jones shape, the typical sampling difficulties near free energy peaks were not encountered. Finally, we also note that in the case of unbiased PIMD simulations the quantum free energy profile can be readily computed from eq 5 or 9 by means of a histogram of the bead collective variable.[17]

Computational Details. The proton transfer reactions studied in this work include a double proton transfer in a formic acid dimer, a sigmatropic proton rearrangement in pentadiene, and the tautomerization of acetaldehyde to vinyl alcohol (Figure 2). The free energy profile of each proton transfer was calculated using umbrella sampling in combination with a machine learning potential (MLP), which significantly reduces the computational cost of the simulations. To construct an initial classical free energy profile and to collect the necessary training data to build an MLP for each of the molecules, *ab initio* umbrella sampling simulations were performed with PSI4,[18] using a PBE0 functional[19] and a 6-311G(3df,3pd) Pople basis set.[20] From every *ab initio* umbrella simulation, the energies and forces of snapshots taken every 5 fs were used to train an equivariant MLP with our in-house developed code available at https://github.com/mcoolsce/NNFFLIB and archived on 10.5281/zenodo.6606271. The neural network architecture of the MLP is inspired by the Neural Equivariant Interatomic Potential (NequIP),[21] but the rotation order of the equivariant features is limited to $\ell = 1$ (see Supporting Information Section S2). Both classical and quantum free energy profiles were constructed with the MLP to test its stability, the performance with respect to the *ab initio* simulations, and to extract additional configurations that were not present in the initial data set. The final MLP was then obtained by training to this extended data set. More details regarding the training of the MLP are provided in Section S3 of the Supporting Information.

The test mean absolute error on the energy and the forces is limited to respectively 0.4 meV and 1.3 meV/Å for the formic acid dimer, 1.1 meV and 4.5 meV/Å for pentadiene, and 0.3 meV and 1.9 meV/Å for acetaldehyde/vinyl alcohol. A comparison between the *ab initio* and MLP free energy profiles, obtained both classically or with the inclusion of NQEs, is given in Figures S1−S6 of the Supporting Information. For the classically sampled proton transfers, the 20 ps *ab initio* umbrella sampling simulations are not fully converged, which can be easily resolved by the MLP by extending the simulation time to 250 ps, given that the MLP tremendously accelerates the evaluation of the PES (see Supporting Information Section S4). In the enhanced PIMD simulations, the spatially extended ring polymer describing the proton facilitates the sampling of the proton transfer, so that the *ab initio* free energy profiles are in excellent agreement with the MLP free energy profiles (which have an increased simulation time of 50 ps). However, from the convergence of the energy around the transition states as a function of the number of beads (Figures S7−S9), it follows that more beads are required than the 16 beads used to construct the *ab initio*

https://doi.org/10.1021/acs.jctc.2c00874
J. Chem. Theory Comput. 2023, 19, 18−24

Journal of Chemical Theory and Computation pubs.acs.org/JCTC Letter

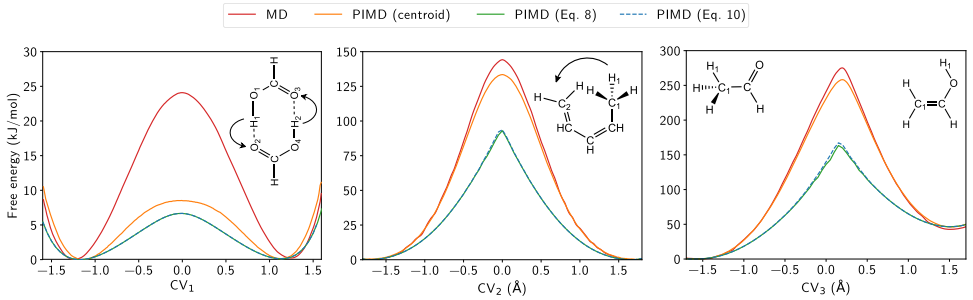

Figure 3. Free energy profiles of a double proton transfer in a formic acid dimer at 200 K (*left*), a sigmatropic proton rearrangement in pentadiene at 450 K (*middle*), and the tautomerization of acetaldehyde to vinyl alcohol at 450 K (*right*). For each proton transfer, both the classical free energy (MD) and the quantum free energy (PIMD) are reported. The PIMD (centroid) profile represents the free energy that is directly obtained when sampling along the centroid CV, before applying the appropriate transformation of eq 8 or 10.

free energy profiles. The differences between the free energy profiles derived with 16 beads or 64 beads are nevertheless limited (Figure S11).

To steer the enhanced sampling of the proton transfers using umbrella sampling, each molecule is biased according to a specific collective variable (CV). For the formic acid dimer, the collective variable for the double proton transfer is given by a difference in coordination numbers

$$CV_1 = CN_{O_1,H_1} - CN_{O_2,H_1} - CN_{O_3,H_2} + CN_{O_4,H_2} \quad (11)$$

with

$$CN_{i,j} = \frac{1 - \left(\frac{r_{ij}}{r_0}\right)^6}{1 - \left(\frac{r_{ij}}{r_0}\right)^{12}} \quad (12)$$

where $\mathbf{r}_{ij}$ is the interatomic distance between atoms i and j, and $\mathbf{r}_0$ = 1.4 Å. The labels of the atoms in eq 11 are indicated in Figure 2. Given that the double proton transfer in the formic acid dimer was shown to be concerted but not correlated (see Supporting Information S7),[22] a simultaneous proton transfer is assumed in the definition of CV_1. For the proton transfers in pentadiene (CV_2) and acetaldehyde (CV_3), a simple difference in interatomic distances can be used as a collective variable

$$CV_2 = \left|\left|\mathbf{r}_{C_1-H_1}\right|\right| - \left|\left|\mathbf{r}_{C_2-H_1}\right|\right| \quad (13)$$

$$CV_3 = \left|\left|\mathbf{r}_{C_1-H_1}\right|\right| - \left|\left|\mathbf{r}_{O-H_1}\right|\right| \quad (14)$$

for which the atomic labels are also indicated in Figure 2. All the simulations in this work relied on `PLUMED` 2.8 to implement the bias potential,[23,24] which was coupled to `Yaff`[25] to perform enhanced classical MD and to `i-PI`[26] to perform enhanced PIMD. An overview of the umbrella force constants and equilibrium values for every reaction is provided in Table S4. The temperature of the classical MD simulations was controlled by a 3-bead Nosé–Hoover chain thermostat,[27] whereas the PIMD simulations made use of a PILE-L thermostat,[16] both using a time constant of 100 fs. The classical MD and PIMD simulations used a time step of respectively 0.5 and 0.25 fs.

RESULTS AND DISCUSSION

The classical and quantum free energy profiles for a double proton transfer in a formic acid dimer, a sigmatropic proton rearrangement in pentadiene, and the tautomerization of acetaldehyde to vinyl alcohol are shown in Figure 3. These three proton transfer reactions span a classical free energy range of about 25–275 kJ/mol, which makes them ideally suited to investigate the influence of the inclusion of NQEs on the free energy. The concerted double proton transfer in the formic acid dimer has the lowest classical free energy barrier (24.1 kJ/mol at 200 K), which is reduced by a factor of about three when the atomic nuclei are treated quantum mechanically. The centroid free energy profile, which corresponds to the collective variable in which the enhanced PIMD sampling was performed, exhibits only small deviations from the actual quantum free energy profile, that is obtained after performing the transformation given by eq 8 or 10. The barrier height changes from 8.5 kJ/mol for the centroid profile to 7.3 kJ/mol for the bead profile, which is a small absolute difference (similar to the one found by Tuckerman *et al.* for hydrogen diffusion in an sII clathrate[6]), but nevertheless a reduction of 14%. Both transformations are also observed to yield the same quantum free energy profile (Figure 3), indicating a proper sampling of all PIMD beads and of the conditional probability used in the transformation.

For the proton transfer in pentadiene and acetaldehyde, by contrast, there is a striking difference between the centroid and bead profiles. By switching from a classical sampling to a quantum sampling in a centroid collective variable, the free energy barrier of the proton transfer in pentadiene is lowered by about 11 kJ/mol (from 144.2 to 133.5 kJ/mol at 450 K). After transformation to a bead collective variable, the resulting quantum free energy profile has a barrier of 93 kJ/mol, thereby reducing the barrier by an additional 40 kJ/mol, yielding a total reduction of 35% with respect to the classical description. For acetaldehyde, the reduction is even larger. The classical free energy barrier of 275.1 kJ/mol drops to 258.2 kJ/mol in a centroid description and to 163.5 kJ/mol for the actual quantum free energy profile, resulting in a diminution of 40% with respect to the classical barrier. Due to the high activation energy of the reaction, the transition state region is sampled less easily, so that a discrepancy of the order of 5 kJ/mol remains present between the two different transformation approaches of eqs 8 and 10 due to the sensitivity of eq 8 to

https://doi.org/10.1021/acs.jctc.2c00874
J. Chem. Theory Comput. 2023, 19, 18–24

Journal of Chemical Theory and Computation pubs.acs.org/JCTC Letter

inequivalences between the beads, as explained in more detail in Section S10 of the Supporting Information. At lower temperatures, the reduced thermal motion also tends to increase the inequivalences in the sampling of the beads, as shown for pentadiene in Section S10.

Each of the three proton transfer reactions clearly demonstrates the importance of an adequate quantum mechanical description of the atomic nuclei in calculating a free energy profile, in line with other proton transfers studied in the literature.[28−30] Even at a temperature of 450 K, NQEs are observed to significantly alter the classical behavior of pentadiene and acetaldehyde. The full extent of the NQEs on the free energy becomes clear when exchanging the quasi-classical centroid description for a description at the level of the bead quanta. Due to the quantum uncertainty on the position of the nuclei, mimicked by the spatial extension of the path integral ring polymer, the bead quanta experience a lower energy barrier since they are not precisely pinned to the transition state but rather envelop it (Figures 1 and 4). As the free energy barriers grow higher and are more sharply peaked, this effect is reinforced, and the dissimilarity between the centroid and the beads increases. In Figure 5, the probability density of the radius of gyration r_{gyr} and the maximal extent r_{max} of the ring polymer of the transitioning proton(s) are shown as a function of the collective variable for each molecule, with

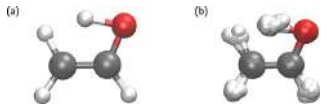

Figure 4. Centroid (a) and bead (b) representation of vinyl alcohol from an umbrella simulation with CV_3 = 0.2. In the bead representation, every atom is replaced by a ring polymer of 64 beads.

$$r_{gyr} = \sqrt{\frac{1}{P}\sum_{k=1}^{P}\left\|\mathbf{r}_H^{(k)} - \mathbf{r}_H^{(c)}\right\|^2} \tag{15}$$

$$r_{\max} = \max_{k\in\{1,\ldots,P\}}\left\|\mathbf{r}_H^{(k)} - \mathbf{r}_H^{(c)}\right\| \tag{16}$$

Both probability densities exhibit a sparser probability distribution around the transition state, in particular for acetaldehyde, thus confirming the increased stretching of the proton's ring polymer around the transition state. Although the spatial expansion of the proton is most pronounced, also the neighboring oxygen or carbon atoms effectively increase in size, which can further aid the reaction mechanism. This is reflected in the quantum radial distribution functions (RDFs) reported in Figures S13−S16, which show a significant broadening for the peaks of the O−H and C−H atom pairs involved in the proton transfer reaction in comparison with the classical RDFs. Furthermore, the peak broadening is also observed to be more prominent near the transition state than near the free energy minima, in agreement with the proton radius of gyration.

CONCLUSIONS

Notwithstanding the well-known impact of nuclear quantum effects (NQEs) on the behavior of protons and their tendency

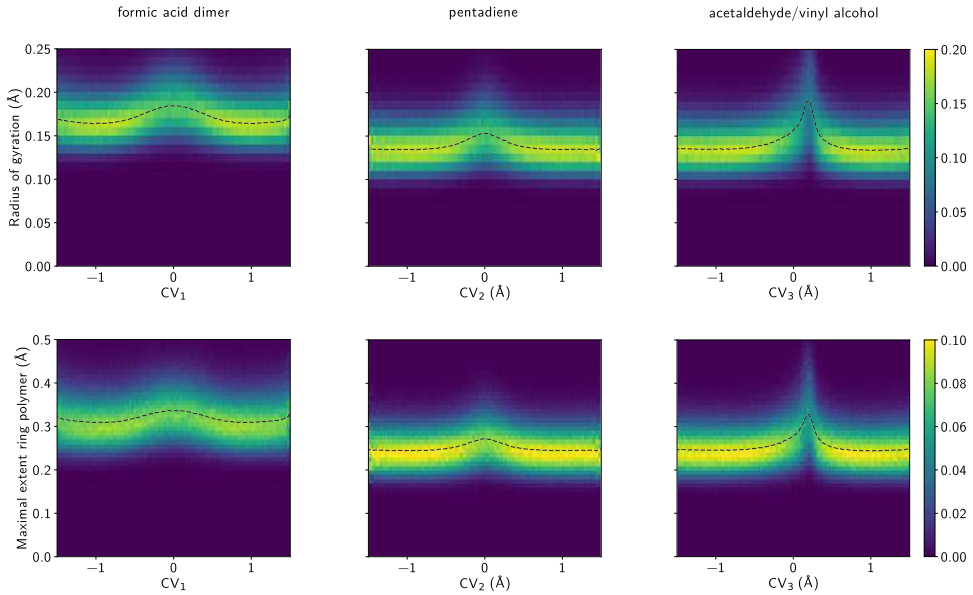

Figure 5. Conditional probability density $p(r_{gyr/max}|CV_i)$ of the radius of gyration (*top row*) and maximal ring polymer extent (*bottom row*) (eqs 15 and 16) of the transitioning proton(s) in formic acid, pentadiene, and acetaldehyde/vinyl alcohol as a function of the collective variable. The average of the probability density as a function of the collective variable is indicated by a dashed black line.

https://doi.org/10.1021/acs.jctc.2c00874
J. Chem. Theory Comput. 2023, 19, 18−24

to lower the activation energy of proton transfer reactions, this work demonstrates that also the quasi-classical approximation of the free energy, using the path integral centroid, is unable to explicitly represent the full impact of NQEs. In enhanced sampling simulations, a bias on the path integral centroid is however most convenient and computationally efficient and can provide all the required information to generate the quantum free energy profile at the level of the individual path integral beads through a postprocessing transformation. Using three molecular proton transfer reactions, spanning a classical free energy range of about 25−275 kJ/mol, the quantum free energy profiles were shown to significantly deviate from the quasi-classical centroid approximations, due to the large spatial extent of the path integral ring polymer. As the free energy barrier becomes higher and more sharply peaked, the deviation is observed to increase, as the difference between the free energy experienced by the centroid and beads is more pronounced. In order to reduce the computational cost associated with *ab initio* path integral molecular dynamics (PIMD), machine learning potentials (MLPs) were trained to accelerate the evaluation of the potential energy surface while maintaining an *ab initio* accuracy. By further exploiting the effective cost reduction of *ab initio* PIMD through the use of MLPs and by combining the MLP with PIMD acceleration techniques, NQEs can also systematically be accounted for in chemical reactions of larger molecular systems. For proton transfer reactions in particular, which are omnipresent in chemical processes, an adequate description of NQEs is indispensable to obtain reliable quantum free energy profiles.

■ ASSOCIATED CONTENT

Supporting Information

The Supporting Information is available free of charge at https://pubs.acs.org/doi/10.1021/acs.jctc.2c00874.

Mathematical details of transformation between centroid and bead free energy profiles, elaborate discussion of MLP architecture and generation of training data sets, *ab initio* validation of MLP free energy profiles, convergence of PIMD simulations, RDFs of different molecules, and temperature dependence of proton transfer in pentadiene (PDF)

MLPs of the formic acid dimer, pentadiene, and acetaldehyde/vinyl alcohol (ZIP)

■ AUTHOR INFORMATION

Corresponding Author

Veronique Van Speybroeck − *Center for Molecular Modeling (CMM), Ghent University, 9052 Zwijnaarde, Belgium;* orcid.org/0000-0003-2206-178X; Email: Veronique.VanSpeybroeck@UGent.be

Authors

Aran Lamaire − *Center for Molecular Modeling (CMM), Ghent University, 9052 Zwijnaarde, Belgium;* orcid.org/0000-0003-0093-5490

Maarten Cools-Ceuppens − *Center for Molecular Modeling (CMM), Ghent University, 9052 Zwijnaarde, Belgium;* orcid.org/0000-0002-7363-7534

Massimo Bocus − *Center for Molecular Modeling (CMM), Ghent University, 9052 Zwijnaarde, Belgium;* orcid.org/0000-0001-9474-6644

Toon Verstraelen − *Center for Molecular Modeling (CMM), Ghent University, 9052 Zwijnaarde, Belgium;* orcid.org/0000-0001-9288-5608

Complete contact information is available at: https://pubs.acs.org/10.1021/acs.jctc.2c00874

Notes

The authors declare no competing financial interest.

■ ACKNOWLEDGMENTS

This work was supported by the Fund for Scientific Research Flanders (FWO), Flanders Industry Innovation Moonshot (ARCLATH II, No. HBC.2021.0254), and the Research Board of Ghent University (BOF). The computational resources (Stevin Supercomputer Infrastructure) and services used in this work were provided by the VSC (Flemish Supercomputer Center), funded by Ghent University, FWO, and the Flemish Government−department EWI.

■ REFERENCES

(1) Markland, T. E.; Ceriotti, M. Nuclear quantum effects enter the mainstream. *Nat. Rev. Chem.* **2018**, *2*, 0109.

(2) Feynman, R. P. Space-Time Approach to Non-Relativistic Quantum Mechanics. *Rev. Mod. Phys.* **1948**, *20*, 367−387.

(3) Unke, O. T.; Chmiela, S.; Sauceda, H. E.; Gastegger, M.; Poltavsky, I.; Schütt, K. T.; Tkatchenko, A.; Müller, K.-R. Machine Learning Force Fields. *Chem. Rev.* **2021**, *121*, 10142−10186.

(4) Friederich, P.; Häse, F.; Proppe, J.; Aspuru-Guzik, A. Machine-learned potentials for next-generation matter simulations. *Nat. Mater.* **2021**, *20*, 750−761.

(5) Deringer, V. L.; Bartók, A. P.; Bernstein, N.; Wilkins, D. M.; Ceriotti, M.; Csányi, G. Gaussian Process Regression for Materials and Molecules. *Chem. Rev.* **2021**, *121*, 10073−10141.

(6) Cendagorta, J. R.; Shen, H.; Bačić, Z.; Tuckerman, M. E. Enhanced Sampling Path Integral Methods Using Neural Network Potential Energy Surfaces with Application to Diffusion in Hydrogen Hydrates. *Adv. Theory Simul.* **2021**, *4*, 2000258.

(7) Li, C.; Voth, G. A. Using Machine Learning to Greatly Accelerate Path Integral Ab Initio Molecular Dynamics. *J. Chem. Theory Comput.* **2022**, *18*, 599−604.

(8) Torrie, G.; Valleau, J. Nonphysical sampling distributions in Monte Carlo free-energy estimation: Umbrella sampling. *J. Comput. Phys.* **1977**, *23*, 187−199.

(9) Laio, A.; Parrinello, M. Escaping free-energy minima. *Proc. Natl. Acad. Sci. U.S.A.* **2002**, *99*, 12562−12566.

(10) Valsson, O.; Parrinello, M. Variational Approach to Enhanced Sampling and Free Energy Calculations. *Phys. Rev. Lett.* **2014**, *113*, 090601.

(11) Quhe, R.; Nava, M.; Tiwary, P.; Parrinello, M. Path Integral Metadynamics. *J. Chem. Theory Comput.* **2015**, *11*, 1383−1388.

(12) Bishop, K. P.; Roy, P.-N. Quantum mechanical free energy profiles with post-quantization restraints: Binding free energy of the water dimer over a broad range of temperatures. *J. Chem. Phys.* **2018**, *148*, 102303.

(13) Tuckerman, M. E.*Statistical Mechanics: Theory and Molecular Simulation*; OUP Oxford: 2010.

(14) Peters, B. Reaction Coordinates and Mechanistic Hypothesis Tests. *Annu. Rev. Phys. Chem.* **2016**, *67*, 669−690.

(15) Craig, I. R.; Manolopoulos, D. E. A refined ring polymer molecular dynamics theory of chemical reaction rates. *J. Chem. Phys.* **2005**, *123*, 034102.

(16) Ceriotti, M.; Parrinello, M.; Markland, T. E.; Manolopoulos, D. E. Efficient stochastic thermostatting of path integral molecular dynamics. *J. Chem. Phys.* **2010**, *133*, 124104.

(17) Rossi, M.; Ceriotti, M.; Manolopoulos, D. E. Nuclear Quantum Effects in H^+ and OH^- Diffusion along Confined Water Wires. *J. Phys. Chem. Lett.* **2016**, *7*, 3001−3007.
(18) Smith, D. G. A.; Burns, L. A.; Simmonett, A. C.; Parrish, R. M.; Schieber, M. C.; Galvelis, R.; Kraus, P.; Kruse, H.; Di Remigio, R.; Alenaizan, A.; James, A. M.; Lehtola, S.; Misiewicz, J. P.; Scheurer, M.; Shaw, R. A.; Schriber, J. B.; Xie, Y.; Glick, Z. L.; Sirianni, D. A.; O'Brien, J. S.; Waldrop, J. M.; Kumar, A.; Hohenstein, E. G.; Pritchard, B. P.; Brooks, B. R.; Schaefer, H. F.; Sokolov, A. Y.; Patkowski, K.; DePrince, A. E.; Bozkaya, U.; King, R. A.; Evangelista, F. A.; Turney, J. M.; Crawford, T. D.; Sherrill, C. D. PSI4 1.4: Open-source software for high-throughput quantum chemistry. *J. Chem. Phys.* **2020**, *152*, 184108.
(19) Adamo, C.; Barone, V. Toward reliable density functional methods without adjustable parameters: The PBE0 model. *J. Chem. Phys.* **1999**, *110*, 6158−6170.
(20) Frisch, M. J.; Pople, J. A.; Binkley, J. S. Self-consistent molecular orbital methods 25. Supplementary functions for Gaussian basis sets. *J. Chem. Phys.* **1984**, *80*, 3265−3269.
(21) Batzner, S.; Musaelian, A.; Sun, L.; Geiger, M.; Mailoa, J. P.; Kornbluth, M.; Molinari, N.; Smidt, T. E.; Kozinsky, B. E(3)-equivariant graph neural networks for data-efficient and accurate interatomic potentials. *Nat. Commun.* **2022**, *13*, 2453.
(22) Ivanov, S. D.; Grant, I. M.; Marx, D. Quantum free energy landscapes from ab initio path integral metadynamics: Double proton transfer in the formic acid dimer is concerted but not correlated. *J. Chem. Phys.* **2015**, *143*, 124304.
(23) Tribello, G. A.; Bonomi, M.; Branduardi, D.; Camilloni, C.; Bussi, G. PLUMED 2: New feathers for an old bird. *Comput. Phys. Commun.* **2014**, *185*, 604−613.
(24) Bonomi, M.; Bussi, G.; Camilloni, C.; Tribello, G. A.; The PLUMED Consortium. Promoting transparency and reproducibility in enhanced molecular simulations. *Nat. Methods* **2019**, *16*, 670−673.
(25) Verstraelen, T.; Vanduyfhuys, L.; Vandenbrande, S.*Yaff, yet another force field*. http://molmod.ugent.be/software/ (accessed 2022-02-28).
(26) Kapil, V.; Rossi, M.; Marsalek, O.; Petraglia, R.; Litman, Y.; Spura, T.; Cheng, B.; Cuzzocrea, A.; Meißner, R. H.; Wilkins, D. M.; Juda, P.; Bienvenue, S. P.; Fang, W.; Kessler, J.; Poltavsky, I.; Vandenbrande, S.; Wieme, J.; Corminboeuf, C.; Kühne, T. D.; Manolopoulos, D. E.; Markland, T. E.; Richardson, J. O.; Tkatchenko, A.; Tribello, G. A.; Van Speybroeck, V.; Ceriotti, M. i-PI 2.0: A universal force engine for advanced molecular simulations. *Comput. Phys. Commun.* **2019**, *236*, 214−223.
(27) Martyna, G. J.; Klein, M. L.; Tuckerman, M. Nosé-Hoover chains: The canonical ensemble via continuous dynamics. *J. Chem. Phys.* **1992**, *97*, 2635−2643.
(28) Tuckerman, M. E.; Marx, D.; Klein, M. L.; Parrinello, M. On the Quantum Nature of the Shared Proton in Hydrogen Bonds. *Science* **1997**, *275*, 817−820.
(29) Cassone, G. Nuclear Quantum Effects Largely Influence Molecular Dissociation and Proton Transfer in Liquid Water under an Electric Field. *J. Phys. Chem. Lett.* **2020**, *11*, 8983−8988.
(30) Slocombe, L.; Sacchi, M.; Al-Khalili, J. An open quantum systems approach to proton tunnelling in DNA. *Commun. Phys.* **2022**, *5*, 109.

https://doi.org/10.1021/acs.jctc.2c00874
J. Chem. Theory Comput. 2023, 19, 18−24

Paper VIII

Nuclear quantum effects on zeolite proton hopping kinetics explored with machine learning potentials and path integral molecular dynamics

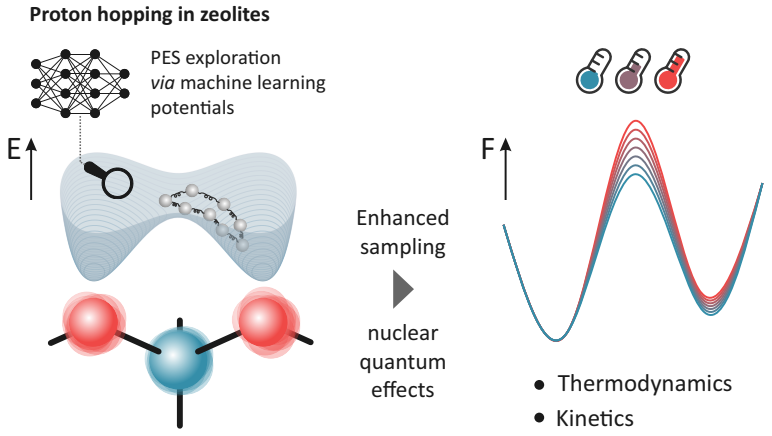

M. Bocus‡, R. Goeminne‡, A. Lamaire, M. Cools-Ceuppens, T. Verstraelen, V. Van Speybroeck

Nature Communications, **2023**, 14 (1), 1008

A. Lamaire performed the PIMD DFT simulations, provided the technical support for the PIMD MLP simulations, and contributed in the analysis and discussion of the results. In this work, the methodology regarding quantum free energy profiles, developed in **Paper VII**, was used.

nature communications

Article

https://doi.org/10.1038/s41467-023-36666-y

Nuclear quantum effects on zeolite proton hopping kinetics explored with machine learning potentials and path integral molecular dynamics

Received: 26 July 2022

Accepted: 10 February 2023

Published online: 23 February 2023

Check for updates

Massimo Bocus[1,2], Ruben Goeminne[1,2], Aran Lamaire[1], Maarten Cools-Ceuppens[1], Toon Verstraelen[1] & Veronique Van Speybroeck[1]

Proton hopping is a key reactive process within zeolite catalysis. However, the accurate determination of its kinetics poses major challenges both for theoreticians and experimentalists. Nuclear quantum effects (NQEs) are known to influence the structure and dynamics of protons, but their rigorous inclusion through the path integral molecular dynamics (PIMD) formalism was so far beyond reach for zeolite catalyzed processes due to the excessive computational cost of evaluating all forces and energies at the Density Functional Theory (DFT) level. Herein, we overcome this limitation by training first a reactive machine learning potential (MLP) that can reproduce with high fidelity the DFT potential energy surface of proton hopping around the first Al coordination sphere in the H-CHA zeolite. The MLP offers an immense computational speedup, enabling us to derive accurate reaction kinetics beyond standard transition state theory for the proton hopping reaction. Overall, more than 0.6 μs of simulation time was needed, which is far beyond reach of any standard DFT approach. NQEs are found to significantly impact the proton hopping kinetics up to ~473 K. Moreover, PIMD simulations with deuterium can be performed without any additional training to compute kinetic isotope effects over a broad range of temperatures.

Brønsted-acidic zeolites are versatile, resistant catalysts that for decades have been recognized as the workhorse of the petrochemical industry[1]. Furthermore, they are also expected to play a vital role in next-generation biorefineries for the conversion of non-fossil feedstocks[2]. From a theoretical point of view, zeolites belong to the most studied materials in the field of heterogeneous computational catalysis[3]. In their ideal, defect-free crystalline form, Brønsted-acidic zeolites are composed of interconnected SiO_4 tetrahedra, where a fraction of the Si^{4+} ions is substituted by Al^{3+}. The excess of negative charge is compensated by the addition of a proton—the Brønsted Acid Site (BAS)—on one of the oxygens in the first coordination sphere of the Al substitution. Interestingly, the BAS is not confined to a specific oxygen of the Al tetrahedron, but it can jump from one oxygen atom to another in what is commonly known as the 'proton hopping' reaction. This process is one of the most fundamental activated events within zeolite chemistry (Fig. 1a) and represents the archetypal proton-transfer reaction which is at the base of any Brønsted acid-catalyzed reaction.

Because of its apparent simplicity, proton hopping is an ideal case study for both experiment and theory, hence various methods have been used to investigate the process kinetics. Experimentally, Nuclear Magnetic Resonance (NMR)[4–6], Impedance Spectroscopy (IS)[7] and

[1]Center for Molecular Modeling, Ghent University, Technologiepark 46, 9052 Zwijnaarde, Belgium. [2]These authors contributed equally: Massimo Bocus, Ruben Goeminne. e-mail: Veronique.Vanspeybroeck@Ugent.be

Article https://doi.org/10.1038/s41467-023-36666-y

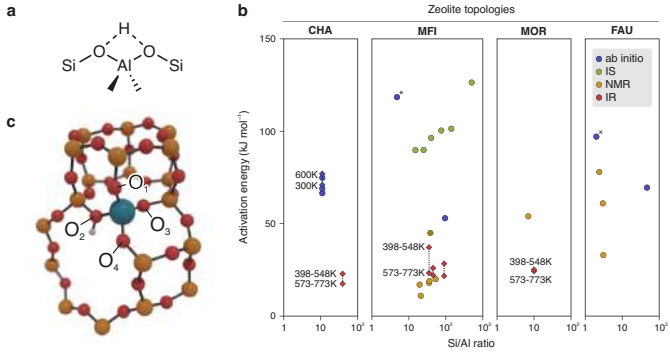

Fig. 1 | Poor agreement is found in the available literature for the activation energy of the proton hopping reaction. a Schematic depiction of the proton hopping reaction. **b** Activation energy for the proton hopping process as function of the Si/Al ratio for multiple zeolites, as derived from the available literature[75]. The data was obtained from ab initio calculations (blue, the points with an asterisk correspond to cluster calculations and, therefore, the Si/Al ratio is meaningless) or IR (red), NMR (yellow) and IS (green) spectroscopies. If more values are available for different temperatures, they are reported with diamonds interconnected by a dotted line. For more details about the reported values and a full list of references, the interested reader is referred to Supplementary Note 1. **c** Part of the H-CHA unit cell, showing the conventional nomenclature of the oxygen atoms in the first coordination sphere of the Al defect adopted herein (Si is in yellow, O in red, Al in blue and H in white).

InfraRed spectroscopy (IR)[8] have been employed to retrieve the activation energies for the proton hopping process. From the theoretical side, the reaction has been tackled with various methodologies ranging from static simulations[9–15] to enhanced-sampling techniques based on molecular dynamics (MD)[16]. Given this plethora of scientific reports, it would be tempting to assume that every detail of the proton hopping reaction is now revealed. However, when surveying the available literature, a huge spread in both the theoretically and experimentally obtained activation energies for proton hopping barriers can be found (Fig. 1b).

In general, activation energies derived from NMR spectroscopy are lower than the theoretical ones. From IR experiments, two different activation energies were obtained for two different temperature ranges (398-548 and 573–773 K, see red diamonds in Fig. 1), a fact that was attributed to the switch from intra-site hopping to inter-site hopping[8]. However, a more recent investigation has disproven such interpretation and indicated active site proximity effects as the main cause for the observed change in activation energy[17]. Inter-site hopping was also suggested to be responsible for the high activation energies retrieved with IS[7].

To understand this lack of consistency, it is important to consider the main possible sources of discrepancy between the proton hopping barriers from literature. First, the residual presence of water in the catalyst is often indicated as the main source for the—in general—low experimental barriers[10], as it is almost impossible to achieve a completely dry material with routine drying procedures[18]. Moreover, the presence of defective sites like extra-framework aluminum species is known to alter the BAS' acidity compared to the pristine material[19]. On the theoretical side, most of the calculations performed so far did not explicitly account for the quantum nature of the hydrogen nucleus. Instead, the nuclei in the system are treated as classical particles moving on an underlying Potential Energy Surface (PES), which is obtained by solving the electronic many-body problem using quantum many-body techniques. This is normally done using Density Functional Theory (DFT) for the sake of computational efficiency. In what follows, the terminology 'classical DFT PES' will be used to refer to nuclei that are treated as classical particles on a DFT-determined PES, thus the electronic degrees of freedom are treated quantum mechanically whereas the nuclei are treated as classical particles. To include Nuclear Quantum Effects (NQEs), approximative methods have been used. For example, tunneling corrections have sometimes been applied to account for NQEs[12]. To more rigorously account for NQEs, one should resort to computationally more expensive methods such as the Path Integral Molecular Dynamics (PIMD) approach, which relies on Feynman's path integral formulation of quantum mechanics. Within PIMD simulations, the statistics of quantum particles are retrieved using a classical ring polymer consisting of P replicas of the system[20]. Each replica runs on the classical DFT PES, making PIMD P times more expensive than a standard MD simulation. This is because an independent DFT-level energy and force evaluation must be performed every MD step for each replica. Within the field of heterogeneous-catalyzed reactions such simulations have so far been mostly unfeasible due to the high computational cost of each PIMD step, as at least 10 replicas are usually required to achieve converged results—making the simulations prohibitively expensive[21]. Nonetheless, there is clear evidence that NQEs may have a significant impact on the physicochemical properties of systems containing light atoms[20,22–24]. For example, it is well-known that they can significantly affect the strength of hydrogen bonds in a variety of systems[25,26]. NQEs have never been explicitly included in zeolite-related reactions and thus it remains unclear to what extent they would affect the rate of proton hopping and by extension any proton-transfer reactions within the field of zeolite catalysis.

To fill this gap of knowledge, we present in the current contribution a methodology that may allow to systematically include NQEs when investigating activated hydrogen transfer events. To this end, proton hopping in H-CHA with isolated active sites is used as a case study (Fig. 1c), for which we first trained an accurate Machine Learning Potential (MLP) based on an underlying set of high-temperature DFT Umbrella Sampling (US) simulations. The use of enhanced-sampling simulations is essential to explore in an efficient way the less-probable highly energetic regions of the PES, which are typically associated with reactive events. The underlying DFT simulations at finite temperatures serve as input to train a deep neural network MLP (Fig. 2). Once an accurate MLP is constructed, an enormous computational speedup can be achieved, which allowed to: (i) compute the Free Energy Surfaces (FESs) of all possible hoppings around an isolated Al defect in the temperature range 273–873 K with a large number of umbrellas and long simulation times to obtain well-converged results, (ii) explicitly include NQEs through the PIMD approach, (iii) derive accurate kinetic

Article https://doi.org/10.1038/s41467-023-36666-y

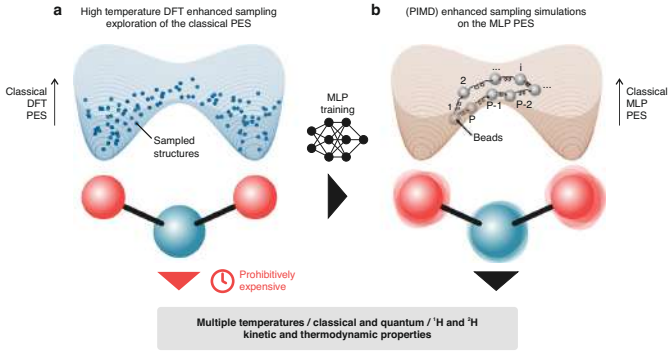

Fig. 2 | Kinetic and thermodynamic properties with and without NQEs over a wide range of temperatures can be computed using an MLP trained on high-temperature enhanced-sampling DFT simulations. The pictures show a simplified schematic representation of the PES experienced by the proton when hopping between two oxygens around the Al site (red and blue spheres, respectively), sampled with DFT simulations (**a**) and subsequently learned with the MLP (**b**). In **b** a schematic view of the hydrogen ring polymer with P beads running on the classical MLP PES is shown.

constants beyond the Transition State Theory (TST) approximation, taking barrier recrossing into account via the reactive flux formalism[27] and (iv) perform an additional set of simulations with deuterium instead of protium to explicitly compute the Kinetic Isotope Effect (KIE) on the reaction.

We show that even at catalytically relevant temperatures (>400 K) NQEs may still be important to consider when computing reaction kinetics and their relevance is not restricted to the absolute low temperature regime. While the work performed here is illustrative for the most basic proton hopping reaction in zeolites, it provides the means to routinely include NQEs and explicitly calculate KIEs when studying any proton-transfer event in heterogeneous catalysis.

Results

Construction of a reactive MLP with DFT accuracy

To train an accurate MLP, a sufficiently large set of DFT datapoints is required, which should cover the relevant regions of the reaction phase space. To this end, high-temperature (873 K) DFT US simulations were performed on a CHA conventional cell containing 36 T Si atoms, where 1 silicon is replaced by Al to give a final Si/Al ratio of 35. The temperature choice of 873 K is arbitrary but, in general, on the higher end of typical zeolite-catalyzed processes[1]. In the CHA topology, all T atoms are equivalent. However, the four O atoms in the first coordination sphere of the Al defect are not (Fig. 1c). This leads to 6 distinct hopping paths, which are all considered in this work. To assess whether any path could be significantly disfavored, activation free energies were initially screened with static calculations. The results suggest that all 6 possible hopping paths have relatively similar activation free energies (within ~20 kJ mol^{-1}) and no single one is strongly (dis)favored (Supplementary Note 2). Therefore, 6 separate DFT US simulations at 873 K were performed to sample all the possible hoppings. A difference in coordination numbers between the proton and the two oxygen atoms involved in the hopping was used as main collective variable to bias the system (see "Methods" section and Supplementary Note 3). One-dimensional umbrellas were used to sample the reaction path and, if needed, additional two-dimensional umbrellas were added to improve the sampling of scarcely visited regions of the phase space (more details are reported in Supplementary Note 3.2). A full overview of the DFT US results is reported in Supplementary Note 4.

Energies and forces were extracted every 5 fs from the DFT US trajectories, yielding a total of ~1,200,000 structures which were used to train an MLP with the SchNetPack package (see "Methods" section and Fig. 2)[28,29]. Performing MD simulations with the MLP provides a dramatic speedup in computational time, going from ~8.3 s/step on 56 Xeon E5-2680v4 CPUs@2.4 GHz cores to ~0.01 s/step on a single NVIDIA Volta V100 GPU. As part of the MLP validation, well-converged 873 K DFT FESs were generated to compare them with the MLP-derived ones within a reasonably small uncertainty. To this end, about 50 ps of simulation time was required for each DFT umbrella. Considering that 19 umbrellas are needed to sample each of the 6 hoppings, this was a computationally demanding task. On the other hand, it also provided us with a very large number of DFT datapoints, hence the large number of structures used to train the MLP. With the acquired knowledge that a mean absolute error on the force of about 40 meV Å^{-1} is sufficient to obtain very accurate FESs (vide infra), we also tested the performance of newer and more data efficient equivariant neural networks[30], where preliminary results indicate that a few hundred fs per umbrella are sufficient to achieve converged results (Supplementary Note 10), providing an enormous computational saving in the DFT data generation.

To further validate the trained MLP, we also tested whether it could reproduce FESs at lower temperatures than the training one. To this end, three additional sets of DFT US simulations were performed. The 2–3 hopping was tested at 573 and 273 K, while the 1–4 hopping was tested at 273 K. With this choice, the hoppings with the smallest activation energies are tested and all four oxygens are considered at the lowest temperature. For the sake of clarity, a detailed comparison between the MLP and DFT results is presented in Supplementary Note 6.1, while here only the 2–3 hopping is discussed in detail. As shown in Fig. 3, the DFT and MLP FESs exhibit an almost perfect overlap, with most variations contained well within the error bars. The free energy barrier exhibits a clear increase with temperature, which is in line with a rigid transition state associated with a negative entropy variation. It must be pointed out that, thanks to the large computational speedup enabled by the MLP, longer simulation times (100 ps vs. 50 ps per umbrella) and a larger number of umbrellas (39 vs. 19 per hopping) were easily achievable. This led to a vastly improved sampling of the reaction PES, thereby obtaining much better converged FESs. Moreover, all MLP simulations were repeated three separate times starting from different initial velocities and the associated results and uncertainties were obtained by averaging over these three independent runs. Initially, the 573 K DFT profile presented a moderate spike in the transition state region, which was not present in the MLP profile. Therefore, 2 additional umbrellas were added in the proximity of the transition state and an additional 40 ps of simulation was performed in every umbrella, for a total of 90 ps. The final DFT profile

Article https://doi.org/10.1038/s41467-023-36666-y

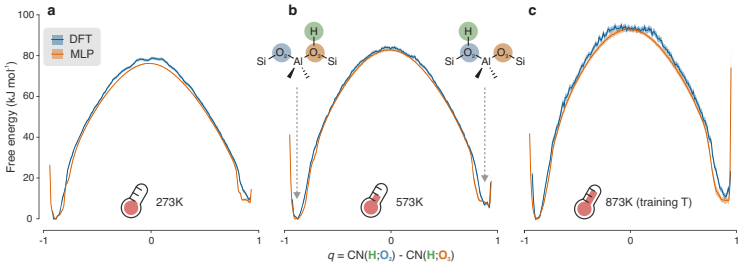

Fig. 3 | The trained MLP can reproduce DFT FESs with high accuracy. The MLP and DFT FESs (in orange and blue, respectively) of the 2–3 hopping at 273 (**a**), 573 (**b**) and 873 K (**c**) are almost perfectly superimposable, even though the MLP model is only trained on snapshots at the highest temperature. A comparison with the other available FESs is shown in Supplementary Fig. 10. For a more detailed definition of the collective variable (q) used to build the FESs, the interested reader is referred to the "Methods" section. Uncertainties (shaded areas around the FESs) on the MLP FESs are obtained by averaging over three independent runs (Supplementary Note 6.1) while for DFT they are estimated according to the procedure summarized in Supplementary Note 3.1.3. Source data are provided as Source Data File.

reaches almost perfect agreement with the MLP one, highlighting how the (small) differences between MLP and DFT FESs are almost certainly caused by sampling issues rather than by significant deviations in the underlying PES. The results show that (i) the trained MLP is effectively capable of encoding chemical reactivity and (ii) high accuracy on the computed FESs is retained also for temperatures lower than the training one, offering thermodynamic transferability in terms of operating conditions.

While directly superimposing FESs provides an intuitive visual means of comparison, the FES itself is not experimentally measurable. The final macroscopic quantity of interest is the kinetic constant of the reaction, which does not depend on the choice of the collective variable used to represent the FES[31,32]. By means of classical (TST), the forward and backward kinetic constants for the 6 high-temperature hoppings, the 2–3 hopping at 573 K and the 1–4 and 2–3 hoppings at 273 K were retrieved (see "Methods" section). Fig 4 reports a graphical comparison between the DFT and MLP rates, where the computed kinetic constants are converted to a corresponding phenomenological barrier using Eyring's equation[32]. The sole purpose of the latter is to provide a more tangible equivalent to the kinetic constant, without comparing values that can span multiple orders of magnitude (more details are provided in the "Methods" section). None of the computed barriers differ more than ~5 kJ mol^{-1} and, for most of the hoppings, the MLP values lie within the error bars of the DFT ones. These results indicate that the MLP accurately reproduces the DFT PES underlying the proton hopping reaction in H-CHA and can therefore be used to compute reaction rates at any temperature of interest and to explicitly introduce NQEs through the PIMD approach (Fig. 2).

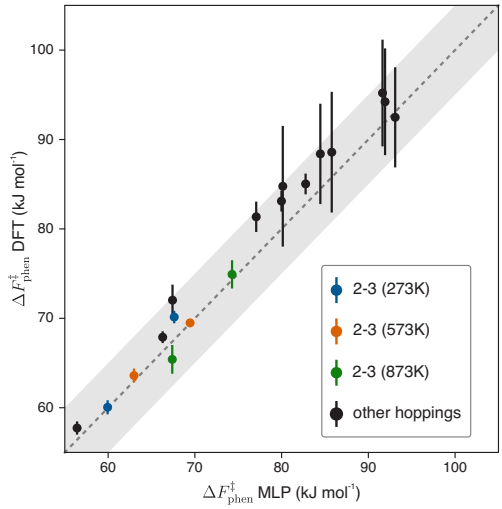

Fig. 4 | The DFT and MLP phenomenological barriers are in excellent agreement. The available DFT phenomenological barriers (12 forward and backward barriers for the 873 K hoppings, the forward and backward barriers of the 2–3 hopping at 573 K and the forward and backward barrier of the 1–4 and 2–3 hoppings at 273 K) are all within about ±5 kJ mol^{-1} from the MLP ones, as highlighted by the gray shaded area. The phenomenological barriers of the 2–3 hopping at various temperatures, corresponding with the free energy profiles of Fig. 3, are highlighted in different colors (273 K in blue, 573 K in orange and 873 K in green). Uncertainties on the MLP barriers are obtained by averaging over three independent runs (although their magnitude is so low that they are barely visible in the figure) while for DFT they are estimated according to the procedure summarized in Supplementary Note 3.3. Source data are provided as Source Data File.

Full characterization of the hopping kinetics

Having validated the MLP to faithfully reproduce the proton hopping FESs over a broad temperature range (273-873 K), additional US simulations were performed to retrieve the full reaction kinetics considering all hopping paths. Moreover, NQEs can be systematically included in the reaction investigation as the PIMD formalism becomes accessible, thanks to the large computational efficiency of the MLP. To obtain well-converged FESs, at least 16 system replicas (also referred to as beads) are required in the ring polymer (Supplementary Note 7.1). A graphical visualization of the spread of the beads around the transition state region compared with the classical case is shown in Fig. 5, where it becomes clear that quite some uncertainty is present on the proton's position compared to the classical deterministic trajectories. A full overview of the classical and quantum FESs is reported in Supplementary Notes 6.1 and 7.3, respectively. Introducing NQEs leads to a general decrease of the free energy barriers compared to the case where nuclei are treated classically. This effect tends to lessen with increasing temperatures, in accordance with the expected convergence between the quantum and classical behavior for high temperatures.

Not only does the MLP allow to include in a reliable—yet computationally feasible—way NQEs, but it also allows to determine reaction kinetics beyond classical TST and explicitly include barrier recrossing through the reactive flux formalism (obtaining the true

Article https://doi.org/10.1038/s41467-023-36666-y

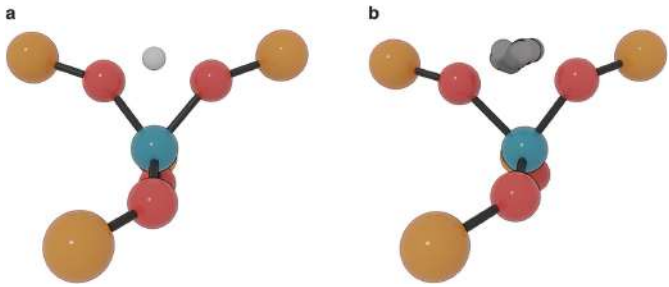

Fig. 5 | The use of PIMD leads to a significant spread in the proton location. These two snapshots, arbitrarily extracted from the transition state umbrella of the 2–3 hopping, highlight how the system beads in PIMD (**b**) can be spread quite significantly in space with respect to the classical case (**a**). For the sake of clarity, only the H-SSZ-13 atoms up to the second coordination sphere around the Al site are shown and in **b** a superposition of all beads is only present for the proton. Si is depicted in yellow, O in red, Al in blue and H in white.

kinetic constant of the reaction)[27,33], which is in its turn part of the Bennett-Chandler reaction rate theory[34,35]. In this approach, multiple unbiased simulations (5000 in this case) are initialized atop the transition state and monitored through time, to retrieve whether they end up in the product basin or whether they recross the barrier towards the reactant basin (see "Methods" section). This approach is most appropriate when NQEs are included, as quantum TST approximations such as ring polymer molecular dynamics (RPMD) TST do not yield a strict upper bound for the quantum rate (more details can be found in Supplementary Note 7.4)[36]. Overall, the MLP US simulations allowed to compute three different kinetic constants for all hopping paths and all temperatures: a classical TST-based one (k^{c}_{TST}), derived from classical MD and the TST approximation, a classical Bennett-Chandler one (k^{c}_{BC}), where barrier recrossing is now explicitly taken into account and, finally, a quantum Bennett-Chandler one (k^{q}_{BC}), analogous to k^{c}_{BC} but derived from the RPMD simulations and thus including NQEs. Remark that the amount of data used to obtain them is well beyond the reach of any pure ab initio methodology where all energy and force evaluations are performed at the DFT level. Even when excluding the thousands of short trajectories required to obtain well-converged k_{BC} values, computing the quantum FESs requires 42 sets of US simulations (6 hopping paths at 7 different temperatures), each consisting of 39 umbrellas simulated with 16 parallel beads—for a total of more than 0.6 μs of simulation time. Such simulation lengths are clearly beyond the limit of any DFT-based MD simulation.

While demonstrating the impact of NQEs on the reaction rate is important to highlight the cases in which NQEs cannot be neglected and should thus be accounted for computationally, the resulting 'quantum speedup' is not experimentally measurable as NQEs are an intrinsic part of nature. What is often measured experimentally, on the other hand, is the KIE—namely the change in rate when the hydrogen atoms in the system are substituted with deuterium (other isotopic substitutions are of course also possible[37]). Interestingly, the MLP trained on ^{1}H simulations can be directly used for KIE calculations, as the reaction PES does not depend on the atomic masses but only on their charge. An additional set of PIMD simulations was therefore performed at 273, 573 and 873 K with the BAS mass set to 2 a.m.u. Given the linear behavior of $\ln(k^{q}_{BC})$ over the whole temperature range (vide infra, Fig. 7), the intermediate temperatures were no longer considered. A full overview of the simulations' results is reported in Supplementary Note 7.5. The error on the MLP forces with respect to DFT remains basically unaffected by the change in the hydrogen mass, confirming that both simulations sample analogous PES regions (Supplementary Fig. 20). The reactive flux kinetic constant for the PIMD simulations with deuterium will be indicated with $k^{q}_{BC}(^{2}H)$, while for protium simulations the isotope label will be omitted.

Using the computed kinetic constants, the equilibrium coverage of the 4 oxygen sites (θ_i, $i = 1-4$) was determined as a function of temperature (more details can be found in Supplementary Note 8). The results for ^{1}H are shown in Fig. 6a–c. When considering the k^{c}_{TST} and k^{c}_{BC} kinetic constants, similar equilibrium populations are obtained within the limits of uncertainty (Fig. 6a, b), which is a consequence of the similar recrossing rate between the forward and backward barriers. In general, O_1 and O_3 are the most populated sites at any temperature, followed by O_2 and O_4. In the classical case, O_3 has the largest population up to 373 K, while at higher temperatures its population becomes nearly identical to O_1. Significantly different results are obtained when the quantum kinetic constants (k^{q}_{BC}, Fig. 6c) are considered, where θ_3 remains significantly larger than θ_1 at all temperatures. A similar trend is obtained for the PIMD simulations with deuterium (Supplementary Fig. 19). When the proton is on O_3, it finds itself oriented towards the center of the 6 T atoms ring (Fig. 6d) and can, therefore, interact with the oxygens on the opposite side. To understand more profoundly the impact of these intra-framework interactions, we performed a 273 K classical MD and PIMD simulations of the zeolite with the proton located on O_3. We then analyzed the radial distribution functions (RDFs) of the proton with the 6 oxygens sharing the Si and Al with O_3 ('adjacent' in Fig. 6e) and all the other oxygens in the unit cell ('others'). We found that—as expected— the BAS lies within 2–3 Å from the oxygens on the other side of the 6-Si ring and will therefore interact with them. By comparing the classical and quantum RDFs (Fig. 6e), it can be seen how the maximum in the RDF H-O (others) occurs at slightly shorter distances in the quantum case and, moreover, shorter distances—in the order of ~2 Å—are explored more often. Based on these findings, it appears that when the quantum nature of the hydrogen nucleus is considered the weak interaction between the non-adjacent framework oxygens and the proton becomes stronger and, as a result, O_3 becomes further stabilized with an increase in θ_3. No other site interacts with other framework oxygens within 3 Å (Supplementary Fig. 18). Previous reports in the literature, based on geometrical considerations concerning the crystallographic zeolite unit cell, suggested that none of the four BAS locations are suited to form H-bonds with other oxygens in the framework[38]. This no longer seems to be the case when temperature effects and NQEs are explicitly taken into account. The number of zeolite frameworks presenting this type of intra-framework interaction could thus be higher than previously thought[38] at realistic operando conditions.

Once all the equilibrium coverages as a function of temperature are known, the overall hopping rate can be computed using the

Article https://doi.org/10.1038/s41467-023-36666-y

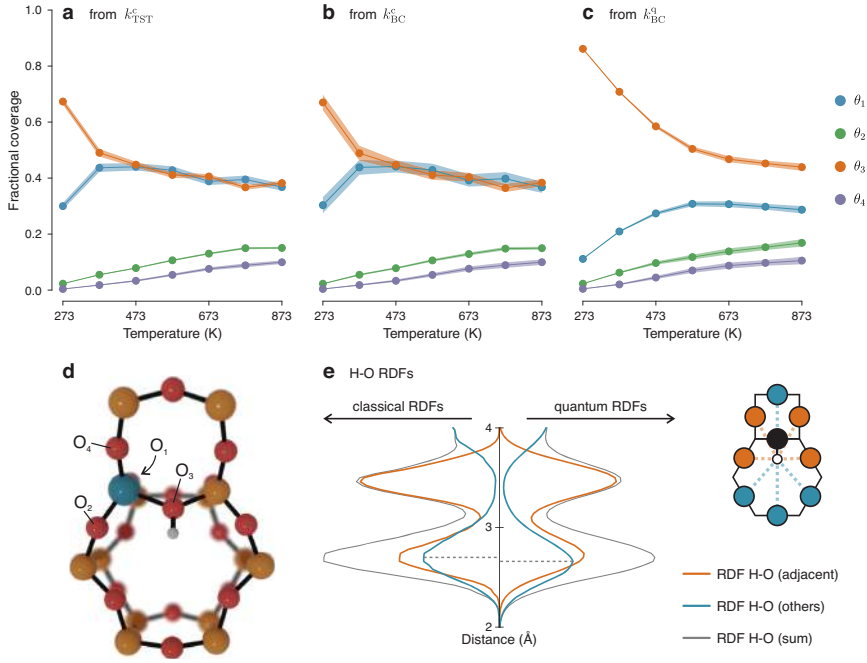

Fig. 6 | Including NQEs can change the computed equilibrium proton coverages. a–c Equilibrium coverages (θ_i) of the 4 oxygen sites around the Al defect as function of temperature, computed from the k^c_{TST}, k^c_{BC} and k^q_{BC} kinetic constants. **d** Portion of the H-CHA framework as seen along the c cell vector, showing the optimized structure of the BAS on O_3. Si is depicted in yellow, O in red, Al in blue and H in white. **e** RDFs between the BAS lying on O_3 and the 6 oxygens sharing the same Si and Al as O_3 (orange line) and the BAS and all other oxygens in the unit cell (blue line), from classical and NQE simulations. The schematic drawing is seen from the same perspective as d and highlights some of the oxygens belonging to 'adjacent' and 'others'. Source data are provided as Source Data File.

formula:

$$r = \sum_{i=1}^{4}\sum_{j\neq i}^{4} k_{ij}\theta_i, \quad (1)$$

where k_{ij} is the kinetic constant of the hopping from O_i to O_j and θ_i the coverage of O_i. From this, an Arrhenius plot for the hopping rate as a function of the temperature is computed (Fig. 7a), whose activation energy should be comparable with experiment. First, we analyzed in how far each of the hoppings is contributing to the overall rate. In all cases, only two hopping paths dominate the rate kinetics (Fig. 7b), namely the $1 \leftrightarrow 4$ and $2 \leftrightarrow 3$ paths, as one could expect based on their low free energy barriers. Note that the forward and backward rates have similar contributions, as a higher free energy of the minimum corresponds to both a lower coverage and a lower free energy barrier to hop towards a stabler minimum. These two factors tend to cancel each other when computing $k_{ij}\theta_i$. Minor contributions are given by the $1 \leftrightarrow 2$ and $2 \leftrightarrow 4$ paths, while the remaining two paths ($1 \leftrightarrow 3$ and $3 \leftrightarrow 4$) only have noticeable contributions at the highest temperatures. In the deuterium case, the $2 \leftrightarrow 3$ path becomes even more dominant at the expenses of $1 \leftrightarrow 4$ as it appears that the transition state energy is not shifted consistently by the isotope substitution (Supplementary Fig. 18).

By considering the slope of the best fit lines in the Arrhenius plots (Fig. 7a) it is possible to retrieve an effective activation energy for the proton hopping reaction. The k^c_{TST} results yield an activation energy of 67.1 kJ mol^{-1}. Going beyond the TST approximation and explicitly including recrossing (k^c_{BC}) does not significantly change the results, with a consistent—but almost negligible—decrease in the rate across the whole temperature range. When NQEs are included (k^q_{BC}), in contrast, the activation energy decreases with about 11 kJ mol^{-1} due to the possibility of the proton to tunnel through the potential energy barriers. When analyzing the rates related to a specific hopping (Supplementary Fig. 17), it was noticed that this effect is not constant, and becomes more prominent in the hopping paths with a more sharply peaked FES around the transition state region (Supplementary Figs. 15 and 16). This is because a narrower barrier increases the probability of tunneling, which in practice means that the beads of the ring polymer are easily located on both sides of the potential energy barrier experiencing on average a lower free energy. These results show that the impact of NQEs is not systematic in nature and can therefore be challenging to capture with ad hoc corrections. Indeed, previous investigations which included NQEs through an a posteriori tunneling correction suggested that above room temperature no significant effect should be observed[12]. Our results, on the other hand, show that the reaction proceeds 65 times faster at 273 K if NQEs are included and, even at 373 K, a 16-fold increase in the computed rate is still present (Fig. 7c). At 473 K, the reaction remains 7 times faster while the speedup, as expected, tends to become negligible at higher temperatures. It appears therefore that for zeolite-catalyzed processes conducted at milder conditions, among which the ones related to biomass conversion are a predominant example[2], NQEs might be non-negligible when computing the kinetics of proton-transfer steps. A few examples where these effects might be important are the aqueous cyclohexanol

Article https://doi.org/10.1038/s41467-023-36666-y

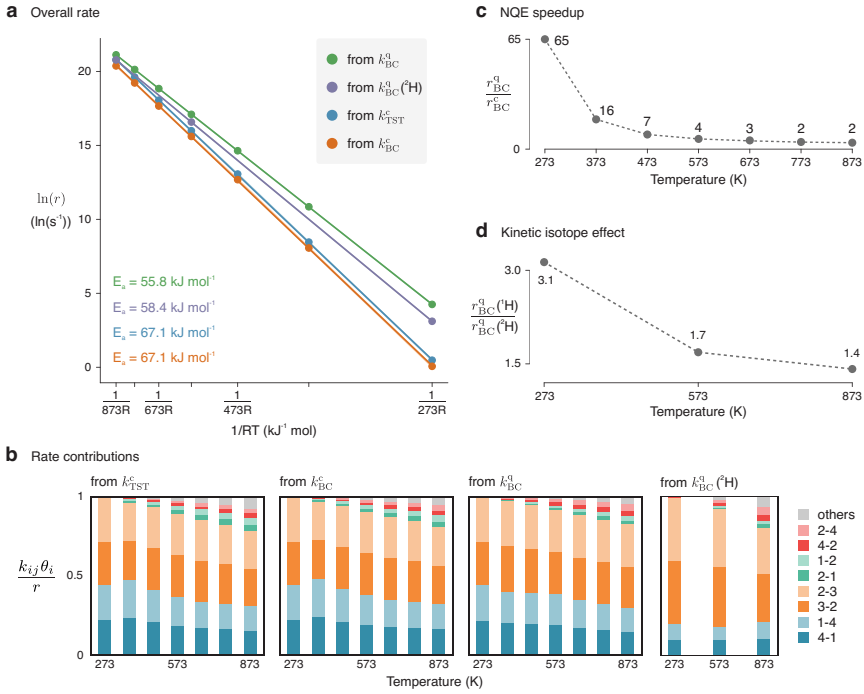

Fig. 7 | NQEs have a significant effect on the computed hopping rate. **a** Arrhenius plot showing the overall hopping rate as function of 1/RT. **b** Contributions to the overall rate from the different hopping paths, as function of temperature and methodology used. **c** Speedup in the rate due to the inclusion of the NQEs. **d** KIE as function of reaction temperature. Source data are provided as Source Data File.

dehydration in H-Beta zeolite at temperatures of about 400 K[39] and the oxidation of methane to methanol in copper-loaded zeolites carried out at ~473 K[40]. These two cases serve as examples of the relevant application area and conditions influenced by NQEs in zeolites. However, it is clear that many more cases could be affected by the inclusion of NQEs.

When protium is substituted by deuterium ($k^q_{BC}(^2H)$) the activation energy becomes 58.4 kJ mol^{-1}, yielding a small increase of 2.6 kJ mol^{-1}. This is in line with the modest magnitude of the predicted KIE (given by the ratio between the total rate with protium and with deuterium, Fig. 7d), which equals 3.1 at 273 K and decreases to 1.4 at 873 K, in line with standard Bigeleisen-Mayer KIE theory[41,42]. It can be noted how the deuterium rates remain significantly larger than the classical k^c_{BC} ones, indicating that the increase in mass is not sufficient to fully suppress the quantum behavior. Unfortunately, there has not been any experimental attempt so far to measure the KIE for proton hopping in zeolites. Theoretically, an early investigation based on static cluster calculations was performed by Fermann and Auerbach[43]. According to their semiclassical TST model, the differences between ^{1}H and ^{2}H are limited above room temperature, in line with our results.

So far, the study focused on H-CHA, which has a single indistinguishable T-site and a small unit cell. To broaden our scope, it is important to assess the MLP capability of describing other zeolite frameworks on which the MLP was not trained. To this end, the transferability of the MLP to other zeolite topologies was investigated. More specifically, we selected five all-silica frameworks from the international zeolite (IZA) database[44] that are of interest for catalytic applications[3] (AFX, CHA, FER, MFI and MOR) and performed a 100 ps NVT DFT MD simulation using the crystallographic unit cell parameters reported in the IZA database (see Supplementary Note 9). The CHA topology was included as a control system, to ensure that the MLP is robust with respect to changes in the unit cell volume. None of the MLP simulations presented obvious instabilities and the error on the forces is not excessive, even for frameworks that do not share any secondary building unit with CHA, varying between 196 meV Å^{-1} for MOR and 258 meV Å^{-1} for MFI. The quality of the zeolite trajectories, monitored through the Si–O and Si–Si RDFs, remains reasonably good with only small long-range differences for MFI (Supplementary Fig. 19). Testing the proton hopping reactivity in a systematic way for more frameworks would require a further set of expensive ab initio US simulations and, therefore, is outside the scope of this work. The results obtained on the all-silica frameworks, nonetheless, still indicate that the MLP can capture to a large extent the chemistry of Si–O–Si bonds and, therefore, we expect that not many additional DFT simulations would be needed to retrain it and extend its accuracy to new zeolite frameworks, for instance building on the transferable MLP for siliceous frameworks by Erlebach et al.[45] towards aluminum-containing zeolites of catalytic interest.

Discussion

Proton-transfer reactions are of primordial importance within zeolite catalysis. Thus far, it was unclear in how far NQEs affect the barriers and rates of proton hopping processes at realistic operating conditions, as their explicit inclusion through PIMD was prohibitively expensive if the underlying classical PES is evaluated at a DFT level of theory. Herein, we showed that a reactive MLP can be trained based on

Article https://doi.org/10.1038/s41467-023-36666-y

underlying high-temperature (873 K) US simulations at the DFT level, that provides kinetic results with a similar accuracy as the underlying DFT data. However, thanks to the enormous computational speedup gained by describing the PES based on the MLP compared to the original DFT energy and force calculations, the MLP can be used to perform virtually any type of simulation that relies on the classical PES of the considered reaction(s) over a broad range of temperatures. The proposed methodology thus not only succeeds in reproducing the underlying DFT simulations but comes with a series of advantages that were so far unreachable due to the prohibitively excessive computational cost.

First, the convergence of the free energy surfaces obtained from enhanced-sampling techniques can be improved by using many more umbrellas and by simulating for a longer time. Secondly, PIMD can be employed to explicitly account for the quantum nature of the nuclei in the system. While the inclusion of NQEs through MLPs has already been proposed in the literature[22,46,47], the application of PIMD/MLP to an activated event in heterogenous catalysis was still unexplored. We remark that for simulations at cryogenic temperatures the number of beads required to achieve converged results could become very large even for the MLP. This problem can be mitigated by coupling the MLP simulations with path integral acceleration techniques[20]. Thirdly, it also becomes possible to go beyond the TST approximation and explicitly include barrier recrossing via the reactive flux formalism, thereby obtaining the true kinetic constant of the reaction. Because of the thousands of short MD trajectories that have to be initialized atop the transition state, this type of calculation was so far too expensive to be performed at a DFT level of theory. The more efficient methodology for describing the forces and energies may also open the window to use methods like transition path sampling within the field of zeolite catalysis, which were thus far not truly accessible due to the large number of paths that needs to be sampled at the DFT level[48]. Finally, KIEs can be explicitly computed if the PIMD simulations are performed with different nuclear masses, as this does not affect the underlying PES learned by the MLP.

Our results show that the expected Arrhenius activation energy for the hopping process, considering all six hoppings and the coverages of the four oxygen sites, is 67.1 kJ mol^{-1} in the absence of NQEs, whereas including the quantum nature of the proton brings the activation energy down to 55.8 kJ mol^{-1}. When quantitively comparing this activation energy to experimental results, it is important to note that this study makes use of the revPBE-D3 level of theory, which is known to underestimate the activation energies of chemical reactions[16,49,50]. In this sense, our barriers will present a lower boundary for the chemically accurate activation energy. Because of the large improvement in data efficiency of newer MLP architectures (Section S10 of the Supplementary Information), we believe that training an accurate model based on a more expensive albeit more reliable exchange-correlation functionals should become feasible. The computed activation energy remains relatively higher than the experimentally available ones. The most likely source of discrepancy lies in the perfect crystalline nature of the adopted zeolite model. The presence of residual water molecules, defects (EFAL species, for instance) and an heterogeneous aluminum distribution are basically unavoidable at the macroscale and all these factors are known to potentially affect the behavior of protons in zeolites[17,19,51]. According to the simulations, a primary KIE of about 3 is expected at 273 K but no experimental evidence is available thus far to corroborate this result.

This proof-of-concept study presents a general scheme to obtain MLP models that can simulate proton hoppings and activated processes in zeolite catalysis with improved realism. The proposed methodology is, in principle, extendible to additional reactions and reactive environments, making it a valuable tool for studying a wide range of catalytic phenomena[52].

Methods

Umbrella sampling simulations

The hopping of the H-CHA BAS between the oxygens in the first coordination sphere of the Al defect was studied by means of umbrella sampling simulations[53,54]. In this approach, quadratic bias potentials (the 'umbrellas') are placed along a certain collective variable (q) which should smoothly vary between reactants and products. The bias has the form $V_i(q) = 1/2K_i(q - q_{0,i})^2$, where K_i is the force constant of the ith umbrella and $q_{0,i}$ its center. An MD simulation is then performed within each umbrella. To study the proton hopping, the chosen collective variable is a difference of coordination numbers (CNs) between the BAS and the two oxygens involved in the hopping:

$$q = \mathrm{CN}(\mathrm{O}_i;\mathrm{H}) - \mathrm{CN}\left(\mathrm{O}_j;\mathrm{H}\right) = \frac{1-\left(\frac{r_{\mathrm{O}_i\mathrm{H}}}{r_0}\right)^N}{1-\left(\frac{r_{\mathrm{O}_i\mathrm{H}}}{r_0}\right)^{2N}} - \frac{1-\left(\frac{r_{\mathrm{O}_j\mathrm{H}}}{r_0}\right)^N}{1-\left(\frac{r_{\mathrm{O}_j\mathrm{H}}}{r_0}\right)^{2N}} \quad (2)$$

The specific values of the N and r_0 parameters were adapted based on the reaction conditions, more information can be found in Supplementary Note 5.2. The bias potential was applied using PLUMED[55,56] and the final statistical analysis of the data was performed with our in-house developed ThermoLIB library[57]. For some of the hoppings, additional wall potentials were required to prevent undesired side reactions; further details are reported in Supplementary Note 3.1.4

DFT molecular dynamics

To perform the DFT MD simulations, the CP2K software package (version 7.1)[58,59] was employed to compute energies and forces at a revPBE-D3/TZVP[60–62] level of theory. Because of the mixed plane waves −atom-centered orbitals approach[63] used by CP2K, the plane waves energy cutoff was set to 350 Ry and GTH pseudopotentials[64] were used to smooth the electron density in the proximity of the nuclei. A significant dependency of the forces on the plane waves cutoff was found, but this was shown to have a negligible impact on the final FESs when much higher settings are used (Supplementary Note 3.1.5). The time step for the integration of the equations of motion was set to 0.5 fs. After equilibration of the unit cell (Supplementary Note 3.3.1), production runs were performed in the NVT ensemble using a Nosé-Hoover thermostat with a chain consisting of five beads[65,66] to control the temperature and a time constant of 334 fs (100 cm^{-1}).

MLP training and usage

A SchNet MLP was trained with the SchNetPack package on the DFT energies and forces which were extracted every 5 fs from the DFT US simulations at 873 K[28,29]. First, the energies and forces were unbiased by subtracting the bias potential applied in the US simulations with PLUMED[55,56]. The unbiased DFT datapoints were randomly divided in a training and validation set with a 80:20 ratio. Subsequently, the MLP was trained with a cutoff of 6 Å, 128 features, 50 gaussians and 6 interaction blocks. The resulting MAE on the validation set is 41.9 meV/Å. More details on the training are provided in Supplementary Note 5.1. Classical unbiased and US simulations with the trained MLP were performed with our in-house code YAFF[67] using a time step of 0.5 fs and a Nosé-Hoover thermostat with three beads for temperature control[65,66]. PIMD simulations were performed with the i-PI driver[68] using a time step of 0.25 fs and a PILE thermostat[69] with a time constant of 100 fs for temperature control. Because of the harmonic repulsion between the beads, some of them might explore regions of the phase space that are not necessarily well-sampled in classical DFT US. Therefore, we also performed an extra DFT PIMD US simulation for the 2–3 hopping (Supplementary Note 7.2) and the resulting FES shows an excellent agreement with the MLP one. It is important to remark that this agreement is very likely not generalizable to other systems or reactions and should always be tested appropriately[70]. In both the classical and PIMD US simulations, PLUMED was used to apply the bias.

Article https://doi.org/10.1038/s41467-023-36666-y

Kinetic rate constant calculation

The plain activation free energy obtained from a FES is largely dependent on the choice of collective variable[31,32]. To remove such dependency, it is necessary to move towards a more general macroscopic property of the process under study, namely the kinetic rate constant. In the Bennett-Chandler approach to transition state theory[34,35], the rate constant of a reaction can be written as[71]:

$$k_{\mathrm{BC}}(t) = \left\langle \dot{q}(0)\theta\left(q(t) - q^*\right)\right\rangle_{q(0)=q^*} \frac{e^{-\beta F(q^*)}}{\int_{-\infty}^{q^*} e^{-\beta F(q)}\mathrm{d}q}, \tag{3}$$

where the first term is the ensemble average of the time derivatives of q for trajectories that, starting atop the transition state ($q(0) = q^*$), end up in the product basin (as imposed by the Heavyside function $\theta(q(t) - q^*)$). With the MLP, it is possible to explicitly compute the first term by performing a large number of unbiased MD simulations (5000 in this case) starting on the transition state and monitor how many of them effectively end up in the product basin[27,33]. The true rate constant is, in principle, given by $k_{\mathrm{BC}} = \lim_{t\to+\infty} k_{\mathrm{BC}}(t)$. Luckily, its value quickly reaches a plateau and 50 fs of simulation were sufficient to obtain well-converged results (Supplementary Note 6.2). The rate constant calculated in this manner is referred to as the Bennett-Chandler one (k_{BC}).

In general, this approach is too expensive, especially for the DFT case, so that only the approximate transition state theory constant ($k_{\mathrm{TST}} = \lim_{t\to 0^+} k_{\mathrm{BC}}(t)$) can be computed from the US trajectories, thereby avoiding the need for additional simulations. While k_{TST} represents an upper limit of the true kinetic constant, assuming a recrossing probability equal to zero, it can be used to compare the DFT and MLP results. Further details are reported in Supplementary Note 3.3. To calculate the quantum rate constants, taking NQEs into account, the approximate technique of RPMD was used (see Supplementary Note 7.4)[72]. Although this approximation can only capture short-time quantum effects, it has been shown to yield good quantum rates in comparison with other approximations[73] or quantum mechanical calculations[74].

As the kinetic constant values can span several orders of magnitude, we often make use of Eyring's equation to convert them into phenomenological barriers, which encode the same information while being – in our opinion – more tangible than a reaction rate.

$$\triangle F^{\ddagger}_{\mathrm{phen}} = -\frac{1}{\beta}\ln(\beta h k) \tag{4}$$

Data availability

The complete training set, examples of input files, processing scripts and the trained MLP have been deposited in the Zenodo database (https://zenodo.org/record/7267913#.Y2U8tHbMK3A). Any additional data is available from the authors upon request. An extended discussion of the results can be found in the Supplementary Information. Source data are provided with this paper.

Code availability

CP2K (https://github.com/cp2k/cp2k), PLUMED (https://github.com/plumed/plumed2), SchNetPack (https://github.com/atomistic-machine-learning/schnetpack) and YAFF (https://github.com/molmod/yaff) are all open source and freely available at the provided links. ThermoLIB is available upon request at https://molmod.ugent.be/software/thermolib.

References

1. Weissermel, K. & Arpe, H.-J. *Industrial Organic Chemistry* (Wiley-VCH Verlag GmbH, Weinheim, Germany, 2003).
2. Ennaert, T. et al. Potential and challenges of zeolite chemistry in the catalytic conversion of biomass. *Chem. Soc. Rev.* **45**, 584–611 (2016).
3. Van Speybroeck, V. et al. Advances in theory and their application within the field of zeolite chemistry. *Chem. Soc. Rev.* **44**, 7044–7111 (2015).
4. Baba, T., Inoue, Y., Shoji, H., Uematsu, T. & Ono, Y. Temperature-dependent lineshape of 1H magic-angle spinning nuclear magnetic resonance spectra of acidic hydroxyl groups in zeolites. *Microporous Mater.* **3**, 647–655 (1995).
5. Sarv, P., Tuherm, T., Lippmaa, E., Keskinen, K. & Root, A. Mobility of the acidic proton in Brønsted sites of H-Y, H-mordenite, and H-ZSM-5 zeolites, studied by high-temperature 1H MAS NMR. *J. Phys. Chem.* **99**, 13763–13768 (1995).
6. Baba, T., Komatsu, N. & Ono, Y. Mobility of the acidic protons in H-ZSM-5 as studied by variable temperature ^{1}H MAS NMR. *J. Phys. Chem. B* **102**, 804–808 (1998).
7. Franke, M. E. & Simon, U. Proton mobility in H-ZSM5 studied by impedance spectroscopy. *Solid State Ion.* **118**, 311–316 (1999).
8. Osuga, R., Yokoi, T., Doitomi, K., Hirao, H. & Kondo, J. N. Infrared investigation of dynamic behavior of Brønsted acid sites on zeolites at high temperatures. *J. Phys. Chem. C.* **121**, 25411–25420 (2017).
9. Fermann, J. T., Blanco, C. & Auerbach, S. Modeling proton mobility in acidic zeolite clusters. I. Convergence of transition state parameters from quantum chemistry. *J. Chem. Phys.* **112**, 6779–6786 (2000).
10. Ryder, J. A., Chakraborty, A. K. & Bell, A. T. Density functional theory study of proton mobility in zeolites: Proton migration and hydrogen exchange in ZSM-5. *J. Phys. Chem. B* **104**, 6998–7011 (2000).
11. Sierka, M. & Sauer, J. Finding transition structures in extended systems: a strategy based on a combined quantum mechanics-empirical valence bond approach. *J. Chem. Phys.* **112**, 6983–6996 (2000).
12. Sierka, M. & Sauer, J. Proton mobility in chabazite, faujasite, and ZSM-5 zeolite catalysts. Comparison based on ab initio calculations. *J. Phys. Chem. B* **105**, 1603–1613 (2001).
13. Tuma, C. & Sauer, J. A hybrid MP2/planewave-DFT scheme for large chemical systems: proton jumps in zeolites. *Chem. Phys. Lett.* **387**, 388–394 (2004).
14. Wang, Y. et al. Density functional theory study of proton hopping in MCM-22 zeolite. *Chem. Phys. Lett.* **388**, 363–366 (2004).
15. Franke, M. E., Sierka, M., Simon, U. & Sauer, J. Translational proton motion in zeolite H-ZSM-5. Energy barriers and jump rates from DFT calculations. *Phys. Chem. Chem. Phys.* **4**, 5207–5216 (2002).
16. Bučko, T., Gešvandtnerová, M. & Rocca, D. Ab initio calculations of free energy of activation at multiple electronic structure levels made affordable: an effective combination of perturbation theory and machine learning. *J. Chem. Theory Comput.* **16**, 6049–6060 (2020).
17. Kester, P. M., Crum, J. T., Li, S., Schneider, W. F. & Gounder, R. Effects of Brønsted acid site proximity in chabazite zeolites on OH infrared spectra and protolytic propane cracking kinetics. *J. Catal.* **395**, 210–226 (2021).
18. Huo, H., Peng, L. & Grey, C. P. Low temperature 1H MAS NMR spectroscopy studies of proton motion in zeolite HZSM-5. *J. Phys. Chem. C.* **113**, 8211–8219 (2009).
19. Li, G. & Pidko, E. A. The nature and catalytic function of cation sites in zeolites: a computational perspective. *ChemCatChem* **11**, 134–156 (2019).
20. Markland, T. E. & Ceriotti, M. Nuclear quantum effects enter the mainstream. *Nat. Rev. Chem.* **2**, 0109 (2018).
21. Li, C. & Voth, G. A. Using machine learning to greatly accelerate path integral ab initio molecular dynamics. *J. Chem. Theory Comput.* **18**, 599–604 (2022).

22. Rossi, M. Progress and challenges in ab initio simulations of quantum nuclei in weakly bonded systems. *J. Chem. Phys.* **154**, 170902 (2021).
23. Sauceda, H. E., Vassilev-Galindo, V., Chmiela, S., Müller, K. R. & Tkatchenko, A. Dynamical strengthening of covalent and non-covalent molecular interactions by nuclear quantum effects at finite temperature. *Nat. Commun.* **12**, 442 (2021).
24. Ceriotti, M. et al. Nuclear quantum effects in water and aqueous systems: experiment, theory, and current challenges. *Chem. Rev.* **116**, 7529–7550 (2016).
25. Li, X. Z., Walker, B. & Michaelides, A. Quantum nature of the hydrogen bond. *Proc. Natl Acad. Sci. USA* **108**, 6369–6373 (2011).
26. Ceriotti, M., Cuny, J., Parrinello, M. & Manolopoulos, D. E. Nuclear quantum effects and hydrogen bond fluctuations in water. *Proc. Natl Acad. Sci. USA* **110**, 15591–15596 (2013).
27. Peters, B. Reactive flux. In *Reaction Rate Theory and Rare Events Simulations*, 335–362 (Elsevier Inc., Amsterdam, 2017).
28. Schütt, K. T., Sauceda, H. E., Kindermans, P. J., Tkatchenko, A. & Müller, K. R. SchNet - a deep learning architecture for molecules and materials. *J. Chem. Phys.* **148**, 241722 (2018).
29. Schütt, K. T. et al. SchNetPack: a deep learning toolbox for atomistic systems. *J. Chem. Theory Comput.* **15**, 448–455 (2019).
30. Batzner, S. et al. E(3)-equivariant graph neural networks for data-efficient and accurate interatomic potentials. *Nat. Commun.* **13**, 2453 (2022).
31. Bailleul, S. et al. Ab initio enhanced sampling kinetic study on MTO ethene methylation reaction. *J. Catal.* **388**, 38–51 (2020).
32. Bučko, T., Chibani, S., Paul, J. F., Cantrel, L. & Badawi, M. Dissociative iodomethane adsorption on Ag-MOR and the formation of AgI clusters: an ab initio molecular dynamics study. *Phys. Chem. Chem. Phys.* **19**, 27530–27543 (2017).
33. Anderson, J. B. Statistical theories of chemical reactions. Distributions in the transition region. *J. Chem. Phys.* **58**, 4684–4692 (1973).
34. Bennett, C. H. Molecular dynamics and transition state theory: the simulation of infrequent events. In *Algorithms for Chemical Computations*, 63–97 (American Chemical Society, 1977).
35. Chandler, D. Statistical mechanics of isomerization dynamics in liquids and the transition state approximation. *J. Chem. Phys.* **68**, 2959–2970 (1978).
36. Hele, T. J. H. & Althorpe, S. C. Derivation of a true (t → 0+) quantum transition-state theory. I. Uniqueness and equivalence to ring-polymer molecular dynamics transition-state-theory. *J. Chem. Phys.* **138**, 084108 (2013).
37. Dale, H. J. A., Leach, A. G. & Lloyd-Jones, G. C. Heavy-atom kinetic isotope effects: primary interest or zero point? *J. Am. Chem. Soc.* **143**, 21079–21099 (2021).
38. Schroeder, C. et al. Hydrogen bond formation of Brønsted acid sites in zeolites. *Chem. Mater.* **32**, 1564–1574 (2020).
39. Vjunov, A. et al. Following solid-acid-catalyzed reactions by MAS NMR spectroscopy in liquid phase - Zeolite-catalyzed conversion of cyclohexanol in water. *Angew. Chem. Int. Ed.* **53**, 479–482 (2014).
40. Tomkins, P., Ranocchiari, M. & Van Bokhoven, J. A. direct conversion of methane to methanol under mild conditions over Cu-zeolites and beyond. *Acc. Chem. Res.* **50**, 418–425 (2017).
41. Bigeleisen, J. & Mayer, M. G. Calculation of equilibrium constants for isotopic exchange reactions. *J. Chem. Phys.* **15**, 261–267 (1947).
42. Bigeleisen, J. & Wolfsberg, M. Theoretical and experimental aspects of isotope effects in chemical kinetics. In *Advances in Chemical Physics* (ed. Prigogine, I.) 15–76 (John Wiley & Sons, Ltd, 1957).
43. Fermann, J. T. & Auerbach, S. Modeling proton mobility in acidic zeolite clusters. II. Room temperature tunneling effects from semiclassical rate theory. *J. Chem. Phys.* **112**, 6787–6794 (2000).
44. IZA Database of Zeolite Structures (accessed 28 March 2022). http://www.iza-structure.org/databases/.
45. Erlebach, A., Nachtigall, P. & Grajciar, L. Accurate large-scale simulations of siliceous zeolites by neural network potentials. *npj Comput. Mater.* **8**, 174 (2022).
46. Cendagorta, J. R., Shen, H., Bačić, Z. & Tuckerman, M. E. Enhanced sampling path integral methods using neural network potential energy surfaces with application to diffusion in hydrogen hydrates. *Adv. Theory Simul.* **4**, 2000258 (2021).
47. Hellström, M., Ceriotti, M. & Behler, J. Nuclear quantum effects in sodium hydroxide solutions from neural network molecular dynamics simulations. *J. Phys. Chem. B* **122**, 10158–10171 (2018).
48. Bolhuis, P. G., Chandler, D., Dellago, C. & Geissler, P. L. Transition path sampling: throwing ropes over rough mountain passes, in the dark. *Annu. Rev. Phys. Chem.* **53**, 291–318 (2002).
49. Sauer, J. Ab initio calculations for molecule-surface interactions with chemical accuracy. *Acc. Chem. Res.* **52**, 3502–3510 (2019).
50. Goncalves, T. J., Plessow, P. N. & Studt, F. On the accuracy of density functional theory in zeolite catalysis. *ChemCatChem* **11**, 4368–4376 (2019).
51. Liu, P. & Mei, D. Identifying free energy landscapes of proton-transfer processes between Brønsted acid sites and water clusters inside the zeolite pores. *J. Phys. Chem. C.* **124**, 22568–22576 (2020).
52. Ma, S. & Liu, Z. P. Machine learning potential era of zeolite simulation. *Chem. Sci.* **13**, 5055–5068 (2022).
53. Torrie, G. M. & Valleau, J. P. Monte Carlo free energy estimates using non-Boltzmann sampling: Application to the sub-critical Lennard-Jones fluid. *Chem. Phys. Lett.* **28**, 578–581 (1974).
54. Torrie, G. M. & Valleau, J. P. Monte Carlo study of a phase-separating liquid mixture by umbrella sampling. *J. Chem. Phys.* **66**, 1402–1408 (1977).
55. Tribello, G. A., Bonomi, M., Branduardi, D., Camilloni, C. & Bussi, G. PLUMED 2: new feathers for an old bird. *Comput. Phys. Commun.* **185**, 604–613 (2014).
56. The PLUMED consortium. Promoting transparency and reproducibility in enhanced molecular simulations. *Nat. Methods* **16**, 667–673 (2019).
57. ThermoLIB | Center for Molecular Modeling (accessed 19 November 2021) https://molmod.ugent.be/software/thermolib.
58. Vandevondele, J. et al. Quickstep: fast and accurate density functional calculations using a mixed Gaussian and plane waves approach. *Comput. Phys. Commun.* **167**, 103–128 (2005).
59. Kühne, T. D. et al. CP2K: An electronic structure and molecular dynamics software package -Quickstep: Efficient and accurate electronic structure calculations. *J. Chem. Phys.* **152**, 194103 (2020).
60. Perdew, J. P., Burke, K. & Ernzerhof, M. Generalized gradient approximation made simple. *Phys. Rev. Lett.* **77**, 3865–3868 (1996).
61. Yang, K., Zheng, J., Zhao, Y. & Truhlar, D. G. Tests of the RPBE, revPBE, τ -HCTHhyb, ωb97X-D, and MOHLYP density functional approximations and 29 others against representative databases for diverse bond energies and barrier heights in catalysis. *J. Chem. Phys.* **132**, 1–10 (2010).
62. Grimme, S., Antony, J., Ehrlich, S. & Krieg, H. A consistent and accurate ab initio parametrization of density functional dispersion correction (DFT-D) for the 94 elements H-Pu. *J. Chem. Phys.* **132**, 154104 (2010).
63. Lippert, G., Hutter, J. & Parrinello, M. The Gaussian and augmented-plane-wave density functional method for ab initio molecular dynamics simulations. *Theor. Chem. Acc.* **103**, 124–140 (1999).
64. Goedecker, S., Teter, M. & Hutter, J. Separable dual-space Gaussian pseudopotentials. *Phys. Rev. B - Condens. Matter Mater. Phys.* **54**, 1703–1710 (1996).
65. Nosé, S. A molecular dynamics method for simulations in the canonical ensemble. *Mol. Phys.* **52**, 255–268 (1984).
66. Martyna, G. J., Klein, M. L. & Tuckerman, M. Nosé-Hoover chains: the canonical ensemble via continuous dynamics. *J. Chem. Phys.* **97**, 2635–2643 (1992).

Article https://doi.org/10.1038/s41467-023-36666-y

67. Verstraelen, T., Vanduyfhuys, L., Vandenbrande, S. & Rogge, S. M. J. Yaff, Yet Another Force Field. http://molmod.github.io/yaff/index.html.
68. Kapil, V. et al. i-PI 2.0: A universal force engine for advanced molecular simulations. *Comput. Phys. Commun.* **236**, 214–223 (2019).
69. Ceriotti, M., Parrinello, M., Markland, T. E. & Manolopoulos, D. E. Efficient stochastic thermostatting of path integral molecular dynamics. *J. Chem. Phys.* **133**, 124104 (2010).
70. Li, C., Paesani, F. & Voth, G. A. Static and dynamic correlations in water: comparison of classical ab initio molecular dynamics at elevated temperature with path integral simulations at ambient temperature. *J. Chem. Theory Comput.* **18**, 2124–2131 (2022).
71. Frenkel, D. & Smit, B. Rare events. In *Understanding Molecular Simulation* 431–464 (Academic Press, 2002).
72. Craig, I. R. & Manolopoulos, D. E. A refined ring polymer molecular dynamics theory of chemical reaction rates. *J. Chem. Phys.* **123**, 034102 (2005).
73. Voth, G. A., Chandler, D. & Miller, W. H. Rigorous formulation of quantum transition state theory and its dynamical corrections. *J. Chem. Phys.* **91**, 7749–7760 (1989).
74. Suleimanov, Y. V., Javier Aoiz, F. & Guo, H. Chemical reaction rate coefficients from ring polymer molecular dynamics: Theory and practical applications. *J. Phys. Chem. A* **120**, 8488–8502 (2016).
75. Bocus, M., Neale, S. E., Cnudde, P. & Van Speybroeck, V. Dynamic evolution of catalytic active sites within zeolite catalysis. In *Reference Module in Chemistry, Molecular Sciences and Chemical Engineering* (Elsevier Inc., Amsterdam, 2021).

Acknowledgements

This work was supported by the Fund for Scientific Research Flanders (FWO, BioFact Excellence of Science project G0H0918N, ID EOS: 30902231, and project G024019N), the Flanders Industry Innovation Moonshot (ARCLATH II, No. HBC.2021.0254) and the Research Board of Ghent University (BOF). The computational resources (Stevin Supercomputer Infrastructure) and services used in this work were provided by the VSC (Flemish Supercomputer Center), funded by Ghent University, FWO, and the Flemish Government – department EWI.

Author contributions

M.B. and V.V.S. initiated the discussion and designed the scope of the project. M.B. performed the classical DFT simulations. A.L. provided technical support for the PIMD simulations and performed the PIMD DFT simulations. Under the supervision of T.V., R.G. trained the MLP and performed the related simulations, with support from M.C.C. M.B., R.G. and A.L. analyzed the results, which were discussed among all authors. M.B. and V.V.S. wrote the manuscript, with contributions from all authors.

Competing interests

The authors declare no competing interests.

Additional information

Supplementary information The online version contains supplementary material available at https://doi.org/10.1038/s41467-023-36666-y.

Correspondence and requests for materials should be addressed to Veronique Van Speybroeck.

Peer review information *Nature Communications* thanks Donghai Mei and the other, anonymous, reviewer(s) for their contribution to the peer review of this work. Peer reviewer reports are available.

Paper IX

Quantum tunneling rotor as a sensitive atomistic probe of guests in a metal-organic framework

K. Titov, M.R. Ryder, A. Lamaire, Z. Zeng, A.K. Chaudhari, J. Taylor, E.M. Mahdi, S.M.J. Rogge, S. Mukhopadhyay, S. Rudić, V. Van Speybroeck, F. Fernandez-Alonso, and J.-C. Tan

Physical Review Materials, **2023**, 7 (7), 073402

A. Lamaire performed the DFT calculations and contributed to the analysis, discussion, and interpretation of the results and the writing of the manuscript.

PHYSICAL REVIEW MATERIALS **7**, 073402 (2023)

Quantum tunneling rotor as a sensitive atomistic probe of guests in a metal-organic framework

Kirill Titov,[1] Matthew R. Ryder,[1,2,3] Aran Lamaire,[4] Zhixin Zeng,[1] Abhijeet K. Chaudhari,[1,5] James Taylor,[2] E. M. Mahdi,[1] Sven M. J. Rogge,[4] Sanghamitra Mukhopadhyay,[2] Svemir Rudić,[2,*] Veronique Van Speybroeck,[4,†] Felix Fernandez-Alonso,[6,7,8,9,‡] and Jin-Chong Tan[1,§]

[1]*Multifunctional Materials & Composites (MMC) Laboratory, Department of Engineering Science, University of Oxford, Parks Road, Oxford OX1 3PJ, United Kingdom*

[2]*ISIS Neutron and Muon Source, Science and Technology Facility Council, UKRI, Rutherford Appleton Laboratory, Chilton, Didcot OX11 0QX, United Kingdom*

[3]*Materials Science and Technology Division, Oak Ridge National Laboratory, Oak Ridge, Tennessee 37831, USA*

[4]*Center for Molecular Modeling (CMM), Ghent University, Technologiepark-Zwijnaarde 46, 9052 Zwijnaarde, Belgium*

[5]*Department of Chemistry, Christ University, Hosur Road, Bangalore 560029, India*

[6]*Materials Physics Center, CSIC-UPV/EHU, Paseo Manuel de Lardizabal 5, 20018 Donostia - San Sebastian, Spain*

[7]*Donostia International Physics Center (DIPC), Paseo Manuel de Lardizabal 4, 20018 Donostia - San Sebastian, Spain*

[8]*Department of Physics and Astronomy, University College London, Gower Street, London WC1E 6BT, United Kingdom*

[9]*IKERBASQUE, Basque Foundation for Science, Plaza Euskadi 5, 48009 Bilbao, Spain*

(Received 12 November 2022; revised 26 June 2023; accepted 27 June 2023; published 19 July 2023)

Quantum tunneling rotors in a zeolitic imidazolate framework ZIF-8 can provide insights into local gas adsorption sites and local dynamics of porous structure, which are inaccessible to standard physisorption or x-ray diffraction sensitive primarily to long-range order. Using *in situ* high-resolution inelastic neutron scattering at 3 K, we follow the evolution of methyl tunneling with respect to the number of dosed gas molecules. While nitrogen adsorption decreases the energy of the tunneling peak, and ultimately hinders it completely (0.33 meV to zero), argon substantially increases the energy to 0.42 meV. *Ab initio* calculations of the rotational barrier of ZIF-8 show an exception to the reported adsorption sites hierarchy, resulting in anomalous adsorption behavior and linker dynamics at subatmospheric pressure. The findings reveal quantum tunneling rotors in metal-organic frameworks as a sensitive atomistic probe of local physicochemical phenomena.

DOI: 10.1103/PhysRevMaterials.7.073402

I. INTRODUCTION

Gas adsorption studies are ubiquitous in metal-organic framework (MOF) research. Nevertheless, conflicting reports of MOF behavior persist in the literature, for example, on the fundamental question of structural flexibility [1] vs rigidity [2] because the information provided by gas adsorption experiments, together with other long-range techniques such as x-ray diffraction (XRD), is not always sufficient to advance the understanding of dynamic and transient phenomena [3]. Likewise, research on molecular rotors in MOFs is gaining attention, revealing a range of rotational linker dynamics (either free or hindered motions) [4,5] with implications on physical and chemical properties of the framework structure [6]. The much-contested behavior of a widely studied MOF, Zeolitic Imidazolate Framework-8 (ZIF-8), is a case in point. ZIF-8′s so-called gate-opening behavior [1], and its linker movements in general [7,8], are still not fully understood despite 25 years of active research [9]. Inelastic neutron scattering (INS) [10], specifically by quantum rotational tunneling of methyl ($-CH_3$) groups in ZIF-8, offers the possibility to resolve many unanswered questions. Rotational tunneling is the phenomenon of the librational states of a molecule whose rotating atoms, in this case, the three H atoms, are indistinguishable [11,12] and is illustrated schematically in Fig. 1(a). These methyl rotors, which account for 24 $-CH_3$ groups for each unit cell of ZIF-8, are sensitive to changes in the surrounding potentials and, therefore, can act as local probes of their atomic environments inside the framework pores. This sprawling network of quantum tunneling sensors can be harnessed to track gas adsorption processes, revealing local mechanisms at the atomic level. Although the methyl rotor in an empty ZIF-8 has been previously linked to quantum tunneling by Yildirim *et al.* [13], they have not investigated the effect of gas dosing on the tunneling phenomenon.

Early studies of the ZIF-8 structure and its behavior in response to gases recognized two extreme states, mainly defined by the orientation of the 2-methylimidazolate (mIm) linker, termed the "closed" and "open" gate. The exact mechanism

*svemir.rudic@stfc.ac.uk
†veronique.vanspeybroeck@ugent.be
‡felix.fernandez@ehu.eus
§jin-chong.tan@eng.ox.ac.uk

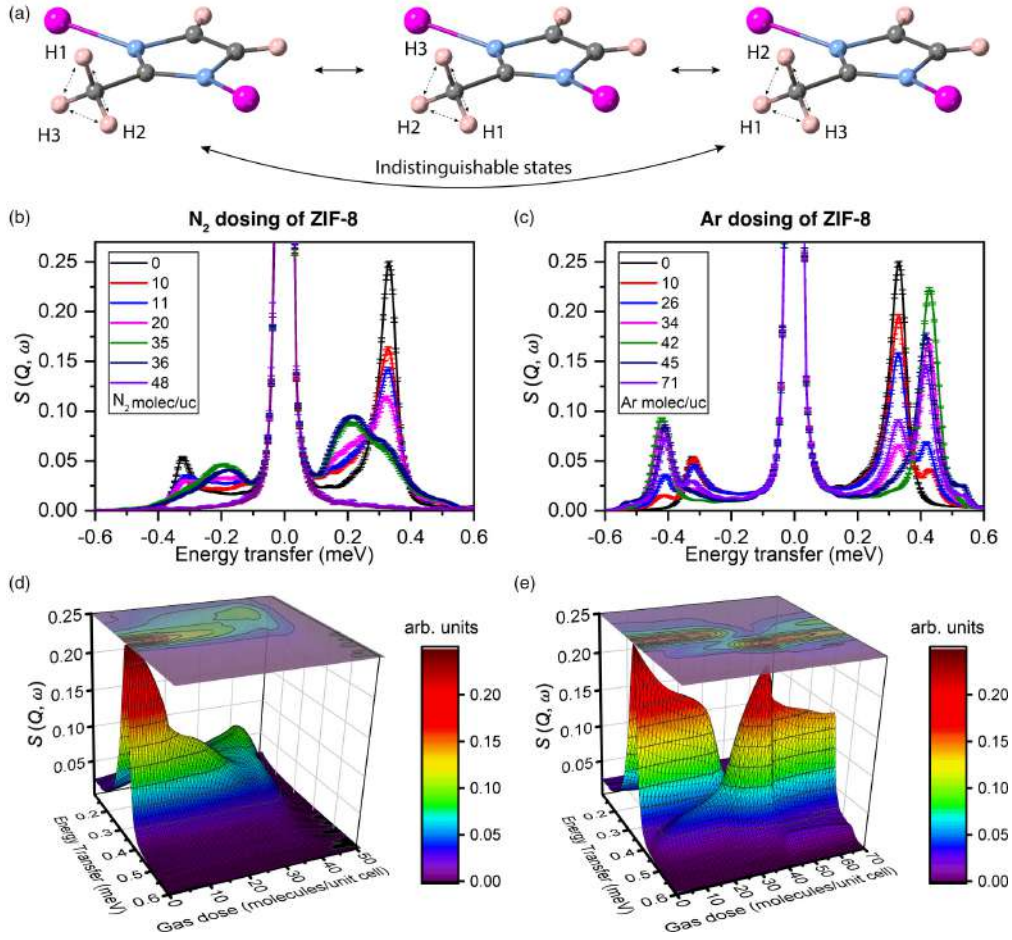

FIG. 1. Methyl tunneling in ZIF-8 with adsorbed guests, measured at 3 K. (a) Indistinguishable librational states of CH_3 rotors in ZIF-8 under quantum rotational tunneling. Color scheme: Zn (pink), C (gray), N (blue), and H (beige). (b), (c) Inelastic neutron-scattering (INS) spectra (collected at 3 K) of ZIF-8 powder dosed at 77 K with varying amounts of N_2 and Ar gas, respectively. (d), (e) Three-dimensional interpolated surfaces of INS spectra in (b) and (c), respectively.

behind the transformation was unclear and was complicated by the experimental technique—applying high hydrostatic pressure to a single crystal and tracking averaged structural changes in XRD patterns [14]. Based on these observations, it was recognized that both states were needed to simulate the gas adsorption behavior of ZIF-8 [1,15], but the existence of preferential adsorption sites was rejected based on early theoretical studies [16]. Subsequent studies, which included INS experiments and density-functional theory calculations of terahertz (THz) vibrational modes of ZIF-8, revealed that the linker orientation could change dynamically, including via "swing" motions of intermediate states that would open and close the pore window aperture into the sodalite cage without the need for guest adsorption [7]. Further experiments showed these motions in THz spectroscopy [17,18] and nuclear magnetic resonance experiments [19], which in conjunction with theoretical simulations have identified multiple vibrational motions of the ZIF-8′s structural moieties. By simulating and synthesizing ZIF-8 variants with various substitutes for the $-CH_3$ groups of mIm linkers, it was also shown that these motions were affected by the chemistry of the framework, which in turn affected gas adsorption behavior [6,20–23]. The work by Moggach and co-workers [24] enriched this expanding view of ZIF-8 by showing that there exist preferential adsorption sites within the framework's pores, despite earlier suggestions [16] to the contrary. This literature, together with

our results from the local quantum tunneling probes presented here, confer a rich view of ZIF-8′s behavior, whereby dynamic vibrational modes and adsorption energies at specific sites, all guided by the underlying physics and chemistry of the porous framework, play radical roles in observed phenomena.

II. EXPERIMENTAL AND THEORETICAL METHODS

A. Materials

ZIF-8 was purchased from Sigma-Aldrich. For a typical sample, 1.2 g of ZIF-8 powder (particle size $\sim$1 μm) was loaded into a perforated Al sachet and evacuated at 200 °C overnight to ensure the sample was desolvated prior to the gas dosing experiments.

B. INS and neutron powder diffraction

The high-resolution INS and neutron powder-diffraction (NPD) data [10,25,26] were collected on the OSIRIS spectrometer at the ISIS Pulsed Neutron and Muon Source at the Rutherford Appleton Laboratory in Chilton, UK. OSIRIS is a high-resolution (25.4 μeV) indirect-geometry neutron spectrometer with long-wavelength diffraction capabilities [27–29]. The secondary spectrometer is positioned at $\sim$34 m from the 25 K liquid hydrogen moderator. Optimized for low-energy, high-resolution inelastic neutron-scattering studies, OSIRIS uses a broadband of incident wavelengths which are Bragg scattered from a crystal-analyzer array following interaction with the sample. For the INS experiment, the (002) plane of the pyrolytic graphite analyzer was used, thus defining the single final energy of detected neutrons as 1.84 meV. The cooled beryllium filter between the sample and the analyzer suppressed higher-order reflections of the graphite analyzer. Due to utilizing a pulsed neutron source, time-of-flight methods are used to determine energies at each particular scattering angle. Using the repetition rate of 16 Hz, which is one-third of the repetition rate of ISIS Target Station 1, an energy transfer range of 20 meV ($\sim$5 THz) was achieved. The scattered neutrons were detected in an angular range corresponding to the momentum transfer (Q) range 0.42−1.82 Å^{-1}. The scattered data from all Q values in this range were summed up to produce the INS spectrum. The neutron-diffraction data were obtained from the instrument as a by-product of the spectroscopy experiments from diffraction detectors in the backscattered geometry. Its resolution amounts to $\Delta d/d = 2.5 \times 10^{-3}$, where Δd is the full width at half maximum of diffraction peaks in d spacing.

C. Gas dosing

The sample was loaded into a cylindrical vanadium can connected to a gas-handling system. N_2 and Ar gas loading was done volumetrically at 77 K to emulate the Brunauer-Emmett-Teller (BET) test conditions (see below) and to ensure that the sample adsorbed the gas. The sample was degassed at 10^{-7} mbar between gas dosing experiments. At each gas dose, the system was allowed to equilibrate for at least 30 min. The sample was then gradually cooled down to 3 K (within $\sim$1 h), where the INS measurements were performed. This methodology of dosing at 77 K and probing at 3 K has previously been adopted to investigate the gas adsorption process within MOFs utilizing INS [30].

D. Gas adsorption measurements

BET isotherms of ZIF-8 for N_2 and Ar were measured on a Quantachrome Autosorb iQ-Chemi instrument at 77 K.

E. Electronic structure calculations

To determine the rotational energy barrier of a "methyl top" (i.e., $-CH_3$ rotor) in ZIF-8, with and without adsorbed N_2 molecules or Ar atoms, each ZIF-8 structure was optimized using CP2K [31,32] in combination with the ASE (atomic simulation environment) [33]. Given that the methyl tops in ZIF-8 behave as quasifree rotors, the energy differences associated with their rotation are very small and sensitive to minor structural differences, which makes their optimization more difficult. Therefore, the crystal symmetry (space group $I\bar{4}3m$) was kept fixed during the optimization, to maintain the equivalence of the different methyl tops. As only structures with full occupation of all equivalent N_2 or Ar adsorption sites were considered, the N_2 molecules or Ar atoms were also required to adhere to the crystal symmetry. The optimizations converged when the forces on all atoms were smaller than 0.0025 eV/Å.

Subsequently, the rotational energy barrier was obtained by rotating one of the methyl tops around the axis of the C–C bond to which it was connected. After every rotational step, an intermediate optimization was performed for the hydrogen atoms of the methyl top, as these hydrogen atoms were not necessarily equivalent due to their different local environment in the structure. During this intermediate optimization, the other atoms were kept fixed.

All the calculations used the optimal unit cell for ZIF-8, which was determined by fitting an equation of state for the empty framework (guest-free). Furthermore, all the calculations were performed using the Perdew–Burke-Ernzerhof functional with the D3 dispersion scheme and Becke-Johnson damping (PBE-D3(BJ)) [34–36], combined with Goedecker-Teter-Hutter pseudopotentials [37], a plane-wave basis set with a cutoff of 800 Ry and a relative cutoff of 60 Ry, and Gaussian TZVP-MOLOPT [38] basis sets for all elements except Ar, as for this element only a DZVP-MOLOPT basis set is available.

F. Rotational energy levels

Once the rotational energy barrier of the methyl top was determined from electronic structure calculations, as outlined in the previous section, the discrete rotational energy levels can be obtained by numerically solving the Schrödinger equation for a hindered rotor, for which we use the so-called direct matrix method [39,40]. Using Numerov's method, a fourth-order approximation to the wave function can be obtained:

$$\psi_{i+1}\left(1+\frac{(\Delta\varphi)^2}{12}f_{i+1}\right) = 2\psi_i\left(1-\frac{5(\Delta\varphi)^2}{12}f_i\right)-\psi_{i-1}\left(1+\frac{(\Delta\varphi)^2}{12}f_{i-1}\right)+\mathcal{O}(\Delta\varphi^6), \quad (1)$$

with $\Delta\varphi = \varphi_{i+1} - \varphi_i$, $\psi_i = \psi(\varphi_i)$, and $f_i = f(\varphi_i) = -\frac{V_i - E}{B}$. For a hindered rotor, characterized by the Hamiltonian

$$\mathcal{H} = -B\frac{\mathrm{d}^2}{\mathrm{d}\varphi^2} + V(\varphi), \tag{2}$$

with

$$B = \frac{1}{2I} = \frac{1}{2\sum_i m_i r_i^2}, \tag{3}$$

the Schrödinger equation can be rewritten as

$$-B\,\frac{\psi_{i-1} - 2\psi_i + \psi_{i+1}}{(\Delta\varphi)^2} + \frac{V_{i-1}\psi_{i-1} + 10V_i\psi_i + V_{i+1}\psi_{i+1}}{12} = E\,\frac{\psi_{i-1} + 10\psi_i + \psi_{i+1}}{12}. \tag{4}$$

Using the matrix representations

$$\boldsymbol{\psi} = \begin{pmatrix} \psi_1 \\ \vdots \\ \psi_i \\ \vdots \\ \psi_N \end{pmatrix},\ \mathbf{A} = \mathbf{I}_{-1} - 2\mathbf{I}_0 + \mathbf{I}_1,\ \mathbf{C} = \mathbf{I}_{-1} + 10\mathbf{I}_0 + \mathbf{I}_1,$$

$$\mathbf{V} = \begin{pmatrix} V_1 \\ \vdots \\ V_i \\ \vdots \\ V_N \end{pmatrix}, \tag{5}$$

with $\mathbf{I}_p$ a matrix with $[\mathbf{I}_p]_{i,i+p} = 1$ ($i \in \{1, \ldots, N\}$) and zeros elsewhere, the fourth-order Numerov approximation of the Schrödinger equation can be transformed into an eigenvalue equation:

$$-\frac{12B}{(\Delta\varphi)^2}\,\mathbf{C}^{-1}\mathbf{A}\,\boldsymbol{\psi} + \mathbf{V}\,\boldsymbol{\psi} = E\,\boldsymbol{\psi}. \tag{6}$$

To impose periodic boundary conditions (i.e., $\psi_0 = \psi_N$), as implied when using an angular coordinate such as φ, one sets $\mathbf{A}_{1N} = \mathbf{A}_{N1} = \mathbf{C}_{1N} = \mathbf{C}_{N1} = 1$. From the rotational energy barriers obtained from electronic structure calculations, it follows that the potential energy of the hindered methyl rotors can be parametrized by

$$V(\varphi) = c_0 + c_1\sin(3\varphi) + c_2\cos(3\varphi) + c_3\sin(6\varphi) + c_4\cos(6\varphi), \tag{7}$$

with the parameters c_i obtained from least-squares linear regression. The resulting potential fits are shown in Supplemental Material, Fig. S4 (for adsorption of Ar atoms) and Fig. S5 (for adsorption of N_2 molecules) [41], and the corresponding parameters c_i are listed in Tables S1 and S4 [41], respectively. These tables illustrate that the inclusion of the $\cos(6\varphi)$ term plays an important role in obtaining an accurate fit. The barrier height is defined as the difference between the highest value of the rotational energy barrier (E_B) and the lowest rotational energy level (E_0), i.e., ($E_B - E_0$), to adequately take the zero-point energy of the rotor into account. The energy at which the experimental tunneling peak is located is compared with the energy of the rotational transition between the two lowest-energy levels ($0 \rightarrow 1$), i.e., ($E_1 - E_0$).

III. RESULTS AND DISCUSSION

The tunneling transitions appear in INS spectra recorded on the OSIRIS spectrometer [27–29] under high vacuum and at temperatures below 30 K as a well-defined peak at 0.33 meV [see the black spectra in Figs. 1(b) and 1(c)], matching the energy determined by Yildirim and co-workers [13] who studied the tunneling of methyl rotors in ZIF-8 without adsorbed guest molecules. When ZIF-8 is loaded with N_2 or Ar gas molecules, the tunneling peak changes its intensity and shifts in energy, signaling a change in the rotational energy of the rotors, which implies a change in their rotational barriers. These changes are induced by the interactions of the gas molecules with the framework. Individual tunneling spectra for increasing doses of the respective gases are shown in Figs. 1(b) and 1(c). These spectra were used to fit piecewise cubic Hermite interpolating polynomial lines through individual energy-transfer data points along the gas dose dimension. This allows us to construct 3D surfaces to reveal the evolution of the tunneling peak with increasing gas doses. The results are shown in Figs. 1(d) and 1(e), together with their 2D projections onto an energy-transfer (meV)−gas dose (molecules per unit cell) plane. Neutron powder-diffraction (NPD) patterns, collected together with the scattering spectra, are interpolated in the same way and plotted as 2D projections of 3D surfaces. INS spectra and NPD data are then plotted on a common gas dose axis with the corresponding BET adsorption isotherms for the same sample. Figures 2(a) and 2(b) show these results for N_2- and Ar-dosed ZIF-8, respectively.

Gas adsorption leads to changes in intensity and shifts of the tunneling peak for both N_2 and Ar dosing. The difference is that N_2 decreases the energy of the tunneling and eventually hinders it completely, whereas Ar increases the energy. Despite this opposite result, the level of gas loading at which these changes occur is within similar ranges that can be defined in terms of adsorption site occupancy. The levels for cumulative full occupancy of each adsorption site are shown as dashed-dotted lines in Figs. 2(a) and 2(b): at 8 molecules per unit cell (molec/uc) there is enough gas in the system to occupy all sites 1, by 32 molec/uc there is enough gas to occupy both sites 1 and sites 2, and so on (further details about adsorption sites are given in the Supplemental Material [41]). The phenomena observed in the adsorption isotherms, INS spectra, and NPD patterns all fit within these adsorption site brackets and should be understood to result from gas molecules occupying those adsorption sites. Figure 2(c) shows adsorption sites 1 to 5, previously identified by Moggach and co-workers [24]. *Ab initio* calculations were performed as part of this study to confirm this assertion of preferential adsorption sites playing a key role in observed tunneling phenomena. The results are summarized below.

Rotational energy barriers of a methyl top (rotor) upon Ar gas adsorption are shown in Fig. 2(d). The rotational barrier heights and the corresponding rotational transitions between the two lowest energy levels ($0 \rightarrow 1$) are listed in Table I for the "empty" ZIF-8 framework (i.e., without gas), and a sequential filling of the first three argon adsorption sites. The five lowest rotational energy levels are listed in Table S3 of the Supplemental Material [41]. For the empty framework, the experimental tunneling peak is observed at 0.33 meV [13],

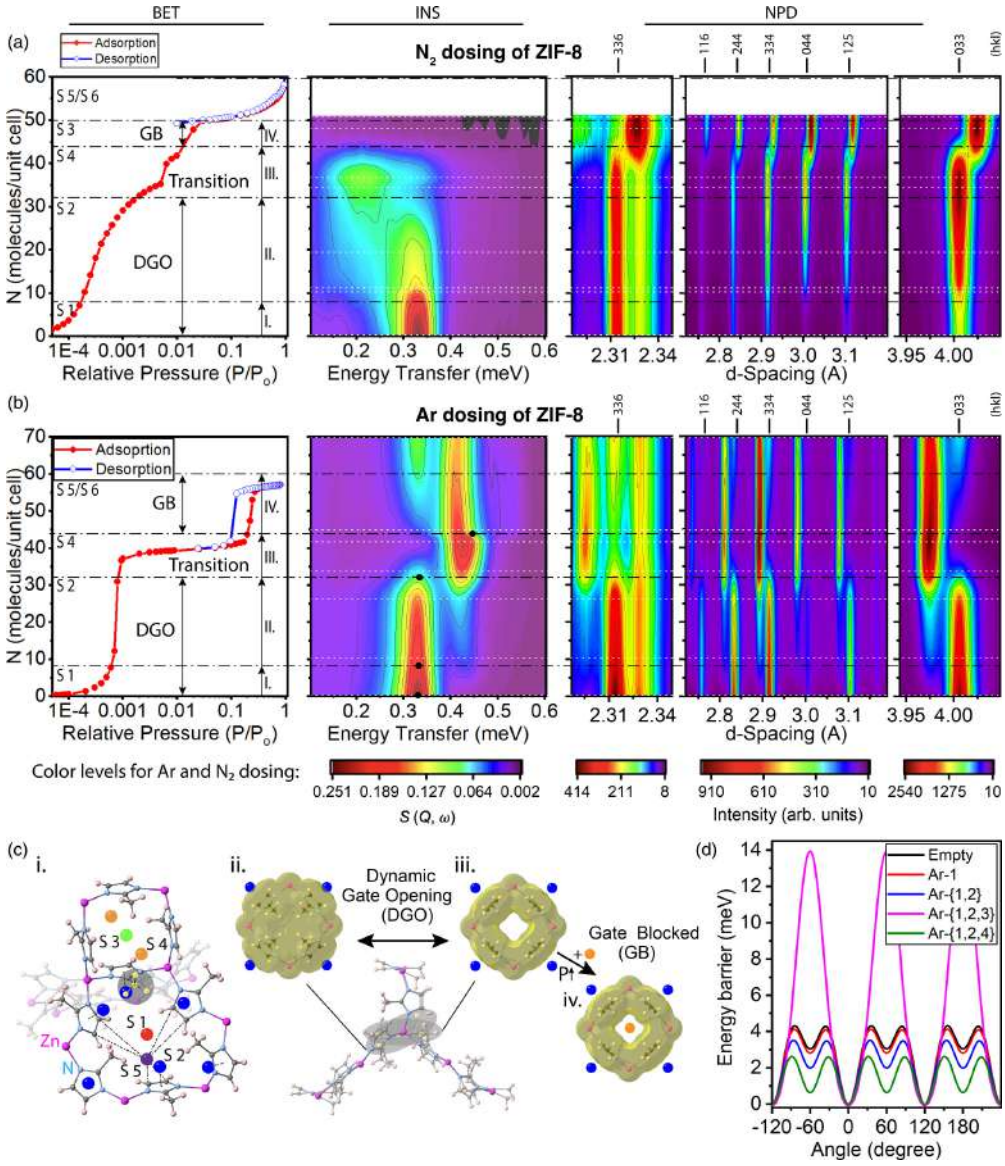

FIG. 2. (a), (b) BET adsorption measurements correlated with interpolated inelastic neutron-scattering spectra and interpolated neutron-diffraction patterns of ZIF-8 dosed with N_2 and Ar gas, respectively. BET measurements were performed at 77 K while neutron measurements were at 3 K. Dosing with gases for neutron experiments was done at 77 K to emulate BET adsorption conditions. Black dashed-dotted lines mark levels of cumulative full occupancy of each adsorption site. White dotted lines mark gas doses at which measurements were performed. (c)i Positions of adsorption sites 1 to 5 in ZIF-8, reproduced from Ref. [19]. Illustrations of average (c)ii closed and (c)iii open states (crystallographic information files (CIFs) from Ref. [14]) reached by 4-membered rings (4-MRs) as they undergo dynamic gate opening (DGO) motions. (c)iv 'Gate-blocked' (GB) state is illustrated as a result of site 4 occupied by gas molecules. van der Waals surfaces are marked in yellow. (d) Theoretically calculated rotational energy barrier of a methyl top in ZIF-8 with a sequential filling of the respective argon adsorption sites; for every adsorption site, all equivalent adsorption positions are occupied simultaneously.

TABLE I. Rotational constant B, optimal N–C–C–H dihedral angle φ_0, maximum of rotational barrier E_B, rotational energy barrier $E_B - E_0$, and energy $E_1 - E_0$ of $0 \rightarrow 1$ rotational transition for different Ar adsorption sites in ZIF-8. All energy quantities are given in meV. Theoretical energy $E_1 - E_0$ is scaled by a factor of 0.8 to resemble the experimental tunneling peak of empty ZIF-8 at 0.33 meV. Note that scaled theoretical values applied here are for ease of comparison with experimental data and do not alter any conclusions.

	No. Ar atoms	B	φ_0 (°)	E_B	$E_B - E_0$	$E_1 - E_0$	$(E_1 - E_0)*0.8$
ZIF-8 (empty)	0	0.573	88.2	4.308	1.821	0.410	0.328
ZIF-8 + Ar-1	8	0.573	88.2	4.119	1.728	0.428	0.342
ZIF-8 + Ar-{1, 2}	32	0.573	88.2	3.511	1.475	0.487	0.389
ZIF-8 + Ar-{1, 2, 3}	38	0.574	86.9	13.95	10.97	0.071	0.057
ZIF-8 + Ar-{1, 2, 4}	44	0.573	88.1	2.623	1.214	0.560	0.448

which is slightly overestimated computationally, yielding a value of 0.41 meV. In contrast, it is worth noting that Ruggiero and co-workers [42] reported a substantially lower computational value of 0.225 meV for the first rotational transition, which is in discrepancy with experiments.

When filling the first type of adsorption sites in ZIF-8 (denoted as Ar-1), requiring a total of 8 argon atoms per unit cell, the energy of the first rotational transition ($E_1 - E_0$) remains virtually unaltered (Table I). If also the second type of adsorption sites (denoted as Ar-2) are filled, yielding a total of 32 argon atoms across sites 1 and 2 per unit cell, the rotational energy barrier (E_B) of the methyl top is lowered by about 0.6 meV, resulting in a modest increase in the energy of the first rotational transition. The addition of 6 further argon atoms per unit cell, occupying the third type of adsorption sites (denoted as Ar-3, as highlighted in Table I), substantially increases the rotational energy barrier so that the energy of the first rotational transition decreases drastically to 0.07 meV, and the methyl top changes its behavior from a quasifree rotor to an almost hindered rotor, frozen in a particular rotation state. However, suppose the fourth type of adsorption site (denoted as Ar-4) is occupied instead of the third type (Ar-3). In that case, the rotational energy barrier of the methyl top decreases instead of increasing so that the energy of the first rotational transition rises, similar to the experimentally observed trend. This finding concludes that site 3 is not filled during subatmospheric adsorption experiments (unlike at high pressure [24]); otherwise, the tunneling peak would have disappeared at a dose of 38 molec/uc, which contradicts our experimental observations.

Likewise, *ab initio* calculations were performed to interrogate the effects of N_2 adsorption on the rotational tunneling energy of ZIF-8 (see details in Sec. II). As in the case of Ar, the computational results (Table S5 [41]) predict that after filling the first and second adsorption sites, the additional nitrogen molecules occupy the fourth type of adsorption sites, rather than the third type. For this adsorption sequence, the first rotational transition ($E_1 - E_0$) decreases by about $0.02 - 0.04$ meV after the initial adsorption of N_2 (by the occupation of sites 1 and 2). When also filling adsorption sites 4, the rotational transition decreased further by 0.07 meV, so that the tunneling transition is lowered by $\sim$0.1 meV with respect to the empty ZIF-8, hence in good agreement with the experimental INS spectra [Fig. 2(a)] where the tunneling peak is shifted to lower energy. Subsequently, it is observed experimentally that the tunneling peaks disappear [Fig. 1(b)], which suggests the nitrogen molecules eventually do start to occupy site 3, for which *ab initio* calculations (Table S5 [41]) predicted a high rotational energy barrier (E_B).

Based on the tunneling phenomena, the adsorption process of ZIF-8 can be subdivided into four stages, as designated in Figs. 2(a) and 2(b). The first stage (I) of the process—between 0 and 8 molec/uc—supplies enough gas to occupy all sites 1 [designated as S1 in Fig. 2(c)]. This phase is the initial loading of the framework, during which the isotherm starts sloping upwards while the intensity of the tunneling peak decreases. Therefore, no shifts of INS or NPD peaks occur during this phase.

The second stage (II)–between 8 and 32 molec/uc—supplies enough gas to occupy all sites 2 in addition to sites 1. During this phase the isotherm rises rapidly for both gases, but more so for Ar. The tunneling peak at around 0.33 meV decreases gradually, and the "dosed" tunneling peaks emerge at energies of 0.22 meV for N_2 and 0.42 meV for Ar. This change in energy of the tunneling peak is not gradual, however. The tunneling energy shifts from one energy to another for some methyl rotors before others, but the shift is sudden rather than gradual. This shift is not completed until the end of the next stage of the adsorption process.

The third stage (III)–between 32 and 44 molec/uc—fills sites 4 in addition to sites 1 and 2. Isotherms level off in this phase before turning upwards again, the tunneling peaks convert completely to their lower and higher energies for N_2 and Ar, respectively, and shifts in NPD peaks occur for both gases: for N_2, the unit cell of ZIF-8 expands (1.4% volumetric expansion), while for Ar, it contracts (2.2% volumetric contraction). These contrasting changes for the two gases show that despite being considered inert at these conditions, adsorption of these gases results in physicochemical interactions with the framework, which produce changes in local potentials and accumulate to trigger structural transformation in the long-range order of the framework. Furthermore, we propose that these contrasting changes are, for instance, influenced by the difference in size of the guest molecules (N_2 > Ar) or the quadrupole moment of N_2, rendering differential host-guest interactions, albeit unraveling the precise mechanism responsible for this effect will warrant further investigation.

In the fourth stage (IV)—for Ar, between 44 and 60 molec/uc—sites 5 and 6 are filled in addition to sites 1, 2, and 4. Hysteresis loops can be seen forming in the adsorption-desorption isotherms [16]. Our results suggest that the interaction energies at specific adsorption sites have a role to play in the observed effect. More precisely, the tunneling peak does not disappear for Ar, but it splits into

three components—indicating that different methyl groups see three types of environments. Crucially, however, the 0.42-meV tunneling peak dominates the additional higher- and lower-energy peaks. Therefore, the methyl groups of ZIF-8 subject to high Ar loading still exhibit rotational tunneling, albeit at different energies. For N_2 adsorption, however, the tunneling peaks observed in experiments completely disappear after site 3 starts to be occupied [Fig. 2(a)]. A full occupation of site 3 occurs at 50 molec/uc, coinciding with the point at which the experimental adsorption isotherm also changes in shape.

IV. CONCLUDING REMARKS

Our experimental results supplemented with *ab initio* calculations show that the reported adsorption sites hierarchy based on interaction energy inside the ZIF-8 pores (observed under GPa pressure by Moggach and co-workers [24]) holds for low-pressure conditions with one exception: the adsorption sites inside 4-membered rings [sites 3 in Fig. 2(c)] of ZIF-8 are not occupied by argon gas molecules at subatmospheric pressure. Nevertheless, for both gases the adsorption sites on either side of the four-membered rings (4-MRs, sites 4) are indeed occupied when enough gas is supplied, which is key to understanding ZIF-8′s adsorption behavior: the steps in adsorption isotherms and the shifts in long-range order of ZIF-8 occur after sites 1 and 2 have been filled and in the process of filling sites 4 [see Figs. 2(a) and 2(b)]. Structurally, this necessitates linker rotations to make sites 4 accessible—the dynamic "gate-opening" motions—explaining the results observed in other experiments [see Figs. 2(c)ii and 2(c)iii for a schematic]. However, it also implies a "gate-blocked" structure in which the linkers of ZIF-8 are no longer able to rotate to a gate-closed position due to guest molecules adsorbed in sites 4 [see Figs. 2(c)iii and 2(c)iv for a schematic]—this is accompanied by a shift in the long-range order of the framework observed in neutron powder-diffraction patterns [Figs. 2(a) and 2(b)].

In conclusion, *in situ* high-resolution INS spectroscopy [27–29] observes the methyl tunneling rotors while simultaneously yielding neutron powder-diffraction patterns containing structural information. This combination enriches gas adsorption isotherms with previously unobserved insights, and could inspire future investigations of porous hybrid materials exhibiting tunneling phenomena.

ACKNOWLEDGMENTS

MMC Laboratory is supported by the ERC Consolidator Grant (PROMOFS Grant Agreement No. 771575) and EPSRC Awards (Grants No. EP/N014960/1 and No. EP/R511742/1). We thank ISIS Facility for the awarded OSIRIS beamtime (Grants No. RB1410426, No. RB1510529, and No. RB1610180), DOIs 10.5286/ISIS.E.RB1410426, 10.5286/ISIS.E.RB1510529, and 10.5286/ISIS.E.RB1610180, as well as the Cryogenics, and Pressure & Furnaces teams for their exemplary support. M.R.R. acknowledges the U.S. DOE Office of Science, Office of Basic Energy Sciences, Chemical Sciences, Geosciences, and Biosciences Division (Separation Sciences). This work is further supported by the Fund for Scientific Research Flanders (FWO) through a Ph.D. fellowship for A.L. (Grant No. 11D2220N) and a postdoctoral fellowship for S.M.J.R. (Grant No. 12T3522N). Financial support for F.F.-A. from the Spanish Ministry of Science and Innovation (Grant No. PID2020-114506GB-I00 funded by MCIN/AEI/10.13039/501100011033 and Grant No. TED2021-129457B-I00 funded by MCIN/AEI/10.13039/501100011033 and the European Union NextGenerationEU/PRTR) as well as the Basque Government (Grant No. PIBA-2021-0026) is gratefully acknowledged. We also acknowledge the financial support received from the IKUR Strategy under the collaboration agreement between Ikerbasque Foundation and the Materials Physics Center on behalf of the Department of Education of the Basque Government. We acknowledge the Research Complex at Harwell (RCaH) for access to materials characterization facilities. The computational resources and services used in this work were provided by the VSC (Flemish Supercomputer Center), funded by the Research Foundation–Flanders (FWO) and the Flemish Government–department EWI.

The authors declare no competing financial interest.

[1] D. Fairen-Jimenez, S. A. Moggach, M. T. Wharmby, P. A. Wright, S. Parsons, and T. Düren, J. Am. Chem. Soc. **133**, 8900 (2011).

[2] W. Morris, C. J. Stevens, R. E. Taylor, C. Dybowski, O. M. Yaghi, and M. A. Garcia-Garibay, J. Phys. Chem. C **116**, 13307 (2012).

[3] *Mechanical Behaviour of Metal–Organic Framework Materials*, edited by J. C. Tan (The Royal Society of Chemistry, London, UK, 2023).

[4] A. Comotti, S. Bracco, and P. Sozzani, Acc. Chem. Res. **49**, 1701 (2016).

[5] M. R. Ryder, B. Van de Voorde, B. Civalleri, T. D. Bennett, S. Mukhopadhyay, G. Cinque, F. Fernandez-Alonso, D. De Vos, S. Rudic, and J. C. Tan, Phys. Rev. Lett. **118**, 255502 (2017).

[6] A. Gonzalez-Nelson, F. X. Coudert, and M. A. van der Veen, Nanomaterials **9**, 330 (2019).

[7] M. R. Ryder, B. Civalleri, T. D. Bennett, S. Henke, S. Rudić, G. Cinque, F. Fernandez-Alonso, and J. C. Tan, Phys. Rev. Lett. **113**, 215502 (2014).

[8] F. Formalik, B. Mazur, M. Fischer, L. Firlej, and B. Kuchta, J. Phys. Chem. C **125**, 7999 (2021).

[9] R. Freund, S. Canossa, S. M. Cohen, W. Yan, H. Deng, V. Guillerm, M. Eddaoudi, D. G. Madden, D. Fairen-Jimenez, H. Lyu *et al.*, Angew. Chem. Int. Ed. **60**, 23946 (2021).

[10] *Neutron Scattering — Fundamentals*, edited by F. Fernandez-Alonso and D. L. Price (Academic Press, New York, 2013).

[11] J. Eckert, Spectroc. Acta A: Mol. Biomol. Spectrosc. **48**, 271 (1992).

[12] M. Prager and A. Heidemann, Chem. Rev. **97**, 2933 (1997).

[13] W. Zhou, H. Wu, T. J. Udovic, J. J. Rush, and T. Yildirim, J. Phys. Chem. A **112**, 12602 (2008).

[14] S. A. Moggach, T. D. Bennett, and A. K. Cheetham, Angew. Chem. Int. Ed. **48**, 7087 (2009).

[15] D. Fairen-Jimenez, R. Galvelis, A. Torrisi, A. D. Gellan, M. T. Wharmby, P. A. Wright, C. Mellot-Draznieks, and T. Duren, Dalton Trans. **41**, 10752 (2012).

[16] C. O. Ania, E. Garcia-Perez, M. Haro, J. J. Gutierrez-Sevillano, T. Valdes-Solis, J. B. Parra, and S. Calero, J. Phys. Chem. Lett. **3**, 1159 (2012).

[17] N. Y. Tan, M. T. Ruggiero, C. Orellana-Tavra, T. Tian, A. D. Bond, T. M. Korter, D. Fairen-Jimenez, and J. A. Zeitler, Chem. Commun. **51**, 16037 (2015).

[18] T. Tanno, Y. Watanabe, K. Umeno, A. Matsuoka, H. Matsumura, M. Odaka, and N. Ogawa, J. Phys. Chem. C **121**, 17921 (2017).

[19] D. I. Kolokolov, A. G. Stepanov, and H. Jobic, J. Phys. Chem. C **119**, 27512 (2015).

[20] F. Formalik, M. Fischer, J. Rogacka, L. Firlej, and B. Kuchta, Micropor. Mesopor. Mat **304**, 109132 (2020).

[21] F. X. Coudert, ChemPhysChem **18**, 2732 (2017).

[22] G. Chaplais, G. Fraux, J.-L. Paillaud, C. Marichal, H. Nouali, A. H. Fuchs, F.-X. Coudert, and J. Patarin, J. Phys. Chem. C **122**, 26945 (2018).

[23] C. L. Hobday, T. D. Bennett, D. Fairen-Jimenez, A. J. Graham, C. A. Morrison, D. R. Allan, T. Duren, and S. A. Moggach, J. Am. Chem. Soc. **140**, 382 (2018).

[24] C. L. Hobday, C. H. Woodall, M. J. Lennox, M. Frost, K. Kamenev, T. Duren, C. A. Morrison, and S. A. Moggach, Nat. Commun. **9**, 1429 (2018).

[25] *Neutron Scattering–Magnetic and Quantum Phenomena*, edited by F. Fernandez-Alonso and D. L. Price (Academic Press, New York, 2015).

[26] *Neutron Scattering–Applications* in *Biology, Chemistry, and Materials Science*, edited by F. Fernandez-Alonso and D. L. Price (Academic Press, New York, 2017).

[27] F. Demmel, D. McPhail, J. Crawford, D. Maxwell, K. Pokhilchuk, V. Garcia-Sakai, S. Mukhopadyay, M. T. F. Telling, F. J. Bermejo, N. T. Skipper *et al.*, EPJ Web. Conf. **83**, 03003 (2015).

[28] M. T. F. Telling and K. H. Andersen, Phys. Chem. Chem. Phys. **7**, 1255 (2005).

[29] M. T. F. Telling, S. I. Campbell, D. Engberg, Y. M. D. Martin, and K. H. Andersen, Phys. Chem. Chem. Phys. **18**, 8243 (2016).

[30] T. L. Easun, F. Moreau, Y. Yan, S. H. Yang, and M. Schroder, Chem. Soc. Rev. **46**, 239 (2017).

[31] J. VandeVondele, M. Krack, F. Mohamed, M. Parrinello, T. Chassaing, and J. Hutter, Comput. Phys. Commun. **167**, 103 (2005).

[32] J. Hutter, M. Iannuzzi, F. Schiffmann, and J. VandeVondele, WIREs Comput. Mol. Sci. **4**, 15 (2014).

[33] A. Hjorth Larsen, J. Jorgen Mortensen, J. Blomqvist, I. E. Castelli, R. Christensen, M. Dulak, J. Friis, M. N. Groves, B. Hammer, C. Hargus *et al.*, J. Phys.: Condens. Matter. **29**, 273002 (2017).

[34] J. P. Perdew, K. Burke, and M. Ernzerhof, Phys. Rev. Lett. **77**, 3865 (1996).

[35] S. Grimme, J. Antony, S. Ehrlich, and H. Krieg, J. Chem. Phys. **132**, 154104 (2010).

[36] S. Grimme, S. Ehrlich, and L. Goerigk, J. Comput. Chem. **32**, 1456 (2011).

[37] S. Goedecker, M. Teter, and J. Hutter, Phys. Rev. B **54**, 1703 (1996).

[38] J. VandeVondele and J. Hutter, J. Chem. Phys. **127**, 114105 (2007).

[39] J. Izaac and J. Wang, *Computational Quantum Mechanics* (Springer, Cham, Switzerland, 2018).

[40] M. Pillai, J. Goglio, and T. G. Walker, Am. J. Phys. **80**, 1017 (2012).

[41] See Supplemental Material at http://link.aps.org/supplemental/10.1103/PhysRevMaterials.7.073402 for supplemental text on ZIF-8 adsorption sites; supplemental figures on different adsorption sites in sodalite cage of ZIF-8; crystallographic adsorption sites; temperature ramp study of the methyl tunneling of empty ZIF-8 under high vacuum; calculated rotational energy barrier of a methyl top in ZIF-8 with filling of Ar or N_2; and supplemental tables of the calculated rotational energies of the methyl rotor in empty ZIF-8 and with sequential filling of Ar or N_2. The Supplemental Material also contains Ref. [23].

[42] Q. Li, A. J. Zaczek, T. M. Korter, J. A. Zeitler, and M. T. Ruggiero, Chem. Commun. **54**, 5776 (2018).

Paper X

Water motifs in zirconium metal-organic frameworks induced by nanoconfinement and hydrophilic adsorption sites

A. Lamaire, J. Wieme, S. Vandenhaute, R. Goeminne, S.M.J. Rogge, V. Van Speybroeck

Manuscript in revision

A. Lamaire performed the research and wrote the manuscript with contributions from all authors.

Water motifs in zirconium metal-organic frameworks induced by nanoconfinement and hydrophilic adsorption sites

Aran Lamaire, Jelle Wieme, Sander Vandenhaute, Ruben Goeminne, Sven M. J. Rogge, and Veronique Van Speybroeck*

Center for Molecular Modeling (CMM), Ghent University, Technologiepark-Zwijnaarde 46, 9052 Zwijnaarde, Belgium

E-mail: Veronique.VanSpeybroeck@UGent.be

Abstract

The intricate hydrogen bond network of water gives rise to various structures with anomalous properties at different thermodynamic conditions. Nanoconfinement can further modify the water structure and properties, and induce specific water motifs, which are instrumental for technological applications such as atmospheric water harvesting. However, so far, a causal relationship between nanoconfinement and the presence of specific hydrophilic adsorption sites is lacking, hampering the further design of nanostructured materials for water templating. Therefore, this work investigates the organisation of water in zirconium-based metal-organic frameworks (MOFs) with varying topologies, pore sizes, and chemical composition, to extract design rules to shape water. The highly tuneable pores and hydrophilicity of MOFs makes them ideally suited for this purpose. We find that small nanopores favour orderly water clusters that nucleate at hydrophilic adsorption sites. Favourably positioning the secondary

adsorption sites, hydrogen-bonded to the primary adsorption sites, allows larger clusters to form at moderate adsorption conditions. To disentangle the importance of nanoconfinement and hydrophilic nucleation sites in this process, we introduce an analytical model with precise control of the adsorption sites. This sheds a new light on design parameters to induce specific water clusters and hydrogen-bonded networks, thus rationalising the application space of water in nanoconfinement.

Introduction

Liquid water is well-known for its anomalous behaviour in comparison with other liquids, including a density maximum at 4 °C – resulting in the famous expansion upon freezing – and a high surface tension.[1] These anomalies are linked with the unusual structure of water, which is determined by an intricate network of hydrogen bonds.[2,3] At lower temperatures, the hydrogen bond networks manifest most orderly in ice crystals[4] or in clathrate hydrates, which are ice-like cage structures that encapsulate clean energy vectors such as methane or hydrogen[5,6]. When confining water molecules to nanosized pores or channels, the hydrogen bond network can be heavily disrupted, thereby significantly altering the physical properties of nanoconfined water compared to bulk water. A reduced dielectric constant can for instance persist in water layers up to 100 nm before recovering bulk behaviour.[7] A thorough understanding of the different factors that influence the nanoconfined water's intricate hydrogen bond network is critical to exploit these unusual properties towards practical applications such as water harvesting[8–10] or shock absorbers[11]. Herein, we further contribute to such understanding by systematically investigating the origins of different hydrogen bond motifs in structurally nanoconfined water.

Carbon nanotubes (CNTs) were one of the first materials investigated in the context of water confinement. Depending on the nanotube diameter and thermodynamic conditions, water molecules in CNTs were reported to form one-dimensional hydrogen bonded chains along the hydrophobic nanotubes[12,13], as well as shell-chain structures with a cylindrical

square-ice shell surrounding the water chain[14], or structured stackings of n-membered water rings[15,16]. The one-dimensional cylindrical confinement of water thus induces the formation of ice-like phases which are unstable in a bulk phase and possess altered properties such as an enhanced diffusion rate. In the case of two-dimensional water confinement, for instance between two graphene sheets, transmission electron microscopy (TEM) measurements showed the existence of a square ice phase, which deviates from the tetrahedral hydrogen bond coordination of bulk ice.[17] For the specific case of a monolayer of nanoconfined water, Kapil *et al.*[18] demonstrated that the phase diagram also contains other stable polymorphs of ice, such as hexagonal, pentagonal, and hexatic ice.

Over the past few years, water confined in three-dimensional nanostructures has systematically gained more attention in view of several applications. To exploit the extraordinary properties of three-dimensionally confined water, metal-organic frameworks (MOFs) are ideal host materials, thanks to their highly tunable nature.[19–21] Their modular composition of metal nodes and organic linkers gives rise to a wide variation in water-confining environments, so that they can be tailored for various applications. Just as in the case of one- and two-dimensional confinement of water, also three-dimensionally confined water in the pores of MOFs behaves differently from bulk water. In flexible MOFs, such as MIL-53(Ga), water adsorption can induce new phases besides the narrow- and large-pore phases known for the empty framework.[22] Furthermore, the confinement of water in MOFs is also known to slow down the water reorientation dynamics and affect the hydrogen bond network, along with the related tetrahedral order.[22,23]

The most notable opportunities three-dimensional water confinement in MOFs offers are atmospheric water harvesting[8–10], water purification[24–26], shock absorption[11], and adsorbent-based heat-pumps and chillers with water as a green working fluid[27–29]. Some frameworks with a hydrophobic character, such as the zeolitic imidazolate framework ZIF-8, possess the ability to function as shock absorbers due to their resistance to water intrusion. In ZIF-8, the spontaneous intrusion of water requires the formation of water clusters with a critical

number of molecules to start filling one of the nanopores. If the strain rate of the water intrusion exceeds the intrinsic rate for the nucleation of critical-sized water clusters, the high-rate mechanical impact is attenuated as a consequence of the energy dissipated in the forced intrusion process.[11]

In many MOFs, however, both hydrophilic and hydrophobic sites are present, which determine the specific adsorption behaviour of the material. The aromatic linkers are typically hydrophobic, while open metal sites and μ-OH groups are hydrophilic and act as nucleation sites in the formation of water clusters.[30,31] This initial step in the water adsorption process was labelled the seeding stage by Hanikel *et al.*[32] in the analysis of water adsorption in MOF-303, a MOF that is exceptionally well suited for atmospheric water harvesting. After the seeding stage, water adsorption in MOF-303 continues through a clustering and networking stage, during which the first adsorbed water molecules grow into clusters and eventually unite into an extended hydrogen-bonded water network. This adsorption mechanism occurs in many MOFs (*e.g.*, CAU-10-H[31], MOF-801[27,33,34], MIL-101[35], Co_2Cl_2BTDD[23]), as well as in the purely covalently bonded equivalent of MOFs, known as covalent organic frameworks (COFs)[36].

During the seeding stage, the hydrophilic sites in the framework play a decisive role, which can be easily demonstrated by the addition or removal of such sites. When pyrazole is substituted by less hydrophilic furan[32] or thiophene[37] in MOF-303, the primary water adsorption sites of the framework are altered, which diminishes the water uptake at low relative humidities. Similarly, the incorporation of hydrophilic linker functionalities for UiO-66 enhances the water uptake at low pressures, whereas incorporating hydrophobic linker functionalities has the opposite effect.[38,39]

In this work, we present a systematic investigation of how the meticulous tuning of nanoconfinement, hydrophobic, and hydrophilic sites may induce the formation of particular water clusters. To this end, a series of zirconium MOFs with different topologies but similar building units is considered, including UiO-66, UiO-67, UiO-68, MOF-801, MOF-808, MOF-

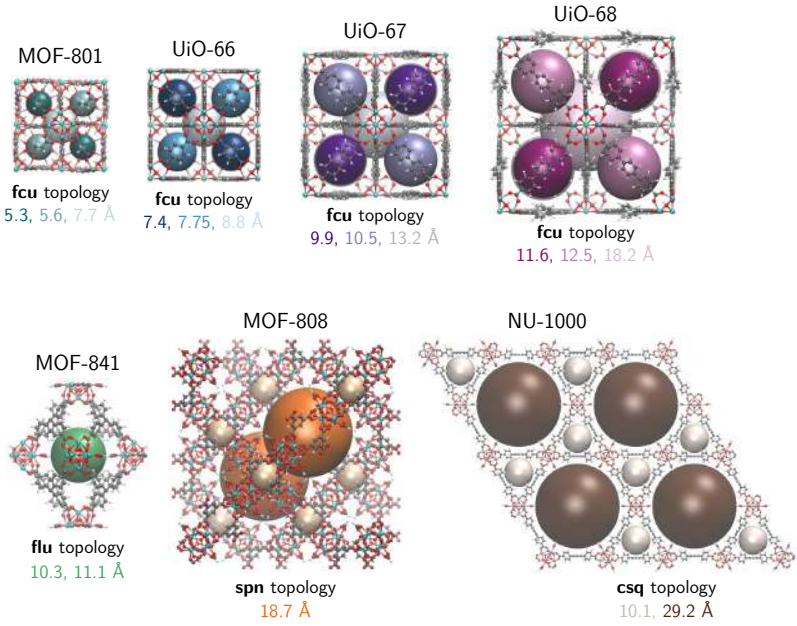

Figure 1: Overview of the structures of the zirconium MOFs investigated in this work. The pores of each framework are indicated with coloured spheres and the corresponding pore diameters are listed below the figure. Note that the structure of NU-1000 is rescaled with a factor of 0.65 compared to the other structures.

841, and NU-1000, as shown in Figure 1. This specific choice of materials allows to evaluate the influence of varying pore sizes (see Figure 1 and Table S1) and degrees of hydrophilicity on the water organisation in highly similar frameworks. MOF-801, UiO-66, UiO-67, and UiO-68 share for instance the same topology and metal nodes, which are connected by linkers of different length, leading to various degrees of confinement. The selected systems can thus be seen as model systems for highly tunable nanostructures, which enable a systematic investigation of the features affecting the organisation of nanoconfined water.

Using different structural identifiers, water confined in the smaller MOFs is shown to deviate substantially from bulk water, as the structural organisation of water is strongly templated by the host framework. To disentangle the role of confinement and the impor-

tance of hydrophilic and hydrophobic regions within the framework, an analytical model is constructed to rationalise the observed behaviour in the MOFs. This model provides a more fundamental insight into the strong interplay between primary and secondary adsorption sites in MOF-801 and UiO-66, which can significantly influence the clustering and networking stages during water adsorption and thus shape the water adsorption isotherms. This understanding can be used to further guide the design of tunable nanostructures for applications that involve water confinement.

Results

For each of the zirconium MOFs in Figure 1 different water loadings are investigated, with a maximal loading determined from grand canonical Monte Carlo (GCMC) simulations at 1 bar and 300 K. As explained in more detail in the Methods section, path integral molecular dynamics (PIMD) simulations are performed to determine the structural properties of the confined water. The computationally more expensive path integral formalism is used as water molecules are prone to nuclear quantum effects (NQEs), which can significantly affect the description of hydrogen bonds.[40] When introducing water molecules in the nanoporous frameworks, each MOF exhibits a cell volume contraction (see Figure S2). Initially, this contraction increases with the number of water molecules until a relative volume reduction of about 2 % is reached. When more guests are added to the framework, the material starts to expand again and can exceed the unit cell volume of the empty framework.

To capture the structural organisation of a network of water molecules, one can consider the number of hydrogen bonds in which each molecule participates. In Figure 2 and Figure S3 of the Supporting Information the probability of different hydrogen bond connectivities is shown for the different frameworks with various water loadings alongside the reference distribution of bulk water. For bulk liquid water, every molecule tends to partake on average in 2.7 hydrogen bonds, as configurations with 2 to 4 hydrogen bonds are most likely.

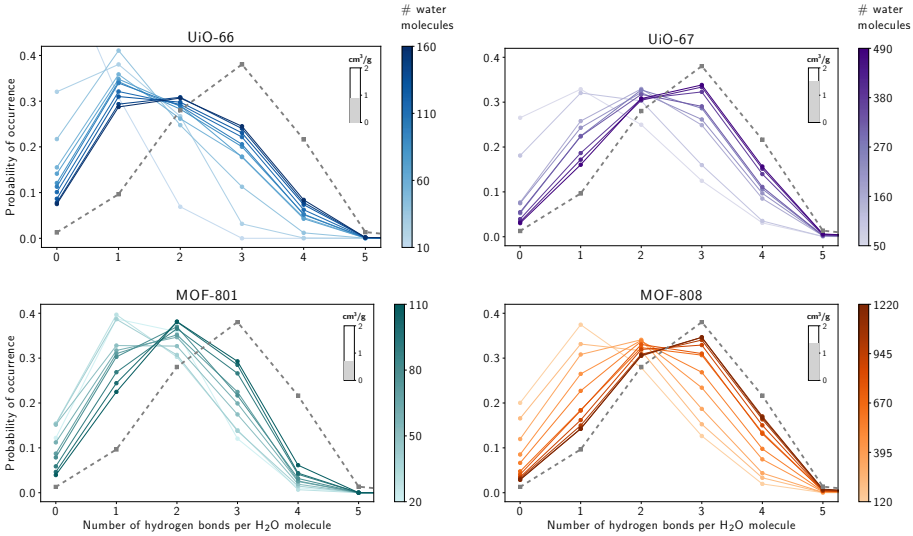

Figure 2: Probability distribution of the number of hydrogen bonds per water molecule for confinement in different MOFs. For each framework, a gradient colour scale is used to indicate the water loading in the unit cell. The hydrogen bond distribution of bulk water is indicated with a grey dashed line. The specific volume of each framework is indicated in the upper right corner of every pane.

For confined water, the hydrogen bond network can be heavily disrupted by the confining framework depending on the size of the pores. When few water molecules are present, the hydrogen bond distribution is skewed towards 0 or 1, as only a limited number of hydrogen bonds can be formed. For higher water loadings, the influence of the framework becomes apparent for smaller frameworks such as UiO-66, MOF-801, and MOF-841, as their hydrogen bond distribution does not converge to the one of bulk water. The materials with larger nanopores, such as UiO-67, UiO-68, MOF-808, and NU-1000, do show hydrogen bond distributions similar to liquid water.

Structural information beyond the first solvation shell around every water molecule can be obtained from radial distribution functions (RDFs) of the oxygen atoms (see Figure 3 and Figure S4). The first peak of the RDF represents neighbouring water molecules and

thus provides similar information as the hydrogen bond distributions. In comparison with ordinary liquid water, this peak is mainly modulated in intensity, whereas its shape and position are only minorly different. The first minimum, on the contrary, does show an appreciable shift for the smaller UiO-66 and MOF-801 frameworks of respectively 0.2 Å and 0.4 Å towards larger interatomic distances. As MOF-801 has the smallest pores, the structural perturbation is clearly most pronounced for this framework, yielding a broader and flatter minimum. This perturbation also pervades the second solvation shell represented by the second RDF peak, which becomes sharper than in bulk water and is shifted to larger distances by 0.4–0.5 Å. For frameworks containing larger pores, such as UiO-67 and MOF-808, the RDF is observed to closely approach the bulk equivalent for larger water loadings, with only small shifts in the peak positions of about 0.15 Å.

The origin of the deviating structural organisation of water in the MOF's nanopores can be traced back to the formation of clusters that nucleate at hydrophilic sites. Particular contributions of the clusters to the RDFs of UiO-66 and MOF-801 are shown in the insets of Figure 3 and in Figure S5. To visualise the preferential adsorption sites and the structures that emerge from it, the water density in the MOFs is shown for different slabs in Figure 4a and Figures S6–S9. A schematic representation of the MOFs with an fcu topology is also depicted in Figure 4a, with the tetrahedral pores indicated in green and pink, whereas the octahedral pore of the framework is filled with an orange sphere. Two types of tetrahedral pores are present, with respectively μ-OH groups (green pores, labelled T1) or μ-O groups (pink pores, labelled T2) on the cornering metal clusters. For MOF-801, distinct geometrical water patterns can be discerned, which closely reflect the framework's structure. In the tetrahedral T1 pores, the cornering μ-OH groups serve as anchor points for the formation of a cubic structure that was also resolved experimentally by Furukawa *et al.* through X-ray diffraction.[33] Starting from the adsorbed water molecules at the four μ-OH groups within the pore (site 1 in Figure 4a), the cube is completed by additional water molecules that hydrogen bond to these anchor points (site 2 in Figure 4a). Furthermore, these additional

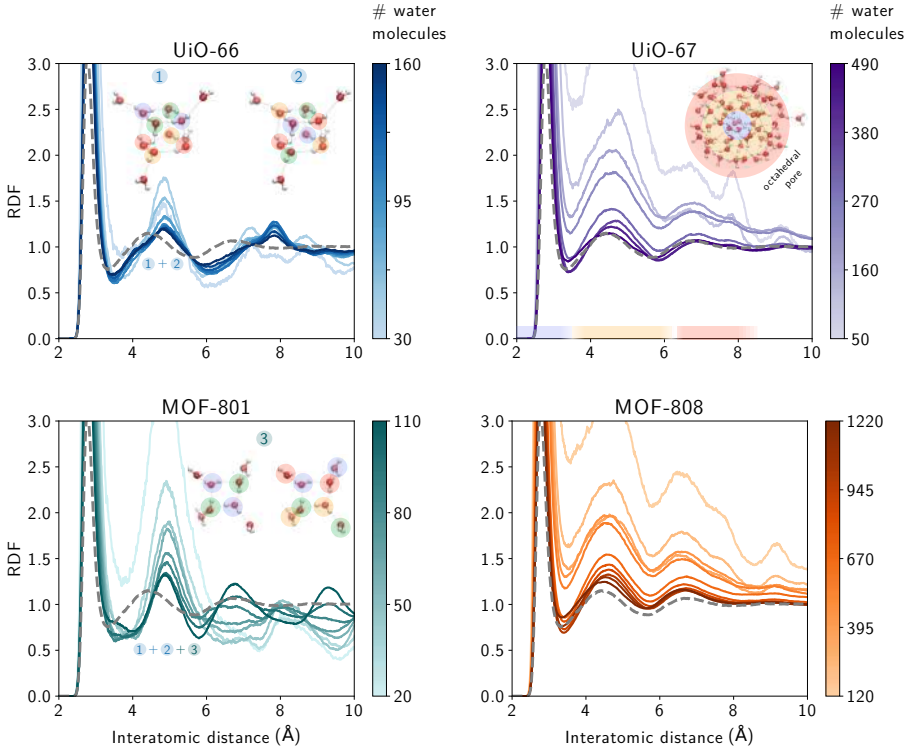

Figure 3: Radial distribution functions (RDFs) between the oxygen atoms of the water molecules in different MOFs. For each framework, a gradient colour scale is used to indicate the water loading in the unit cell. The O–O RDF of bulk water is indicated with a grey dashed line. The insets for UiO-66 and MOF-801 (labelled 1–3) show the contributions of representative O–O pairs to the second peak of the RDF. The inset for UiO-67 shows the bulk-like shell structure in the octahedral pore.

water molecules, in their turn, can engage in a hydrogen bond that connects the tetrahedral pore with the neighbouring octahedral pore (site 3 in Figure 4a). At lower water loadings, the tetrahedral pore of MOF-801 can also accommodate a square cluster instead of a cubic cluster, as shown in Figure S7.

When increasing the pore size by going from MOF-801 to UiO-66, thus increasing the diameter of the tetrahedral pore by about 2 Å (by changing the fumerate linkers by benzenedicarboxylate linkers), two different density profiles appear within the T1- and T2-type tetrahedral pores (in Figure 4a). The T1-type pore still accommodates cubic water clusters that nucleate at the μ-OH groups located in the corners of the pore. The T2-type pore, on the contrary, has μ-O instead of μ-OH groups in its corners, which displaces the primary adsorption sites. In the T2-type pores, the primary adsorption sites are located closer to the corners (site 4 in Figure 4a), which misaligns the nucleation points for a pore-filling cubic water cluster. The absence of an optimal water cluster to fill the pore results in more freedom for the hydrogen bonds formed with the adsorption sites, which is reflected in the reduced and dispersed density surrounding these sites. For MOF-801, by contrast, the smaller size of the tetrahedral pores allows to also stabilise the cubic water cluster in the T2-type pore, as the adsorption sites are located closer to the centre of the pore and thus provide the required hydrogen bonds to complete the cube (just as in the T1-type pore). Note that a distinction in adsorption sites between the tetrahedral pores was also experimentally observed by Furukawa *et al.*[33], but the difference in adsorption sites was not resolved atomically with respect to the patterns induced by the specific terminations of the metal nodes.

To rationalise the adsorption behaviour in a confined environment such as MOF-801 or UiO-66, an analytical potential was used to separate the effects of geometrical confinement from the presence of hydrophilic adsorption sites. To this end, a repulsive cubic box with different side lengths was used, which contains either no adsorption sites, tetrahedrally arranged adsorption sites, or cubically arranged adsorption sites (see Figures 4b, Section S10, and the Methods Section). In the absence of hydrophilic sites (Figure S15), a collection of

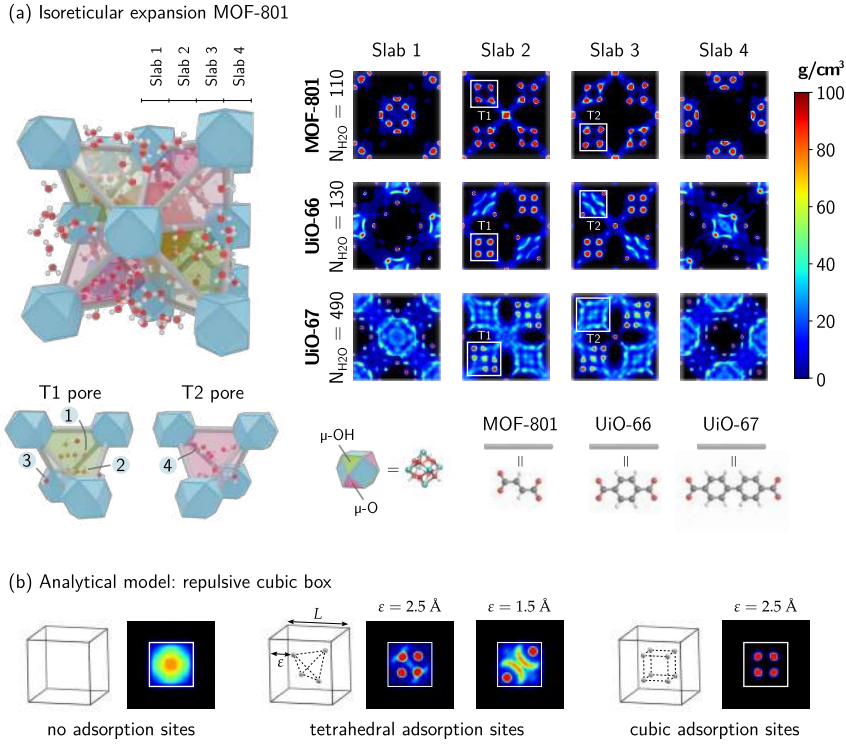

Figure 4: Density plots of water molecules confined in (a) different MOFs and (b) a repulsive cubic box (see Methods section). Pane (a) also contains a schematic representation of a water-filled MOF, with examples of the water clusters present in the T1 and T2 pore. The different adsorption sites are labelled as follows: (1) adsorbed at a μ-OH group of the metal node, (2) hydrogen bonded to sites 1, (3) connecting tetrahedral and octahedral pores, and (4) adsorbed at a μ-O group of the metal node (see also Figure S10). Densities lower than 0.001 g/cm^3 are attributed the colour black. The densities of the MOFs are symmetrized using the space group of the framework (see Supporting Information S8), so that only four slabs of one half of the framework are shown. The densities of the repulsive cubic boxes are symmetrised using the P$\bar{4}$3m space group, so that only the density in the top half of the box is shown. The box has a side $L = 8$ Å and adsorption sites with a strength of $K = 20$ kJ/mol. Results for different box parameters are reported in Section S10 of the Supporting Information.

eight water molecules only takes on a cubic shape for very small box lengths (smaller than 6 Å). As the water molecules are located closely near the edges of the box, attempting to escape the box, it is rather unlikely that this number of water molecules would be present in a realistic pore. In the presence of tetrahedrally arranged hydrophilic sites, the adsorption patterns observed in UiO-66 can be reproduced with an appropriate placement of the adsorption sites (Figures S16–S23). For box lengths varying from 6 to 10 Å, a cubic water cluster is formed when the tetrahedral adsorption sites outline a cube with a side of about 3 Å. In this case, the corners of the cube which do not contain an adsorption site are located at a hydrogen bond distance from the tetrahedral adsorption sites, thus favouring the formation of a cubic water cluster. If the adsorption sites are further apart and define a cube with a side of about 4 Å, the tetrahedral arrangement of the T2-type pores in UiO-66 is retrieved. When the tetrahedrally arranged hydrophilic sites are replaced by a cubical arrangement, the cubic water clusters can be stabilised at lower adsorption energies and over a wider range of distances (*i.e.*, a cube with a side of about 3–4 Å). This analytical model therefore not only demonstrates the importance of hydrophilic sites in the formation of water clusters, but also a possible design principle in which a set of primary adsorption sites outlines a larger cluster with secondary adsorption sites located at hydrogen bond distances from the primary sites. By exploiting this principle, it is also possible to construct larger clusters as shown in Figures S25–S26.

The interplay between primary and secondary adsorption sites also strongly influences the water adsorption behaviour. In the context of atmospheric water harvesting, the ideal adsorption behaviour is characterised by a step-shaped isotherm with a steep uptake at a relative pressure between 0.1 and 0.3, to allow for an easy adsorption at low pressures while retaining moderate regeneration conditions.[8,41] In Figure 5, water adsorption isotherms are shown for a virtual cubic pore with a side of 6 Å and tetrahedrally arranged adsorption sites at different positions. With the aid of secondary adsorption sites, the desired adsorption behaviour for atmospheric water harvesting can be retrieved for primary adsorption sites

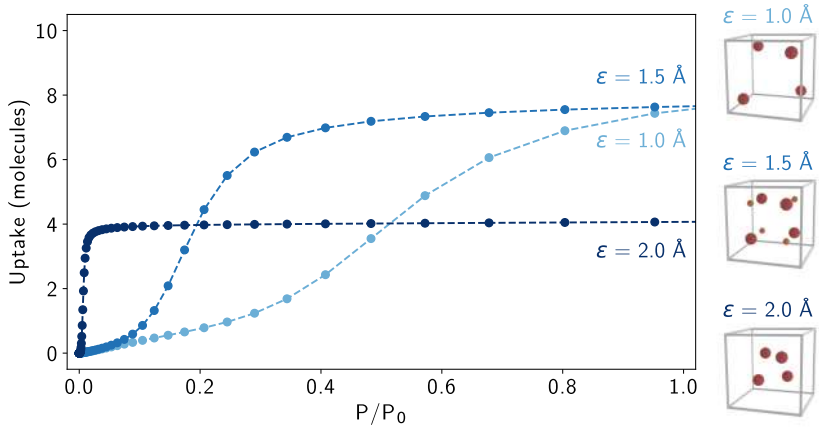

Figure 5: Water adsorption isotherms for water molecules confined in a repulsive cubic box with a side length of 6 Å and tetrahedrally arranged adsorption sites. The position of the adsorption sites is varied with the parameter ε. The four primary adsorption sites have a strength of 35 kJ/mol and are indicated in red. The secondary adsorption sites only occur for $\varepsilon = 1.5$ Å and are indicated in orange.

with a moderate strength of 35 kJ/mol. In the absence of secondary adsorption sites, a larger spacing between the adsorption sites is observed to flatten the isotherm, whereas a closer spacing of the sites shifts the isotherm to lower relative pressures. Both mechanisms significantly reduce the working capacity of the virtual pore. A more elaborate discussion of the influence of different parameters on the adsorption isotherms, including the adsorption strength, is given in Section S10.2 of the Supporting Information.

A further increase of the pore size by going from UiO-66 to UiO-67 yields a more attenuated image of the water density (Figure 4a). The μ-OH groups in the T1-type pores remain preferential adsorption sites that can branch out cubically, thus preserving a specific order within the additional spatial freedom of the larger pore. A unique cubic cluster as in the T1-type pores of UiO-66 is however no longer present. In the T2-type pores, the spatial freedom further thins the water density, although the adsorption sites near the corners of the pore are still clearly visible. For UiO-68, the trend associated with increasing pore sizes continues, with a more diluted density in the pores that remains pierced by the adsorption

sites (Figure S6). Alternatively, the pore size of UiO-66 can also be increased by introducing defects in the framework. By removing one or two linkers in the model of UiO-66, along with the protons on the connected zirconium bricks for charge balance, some primary adsorption sites change from μ-OH to μ-O, so that together with the increase in pore size the preferential secondary adsorption sites disappear (Figure S9). A specific organisation of water in clusters is therefore only to be expected for MOFs with appropriately tuned pore sizes and favourably located hydrophilic sites, which are key features in the design and performance of atmospheric MOF water harvesters.

Similarly to MOF-801 and UiO-66, other framework-induced water motifs can be observed in zirconium MOFs with a different topology. In the tetrahedral MOF-841 crystal, the μ-O and μ-OH adsorption sites are again surrounded by a second layer of adsorbed water molecules, but are no longer enclosed in a cubical pore (Figure S6). In MOF-808, the μ-O(H) adsorption sites are located both in the smaller tetrahedral pores and in the large adamantane cages, which yields a layer of water molecules that envelops the framework. In the larger pores, just as for UiO-68, the spatial freedom of the molecules dilutes the density. Also in NU-1000 (Figure S8), a specific clustered water organisation is absent in the large pores, but in the space confined between the linkers, ring-like structures can be discerned.

As illustrated by this selection of zirconium MOFs, structured water clusters can be formed within MOFs in the presence of hydrophilic adsorption sites. If the confining pore is sufficiently small, it fully templates the hydrogen-bonded network of water molecules it contains. Another example of this behaviour is for instance given by the one-dimensional water wires that are present in the narrow-pore phase of MIL-53.[42,43] However, when the volume of the framework increases and the material transitions to the large-pore phase, the larger pores can adsorb more water molecules and a more disordered water network replaces the water wires. Also in Co_2Cl_2BTDD water wires are formed, which nucleate at the open metal sites of the framework and instigate the subsequent pore filling process.[23] In PCP-1, an ordered stacking of two-dimensional square water structures was revealed with single-

crystal X-ray diffraction,[44] which demonstrates once more the possibility to form ice-like ordered structures at room temperature. In CAU-10-H, a water cluster is built around a double pentamer, which cannot be hosted in CAU-10-CH_3 due to the presence of the methyl groups.[31]

Additional information about the substructure of the hydrogen bonded network can be obtained by means of a graph search for specific structures. More particularly, one can scan the network for square, pentagonal, and hexagonal ring structures, which are the constituents of clathrate hydrates or ice.[4,5] In bulk water, the pentagonal and hexagonal rings are more prevalent than the square ones, as shown in Figures S14–S16. In confinement, the pore size and shape determine the relative occurrence of the different ring structures. The small tetrahedral pores in UiO-66 and MOF-801 result in a larger amount of square rings, which makes them equally or more prevalent than the larger pentagonal and hexagonal rings. When the pore size of the framework increases, the bulk-like behaviour re-emerges for high water loadings and the pentagonal and hexagonal rings are again most numerously present.

Discussion

Using a diverse set of zirconium MOFs, with similar building units but varying topologies and pore sizes, the organisation of water in different nanoconfining environments was systematically investigated to unravel to which extent water can be templated by the host framework. Only for large pores, the bulk-like behaviour of water can be retrieved. In the smaller pores, the network of water molecules – and the resulting properties – are shaped by the pore that hosts them. To form orderly water clusters in a pore, hydrophilic adsorption sites play a pivotal role, as demonstrated by the analytical model that was devised in this work. Besides the importance of hydrophilic sites in the nucleation of water clusters, they may also induce secondary adsorption sites through hydrogen bonding, which allows for the construction of larger orderly water clusters with a limited number of hydrophilic sites. The

cubic water cluster observed in the tetrahedral pores of MOF-801 and UiO-66 is an example of such an interplay of primary and secondary adsorption sites, as rationalised by the analytical model. Given the decisive role of water clusters in the adsorption behaviour of nanoporous materials, secondary adsorption sites can assist in shaping the water adsorption isotherms by improving the adsorption capacity of the material while maintaining modest desorption energies, as required for instance in atmospheric water harvesting.

Methods

Force fields

For each MOF considered in this work, a flexible force field was derived from first-principles data using the `QuickFF` protocol.[45] By relying on the equilibrium structure and the Hessian of isolated clusters distilled from the framework, the potential energy surface of the framework can be cast into an analytical representation. The first-principles calculations of the clusters were performed with `Gaussian 16`[46], using a B3LYP level of theory[47], a LanL2DZ basis set and effective core potential for the zirconium atoms[48], and a 6-311g(d,p) basis set[49] for the hydrogen, carbon, and oxygen atoms. The framework charges were obtained from MBIS partitioning[50] of the electron density calculated with `GPAW`[51], whereas the van der Waals interactions were described with Dreiding Lennard-Jones parameters[52]. For the water molecules, the q-TIP4P/f force field was used to avoid a double counting of the nuclear quantum effects (NQEs) when using path integral molecular dynamics (PIMD).[53] More details regarding the energy expression of the force fields are provided in Section S2.1 of the Supporting Information.

For MOF-801, the force field simulations were also compared with PIMD simulations performed with a machine learning potential (MLP), to assess the robustness of the results. In the MLP, the atomic interactions are represented by a neural network with a MACE[54] architecture that is trained on PBE-D3(BJ)[55,56] energies and forces of configurations generated

with the `Psiflow`[57] methodology, as detailed in Section S2.2 of the Supporting Information. Both descriptions of water in MOF-801 are observed to yield similar results, as demonstrated in Section S8 of the Supporting Information.

PIMD simulations

To generate initial configurations with different water loadings for each MOF, grand canonical Monte Carlo (GCMC) simulations at 300 K and 1 bar were performed with RASPA[58], using equal translation, rotation, and insertion probabilities. Subsequently, the GCMC snapshots were used as initial configurations for path integral molecular dynamics (PIMD) simulations performed with `i-PI`[59]. PIMD was used instead of regular MD as nuclear quantum effects (NQEs) can play an important role in the description of water.[40] A brief outline of PIMD is provided in Section S3 of the Supporting Information. The temperature of the PIMD simulations was set to 300 K and controlled by a Langevin thermostat[60] with a time constant of 100 fs. The pressure was set to 1 bar and controlled by a Raiteri-Gale-Bussi barostat[61] with a timeconstant of 1 ps. For every atom 32 beads were used to evaluate the short-range interactions, whereas the long-range interactions were evaluated on a contracted ring-polymer of 8 beads. The force evaluation in `i-PI` was delegated to `Yaff`[62] in combination with `LAMMPS`[63] to speed up the calculation of the non-covalent interactions. Every simulation was run with a time step of 0.25 fs and has a total simulation time of 250 ps. The reference simulation for bulk water used a box with 216 water molecules with a density of 997 kg/m^3. This simulation was run for 200 ps with a constant volume.

Analytical model

As a toy model, three artificial confining environments were considered (see Figure 4). A first environment consists of a repulsive cubic box in which water molecules can move freely

and are restrained by repulsive walls modelled by the following potential:

$$\begin{aligned} V(x,y,z) = &\frac{\kappa}{2}(x-x_0)^2\,\mathcal{H}(x-x_0) + \frac{\kappa}{2}(y-y_0)^2\,\mathcal{H}(y-y_0) + \\ &\frac{\kappa}{2}(z-z_0)^2\,\mathcal{H}(z-z_0) + \frac{\kappa}{2}(x+x_0)^2\,(1-\mathcal{H}(x+x_0)) + \\ &\frac{\kappa}{2}(y+y_0)^2\,(1-\mathcal{H}(y+y_0)) + \frac{\kappa}{2}(z+z_0)^2\,(1-\mathcal{H}(z+z_0)), \end{aligned} \tag{1}$$

with $\mathcal{H}$ the Heaviside function, κ the strength of the repulsive walls, and $2\,\|\mathbf{r}_0\|$ the length of a side of the repulsive cube. For all simulations, a κ value of 100 kJ/(mol Å^2) was used. The second and third confining environment closely mimic the tetrahedral pores of UiO-66 by introducing local adsorption sites in the above mentioned repulsive cubic box with the following analytical potential:

$$V(x,y,z) = -K\sum_i \cos\left(\frac{\pi}{w}\,\|\mathbf{r}-\mathbf{r}_{0,i}\|\right)\;\mathcal{H}\left(-\|\mathbf{r}-\mathbf{r}_{0,i}\| + \frac{w}{2}\right), \tag{2}$$

with K, w, and $\mathbf{r}_{0,i}$ respectively the strength, width, and position of the adsorption sites. Both a tetrahedral and a cubic arrangement of the adsorption sites were considered, as illustrated in Figure 4, with $\mathbf{r}_{0,i} = \left[\pm\left(\frac{L}{2}-\varepsilon\right), \pm\left(\frac{L}{2}-\varepsilon\right), \pm\left(\frac{L}{2}-\varepsilon\right)\right]$ and L the box edge length. The width w of the adsorption sites was set to 3 Å.

To construct water adsorption isotherms for the analytical models with adsorption sites, the transition matrix Monte Carlo methodology (TMMC) was used.[64] After an initial canonical Monte Carlo equilibration of 10^5 steps at 300 K, a classical MD simulation of 500 ps is performed with a virtual Widom insertion and deletion after every MD step. By performing these simulations for different water loadings, the water adsorption isotherm can be determined. A more elaborate discussion of the water adsorption isotherms for the analytical models, using both the q-TIP4P/f force field and the MBX water model[65], can be found in Section S10 of the Supporting Information.

Acknowledgement

This work was supported by the Research Foundation – Flanders (FWO, grant nos. 11D2220N (A.L.), 12T3522N (S.M.J.R.), and 11H6821N (S.V.)), Flanders Industry Innovation Moonshot (ARCLATH II, No. HBC.2021.0254 and MOONRISE, No. HBC.2020.2612), and the Research Board of Ghent University (BOF). The main computational resources (Stevin Supercomputer Infrastructure) and services used in this work were provided by the VSC (Flemish Supercomputer Center), funded by Ghent University, FWO, and the Flemish Government – department EWI. A part of the simulations were performed on the Luxembourg national supercomputer MeluXina. The authors gratefully acknowledge the Lux-Provide teams for their expert support. We also acknowledge the EuroHPC Joint Undertaking for awarding this project access to the EuroHPC supercomputer LUMI, hosted by CSC (Finland) and the LUMI consortium through a EuroHPC Regular Access call. Finally, we would also like to thank Venkat Kapil and Ben Clifford for their help with `Psiflow` implementations regarding `i-PI` and `Parsl`, respectively.

Author contributions

A.L., S.M.J.R., J.W., and V.V.S. designed the research. A.L. performed all the simulations and analysed the results, which were discussed among all authors. Under the supervision of V.V.S., the methodology was developed by A.L., J.W., S.M.J.R, S.V., and R.G. J.W. derived the MOF force fields. S.V. trained the MLP of MOF-801. R.G. provided the required expertise to calculate the water adsorption isotherms using TMMC simulations. A.L. wrote the manuscript with contributions from all authors.

Data availability

The structure and force field input files are available from the online GitHub repository at `https://github.com/AranLamaire/Supporting_Information`. Any additional data is available from the authors upon request.

Code availability

`YAFF` (https://github.com/molmod/yaff), `i-PI` (https://github.com/i-pi/i-pi), `Psiflow` (https://github.com/molmod/psiflow), `MACE` (https://github.com/acesuit/mace), and `CP2K` (https://github.com/cp2k/cp2k) are open source codes which are freely available at the provided links.

References

(1) Pettersson, L. G. M.; Henchman, R. H.; Nilsson, A. Water – The Most Anomalous Liquid. *Chemical Reviews* **2016**, *116*, 7459–7462.

(2) Breynaert, E.; Houlleberghs, M.; Radhakrishnan, S.; Grübel, G.; Taulelle, F.; Martens, J. A. Water as a tuneable solvent: a perspective. *Chem. Soc. Rev.* **2020**, *49*, 2557–2569.

(3) Seki, T.; Chiang, K.-Y.; Yu, C.-C.; Yu, X.; Okuno, M.; Hunger, J.; Nagata, Y.; Bonn, M. The Bending Mode of Water: A Powerful Probe for Hydrogen Bond Structure of Aqueous Systems. *J. Phys. Chem. Lett.* **2020**, *11*, 8459–8469.

(4) Cui, B.; Xu, P.; Li, X.; Fan, K.; Guo, X.; Tong, L. Low-Dimensional and Confined Ice. *Annual Review of Materials Research* **2023**, *53*, 371–397.

(5) Gupta, A.; Baron, G. V.; Perreault, P.; Lenaerts, S.; Ciocarlan, R.-G.; Cool, P.; Mileo, P. G.; Rogge, S.; Van Speybroeck, V.; Watson, G.; Van Der Voort, P.; Houlle-

berghs, M.; Breynaert, E.; Martens, J.; Denayer, J. F. Hydrogen Clathrates: Next Generation Hydrogen Storage Materials. *Energy Storage Materials* **2021**, *41*, 69–107.

(6) Wang, P.; Teng, Y.; Zhu, J.; Bao, W.; Han, S.; Li, Y.; Zhao, Y.; Xie, H. Review on the synergistic effect between metal–organic frameworks and gas hydrates for CH_4 storage and CO_2 separation applications. *Renewable and Sustainable Energy Reviews* **2022**, *167*, 112807.

(7) Fumagalli, L.; Esfandiar, A.; Fabregas, R.; Hu, S.; Ares, P.; Janardanan, A.; Yang, Q.; Radha, B.; Taniguchi, T.; Watanabe, K.; Gomila, G.; Novoselov, K. S.; Geim, A. K. Anomalously low dielectric constant of confined water. *Science* **2018**, *360*, 1339–1342.

(8) Hanikel, N.; Prévot, M. S.; Yaghi, O. M. MOF water harvesters. *Nat. Nanotechnol.* **2020**, *15*, 348–355.

(9) Yilmaz, G.; Meng, F. L.; Lu, W.; Abed, J.; Peh, C. K. N.; Gao, M.; Sargent, E. H.; Ho, G. W. Autonomous atmospheric water seeping MOF matrix. *Sci. Adv.* **2020**, *6*, eabc8605.

(10) Almassad, H. A.; Abaza, R. I.; Siwwan, L.; Al-Maythalony, B.; Cordova, K. E. Environmentally adaptive MOF-based device enables continuous self-optimizing atmospheric water harvesting. *Nat. Commun.* **2022**, *13*, 4873.

(11) Sun, Y.; Rogge, S. M. J.; Lamaire, A.; Vandenbrande, S.; Wieme, J.; Siviour, C. R.; Van Speybroeck, V.; Tan, J.-C. High-rate nanofluidic energy absorption in porous zeolitic frameworks. *Nat. Mater.* **2021**, *20*, 1015–1023.

(12) Hummer, G.; Rasaiah, J. C.; Noworyta, J. P. Water conduction through the hydrophobic channel of a carbon nanotube. *Nature* **2001**, *414*, 188–190.

(13) Wang, D.; Tian, Y.; Jiang, L. Abnormal Properties of Low-Dimensional Confined Water. *Small* **2021**, *17*, 2100788.

(14) Kolesnikov, A. I.; Zanotti, J.-M.; Loong, C.-K.; Thiyagarajan, P.; Moravsky, A. P.; Loutfy, R. O.; Burnham, C. J. Anomalously Soft Dynamics of Water in a Nanotube: A Revelation of Nanoscale Confinement. *Phys. Rev. Lett.* **2004**, *93*, 035503.

(15) Koga, K.; Gao, G. T.; Tanaka, H.; Zeng, X. C. Formation of ordered ice nanotubes inside carbon nanotubes. *Nature* **2001**, *412*, 802–805.

(16) Takaiwa, D.; Hatano, I.; Koga, K.; Tanaka, H. Phase diagram of water in carbon nanotubes. *Proc. Natl. Acad. Sci.* **2008**, *105*, 39–43.

(17) Algara-Siller, G.; Lehtinen, O.; Wang, F. C.; Nair, R. R.; Kaiser, U.; Wu, H. A.; Geim, A. K.; Grigorieva, I. V. Square ice in graphene nanocapillaries. *Nature* **2015**, *519*, 443–445.

(18) Kapil, V.; Schran, C.; Zen, A.; Chen, J.; Pickard, C. J.; Michaelides, A. The first-principles phase diagram of monolayer nanoconfined water. *Nature* **2022**,

(19) Freund, R. et al. 25 Years of Reticular Chemistry. *Angewandte Chemie International Edition* **2021**, *60*, 23946–23974.

(20) Mouchaham, G.; Cui, F. S.; Nouar, F.; Pimenta, V.; Chang, J.-S.; Serre, C. Metal-Organic Frameworks and Water: 'From Old Enemies to Friends'? *Trends in Chemistry* **2020**, *2*, 990–1003.

(21) Zhang, B.; Zhu, Z.; Wang, X.; Liu, X.; Kapteijn, F. Water Adsorption in MOFs: Structures and Applications. *Adv. Func. Mater.* **2024**, *n/a*, 2304788.

(22) Coudert, F.-X. Water Adsorption in Soft and Heterogeneous Nanopores. *Acc. Chem. Res.* **2020**, *53*, 1342–1350.

(23) Rieth, A. J.; Hunter, K. M.; Dincă, M.; Paesani, F. Hydrogen bonding structure of confined water templated by a metal-organic framework with open metal sites. *Nat. Commun.* **2019**, *10*, 4771.

(24) Drout, R. J.; Robison, L.; Chen, Z.; Islamoglu, T.; Farha, O. K. Zirconium Metal-Organic Frameworks for Organic Pollutant Adsorption. *Trends in Chemistry* **2019**, *1*, 304–317.

(25) Rojas, S.; Horcajada, P. Metal–Organic Frameworks for the Removal of Emerging Organic Contaminants in Water. *Chem. Rev.* **2020**, *120*, 8378–8415.

(26) Jun, B.-M.; Al-Hamadani, Y. A.; Son, A.; Park, C. M.; Jang, M.; Jang, A.; Kim, N. C.; Yoon, Y. Applications of metal-organic framework based membranes in water purification: A review. *Separation and Purification Technology* **2020**, *247*, 116947.

(27) Canivet, J.; Fateeva, A.; Guo, Y.; Coasne, B.; Farrusseng, D. Water adsorption in MOFs: fundamentals and applications. *Chem. Soc. Rev.* **2014**, *43*, 5594–5617.

(28) Wang, S.; Lee, J. S.; Wahiduzzaman, M.; Park, J.; Muschi, M.; Martineau-Corcos, C.; Tissot, A.; Cho, K. H.; Marrot, J.; Shepard, W.; Maurin, G.; Chang, J.-S.; Serre, C. A robust large-pore zirconium carboxylate metal–organic framework for energy-efficient water-sorption-driven refrigeration. *Nat. Energy* **2018**, *3*, 985–993.

(29) Lenzen, D.; Zhao, J.; Ernst, S.-J.; Wahiduzzaman, M.; Ken Inge, A.; Fröhlich, D.; Xu, H.; Bart, H.-J.; Janiak, C.; Henninger, S.; Maurin, G.; Zou, X.; Stock, N. A metal–organic framework for efficient water-based ultra-low-temperature-driven cooling. *Nat. Commun.* **2019**, *10*, 3025.

(30) Liu, X.; Wang, X.; Kapteijn, F. Water and Metal-Organic Frameworks: From Interaction toward Utilization. *Chem. Rev.* **2020**, *120*, 8303–8377.

(31) van der Veen, M. A.; Canossa, S.; Wahiduzzaman, M.; Nenert, G.; Frohlich, D.; Rega, D.; Reinsch, H.; Shupletsov, L.; Markey, K.; De Vos, D. E.; Bonn, M.; Stock, N.; Maurin, G.; Backus, E. H. G. Confined Water Cluster Formation in Water Harvesting by Metal-Organic Frameworks: CAU-10-H versus CAU-10-CH_3. *Adv. Mater.* **2024**, *36*, 2210050.

(32) Hanikel, N.; Pei, X.; Chheda, S.; Lyu, H.; Jeong, W.; Sauer, J.; Gagliardi, L.; Yaghi, O. M. Evolution of water structures in metal-organic frameworks for improved atmospheric water harvesting. *Science* **2021**, *374*, 454–459.

(33) Furukawa, H.; Gándara, F.; Zhang, Y.-B.; Jiang, J.; Queen, W. L.; Hudson, M. R.; Yaghi, O. M. Water Adsorption in Porous Metal-Organic Frameworks and Related Materials. *J. Am. Chem. Soc.* **2014**, *136*, 4369–4381.

(34) Fuchs, A.; Knechtel, F.; Wang, H.; Ji, Z.; Wuttke, S.; Yaghi, O. M.; Ploetz, E. Water Harvesting at the Single-Crystal Level. *J. Am. Chem. Soc.* **2023**, *145*, 14324–14334.

(35) Yanagita, K.; Hwang, J.; Shamim, J. A.; Hsu, W.-L.; Matsuda, R.; Endo, A.; Delaunay, J.-J.; Daiguji, H. Kinetics of Water Vapor Adsorption and Desorption in MIL-101 Metal-Organic Frameworks. *Journal of Physical Chemistry C* **2019**, *123*, 387–398.

(36) Tan, K. T.; Tao, S.; Huang, N.; Jiang, D. Water cluster in hydrophobic crystalline porous covalent organic frameworks. *Nat. Commun.* **2021**, *12*, 6747.

(37) Zheng, Z.; Hanikel, N.; Lyu, H.; Yaghi, O. M. Broadly Tunable Atmospheric Water Harvesting in Multivariate Metal–Organic Frameworks. *Journal of the American Chemical Society* **2022**, *144*, 22669–22675.

(38) Lu, F.-F.; Gu, X.-W.; Wu, E.; Li, B.; Qian, G. Systematic evaluation of water adsorption in isoreticular UiO-type metal-organic frameworks. *J. Mater. Chem. A* **2023**, *11*, 1246–1255.

(39) Zhang, J.; Paesani, F.; Lessio, M. Computational insights into the interaction of water with the UiO-66 metal–organic framework and its functionalized derivatives. *J. Mater. Chem. C* **2023**, *11*, 10247–10258.

(40) Ceriotti, M.; Fang, W.; Kusalik, P. G.; McKenzie, R. H.; Michaelides, A.; Morales, M. A.; Markland, T. E. Nuclear Quantum Effects in Water and Aqueous

Systems: Experiment, Theory, and Current Challenges. *Chem. Rev.* **2016**, *116*, 7529–7550.

(41) Kalmutzki, M. J.; Diercks, C. S.; Yaghi, O. M. Metal-Organic Frameworks for Water Harvesting from Air. *Adv. Mater.* **2018**, *30*, 1704304.

(42) Paesani, F. Water in metal-organic frameworks: structure and diffusion of H_2O in MIL-53(Cr) from quantum simulations. *Mol. Simul.* **2012**, *38*, 631–641.

(43) Lamaire, A.; Wieme, J.; Hoffman, A. E. J.; Van Speybroeck, V. Atomistic insight in the flexibility and heat transport properties of the stimuli-responsive metal–organic framework MIL-53(Al) for water-adsorption applications using molecular simulations. *Faraday Discuss.* **2021**, *225*, 301–323.

(44) Ichii, T.; Arikawa, T.; Omoto, K.; Hosono, N.; Sato, H.; Kitagawa, S.; Tanaka, K. Observation of an exotic state of water in the hydrophilic nanospace of porous coordination polymers. *Commun. Chem.* **2020**, *3*, 16.

(45) Vanduyfhuys, L.; Vandenbrande, S.; Wieme, J.; Waroquier, M.; Verstraelen, T.; Van Speybroeck, V. Extension of the QuickFF force field protocol for an improved accuracy of structural, vibrational, mechanical and thermal properties of metal-organic frameworks. *J. Comput. Chem.* **2018**, *39*, 999–1011.

(46) Frisch, M. J. et al. Gaussian 16 Revision C.01. 2016; Gaussian Inc. Wallingford CT.

(47) Becke, A. D. Density-functional exchange-energy approximation with correct asymptotic behavior. *Phys. Rev. A* **1988**, *38*, 3098–3100.

(48) Hay, P. J.; Wadt, W. R. Ab initio effective core potentials for molecular calculations. Potentials for the transition metal atoms Sc to Hg. *Journal of Chemical Physics* **1985**, *82*, 270–283.

(49) Krishnan, R.; Binkley, J. S.; Seeger, R.; Pople, J. A. Self-consistent molecular orbital methods. XX. A basis set for correlated wave functions. *J. Chem. Phys.* **1980**, *72*, 650–654.

(50) Verstraelen, T.; Vandenbrande, S.; Heidar-Zadeh, F.; Vanduyfhuys, L.; Van Speybroeck, V.; Waroquier, M.; Ayers, P. W. Minimal Basis Iterative Stockholder: Atoms in Molecules for Force-Field Development. *J. Chem. Theory Comput.* **2016**, *12*, 3894–3912.

(51) Enkovaara, J. et al. Electronic structure calculations with GPAW: a real-space implementation of the projector augmented-wave method. *J. Phys. Condens. Matter* **2010**, *22*, 253202.

(52) Mayo, S. L.; Olafson, B. D.; Goddard, W. A. DREIDING: a generic force field for molecular simulations. *J. Phys. Chem.* **1990**, *94*, 8897–8909.

(53) Habershon, S.; Markland, T. E.; Manolopoulos, D. E. Competing quantum effects in the dynamics of a flexible water model. *J. Chem. Phys.* **2009**, *131*, 024501.

(54) Batatia, I.; Kovacs, D. P.; Simm, G.; Ortner, C.; Csanyi, G. MACE: Higher Order Equivariant Message Passing Neural Networks for Fast and Accurate Force Fields. Advances in Neural Information Processing Systems. 2022; pp 11423–11436.

(55) Perdew, J. P.; Burke, K.; Ernzerhof, M. Generalized Gradient Approximation Made Simple. *Phys. Rev. Lett.* **1996**, *77*, 3865–3868.

(56) Grimme, S.; Antony, J.; Ehrlich, S.; Krieg, H. A consistent and accurate ab initio parametrization of density functional dispersion correction (DFT-D) for the 94 elements H-Pu. *J. Chem. Phys.* **2010**, *132*, 154104.

(57) Vandenhaute, S.; Cools-Ceuppens, M.; DeKeyser, S.; Verstraelen, T.; Van Spey-

broeck, V. Machine learning potentials for metal-organic frameworks using an incremental learning approach. *npj Comput. Mater.* **2023**, *9*, 19.

(58) Dubbeldam, D.; Calero, S.; Ellis, D. E.; Snurr, R. Q. RASPA: molecular simulation software for adsorption and diffusion in flexible nanoporous materials. *Mol. Simulat.* **2016**, *42*, 81–101.

(59) Kapil, V. et al. i-PI 2.0: A universal force engine for advanced molecular simulations. *Comput. Phys. Commun.* **2018**, *236*, 214–223.

(60) Ceriotti, M.; Parrinello, M.; Markland, T. E.; Manolopoulos, D. E. Efficient stochastic thermostatting of path integral molecular dynamics. *J. Chem. Phys.* **2010**, *133*, 124104.

(61) Raiteri, P.; Gale, J. D.; Bussi, G. Reactive force field simulation of proton diffusion in $BaZrO_3$ using an empirical valence bond approach. *J. Phys. Condens. Matter* **2011**, *23*, 334213.

(62) Verstraelen, T.; Vanduyfhuys, L.; Vandenbrande, S. Yaff, yet another force field. https://github.com/molmod/yaff.

(63) Plimpton, S. Fast Parallel Algorithms for Short-Range Molecular Dynamics. *J. Comput. Phys.* **1995**, *117*, 1–19.

(64) Witman, M.; Mahynski, N. A.; Smit, B. Flat-Histogram Monte Carlo as an Efficient Tool To Evaluate Adsorption Processes Involving Rigid and Deformable Molecules. *J. Chem. Theory Comput.* **2018**, *14*, 6149–6158.

(65) Riera, M.; Knight, C.; Bull-Vulpe, E. F.; Zhu, X.; Agnew, H.; Smith, D. G. A.; Simmonett, A. C.; Paesani, F. MBX: A many-body energy and force calculator for data-driven many-body simulations. *J. Chem. Phys.* **2023**, *159*, 054802.

Supporting Information for

Water motifs in zirconium metal-organic frameworks induced by nanoconfinement and hydrophilic adsorption sites

Aran Lamaire, Jelle Wieme, Sander Vandenhaute, Ruben Goeminne,
Sven M. J. Rogge, and Veronique Van Speybroeck

Center for Molecular Modeling (CMM), Ghent University,
Technologiepark-Zwijnaarde 46, 9052 Zwijnaarde, Belgium

Contents

S1 MOF topologies

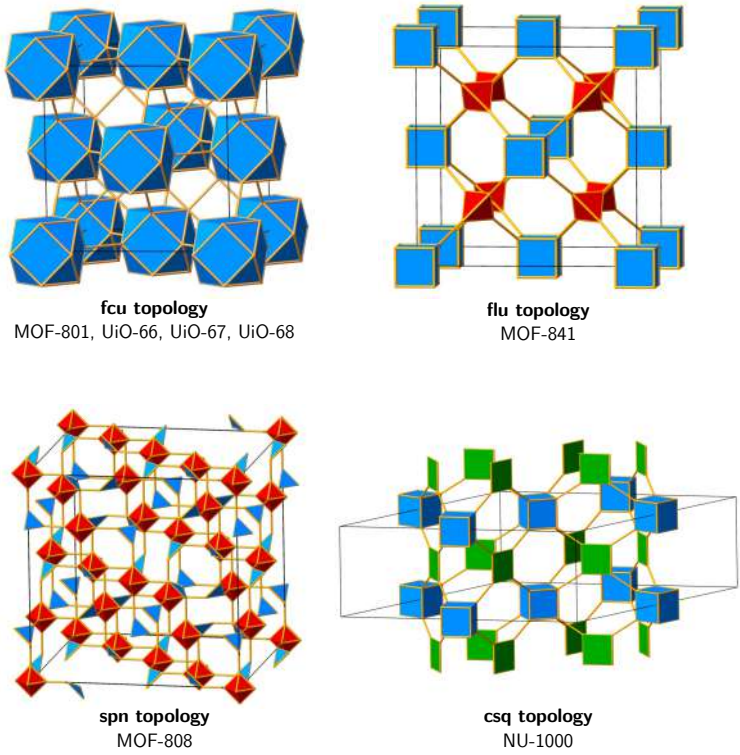

Figure S1: Schematic representation of the topologies of the zirconium MOFs considered in this work. Figures adopted from `https://crystalsymmetry.wordpress.com/nets/mof-nets/`.

S2 Description of the potential energy surface

S2.1 Force field parametrisation

For each metal-organic framework (MOF) considered within this work, the corresponding potential energy surface was described by a force field constructed according to the `QuickFF` protocol[1,2]. In this protocol, the *ab initio* equilibrium structure and the Hessian of isolated clusters of the structure at the B3LYP level of theory[3] are used to parametrise the covalent part of the force field

$$
\begin{aligned}
V_{cov}^{FF} &= V_{bond} + V_{bend} + V_{torsion} + V_{oopdist} + V_{cross} \qquad \text{(S2.1)}\\
&= V_{bond} + \sum_{\substack{i,j,k\\(i\neq j\neq k)}} \frac{K_{ijk}^{\theta}}{2}(\theta_{ijk}-\theta_{ijk,0})^2\Big[1-0.14\,(\theta_{ijk}-\theta_{ijk,0})+5.6\cdot 10^{-5}(\theta_{ijk}-\theta_{ijk,0})^2-7\cdot 10^{-7}(\theta_{ijk}-\theta_{ijk,0})^3\\
&\quad + 2.2\cdot 10^{-8}(\theta_i-\theta_{i,0})^4\Big] + \sum_i \frac{K_i^{\phi}}{2}[1-\cos(m_{\phi,i}(\phi_i-\phi_{i,0}))] + \sum_i \frac{K_i^{d}}{2}(d_i-d_{i,0})^2\\
&\quad + \sum_{\substack{i,j,k\\(i\neq j\neq k)}} K_{ijk}^{rr}(r_{ij}-r_{ij,0})(r_{jk}-r_{jk,0}) + \sum_{\substack{i,j,k\\(i\neq j\neq k)}} \Big[K_{ijk}^{rr\theta}(r_{ij}-r_{ij,0})+K_{ijk}^{rr\theta'}(r_{jk}-r_{jk,0})\Big](\theta_{ijk}-\theta_{ijk,0}),
\end{aligned}
$$

with V_{bond}, V_{bend}, $V_{torsion}$, $V_{oopdist}$, and V_{cross} the force field contributions of the bonds, bends, torsion angles, out-of-plane distances (oopdist), and cross terms respectively. Each contribution is parametrised by the appropriate internal coordinates, including the bond distances r_i, the bend angles θ_i (*vide infra*), the out-of-plane distances d_i, and the dihedral angles ϕ_i. The rest values of these internal coordinates are denoted by $r_{ij,0}$, $\theta_{ijk,0}$, $d_{i,0}$, and $\phi_{i,0}$. The multiplicity of the dihedral angles is denoted by $m_{\phi,i}$ and the force constants are labelled K_{ij}^{r}, K_{ijk}^{θ}, K_i^{d}, K_i^{ϕ}, K_{ijk}^{rr}, and $K_{ijk}^{rr\theta}$. All the bonds, except for the one characterising the μ_3–OH moieties, are parametrised by the following quartic potential

$$
V_{bond} = \sum_{\substack{i,j\\(i\neq j)}} \frac{K_{ij}^{r}}{2}(r_{ij}-r_{ij,0})^2\left[1-2.55\,(r_{ij}-r_{ij,0})+\frac{7}{12}(2.55\,(r_{ij}-r_{ij,0}))^2\right], \qquad \text{(S2.2)}
$$

whereas the μ_3–OH moieties are parametrised by a harmonic bond potential

$$
V_{bond} = \sum_{\substack{i,j\\(i\neq j)}} \frac{K_{ij}^{r}}{2}(r_{ij}-r_{ij,0})^2. \qquad \text{(S2.3)}
$$

The non-covalent part of the force field, containing the electrostatic and van der Waals interactions, is given by

$$
V_{noncov}^{FF} = \frac{1}{2}\sum_{\substack{i,j\\(i\neq j)}} \frac{q_i q_j}{4\pi\varepsilon_0 r_{ij}}\,\mathrm{erf}\left(\frac{r_{ij}}{d_{ij}}\right) + \sum_{\substack{i,j\\(i\neq j)}} 4\varepsilon_{ij}\left[\left(\frac{\sigma_{ij}}{r_{ij}}\right)^{12}-\left(\frac{\sigma_{ij}}{r_{ij}}\right)^{6}\right], \qquad \text{(S2.4)}
$$

with q_i the charge of atom i, r_{ij} the distance between atoms i and j, $d_{ij} = \sqrt{d_i^2+d_j^2}$ a mixed charge radius

derived from the individual Gaussian charge distribution radii d_i and d_j, erf the error function, ε_{ij} the well depth of the Lennard-Jones potential, and σ_{ij} the distance at which the Lennard-Jones potential equals zero. The parameters of the Gaussian charge distributions are derived using the Minimal Basis Iterative Stockholder (MBIS) method[4], whereas the Lennard-Jones parameters for the interaction between atoms i and j are determined from the Dreiding parameters tabulated in Ref. 5 by means of the Lorentz-Berthelot mixing rules: $\sigma_{ij} = \frac{\sigma_i+\sigma_j}{2}$ and $\varepsilon_{ij} = \sqrt{\varepsilon_i \varepsilon_j}$. As there are no Dreiding parameters for zirconium atoms, UFF Lennard-Jones parameters[6] were used for the zirconium atoms. In previous work of some of the authors, similar force field parametrisations were proven to be very successful in describing the behaviour of both pristine and defect UiO-type MOFs.[7]

The water molecules are described by the q-TIP4P/f water model of Habershon *et al.*[8], which was particularly devised for path integral molecular dynamics simulations (see Section S3) to avoid a possible double counting of the nuclear quantum effects when fitting to experimental data. The q-TIP4P/f model was derived from the well-known classical rigid TIP4P/2005 model of Abascal and Vega[9], which also contains four interaction sites including three charge centres and one Lennard-Jones centre. The Lennard-Jones centre coincides with the oxygen atom of the water molecule, whereas the charge centres consist of the hydrogen atoms supplemented by an additional charge site, the so-called M site, which is located on the bisector of the H–O–H angle:

$$\mathbf{r}_M = \gamma \mathbf{r}_O + (1-\gamma)\,\frac{\mathbf{r}_{H_1} + \mathbf{r}_{H_2}}{2}, \tag{S2.5}$$

with $\gamma = 0.73612$. By displacing the negative charge from the oxygen atom to the M site, a better mean-field description of the polarization of the water molecules can be obtained. The q-TIP4P/f water model has been proven to successfully reproduce many properties of water (including its density, radial distribution functions, melting point, diffusion coefficient, and infrared spectrum) and has therefore been used in many studies.[10–14]

S2.2 Machine learning potential for MOF-801 and *ab initio* modelling of UiO-66

To verify the results obtained with the force fields described in Section S2.1, *ab initio* molecular dynamics (MD) simulations were performed for MOF-801 and UiO-66 for a high water loading (110 and 130 water molecules, respectively). These *ab initio* calculations were performed with `CP2K`,[15] with the PBE functional with D3(BJ) dispersion corrections,[16–18] GTH pseudopotentials,[19] and TZV2P-MOLOPT basis sets in combination with a plane wave basis set with a cutoff energy of 1000 Ry (and a relative cutoff energy of 60 Ry).[20] For each framework, five MD simulations were run with different initial water configurations for 2.5 or 5 ps for MOF-801 and UiO-66, respectively.

To further examine the implications of an *ab initio* description of the interatomic interactions, using more advanced path integral MD simulations (PIMD) (see Section S3) for different water loadings, a machine learning potential (MLP) with a MACE architecture was trained for MOF-801.[21] To this end, a dataset of 11 341 structures was generated, which was randomly split into a training and validation set according to a 90:10 ratio. This dataset is archived on 10.5281/zenodo.12664241. An initial, pre-training dataset

was generated by means of classical MD simulations at 150 K, 300 K, and 600 K using MACE-MP-0.[22] For each temperature, 100 simulations of 20 ps were performed, with different initial seeds, from which configurations were extracted every 2.5 ps. All these configurations were subsequently evaluated with CP2K, using the same settings as the *ab initio* simulations discussed in the previous paragraph. Starting from this pre-training dataset, 300 PIMD simulations (with 32 beads) were propagated in parallel within an active learning scheme, using 100 simulations for each temperature (100 K, 300 K, and 600 K) and a variety of water loadings. Using `Psiflow 4` (pre-release),[23] four iterations were performed within the active learning scheme. Additional data for the MLP was obtained from PIMD simulations with a lower number of beads (*i.e.* 2, 4, 8, or 16) and different temperatures (including 600 K and 900 K). As PIMD induces larger interatomic forces on the beads than classical MD, which increases the risk of numerical instability, the active learning workflow was complemented by stochastic weight averaging (SWA) as it has been empirically shown that this can reduce overfitting and improve the generalisation performance.[24] Within the 300 epochs used for training, SWA was only employed during the last 200 epochs. The learning rate scheduler was set to reduce the learning rate if the validation loss did not decrease for 20 epochs. In the loss function, the energy weight equals 100 times the weight of the forces to obtain a sufficiently accurate description of the relative stability of various water geometries. A cutoff radius of 6.5 Å was used to ensure sufficient overlap between the atomic environments at low water loadings. The atomic features consist of 16 scalar features ($\ell = 0$) and 16 vector features ($\ell = 1$). The learning rate was set to 0.02 and the batch size to 8 as the MOF-801 structure contains many crystallographically equivalent atomic environments. The MACE model uses a correlation order of three and a default angular resolution $\ell_{\text{max}} = 3$. The resulting validation errors of the MLP for the energy and forces are 0.8 meV/atom and 40.3 meV/Å, respectively.

S3 Path integral MD

To include nuclear quantum effects (NQEs) such as zero-point energy or tunnelling in molecular dynamics (MD) simulations, one can make use of the (second order) path integral MD (PIMD) formalism, where the canonical density matrix $e^{-\beta\hat{H}}$ of an N-atom system is approximated by the following Trotter factorisation

$$e^{-\beta\hat{H}} \approx \left[e^{-\frac{\beta}{2P}\hat{V}} e^{-\frac{\beta}{P}\sum_{i=1}^{N}\frac{\hat{\mathbf{p}}_i^2}{2m_i}} e^{-\frac{\beta}{2P}\hat{V}}\right]^P, \tag{S3.1}$$

with $\beta = (k_B T)^{-1}$ the inverse temperature, $\mathbf{p}_i$ and $\mathbf{r}_i$ respectively the momentum and position of the i-th particle, and $V(\mathbf{r}_1, \ldots, \mathbf{r}_N)$ the potential energy surface. Within this approximation, the quantum mechanical canonical partition function $Z = \text{Tr}[e^{-\beta\hat{H}}]$ can be reduced to

$$Z_P = \prod_{k=1}^{P}\prod_{i=1}^{N}\int \mathrm{d}\mathbf{p}_i^{(k)} \int \mathrm{d}\mathbf{r}_i^{(k)} e^{-\beta H_P}, \tag{S3.2}$$

so that the Hamiltonian $\hat{H}$ of the N-atom system is replaced by the Hamiltonian $H_P = H_P^0 + V_P$ of an

extended molecular system, with

$$H_P^0 = \sum_{k=1}^{P} \sum_{i=1}^{N} \left[\frac{\mathbf{p}_i^{(k)^2}}{2m_i} + \frac{1}{2} m_i \omega_P^2 \left(\mathbf{r}_i^{(k+1)} - \mathbf{r}_i^{(k)} \right)^2 \right] \qquad \text{and} \qquad V_P = \frac{1}{P} \sum_{k=1}^{P} V(\mathbf{r}_1^{(k)}, \ldots, \mathbf{r}_N^{(k)}), \tag{S3.3}$$

with $\mathbf{r}_i^{(k)}$ and $\mathbf{p}_i^{(k)}$ respectively the position and momentum of the k-th bead of the i-th particle, P the number of beads, $\omega_P = \frac{\sqrt{P}}{\beta\hbar}$ the angular frequency of the harmonic nearest-neighbour interaction, and $\mathbf{r}_i^{(P+1)} = \mathbf{r}_i^{(1)}$. By introducing the effective Hamiltonian H_P, in which every atom of the system is replaced by a ring polymer of P atom replicas that interact harmonically with their nearest-neighbours, one can mimic NQEs in MD simulations. When the number of beads P tends to infinity, the classical ring polymer isomorphism yields quantum mechanically exact results.

S4 Pore diameters and unit cells

Table S1: Pore diameters of the different MOFs and their average GCMC loading of H_2O molecules (at 1 bar). The pore diameter distribution in `zeo++`[25] was calculated for the optimised MOF structures.

	Pore diameter exp. (Å)	**Pore diameter `zeo++` (Å)**	**GCMC loading unit cell**
UiO-66	7.4 and 8.4[26]	7.4, 7.75, and 8.8	153
UiO-67		9.9, 10.5, and 13.2	486
UiO-68		11.6, 12.5, and 18.2	1011
MOF-801	4.8, 5.6, and 7.4[26]	5.3, 5.6, and 7.7	
MOF-808	18.4[26]	18.7	1212
MOF-841	9.2[26]	10.3 and 11.1	151
NU-1000	31[27,28]	10.1 and 29.2	671

Table S2: Unit cell information of the different MOFs. The cell lengths and angles are averages obtained from PIMD simulations at the lowest water loading (*i.e.* 20 water molecules per unit cell for UiO-68 and MOF-808, and 10 water molecules per unit cell for the other frameworks).

	Number of atoms	**Mass (amu)**	**Cell lengths (Å)**	**Cell angles (degrees)**
UiO-66	456	6656.24	21.33, 21.33, 21.34	90.0, 90.0, 90.0
UiO-67	696	8482.55	27.54, 27.54, 27.54	90.0, 90.0, 90.0
UiO-68	936	10308.85	33.70, 33.72, 33.71	90.0, 90.0, 90.0
MOF-801	312	5454.83	18.34, 18.34, 18.33	90.0, 90.0, 90.0
MOF-808	1248	21819.34	36.30, 36.33, 36.33	90.0, 90.0, 89.9
MOF-841	280	3688.61	15.69, 15.72, 28.20	89.5, 90.3, 89.1
NU-1000	546	6650.17	40.51, 40.53, 16.80	90.0, 89.9, 120.0

S5 Volume dependence guest loading

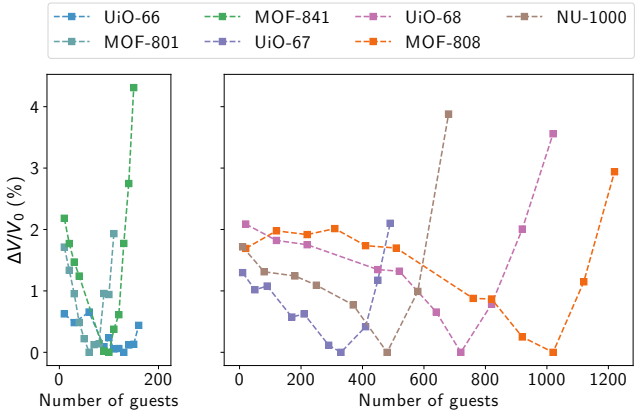

Figure S2: Relative change in the unit cell volume as a function of the number of adsorbed water molecules in different MOFs.

S6 Hydrogen bond distributions

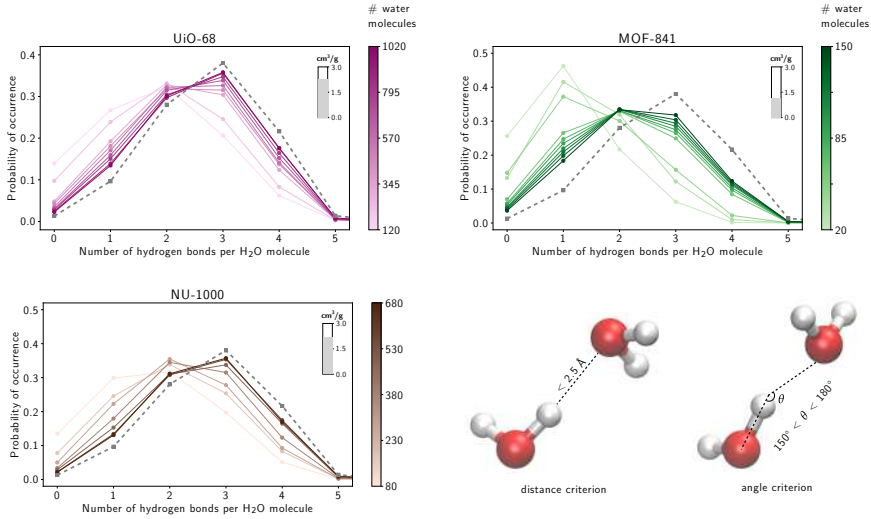

Figure S3: Probability distribution of the number of hydrogen bonds per water molecule for confinement in different MOFs. For each framework, a gradient colour scale is used to indicate the water loading in the unit cell. The hydrogen bond distribution of bulk water is indicated with a grey dashed line. The bottom right pane depicts the geometrical criteria used to define a hydrogen bond.

S7 Radial distribution functions

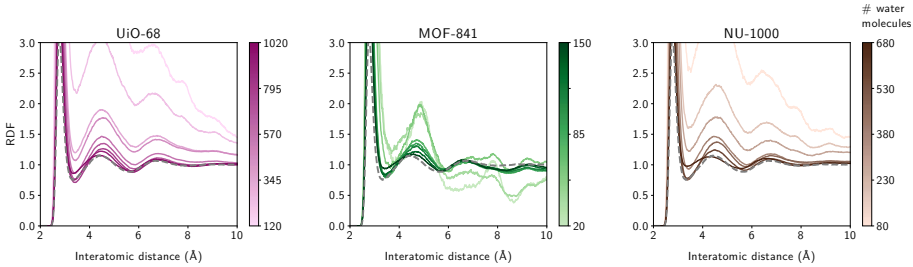

Figure S4: Radial distribution functions (RDFs) between the oxygen atoms of the water molecules in different MOFs. For each framework, a gradient colour scale is used to indicate the water loading in the unit cell. The O–O RDF of bulk water is indicated with a grey dashed line.

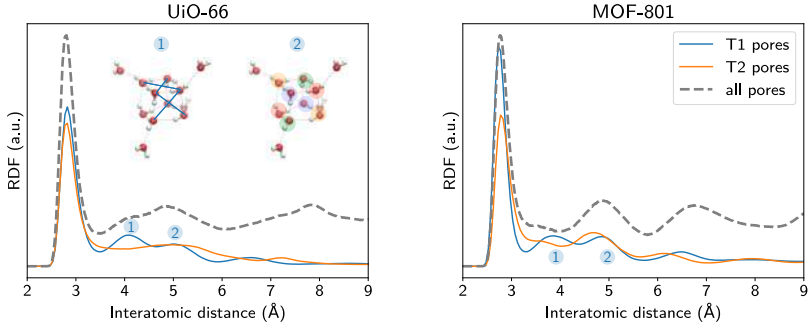

Figure S5: RDFs between the oxygen atoms of the water molecules in UiO-66 (loaded with 140 water molecules) and MOF-801 (loaded with 110 water molecules) and the isolated contributions of the molecules in the T1 pores (blue) or T2 pores (orange). For the clarity of visualisation, the RDF contributions of the T1 and T2 pores were rescaled. Representative O–O pairs contributing to the peaks labelled 1 and 2 for the T1 pores are visualised in the insets.

S8 Density

To construct the density plots in Figure 4 and Figure S6, the discretised water density in each material was symmetrised using the space group of the framework. More specifically, the symmetrised water density can be calculated by averaging over the three-dimensional matrices of the discretised water density that are obtained by applying the rotation and translation symmetry operations of the space group. In Figure S7, the unsymmetrised densities of MOF-801 are shown for different water loadings. For the highest water loading, the unsymmetrised density can be compared with the symmetrised density in Figure 4. The unsymmetrised densities of NU-1000 are shown in Figure S8.

In Figure S9, a density plot of pristine UiO-66 is compared with density plots of defective UiO-66, with one or two missing linkers. To model the defective UiO-66 structures, a proton on each of the zirconium bricks connected to the linker is also removed for charge balance. The tetrahedral pores of the framework that are merged by the linker defects do no longer give rise to the cubic water clusters of pristine UiO-66. This is a consequence of the additional spatial freedom of the water molecules in the pore (similarly to frameworks with larger pore sizes), in combination with the mutation of some μ-OH adsorption sites into μ-O sites.

In Figures S11 and S12, the water densities in MOF-801 and UiO-66 obtained from force field PIMD simulations are compared with *ab initio* MD simulations (for a high water loading). For MOF-801, both descriptions of the interatomic interactions give rise to a similar water density, with cubic water clusters in both tetrahedral pores. Around the zirconium bricks, small differences in the density are present due to small displacements of certain adsorption sites. In UiO-66, also the μ-O adsorption sites in the T2 pore exhibit a small displacement when comparing force field simulations to *ab initio* simulations. As a consequence, the preferential distance from a water molecule to a μ-O site slightly increases, so that the T2 pore of UiO-66 can now also accommodate cubic water clusters, although these are not as stable as in MOF-801, as indicated by the lower water density for the four secondary adsorption sites.

A further investigation of the water density in MOF-801 for different water loadings, using the MLP described in Section S2.2 to perform PIMD simulations with an *ab initio* accuracy, also demonstrates a good resemblance with the force field results. As shown in Figure S13, the water molecules at lower water loadings tend to adsorb first around the zirconium bricks of the framework and occupy the primary μ-OH adsorption sites in the T1 pores, just as in Figure S7.

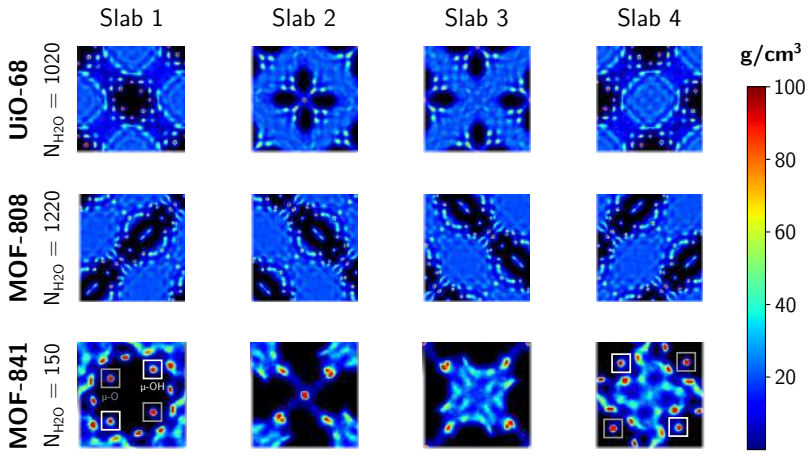

Figure S6: Density plots of water molecules confined in different MOFs. The densities are symmetrised using the space group of the framework, so that only four slabs along the *c*-axis are shown. For MOF-841, the primary adsorption sites at the μ-OH and μ-O sites of the metal nodes are indicated with respectively white or grey squares.

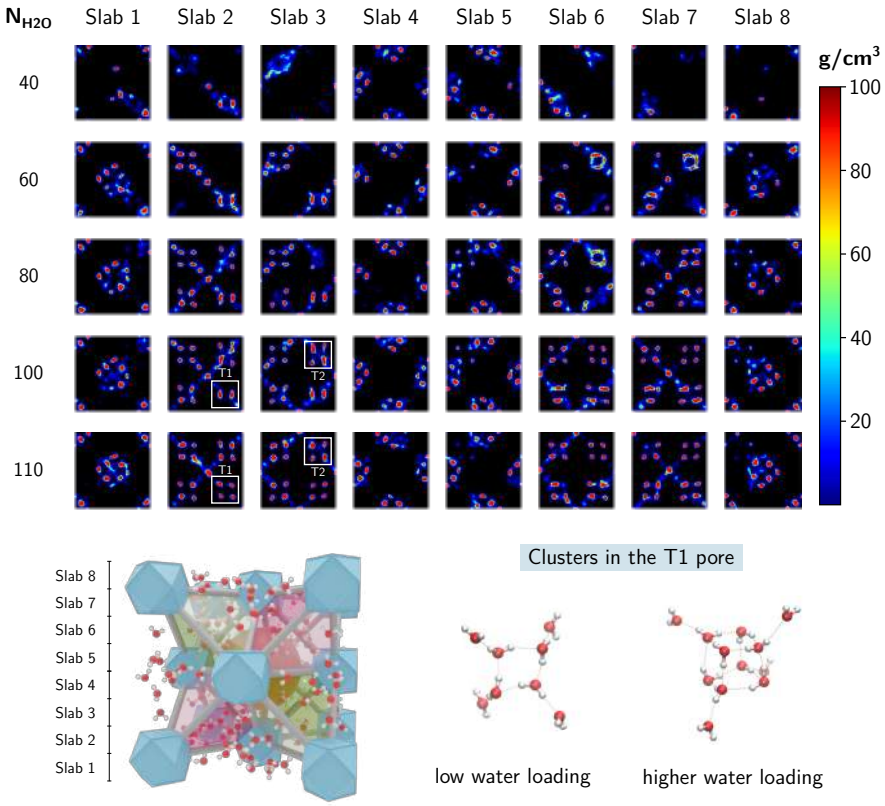

Figure S7: Density plots of water molecules confined in MOF-801 showing eight slabs along the *c*-axis. The slabs are indicated on a schematic representation of the framework on the bottom of the figure, alongside the two types of water clusters identified in the T1 tetrahedral pore at low and higher water loadings of the pore.

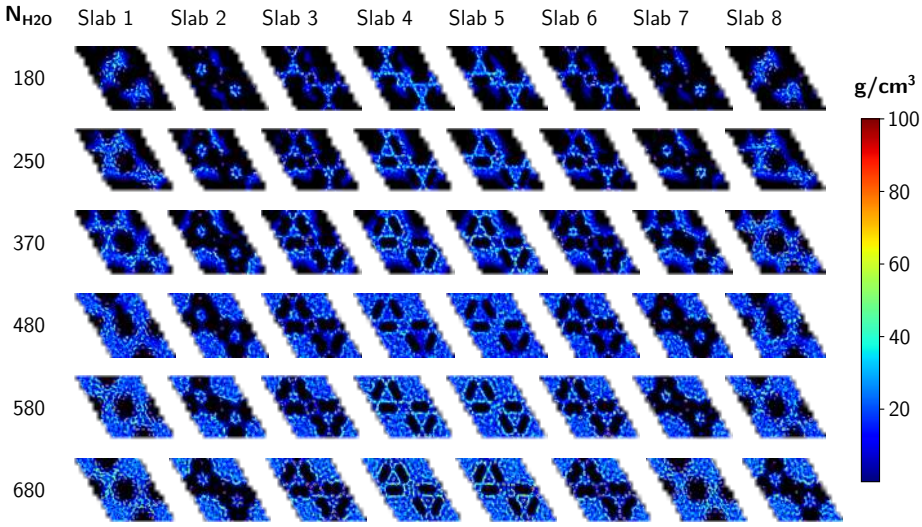

Figure S8: Density plots of water molecules confined in NU-1000 showing eight slabs along the c-axis.

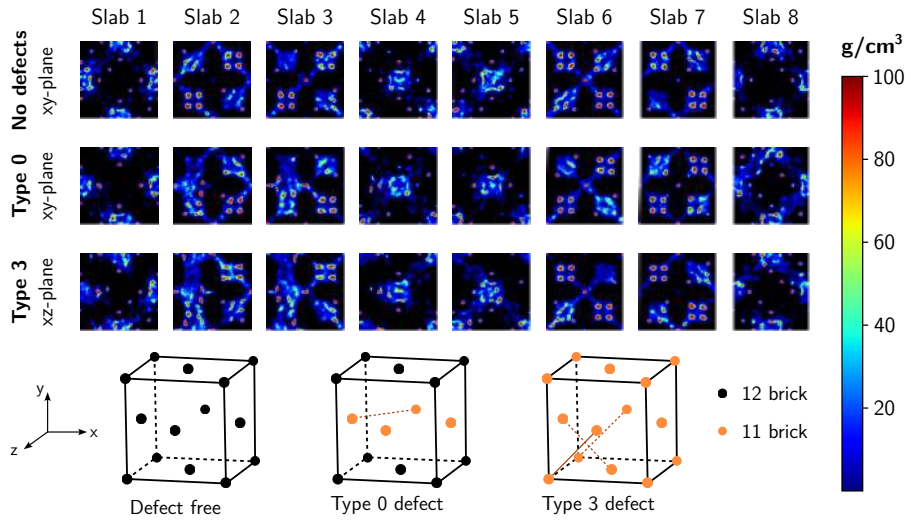

Figure S9: Density plots of 120 water molecules confined in UiO-66 without defects, one missing linker (type 0 defect), and two missing linkers (type 3 defect). For each framework eight slabs are shown along the y-axis or z-axis.

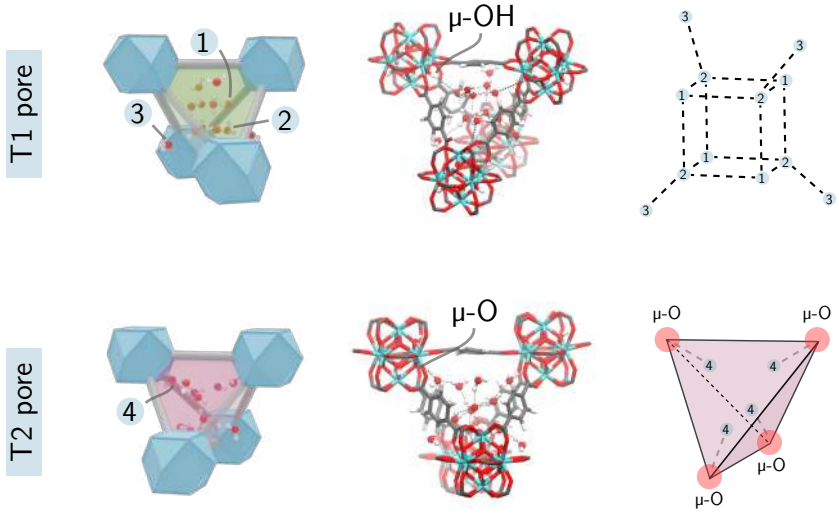

Figure S10: Adsorption sites in the T1 and T2 tetrahedral pores of pristine UiO-66. The different adsorption sites are labelled as follows: (1) adsorbed at a μ-OH group of the metal node, (2) hydrogen bonded to sites 1, (3) connecting tetrahedral and octahedral pores, and (4) adsorbed at a μ-O group of the metal node.

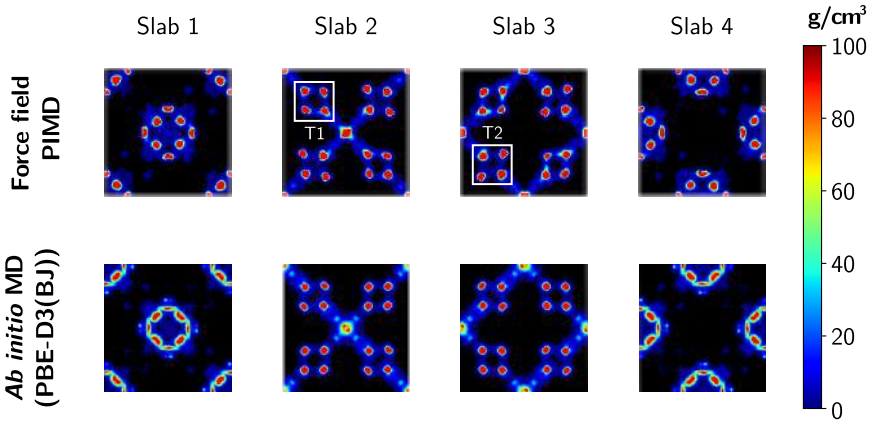

Figure S11: Density plots of 110 water molecules confined in MOF-801 obtained with force field PIMD simulations with 32 beads (see Section S2.1) or *ab initio* MD simulations at a PBE-D3(BJ) level of theory. The densities are symmetrised using the space group of the framework, so that only four slabs along the *c*-axis are shown.

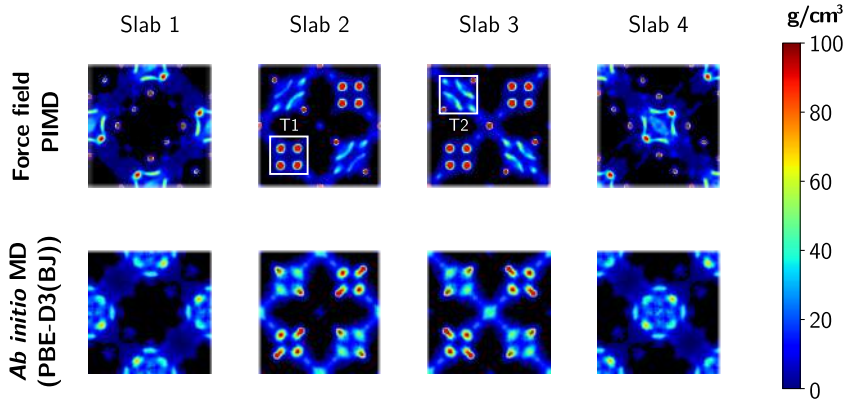

Figure S12: Density plots of 130 water molecules confined in UiO-66 obtained with force field PIMD simulations with 32 beads (see Section S2.1) or *ab initio* MD simulations at a PBE-D3(BJ) level of theory. The densities are symmetrised using the space group of the framework, so that only four slabs along the *c*-axis are shown.

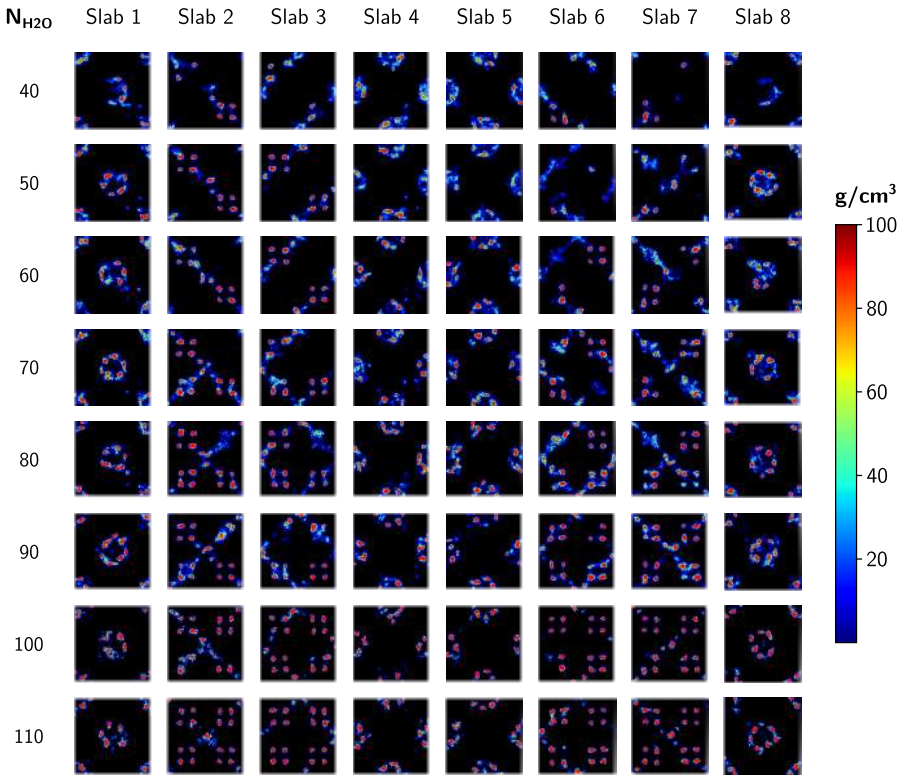

Figure S13: Density plots of water molecules confined in MOF-801 showing eight slabs along the *c*-axis as obtained from 16 bead PIMD simulations with a neural network MLP. The slabs are indicated on a schematic representation of the framework on the bottom of Figure S7.

S9 Cluster analysis

To identify water clusters in the MOFs, we first determine the hydrogen bonds between the adsorbed water molecules for every time step and every bead of the PIMD simulation (see Section S6). Subsequently, these hydrogen bonds are converted into the edges of a graph, from which we remove the bridges to isolate connected subgraphs. Finally, these subgraphs are screened for isomorphisms with the graphs of the different water clusters mentioned in Ref. 29 (which contain up to 10 water molecules). The `NetworkX`[30] Python package was used for all graph manipulations. The probability of finding square, pentagonal, or hexagonal water clusters in the different MOFs is shown in Figures S14–S16 for different water loadings.

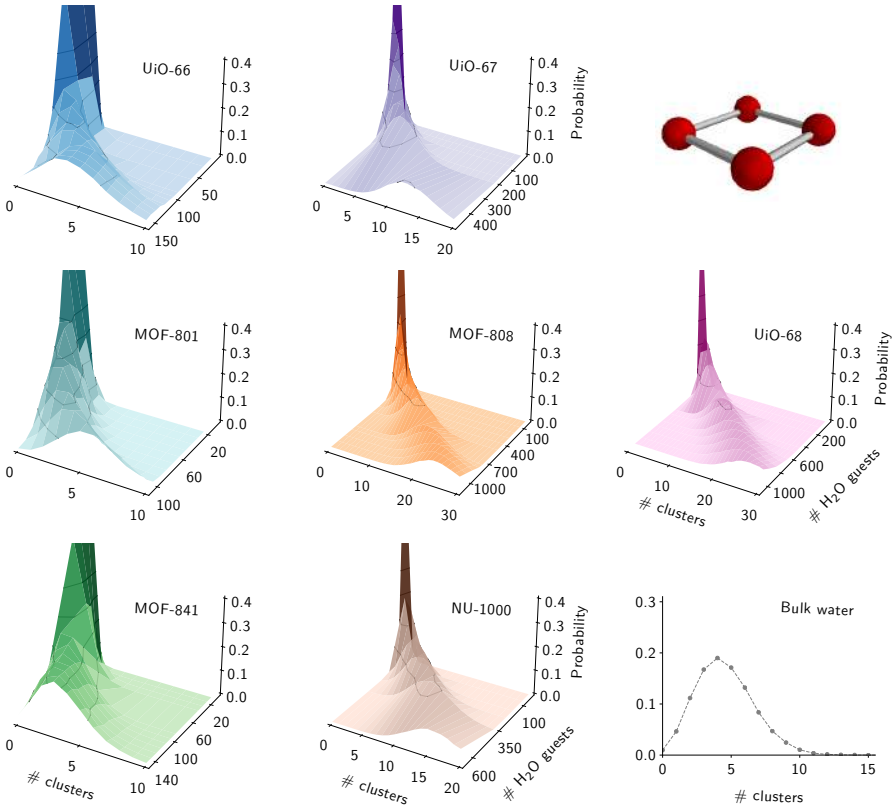

Figure S14: Probability of the occurrence of a certain number of square-shaped water clusters for different water loadings in different zirconium MOFs. The probability for a simulation of bulk water with 216 water molecules is shown in the bottom right corner.

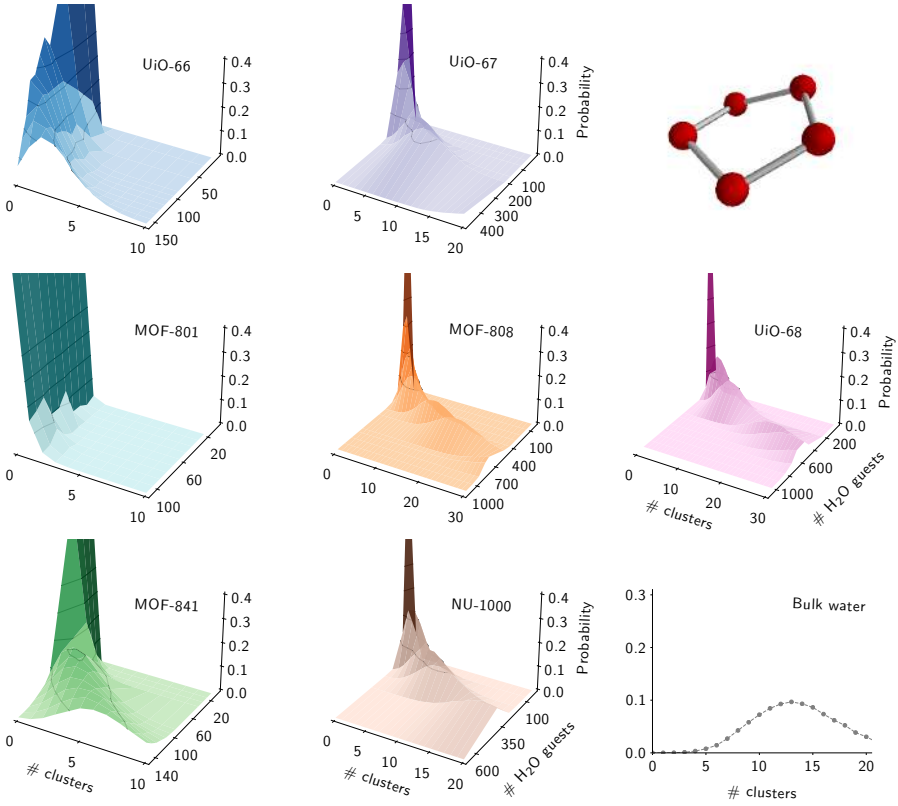

Figure S15: Probability of the occurrence of a certain number of pentagonal-shaped water clusters for different water loadings in different zirconium MOFs. The probability for a simulation of bulk water with 216 water molecules is shown in the bottom right corner.

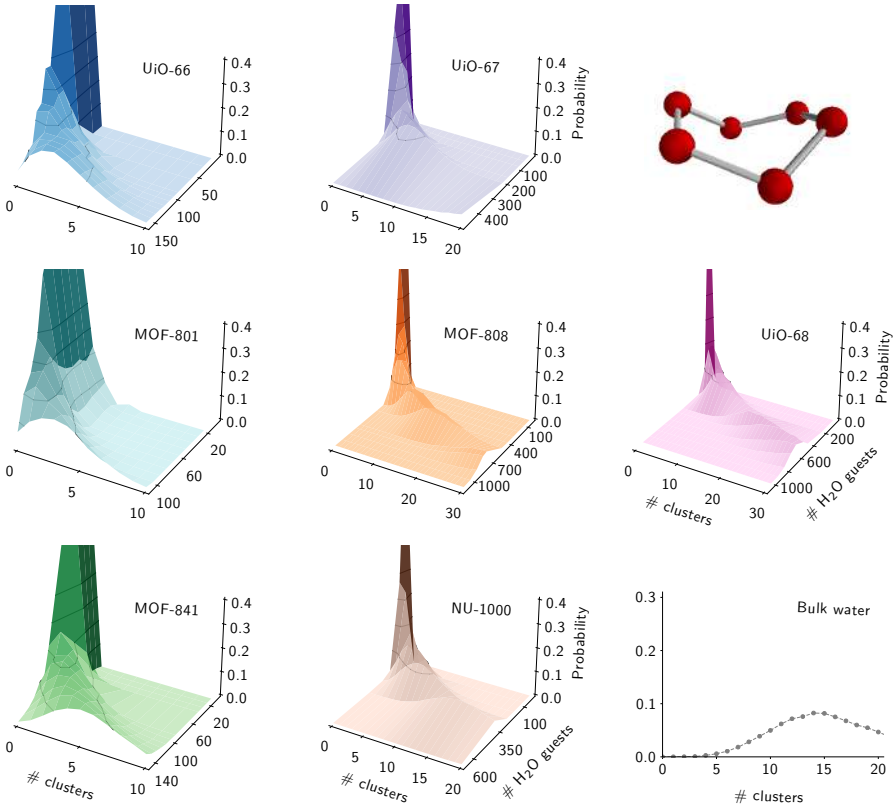

Figure S16: Probability of the occurrence of a certain number of hexagonal-shaped water clusters for different water loadings in different zirconium MOFs. The probability for a simulation of bulk water with 216 water molecules is shown in the bottom right corner.

S10 Analytical potentials

S10.1 Density

To rationalise the water clusters observed in MOF-801 and UiO-66, different analytical potentials are considered (Figure S17), as explained in the Methods section, which reduce the MOF–water interactions to a simple set of primary adsorption sites. The density plots obtained for these potentials (with different parametrisations) are shown in Figures S18–S26. The RDFs for the analytical potentials containing tetrahedrally or cubically arranged adsorption sites are shown in Figure S27.

Remark that for a repulsive box without adsorption sites (Figure S18), a small box size forces the water molecules into a water–water repulsion regime, so that the least energetically disfavoured configuration is observed with the water molecules near or in the weakly repulsive region of the walls. For moderate box sizes, the highest water density is still observed near the edges of the box, because the dynamically changing network of hydrogen bonds still creates structures that encounter the repulsive walls of the box. Moreover, the largest volume of the box is also contained in this edge region, *e.g.* 70% of the volume of a box with a side length of 6 Å is located in a 2 Å edge region of the box (*i.e.* when excluding an inner cube with a side length of 4 Å). For large box sizes, the water molecules can move freely within the box and the highest density is located in the centre of the box.

To demonstrate the potential of well-considered primary adsorption sites that can give rise to an extended water cluster through secondary adsorption sites, which are hydrogen bonded to the primary sites, an additional analytical potential is considered in Figure S28. In this potential, eight adsorption sites are defined in a repulsive cubic box containing 27 water molecules. The adsorption sites are positioned in such a way that a cubic 3 x 3 water grid can be formed, as all the grid points are either primary adsorption sites or located within a hydrogen bonding distance of two neighbouring primary adsorption sites (see Figure S29). For a relatively small box with a side of 8 Å (Figure S28), this average water density is indeed a cubic 3 x 3 grid. For larger box sizes (*e.g.* 10 or 11 Å in Figure S28), not all grid positions are systematically occupied, but in the middle layer (slab 2) along the *z*-axis the order induced by the secondary adsorption sites is clearly visible.

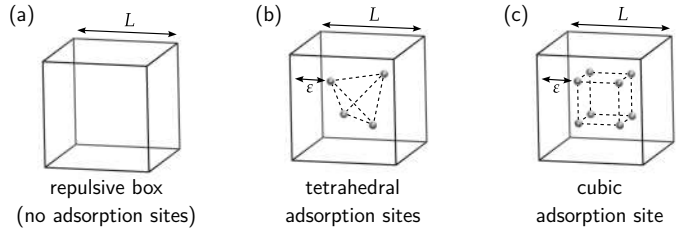

Figure S17: Graphical representation of three analytical toy models which confine water molecules in a repulsive cubic box with side length L. The repulsive box can contain (a) no adsorption sites, (b) tetrahedrally arranged adsorption sites, or (c) cubically arranged adsorption sites.

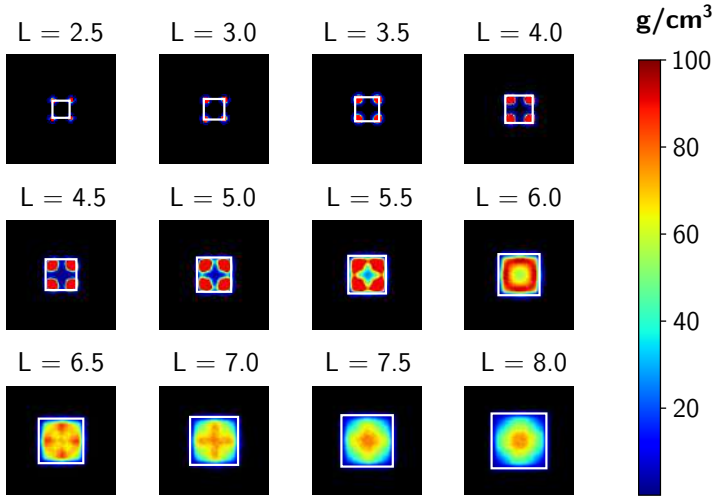

Figure S18: Density plots of eight water molecules confined in a repulsive cubic box with side length L (in Å). The densities are symmetrized using the $P\bar{4}3m$ space group, so that only the density in the top half of the box is shown. The edges of the simulation box are indicated in white.

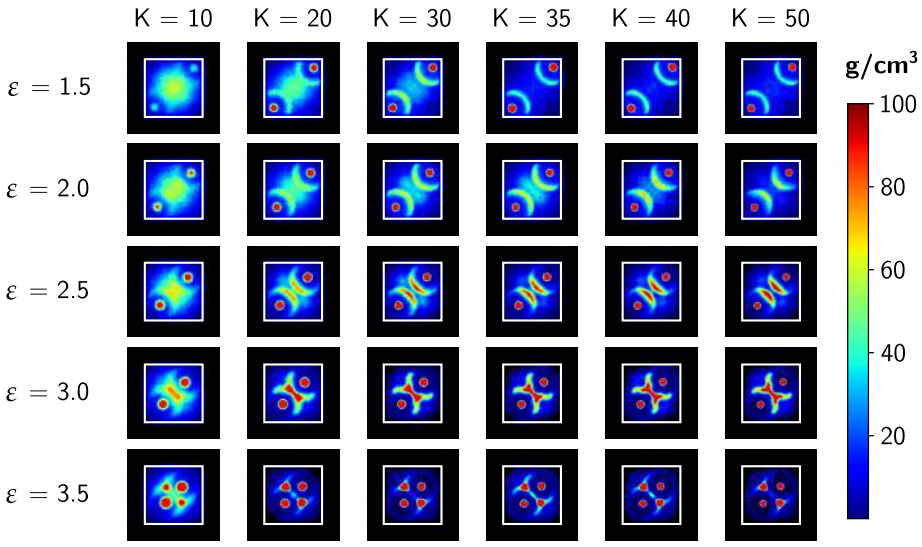

Figure S19: Density plots of eight water molecules confined in a repulsive cubic box with a side length of 10 Å and tetrahedrally arranged adsorption sites. The strength K of the adsorption sites is given in kJ/mol and the distance of the sites to the box walls ε is given in Å. The densities are symmetrized using the $P\bar{4}3m$ space group, so that only the density in the top half of the box is shown. The edges of the simulation box are indicated in white.

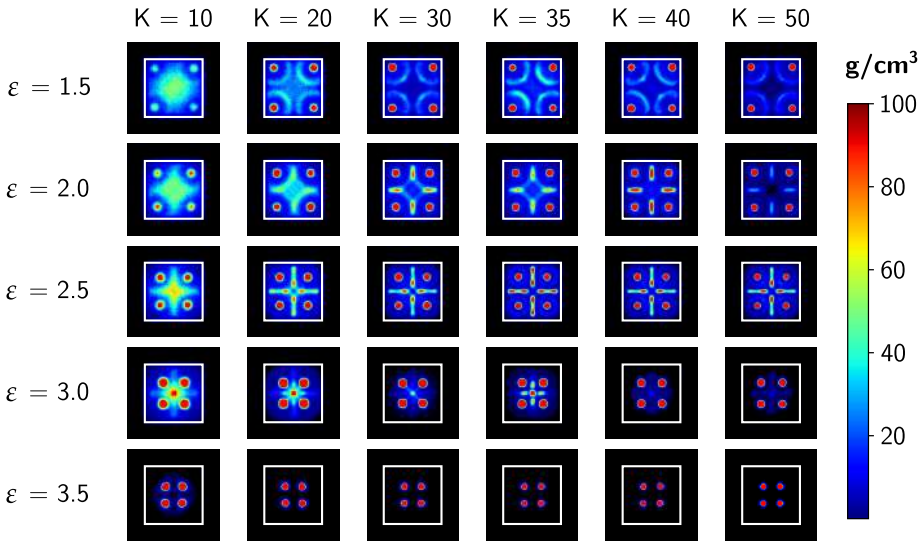

Figure S20: Density plots of eight water molecules confined in a repulsive cubic box with a side length of 10 Å and cubically arranged adsorption sites. The strength K of the adsorption sites is given in kJ/mol and the distance of the sites to the box walls ε is given in Å. The densities are symmetrized using the $P\bar{4}3m$ space group, so that only the density in the top half of the box is shown. The edges of the simulation box are indicated in white.

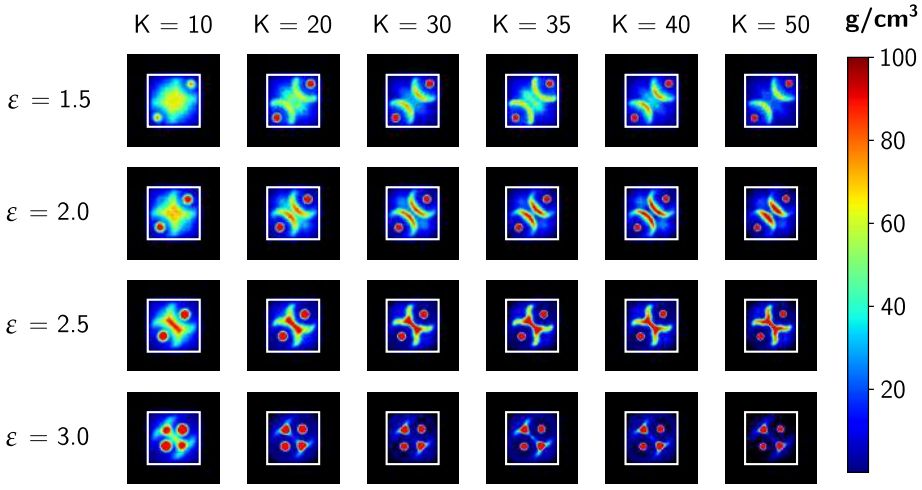

Figure S21: Density plots of eight water molecules confined in a repulsive cubic box with a side length of 9 Å and tetrahedrally arranged adsorption sites. The strength K of the adsorption sites is given in kJ/mol and the distance of the sites to the box walls ε is given in Å. The densities are symmetrized using the $P\bar{4}3m$ space group, so that only the density in the top half of the box is shown. The edges of the simulation box are indicated in white.

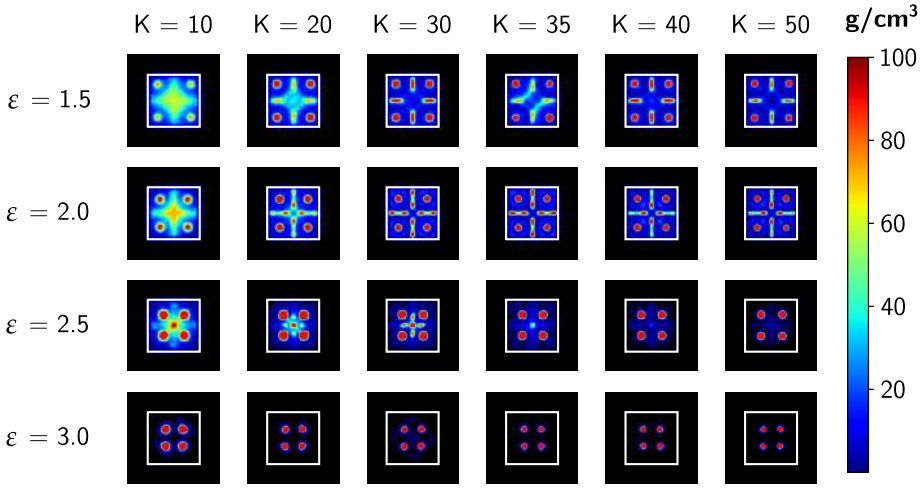

Figure S22: Density plots of eight water molecules confined in a repulsive cubic box with a side length of 9 Å and cubically arranged adsorption sites. The strength K of the adsorption sites is given in kJ/mol and the distance of the sites to the box walls ε is given in Å. The densities are symmetrized using the P$\bar{4}$3m space group, so that only the density in the top half of the box is shown. The edges of the simulation box are indicated in white.

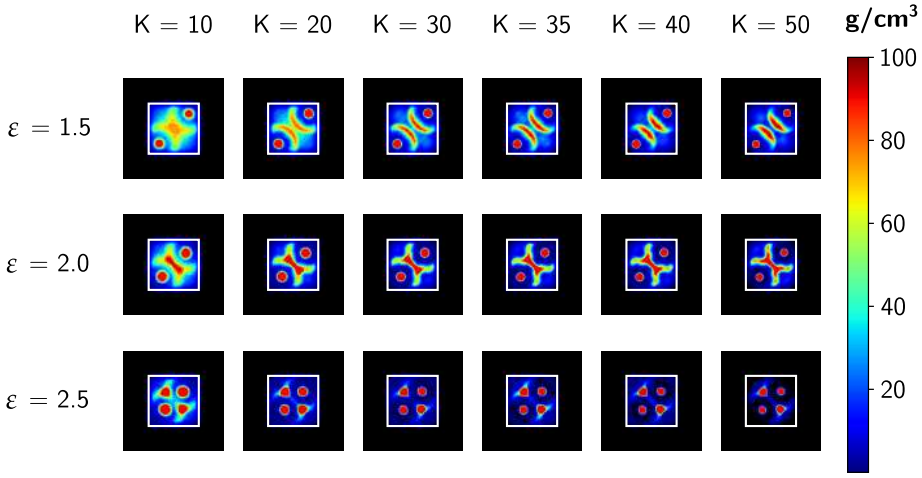

Figure S23: Density plots of eight water molecules confined in a repulsive cubic box with a side length of 8 Å and tetrahedrally arranged adsorption sites. The strength K of the adsorption sites is given in kJ/mol and the distance of the sites to the box walls ε is given in Å. The densities are symmetrized using the $P\bar{4}3m$ space group, so that only the density in the top half of the box is shown. The edges of the simulation box are indicated in white.

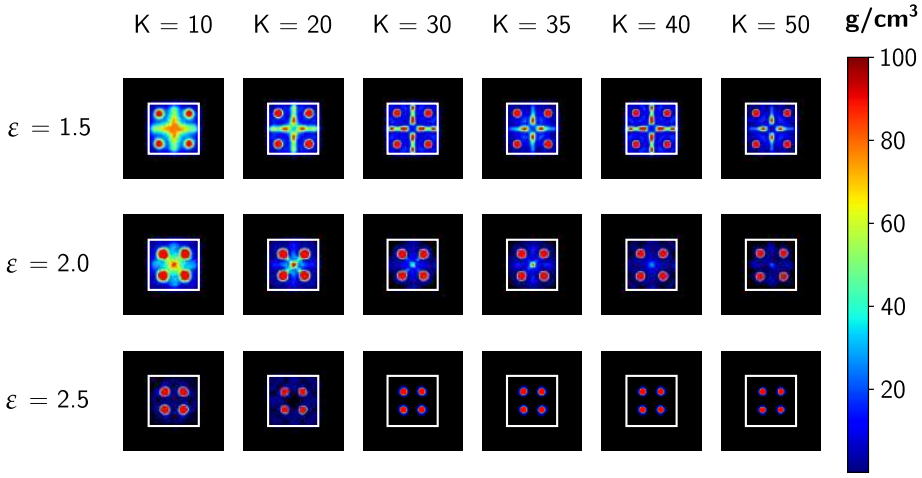

Figure S24: Density plots of eight water molecules confined in a repulsive cubic box with a side length of 8 Å and cubically arranged adsorption sites. The strength K of the adsorption sites is given in kJ/mol and the distance of the sites to the box walls ε is given in Å. The densities are symmetrized using the P$\bar{4}$3m space group, so that only the density in the top half of the box is shown. The edges of the simulation box are indicated in white.

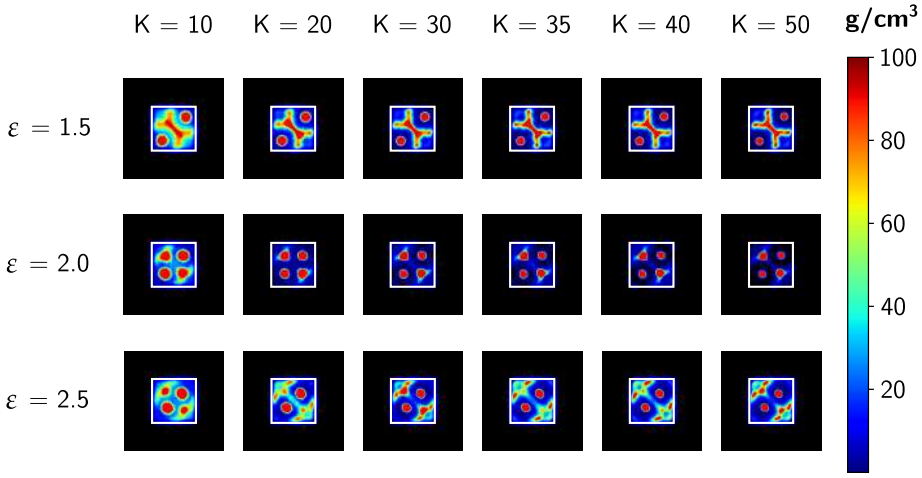

Figure S25: Density plots of eight water molecules confined in a repulsive cubic box with a side length of 7 Å and tetrahedrally arranged adsorption sites. The strength K of the adsorption sites is given in kJ/mol and the distance of the sites to the box walls ε is given in Å. The densities are symmetrized using the $P\bar{4}3m$ space group, so that only the density in the top half of the box is shown. The edges of the simulation box are indicated in white.

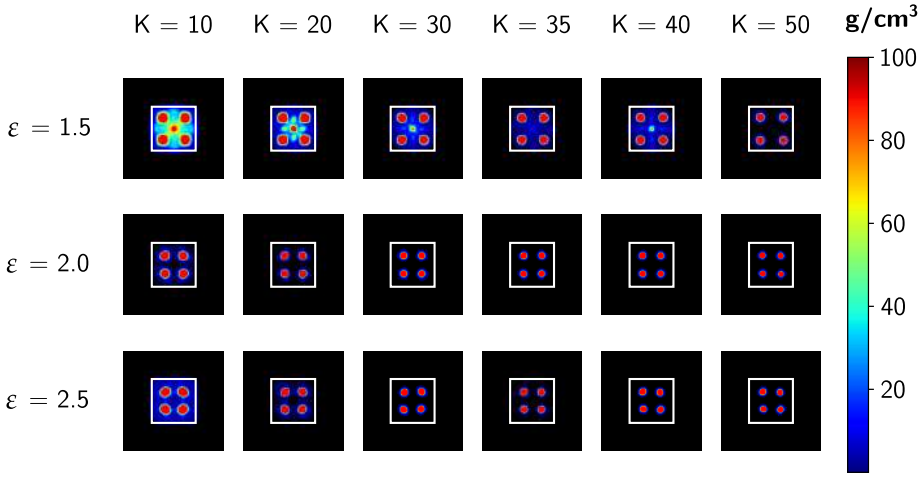

Figure S26: Density plots of eight water molecules confined in a repulsive cubic box with a side length of 7 Å and cubically arranged adsorption sites. The strength K of the adsorption sites is given in kJ/mol and the distance of the sites to the box walls ε is given in Å. The densities are symmetrized using the $P\bar{4}3m$ space group, so that only the density in the top half of the box is shown. The edges of the simulation box are indicated in white.

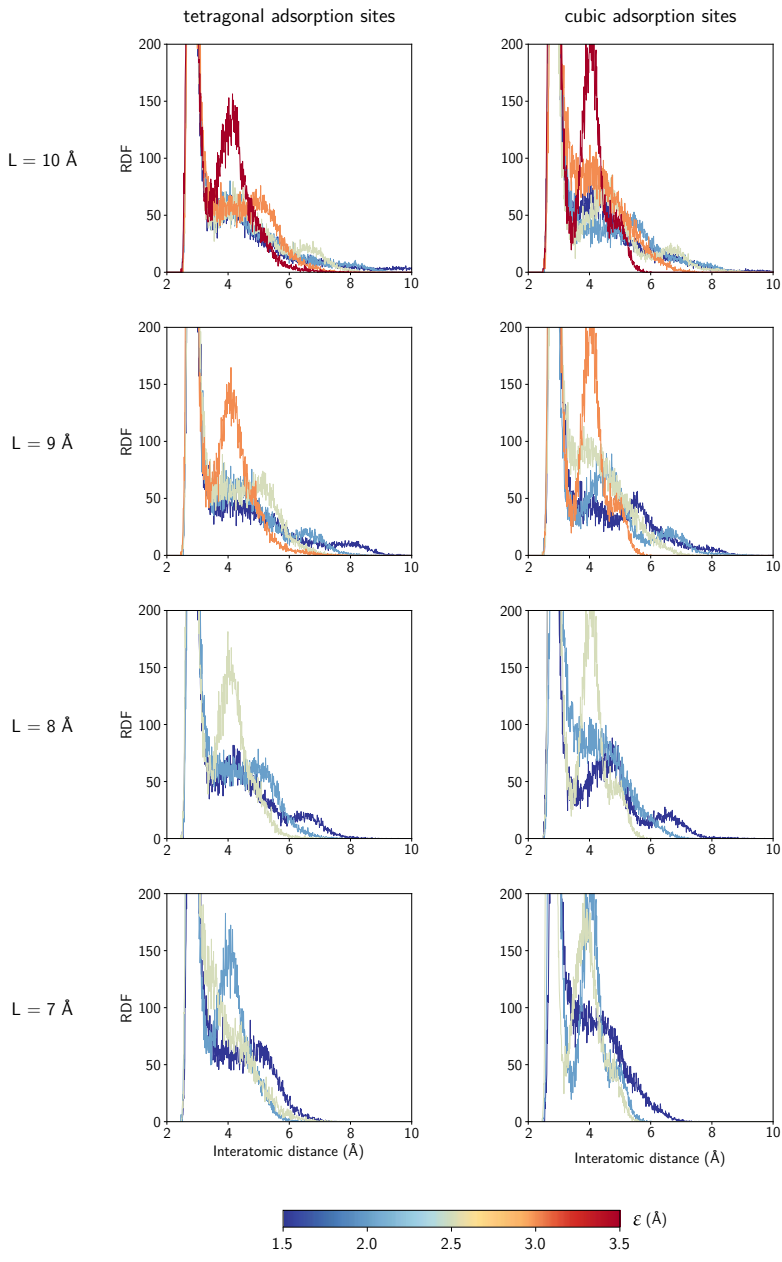

Figure S27: O–O RDFs of eight water molecules in the repulsive cubic box with tetrahedrally (left column) and cubically (right column) arranged adsorption sites with a strength K = 25 kJ/mol for different distances ε to the box walls and different box side lengths L. The peaks around 4 and 5 Å are in agreement with the cluster contributions identified for UiO-66 and MOF-801 (Figure S5).

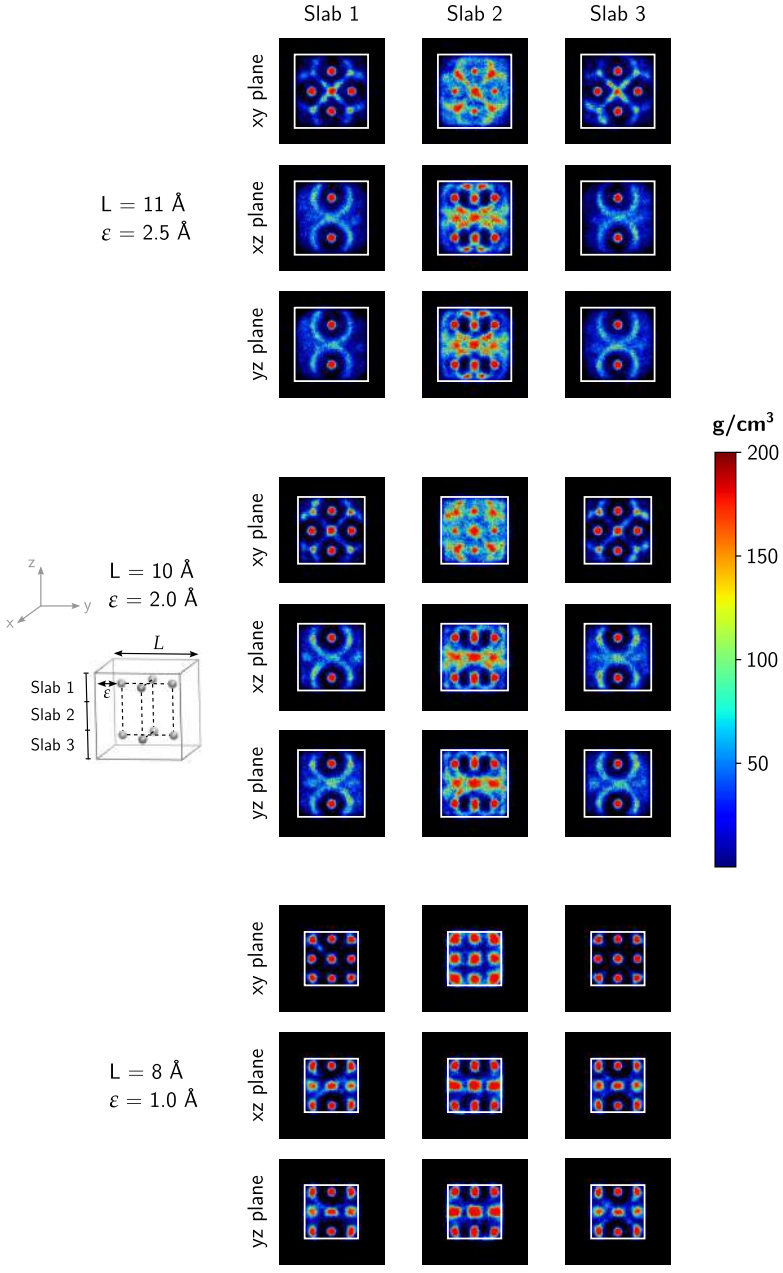

Figure S28: Density plots of 27 water molecules confined in a repulsive cubic box with side length L and adsorption sites with a strength K = 35 kJ/mol and distance ε to the box walls. The eight adsorption sites are visualised in the middle pane.

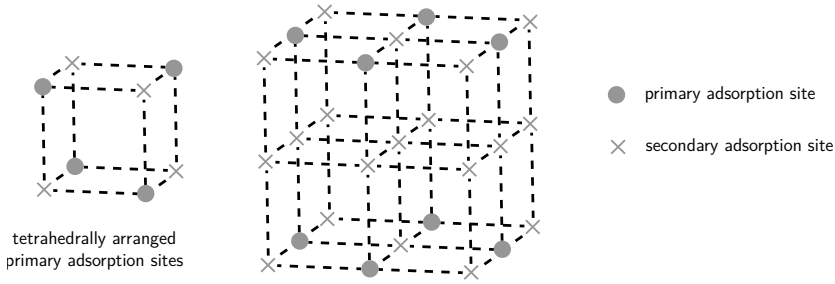

Figure S29: Schematic representation of the primary and secondary adsorption sites for tetrahedrally arranged primary adsorption sites (left) or the arrangement of primary adsorption sites from Figure S28 (right).

S10.2 Water adsorption isotherms

To illustrate the importance of secondary adsorption sites in the context of atmospheric water harvesting, Figures S30–S33 show the water adsorption isotherms for the analytical potentials with a tetrahedral or cubic arrangement of the adsorption sites for box sizes of 6 or 8 Å. The ideal water adsorption behaviour for atmospheric water harvesting is characterised by a step-shaped isotherm with a steep uptake for a relative pressure P/P_0 between 0.1 and 0.3, which allows for an easy water adsorption at low pressures, while retaining moderate regeneration conditions.[31,32] For a repulsive cubic box with a side length of 6 Å and tetrahedrally arranged adsorption sites (Figure S30), this ideal adsorption behaviour is retrieved for adsorption sites at a distance $\varepsilon = 1.5$ Å from the box walls and an adsorption strength of 35 kJ/mol. In this configuration, the tetrahedrally arranged adsorption sites outline a cube with a side of about 3 Å, which implies the presence of four secondary adsorption sites that are hydrogen bonded to the four primary tetrahedral adsorption sites. At low relative pressures, these secondary sites can be filled alongside the primary adsorption sites, yielding an uptake of about eight water molecules. When increasing the strength of the primary adsorption sites, the uptake at these sites shift to lower relative pressures, which limits the working capacity of the pore as these water molecules cannot be desorbed at moderate thermodynamic conditions. Remark that for a comparison with experimental results, the heat of adsorption should be used rather than the strength of the primary adsorption sites. As the heat of adsorption also accounts for the internal energy of the water molecules and the interaction energy between the different water molecules, this yields a lower number than the pure interaction energy of the adsorption sites, as shown in Figure S36.

When the primary adsorption sites are placed closer together ($\varepsilon = 2$ Å), the same uptake at very low relative pressures is observed. However, as there are no secondary adsorption sites for this configuration, the total uptake is limited to the four primary adsorption sites. When the primary adsorption sites are

placed further apart ($\varepsilon = 1$ Å), the secondary adsorption sites are also absent and the lack of cooperative adsorption among the sites significantly decreases the steepness of the isotherm step, which also limits the working capacity associated with the pore.

For a box with a side length of 8 Å (Figure S32), similar conclusions can be drawn. The most interesting isotherm for atmospheric water harvesting is again obtained in the presence of secondary adsorption sites ($\varepsilon = 2.5$ Å and $K = 35$ kJ/mol). When the primary adsorption sites are placed further apart ($\varepsilon = 2.5$ Å), the isotherm step is again flattened across the pressure range.

When the secondary adsorption sites are replaced by primary adsorption sites in the box with a side length of 6 Å (Figure S31, $\varepsilon = 1.5$ Å), the strong cooperative interaction between the cubically arranged adsorption sites results in an immediate occupation of the sites at the lowest pressures. If the eight (primary) adsorption sites are placed further apart ($\varepsilon = 1$ Å), near the corners of the repulsive box, an appropriate step isotherm can be retrieved for an adsorption strength of $K = 30$ kJ/mol with a slightly higher uptake than in the case of only four primary adsorption sites. For the larger box with a side length of 8 Å, similar conclusions can be drawn. The most effective adsorption behaviour is obtained when placing the eight primary adsorption sites in the corners of the cubic box (Figure S33, $\varepsilon = 1.0$ or 1.5 Å), yielding an appropriate step isotherm for adsorption sites with a strength of 30 kJ/mol. When the primary adsorption sites are located near the corners of the box, apart from one another, other water molecules can hydrogen bond to these sites (Figure S35), thus creating a hydrogen bonded structure which maximally exploits the volume of this larger box and increases the uptake. Remark that for $\varepsilon = 1.0$ the distance between the adsorption sites equals about two hydrogen bonds, so that a water molecule can be adsorbed in between the primary adsorption sites. In larger pores, more adsorption sites located near the edges are thus more advantageous than a small cubic water cluster in the centre of the pore to obtain a higher water uptake.

To assess the approximation of only considering an isolated virtual cubic pore in the analytical model, we also consider a configuration of two neighbouring cubic pores (each with a side length of 6 Å) which are separated by a repulsive wall with a non-repulsive window (Figure S34). The non-repulsive window takes up one quarter of the separating wall, which is 2 Å thick. Only one of the two pores contains tetrahedrally arranged adsorption sites, while the other box contains no adsorption sites. Within the pressure range relevant for atmospheric water harvesting, the water adsorption isotherm differs only negligibly from an isolated cubic box with the same adsorption sites, thus confirming the relevance of the approximate analytical model with a single isolated pore.

The vapor pressure P_0 (at 300 K) used to determine the relative pressure in Figures S30–S34 is 0.03567 bar.

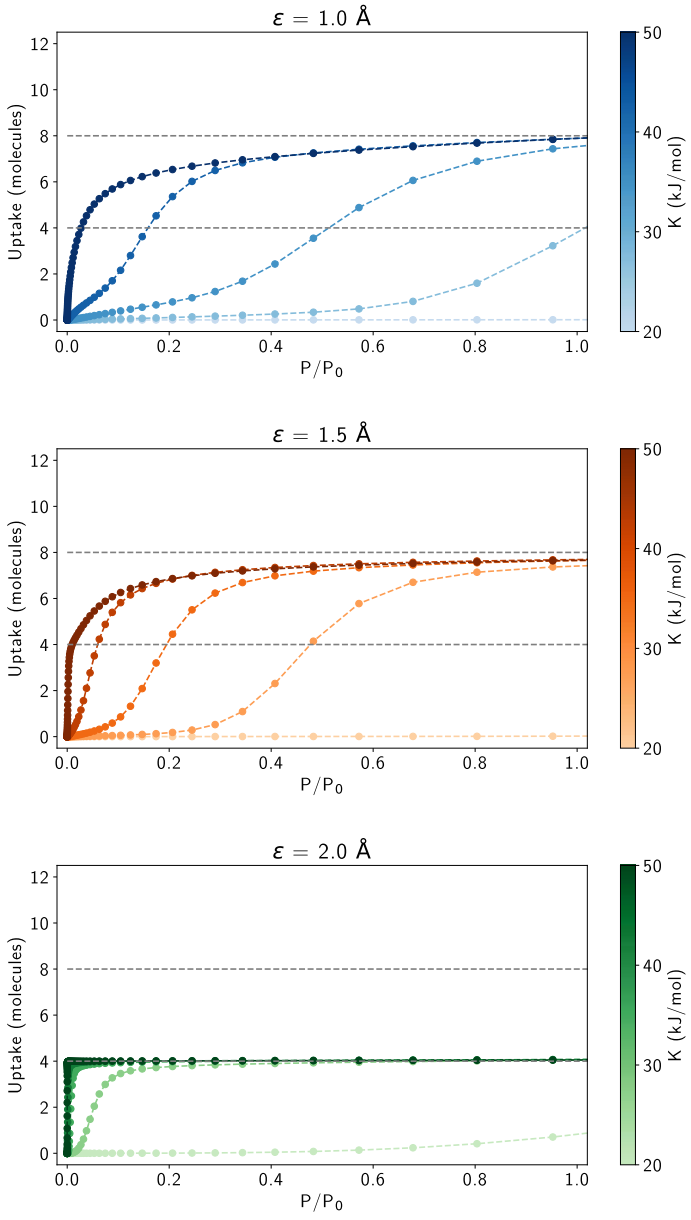

Figure S30: Water adsorption isotherms for water molecules confined in a repulsive cubic box with a side length of 6 Å and tetrahedrally arranged adsorption sites. K is the strength of the adsorption sites (taking values of 20, 30, 35, 40, and 50 kJ/mol) and ε is the distance of the sites to the box walls.

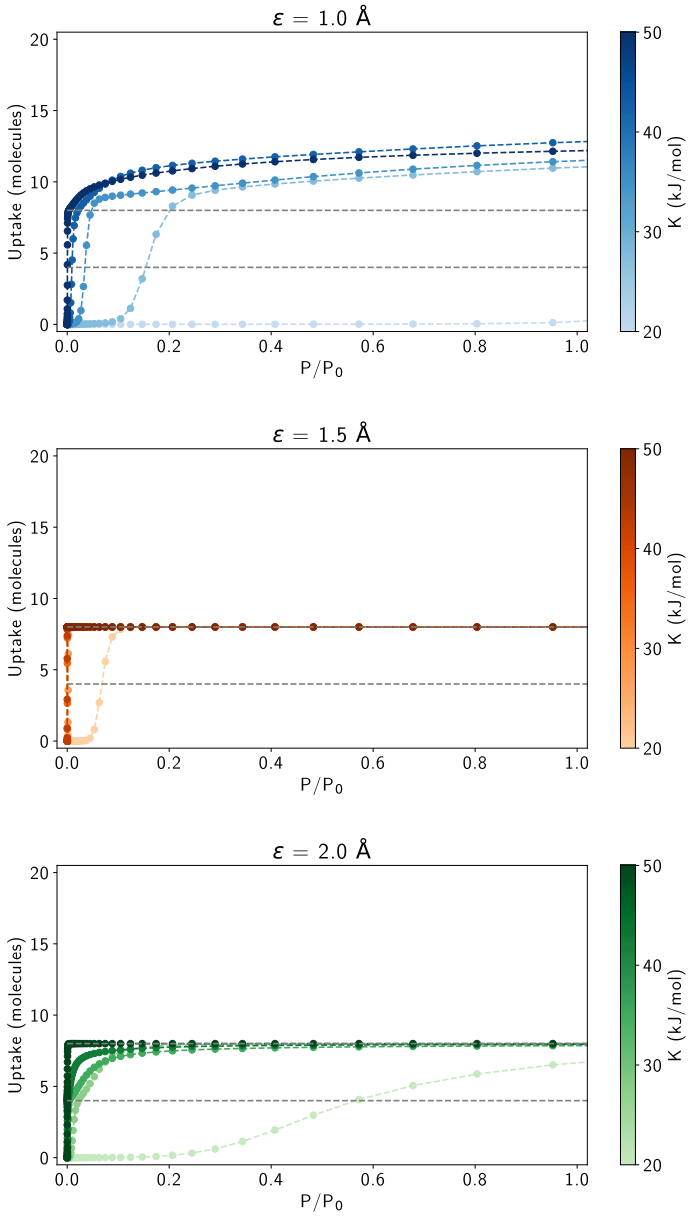

Figure S31: Water adsorption isotherms for water molecules confined in a repulsive cubic box with a side length of 6 Å and cubically arranged adsorption sites. K is the strength of the adsorption sites (taking values of 20, 30, 35, 40, and 50 kJ/mol) and ε is the distance of the sites to the box walls.

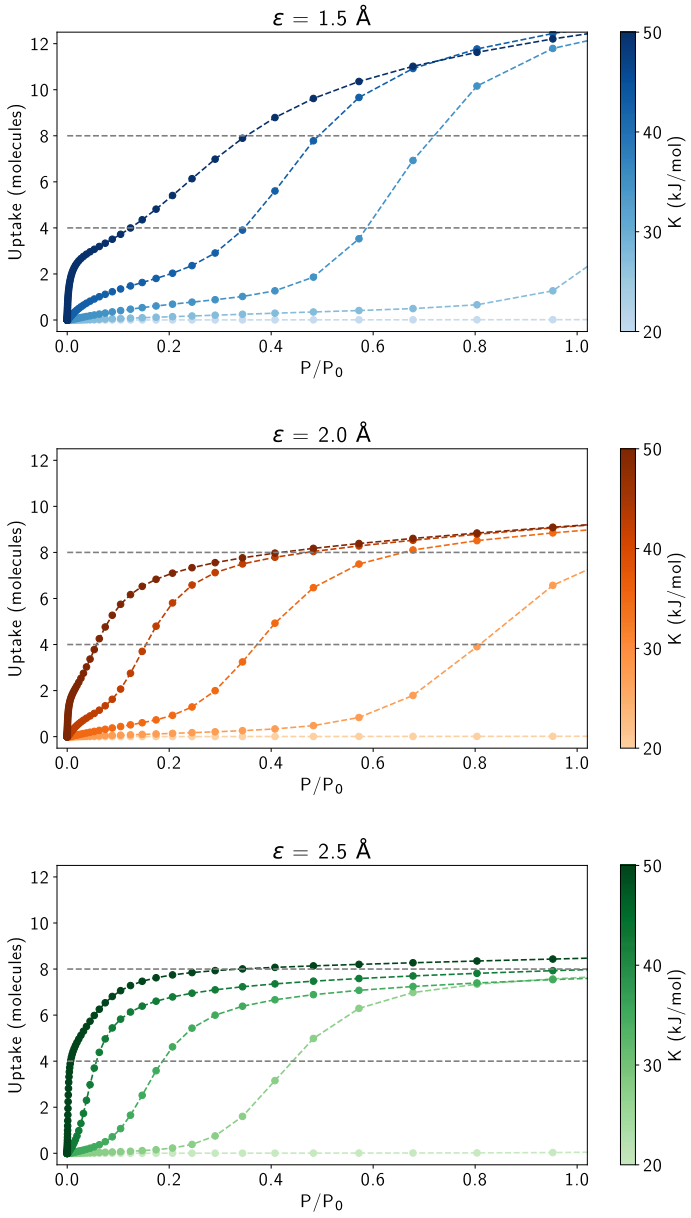

Figure S32: Water adsorption isotherms for water molecules confined in a repulsive cubic box with a side length of 8 Å and tetrahedrally arranged adsorption sites. K is the strength of the adsorption sites (taking values of 20, 30, 35, 40, and 50 kJ/mol) and ε is the distance of the sites to the box walls.

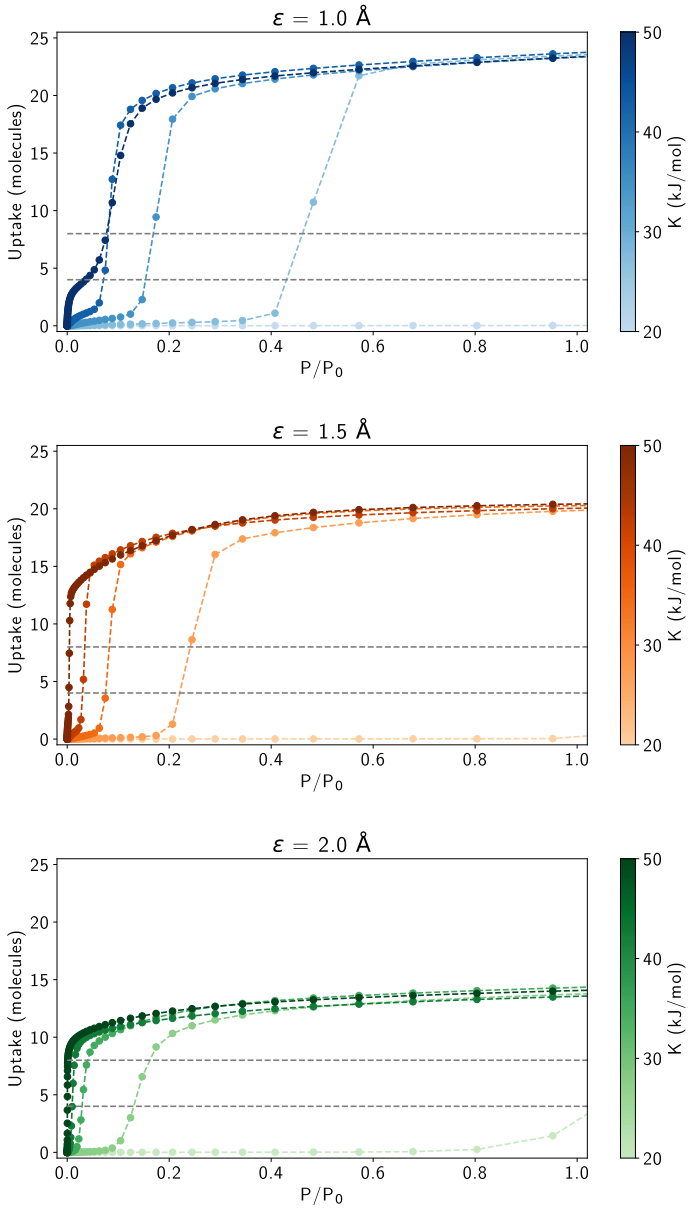

Figure S33: Water adsorption isotherms for water molecules confined in a repulsive cubic box with a side length of 8 Å and cubically arranged adsorption sites. K is the strength of the adsorption sites (taking values of 20, 30, 35, 40, and 50 kJ/mol) and ε is the distance of the sites to the box walls.

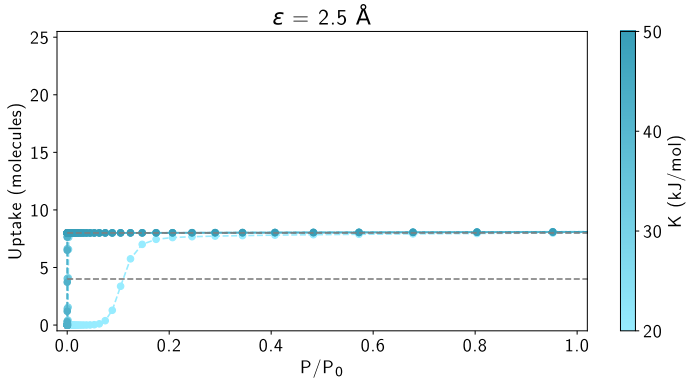

Figure S33: Water adsorption isotherms for water molecules confined in a repulsive cubic box with a side length of 8 Å and cubically arranged adsorption sites. K is the strength of the adsorption sites (taking values of 20, 30, 35, 40, and 50 kJ/mol) and ε is the distance of the sites to the box walls.

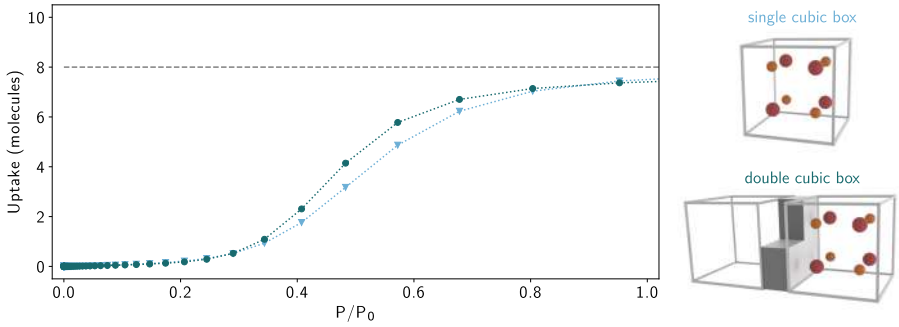

Figure S34: Water adsorption isotherms for water molecules confined in a repulsive cubic box. Two different configurations are considered: (i) an isolated cubic box with a side length of 6 Å and tetrahedrally arranged adsorption sites and (ii) two neighbouring cubic boxes with a side length of 6 Å, separated by a repulsive wall with a non-repulsive window; only one of the two boxes contains tetrahedrally arranged adsorption sites, while the other contains no adsorption sites. The adsorption sites have a strength of 30 kJ/mol and are placed at a distance ε = 1.5 Å from the box walls. The four primary adsorption sites are indicated with red spheres, whereas the secondary adsorption sites are indicated with orange spheres.

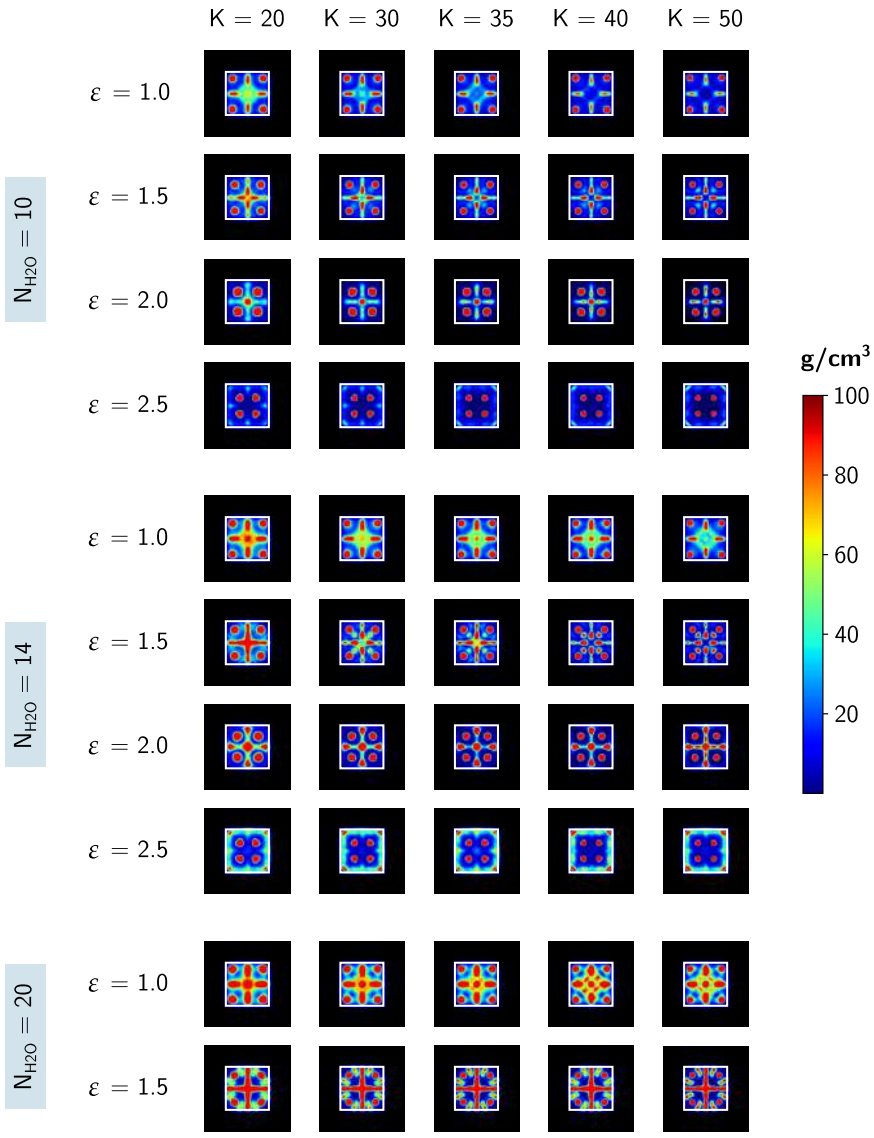

Figure S35: Density plots of different numbers of water molecules confined in a repulsive cubic box with a side length of 8 Å and cubically arranged adsorption sites. The strength K of the adsorption sites is given in kJ/mol and the distance of the sites to the box walls ε is given in Å. The densities are symmetrized using the P$\bar{4}$3m space group, so that only the density in the top half of the box is shown. The edges of the simulation box are indicated in white.

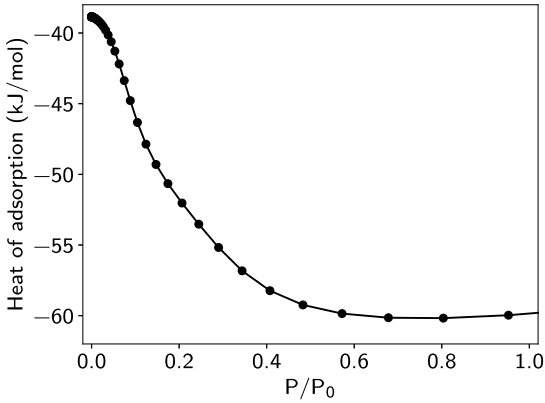

Figure S36: Isosteric heat of adsorption for water molecules confined in a repulsive cubic box with a side length of 6 Å and tetrahedrally arranged adsorption sites with a strength of 35 kJ/mol. The distance ε of the sites to the box walls equals 1.5 Å. The isosteric heat of adsorption was calculated from the TMMC calculations using Eq. (8) of Ref. 33.

Influence of the water model on the adsorption isotherms

As water adsorption isotherms are notoriously difficult to compute, due to their sensitivity to small deviations in interaction energies, we evaluate the robustness of the results obtained with the q-TIP4P/f force field through a comparison with the MBX water model.[34] As MBX has been fitted on a large dataset of CCSD(T) energies, this model yields a higher accuracy for the interaction energies of water clusters than most other water models.

Structurally, the same water clusters are predicted by both models, as shown in Figure S37 for the specific case of eight water molecules in a box with tetrahedrally arranged adsorption sites. Energetically, a re-evaluation of the energy of clusters up to eight water molecules obtained from MBX MD simulations with the q-TIP4P/f force field, or vice versa, yield an energy difference of 1–1.5 kJ/mol per interaction between water molecules. For a cluster of eight water molecules, the total energy difference per molecule is observed to be about 5 kJ/mol. Although this difference in energy does not affect the structural properties, it is expected to be of importance for the adsorption characteristics, as small discrepancies in interaction energies can strongly influence adsorption isotherms. In Figure S38, the MBX water adsorption isotherms for a box with cubically arranged adsorption sites are shown, which are similar to the isotherms obtained with q-TIP4P/f (Figure S31). Due to the difference in interaction energy between both models, the MBX isotherms are however shifted towards larger relative pressures. Nevertheless, the main conclusions remain valid. For ε = 1.5 Å, for example, only very weak primary adsorption sites of 20 kJ/mol can yield a step isotherm, as stronger adsorption sites get immediately occupied at the lowest pressures. Also for

ε = 2.0 Å, the gradual uptake after the first four water molecules is shifted towards larger relative pressures and is stretched across a wider pressure range.

When considering only four primary adsorption sites, in a tetrahedral arrangement, the differences between both water models are more pronounced (Figure S39). In contrast to the step isotherms obtained with q-TIP4P/f (Figure S30), the energetic differences in the MBX model yield isotherms that are significantly stretched across a larger pressure range and only yield the cubic water clusters at larger pressures. Given the sensitivity of isotherms to small differences in interaction energies and the higher accuracy of the MBX interaction energies, this reveals an artefact of the simplification of the analytical model in explaining the behaviour of MOF water adsorption isotherms. As shown in Figure S40, MOFs such as MOF-801 do not only contain isolated primary adsorption sites (*e.g.* from μ–OH sites), but also stabilise water molecules within the remainder of the pore due to weak interactions with the framework. When introducing these weak interactions in the form of weak secondary sites (with a strength of 5–10 kJ/mol), as shown in Figure S39, a step isotherm shape can be retrieved within the relevant pressure range. Therefore, MBX predicts that the important secondary adsorption sites required to produce the desired adsorption behaviour contain both contributions from the water molecules adsorbed at primary adsorption sites and from weak interactions with the MOF framework.

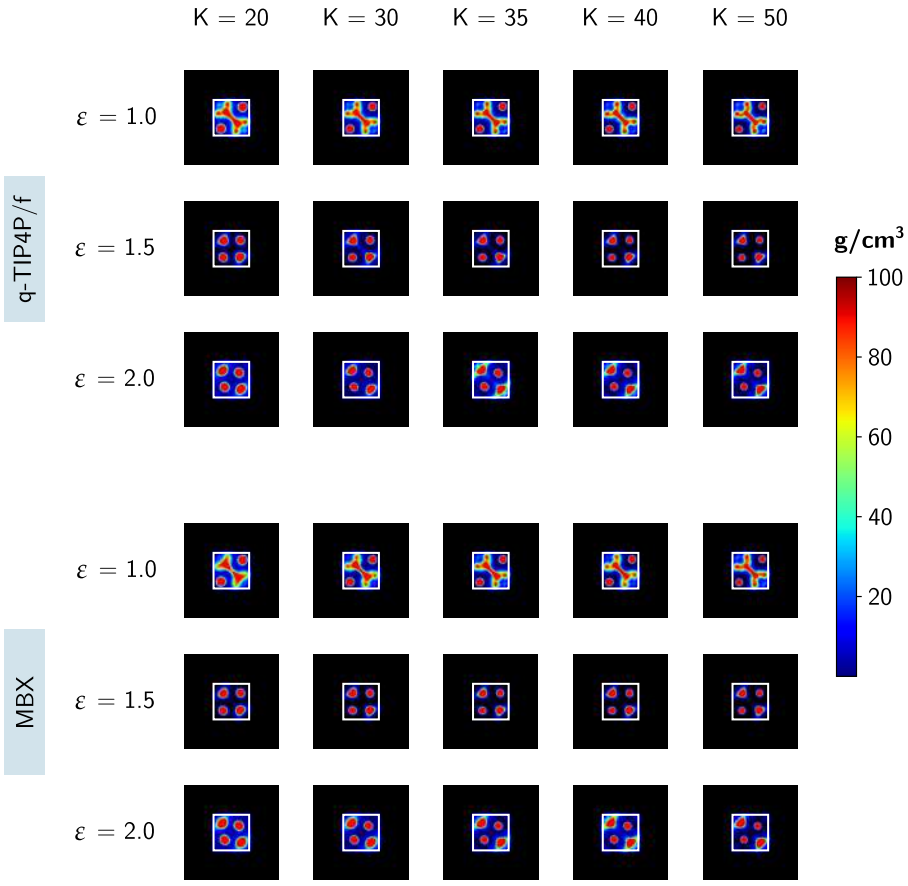

Figure S37: Density plots of eight water molecules confined in a repulsive cubic box with a side length of 6 Å and tetrahedrally arranged adsorption sites, comparing the q-TIP4P/f and MBX water models. The strength K of the adsorption sites is given in kJ/mol and the distance of the sites to the box walls ε is given in Å. The densities are symmetrized using the $P\bar{4}3m$ space group, so that only the density in the top half of the box is shown. The edges of the simulation box are indicated in white.

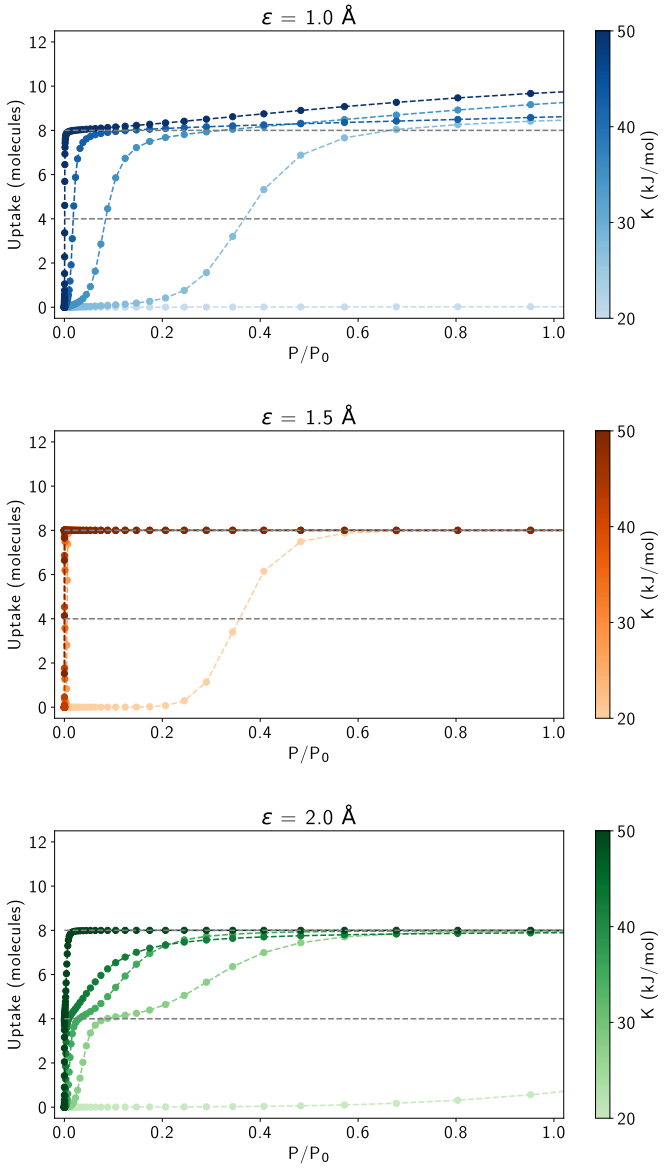

Figure S38: Water adsorption isotherms for water molecules confined in a repulsive cubic box with a side length of 6 Å and cubically arranged adsorption sites, obtained with the MBX water model. K is the strength of the adsorption sites (taking values of 20, 30, 35, 40, and 50 kJ/mol) and ε is the distance of the sites to the box walls.

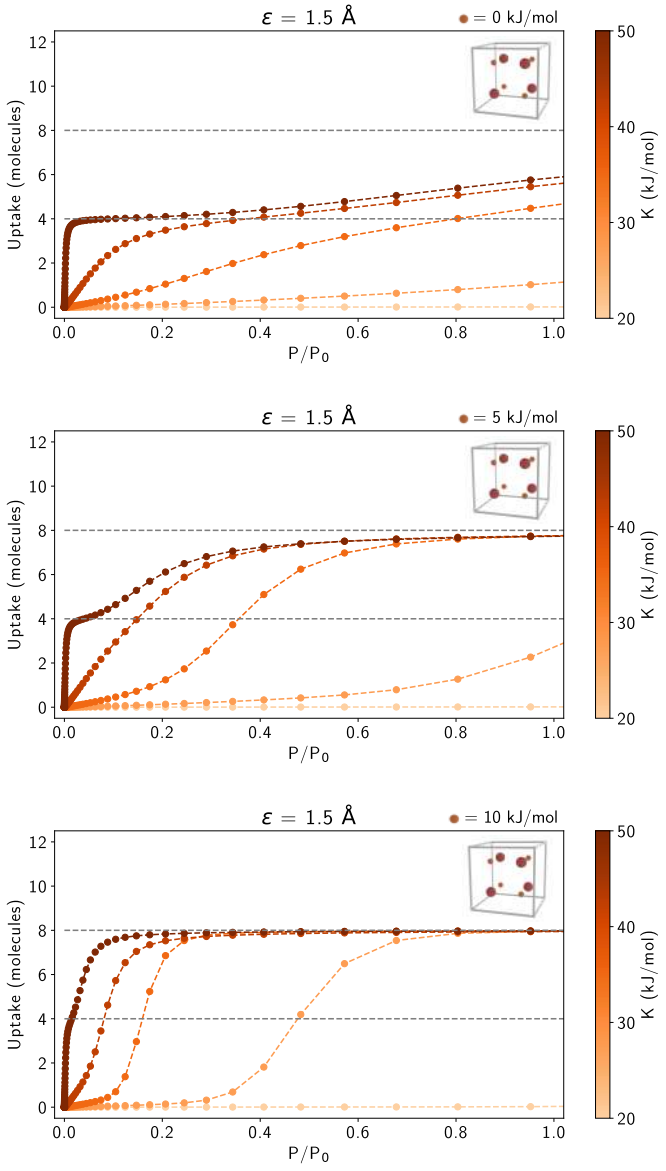

Figure S39: Water adsorption isotherms for water molecules confined in a repulsive cubic box with a side length of 6 Å and cubically arranged adsorption sites, obtained with the MBX water model. K is the strength of the red, primary adsorption sites in the inset (taking values of 20, 30, 35, 40, and 50 kJ/mol), while the strength of the orange, secondary adsorption sites is varied from 0 to 10 kJ/mol in the separate panes. ε is the distance of the sites to the box walls.

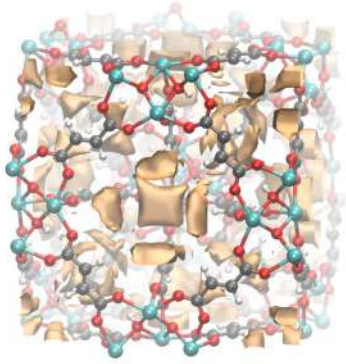

Figure S40: Isosurface of a water molecule in MOF-801 for an adsorption energy of -15 kJ/mol, obtained with the q-TIP4P/f force field using the methodology outlined in Ref. 35.

References

(1) Vanduyfhuys, L.; Vandenbrande, S.; Verstraelen, T.; Schmid, R.; Waroquier, M.; Van Speybroeck, V. QuickFF: A program for a quick and easy derivation of force fields for metal-organic frameworks from ab initio input. *J. Comput. Chem.* **2015**, *36*, 1015–1027.

(2) Vanduyfhuys, L.; Vandenbrande, S.; Wieme, J.; Waroquier, M.; Verstraelen, T.; Van Speybroeck, V. Extension of the QuickFF force field protocol for an improved accuracy of structural, vibrational, mechanical and thermal properties of metal-organic frameworks. *J. Comput. Chem.* **2018**, *39*, 999–1011.

(3) Becke, A. D. Density-functional exchange-energy approximation with correct asymptotic behavior. *Phys. Rev. A* **1988**, *38*, 3098–3100.

(4) Verstraelen, T.; Vandenbrande, S.; Heidar-Zadeh, F.; Vanduyfhuys, L.; Van Speybroeck, V.; Waroquier, M.; Ayers, P. W. Minimal Basis Iterative Stockholder: Atoms in Molecules for Force-Field Development. *J. Chem. Theory Comput.* **2016**, *12*, 3894–3912.

(5) Mayo, S. L.; Olafson, B. D.; Goddard, W. A. DREIDING: a generic force field for molecular simulations. *J. Phys. Chem.* **1990**, *94*, 8897–8909.

(6) Rappe, A. K.; Casewit, C. J.; Colwell, K. S.; Goddard, W. A. I.; Skiff, W. M. UFF, a full periodic table force field for molecular mechanics and molecular dynamics simulations. *J. Am. Chem. Soc.* **1992**, *114*, 10024–10035.

(7) Rogge, S. M. J.; Wieme, J.; Vanduyfhuys, L.; Vandenbrande, S.; Maurin, G.; Verstraelen, T.; Waroquier, M.; Van Speybroeck, V. Thermodynamic Insight in the High-Pressure Behavior of UiO-66: Effect of Linker Defects and Linker Expansion. *Chem. Mater.* **2016**, *28*, 5721–5732.

(8) Habershon, S.; Markland, T. E.; Manolopoulos, D. E. Competing quantum effects in the dynamics of a flexible water model. *J. Chem. Phys.* **2009**, *131*, 024501.

(9) Abascal, J. L. F.; Vega, C. A general purpose model for the condensed phases of water: TIP4P/2005. *J. Chem. Phys.* **2005**, *123*, 234505.

(10) Ramírez, R.; Herrero, C. P. Kinetic energy of protons in ice Ih and water: A path integral study. *Phys. Rev. B* **2011**, *84*, 064130.

(11) Markland, T. E.; Berne, B. J. Unraveling quantum mechanical effects in water using isotopic fractionation. *Proc. Natl. Acad. Sci. U.S.A.* **2012**, *109*, 7988–7991.

(12) Cheng, B.; Behler, J.; Ceriotti, M. Nuclear Quantum Effects in Water at the Triple Point: Using Theory as a Link Between Experiments. *J. Phys. Chem. Lett.* **2016**, *7*, 2210–2215.

(13) Kapil, V.; Cuzzocrea, A.; Ceriotti, M. Anisotropy of the Proton Momentum Distribution in Water. *J. Phys. Chem. B* **2018**, *122*, 6048–6054.

(14) Rasti, S.; Meyer, J. Importance of zero-point energy for crystalline ice phases: A comparison of force fields and density functional theory. *J. Chem. Phys.* **2019**, *150*, 234504.

(15) Kühne, T. D. et al. CP2K: An electronic structure and molecular dynamics software package - Quickstep: Efficient and accurate electronic structure calculations. *J. Chem. Phys.* **2020**, *152*, 194103.

(16) Perdew, J. P.; Burke, K.; Ernzerhof, M. Generalized Gradient Approximation Made Simple. *Phys. Rev. Lett.* **1996**, *77*, 3865–3868.

(17) Grimme, S.; Antony, J.; Ehrlich, S.; Krieg, H. A consistent and accurate ab initio parametrization of density functional dispersion correction (DFT-D) for the 94 elements H-Pu. *J. Chem. Phys.* **2010**, *132*, 154104.

(18) Grimme, S.; Ehrlich, S.; Goerigk, L. Effect of the damping function in dispersion corrected density functional theory. *J. Comput. Chem.* **2011**, *32*, 1456–1465.

(19) Goedecker, S.; Teter, M.; Hutter, J. Separable dual-space Gaussian pseudopotentials. *Phys. Rev. B* **1996**, *54*, 1703–1710.

(20) VandeVondele, J.; Hutter, J. Gaussian basis sets for accurate calculations on molecular systems in gas and condensed phases. *J. Chem. Phys.* **2007**, *127*, 114105.

(21) Batatia, I.; Kovacs, D. P.; Simm, G.; Ortner, C.; Csanyi, G. MACE: Higher Order Equivariant Message Passing Neural Networks for Fast and Accurate Force Fields. Advances in Neural Information Processing Systems. 2022; pp 11423–11436.

(22) Batatia, I. et al. A foundation model for atomistic materials chemistry. 2024; `https://arxiv.org/abs/2401.00096`.

(23) Vandenhaute, S.; Cools-Ceuppens, M.; DeKeyser, S.; Verstraelen, T.; Van Speybroeck, V. Machine learning potentials for metal-organic frameworks using an incremental learning approach. *npj Comput. Mater.* **2023**, *9*, 19.

(24) Izmailov, P.; Podoprikhin, D.; Garipov, T.; Vetrov, D.; Wilson, A. G. Averaging Weights Leads to Wider Optima and Better Generalization. 2019; `https://arxiv.org/abs/1803.05407`.

(25) Willems, T. F.; Rycroft, C. H.; Kazi, M.; Meza, J. C.; Haranczyk, M. Algorithms and tools for high-throughput geometry-based analysis of crystalline porous materials. *Micropor. Mesopor. Mat.* **2012**, *149*, 134–141.

(26) Furukawa, H.; Gándara, F.; Zhang, Y.-B.; Jiang, J.; Queen, W. L.; Hudson, M. R.; Yaghi, O. M. Water Adsorption in Porous Metal-Organic Frameworks and Related Materials. *J. Am. Chem. Soc.* **2014**, *136*, 4369–4381.

(27) Deria, P.; Mondloch, J. E.; Tylianakis, E.; Ghosh, P.; Bury, W.; Snurr, R. Q.; Hupp, J. T.; Farha, O. K. Perfluoroalkane Functionalization of NU-1000 via Solvent-Assisted Ligand Incorporation: Synthesis and CO_2 Adsorption Studies. *J. Am. Chem. Soc.* **2013**, *135*, 16801–16804.

(28) Deria, P.; Bury, W.; Hod, I.; Kung, C.-W.; Karagiaridi, O.; Hupp, J. T.; Farha, O. K. MOF Functionalization via Solvent-Assisted Ligand Incorporation: Phosphonates vs Carboxylates. *Inorg. Chem.* **2015**, *54*, 2185–2192.

(29) Temelso, B.; Archer, K. A.; Shields, G. C. Benchmark Structures and Binding Energies of Small Water Clusters with Anharmonicity Corrections. *J. Phys. Chem. A* **2011**, *115*, 12034–12046.

(30) Hagberg, A. A.; Schult, D. A.; Swart, P. J. Exploring Network Structure, Dynamics, and Function using NetworkX. Proceedings of the 7th Python in Science Conference. Pasadena, CA USA, 2008; pp 11–15.

(31) Kalmutzki, M. J.; Diercks, C. S.; Yaghi, O. M. Metal-Organic Frameworks for Water Harvesting from Air. *Adv. Mater.* **2018**, *30*, 1704304.

(32) Hanikel, N.; Prévot, M. S.; Yaghi, O. M. MOF water harvesters. *Nat. Nanotechnol.* **2020**, *15*, 348–355.

(33) Vlugt, T. J. H.; García-Pérez, E.; Dubbeldam, D.; Ban, S.; Calero, S. Computing the Heat of Adsorption using Molecular Simulations: The Effect of Strong Coulombic Interactions. *J. Chem. Theory Comput.* **2008**, *4*, 1107–1118.

(34) Riera, M.; Knight, C.; Bull-Vulpe, E. F.; Zhu, X.; Agnew, H.; Smith, D. G. A.; Simmonett, A. C.; Paesani, F. MBX: A many-body energy and force calculator for data-driven many-body simulations. *J. Chem. Phys.* **2023**, *159*, 054802.

(35) Vandenbrande, S.; Verstraelen, T.; Gutiérrez-Sevillano, J. J.; Waroquier, M.; Van Speybroeck, V. Methane Adsorption in Zr-Based MOFs: Comparison and Critical Evaluation of Force Fields. *J. Phys. Chem. C* **2017**, *121*, 25309–25322.

Paper XI

Design of a tunable mixed matrix membrane platform for high-performance gas separations

X. Tan, S. Robijns, A. Lamaire, R. Goeminne, N. De Witte, M. Dickmann, R. Verbeke, T. Van der Donck, D. Van Havere, R. de Oliveira Silva, Q. Ke, Y. Li, R. Thür, I. Aslam, C. Van Goethem, T. Donckels, D. Sakellariou, V. Van Speybroeck, T. Van Assche, M. Dusselier, I. Vankelecom

Manuscript in revision

A. Lamaire and R. Goeminne performed all simulations and contributed to the analysis, discussion, and interpretation of the results and the writing of the manuscript. The force field and *ab initio* simulations were performed by A. Lamaire, whereas the MLP simulations were performed by R. Goeminne.

Design of a tunable, high-performance mixed matrix membrane platform for gas separations

Authors: Xiaoyu Tan[1]†, Sven Robijns[2]†, Aran Lamaire[3], Ruben Goeminne[3], Niels De Witte[4], Marcel Dickmann[5], Rhea Verbeke[1], Tom Van der Donck[6], Daan Van Havere[1], Rodrigo de Oliveira Silva[1], Quanli Ke[2]‡, Yun Li[1], Raymond Thür[1]‡‡, Imran Aslam[1], Cédric Van Goethem[1], Thibaut Donckels[2], Dimitrios Sakellariou[1], Veronique Van Speybroeck[3], Tom Van Assche[4], Michiel Dusselier[2]*, Ivo Vankelecom[1]*

Affiliations:

[1]Membrane Technology Group (MTG), cMACS division, Faculty of Bioscience Engineering, KU Leuven; Celestijnenlaan 200F, 3001 Leuven, Belgium.

[2]Center for Sustainable Catalysis and Engineering, KU Leuven; Celestijnenlaan 200F, 3001 Leuven, Belgium.

[3]Center for Molecular Modeling, Ghent University; Tech Lane Ghent Science Park, Technologiepark 46, Zwijnaarde, 9052, Belgium.

[4]Department of Chemical Engineering, Vrije Universiteit Brussel; Pleinlaan 2, 1050 Brussels, Belgium.

[5]Heinz Maier Leibnitz Zentrum, Technische Universität München; Lichtenbergstraße 1, Garching, 85748, Germany.

[6]Department of Materials Engineering, KU Leuven; Kasteelpark Arenberg 44, 3001 Leuven, Belgium.

‡Present address: Institute of Catalytic Reaction Engineering, Zhejiang University of Technology; Hangzhou 310014, China.

‡‡ Present address: Agfa-Gevaert NV, Septestraat 27, 2640 Mortsel, Belgium

†These authors contributed equally to this work.

*Corresponding author. Email: ivo.vankelecom@kuleuven.be, michiel.dusselier@kuleuven.be

Summary: Membrane technology could offer substantial economic and environmental benefits for energy-intensive chemical separations. Chabazite-type zeolites, possessing a 3-dimensional channel system with molecular-sieving windows, would be an ideal membrane material, but conditions to synthesize zeolite-only membranes limit optimization strategies. Guided by advanced quantum chemistry calculations on inner-pore molecular interactions, zeolite properties were tailored for different separations and optimised particles incorporated in polyimide at very high loadings. A membrane platform was thus created that largely outperforms state-of-the-art membranes for a broad variety of industry-relevant applications, i.e. carbon capture, natural gas/biogas purification, hydrocarbon and hydrogen recovery. Accurate size-sieving of gas molecules was realized together with rational determination of optimal gas-zeolite interactions. Crucial for industrial applications, these well-tuned membranes displayed excellent non-ageing properties and high flexibility, presented higher mixed-gas selectivities than ideal-gas selectivities, performed even better at low CO_2-partial pressures, and can be made humidity-insensitive.

Introduction

Chemical separations account for 10-15% of the global energy consumption, especially gas separations are particularly challenging and energy-intensive (*1*). Compared to conventional technologies, membrane technology offers a more sustainable alternative, owing to its low energy consumption, small footprint and modular design (*2, 3*). To develop next-generation gas separation membranes, materials that combine molecular-sieving with specific chemical interactions are crucial (*4-9*). However, understanding and manipulating the interaction environment in angstrom-sized porous systems for membranes remains challenging (*10*). The SSZ-13 zeolite (CHA-type) possesses a long-range-ordered 3-dimensional channel system with 3.72 Å windows, exactly located in the range of the kinetic diameters of gases. CHA's gas sorption and transport properties can be readily manipulated via its Si/Al ratio and counterions (*11-13*). CHA excellently separates gases in adsorption processes or as zeolite-only membranes (*14-24*) for natural gas purification, CO_2 capture, syngas treatment, air separation, hydrogen production, and volatile radionuclide separations. However, CHA with a low Si/Al is difficult to prepare as a defect-free zeolite-only film, and CHA with a high Si/Al (>80) does not allow for a proper tuning of selective inner-pore interactions (*25-31*).

To surpass these limitations and fully exploit the potential of this promising type of zeolite, CHA particles were synthesized covering a broad range of Si/Al ratios (~3 to +∞) with different counterions. When subsequently loaded in polymers to form mixed matrix membranes (MMMs), CHA's superior separation properties can be combined with the processibility and flexibility of polymeric membranes. By closely integrating well-designed experimental and computational studies (*32, 33*), manifold possibilities for various size and polarity-based gas separations were reached and membranes with systematically tuned performances were engineered. Essential for the full expression of these properties in the MMM is a high filler loading. Compared to our last report (*34*), by thoroughly optimizing the membrane fabrication strategy, zeolite loadings are now further increased to 60-65wt.%. This leads to a pronounced quasi-continuous zeolite phase across the flexible polymer matrix for the cubic CHA, hence obtaining ultra-permeable and ultra-selective gas pathways with remarkable non-ageing properties. More importantly, in contrast to the earlier reported platelet-shaped SSZ-39 zeolite, CHA zeolites are already commercially exploited (*35, 36*), which makes the CHA-MMMs not only a tunable high-performance membrane platform for various industrial applications but also an economical and practical option for scaling up, hence amplifying potential impact.

Zeolite and membrane characterizations

Highly crystalline, pure CHA zeolites (Fig. S9) with different Si/Al and counterions were synthesized according to modified literature recipes (*37-40*), possessing the micropore volumes of 0.25~0.3 cm^3/g (Fig. S22−S24, Table S3). This value, comparable to the maximal accessible volume, suggests a nearly-perfect 3D-connected channel system. The elemental analysis (Table S2, Fig. S66−S71, Table S19) confirmed the counterion loadings and Si/Al ratios of 3, 5, 10, +∞ (pure silica) of the lab-synthesized zeolites, and a Si/Al=16 for the commercial sample. Zeolite particles were oblate-shaped (CHA-3), spherical-shaped (CHA-5) and cubic-shaped (CHA-10, Si-CHA) (Fig. 1A-1D) with different sizes (0.5–5 μm). Sorption isotherms of CO_2, CH_4, O_2, N_2, Ar and H_2 were measured for Na-CHA-10 at 25°C (Fig. 2D). A sharply rising CO_2 isotherm together with a theoretical maximum CO_2 uptake of 7.36 mmol/g were confirmed (Table S6), attributed to its high CO_2-philicity, thus showing an outstanding capacity for CO_2 capture (*41*). Consistent with literature (*12, 42*), the Na-CHA-10 presents an adsorption capacity decrease in the order of $CO_2 \gg CH_4 > N_2$, while the adsorption capacities of N_2, O_2 and Ar are very similar. As expected, a very low H_2 gas uptake is observed, due to the limited interaction of H_2 with the framework.

MMMs were prepared with CHA via a solution-casting strategy, reaching high zeolite loadings up to 60−65wt.% (Fig. S13−S14). Zeolite crystallinity was preserved in the MMMs after all synthesis steps (Fig. S11) and no chemical changes of the MMM were observed during the membrane preparation (Fig. S19−S21, Fig. S78−S81). Thermal analysis further indicated good polymer-zeolite interactions in the MMM:the glass transition temperature of the polymer matrix increased from 314°C to 325°C with CHA

loading (Fig. S12), pointing towards 'wrapping' of the zeolite by polymer and rigidification of the polymer chains regardless the size (<5μm in this work), shape or Si/Al of the CHA filler. CO_2, CH_4 and N_2 sorption experiments on the annealed unfilled membrane and the 60wt.% Na-CHA-10 MMM denoted a substantially higher gas uptake for the MMMs than the unfilled Matrimid (Fig. S35).

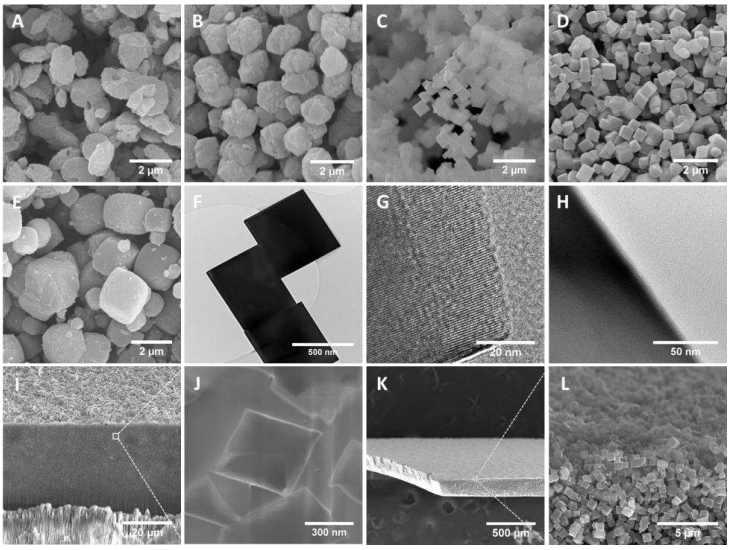

Figure 1. Visualization of CHA zeolites and CHA-MMMs: (**A-E**). lab-synthesized CHA zeolites (from A to D: Si/Al=3, 5, 10, +∞) presenting various sizes and shapes; (**E**). a commercial CHA zeolite (Si/Al=16) with a less regular size and shape than lab-synthesized samples; (**F-G**). cubic-shaped Na-CHA-10 with a high crystallinity; (**H**). 70-nm sectioning of a thermal-annealed Na-CHA-10 MMM, where the dark part is the zeolite and the light part is the polymer matrix, indicating a defect-free zeolite-polymer interface; (**I-J**). cross-section of a 60wt.% thermal-annealed Na-CHA-10 MMM, presenting a defect-free zeolite-polymer interface and high zeolite loading; (**K-L**). an oxidized 60wt.% Na-CHA-10 MMM, with all polymer removed, revealing a self-standing zeolite-only film. (details in SI)

Quasi-continuous, defect-free zeolitic percolation highway

Full removal of the polymer by oxidative treatment at 800°C (Fig. S51) led to a remarkably stable zeolite-only film with a thickness similar to the unoxidized MMM (Fig. 1K−1L, S52−S56), thus demonstrating an ultra-high zeolite loading in a random packing. In addition, the cross-section image of the MMM (Fig. 1I−1J, S45−S50) also indicates that the CHA zeolites are non-aligned, but closely packed within the polymer matrix. This quasi-continuous CHA zeolite phase across the MMM thus creates a selective 'percolation highway' (Fig. 4A) to allow fast and highly selective transport of targeted gas molecules (*34*).

The free volume and atomic-level defects (0.1−1 nm) of the MMM were quantified via positron annihilation lifetime spectroscopy (PALS, Fig. S27−S32) and the voids (>1 nm) at the zeolite/polymer interface were investigated by high-resolution electron microscopes (Fig. 1H-1J). All showed an effective elimination of defects by thermal annealing and thus a good zeolite-polymer interface. According to PALS, two types of free-volume elements appear in the MMM and the overall free volume of MMMs slightly decreased after thermal annealing (Table S5). The bigger free-volume elements of the MMM (mean radius of 0.37 nm) originate from the CHA filler. The smaller free-volume elements (mean radius of 0.12-0.14 nm) probably point to the polymer-filler interfaces, which are smaller than the kinetic diameter of gas molecules, and thus won't impact the gas separations.

Tuning of the inner-pore molecular interactions

Intermolecular interactions within CHA pronouncedly influence the gas transport of the MMM, where Al-content and associated counterions play decisive roles. Particularly, with increasing Al-content (more

charge-balancing counterions), the affinity of CHA for gas molecules is enhanced through stronger (di- or quadru)polar interactions (*12, 20, 33*). To manipulate these interactions, Na^+-exchanged CHA (Na-CHA) samples with Si/Al = 3, 5, 10, +∞ were synthesized (Fig.1A-1D) for 50 wt.% CHA-MMMs preparation. For equimolar CO_2/CH_4 at 25°C/2 bar, Na-CHA-3 MMM showed a CO_2 permeability of ~30 Barrer and a CO_2/CH_4 selectivity of ~68, i.e. a much lower performance than its higher Si/Al counterparts (Fig. 2A). Na-CHA-5 MMM presented an improved permeability of ~350 Barrer and selectivity of 135, whereas the Na-CHA-10 MMM obtained >2100 Barrer (i.e. >70-times more permeable than Na-CHA-3 MMM), and a selectivity >230. Interestingly, CHA-MMMs with Si/Al>10 again presented declined separation performance, where the Si-CHA MMM exhibited a CO_2 permeability of ~1140 Barrer and a selectivity of ~170. The equimolar CO_2/N_2 mixed-gas separations with these MMMs further confirmed this trend for CO_2 permeabilities (Fig. 2B). While the selectivity difference between Na-CHA-5 and Na-CHA-10 MMMs was small (~55), and Na-CHA-3 MMM showed a relatively low selectivity (~45) because of its hindered CO_2 permeation pathway, Si-CHA MMMs presented a sharp selectivity drop to ~33 due to the absence of Al, causing weakened competitive sorption between CO_2 and N_2. The Na-CHA-10 MMM thus presented superior CO_2 separation performances over all others.

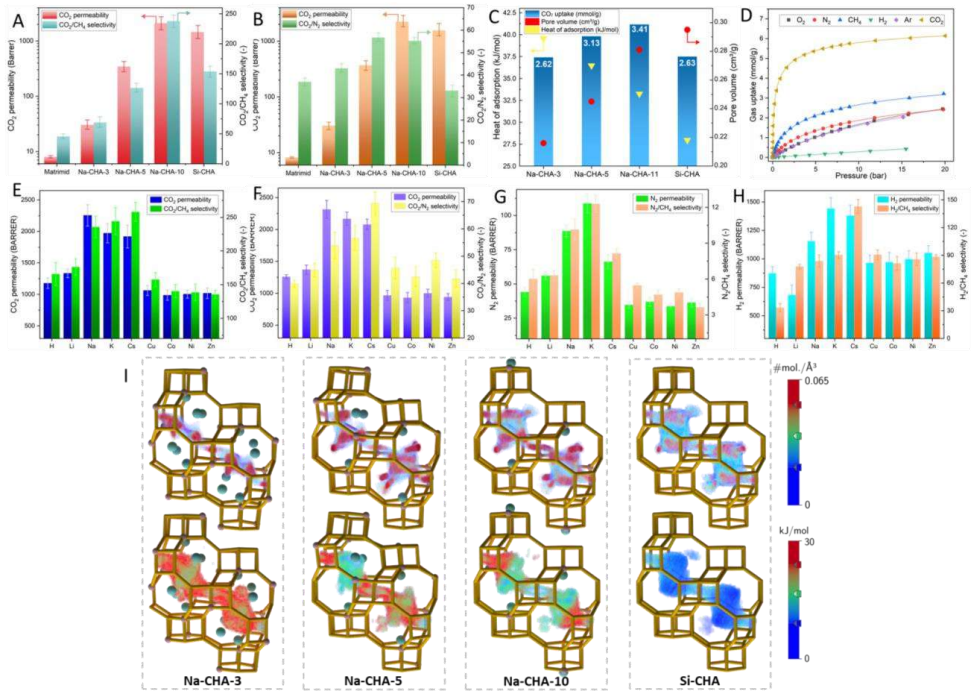

Figure 2. Influence of interaction environment in CHA and CHA-MMMs performances: (**A-B**). Equimolar CO_2/CH_4 and CO_2/N_2 separation performances for unfilled Matrimid and 50 wt.% Na-CHA-3, Na-CHA-5, Na-CHA-10 and Si-CHA MMMs under 25°C/2 bar; (**C**). CO_2 uptake, micropore volume and heat of CO_2 adsorption for Na-CHA-3, Na-CHA-5, Na-CHA-11, Si-CHA zeolites under 25°C/1 bar via simulation; (**D**). H_2, Ar, O_2, N_2, CO_2 and CH_4 adsorption isotherms of Na-CHA-10 zeolite under 25°C; (**E-H**). gas separation performances of 50 wt.% CHA-10 MMMs with different counterions (H^+, Li^+, Na^+, K^+, Cs^+, Cu^{2+}, Co^{2+}, Ni^{2+}, Zn^{2+}) for equimolar mixed-gas CO_2/CH_4 separation, CO_2/N_2 separation, N_2/CH_4 separation and ideal-gas H_2/CH_4 separation; (**I**). CO_2 adsorption isosurface plots (upper) and CO_2 diffusion free energy profiles (bottom) for Na-CHA-3, Na-CHA-5, Na-CHA-11 and Si-CHA at 25°C/1 bar via GCMC and MD simulations, where the higher density areas and high diffusion energy areas are indicated in red and the lower ones by blue. (detail in SI)

To understand the influence of the Si/Al ratio, the inner-pore molecular interactions were simulated using a machine learning potential with a first-principles accuracy (*43*). The largest CO_2 uptake was obtained for Na-CHA-11 (Na^+/cage=1), which can be rationalized based on the opposite trends for the heat of adsorption

and the pore volume as a function of the Si/Al (Fig. 2C). When the Na^+-content exceeds two Na^+/cage (e.g. Na-CHA-3), the viable gas diffusion pathways decrease, as diffusion through some windows is hindered by the presence of Na^+ (Fig. 2I). Furthermore, the free energy barriers to diffuse between cages also increase with Na^+-content, due to its high CO_2 affinity. Fig. 2I displays the free energy barriers for the diffusion of a single CO_2 molecule through a window. In Na-CHA-11, the surrounding of a Na^+ represents a region of low free energy, implying a high probability of encountering a CO_2 molecule in that region. Due to the high CO_2-Na^+ affinity, the CO_2 molecule is less likely to reside in Na^+-free regions. Therefore, in Na-CHA-11, preferential diffusion pathways connect Na^+ along windows. For lower Si/Al, strong CO_2-Na^+ interactions eliminate the diffusion pathways with a low free energy barrier (Fig. S39), further reducing the CO_2 mobility, as observed by the sharp permeability drop of relevant CHA-MMMs. Additionally, calculated CO_2 diffusion coefficients (Table S18) exhibit a monotonic decrease of two orders of magnitude from Si-CHA to Na-CHA-3.

Counterion nature, location and amount (*33*) strongly define interaction potentials and pore morphologies. The counterion loading influences the pore volume profoundly for low Si/Al zeolites, but no significant pore volume change is observed in CHA-10 since it only hosts a limited number of counterions (Table S3). The interaction strength is in general inversely proportional to the charge density or ionic radius of the counterion. Only H^+ is an exception being strongly shielded by the zeolite framework. This finally leads to the following rank in interaction potentials: divalent counterions$\gg Li^+ > Na^+ > K^+ > Cs^+ > H^+$ (*12, 19, 44*).

The role of counterions was studied by comparing the performance of 50wt.% CHA-10 MMMs including monovalent and divalent ones (H^+, Li^+, Na^+, K^+, Cs^+, Cu^{2+}, Ni^{2+}, Zn^{2+}, Co^{2+}). Their mixed-gas (CO_2/CH_4, CO_2/N_2, N_2/CH_4) and ideal-gas (H_2/CH_4) separation results at 25°C are shown in Fig. 2E-2H. Interestingly, even for CHA-10 MMMs, a higher interaction potential is not always beneficial to gas permeation. For CO_2–related separations, the CO_2 permeability follows the order $Na^+ > K^+ > Cs^+ > Li^+ > H^+$>divalent cation forms, because the CO_2–philicity of CHA-10 follows the order of $Na^+ > K^+ > Cs^+ > H^+$. Excessive interaction potentials of Li^+ and divalent counterions (Cu^{2+}, Ni^{2+}, Zn^{2+}, Co^{2+}) thus impair gas transport. For H_2 and N_2 permeation, K-CHA-10 MMM presents the highest gas flux, attributed to preferential interaction, and the Cs-CHA-10 MMM shows the best CO_2/CH_4, CO_2/N_2 and H_2/CH_4 selectivity, probably due to the large size of Cs^+. Overall, Na^+, K^+, Cs^+ loaded CHA-10 MMMs present better permeability-selectivity combinations for gas pairs than stronger or weaker interacting counterions, indicating an ideal, intermediate interaction potential for optimal gas permeation and competitive adsorption properties. Among them, Na-CHA-11 possesses a calculated heat of CO_2 adsorption of ~33 kJ/mol, pointing to an optimal interaction range for high-performance membrane development.

Ultrafast and precise gas separations

Comprehensive gas permeation testing was conducted for CHA-MMMs with different Si/Al and counterions. Ideal-gas permeabilities of 60wt.% Na-CHA-10 MMM are plotted as a function of the kinetic diameter of the gases in Fig. 3A, clearly presenting the pivotal role of both size exclusion and interaction aspects, specifically for CO_2. Based on physisorption and ideal-gas permeations, solubilities and diffusivities of H_2, Ar, CO_2, O_2, N_2 and CH_4 were calculated for the 60wt.% Na-CHA-10 MMM (Table S16). Compared to the unfilled membrane, the MMM displayed a 170-fold greater CO_2 diffusivity, whereas the CH_4 diffusivity increased 19-fold only. The pronounced enhancement of CO_2/CH_4 diffusivity selectivity thus clearly demonstrates the sharp size-sieving mechanism.

Because the window size of CHA (3.72 Å) is in-between the kinetic diameter of hydrocarbons and light gases, CHA-MMMs present great opportunities for such separations (Fig. 3). For instance, the 60wt.% Na-CHA-10 MMM shows stunning ideal selectivities: CO_2/C_3H_8 >6500, CO_2/C_3H_6 ~5000, CO_2/C_2H_6 >1400, CO_2/C_2H_4 ~280, together with an ideal CO_2 permeability of ~7300 Barrer (1 bar/25°C). This makes it an outstanding candidate to recover hydrocarbons from e.g. CO_2 hydrogenation processes (*45, 46*). Another potential application could be hydrocarbon recovery in polyolefin production, where N_2 should be removed. 60 wt.% Na-CHA-10 MMM exhibits impressive ideal selectivities: N_2/C_3H_8 ~330, N_2/C_3H_6 ~250, N_2/C_2H_6 ~70, N_2/C_2H_4 ~15, N_2/CH_4 ~10, combined with an ideal N_2 permeability >370 Barrer (1bar/25°C). 60 wt.%

Na-CHA-10 MMM also presents attractive industry-relevant H_2/CH_4 separation performance, where the ideal selectivity reaches ~90 and H_2 permeability >3800 Barrer (1 bar/25°C).

In addition to the dominant role of size-exclusion, strong competitive adsorption of CHA also enhances separation performance, thus the mixed-gas selectivities of CHA-MMMs were significantly higher than their ideal-gas selectivities for separations involving polar gases. This feature can be attributed to the strong competitive sorption of polar gas molecules (such as CO_2) in the CHA filler (*32*). For example, thanks to the high CO_2–philicity of CHA, strongly adsorbing CO_2 occupies the adsorption sites of CHA, making zeolite channels partly inaccessible to weakly adsorbing gases like CH_4, N_2, O_2, thus inhibiting their permeation and improving selectivity.

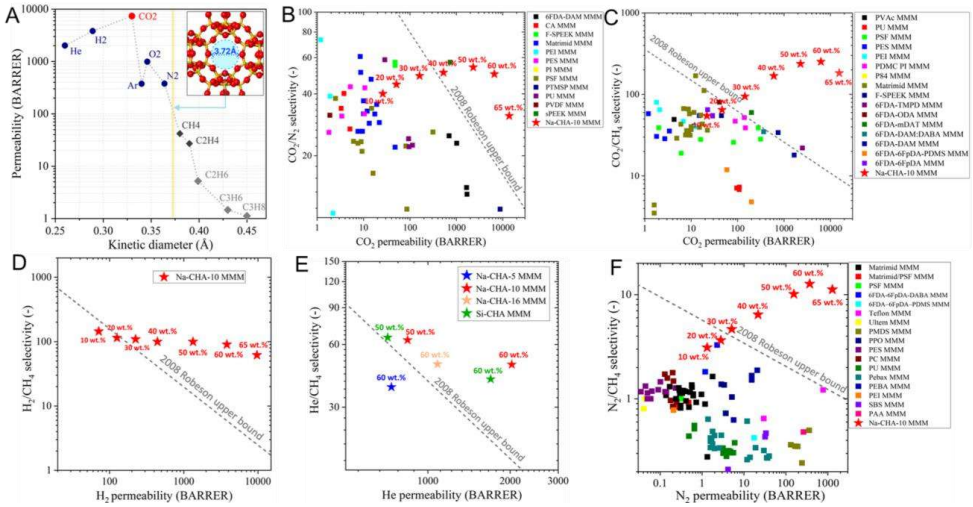

Figure 3. Gas separation performance for CHA-MMMs: (**A**). ideal-gas permeabilities of 60 wt.% Na-CHA-10 MMM for gases with different sizes and polarities. A clear size-sieving effect by the window of CHA and preferential diffusion of polar gases, like CO_2, are observed; (**B**). mixed-gas CO_2/N_2 separation of Na-CHA-10 MMMs; (**C**). mixed-gas CO_2/CH_4 separation of Na-CHA-10 MMMs; (**D**). ideal-gas H_2/CH_4 separation of Na-CHA-10 MMMs; (**E**). ideal-gas He/CH_4 separation by high-loading CHA-MMMs; (**F**). mixed-gas N_2/CH_4 separation of Na-CHA-10 MMMs.

For example, for the 60 wt.% Na-CHA-10 MMM, the CO_2/CH_4 ideal-gas selectivity was ~175 (1 bar/25°C), whereas its equimolar CO_2/CH_4 mixed-gas selectivity reached >250 with a CO_2 permeability up to 6200 Barrer (2 bar/25°C). Likewise, the CO_2/N_2 ideal-gas selectivity at 1 bar/25°C was ~20, while its mixed-gas selectivity (2 bar/25°C) increased to 50 together with a CO_2 permeability of ~7000 Barrer (Fig. 3B). When depicted on selectivity-permeability trade-off plots, the Na-CHA-10 MMMs largely surpass several Robeson upper bounds, such as for CO_2/CH_4, CO_2/N_2, H_2/CH_4, N_2/CH_4, He/CH_4 (Fig. 3) and presents good potential for many other industry-relevant separations (CO_2/olefins, H_2/hydrocarbons, N_2/hydrocarbons, CO_2/O_2).

With increasing temperature (Fig. S38), the CHA affinity decreases for most gases (*12, 32*). The reduced adsorption lowers gas permeability and selectivity. For instance, both Na-CHA-10 and Si-CHA MMMs exhibit reduced CO_2 permeability and CO_2/CH_4 selectivity when the temperature increases from 25°C to 65°C. However, with lower Si/Al ratios of CHA filler, this performance decline is much less pronounced (Table S12). Their strong interaction strength minimizes affinity loss and allows MMMs to work at higher-temperature applications. Moreover, thanks to its high CO_2-philicity, the CHA filler could get quasi-saturated with CO_2 at low pressure, Na-CHA-10 MMMs thus exhibit enhanced performance in feeds with low CO_2 partial pressures (as found in many industrial applications), where the CO_2/CH_4 selectivity could reach 310 with a CO_2 permeability ~8000 Barrer (Table S14).

Towards industrial applications

Both CHA and Matrimid are commercially available, hence making CHA-MMMs a particularly promising candidate for large-scale, industrial applications. A commercial zeolite (Na-CHA-16, Fig. 1E) was utilized for MMM preparation up to 60wt.% zeolite loading (Fig. S64) and sizes up to ~19 cm (Fig. 4B). As expected, due to its lower pore volume (Table S3, Fig. S36) and imperfect particle size distribution, for equimolar CO_2/CH_4 separation, the 50wt.% Na-CHA-16 MMM gives a lower CO_2 permeability (~400 Barrer) and selectivity (~100) than its lab-made counterparts, but still clearly surpasses the current state-of-the-art. Importantly, CHA-MMMs retain the desired flexibility that should allow for module construction (Fig. 4C), and excellent non-aging properties were observed with consistent CO_2/CH_4 selectivity and CO_2 permeability one year after preparation.

In industrial applications, impurities may cause severe membrane performance decline. The most common impurity, H_2O, with its high dipole moment, exhibits a far stronger affinity for CHA than CO_2, CH_4 or N_2, thus pushing them away from the adsorption site. Outperforming all other CHA-MMMs (Fig. 4D), the Si-CHA MMM presents outstanding anti-moisture properties for CO_2/CH_4 separation: quasi-consistent gas permeability and selectivity were maintained in wet conditions (Table S10-S11). This arises from the absence of counterions in Si-CHA, preventing strong competitive adsorption of H_2O and making them particularly interesting for industrial applications with polar impurities.

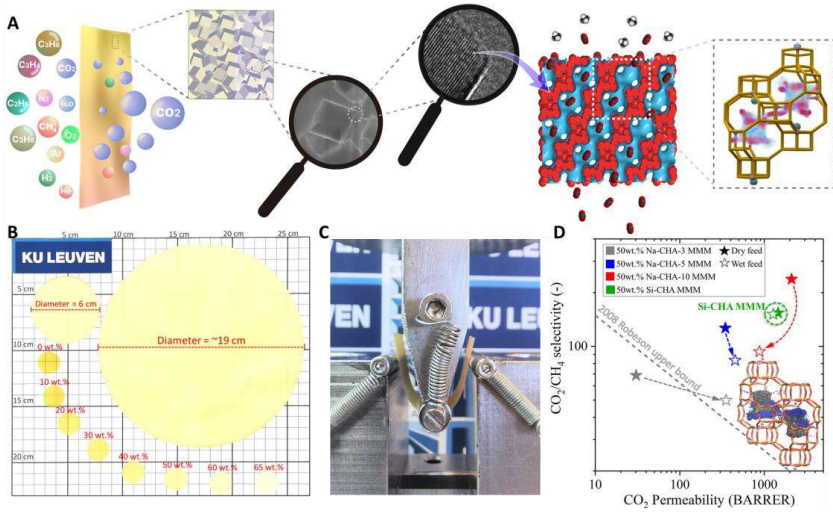

Figure 4. Characterization and illustrations of CHA-MMMs: (A). Schematic illustration of CHA-MMMs for gas separations, with a zeolitic percolation highway across the membrane and unhindered gas permeation through tunable, size-sieving fillers; **(B)** Appearance of Na-CHA-10 MMMs, up to 65wt.% zeolite loading (diameter of 2 cm), and 50wt.% Na-CHA-16 MMMs with diameters of 6 cm and 19 cm. **(C).** The flexibility of a 50 wt.% Na-CHA-16 MMM; **(D)**. Equimolar CO_2/CH_4 separations for 50wt.% CHA-MMMs for both wet (relative humidity=70%) and dry feeds under 25°C/2 bar, plotted with the 2008 Robeson upper bound, proving the anti-moisture properties of Si-CHA MMM. Insert image: adsorption density plot of Na-CHA-11 for the competitive adsorption of H_2O and CO_2 in GCMC simulations (under 25°C/1 bar).

References

1. D.S. Sholl, R. P. Lively, Seven chemical separations. *Nature* **532**, 435–437 (2016). https://doi.org/10.1038/532435a
2. R. W. Baker, Membrane Technology and Applications (JohnWiley & Sons, Inc., ed. 3, Hoboken, NJ, 2012).
3. S. P. Nunes, K.-V. Peinemann, *Membrane Technology: In the Chemical Industry* (Wiley-VCH, ed. 2, Weinheim, Germany, 2006).
4. R. W. Baker, B. T. Low, Gas Separation Membrane Materials: A Perspective. *Macromolecules* **47**, 6999–7013 (2014). https://doi.org/10.1021/ma501488s
5. W. J. Koros, C. Zhang, Materials for next-generation molecularly selective synthetic membranes. *Nat. Mater.* **16**, 289–297 (2017). doi:10.1038/nmat4805
6. S. Zhou, O. Shekhah, A. Ramírez, et al. Asymmetric pore windows in MOF membranes for natural gas valorization. *Nature* **606**, 706–712 (2022). https://doi.org/10.1038/s41586-022-04763-5
7. G. Liu et al., Mixed matrix formulations with MOF molecular sieving for key energy-intensive separations. *Nat. Mater*. **17**, 283-289 (2018). https://doi.org/10.1038/s41563-017-0013-1
8. M. Jeon, D. Kim, P. Kumar, et al. Ultra-selective high-flux membranes from directly synthesized zeolite nanosheets. *Nature* 543, 690–694 (2017). https://doi.org/10.1038/nature21421
9. K. Hazazi, Y. Wang, B. Ghanem, et al. Precise molecular sieving of ethylene from ethane using triptycene-derived submicroporous carbon membranes. *Nat. Mater.* 22, 1218–1226 (2023). https://doi.org/10.1038/s41563-023-01629-7
10. R. Krishna and J. M. Van Baten. Highlighting the anti-synergy between adsorption and diffusion in cation-exchanged Faujasite zeolites. *ACS Omega* **7**, 13050−13056 (2022). https://doi.org/10.1021/acsomega.2c00427
11. Ch. Baerlocher, L. B. McCusker, Database of Zeolite Structures (2017); http://www.iza-structure.org/databases
12. T. D. Pham, Q. Liu, R. F. Lobo, Carbon dioxide and nitrogen adsorption on cation-exchanged SSZ-13 zeolites. *Langmuir* **29**, 832–839 (2013). https://doi.org/10.1021/la304138z
13. M. Dusselier, M. E. Davis, Small-Pore Zeolites: Synthesis and Catalysis. *Chem. Rev.* **118**, 5265–5329 (2018). doi:10.1021/acs.chemrev.7b00738
14. X. Wang et al., High-silica CHA zeolite membrane with ultra-high selectivity and irradiation stability for Krypton/xenon separation. *Angew. Chem*. **133**, 9114–9119 (2021). https://doi.org/10.1002/anie.202100172
15. M. Debost et al., Synthesis of discrete CHA zeolite nanocrystals without organic templates for selective CO_2 capture. *Angew. Chem*. **132**, 23697–23701 (2020). https://doi.org/10.1002/anie.202009397
16. J. Yang et al., K-chabazite zeolite nanocrystal aggregates for highly efficient methane separation. *Angew. Chem. Int. Ed*. **61**, 23491–23495 (2021). https://doi.org/10.1002/anie.202116850
17. M. R. Hudson et al., Unconventional, highly selective CO_2 adsorption in zeolite SSZ-13. *J. Acm. Chem. Soc.* **134**, 1970–1973 (2012). https://doi.org/10.1021/ja210580b
18. D. Fu, Y. Park, M. E. Davis, Zinc containing small-pore zeolites for capture of low concentration carbon dioxide. *Angew. Chem. Int. Ed.* **61**, e202112916 (2021). https://doi.org/10.1002/anie.202112916

19. M. Sun, Q. Gu, A. Hanif, T. Wang, J. Shang, Transition metal cation-exchanged SSZ-13 zeolites for CO_2 Capture and separation from N_2. *Chem. Eng. J.* **370**, 1450–1458 (2019). https://doi.org/10.1016/j.cej.2019.03.234

20. J. Shang, G. Li, R. Singh, Q. Gu, K. M. Nairn, T. J. Bastow, N. Medhekar, C. M. Doherty, A. J. Hill, J. Z. Liu, P. A. Webley, Discriminative separation of gases by a "molecular trapdoor" mechanism in chabazite zeolites. *J. Acm. Chem. Soc.* **134**, 19246–19253 (2012). doi:10.1021/ja309274y

21. M. Miyamoto, Y. Fujioka, K. Yogo, Pure silica CHA type zeolite for CO_2 separation using pressure swing adsorption at high pressure. *J. Mater. Chem.* **22**, 20186–20189 (2012). doi:10.1039/c2jm34597h

22. Y. Zheng, N. Hu, H. Wang, N. Bu, F. Zhang, R. Zhou, Preparation of steam-stable high-silica CHA (SSZ-13) membranes for CO_2/CH_4 and C_2H_4/C_2H_6 separation. *J. Memb. Sci.* **475**, 303–310 (2015). doi:10.1016/j.memsci.2014.10.048

23. B. Wang, Y. Zheng, J. Zhang, W. Zhang, F. Zhang, W. Xing, R. Zhou, Separation of light gas mixtures using zeolite SSZ-13 membranes. *Microporous Mesoporous Mater.* **275**, 191–199 (2019). doi:10.1016/j.micromeso.2018.08.032

24. K. Kida, Y. Maeta, K. Yogo, Preparation and gas permeation properties on pure silica CHA-type zeolite membranes. *J. Memb. Sci.* **522**, 363–370 (2017). doi:10.1016/j.memsci.2016.09.002

25. T. D. Pham, R. F. Lobo, Adsorption equilibria of CO_2 and small hydrocarbons in AEI-, CHA-, STT-, and RRO-type siliceous zeolites. *Microporous Mesoporous Mater.* **236**, 100-108 (2016). doi:10.1016/j.micromeso.2016.08.025

26. B. Wang, Y. Wang, X. Li, S. Zhong, R. Zhou, Highly CO_2-selective and moisture-resistant bilayer silicalite-1/SSZ-13 membranes with gradient pores for wet CO_2/CH_4 and CO_2/N_2 separations. *J. Memb. Sci.* **636**, 119565 (2021). doi:10.1016/j.memsci.2021.119565

27. D. H. Olson, M. A. Camblor, L. A. Villaescusa, G. H. Kuehl, Light hydrocarbon sorption properties of pure silica Si-CHA and ITQ-3 and high silica ZSM-58. *Microporous Mesoporous Mater.* **67**, 27–33 (2004). doi:10.1016/j.micromeso.2003.09.025

28. Y. Li, H. Yi, X. Tang, F. Li, Q. Yuan, Adsorption separation of CO_2/CH_4 gas mixture on the commercial zeolites at atmospheric pressure. *Chem. Eng. J.* **229**, 50–56 (2013). doi:10.1016/j.cej.2013.05.101

29. F. Hirosawa, M. Miyagawa, H. Takaba, Selectivity enhancement by the presence of grain boundary in chabazite zeolite membranes investigated by non-equilibrium molecular dynamics. *J. Memb. Sci.* **632**, 119348 (2021). doi:10.1016/j.memsci.2021.119348

30. N. Kosinov, C. Auffret, G. J. Borghuis, V. G. P. Sripathi, E. J. M. Hensen, Influence of the Si/Al ratio on the separation properties of SSZ-13 zeolite membranes. *J. Memb. Sci.* **484**, 140–145 (2015). https://doi.org/10.1016/j.memsci.2015.02.044

31. R. Rangnekar, N Mittal, B. Elyassi, J. Caro, M. Tsapatsis, Zeolite membranes - a review and compatison with MOFs. *Chem. Soc. Rev.* **44**, 7128-7154 (2015). https://doi.org/10.1039/C5CS00292C

32. F. N. Ridha, P. A. Webley, Entropic effects and isosteric heats of nitrogen and carbon dioxide adsorption on chabazite zeolites. *Microporous and Mesoporous Mater.* **132**, 22–30 (2010). https://doi.org/10.1016/j.micromeso.2009.07.025

33. T. D. Pham, M. R. Hudson, C. M. Brown, R. F. Lobo, Molecular basis for the high CO_2 adsorption capacity of chabazite zeolites. *ChemSusChem*. **7**, 3031–3038 (2014). doi:10.1002/cssc.201402555

34. X. Tan, et al. Truly combining the advantages of polymeric and zeolite membranes for gas separations. *Science* **378**, 1189-1194 (2022). https://www.science.org/doi/10.1126/science.ade1411

35. P. Tian, Y. Wei, M. Ye, Z. Liu. Methanol to Olefins (MTO): From Fundamentals to

Commercialization. *ACS. Cat.* **5**, 1922-1938 (2015). https://doi.org/10.1021/acscatal.5b00007

36. L. Han, S. Cai, M. Gao, J.-Y. Hasegawa, P. Wang, J. Zhang, L. Shi, D. Zhang, Selective Catalytic Reduction of NO_x with NH_3 by Using Novel Catalysts: State of the Art and Future Prospect. *Chem. Rev.* **119**, 10916-10976 (2019). https://doi.org/10.1021/acs.chemrev.9b00202

37. J. Diaz-Cabañas, P. A. Barrett, M. A. Camblor, Synthesis and structure of pure SiO_2 chabazite: the SiO_2 polymorph with the lowest framework density. *Chem. Commun.* 1881-1882 (1998). https://doi.org/10.1039/A804800B

38. N. Nakazawa, S. Inagaki, Y. Kubota, Direct Hydrothermal Synthesis of High-silica SSZ-39 Zeolite with Small Particle Size. *Chem. Lett.* **45**, 919–921 (2016). https://doi.org/10.1246/cl.160370

39. T. Nishitoba, T. Nozaki, S. Park, Y. Wang, J. N. Konda, H. Gies, T. Yokoi, CHA-Type Zeolite Prepared by Interzeolite Conversion Method Using FAU and LTL-Type Zeolite: Effect of the Raw Materials on the Crystallization Mechanism, and Physicochemical and Catalytic Properties. *Catalysts*. **10**, 1204 (2020). https://doi.org/10.3390/catal10101204

40. L. Van Tendeloo, E. Gobechiya, E. Breynaert, J. A. Martens, C. E. A. Kirschhock, Alkaline cations directing the transformation of FAU zeolites into five different framework types. *Chem. Commun.* **49**, 11737-11739 (2013). https://doi.org/10.1039/C3CC47292B

41. D. G. Boer, P. P. Pescarmona, Zeolites as Selective Adsorbents for CO_2 Separation. *ACS. Appl. Energy Mater.* **6**, 2634-2656 (2023). https://doi.org/10.1021/acsaem.2c03605

42. R. Kaur, P. Webley, Adsorption of N_2, O_2, and Ar in Potassium Chabazite. *Adsorption.* **11**, 173–177 (2005). https://doi.org/10.1007/s10450-005-5918-3

43. S. Batzner, A. Musaelian, L. Sun, M. Geiger, J.P. Mailoa, M. Kornbluth, N. Molinari, T.E. Smidt, B. Kozinsky, E(3)-equivariant graph neural networks for data-efficient and accurate interatomic potentials. *Nat. Comm.* **13**, 2453 (2022). https://doi.org/10.1038/s41467-022-29939-5

44. J. Zhang, R. Singh, P. A. Webley, Alkali and alkaline-earth cation exchanged chabazite zeolites for adsorption-based CO_2 capture. *Microporous and Mesoporous Mater.* **111**, 478–487 (2008). https://doi.org/10.1016/j.micromeso.2007.08.022

45. A. Álvarez et al., Challenges in the greener production of formates/formic acid, methanol, and DME by heterogeneously catalyzed CO_2 hydrogenation processes. *Chem. Rev.* **117**, 9804–9838 (2017). https://doi.org/10.1021/acs.chemrev.6b00816

46. N. Martin, A. Portillo, A. Ateka, F. G. Cirujano, L. Oar-Arteta, A. T. Aguayo, M. Dusselier. MOF-derived/zeolite hybrid catalyst for the production of light olefins from CO_2. *ChemCatChem.* **12**, 5750-5758 (2020). https://doi.org/10.1002/cctc.202001109

Methods

Materials

Isopropanol (>99.5%) and absolute ethanol (>99.8%), cobalt nitrate hexahydrate (98%+), lithium nitrate (anhydrous, 99%), tetraethyl orthosilicate (TEOS, 99%) and tetraethylammonium hydroxide (pentahydrate) were supplied by Fischer Scientific. Diethyl ether (>99%, stabilized), iodomethane (99%, stabilized), methanol (99.9% for analysis) ammonium nitrate (98%), zinc acetate dihydrate (98%), copper nitrate trihydrate (99%) and chloroform (>99%) were supplied by Acros organics. $NaHCO_3$ (-40+140 mesh) and 40 wt.% colloidal silica suspension (Ludox AS-40) were purchased from Sigma-Aldrich. NaOH (pellets, >98 wt.%), KOH (pellets), acetone (technical) and NaCl (>99%) were purchased from VWR Chemical. Trimethyladamantylamonium hydroxide solution (20 wt.%) was supplied by SACHEM. HF (40 wt% Aq.), nickel nitrate (hexahydrate) and cesium nitrate were ordered with Merck Life Science. FAU zeolite (CBV712, CBV300) was supplied by Zeolyst. Ion exchange resin (Dowex Monosphere 550A UPW) was purchased from Dow Chemical. 3,3'-4,4'-benzophenone tetracarboxylic-dianhydride diaminophenylindane (Matrimid® 5218, M_w = 40000 g/mol) was kindly provided by Huntsman (Switzerland). CO_2 (>99.999%), CH_4 (>99.999%), N_2 (>99.999%), H_2 (>99.999%), O_2 (>99.999%), He (>99.999%), Ar (>99.999%), C_2H_4 (>99.995%), C_2H_6 (>99.995%), C_3H_6 (>99.7%) and C_3H_8 (>99.7%) were purchased from Air Liquide and used as delivered.

Synthesis of zeolites

Pure silica CHA (Si-CHA) was synthesised using a seed-assisted fluorine route similar to Camblor et al. (*37*). To produce the seeds, 13 g of TEOS was hydrolyzed in 31.18 g of a 1 M solution of N,N,N-Trimethyladamantylammonium hydroxide (TMAdamOH). This mixture was left to hydrolise until 31.76 g of water and ethanol had evaporated. 1.33 g of 40 wt.% HF was stirred into the gel, which was transferred into a 25 mL PTFE-lined steel autoclave and placed into a forced convection oven (160 °C) for 4 days. (gel composition: 1 SiO2 : 0.5 TMAdamOH : 0.5 HF : 3 H_2O) To reduce the size of the CHA crystals, the synthesis was repeated after exchanging 10 wt.% of the silica by previously synthesised seeds.

For the synthesis of the CHA zeolites with a Si/Al ratio of ~10, 8.5 g of a 20 wt.% TMAdamOH, 3.75 g of a 20 wt.% NaOH solution and 5.08 g of colloidal silica (LUDOX AS-40) were mixed. The obtained gell is heated in an 80°C water bath under 300 rpm of stirring until approximately 8.5 g of water is evaporated. Next, 0.93 g of FAU (CBV712) is manually stirred into the gel. (gell composition 1 SiO_2 : 0.048 AlO_2 : 0.40 NaOH: 0.18 TMAdamOH: 4.83 H_2O). The PTFE liner is placed into a stainless steel autoclave and heated in a forced convection oven (160 °C, 600 rpm stirring) for 4 days. The CHA with a Si/Al = ~5 was prepared using a slightly modified recipe of Nishitoba et al (*39*). 7.2 g of a 35 wt.% solution of N,N,N,N-Tetraethylammonium hydroxide (TEAOH) was stirred with 0.23 g of deionized water, 2.05 g of a 20 wt.% solution of NaOH and 1.44 g of a 20 wt.% solution of KOH inside of a PTFE liner for several minutes until all reagents were homogeneously dispersed. Finally, 6.06 g of FAU (CBV712) zeolite is added to the mixture. The PTFE liner is capped and inserted into a stainless steel autoclave. Finally, hydrothermal synthesis (160°C) was carried out for 4 days. The chabazite with a Si/Al molar ratio of ~2 was synthesised according to a recipe proposed by Van Tendeloo et al (*40*). 1.33 g of FAU (CBV300) was dissolved in 15.67 g of a 7.24 wt.% aqueous solution of KOH. Next, the mixture was placed into a stainless steel autoclave and left to react at 100 °C for 2 days.

After synthesis, the zeolites were washed at least three times with water by suspending them in 40 mL of MQ water (18.2 mΩ), centrifugation and decantation of the top liquid, until the pH reaches 9 or less. Next, they were dried overnight in an oven at 60°C. Zeolites containing organics after synthesis were subjected to a calcination step before being used in ion exchange. Calcination was carried out in a muffle oven under static air. Zeolites were calcined at 580 °C for 6 h (1 °C/min ramp).

Ion exchange took place in two steps, firstly, the freshly calcined zeolites were exchanged to their NH_4^+-form, and next, they were exchanged to be in their respective (alkali)metal-form. Through direct calcination of this zeolite as described above, the H-form was obtained. For the ammonium exchange, 1 g of zeolite was suspended in 150 mL of a 0.5 M solution of NH_4NO_3 for 24 h. After which the solids are separated by vacuum filtration. Next, for the Na^+ and K^+ exchange, 1 g of zeolite was suspended in 150 mL of a 0.5 M solution of NaCl or KCl respectively. This procedure was repeated three times for 16, 8 and 16 h respectively. For the Li^+, Cs^+, Co^{2+}, Ni^{2+}, Cu^{2+} and Zn^{2+} exchange, a different procedure was followed. 1 g of NH_4^+-form zeolite was suspended in 150 mL of 0.1 M solution of the respective nitrate salt (excluding Zn^{2+}, for which zinc acetate was used). The mixture was homogenised and the pH of the solution was lowered using a dilute solution of nitric acid until the pH reached below 5. Next, the solution was placed into a heating mantle and heated for 2 h at 80 °C under 600 rpm of stirring. After these 2 h, the solution was left to cool to room temperature and the solids were recovered using vacuum filtration. After separation from the exchange solution, all samples were washed with copious amounts of MQ H_2O. Finally, the samples were left to dry overnight at 60 °C. Before use, all the zeolites were calcined one final time (vide supra) to ensure the absence of water during membrane preparation.

Preparation of membranes

Pristine Matrimid membranes were prepared by dissolving 0.30 g of Matrimid (pre-dried 24 h at 100 °C) in 3.98 g of chloroform. After continuously stirring on a magnetic stirring plate for 24 h, this homogeneous 7 wt.% polymer solution was poured into a Teflon Petri dish (d = 6 cm) in a glove bag filled with pure nitrogen. Evaporation of the solvent was slowed down by placing a glass funnel with small opening (diameter funnel = 8 cm; diameter opening = 3 mm, interior volume of the funnel ≈ 100 cm^3) upside down over the Petri dish. The glass funnel generated a quasi-saturated chloroform vapor phase above the polymer solution, thus reducing the solvent evaporation speed. This led to delayed solidification of the membrane film which lasted approximately 4 h. The solidified polymer film was kept in the nitrogen bag for 24 h, removed from the Petri dish and dried naturally for 24 h, before thermal treatment.

Mixed-matrix membranes (MMMs) containing different zeolite loading (10, 20, 30, 40, 50, 60, 65 wt.%) with different zeolites (lab-synthesized Na-CHA-2, Na-CHA-5, Na-CHA-10, Si-CHA, H-CHA-2, H-CHA-5, Zn-CHA-5, H-CHA-10, Li-CHA-10, K-CHA-10, Cs-CHA-10, Co-CHA-10, Ni-CHA-10, Cu-CHA-10, Zn-CHA-10 and commercial H-CHA-16) were prepared. Firstly, a calculated amount of Matrimid was dissolved in chloroform to make a 10 wt.% homogeneous Matrimid solution. Next, a certain amount of the zeolite (calcined for 8 hours under atmosphere at 580 °C before use) was added to 1.2-1.5 g chloroform to make zeolite dispersion. The zeolite dispersion was stirred for 2 h and thoroughly sonicated for 1 h. For each zeolite dispersion, a calculated amount of 10 wt.% Matrimid solution was added. The total mass of zeolite together with polymer in the zeolite/polymer solutions for 10, 20, 30 wt.% MMMs were ~0.4 g, and for 40, 50, 60, 65 wt.% MMMs were 0.5 g. All zeolite/polymer solutions were stirred on a magnetic stirring plate for 10 h, and sonicated twice (1 h per turn) in the beginning and at the middle of the stirring process. The final mixture was cast into a Petri dish (diameter = 6 cm) in a nitrogen bag. The polymer concentration was adjusted to be around 6-8 wt.% to obtain a viscous solution that can be cast but will not suffer much from zeolite precipitation during solvent evaporation. Evaporation of chloroform was slowed down by putting a glass funnel with small opening (diameter funnel = 8 cm; diameter opening = 3 mm, interior volume of the funnel ≈ 100 cm^3) upside down over the Petri dish. The glass funnel generated a quasi-saturated chloroform vapor phase above the polymer solution layer, reducing the solvent evaporation speed. This led to slow solidification of the membrane film in approximately 4 h. The solidified membrane was kept in the nitrogen bag for 24 h, removed from the Petri dish and dried naturally for 24 h before thermal treatment. The zeolite loading was calculated by using Equation 1:

$$\text{Zeolite loading (wt.\%)} = 100 \times \left(\frac{m_{zeolite}}{m_{zeolite}+m_{polymer}}\right) \quad (1)$$

where $m_{zeolite}$ and $m_{polymer}$ are the weight of the zeolite and the polymer, respectively.

The dried membranes were then placed between glass plates to prevent curling and placed in a muffle oven. The muffle oven was heated to 260 ºC. The heating protocol entailed heating at 1 ºC/min from room temperature to the final annealing temperature with 30 ºC increments. At each increment, the oven was kept isothermally for 2 h. The membranes remained at the final temperature for 24 h, and were removed after the oven cooled down to room temperature naturally as too fast quenching would have resulted in voids between the polymer matrix and the filler due to the difference in the thermal expansion coefficients of the two materials. By allowing the MMMs to cool down naturally, good adhesion between the polymer chains and the zeolite was assumed to be maintained.

Characterization

X-ray diffraction (XRD) patterns were recorded at room temperature under ambient conditions on a high-throughput STOE STADI P Combi diffractometer in the transmission mode with focusing Ge(111) monochromatic X-ray inlet beams (λ = 1.5406 Å, Cu Kα source). Elemental analysis was performed using an inductively coupled plasma-atomic emission spectrometer (ICP-AES, Perkin Elmer Optima 3300 DV). The chemical structure of the zeolite/polymer interface was analyzed with Raman microspectroscopy, using an upright optical microscope (BX53, Olympus, Japan) installed with a commercial Raman setup (MonoVista CRS+, S&I GmbH, Germany), and Fourier transform infrared spectroscopy (FT-IR) was conducted in dry air by using a transmittance mode Bruker Vertex 70. The morphology of the zeolite filler, membrane top-view, bottom-view and cross-sections were observed with a JEOL JSM-1060LV scanning electron microscope (SEM). Further analysis of the zeolite-polymer interface and membrane's morphology was performed by focused ion beam scanning electron microscopy (FIB-SEM) on Dualbeam Nova Nanolab 600, FEG with Ga source FIB (Sidewinder), ThermoFisher. Scanning transmission electron microscope (STEM) and scanning transmission electron microscopy-energy dispersive X-ray spectroscopy (STEM-EDX) measurements were performed with an aberration-corrected JEOL ARM200F Microscope operating at an acceleration voltage of 200 kV and equipped with a cold FEG. The ^{27}Al solid-state NMR experiments were performed with Bruker Avance I spectrometer using a 4 mm Chemagnetics solids probe at a 500 MHz Oxford wide-bore superconducting magnet. Nitrogen physisorption was performed on Tristar II 3020, micromeritics. Membrane density was determined with the buoyancy method by using a Sartorius YDK 01 Density Determination Kit with water as the buoyancy liquid. Thermogravimetric analysis (TGA) measurements were performed on a TGA/DSC 3+, METTLER TOLEDO. Differential scanning calorimetry (DSC) measurements were performed on a DSC Q2000 (TA instruments). A 3-points bending test was performed on an Instron 5943 for flexural modulus measurement (more details are available in SI).

Gas permeation test

The gas separation performance of the prepared membranes for CO_2/CH_4, CO_2/N_2, N_2/CH_4 mixture feeds and Ar, He, H_2, CO_2, CH_4, O_2, N_2, C_2H_4, C_2H_6, C_3H_6, C_3H_8 pure gas feeds were tested by using a custom-built, high-throughput gas separation system (HTGS) (*47*). HTGS allows for a simultaneous pure gas and mixed-gas testing of up to 8 (or 16) membrane coupons at varying membrane temperatures and feed pressures. Two high throughput gas separation setups (HTGS) have been used in this work, schematic diagrams and more details of both HTGSs can be found in the SI. Mixed-gas separation factors are calculated through the measurement of the permeate composition. This permeate composition is determined using a gas chromatograph (Interscience compact GC with Porabond Q column in HTGS-1, Interscience Compact GC4.0 with Rt-Q-Bond column in HTGS-2) connected to the permeate line. The GCs are calibrated by exposing them to varying gas mixtures of known composition (through the use of MFCs) every 3 months.

In this study, the membranes were tested with 50–50 vol.% CO_2/CH_4, CO_2/N_2, N_2/CH_4 mixture at 25°C/2 bar to study the mixed gas separation performance. Moreover, the Ar, He, H_2, CO_2, CH_4, O_2, N_2, C_2H_4, C_2H_6, C_3H_6, C_3H_8 was tested under 25°C/1 bar to study the ideal-gas permeations of membranes. The membrane stability/steady-state testing was conducted for 72 h continuous running for a 50–50 vol.%

CO_2/CH_4 mixture at 25°C/2 bar. The influence of the moisture in the feed streams on the membrane performance was studied by humidifying the feed stream (RH = 60%) via a humidifier in HTGS-2. For the aging testing, the 60wt.% Na-CHA-10 MMM coupons were measured for 50–50 vol.% CO_2/CH_4 mixture (at 25°C/2 bar) every 3-months after preparation. Since all of the membranes were kept in the open atmosphere, moisture was reversibly absorbed by the zeolite filler, which caused around a 30 % decrease in gas permeability and CO_2/CH_4 selectivity (compared with the dried membranes). To fairly compare them with the original (dried) membranes, the membrane coupons were dried in the oven for 24 h (under 260°C) before the gas permeation testing (to desorb water).

The gas permeability was measured by using a constant-volume, variable-pressure permeation system. The membranes were first allowed to reach a steady-state overnight. The steady-state for membrane permeability and separation factor were tested separately. The final steady-state was confirmed when both the consecutive permeability measurement and consecutive GC measurements gave the same results. Then, 5 more measurements were taken and their average was reported. Each final data point reported is an average of two membranes and 4 coupons from each membrane, thus 8 replicas in total. The mixed-gas permeability of gas i (P_i) was calculated by Equation 2:

$$P_i = 10^{10} \times \frac{y_i \times V \times V_m \times L}{x_i \times p_{up} \times A \times R \times T} \times \frac{dp}{dt} \quad (2)$$

with P_i the gas permeability (Barrer), y_i the mole fraction of component i in the permeate, x_i the mole fraction of component i in the feed, V the downstream volume (cm^3), V_m the molar volume (22.414 L mol^{-1}), A the membrane permeation area (1.91 cm^2), L the membrane thickness (μm), T the operating temperature (ºK), p_{up} the upstream pressure (bar), R the gas constant (0.082 L atm mol^{-1} K^{-1}) and dp/dt the pressure increase (torr s^{-1}).

The mixed-gas separation factors (α^*) were calculated as given in Equation 3. The mole ratio y_i/y_j is determined from the chromatogram peak areas of the permeate (calculated based on the GC calibration), while x_i/x_j is determined by the feed settings.

$$\alpha^*_{i/j} = \frac{y_i/y_j}{x_i/x_j} \quad (3)$$

High-pressure physisorption

High-pressure gas adsorption isotherms measurements were performed using a volumetric setup (VTI, HPA 100), accompanied by a deep vacuum pump capable of reaching 10^{-7} mbar. Prior to each measurement, the samples were outgassed by increasing the temperature (1 °C/min, overnight) under vacuum. The activation temperature for the zeolite samples were 350 °C, while a lower temperature of 260 °C was used for the membrane sample. The measurements were performed between 10-50°C depending on the sample. The adsorption isotherms were fitted using the Toth isotherm model (*48*), which is defined in Equation 4.

$$q_i = \frac{(q_{i,max} K_i * p)}{(1+(K_i * p)^{n_i})^{\frac{1}{n_i}}} \quad (4)$$

The commercial CHA sample was measured at multiple temperatures to investigate the temperature dependence of the isotherm measurements. These isotherms were fitted using the previously mentioned Toth isotherm model, but with a temperature-dependent K_i (Equation 5).

$$K_i = K_i^{\circ} \exp\left(-\frac{\Delta H_i^{\circ}}{R_g T}\right) \quad (5)$$

where q_i is the amount adsorbed (mmol/g) and $q_{i,max}$ is the maximum amount adsorbed (mmol/g), p is the partial pressure (bar), K_i is the adsorption affinity constant (1/bar), n_i is the heterogeneity coefficient (-), K_i° is

the infinite adsorption at zero loading (1/bar), ΔH_i° is the isosteric heat of adsorption at zero loading (kJ/mol), T is the temperature (°K), and R_g is the gas constant (J/mol/°K). (More details are available in SI).

Molecular simulations

To qualitatively probe the adsorption behavior of the Na-CHA zeolite (with Si/Al = 11) for CO_2 and $CO_2/CH_4/H_2O$, Grand Canonical Monte Carlo (GCMC) simulations were performed using RASPA (*49*). For all simulations, the temperature was set to 25 °C and pressures of 0.1 bar, 1 bar and 2 bar were considered. The parameters of the van der Waals interactions between the different atoms and the atomic charges were obtained from the literature (*50, 51, 52*). For the water guest molecules, the TIP5P-Ew model was used (*52*). A 2×2×2-supercell was used to allow for a van der Waals cutoff radius of 11.5 Å and $5{\cdot}10^6$ MC cycles were performed for each simulation. In the case of ternary adsorption, equal mole fractions were used for the CO_2 and CH_4 guest molecules. The H_2O mole fraction was varied from 0.05 to 0.3 or set by the saturation vapor pressure of water at 25 °C (see Supporting Information XX).

The influence of different Si/Al ratios on the adsorption of CO_2 in Na-CHA zeolites is evaluated with a newly trained machine learning potential (MLP) rather than with regular force field potentials (as used in RASPA), to increase the accuracy of the simulations to the level of density functional theory (DFT). To this end, the protocol described in Ref. 73 was used to train a single Neural Equivariant Interatomic Potential (NequIP) MLP (68) for all Si/Al ratios. The energies and forces of each configuration are obtained with DFT using the PBE functional (57) with DFT-D3(BJ) dispersion interactions (58), a cutoff energy of 500 eV, and a single k-point in VASP (74-76). The resulting mean absolute error on the energy and forces of the MLP are 2.3 meV per adsorbate and 7.9 meV/Å, respectively. All the GCMC simulations with this MLP were performed at a temperature of 25 °C and a pressure of 1 bar, using $5{\cdot}10^6$ MC cycles. The Na-CHA zeolite structures with different Si/Al ratios are provided as separate files.

The diffusion behavior of CO_2 in the Na-CHA zeolite was computationally probed by constructing free energy profiles of a CO_2 molecule traversing the zeolite. Given the high computational cost of these simulations for different Si/Al ratios, an MLP was constructed to perform these simulations. In contrast to the MLP used for the GCMC simulations, this MLP allows for a fully flexible description of the framework, which contains a single CO_2 molecule. To significantly speed up the dataset generation, an active learning loop was performed for each Si/Al ratio as described in (77). All the single-point calculations were performed with CP2K (53), using the PBE functional with DFT-D3(BJ) dispersion interactions. GTH pseudopotentials (78) were used in combination with TZVP-MOLOPT basis sets (60), a plane wave cut-off energy of 1000 Ry, and a relative cut-off energy of 60 Ry. The final MLP was trained to mean absolute errors of 0.9 meV per atom and 42.7 meV/Å on the energy and forces, respectively. Three-dimensional free energy profiles were constructed through umbrella sampling simulations performed with OpenMM (79) in combination with PLUMED (61, 62), using a Langevin thermostat to set the temperature to 25 °C. The collective variable (CV) describing the diffusion through the 8MRs is similar to the one used in Refs. (34, 63, 64) so that:

$$q = \left(\boldsymbol{r}_{center,\ CO_2} - \boldsymbol{r}_{center,\ 8MR}\right) \cdot \boldsymbol{n}_{8MR}$$

with $\boldsymbol{n}_{8MR}$ the normal of the central 8MR, defined by four silicon atoms (Fig. S6), $\boldsymbol{r}_{center,\ 8MR}$ the center of this aperture, and $\boldsymbol{r}_{center,\ CO_2}$ the center of mass of the CO_2 molecule. To sample all the CHA cages in the simulated 2x2x2 supercell, a CV-range of -24 Å to 31 Å is used, which covers all the cages of the structure under periodic boundary conditions. Every 0.65 Å, a simulation of 80 ps with an umbrella with a force constant of 100 kJ/(mol Å²) was performed, from which the one-dimensional free energy profiles were constructed using the weighted histogram analysis method (WHAM) (65). Subsequently, these one-dimensional free energy profiles were transformed into three-dimensional free energy profiles (Figure SXX) using the following formula:

$$F(x,y,z) = -\frac{1}{\beta}\ln\left[\int dq\ p_b(\mathrm{x,y,z}|q)\, e^{-\beta F(q)}\right] + C$$

with C a constant, $F(\mathrm{q})$ the one-dimensional free energy profile obtained from WHAM, and $p_b(\mathrm{x,y,z}|q)$ the conditional probability that the three-dimensional collective variable takes the value (x, y, z) in a simulation with a time-independent bias when the one-dimensional collective variable has a value q. By simply keeping track of values of (x, y, z) for every value of q during the umbrella sampling simulations, this transformation is reduced to a simple post-processing step.

Furthermore, also the influence of the presence of H_2O was investigated for the free energy profiles. For these simulations, we restricted ourselves to a CHA unitcell containing 1 Na^+ per cage (yielding a Si/Al ratio of 11) and free energy profiles for only two neighbouring cages. Initial free energy profiles were constructed through *ab initio* umbrella sampling simulations performed with CP2K. For each umbrella, a simulation in the (N, P, $\sigma_a = 0$, T)-ensemble was conducted. The temperature was set to 25 °C and controlled by a Nosé-Hoover thermostat (54, 55) with a time constant of 0.1 ps. The pressure was set to 1 bar and controlled by an MTTK barostat (56) with a time constant of 1 ps. The electronic energies were evaluated with DFT using the same settings as without H_2O, only the plane wave cut-off was reduced to 800 Ry. The umbrella simulations for Na-CHA with both CO_2 and H_2O were run for 15 ps. To improve the convergence of the umbrella sampling simulations, a machine learning potential was trained on the *ab initio* enhanced sampling data to further extend the simulation time of each umbrella with a much lower computational cost. This MLP was trained with the NNFFLIB code (66, 67). The test mean absolute error on the energy and forces is limited to respectively 0.1 meV and 10.5 meV/Å for Na-CHA with CO_2 and H_2O. With the MLP, each umbrella simulation was run for 500 ps to improve the sampling. More computational details regarding the different simulations can be found in the Supporting Information.

Positron Annihilation Lifetime Spectroscopy

A detailed description and the capabilities of PALS with polymers and comparisons to complementary methods can be found in the reference (*69*). All positron annihilation lifetime spectra were obtained using a conventional laboratory lifetime spectrometer consisting of two Photonics XP2020/URQ photomultipliers with BaF_2 scintillators, connected to nuclear electronics in a fast-slow coincidence arrangement. A ^{22}Na salt encapsulated in Kapton foil serves as a positron source. Two identical samples of 1 × 1 cm² size were arranged around the source material in a so-called sandwich geometry. The sample sandwich was placed between the photomultiplier detectors and the emitted gamma radiation was detected, filtered and processed by the nuclear electronics. In the final step, the analogue pulses are digitized by an ADC928 analog-to-digital converter from ORTEC. These data can be read out and histogrammed by a computer, resulting in a typical positron lifetime spectrum. To determine the instrumental function *R(t)* of the spectrometer, silicon single crystals with a well-known positron lifetime were measured. From the instrument function, an overall time resolution of 290 ps (FWHM) can be derived for the spectrometer. The peak-to-background ratio is in the range of 40000:1. The measured lifetime spectra of the polymer samples were analyzed via linear regression by Levenberg-Marquardt algorithm, using Equation 7:

$$N(t) = R(t) * \sum_{i=1}^{n} \frac{I_i}{\tau_i} \exp\left(-\frac{t}{\tau_i}\right) + \text{background} \tag{7}$$

where *N(t)* represents the measured lifetime spectrum and *R(t)* represents the instrument resolution function consisting of a sum of Gaussian functions. Each lifetime component is given by the respective lifetime τ_i and the corresponding intensity I_i. All spectra are overlaid by a random background, which can be assumed to be constant. The total number of lifetime components *n* present in a given spectrum is obtained from the quality of the calculated fit using the reduced χ^2 value, which ranges from 1.0 to 1.15 for all analyzed spectra. The shortest lifetime represents the decay of p-Ps and was fixed at 125 ps. The radius of the sub-1 nm free volume elements (FVEs) can be calculated by a semi-empirical quantum mechanical model, the Tao-Eldrup model (*70, 71*), as Equation 8:

$$\tau = \frac{1}{2}\left[1 - \frac{r}{r+\Delta r} + \frac{1}{2\pi}\sin\left(\frac{2\pi r}{r+\Delta r}\right)\right]^{-1} \text{[ns]} \tag{8}$$

where τ is the measured o-Ps lifetime, r is the mean radius of the FVEs and Δr is an empirical value for the overlap of the o-Ps wave function with the material around the FVEs. The best-fitted value equals 0.166 nm (*70-72*). (More details are available in SI).

References

47. A. L. Khan, S. Basu, A. Cano-Odena, I. F. Vankelecom, Novel high throughput equipment for membrane-based gas separations. *J. Membr. Sci.* **354**, 32-39 (2010). doi:10.1016/j.memsci.2010.02.069

48. J. Tóth, State equation of the solid-gas interface layers. *Acta Chem. Acad. Sci. Hung.* **69**, 311–328 (1971).

49. D. Dubbeldam, S. Calero, D. E. Ellis, R. Q. Snurr, RASPA: molecular simulation software for adsorption and diffusion in flexible nanoporous materials. *Mol. Simulat.* **42**, 81–101 (2016). doi:10.1080/08927022.2015.1010082

50. E. García-Pérez, J. B. Parra, C. O. Ania, A. García-Sánchez, J. M. van Baten, R. Krishna, D. Dubbeldam, and S. Calero, A computational study of CO_2, N_2, and CH_4 adsorption in zeolites. *Adsorption*. **13**, 469–476 (2007). doi:10.1007/s10450-007-9039-z

51. A. Martin-Calvo, J. J. Gutiérrez-Sevillano, J. B. Parra, C. O. Ania, S. Calero, Transferable force fields for adsorption of small gases in zeolites. *Phys. Chem. Chem. Phys.* **17**, 24048–24055 (2015). https://doi.org/10.1039/C5CP03749B

52. J.M. Castillo, J. Silvestre-Albero, F. Rodriguez-Reinoso, T.J.H. Vlugt, S. Calero, Water adsorption in hydrophilic zeolites: experiment and simulation, *Phys. Chem. Chem. Phys*. **15**, 17374-17382 (2013). https://doi.org/10.1039/C3CP52910J

53. T. D. Kühne, M. Iannuzzi, M. Del Ben, V. V. Rybkin, P. Seewald, F. Stein, T. Laino, R. Z. Khaliullin, O. Schütt, F. Schiffmann, D. Golze, J. Wilhelm, S. Chulkov, M. H. Bani-Hashemian, V. Weber, U. Borštnik, M. Taillefumier, A. S. Jakobovits, A. Lazzaro, H. Pabst, T. Müller, R. Schade, M. Guidon, S. Andermatt, N. Holmberg, G. K. Schenter, A. Hehn, A. Bussy, F. Belleflamme, G. Tabacchi, A. Glöß, M. Lass, I. Bethune, C. J. Mundy, C. Plessl, M. Watkins, J. VandeVondele, M. Krack, J. Hutter, CP2K: An electronic structure and molecular dynamics software package - Quickstep: Efficient and accurate electronic structure calculations. *J. Chem. Phys*. **152**, 194103 (2020). doi:10.1063/5.0007045

54. S. Nosé, A molecular dynamics method for simulations in the canonical ensemble. *Mol. Phys*. **52**, 255–268 (1984). doi:10.1080/00268978400101201

55. S. Nosé, A unified formulation of the constant temperature molecular dynamics methods. *J. Chem. Phys*. **81**, 511–519 (1984). doi:10.1063/1.447334

56. G. J. Martyna, D. J. Tobias, M. L. Klein, Constant pressure molecular dynamics algorithms. *J. Chem. Phys*. **101**, 4177–4189 (1994). doi:10.1063/1.467468

57. J. P. Perdew, K. Burke, M. Ernzerhof, Generalized Gradient Approximation Made Simple. *Phys. Rev. Lett*. **77**, 3865–3868 (1996). doi:10.1103/PhysRevLett.77.3865

58. S. Grimme, S. Ehrlich, L. Goerigk, Effect of the damping function in dispersion corrected density functional theory. *J. Comput. Chem.* **32**,1456–1465 (2011). doi:10.1002/jcc.21759

59. S. Grimme, S. Ehrlich, L. Goerigk, Effect of the damping function in dispersion corrected density functional theory. *J. Comput. Chem.* **32**,1456–1465 (2011). doi:10.1002/jcc.21759

60. J. VandeVondele, J. Hutter, Gaussian basis sets for accurate calculations on molecular systems in gas and condensed phases. *J. Chem. Phys.* **127**, 114105, 2007. doi:10.1063/1.2770708

61. M. Bonomi, G. Bussi, C. Camilloni, G. A. Tribello, P. Banáš, A. Barducci, M. Bernetti, P. G. Bolhuis,

S. Bottaro, D. Branduardi, R. Capelli, P. Carloni, M. Ceriotti, A. Cesari, H. Chen, 1W. Chen, F. Colizzi, S. De, M. De La Pierre, D. Donadio, V. Drobot, B. Ensing, A. L. Ferguson, M. Filizola, J. S. Fraser, H. Fu, P. Gasparotto, F. L. Gervasio, F. Giberti, A. Gil-Ley, T. Giorgino, G. T. Heller, G. M. Hocky, M. Iannuzzi, M. Invernizzi, K. E. Jelfs, A. Jussupow, E. Kirilin, A. Laio, V. Limongelli, K. Lindorff-Larsen, T. Löhr, F. Marinelli, L. Martin-Samos, M. Masetti, R. Meyer, A. Michaelides, C. Molteni, T. Morishita, M. Nava, C. Paissoni, E. Papaleo, M. Parrinello, J. Pfaendtner, P. Piaggi, G. Piccini, A. Pietropaolo, F. Pietrucci, S. Pipolo, D. Provasi, D. Quigley, P. Raiteri, S. Raniolo, J. Rydzewski, M. Salvalaglio, G. C. Sosso, V. Spiwok, J. Šponer, D. W. H. Swenson, P. Tiwary, O. Valsson, M. Vendruscolo, G. A. Voth, A. White, T. P. consortium, Promoting transparency and reproducibility in enhanced molecular simulations. *Nat. Methods.* **16**, 670–673 (2019). doi:10.1038/s41592-019-0506-8

62. G. A. Tribello, M. Bonomi, D. Branduardi, C. Camilloni, G. Bussi, PLUMED 2: New feathers for an old bird. *Comput. Phys. Commun*. **185**, 604–613 (2014). doi:10.1016/j.cpc.2013.09.018

63. P. Cnudde, R. Demuynck, S. Vandenbrande, M. Waroquier, G. Sastre, V. V. Speybroeck, Light Olefin Diffusion during the MTO Process on H-SAPO-34: A Complex Interplay of Molecular Factors. *J. Am. Chem. Soc*. **142**, 6007–6017 (2020). doi:10.1021/jacs.9b10249

64. Y. Sun, S. M. J. Rogge, A. Lamaire, S. Vandenbrande, J. Wieme, C. R. Siviour, V. Van Speybroeck, J.-C. Tan, High-rate nanofluidic energy absorption in porous zeolitic frameworks. *Nat. Mater*. **20**, 1015–1023 (2021). doi:10.1038/s41563-021-00977-6

65. A. Grossfield, WHAM: an implementation of the weighted histogram analysis method. http://membrane.urmc.rochester.edu/content/wham/

66. https://github.com/mcoolsce/NNFFLIB

67. A. Lamaire, M. Cools-Ceuppens, M. Bocus, T. Verstraelen, V. Van Speybroeck, Quantum free energy profiles for molecular proton transfers, *J. Chem. Theory Comput.*, **19**, 18-24 (2022). https://doi.org/10.1021/acs.jctc.2c00874

68. S. Batzner, A. Musaelian, L. Sun, M. Geiger, J.P. Mailoa, M. Kornbluth, N. Molinari, T.E. Smidt, B. Kozinsky, E(3)-equivariant graph neural networks for data-efficient and accurate interatomic potentials, *Nat. Comm.* **13**, 2453 (2022). https://doi.org/10.1038/s41467-022-29939-5

69. T. Stassin et al., Porosimetry for thin films of metal–organic frameworks: A comparison of positron annihilation lifetime spectroscopy and adsorption-based methods. *Advanced Materials*. **33**, 2006993 (2021). https://doi.org/10.1002/adma.202006993

70. M. Eldrup, D. Lightbody, J. N. Sherwood, The temperature dependence of positron lifetimes in solid pivalic acid. *Chem. Phys*. **63**, 51–58 (1981). https://doi.org/10.1016/0301-0104(81)80307-2

71. S. J. Tao, Positronium annihilation in molecular substances. *J. Chem. Phys*. **56**, 5499–5510 (1972). https://doi.org/10.1063/1.1677067

72. Y. C. Jean, Positron annihilation spectroscopy for chemical analysis: A novel probe for microstructural analysis of polymers. *Microchemical Journal*. **42**, 72–102 (1990). https://doi.org/10.1016/0026-265X(90)90027-3

73. R. Goeminne, L. Vanduyfhuys, V. Van Speybroeck, T. Verstraelen, DFT-Quality Adsorption Simulations in Metal–Organic Frameworks Enabled by Machine Learning Potentials. *J. Chem. Theory Comput.* **19**, 6313–6325 (2023). https://doi.org/10.1021/acs.jctc.3c00495

74. G. Kresse, J. Hafner, Ab initio molecular dynamics for liquid metals. *Phys. Rev. B* **47**, 558 (1993). https://doi.org/10.1103/PhysRevB.47.558

75. G. Kresse, J. Furthmüller, Efficiency of ab-initio total energy calculations for metals and semiconductors using a plane-wave basis set. *Comput. Mater. Sci.* **6**, 15–50 (1996). https://doi.org/10.1016/0927-0256(96)00008-0

76. G. Kresse, J. Furthmüller, Efficient iterative schemes for ab initio total-energy calculations using a plane-wave basis set. *Phys. Rev. B* **54**, 11169 (1996). https://doi.org/10.1103/PhysRevB.54.11169

77. S. Vandenhaute, M. Cools-Ceuppens, S. DeKeyser, T. Verstraelen, V. Van Speybroeck, Machine learning potentials for metal-organic frameworks using an incremental learning approach. *npj Comput. Mater.* **9**, 19 (2023). https://doi.org/10.1038/s41524-023-00969-x

78. S. Goedecker, M. Teter, J. Hutter, Separable dual-space gaussian pseudopotentials. *Phys. Rev. B* **54**, 1703–1710 (1996). https://doi.org/10.1103/PhysRevB.54.1703

79. P. Eastman, J. Swails, J.D. Chodera, R.T. McGibbon, Y. Zhao, K.A. Beauchamp, L.-P. Wang, A.C. Simmonett, M.P. Harrigan, C.D. Stern, R.P. Wiewiora, B.R. Brooks, V.S. Pande, OpenMM 7: Rapid development of high performance algorithms for molecular dynamics. *PLOS Computational Biology* **13**, e1005659 (2017). https://doi.org/10.1371/journal.pcbi.1005659

B

List of Publications

Publications in international peer–reviewed journals

1. **Design of a tunable mixed matrix membrane platform for high-performance gas separations**
   X. Tan, S. Robijns, A. Lamaire, R. Goeminne, N. De Witte, M. Dickmann, R. Verbeke, T. Van der Donck, D. Van Havere, R. de Oliveira Silva, Q. Ke, Y. Li, R. Thür, I. Aslam, C. Van Goethem, T. Donckels, D. Sakellariou, V. Van Speybroeck, T. Van Assche, M. Dusselier, I. Vankelecom
   In revision

2. **Water motifs in zirconium metal-organic frameworks induced by nanoconfinement and hydrophilic adsorption sites**
   A. Lamaire, J. Wieme, S. Vandenhaute, R. Goeminne, S.M.J. Rogge, V. Van Speybroeck
   In revision

3. **Unraveling the Mechanisms of Zirconium Metal–Organic Frameworks-Based Mixed-Matrix Membranes Preventing Polysulfide Shuttling**
   W. Lu, Z. Pang, A. Lamaire, F. Liu, S. Dai, M.L. Pinto, R. Demir-Cakan, K. Ooi Tan, V. Van Speybroeck, V. Pimenta, C. Serre
   Small Science, **2024**, 4 (6), 2300339
   IF: 11.1, Number of citations: 0

4. **Quantum tunneling rotor as a sensitive atomistic probe of guests in a metal-organic framework**
   K. Titov, M.R. Ryder, A. Lamaire, Z. Zeng, A.K. Chaudhari, J. Taylor, E.M. Mahdi, S.M.J. Rogge, S. Mukhopadhyay, S. Rudić, V. Van Speybroeck, F. Fernandez-Alonso, J.-C. Tan
   Physical Review Materials, **2023**, 7 (7), 073402
   IF: 3.1, Number of citations: 0

5. **Nuclear quantum effects on zeolite proton hopping kinetics explored with machine learning potentials and path integral molecular dynamics**
   M. Bocus, R. Goeminne, A. Lamaire, M. Cools-Ceuppens, T. Verstraelen, V. Van Speybroeck
   Nature Communications, **2023**, 14 (1), 1008
   IF: 14.7, Number of citations: 18

6. **Quantum free energy profiles for molecular proton transfers**
   A. Lamaire, M. Cools-Ceuppens, M. Bocus, T. Verstraelen, V. Van Speybroeck
   Journal of Chemical Theory and Computation, **2023**, 19 (1), 18–24
   IF: 5.7, Number of citations: 2

7. **Truly combining the advantages of polymeric and zeolite membranes for gas separations**
   X. Tan, S. Robijns, R. Thür, Q. Ke, N. De Witte, A. Lamaire, Y. Li, I. Aslam, D. Van Havere, T. Donckels, T. Van Assche, V. Van Speybroeck, M. Dusselier, I. Vankelecom
   Science, **2022**, 378 (6625), 1189–1194
   IF: 44.7, Number of citations: 53

8. **How Reproducible are Surface Areas Calculated from the BET Equation?**
   J.W.M. Osterrieth, J. Rampersad, D. Madden, N. Rampal, L. Skoric, B. Connolly, M.D. Allendorf, V. Stavila, J.L Snider, R. Ameloot, J. Marreiros, C. Ania, D. Azevedo, E. Vilarrasa-Garcia, B.F. Santos, X.-H. Bu, Z. Chang, H. Bunzen, N.R. Champness, S.L. Griffin, B. Cheng, R.-B. Lin, B. Coasne, S. Cohen, J.C. Moreton, Y.J. Colón, L. Chen, R. Clowes, F.-X. Coudert, Y. Cui, B. Hou, D.M. D'Alessandro, P.W. Doheny, M. Dincă, C. Sun, C. Doonan, M.T. Huxley, J.D. Evans, P. Falcaro, R. Ricco, O. Farha, K.B. Idrees, T. Islamoglu, P. Feng, H. Yang, R.S. Forgan, D. Bara, S. Furukawa, E. Sanchez, J. Gascon, S. Telalović, S.K. Ghosh, S. Mukherjee, M.R. Hill, M.M. Sadiq, P. Horcajada, P. Salcedo-Abraira, K. Kaneko, R. Kukobat, J. Kenvin, S. Keskin, S. Kitagawa, K.-i. Otake, R.P. Lively, S.J.A.

DeWitt, P.L. Llewellyn, B.V. Lotsch, S.T. Emmerling, A.M. Pütz, C. Martí-Gastaldo, N.M. Padial, J. García-Martínez, N. Linares, D. Maspoch, J.A. Suárez del Pino, P.Z. Moghadam, R. Oktavian, R.E. Morris, P.S. Wheatley, J. Navarro, C. Petit, D. Danaci, M.J. Rosseinsky, A.P. Katsoulidis, M. Schroeder, X. Han, S. Yang, C. Serre, G. Mouchaham, D.S. Sholl, R. Thyagarajan, D. Siderius, R.Q. Snurr, R.B. Goncalves, S. Telfer, S.J. Lee, V.P. Ting, J.L. Rowlandson, T. Uemura, T. Iiyuka, M.A. van der Veen, D. Rega, V. Van Speybroeck, S.M.J. Rogge, A. Lamaire, K.S. Walton, L.W. Bingel, S. Wuttke, J. Andreo, O. Yaghi, B. Zhang, C.T. Yavuz, T.S. Nguyen, F. Zamora, C. Montoro, H. Zhou, A. Kirchon, D. Fairen-Jimenez
Advanced Materials, **2022**, 34 (27), 2201502
IF: 29.4, Number of citations: 135

9. **Correlating MOF-808 parameters with mixed-matrix membrane (MMM) CO_2 permeation for a more rational MMM design**
R. Thür, D. Van Havere, N. Van Velthoven, S. Smolders, A. Lamaire, J. Wieme, V. Van Speybroeck, D. De Vos, I. Vankelecom
Journal of Materials Chemistry A, **2021**, 9 (21), 12782–12796
IF: 14.5, Number of citations: 26

10. **High rate nanofluidic energy absorption in porous zeolitic frameworks**
Y. Sun, S.M.J. Rogge, A. Lamaire, S. Vandenbrande, J. Wieme, C.R. Siviour, V. Van Speybroeck, J.-C. Tan
Nature Materials, **2021**, 20 (7), 1015–1023
IF: 47.7, Number of citations: 50

11. **Atomistic insight in the flexibility and heat transport properties of the stimuli-responsive metal-organic framework MIL-53(Al) for water-adsorption applications using molecular simulations**
A. Lamaire, J. Wieme, A.E.J. Hoffman, V. Van Speybroeck
Faraday Discussions, **2021**, 225, 301–323
IF: 4.4, Number of citations: 18

12. **Thermal Engineering of Metal-Organic Frameworks for Adsorption Applications: A Molecular Simulations Perspective**
J. Wieme, S. Vandenbrande, A. Lamaire, V. Kapil, L. Vanduyfhuys, V. Van Speybroeck
ACS Applied Materials & Interfaces, **2019**, 11 (42), 38697–38707
IF: 8.8, Number of citations: 66

13. **Modeling the structural and thermal properties of loaded metal-organic frameworks. An interplay of quantum and anharmonic fluctuations**
V. Kapil, J. Wieme, S. Vandenbrande, A. Lamaire, V. Van Speybroeck, M. Ceriotti
Journal of Chemical Theory and Computation, **2019**, 15 (5), 3237–3249
IF: 5.0, Number of citations: 24

14. **On the importance of anharmonicities and nuclear quantum effects in modelling the structural properties and thermal expansion of MOF-5**
A. Lamaire, J. Wieme, S.M.J. Rogge, M. Waroquier, V. Van Speybroeck
Journal of Chemical Physics, **2019**, 150 (9), 094503
IF: 3.0, Number of citations: 19

Conference contributions

Oral presentations

1. **Nuclear quantum effects in proton transfer reactions**
Aran Lamaire, Massimo Bocus, Ruben Goeminne, Sander Vandenhaute, Maarten Cools-Ceuppens, Toon Verstraelen, Veronique Van Speybroeck
Quantum^2 *on machine learning enhanced sampling*, Lausanne, Switzerland, November 29 – December 1, 2023

2. **The influence of nuclear quantum effects on proton hopping kinetics in the H-SSZ-13 zeolite through ab initio derived machine learning potentials**
Massimo Bocus, Ruben Goeminne, Aran Lamaire, Maarten Cools-Ceuppens, Toon Verstraelen, Veronique Van Speybroeck
NCCC XXIII, Noordwijkerhout, The Netherlands, May 9–11, 2022

3. **Harder, better, faster, stronger: Designing hydrophobic cage-type materials as efficient high-rate shock absorbers**
Sven M.J. Rogge, Yueting Sun, Aran Lamaire, Steven Vandenbrande, Jelle Wieme, Clive R. Siviour, Jin–Chong Tan, Veronique Van Speybroeck
EuroMOF2021, Krakow (online), Poland, September 13–15, 2021

4. **ZIF-8 as a high-impact shock absorber? Unraveling the anomalous high-rate water intrusion in ZIF-8 by simulation and experiment**
   Sven M.J. Rogge, Yueting Sun, Aran Lamaire, Steven Vandenbrande, Jelle Wieme, Clive R. Siviour, Jin–Chong Tan, Veronique Van Speybroeck
   MMC, Oxford, United Kingdom, June 18, 2019

5. **Towards a molecular level understanding of chemical and physical phenomena in metal-organic frameworks**
   Jelle Wieme, Chiara Caratelli, Ruben Demuynck, Arthur De Vos, Julianna Hajek, Alexander E.J. Hoffman, Aran Lamaire, Kurt Lejaeghere, Sven M.J. Rogge, Steven Vandenbrande, Louis Vanduyfhuys, Michel Waroquier, Veronique Van Speybroeck
   Congrès français des MOFs, Paris, France, May 16–17, 2018

Poster presentations

1. **Atomistic insight in the flexibility and heat transport properties of MIL-53(Al) for water-adsorption applications**
   Aran Lamaire, Jelle Wieme, Alexander E.J. Hoffman, Veronique Van Speybroeck
   MOF2022, Dresden, Germany, September 4–7, 2022

2. **Computationally modelling hydrogen storage and transport in methane clathrates**
   Aran Lamaire, Sven M.J. Rogge, Paulo G.M. Mileo, Maarten Houlleberghs, Eric Breynaert, Johan A. Martens, Veronique Van Speybroeck
   Hydrogen Research Event @ Advanced Engineering 2022, Antwerp, Belgium, May 12, 2022

3. **Rationalizing the structural organisation of nanoconfined water by tuning the pore architecture of metal-organic frameworks**
   Aran Lamaire, Jelle Wieme, Sven M.J. Rogge, Veronique Van Speybroeck
   EUROMOF2021, Krakow (online), Poland, September 13–15, 2021

4. **Structural organisation of water in zirconium-based metal-organic frameworks** *EUROMOF 2019*, Paris, France, October 27–30, 2019

5. **Structural organisation of water in zirconium-based metal-organic frameworks**
   Aran Lamaire, Jelle Wieme, Sven M.J. Rogge, Veronique Van Speybroeck
   MOFSIM2019, Ghent, Belgium, April 10–12, 2019

6. **Nuclear quantum effects in metal-organic frameworks**
   Aran Lamaire, Jelle Wieme, Sven M.J. Rogge, Liesbeth De Bruecker, Veronique Van Speybroeck
   MOFSIM2019, Ghent, Belgium, April 10–12, 2019

7. **Nuclear quantum effects in metal-organic frameworks**
   Aran Lamaire, Jelle Wieme, Sven M.J. Rogge, Liesbeth De Bruecker, Veronique Van Speybroeck
   Ab initio Modeling in Solid State Chemistry, Torino, Italy, September 2–7, 2018

8. **Nuclear quantum effects in metal-organic frameworks**
   Aran Lamaire, Jelle Wieme, Sven M.J. Rogge, Liesbeth De Bruecker, Veronique Van Speybroeck
   Path Integral Quantum Mechanics: From the Basics to the Latest Developments, Lausanne, Switzerland, June 25–29, 2018

9. **Nuclear quantum effects in metal-organic frameworks**
   Aran Lamaire, Jelle Wieme, Sven M.J. Rogge, Liesbeth De Bruecker, Veronique Van Speybroeck
   Solvay New Horizons Lectures in Chemistry, Zwijnaarde, Belgium, June 1, 2018

10. **On the importance of nuclear quantum effects in modelling the structural properties and thermal expansion of MOF–5**
    Aran Lamaire, Jelle Wieme, Sven M.J. Rogge, and Veronique Van Speybroeck
    MolSim 2018: Understanding Molecular Simulation, Amsterdam, The Netherlands, January 8–19, 2018

11. **On the importance of nuclear quantum effects in modelling the structural properties and thermal expansion of MOF–5**
    Aran Lamaire, Jelle Wieme, Sven M.J. Rogge, and Veronique Van Speybroeck
    EuroMOF 2017, Delft, The Netherlands, October 29 – November 1, 2017

Master's thesis

Introducing nuclear quantum effects via colored-noise thermostats and path integral methods to simulate metal-organic frameworks

Aran Lamaire

Master's thesis performed at the Center for Molecular Modeling (CMM), Ghent University, 2016–2017

Supervisor: prof. dr. ir. Veronique Van Speybroeck

C

List of Software Packages

In the context of this Ph.D. dissertation, various software packages have been used extensively. Below, an overview of these software packages is provided.

CP2K

CP2K is an open source quantum chemistry and solid state physics code that can be used to perform DFT calculations with mixed atomic and plane wave basis sets. It implements several sampling techniques, including normal mode analysis, molecular dynamics, Monte Carlo, and metadynamics. In this PhD dissertation, CP2K was used to perform first-principles (enhanced sampling) molecular dynamics simulations and energy optimisations on zeolites and MOFs. More information about this software is available at https://www.cp2k.org/ and in Ref. [194].

i-PI

i-PI is a universal force engine interface which uses a client-server paradigm to perform (path integral) molecular dynamics simulations based on force calculations of an external client code, such as CP2K, LAMMPS, or Yaff. In this PhD dissertation, i-PI was used to perform path integral and ring polymer molecular dynamics simulations in combination with both first-principles and force field descriptions in CP2K and Yaff, respectively. More information about this software is available at https://ipi-code.org/ and in Refs. [195–197].

LAMMPS

LAMMPS is a classical molecular dynamics code and an acronym for Large-scale Atomic/Molecular Massively Parallel Simulator. It contains an efficient multi-threading parallelisation and GPU acceleration, and implements various force fields and machine learning potentials. In this PhD dissertation, LAMMPS was used in combination with Yaff to accelerate the evaluation of long-range force field contributions. More information about this software is available at https://www.lammps.org/ and in Refs. [198, 199].

MolMod

MolMod is a Python library which implements many auxiliary functions that are useful to write molecular modelling programs. It is the underlying library for many software packages developed at the Center for Molecular Modeling. In this PhD dissertation, MolMod was used as a library within Yaff, TAMkin, and QuickFF. More information about this software is available at http://molmod.github.io/molmod/.

PLUMED

PLUMED is an open source library which implements various enhanced sampling algorithms and free energy methods. It is interfaced with several molecular dynamics engines, including CP2K, i-PI, LAMMPS, and Yaff. In this PhD dissertation, PLUMED was used to perform umbrella sampling simulations with CP2K, i-PI, and Yaff. More information about this software is available at https://www.plumed.org/ and in Refs. [200–202].

PSI4

PSI4 is an open source quantum chemistry code that can be used to perform DFT and wave function-based calculations with atomic basis sets. In this PhD dissertation, PSI4 was used in combination with Yaff and PLUMED to perform first-principles enhanced sampling molecular dynamics simulations for proton transfer reactions in small molecules. More information about this software is available at https://psicode.org/ and in Ref. [203].

QuickFF

QuickFF is a software package developed at the Center for Molecular Modeling, which allows to derive accurate force fields for molecular systems in a quick and easy manner. Starting from an equilibrium structure and a Hessian matrix, obtained from first-principles calculations, QuickFF generates

force field parameters to describe the covalent interactions in a molecular system. In this PhD dissertation, QuickFF force fields were used to simulate various MOFs. More information about this software is available at https://molmod.github.io/QuickFF/ and in Refs. [79, 80].

RASPA

RASPA is a software package that can be used to simulate the adsorption and diffusion of molecules in flexible nanoporous materials. In this PhD dissertation, RASPA was used to construct adsorption isotherms by means of grand canonical Monte Carlo simulations. More information about this software is available at https://iraspa.org/raspa/ and in Ref. [204].

WHAM

WHAM is a memory-efficient implementation of the Weighted Histogram Analysis Method, which allows to compute free energy profiles from biased molecular dynamics trajectories obtained from umbrella sampling simulations. In this PhD dissertation, all one-dimensional free energy profiles were obtained with the WHAM code. More information about this software is available at http://membrane.urmc.rochester.edu/?page_id=126.

Yaff

Yaff is a classical molecular dynamics code developed at the Center for Molecular Modeling, which can be used to perform force field simulations in different thermodynamic ensembles. In this PhD dissertation, Yaff was used to perform classical molecular dynamics simulations and to evaluate the interatomic energies and forces in path integral molecular dynamics simulations in combination with i-PI. More information about this software is available at http://molmod.github.io/yaff/.

D

High-Performance Computing Infrastructure

The computational resources (Stevin Supercomputer Infrastructure) and services used in this work were provided by the VSC (Flemish Supercomputer Center), funded by Ghent University, FWO, and the Flemish Government – department EWI. A list of granted project applications for Tier-1 compute time is provided below.

1. **Hydrogen diffusion pathways in a clathrate**
   Aran Lamaire, Alexander E.J. Hoffman, S. Borgmans, and Veronique Van Speybroeck
   4685824 core hours, March 2023 – November 2023 (Hortense)

2. **Methane diffusion in a clathrate**
   Aran Lamaire, Alexander E.J. Hoffman, and Veronique Van Speybroeck
   4259840 core hours, July 2022 – March 2023 (Hortense)

3. **Calculation of vibrational spectra of the lead-halide perovskite $CsPbBr_3$**
   Alexander E.J. Hoffman, Aran Lamaire, Siebe Vanlommel, Sven M.J. Rogge, and Veronique Van Speybroeck
   4672512 core hours, July 2022 – March 2023 (Hortense)

4. **Hydrogen diffusion in a clathrate**
   Aran Lamaire, Alexander E.J. Hoffman, and Veronique Van Speybroeck
   4259840 core hours, March 2022 – November 2022 (Hortense)

5. **Calculation of vibrational spectra of framework materials via static and dynamic approaches**
   Alexander E.J. Hoffman, Aran Lamaire, Sven M.J. Rogge, and Veronique Van Speybroeck
   3766144 core hours, March 2022 – November 2022 (Hortense)

6. **Data generation for a machine learning potential**
   Aran Lamaire
   500000 core hours (starting grant), March 2022 – July 2022 (Hortense)

7. **Proton diffusion in a zeolite (continuation)**
   Aran Lamaire, Alexander E.J. Hoffman, and Veronique Van Speybroeck
   2709504 core hours, November 2021 – July 2022 (Hortense)

8. **Proton diffusion in a zeolite**
   Aran Lamaire, Alexander E.J. Hoffman, and Veronique Van Speybroeck
   2709504 core hours, July 2021 – March 2022 (Hortense)

9. **Calculation of dynamic Raman spectra via finite difference and linear response**
   Alexander E.J. Hoffman, Aran Lamaire, and Veronique Van Speybroeck
   2220252 core hours, July 2021 – March 2022 (Hortense)

10. **Proton diffusion in a metal-organic framework**
    Aran Lamaire, Alexander E.J. Hoffman, and Veronique Van Speybroeck
    2683700 core hours, March 2021 – November 2021 (Hortense)

11. **Influence of extraframework Ca species on the MTO process in ZSM-5**
    Alexander E.J. Hoffman, Aran Lamaire, and Veronique Van Speybroeck
    3290112 core hours, March 2021 – November 2021 (Hortense)

12. **Development of machine learning potentials for the guest-induced flexibility in MIL-53(Al)**
    Sander Vandenhaute and Aran Lamaire
    4418 node days, November 2020 – July 2021 (BrENIAC)

13. **Characterization of the hydrogen-bonding structure of nanoconfined water in metal-organic frameworks**
    Sander Borgmans, Ruben Goeminne, and Aran Lamaire
    4200 node days, July 2020 – March 2021 (BrENIAC)

14. **Sampling of 3D adsorption energy profiles of nanoporous materials**
    Aran Lamaire, Sander Borgmans, and Veronique Van Speybroeck
    4033 node days, July 2020 – March 2021 (BrENIAC)

15. **Optimization algorithms for structures containing free rotors**
    Aran Lamaire
    500 node days (starting grant), May 2020 – September 2020 (BrENIAC)

16. **Unraveling the MTO process using Raman spectroscopy**
    Alexander E.J. Hoffman, Aran Lamaire, Karen Dedecker, and Veronique Van Speybroeck
    4860 node days, March 2020 – November 2020 (BrENIAC)

17. **Unraveling the MTO process using Raman spectroscopy**
    Alexander E.J. Hoffman, Aran Lamaire, and Veronique Van Speybroeck
    2880 node days, July 2019 – March 2020 (BrENIAC)

18. **Influence of nanoconfined water on the phase stability of flexible nanoporous materials**
    Aran Lamaire, Sander Borgmans, and Veronique Van Speybroeck
    3920 node days, July 2019 – March 2020 (BrENIAC)

19. **Influence of water on the phase stability of flexible nanoporous materials**
    Aran Lamaire, Sander Borgmans, Jelle Wieme, and Veronique Van Speybroeck
    4897 node days, March 2019 – November 2019 (BrENIAC)

20. **Computational study of the lattice dynamics in MIL-47**
    Alexander E.J. Hoffman, Aran Lamaire, and Veronique Van Speybroeck
    1260 node days, March 2019 – November 2019 (BrENIAC)

21. **Structural characterisation of water confined in nanoporous materials**
    Aran Lamaire, J. Wieme, and Veronique Van Speybroeck
    4512 node days, July 2018 – March 2019 (BrENIAC)

22. **Investigating the breathing behavior in flexible metal-organic frameworks using computational vibrational spectroscopy**
    Alexander E.J. Hoffman, Aran Lamaire, and Veronique Van Speybroeck
    1800 node days, July 2018 – March 2019 (BrENIAC)

23. **Investigating the low-frequency vibrational fingerprint of flexible metal-organic frameworks**
    Alexander E.J. Hoffman, Aran Lamaire, Jelle Wieme, and Veronique Van Speybroeck
    1062 node days, March 2018 – November 2018 (BrENIAC)

24. **Benchmarking elastic properties of metal-organic frameworks**
    Jelle Wieme, Aran Lamaire, Kurt Lejaeghere, and Veronique Van Speybroeck
    1296 node days, November 2017 – April 2018 (BrENIAC)

25. **Understanding the high-pressure behavior of a flexible nanoporous material**
    Jelle Wieme, Aran Lamaire, and Veronique Van Speybroeck
    2430 node days, September 2017 – December 2017 (BrENIAC)

Bibliography

[1] G. Galilei, *Dialogo sopra i due massimi sistemi del mondo.* 1632.

[2] M. Ding, R. W. Flaig, H.-L. Jiang, and O. M. Yaghi, "Carbon capture and conversion using metal-organic frameworks and MOF-based materials," *Chem. Soc. Rev.*, vol. 48, pp. 2783–2828, 2019.

[3] D. Fu and M. E. Davis, "Carbon dioxide capture with zeotype materials," *Chem. Soc. Rev.*, vol. 51, pp. 9340–9370, 2022.

[4] Q. Zhang, J. Yu, and A. Corma, "Applications of Zeolites to C1 Chemistry: Recent Advances, Challenges, and Opportunities," *Adv. Mater.*, vol. 32, no. 44, p. 2002927, 2020.

[5] T. Ennaert, J. Van Aelst, J. Dijkmans, R. De Clercq, W. Schutyser, M. Dusselier, D. Verboekend, and B. F. Sels, "Potential and challenges of zeolite chemistry in the catalytic conversion of biomass," *Chem. Soc. Rev.*, vol. 45, pp. 584–611, 2016.

[6] N. Hanikel, M. S. Prévot, and O. M. Yaghi, "MOF water harvesters," *Nat. Nanotechnol.*, vol. 15, no. 5, pp. 348–355, 2020.

[7] Y. Li, L. Li, and J. Yu, "Applications of Zeolites in Sustainable Chemistry," *Chem*, vol. 3, no. 6, pp. 928–949, 2017.

[8] C. Baerlocher, D. Brouwer, B. Marler, and L. McCusker, "Database of Zeolite Structures." https://www.iza-structure.org/databases/.

[9] A. F. Masters and T. Maschmeyer, "Zeolites – From curiosity to cornerstone," *Micropor. Mesopor. Mat.*, vol. 142, no. 2, pp. 423–438, 2011.

[10] B. M. Weckhuysen and J. Yu, "Recent advances in zeolite chemistry and catalysis," *Chem. Soc. Rev.*, vol. 44, pp. 7022–7024, 2015.

[11] R. M. Barrer, "33. Synthesis of a zeolitic mineral with chabazite-like sorptive properties," *J. Chem. Soc.*, pp. 127–132, 1948.

[12] B. Smit and T. L. M. Maesen, "Towards a molecular understanding of shape selectivity," *Nature*, vol. 451, no. 7179, pp. 671–678, 2008.

[13] C. Chizallet, C. Bouchy, K. Larmier, and G. Pirngruber, "Molecular Views on Mechanisms of Brønsted Acid-Catalyzed Reactions in Zeolites," *Chem. Rev.*, vol. 123, no. 9, pp. 6107–6196, 2023.

[14] Y. Liao, R. Zhong, E. Makshina, M. d'Halluin, Y. van Limbergen, D. Verboekend, and B. F. Sels, "Propylphenol to Phenol and Propylene over Acidic Zeolites: Role of Shape Selectivity and Presence of Steam," *ACS Catal.*, vol. 8, no. 9, pp. 7861–7878, 2018.

[15] S. Mardiana, N. J. Azhari, T. Ilmi, and G. T. Kadja, "Hierarchical zeolite for biomass conversion to biofuel: A review," *Fuel*, vol. 309, p. 122119, 2022.

[16] Y. Li and J. Yu, "Emerging applications of zeolites in catalysis, separation and host–guest assembly," *Nat. Rev. Mater.*, vol. 6, no. 12, pp. 1156–1174, 2021.

[17] A. Burrows, J. Holman, A. Parsons, G. Pilling, and G. Price, *Chemistry^3: introducing inorganic, organic, and physical chemistry*. Oxford University Press, 2017.

[18] J. Lehto, R. Koivula, H. Leinonen, E. Tusa, and R. Harjula, "Removal of Radionuclides from Fukushima Daiichi Waste Effluents," *Sep. Purif. Rev.*, vol. 48, no. 2, pp. 122–142, 2019.

[19] X. Tan, S. Robijns, R. Thür, Q. Ke, N. D. Witte, A. Lamaire, Y. Li, I. Aslam, D. V. Havere, T. Donckels, T. V. Assche, V. V. Speybroeck, M. Dusselier, and I. Vankelecom, "Truly combining the advantages of polymeric and zeolite membranes for gas separations," *Science*, vol. 378, no. 6625, pp. 1189–1194, 2022.

[20] D. G. Boer, J. Langerak, and P. P. Pescarmona, "Zeolites as Selective Adsorbents for CO_2 Separation," *ACS Appl. Energy Mater.*, vol. 6, no. 5, pp. 2634–2656, 2023.

[21] P. Z. Moghadam, A. Li, S. B. Wiggin, A. Tao, A. G. P. Maloney, P. A. Wood, S. C. Ward, and D. Fairen-Jimenez, "Development of a Cambridge Structural Database Subset: A Collection of Metal-Organic Frameworks for Past, Present, and Future," *Chem. Mater.*, vol. 29, no. 7, pp. 2618–2625, 2017.

[22] R. Freund, O. Zaremba, G. Arnauts, R. Ameloot, G. Skorupskii, M. Dincă, A. Bavykina, J. Gascon, A. Ejsmont, J. Goscianska, M. Kalmutzki, U. Lächelt, E. Ploetz, C. S. Diercks, and S. Wuttke, "The Current Status of MOF and COF Applications," *Angew. Chem. Int. Ed.*, vol. 60, no. 45, pp. 23975–24001, 2021.

[23] B. P. Block, S. H. Rose, C. W. Schaumann, E. S. Roth, and J. Simkin, "Coordination Polymers with Inorganic Backbones Formed by Double-Bridging of Tetrahedral Elements," *J. Am. Chem. Soc.*, vol. 84, no. 16, pp. 3200–3201, 1962.

[24] E. A. Tomic, "Thermal stability of coordination polymers," *J. Appl. Polym. Sci.*, vol. 9, no. 11, pp. 3745–3752, 1965.

[25] H. Li, M. Eddaoudi, M. O'Keeffe, and O. M. Yaghi, "Design and synthesis of an exceptionally stable and highly porous metal-organic framework," *Nature*, vol. 402, pp. 276–279, 1999.

[26] M. Eddaoudi, J. Kim, N. Rosi, D. Vodak, J. Wachter, M. O'Keeffe, and O. M. Yaghi, "Systematic Design of Pore Size and Functionality in Isoreticular MOFs and Their Application in Methane Storage," *Science*, vol. 295, no. 5554, pp. 469–472, 2002.

[27] H. Furukawa, K. E. Cordova, M. O'Keeffe, and O. M. Yaghi, "The Chemistry and Applications of Metal-Organic Frameworks," *Science*, vol. 341, no. 6149, 2013.

[28] O. M. Yaghi, M. O'Keeffe, N. W. Ockwig, H. K. Chae, M. Eddaoudi, and J. Kim, "Reticular synthesis and the design of new materials," *Nature*, vol. 423, no. 6941, pp. 705–714, 2003.

[29] A. J. Howarth, Y. Liu, P. Li, Z. Li, T. C. Wang, J. T. Hupp, and O. K. Farha, "Chemical, thermal and mechanical stabilities of metal-organic frameworks," *Nat. Rev. Mater.*, vol. 1, no. 3, p. 15018, 2016.

[30] P. Guo, D. Dutta, A. G. Wong-Foy, D. W. Gidley, and A. J. Matzger, "Water Sensitivity in Zn_4O-Based MOFs is Structure and History Dependent," *J. Am. Chem. Soc.*, vol. 137, no. 7, pp. 2651–2657, 2015.

[31] M. Rubio-Martinez, C. Avci-Camur, A. W. Thornton, I. Imaz, D. Maspoch, and M. R. Hill, "New synthetic routes towards MOF production at scale," *Chem. Soc. Rev.*, vol. 46, pp. 3453–3480, 2017.

[32] J. H. Cavka, S. Jakobsen, U. Olsbye, N. Guillou, C. Lamberti, S. Bordiga, and K. P. Lillerud, "A New Zirconium Inorganic Building Brick Forming

Metal Organic Frameworks with Exceptional Stability," *J. Am. Chem. Soc.*, vol. 130, no. 42, pp. 13850–13851, 2008.

[33] S. M. J. Rogge, J. Wieme, L. Vanduyfhuys, S. Vandenbrande, G. Maurin, T. Verstraelen, M. Waroquier, and V. Van Speybroeck, "Thermodynamic Insight in the High-Pressure Behavior of UiO-66: Effect of Linker Defects and Linker Expansion," *Chem. Mater.*, vol. 28, no. 16, pp. 5721–5732, 2016.

[34] J.-B. Lin, T. T. T. Nguyen, R. Vaidhyanathan, J. Burner, J. M. Taylor, H. Durekova, F. Akhtar, R. K. Mah, O. Ghaffari-Nik, S. Marx, N. Fylstra, S. S. Iremonger, K. W. Dawson, P. Sarkar, P. Hovington, A. Rajendran, T. K. Woo, and G. K. H. Shimizu, "A scalable metal-organic framework as a durable physisorbent for carbon dioxide capture," *Science*, vol. 374, no. 6574, pp. 1464–1469, 2021.

[35] W. Xu and O. M. Yaghi, "Metal-Organic Frameworks for Water Harvesting from Air, Anywhere, Anytime," *ACS Cent. Sci.*, vol. 6, no. 8, pp. 1348–1354, 2020.

[36] M. J. Kalmutzki, C. S. Diercks, and O. M. Yaghi, "Metal-Organic Frameworks for Water Harvesting from Air," *Adv. Mater.*, vol. 30, no. 37, p. 1704304, 2018.

[37] F. Fathieh, M. J. Kalmutzki, E. A. Kapustin, P. J. Waller, J. Yang, and O. M. Yaghi, "Practical water production from desert air," *Sci. Adv.*, vol. 4, no. 6.

[38] H. A. Almassad, R. I. Abaza, L. Siwwan, B. Al-Maythalony, and K. E. Cordova, "Environmentally adaptive MOF-based device enables continuous self-optimizing atmospheric water harvesting," *Nat. Commun.*, vol. 13, p. 4873, 2022.

[39] J. Lee, O. K. Farha, J. Roberts, K. A. Scheidt, S. T. Nguyen, and J. T. Hupp, "Metal–organic framework materials as catalysts," *Chem. Soc. Rev.*, vol. 38, pp. 1450–1459, 2009.

[40] J. Liang, Z. Liang, R. Zou, and Y. Zhao, "Heterogeneous Catalysis in Zeolites, Mesoporous Silica, and Metal-Organic Frameworks," *Adv. Mater.*, vol. 29, no. 30, p. 1701139, 2017.

[41] S. M. J. Rogge, A. Bavykina, J. Hajek, H. Garcia, A. I. Olivos-Suarez, A. Sepúlveda-Escribano, A. Vimont, G. Clet, P. Bazin, F. Kapteijn,

M. Daturi, E. V. Ramos-Fernandez, F. X. Llabrés i Xamena, V. Van Speybroeck, and J. Gascon, "Metal-organic and covalent organic frameworks as single-site catalysts," *Chem. Soc. Rev.*, vol. 46, pp. 3134–3184, 2017.

[42] M. de J. Velásquez-Hernández, M. Linares-Moreau, E. Astria, F. Carraro, M. Z. Alyami, N. M. Khashab, C. J. Sumby, C. J. Doonan, and P. Falcaro, "Towards applications of bioentities@MOFs in biomedicine," *Coord. Chem. Rev.*, vol. 429, p. 213651, 2021.

[43] J. W. M. Osterrieth and D. Fairen-Jimenez, "Metal-Organic Framework Composites for Theragnostics and Drug Delivery Applications," *Biotechnol. J.*, vol. 16, no. 2, p. 2000005, 2021.

[44] A. Schneemann, V. Bon, I. Schwedler, I. Senkovska, S. Kaskel, and R. A. Fischer, "Flexible metal-organic frameworks," *Chem. Soc. Rev.*, vol. 43, pp. 6062–6096, 2014.

[45] Z. Chang, D.-H. Yang, J. Xu, T.-L. Hu, and X.-H. Bu, "Flexible Metal-Organic Frameworks: Recent Advances and Potential Applications," *Adv. Mater.*, vol. 27, no. 36, pp. 5432–5441, 2015.

[46] S. Horike, S. Shimomura, and S. Kitagawa, "Soft porous crystals," *Nat. Chem.*, vol. 1, no. 9, pp. 695–704, 2009.

[47] S. A. Moggach, T. D. Bennett, and A. K. Cheetham, "The Effect of Pressure on ZIF-8: Increasing Pore Size with Pressure and the Formation of a High-Pressure Phase at 1.47 GPa," *Angew. Chem. Int. Ed.*, vol. 48, no. 38, pp. 7087–7089, 2009.

[48] D. Fairen-Jimenez, S. A. Moggach, M. T. Wharmby, P. A. Wright, S. Parsons, and T. Düren, "Opening the Gate: Framework Flexibility in ZIF-8 Explored by Experiments and Simulations," *J. Am. Chem. Soc.*, vol. 133, no. 23, pp. 8900–8902, 2011.

[49] S. Krause, V. Bon, I. Senkovska, U. Stoeck, D. Wallacher, D. M. Többens, S. Zander, R. S. Pillai, G. Maurin, F.-X. Coudert, and S. Kaskel, "A pressure-amplifying framework material with negative gas adsorption transitions," *Nature*, vol. 532, no. 7599, pp. 348–352, 2016.

[50] S. Krause, J. D. Evans, V. Bon, I. Senkovska, P. Iacomi, F. Kolbe, S. Ehrling, E. Troschke, J. Getzschmann, D. M. Többens, A. Franz, D. Wallacher, P. G. Yot, G. Maurin, E. Brunner, P. L. Llewellyn, F.-X. Coudert, and S. Kaskel, "Towards general network architecture design criteria for negative gas adsorption transitions in ultraporous frameworks," *Nat. Commun.*, vol. 10, p. 3632, 2019.

[51] G. Férey and C. Serre, "Large breathing effects in three-dimensional porous hybrid matter: facts, analyses, rules and consequences," *Chem. Soc. Rev.*, vol. 38, pp. 1380–1399, 2009.

[52] A. E. J. Hoffman, L. Vanduyfhuys, I. Nevjestić, J. Wieme, S. M. J. Rogge, H. Depauw, P. Van Der Voort, H. Vrielinck, and V. Van Speybroeck, "Elucidating the Vibrational Fingerprint of the Flexible Metal-Organic Framework MIL-53(Al) Using a Combined Experimental/Computational Approach," *J. Phys. Chem. C*, vol. 122, no. 5, pp. 2734–2746, 2018.

[53] L. Vanduyfhuys, S. M. J. Rogge, J. Wieme, S. Vandenbrande, G. Maurin, M. Waroquier, and V. Van Speybroeck, "Thermodynamic insight into stimuli-responsive behaviour of soft porous crystals," *Nat. Commun.*, vol. 9, p. 204, 2018.

[54] R.-B. Lin, S. Xiang, W. Zhou, and B. Chen, "Microporous Metal-Organic Framework Materials for Gas Separation," *Chem*, vol. 6, no. 2, pp. 337–363, 2020.

[55] Y. Shen, A. Tissot, and C. Serre, "Recent progress on MOF-based optical sensors for VOC sensing," *Chem. Sci.*, vol. 13, pp. 13978–14007, 2022.

[56] P. G. Yot, Z. Boudene, J. Macia, D. Granier, L. Vanduyfhuys, T. Verstraelen, V. Van Speybroeck, T. Devic, C. Serre, G. Ferey, N. Stock, and G. Maurin, "Metal-organic frameworks as potential shock absorbers: the case of the highly flexible MIL-53(Al)," *Chem. Commun.*, vol. 50, pp. 9462–9464, 2014.

[57] A. Reinhardt and B. Cheng, "Quantum-mechanical exploration of the phase diagram of water," *Nat. Commun.*, vol. 12, p. 588, 2021.

[58] M. Ceriotti, W. Fang, P. G. Kusalik, R. H. McKenzie, A. Michaelides, M. A. Morales, and T. E. Markland, "Nuclear Quantum Effects in Water and Aqueous Systems: Experiment, Theory, and Current Challenges," *Chem. Rev.*, vol. 116, no. 13, pp. 7529–7550, 2016.

[59] A. C. Doyle, *A Case of Identity*. 1892.

[60] V. Van Speybroeck, S. Vandenhaute, A. E. J. Hoffman, and S. M. J. Rogge, "Towards modeling spatiotemporal processes in metal-organic frameworks," *Trends in Chem.*, vol. 3, no. 8, pp. 605–619, 2021.

[61] F. Giustino, *Materials Modelling Using Density Functional Theory: Properties and Predictions*. Oxford University Press, 2014.

[62] B. Bransden and C. Joachain, *Physics of Atoms and Molecules*. Pearson Education, Prentice Hall, 2003.

[63] R. M. Martin, *Electronic Structure: Basic Theory and Practical Methods*. Cambridge University Press, 2004.

[64] R. G. Parr and Y. Weitao, *Density-Functional Theory of Atoms and Molecules*. Oxford University Press, 1995.

[65] J. P. Perdew, K. Burke, and M. Ernzerhof, "Generalized Gradient Approximation Made Simple," *Phys. Rev. Lett.*, vol. 77, pp. 3865–3868, 1996.

[66] A. D. Becke, "Density-functional exchange-energy approximation with correct asymptotic behavior," *Phys. Rev. A*, vol. 38, pp. 3098–3100, 1988.

[67] C. Lee, W. Yang, and R. G. Parr, "Development of the Colle-Salvetti correlation-energy formula into a functional of the electron density," *Phys. Rev. B*, vol. 37, pp. 785–789, 1988.

[68] J. Sun, A. Ruzsinszky, and J. P. Perdew, "Strongly Constrained and Appropriately Normed Semilocal Density Functional," *Phys. Rev. Lett.*, vol. 115, p. 036402, 2015.

[69] C. Adamo and V. Barone, "Toward reliable density functional methods without adjustable parameters: The PBE0 model," *J. Chem. Phys.*, vol. 110, no. 13, pp. 6158–6170, 1999.

[70] A. D. Becke, "Density-functional exchange-energy approximation with correct asymptotic behavior," *Phys. Rev. A*, vol. 38, pp. 3098–3100, 1988.

[71] J. P. Perdew and K. Schmidt, "Jacob's ladder of density functional approximations for the exchange-correlation energy," *AIP Conf. Proc.*, vol. 577, pp. 1–20, 07 2001.

[72] D. Dubbeldam, K. S. Walton, T. J. H. Vlugt, and S. Calero, "Design, Parameterization, and Implementation of Atomic Force Fields for Adsorption in Nanoporous Materials," *Adv. Theory Simul.*, vol. 2, no. 11, p. 1900135, 2019.

[73] J. E. Lennard-Jones, "Cohesion," *Proc. Phys. Soc.*, vol. 43, no. 5, p. 461, 1931.

[74] S. L. Mayo, B. D. Olafson, and W. A. Goddard, "DREIDING: a generic force field for molecular simulations," *J. Phys. Chem.*, vol. 94, no. 26, pp. 8897–8909, 1990.

[75] N. L. Allinger, Y. H. Yuh, and J. H. Lii, "Molecular mechanics. the MM3 force field for hydrocarbons. 1," *J. Am. Chem. Soc.*, vol. 111, no. 23, pp. 8551–8566, 1989.

[76] A. K. Rappé, C. J. Casewit, K. S. Colwell, W. A. I. Goddard, and W. M. Skiff, "UFF, a full periodic table force field for molecular mechanics and molecular dynamics simulations," *J. Am. Chem. Soc.*, vol. 114, no. 25, pp. 10024–10035, 1992.

[77] M. A. Addicoat, N. Vankova, I. F. Akter, and T. Heine, "Extension of the universal force field to metal–organic frameworks," *J. Chem. Theory Comput.*, vol. 10, no. 2, pp. 880–891, 2014.

[78] S. Bureekaew, S. Amirjalayer, M. Tafipolsky, C. Spickermann, T. K. Roy, and R. Schmid, "MOF-FF - A flexible first-principles derived force field for metal-organic frameworks," *Phys. Status Solidi (B)*, vol. 250, no. 6, pp. 1128–1141, 2013.

[79] L. Vanduyfhuys, S. Vandenbrande, T. Verstraelen, R. Schmid, M. Waroquier, and V. Van Speybroeck, "QuickFF: A program for a quick and easy derivation of force fields for metal-organic frameworks from ab initio input," *J. Comput. Chem.*, vol. 36, no. 13, pp. 1015–1027, 2015.

[80] L. Vanduyfhuys, S. Vandenbrande, J. Wieme, M. Waroquier, T. Verstraelen, and V. Van Speybroeck, "Extension of the QuickFF force field protocol for an improved accuracy of structural, vibrational, mechanical and thermal properties of metal-organic frameworks," *J. Comput. Chem.*, vol. 39, no. 16, pp. 999–1011, 2018.

[81] T. Verstraelen, S. Vandenbrande, F. Heidar-Zadeh, L. Vanduyfhuys, V. Van Speybroeck, M. Waroquier, and P. W. Ayers, "Minimal Basis Iterative Stockholder: Atoms in Molecules for Force-Field Development," *J. Chem. Theory Comput.*, vol. 12, no. 8, pp. 3894–3912, 2016.

[82] N. L. Allinger, X. Zhou, and J. Bergsma, "Molecular mechanics parameters," *J. Mol. Struct.: THEOCHEM*, vol. 312, no. 1, pp. 69–83, 1994.

[83] S. Habershon, T. E. Markland, and D. E. Manolopoulos, "Competing quantum effects in the dynamics of a flexible water model," *J. Chem. Phys.*, vol. 131, no. 2, p. 024501, 2009.

[84] J. J. Potoff and J. I. Siepmann, "Vapor-liquid equilibria of mixtures containing alkanes, carbon dioxide, and nitrogen," *AIChE J.*, vol. 47, no. 7, pp. 1676–1682.

[85] A. C. T. van Duin, S. Dasgupta, F. Lorant, and W. A. Goddard, "ReaxFF: A Reactive Force Field for Hydrocarbons," *J. Phys. Chem. A*, vol. 105, no. 41, pp. 9396–9409, 2001.

[86] M. Cools-Ceuppens, *Incorporating long-range interactions and polarization in machine learning potentials with explicit electrons*. PhD thesis, 2022.

[87] S. Vandenhaute, M. Cools-Ceuppens, S. DeKeyser, T. Verstraelen, and V. Van Speybroeck, "Machine learning potentials for metal-organic frameworks using an incremental learning approach," *npj Comput. Mater.*, vol. 9, no. 1, p. 19, 2023.

[88] K. T. Schütt, H. E. Sauceda, P.-J. Kindermans, A. Tkatchenko, and K.-R. Müller, "SchNet – A deep learning architecture for molecules and materials," *J. Chem. Phys.*, vol. 148, no. 24, p. 241722, 2018.

[89] S. Batzner, A. Musaelian, L. Sun, M. Geiger, J. P. Mailoa, M. Kornbluth, N. Molinari, T. E. Smidt, and B. Kozinsky, "E(3)-equivariant graph neural networks for data-efficient and accurate interatomic potentials," *Nat. Commun.*, vol. 13, p. 2453, 2022.

[90] V. Van Speybroeck, "Challenges in modelling dynamic processes in realistic nanostructured materials at operating conditions," *Phil. Trans. R. Soc. A*, vol. 381, no. 2250, p. 20220239, 2023.

[91] A. E. J. Hoffman, W. Temmerman, E. Campbell, A. A. Damin, I. Lezcano-Gonzalez, A. M. Beale, S. Bordiga, J. Hofkens, and V. Van Speybroeck, "A Critical Assessment on Calculating Vibrational Spectra in Nanostructured Materials," *J. Chem. Theory Comput.*, vol. 20, no. 2, pp. 513–531, 2024.

[92] R. Golesorkhtabar, P. Pavone, J. Spitaler, P. Puschnig, and C. Draxl, "ElaStic: A tool for calculating second-order elastic constants from first principles," *Comput. Phys. Commun.*, vol. 184, no. 8, pp. 1861–1873, 2013.

[93] V. Kapil, J. Wieme, S. Vandenbrande, A. Lamaire, V. Van Speybroeck, and M. Ceriotti, "Modeling the Structural and Thermal Properties of Loaded Metal-Organic Frameworks. An Interplay of Quantum and Anharmonic Fluctuations," *J. Chem. Theory Comput.*, vol. 15, no. 5, pp. 3237–3249, 2019.

[94] D. Frenkel and B. Smit, *Understanding Molecular Simulation: From Algorithms to Applications*. Elsevier Science, 2001.

[95] M. E. Tuckerman, *Statistical Mechanics: Theory and Molecular Simulation.* OUP Oxford, 2010.

[96] S. Nosé, "A molecular dynamics method for simulations in the canonical ensemble," *Mol. Phys.*, vol. 52, no. 2, pp. 255–268, 1984.

[97] W. G. Hoover, "Canonical dynamics: Equilibrium phase-space distributions," *Phys. Rev. A*, vol. 31, pp. 1695–1697, 1985.

[98] G. J. Martyna, M. L. Klein, and M. Tuckerman, "Nosé-Hoover chains: The canonical ensemble via continuous dynamics," *J. Chem. Phys.*, vol. 97, no. 4, pp. 2635–2643, 1992.

[99] G. J. Martyna, D. J. Tobias, and M. L. Klein, "Constant pressure molecular dynamics algorithms," *J. Chem. Phys.*, vol. 101, no. 5, pp. 4177–4189, 1994.

[100] G. J. Martyna, M. E. Tuckerman, D. J. Tobias, and M. L. Klein, "Explicit reversible integrators for extended systems dynamics," *Mol. Phys.*, vol. 87, no. 5, pp. 1117–1157, 1996.

[101] J. Thijssen, *Computational Physics.* Cambridge University Press, 2007.

[102] J. A. Barker, "A quantum-statistical Monte Carlo method; path integrals with boundary conditions," *J. Chem. Phys.*, vol. 70, no. 6, pp. 2914–2918, 1979.

[103] D. M. Ceperley, "Path integrals in the theory of condensed helium," *Rev. Mod. Phys.*, vol. 67, pp. 279–355, 1995.

[104] C. Herrero and R. Ramírez, "Path-integral simulation of solids," *J. Phys. Condens. Matter*, vol. 26, no. 23, p. 233201, 2014.

[105] S. Vandenbrande, M. Waroquier, V. Van Speybroeck, and T. Verstraelen, "Ab Initio Evaluation of Henry Coefficients Using Importance Sampling," *J. Chem. Theory Comput.*, vol. 14, no. 12, pp. 6359–6369, 2018.

[106] R. Goeminne, L. Vanduyfhuys, V. Van Speybroeck, and T. Verstraelen, "DFT-Quality Adsorption Simulations in Metal-Organic Frameworks Enabled by Machine Learning Potentials," *J. Chem. Theory Comput.*, vol. 19, no. 18, pp. 6313–6325, 2023.

[107] S. M. J. Rogge, R. Goeminne, R. Demuynck, J. J. Gutiérrez-Sevillano, S. Vandenbrande, L. Vanduyfhuys, M. Waroquier, T. Verstraelen, and V. Van Speybroeck, "Modeling Gas Adsorption in Flexible Metal-Organic Frameworks via Hybrid Monte Carlo/Molecular Dynamics Schemes," *Adv. Theory Simul.*, vol. 2, no. 4, p. 1800177, 2019.

[108] R. Goeminne, S. Krause, S. Kaskel, T. Verstraelen, and J. D. Evans, "Charting the Complete Thermodynamic Landscape of Gas Adsorption for a Responsive Metal-Organic Framework," *J. Am. Chem. Soc.*, vol. 143, no. 11, pp. 4143–4147, 2021.

[109] M. Witman, N. A. Mahynski, and B. Smit, "Flat-Histogram Monte Carlo as an Efficient Tool To Evaluate Adsorption Processes Involving Rigid and Deformable Molecules," *J. Chem. Theory Comput.*, vol. 14, no. 12, pp. 6149–6158, 2018.

[110] M. Witman, B. Wright, and B. Smit, "Simulating Enhanced Methane Deliverable Capacity of Guest Responsive Pores in Intrinsically Flexible MOFs," *J. Phys. Chem. Lett.*, vol. 10, no. 19, pp. 5929–5934, 2019.

[111] G. Torrie and J. Valleau, "Nonphysical sampling distributions in monte carlo free-energy estimation: Umbrella sampling," *J. Comput. Phys.*, vol. 23, no. 2, pp. 187–199, 1977.

[112] S. Kumar, J. M. Rosenberg, D. Bouzida, R. H. Swendsen, and P. A. Kollman, "THE weighted histogram analysis method for free-energy calculations on biomolecules. I. The method," *J. Comput. Chem.*, vol. 13, no. 8, pp. 1011–1021, 1992.

[113] B. Roux, "The calculation of the potential of mean force using computer simulations," *Comput. Phys. Commun.*, vol. 91, no. 1, pp. 275–282, 1995.

[114] S. Borgmans, *In-depth computational characterization of the structure and dynamics in covalent organic frameworks.* PhD thesis, 2023.

[115] S. Borgmans, S. M. J. Rogge, L. Vanduyfhuys, and V. Van Speybroeck, "OGRe: Optimal Grid Refinement Protocol for Accurate Free Energy Surfaces and Its Application in Proton Hopping in Zeolites and 2D COF Stacking," *J. Chem. Theory Comput.*, vol. 19, no. 24, pp. 9032–9048, 2023.

[116] A. Laio and M. Parrinello, "Escaping free-energy minima," *Proc. Natl. Acad. Sci. USA*, vol. 99, no. 20, pp. 12562–12566, 2002.

[117] O. Valsson and M. Parrinello, "Variational Approach to Enhanced Sampling and Free Energy Calculations," *Phys. Rev. Lett.*, vol. 113, p. 090601, 2014.

[118] S. M. J. Rogge, L. Vanduyfhuys, A. Ghysels, M. Waroquier, T. Verstraelen, G. Maurin, and V. Van Speybroeck, "A Comparison of Barostats for the Mechanical Characterization of Metal-Organic Frameworks," *J. Chem. Theory Comput.*, vol. 11, no. 12, pp. 5583–5597, 2015.

[119] Y. Sugita and Y. Okamoto, "Replica-exchange molecular dynamics method for protein folding," *Chemical Physics Letters*, vol. 314, no. 1, pp. 141–151, 1999.

[120] P. G. Bolhuis and D. W. H. Swenson, "Transition Path Sampling as Markov Chain Monte Carlo of Trajectories: Recent Algorithms, Software, Applications, and Future Outlook," *Adv. Theory Simul.*, vol. 4, no. 4, p. 2000237, 2021.

[121] R. Demuynck, S. M. J. Rogge, L. Vanduyfhuys, J. Wieme, M. Waroquier, and V. Van Speybroeck, "Efficient Construction of Free Energy Profiles of Breathing Metal–Organic Frameworks Using Advanced Molecular Dynamics Simulations," *J. Chem. Theory Comput.*, vol. 13, no. 12, pp. 5861–5873, 2017.

[122] S. Grimme, J. Antony, S. Ehrlich, and H. Krieg, "A consistent and accurate ab initio parametrization of density functional dispersion correction (DFT-D) for the 94 elements H-Pu," *J. Chem. Phys.*, vol. 132, no. 15, p. 154104, 2010.

[123] S. Grimme, S. Ehrlich, and L. Goerigk, "Effect of the damping function in dispersion corrected density functional theory," *J. Comput. Chem.*, vol. 32, no. 7, pp. 1456–1465, 2011.

[124] E. Beerdsen, B. Smit, and D. Dubbeldam, "Molecular Simulation of Loading Dependent Slow Diffusion in Confined Systems," *Phys. Rev. Lett.*, vol. 93, p. 248301, 2004.

[125] D. S. Sholl and R. P. Lively, "Seven chemical separations to change the world," *Nature*, vol. 532, no. 7600, pp. 435–437, 2016.

[126] T. E. Markland and M. Ceriotti, "Nuclear quantum effects enter the mainstream," *Nat. Rev. Chem.*, vol. 2, p. 0109, 2018.

[127] M. Rossi, W. Fang, and A. Michaelides, "Stability of Complex Biomolecular Structures: van der Waals, Hydrogen Bond Cooperativity, and Nuclear Quantum Effects," *J. Phys. Chem. Lett.*, vol. 6, no. 21, pp. 4233–4238, 2015.

[128] L. Wang, S. D. Fried, S. G. Boxer, and T. E. Markland, "Quantum delocalization of protons in the hydrogen-bond network of an enzyme active site," *Proc. Natl. Acad. Sci.*, vol. 111, no. 52, pp. 18454–18459, 2014.

[129] J. E. Lawrence and D. E. Manolopoulos, "Path integral methods for reaction rates in complex systems," *Faraday Discuss.*, vol. 221, pp. 9–29, 2020.

[130] P. Dulong and A. Petit, *Recherches sur la mesure des températures et sur les lois de la communication de la chaleur.* 1818.

[131] L. D. Landau and E. M. Lifshitz, *Statistical Physics.* 1970.

[132] C. L. Hobday, C. H. Woodall, M. J. Lennox, M. Frost, K. Kamenev, T. Düren, C. A. Morrison, and S. A. Moggach, "Understanding the adsorption process in ZIF-8 using high pressure crystallography and computational modelling," *Nat. Commun.*, vol. 9, p. 1429, 2018.

[133] K. Titov, M. R. Ryder, A. Lamaire, Z. Zeng, A. K. Chaudhari, J. Taylor, E. M. Mahdi, S. M. J. Rogge, S. Mukhopadhyay, S. Rudić, V. Van Speybroeck, F. Fernandez-Alonso, and J.-C. Tan, "Quantum tunneling rotor as a sensitive atomistic probe of guests in a metal-organic framework," *Phys. Rev. Mater.*, vol. 7, p. 073402, 2023.

[134] R. M. Dimeo, "Visualization and measurement of quantum rotational dynamics," *Am. J. Phys.*, vol. 71, no. 9, pp. 885–893, 2003.

[135] A. Horsewill, "Quantum tunnelling aspects of methyl group rotation studied by NMR," *Prog. Nucl. Magn. Reson. Spectrosc.*, vol. 35, no. 4, pp. 359–389, 1999.

[136] R. P. Feynman, "Space-Time Approach to Non-Relativistic Quantum Mechanics," *Rev. Mod. Phys.*, vol. 20, pp. 367–387, 1948.

[137] A. Lamaire, M. Cools-Ceuppens, M. Bocus, T. Verstraelen, and V. Van Speybroeck, "Quantum free energy profiles for molecular proton transfers," *J. Chem. Theory Comput.*, vol. 19, no. 1, pp. 18–24, 2023.

[138] S. C. Althorpe, "Path-integral approximations to quantum dynamics," *Eur. Phys. J. B*, vol. 94, no. 7, p. 155, 2021.

[139] M. Ceriotti, D. E. Manolopoulos, and M. Parrinello, "Accelerating the convergence of path integral dynamics with a generalized Langevin equation," *J. Chem. Phys.*, vol. 134, no. 8, p. 084104, 2011.

[140] M. Ceriotti and D. E. Manolopoulos, "Efficient First-Principles Calculation of the Quantum Kinetic Energy and Momentum Distribution of Nuclei," *Phys. Rev. Lett.*, vol. 109, p. 100604, 2012.

[141] I. R. Craig and D. E. Manolopoulos, "Quantum statistics and classical mechanics: Real time correlation functions from ring polymer molecular dynamics," *J. Chem. Phys.*, vol. 121, no. 8, pp. 3368–3373, 2004.

[142] S. Habershon, D. E. Manolopoulos, T. E. Markland, and T. F. Miller III, "Ring-Polymer Molecular Dynamics: Quantum Effects in Chemical Dynamics from Classical Trajectories in an Extended Phase Space," *Annu. Rev. Phys. Chem.*, vol. 64, no. 1, pp. 387–413, 2013.

[143] J. Cao and G. A. Voth, "A new perspective on quantum time correlation functions," *J. Chem. Phys.*, vol. 99, no. 12, pp. 10070–10073, 1993.

[144] S. Jang and G. A. Voth, "Path integral centroid variables and the formulation of their exact real time dynamics," *J. Chem. Phys.*, vol. 111, no. 6, pp. 2357–2370, 1999.

[145] G. R. Medders and F. Paesani, "Infrared and Raman Spectroscopy of Liquid Water through "First-Principles" Many-Body Molecular Dynamics," *J. Chem. Theory Comput.*, vol. 11, no. 3, pp. 1145–1154, 2015.

[146] M. Rossi, M. Ceriotti, and D. E. Manolopoulos, "How to remove the spurious resonances from ring polymer molecular dynamics," *J. Chem. Phys.*, vol. 140, no. 23, p. 234116, 2014.

[147] S. D. Ivanov, A. Witt, M. Shiga, and D. Marx, "Communications: On artificial frequency shifts in infrared spectra obtained from centroid molecular dynamics: Quantum liquid water," *The Journal of Chemical Physics*, vol. 132, no. 3, p. 031101, 2010.

[148] I. R. Craig and D. E. Manolopoulos, "A refined ring polymer molecular dynamics theory of chemical reaction rates," *J. Chem. Phys.*, vol. 123, no. 3, p. 034102, 2005.

[149] R. P. Feynman, "Simulating Physics with Computers," *Int. J. Theor. Phys.*, vol. 21, no. 6, pp. 467–488, 1982.

[150] B. Mu and K. S. Walton, "Thermal Analysis and Heat Capacity Study of Metal-Organic Frameworks," *J. Phys. Chem. C*, vol. 115, no. 46, pp. 22748–22754, 2011.

[151] F. Kloutse, R. Zacharia, D. Cossement, and R. Chahine, "Specific heat capacities of MOF-5, Cu-BTC, Fe-BTC, MOF-177 and MIL-53(Al) over wide temperature ranges: Measurements and application of empirical group contribution method," *Microporous Mesoporous Mater.*, vol. 217, pp. 1–5, 2015.

[152] Y. Ming, J. Purewal, D. Liu, A. Sudik, C. Xu, J. Yang, M. Veenstra, K. Rhodes, R. Soltis, J. Warner, M. Gaab, U. Müller, and D. J. Siegel, "Thermophysical properties of MOF-5 powders," *Microporous Mesoporous Mater.*, vol. 185, pp. 235–244, 2014.

[153] A. Lamaire, J. Wieme, S. M. J. Rogge, M. Waroquier, and V. Van Speybroeck, "On the importance of anharmonicities and nuclear quantum effects in modelling the structural properties and thermal expansion of MOF-5," *J. Chem. Phys.*, vol. 150, no. 9, p. 094503, 2019.

[154] J. Wieme, *Advanced molecular simulations to computationally model phase stability and thermal properties of metal-organic frameworks*. PhD thesis, 2019.

[155] J. R. Cendagorta, H. Shen, Z. Bačić, and M. E. Tuckerman, "Enhanced Sampling Path Integral Methods Using Neural Network Potential Energy Surfaces with Application to Diffusion in Hydrogen Hydrates," *Adv. Theory Simul.*, vol. 4, no. 4, p. 2000258, 2021.

[156] K. P. Bishop and P.-N. Roy, "Quantum mechanical free energy profiles with post-quantization restraints: Binding free energy of the water dimer over a broad range of temperatures," *J. Chem. Phys.*, vol. 148, no. 10, p. 102303, 2018.

[157] M. Bocus, R. Goeminne, A. Lamaire, M. Cools-Ceuppens, T. Verstraelen, and V. Van Speybroeck, "Nuclear quantum effects on zeolite proton hopping kinetics explored with machine learning potentials and path integral molecular dynamics," *Nat. Commun.*, vol. 14, p. 1008, 2023.

[158] M. Bocus, S. E. Neale, P. Cnudde, and V. Van Speybroeck, "6.08 - dynamic evolution of catalytic active sites within zeolite catalysis," in *Comprehensive Inorganic Chemistry III (Third Edition)*, pp. 165–200, Oxford: Elsevier, 2023.

[159] Y. Zhang and W. Yang, "Comment on "generalized gradient approximation made simple"," *Phys. Rev. Lett.*, vol. 80, pp. 890–890, 1998.

[160] K. Yang, J. Zheng, Y. Zhao, and D. G. Truhlar, "Tests of the RPBE, revPBE, τ-HCTHhyb, ωB97X-D, and MOHLYP density functional approximations and 29 others against representative databases for diverse bond energies and barrier heights in catalysis," *J. Chem. Phys.*, vol. 132, no. 16, p. 164117, 2010.

[161] R. Collepardo-Guevara, I. R. Craig, and D. E. Manolopoulos, "Proton transfer in a polar solvent from ring polymer reaction rate theory," *J. Chem. Phys.*, vol. 128, no. 14, p. 144502, 2008.

[162] R. P. Feynman, *The Character of Physical Law*. The M.I.T. Press, 1965.

[163] G. Yilmaz, F. L. Meng, W. Lu, J. Abed, C. K. N. Peh, M. Gao, E. H. Sargent, and G. W. Ho, "Autonomous atmospheric water seeping MOF matrix," *Sci. Adv.*, vol. 6, no. 42, p. eabc8605, 2020.

[164] R. J. Drout, L. Robison, Z. Chen, T. Islamoglu, and O. K. Farha, "Zirconium Metal-Organic Frameworks for Organic Pollutant Adsorption," *Trends in Chemistry*, vol. 1, no. 3, pp. 304–317, 2019.

[165] S. Rojas and P. Horcajada, "Metal-Organic Frameworks for the Removal of Emerging Organic Contaminants in Water," *Chem. Rev.*, vol. 120, no. 16, pp. 8378–8415, 2020.

[166] B.-M. Jun, Y. A. Al-Hamadani, A. Son, C. M. Park, M. Jang, A. Jang, N. C. Kim, and Y. Yoon, "Applications of metal-organic framework based membranes in water purification: A review," *Sep. Purif. Technol.*, vol. 247, p. 116947, 2020.

[167] Y. Sun, S. M. J. Rogge, A. Lamaire, S. Vandenbrande, J. Wieme, C. R. Siviour, V. Van Speybroeck, and J.-C. Tan, "High-rate nanofluidic energy absorption in porous zeolitic frameworks," *Nat. Mater.*, vol. 20, no. 7, pp. 1015–1023, 2021.

[168] J. Canivet, A. Fateeva, Y. Guo, B. Coasne, and D. Farrusseng, "Water adsorption in MOFs: fundamentals and applications," *Chem. Soc. Rev.*, vol. 43, pp. 5594–5617, 2014.

[169] S. Wang, J. S. Lee, M. Wahiduzzaman, J. Park, M. Muschi, C. Martineau-Corcos, A. Tissot, K. H. Cho, J. Marrot, W. Shepard, G. Maurin, J.-S. Chang, and C. Serre, "A robust large-pore zirconium carboxylate metal–organic framework for energy-efficient water-sorption-driven refrigeration," *Nat. Energy*, vol. 3, no. 11, pp. 985–993, 2018.

[170] D. Lenzen, J. Zhao, S.-J. Ernst, M. Wahiduzzaman, A. Ken Inge, D. Fröhlich, H. Xu, H.-J. Bart, C. Janiak, S. Henninger, G. Maurin, X. Zou, and N. Stock, "A metal–organic framework for efficient water-based ultra-low-temperature-driven cooling," *Nat. Commun.*, vol. 10, p. 3025, 2019.

[171] B. Zhang, Z. Zhu, X. Wang, X. Liu, and F. Kapteijn, "Water Adsorption in MOFs: Structures and Applications," *Adv. Func. Mater.*, vol. n/a, no. n/a, p. 2304788, 2024.

[172] K. Koga, G. T. Gao, H. Tanaka, and X. C. Zeng, "Formation of ordered ice nanotubes inside carbon nanotubes," *Nature*, vol. 412, no. 6849, pp. 802–805, 2001.

[173] D. Takaiwa, I. Hatano, K. Koga, and H. Tanaka, "Phase diagram of water in carbon nanotubes," *Proc. Natl. Acad. Sci.*, vol. 105, no. 1, pp. 39–43, 2008.

[174] G. Algara-Siller, O. Lehtinen, F. C. Wang, R. R. Nair, U. Kaiser, H. A. Wu, A. K. Geim, and I. V. Grigorieva, "Square ice in graphene nanocapillaries," *Nature*, vol. 519, no. 7544, pp. 443–445, 2015.

[175] V. Kapil, C. Schran, A. Zen, J. Chen, C. J. Pickard, and A. Michaelides, "The first-principles phase diagram of monolayer nanoconfined water," *Nature*, 2022.

[176] T. Ichii, T. Arikawa, K. Omoto, N. Hosono, H. Sato, S. Kitagawa, and K. Tanaka, "Observation of an exotic state of water in the hydrophilic nanospace of porous coordination polymers," *Commun. Chem.*, vol. 3, no. 1, p. 16, 2020.

[177] M. A. van der Veen, S. Canossa, M. Wahiduzzaman, G. Nenert, D. Frohlich, D. Rega, H. Reinsch, L. Shupletsov, K. Markey, D. E. De Vos, M. Bonn, N. Stock, G. Maurin, and E. H. G. Backus, "Confined Water Cluster Formation in Water Harvesting by Metal-Organic Frameworks: CAU-10-H versus CAU-10-CH_3," *Adv. Mater.*, vol. 36, no. 12, p. 2210050, 2024.

[178] N. Hanikel, X. Pei, S. Chheda, H. Lyu, W. Jeong, J. Sauer, L. Gagliardi, and O. M. Yaghi, "Evolution of water structures in metal-organic frameworks for improved atmospheric water harvesting," *Science*, vol. 374, no. 6566, pp. 454–459, 2021.

[179] H. Furukawa, F. Gándara, Y.-B. Zhang, J. Jiang, W. L. Queen, M. R. Hudson, and O. M. Yaghi, "Water Adsorption in Porous Metal-Organic Frameworks and Related Materials," *J. Am. Chem. Soc.*, vol. 136, no. 11, pp. 4369–4381, 2014.

[180] A. Fuchs, F. Knechtel, H. Wang, Z. Ji, S. Wuttke, O. M. Yaghi, and E. Ploetz, "Water Harvesting at the Single-Crystal Level," *J. Am. Chem. Soc.*, vol. 145, no. 26, pp. 14324–14334, 2023.

[181] K. Yanagita, J. Hwang, J. A. Shamim, W.-L. Hsu, R. Matsuda, A. Endo, J.-J. Delaunay, and H. Daiguji, "Kinetics of Water Vapor Adsorption and Desorption in MIL-101 Metal-Organic Frameworks," *J. Phys. Chem. C*, vol. 123, no. 1, pp. 387–398, 2019.

[182] A. J. Rieth, K. M. Hunter, M. Dincă, and F. Paesani, "Hydrogen bonding structure of confined water templated by a metal-organic framework with open metal sites," *Nat. Commun.*, vol. 10, p. 4771, 2019.

[183] A. Lamaire, J. Wieme, A. E. J. Hoffman, and V. Van Speybroeck, "Atomistic insight in the flexibility and heat transport properties of the stimuli-responsive metal–organic framework MIL-53(Al) for water-adsorption applications using molecular simulations," *Faraday Discuss.*, vol. 225, pp. 301–323, 2021.

[184] N. Guillou, F. Millange, and R. I. Walton, "Rapid and reversible formation of a crystalline hydrate of a metal-organic framework containing a tube of hydrogen-bonded water," *Chem. Commun.*, vol. 47, pp. 713–715, 2011.

[185] F. Paesani, "Water in metal-organic frameworks: structure and diffusion of H_2O in MIL-53(Cr) from quantum simulations," *Mol. Simul.*, vol. 38, no. 8-9, pp. 631–641, 2012.

[186] Z. Zheng, N. Hanikel, H. Lyu, and O. M. Yaghi, "Broadly tunable atmospheric water harvesting in multivariate metal–organic frameworks," *J. Am. Chem. Soc.*, vol. 144, no. 49, pp. 22669–22675, 2022.

[187] F.-F. Lu, X.-W. Gu, E. Wu, B. Li, and G. Qian, "Systematic evaluation of water adsorption in isoreticular UiO-type metal-organic frameworks," *J. Mater. Chem. A*, vol. 11, pp. 1246–1255, 2023.

[188] J. Zhang, F. Paesani, and M. Lessio, "Computational insights into the interaction of water with the UiO-66 metal–organic framework and its functionalized derivatives," *J. Mater. Chem. C*, vol. 11, pp. 10247–10258, 2023.

[189] E. C. Clough, T. A. Plaisted, Z. C. Eckel, K. Cante, J. M. Hundley, and T. A. Schaedler, "Elastomeric Microlattice Impact Attenuators," *Matter*, vol. 1, no. 6, pp. 1519–1531, 2019.

[190] A. Phan, C. J. Doonan, F. J. Uribe-Romo, C. B. Knobler, M. O'Keeffe, and O. M. Yaghi, "Synthesis, Structure, and Carbon Dioxide Capture Properties of Zeolitic Imidazolate Frameworks," *Acc. Chem. Res.*, vol. 43, no. 1, pp. 58–67, 2010.

[191] A. M. Turing, "I.—COMPUTING MACHINERY AND INTELLIGENCE," *Mind*, vol. LIX, no. 236, pp. 433–460, 1950.

[192] E. Brémond, M. Savarese, N. Rega, I. Ciofini, and C. Adamo, "Free Energy Profiles of Proton Transfer Reactions: Density Functional Benchmark from Biased Ab Initio Dynamics," *J. Chem. Theory Comput.*, vol. 18, no. 3, pp. 1501–1511, 2022.

[193] J. Daru, H. Forbert, J. Behler, and D. Marx, "Coupled Cluster Molecular Dynamics of Condensed Phase Systems Enabled by Machine Learning Potentials: Liquid Water Benchmark," *Phys. Rev. Lett.*, vol. 129, p. 226001, 2022.

[194] T. D. Kühne, M. Iannuzzi, M. Del Ben, V. V. Rybkin, P. Seewald, F. Stein, T. Laino, R. Z. Khaliullin, O. Schütt, F. Schiffmann, D. Golze, J. Wilhelm, S. Chulkov, M. H. Bani-Hashemian, V. Weber, U. Borštnik, M. Taillefumier, A. S. Jakobovits, A. Lazzaro, H. Pabst, T. Müller, R. Schade, M. Guidon, S. Andermatt, N. Holmberg, G. K. Schenter, A. Hehn, A. Bussy, F. Belleflamme, G. Tabacchi, A. Glöß, M. Lass, I. Bethune, C. J. Mundy, C. Plessl, M. Watkins, J. VandeVondele, M. Krack, and J. Hutter, "CP2K: An electronic structure and molecular dynamics software package - Quickstep: Efficient and accurate electronic structure calculations," *J. Chem. Phys.*, vol. 152, no. 19, p. 194103, 2020.

[195] M. Ceriotti, J. More, and D. E. Manolopoulos, "i-PI: A Python interface for ab initio path integral molecular dynamics simulations," *Comput. Phys. Commun.*, vol. 185, no. 3, pp. 1019–1026, 2014.

[196] V. Kapil, M. Rossi, O. Marsalek, R. Petraglia, Y. Litman, T. Spura, B. Cheng, A. Cuzzocrea, R. H. Meißner, D. M. Wilkins, P. Juda, S. P. Bienvenue, W. Fang, J. Kessler, I. Poltavsky, S. Vandenbrande, J. Wieme, C. Corminboeuf, T. D. Kühne, D. E. Manolopoulos, T. E. Markland, J. O. Richardson, A. Tkatchenko, G. A. Tribello, V. Van Speybroeck, and M. Ceriotti, "i-PI 2.0: A universal force engine for advanced molecular simulations," *Comput. Phys. Commun.*, vol. 236, pp. 214–223, 2018.

[197] Y. Litman, V. Kapil, Y. M. Y. Feldman, D. Tisi, T. Begušić, K. Fidanyan, G. Fraux, J. Higer, M. Kellner, T. E. Li, E. S. Pós, E. Stocco, G. Trenins, B. Hirshberg, M. Rossi, and M. Ceriotti, "i-PI 3.0: A flexible and efficient framework for advanced atomistic simulations," *J. Chem. Phys.*, vol. 161, no. 6, p. 062504, 2024.

[198] S. Plimpton, "Fast Parallel Algorithms for Short-Range Molecular Dynamics," *J. Comput. Phys.*, vol. 117, no. 1, pp. 1–19, 1995.

[199] A. P. Thompson, H. M. Aktulga, R. Berger, D. S. Bolintineanu, W. M. Brown, P. S. Crozier, P. J. in 't Veld, A. Kohlmeyer, S. G. Moore, T. D. Nguyen, R. Shan, M. J. Stevens, J. Tranchida, C. Trott, and S. J. Plimpton, "LAMMPS - a flexible simulation tool for particle-based materials modeling at the atomic, meso, and continuum scales," *Comp. Phys. Comm.*, vol. 271, p. 108171, 2022.

[200] M. Bonomi, D. Branduardi, G. Bussi, C. Camilloni, D. Provasi, P. Raiteri, D. Donadio, F. Marinelli, F. Pietrucci, R. A. Broglia, and M. Parrinello, "PLUMED: A portable plugin for free-energy calculations with molecular dynamics," *Comput. Phys. Commun.*, vol. 180, no. 10, pp. 1961–1972, 2009.

[201] G. A. Tribello, M. Bonomi, D. Branduardi, C. Camilloni, and G. Bussi, "PLUMED 2: New feathers for an old bird," *Comput. Phys. Commun.*, vol. 185, no. 2, pp. 604–613, 2014.

[202] M. Bonomi, G. Bussi, C. Camilloni, G. A. Tribello, P. Banáš, A. Barducci, M. Bernetti, P. G. Bolhuis, S. Bottaro, D. Branduardi, R. Capelli, P. Carloni, M. Ceriotti, A. Cesari, H. Chen, W. Chen, F. Colizzi, S. De, M. De La Pierre, D. Donadio, V. Drobot, B. Ensing, A. L. Ferguson, M. Filizola, J. S. Fraser, H. Fu, P. Gasparotto, F. L. Gervasio, F. Giberti, A. Gil-Ley, T. Giorgino, G. T. Heller, G. M. Hocky, M. Iannuzzi, M. Invernizzi, K. E. Jelfs, A. Jussupow, E. Kirilin, A. Laio, V. Limongelli, K. Lindorff-Larsen, T. Löhr, F. Marinelli, L. Martin-Samos, M. Masetti, R. Meyer, A. Michaelides, C. Molteni, T. Morishita, M. Nava, C. Paissoni, E. Papaleo, M. Parrinello, J. Pfaendtner, P. Piaggi, G. Piccini, A. Pietropaolo, F. Pietrucci, S. Pipolo, D. Provasi, D. Quigley, P. Raiteri, S. Raniolo, J. Rydzewski, M. Salvalaglio, G. C. Sosso, V. Spiwok, J. Šponer, D. W. H. Swenson, P. Tiwary, O. Valsson, M. Vendruscolo, G. A. Voth, A. White, and T. P. consortium, "Promoting transparency and reproducibility in enhanced molecular simulations," *Nat. Methods*, vol. 16, no. 8, pp. 670–673, 2019.

[203] D. G. A. Smith, L. A. Burns, A. C. Simmonett, R. M. Parrish, M. C. Schieber, R. Galvelis, P. Kraus, H. Kruse, R. Di Remigio, A. Alenaizan, A. M. James, S. Lehtola, J. P. Misiewicz, M. Scheurer, R. A. Shaw, J. B. Schriber, Y. Xie, Z. L. Glick, D. A. Sirianni, J. S. O'Brien, J. M. Waldrop, A. Kumar, E. G. Hohenstein, B. P. Pritchard, B. R. Brooks, H. F. Schaefer, A. Y. Sokolov, K. Patkowski, A. E. DePrince, U. Bozkaya, R. A. King, F. A. Evangelista, J. M. Turney, T. D. Crawford, and C. D. Sherrill, "Psi4 1.4: Open-source software for high-throughput quantum chemistry," *J. Chem. Phys.*, vol. 152, no. 18, p. 184108, 2020.

[204] D. Dubbeldam, S. Calero, D. E. Ellis, and R. Q. Snurr, "RASPA: molecular simulation software for adsorption and diffusion in flexible nanoporous materials," *Mol. Simulat.*, vol. 42, no. 2, pp. 81–101, 2016.

This research was supported by the Research Foundation Flanders (FWO) through a personal mandate (Grant Nos. 11D2218N and 11D2220N) and a Flanders Industry Innovation Moonshot (ARCLATH II, No. HBC.2021.0254).

The computational resources (Stevin Supercomputer Infrastructure) and services used in this work were provided by the VSC (Flemish Supercomputer Center), funded by Ghent University, FWO, and the Flemish Government – department EWI.